Use of a Novel Bioreactor Configuration in the Form of High Solid Digestion for Municipal Organic Wastes at Pilot Scale

Kubra Arslan[1],Tugba Keskin Gundogdu[1], Duygu KaraalpYavuzyılmaz [1], Nuri Azbar[1]*

Abstract

The objective of this study was to investigate the performance and process stability of a novel dry anaerobic digestion system. For this purpose, a solid state anaerobic digester (100 L) with percolation system (200 L) was designed at pilot scale. Municipal solid wastes were fed into the dry fermentation unit and system was operated with intermittent recycling of leachate through percolation unit back to the dry fermentation unit twice a day. Gas production in both unit was recorded daily and gas content and leachate analysis were carried out twice a week. A batch feeding of solid waste (17.5 kg waste) having less than 5 cm particle size with a dry matter of 13% and organic dry matter of 85% was carried out and process was operated for 60 days. Results indicated that 560 L methane per kg organic dry matter was produced. This corresponds to biogas production 119 m^3 per ton of wet solid waste. It was also observed that the main gas production took place in percolation tank and the solid digester acted as a hydrolysis and acid reactor indicated by the low gas production and acidic leachate characteristics. There were also almost no digestate generation which eliminates costly post treatment units before the discharge of digestate, which is a critical problem for wet digestion counterpart.

Keywords: *Anaerobic digestion, high solid fermentation, municipal solid waste*

1. INTRODUCTION

Industrialization and rapid urbanization has increased significantly the generation of municipal solid wastes (MSW) and as in many developing countries it is a big environmental problem for Turkey. In 2014, MSW generation rate was 1.08 kg/cap.day, 28 million tons of MSW generated, and this waste was landfilled either in sanitary landfills (63.6%) or dumpsites (35.5%), composted (4%) and disposed with other ways (5%) [1]. Typical MSW composition in Turkey contains high biodegradable organic fraction (40-75%) as it can be seen in Table 1 [2]. On the other hand, MSW management has been a pressure point for Turkey while being a candidate country for EU accession and EU 27 targets .In order to decrease the amount of organic biodegradable waste sent to landfill sites and to set up a waste management system, most of the EU waste management directives have been transposed into Turkey's national legislation. Therefore the reduction of biodegradable waste amounts which is landfilled and proper treatment of MSW is an important task for Turkey [3].

Table 1.Composition of MSW in Turkey

Components	Range in weight (%)
Organics	40-65
Paper/cardboard	7-18
Plastics	5-14
Metal	1-6
Glass	2-6
Others	7-24

Anaerobic digestion (AD) is a promising solution as it is a biological treatment capable to decompose the organic matter under oxygen free conditions [4]. Furthermore, the end product of AD includes biogas (60–70% methane) which is a renewable energy resources, and the effluent which is an organic residue rich in nitrogen can be used as soil conditioner or fertilizer [5,6].

[1] *Ege University, Graduate School of Natural And Applied Science, Environmental Sciences Departmant, İzmir, Turkey,* arslankubra03@gmail.com

AD process is based on four steps: hydrolysis, acidogenesis, acetogenesis and methanogenesis [7] and can be classified based on operating parameters and reactor design [4]. Depending on the total solid (TS) concentration of the feedstock the AD process can be divided into wet (<10% TS) and dry (10% TS) digestion processes [8].

Compared to wet digestion, dry digestion, also known as ‘‘high-solid’’ anaerobic processes [8] is advantageous in terms of smaller reactor volume, lower energy consumption for heating, higher volumetric methane productivity [6], less wastewater generation, low-moisture digestate that is easier to handle and lower total energy loss [4]. However, in dry digestion due to the contact between microorganism and feedstock is poor the biogas yield is generally low and there is a high tendency to inhibition caused by accumulation of ammonia and volatile fatty acids (VFAs) [9]. The digestate or leachate of dry AD can be recycled to inoculate the fresh feedstock on the purpose of improving the biogas yield [10]. Systems that recycle leachate into the reactor vessel are called percolation systems. Leachate recycling approach provides a good transportation for microorganism throughout the digester and prevent the inhibition caused by accumulation of VFAs and ammonia [4].

The objectives of this study was to investigate the process performance and stability of a novel anaerobic digester configuration which employs dry fermentation of municipal solid wastes.

2. MATERIALS AND METHODS

2.1. Feedstock and Inoculum

MSW were obtained from Izmir Metropolitan City, Solid Waste Management Department in Izmir, Turkey and it mainly consisted of seasonal vegetable and fruits. The wastes were whittled to have a particle size around 5 cm before filled in reactor. Representative samples of MSW (small pieces taken from each fruit and vegetable) were crushed using an electrical blender and used to perform analytical analysis. Anaerobic inoculum was taken from an up-flow anaerobic sludge blanket (UASB) reactor fed with wastewater of a beer factory located in Izmir.

2.2. Process Description

The process consists of a batch dry anaerobic reactor with 100 L total volume and a percolation tank with 200 L total volume. Inside the reactor there was a stainless steel basket which has holes at the bottom and the side and keeps the solid material inside reactor. On the top of the reactor the inoculum-percolate distribution device which is basically a perforated plate was placed and allowed the distribution of percolate over the feedstock. The temperature and humidity probe were also set on the top of the reactor.

In the beginning of the study the percolation tank was filled with the liquid anaerobic inoculum equipped with an agitator and a pump. Once a day this liquid inoculum was sprayed over the feedstock in the dry digester, passed through the substrate stack and reached into the percolation tank from the pipeline which is placed between the bottom of the dry digester and percolation tank (leachate circulation line). A sampling point was located on the leachate circulation line, every 2 or 3 days, samples from leachate were taken from this line and analyzed for VFA and total ammonia nitrogen (TAN).

The percolation tank and digester were heated by hot water circulation through the heating pipe installed inside the tanks to keep the temperature at 37 °C and isolated for heat preservation. Biogas production was measured by a drum type gas meter for both dry digester and percolation tank, and biogas sampling was done from the line between reactor and gas meter.

2.3. Analytical Methods

VS and TS contents were analyzed according to the APHA Standard Methods for the Examination of Water and Wastewater. TAN was determined using a colorimetric method with an ammonia nitrogen kit, and a spectrophotometer. VFAs in the AD leachate were measured using a gas chromatography (GC). Leachate samples were centrifuged then supernatant was filtered through 0,45 µm nylon syringe filter for GC analysis. The volume of biogas was measured by a drum type gas meter (Ritter, Germany) and the composition of biogas (H_2, CH_4 and CO_2) was analyzed by Agilent gas chromatograph equipped with a flame ionization detector and a DB-FFAP 30 m × 0.32 mm × 0.25 mm capillary column.

3. RESULTS AND DISCUSSION

3.1. Characteristics of MSW

The characteristics of MSW used in this study are shown in Table 2. As the content of MSW varied depending on different seasons, in summer MSW consist of mostly juicy fruits and vegetables therefore TS of the MSW used in this study was 13%, and VS was 85% of TS respectively.

Table 2.Characteristics of MSW

Parameters	MSW
TS (%)	13
VS (%TS)	85
NH_4^+-N(g/L)	0.1
pH	4.55

3.2. Biogas and Methane Production

The chemical characteristics of inoculum inside the percolation tank were measured in the beginning of the study. TS and VS of the inoculum was about 3% and 77% (of TS), respectively. Another pH probe was set on the spray pipeline which shows the pH trend of the inoculum. During the study the pH value of the inoculum was very stable and ranged from 7.4 to 7.8 this proves the methanogenic activity was dominant in the percolation tank during the experiment.
Daily biogas production and methane content in biogas at percolation tank and digester are shown in Fig. 2. The start-up of the process followed different trend in percolation tank and digester. During first four days while big amounts of biogas was produced in percolation tank there was no biogas production in dry digester. The total biogas produced in percolation tank for first four days was 880 L which is the 50% of the total biogas production value reached after 60 days. It is reported that the fruit and vegetable waste has a big part of easily digestible fraction, which might produce excessive VFAs at the beginning of the dry digestion [11]. This soluble VFA leached from dry digester washed into the percolation tank and digested to biogas which might be the reason of high amount of biogas production in percolation tank in the first four days. However, the biogas production of the percolation tank decreased to a stable level after 10 days and after 40 days the biogas production progressively decreased and reached values around 5-3.

Fig. 2 shows that a lag phase of 4 days occurred at dry digester. The degradation rate of the feedstock depends on the maximum contact between the substrate and microorganism which is mainly carried out by high mechanical agitation in the liquid digester [11]. On the other hand, this contact was achieved by recycling the microorganism in percolation tank back onto the feedstock in the dry digester. It is reported that the percolate recirculation at a high flow rate allowed accelerating the solid–liquid mass transfer and increase the biogas production dramatically. It is also shown that increasing the percolate recirculation rate in intermittent and short recirculation operations improves the stability and speed of the dry anaerobic digestion[12].

Afterward the biogas production of the dry digester increased and reached to a stable level and the digester showed a steady biogas production for 40 days.

In percolation tank the methane content in the biogas was between 55-60% during the experiment as it is shown in Fig. 2. In dry digester methane content in the biogas was 15% in the beginning of the experiment, from the start-up the methane content in the biogas progressively increased and reached values around 45%.

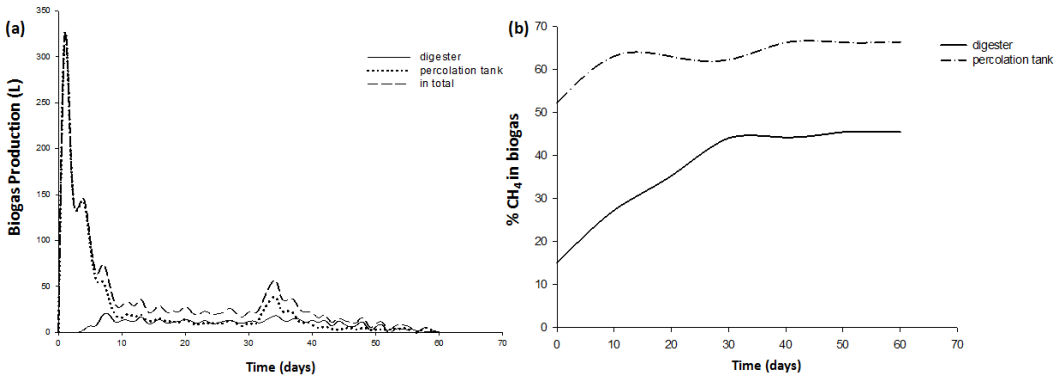

Figure 2. Daily biogas production and methane content of biogas: (a) Daily biogas production of percolation tank, digester and in total; (b) Methane content of the biogas in percolation tank and digester

The biogas and methane production of dry digester and percolation tank is shown in Table 3. Dry digester and percolate tank totally produced biogas of 2095 L, of which 550 L of biogas produced from dry digester, and 1545 L of biogas produced from the percolate tank which is the 75% of total biogas production.

Table 3. Biogas and methane production of percolation tank and digester

	Biogas production (L)	**CH_4 production (L)**
Percolation Tank	1545	210
Digester	550	875
Total	2095	1085

These results indicated that a big amount of VFAs produced in dry digester and with the recirculation of percolate they washed into the percolation tank and converted to biogas . During the first 40 days, the process was separated into two-phase system of hydrolysis and acetogenesis in dry digester and methanogenesis in percolation tank. However, with recirculation of percolate the methanogens was irrigated into the digester and biogas and methane was produced both in percolation tank and dry digester. Depending on biogas and methane production values the AD efficiency of the percolation tank was much higher than dry digester. Some studies also reported the same results that two-phase dry AD has advantages of more stable processing ([11], [12]).

The specific biogas and methane yields reached after 60 days were 1085 L biogas kg^{-1} VS and 560 L CH_4 kg^{-1} VS, respectively.

It is reported that the biogas yield of fruit and vegetable wastes varied from 650-700 L biogas kg^{-1} VS depending on different TS values [13]. It is also investigated that the methane yield of different content of solid organic wastes varied from 200-850 L CH_4 kg^{-1} VS [14]. Compared with literatures, the results showed that biogas yield in this experiment much more higher than literature values, methane yield was in an avarage range.

3.3. Leachate Analysis

Every 2 or 3 days samples from leachate were taken from the circulation pipeline and analyzed for VFA and total ammonia nitrogen (TAN) to follow the stability of the dry digestion process. Also a pH probe was placed in the circulation pipeline and pH changes are followed. Fig 3 shows the pH and VFA trends of the leachate.

The pH values of the leachate as can be seen in Fig.3b was around 4 in the beginning of the experiment hence the high VFA concentrations in leachate. Afterward the pH value of leachate reached 5.5 in following four days and remained around 5.5-6.0 between days 4 and 30. The optimum pH of hydrolysis and acidogenesis has been reported as being between 5.5-6.0 and the optimum pH of methanogenesis is over 7.0 [15]. During the first 30 days of experiment pH of leachate stayed under 7.0. As can be observed in Fig 2b methane content in the biogas in dry digester also stayed under %40. This proves that during first 30 days while hydrolysis and acetogenesis occurred in dry digester methanogenesis occurred in percolation tank. However, for the rest of experiment pH of leachate stayed over 7 and also methane content in the biogas in dry digester remained over 45%.

VFAs namely, acetic acid, propionic acid, butyric acid, isobutyric acid, valeric acid and isovaleric acid are intermediates of anaerobic digestion and are produced during the hydrolysis and acidogenesis steps[15]. During the AD the process efficiency may affect due to the inhibition caused by VFA or ammonia accumulation. As can be observed in Fig 3a during first 30 days a sharp increase occurred in butyric acid with a maximum concentration of 20,000 mg L^{-1} then two other peak in butyric acid occurred on day 15 and 25 with the concentration of 25,000 mg L^{-1} and 20,000 mg L^{-1}, respectively. Due to the high concentration of butyric acid methanogenic activity in the dry digester might be inhibited and resulted with the low methane content of the biogas in dry digester.

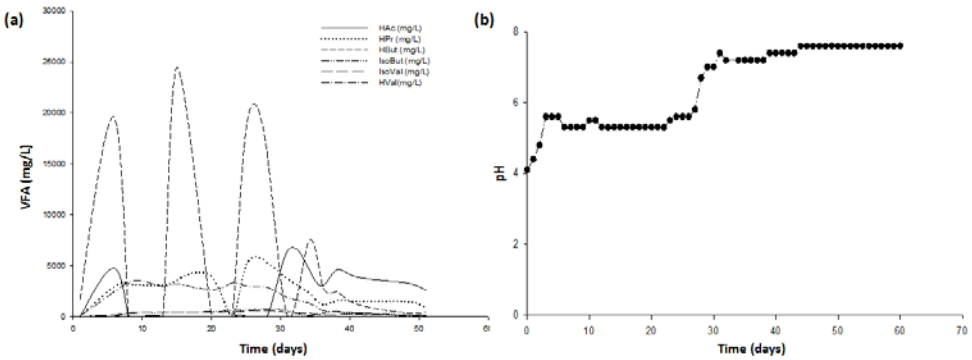

Figure 3. (a)VFAs in leachate ;(b) pH in leachate

The TAN concentration of the leachate is shown in Fig. 4. During the experiment TAN concentration remained under 150 mg/L which is reasonable for the AD process stability. It is reported that anaerobic microorganisms need nitrogen as an essential nutrient and TAN concentrations below 200 mg/L are considered to be advantageous while concentrations over 1500

mg/L can be inhibitory [12]. As it can be seen in Fig. 4 TAN concentrations stayed between beneficial range and no inhibition effect caused by ammonia accumulation occurred during the study.

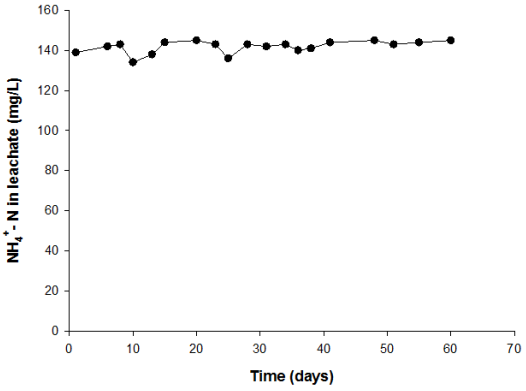

Figure 4. TAN concentration in leachate

4. CONCLUSIONS

The objective of this study was to investigate the performance and process stability of a novel dry anaerobic digestion system and has demonstrated that the system is technically feasible for high solid anaerobic digestion of MSW.

The results also showed that the main gas production took place in percolation tank and the solid digester acted as a hydrolysis and acid reactor indicated by the low gas production and acidic leachate characteristics.

The main advantage of this system is that there was also almost no digestate generation which eliminates costly post treatment units before the discharge of digestate, which is a critical problem for wet digestion systems all over the world.

ACKNOWLEDGMENT

The authors wish to thank Scientific and Technological Research Council of Turkey (TUBITAK) - CAYDAG under the grant No 113Y534 and COST for the financial support of this study. The data presented in this article was produced within the project above, however it is only the authors of this article who are responsible for the results and discussions made herein. The authors would also thank to Izmir Metropolitan Municipality and General Directory of IZSU for their supports.

REFERENCES

[1]. (2016) The TurkStat website. [Online]. Available: http://www.tuik.gov.tr/
[2]. N. G. Turan, S. Çoruh, A. Akdemir, O. N. Ergun, "Municipal solid waste management strategies in Turkey", *Waste Management*, vol. 29, pp. 465-469, 2009.
[3]. I. Bakas, L. Milios, " Municipal waste management in Turkey" , European Environment Agency, 2013
[4]. Y. Li, S. Y. Park, J. Zhu, "Solid-state anaerobic digestion for methane production from organic waste," *Renewable and Sustainable Energy Reviews*, vol. 15, pp. 821-826, 2011
[5]. I. M. Nasir, T. I. M. Ghazi, R. Omar, "Production of biogas from solid organic wastes through anaerobic digestion: a review,"*Appl Microbiol Biotechnol*, vol. 95, pp. 321-329, 2012
[6]. T. Yang, Y. Li, J. Gao, C. Huang, B. Chen, L. Zhang, X. Wang, Y. Zhao, B. Xi, X. Li, "Performance of dry anaerobic technology in the co-digestion of rural organic solid wastes in China," *Energy*, vol. 93, pp. 2497-2502, 2015.
[7]. J. Fernández-Rodríguez, M. Pérez, L.I. Romero, "Dry thermophilic anaerobic digestion of the organic fraction of municipal solid wastes: Solid retention time optimization," *Chemical Engineering Journal*, vol. 251, pp. 435-440, 2014.
[8]. S. K. Cho, W. T. Im, D. H. Kim, M. H. Kim, H. S. Shin, S. E. Oh, " Dry anaerobic digestion of food waste under meshophilic conditions: Performance and methanogenic community analysis," *Bioresource Technology*, vol. 131, pp. 210-217, 2013.
[9]. X. Ge, F. Xu, Y. Li, "Solid-state anaerobic digestion of lignocellulosic biomass: Recent progress and perspectives," *Bioresource Technlogy*, vol. , pp. 239-249, 2016.
[10]. J. Zhu, Y. Zheng, F. Xu, Y. Li, "Solid-state anaerobic co-digestion of hay and soybean processing waste for biogas production", *Bioresource Technlogy*, vol. 154, pp. 240-247, 2014.
[11]. M.Y. Qian, R. H. Li, J. Li, H. Wedwitschka, M. Nelles, W. Stinner, H.J. Zhou, "Industrial scale garage-type dry fermentation of municipal solid waste to biogas," *Bioresource Technology*, in press, 2016.
[12]. C. Rico, J. A. Montes, N. Munoz, J. L. Rico, "Thermophilic anaerobic digestion of the screened solid fraction of dairy manure in a solid-phase percolating reactor system," *Journal of Cleaner Production*, vol. 102, pp. 512- 520, 2015.
[13]. D. Y. C. Leung, J. Wang, "An overwiev on biogas generation from anaerobic digestion of food waste," *International Journal of Green Energy*, vol. 13:2, pp.119-131, 2016
[14]. A. Khalid, M. Arshad, M. Anjum, T. Mahmood, L. Dawson, "The anaerobic digestion of solid organic waste," *Waste Management*, vol. 31, pp. 1737-1744, 2011.
[15]. D. J. Lee, S. Y. Lee, J. s. Bae, J. G. Kang, K. H. Kim, S. S. Rhee, J. H. Park, J. S. Cho, J. Chung, D. C. Seo, " Effet of volatile fatty acid concentration on anaerobic degredation rate from field anaerobic digestion facilities treating food waste leachate in South Korea, " *Journal of Chemistry*, vol. 2015, 2015

BIOGRAPHY

Kubra Arslan was graduated from Ege University, Bioengineering Department in 2014. She has been doing her MSc degree at Ege University, Environmental Sciences Department. She is currently working under a project which is supported by TUBITAK. Her research interest focuses on environmental biotechnology, solid-state anaerobic digestion, biogas production.

Analysis of Temperature Distribution Between Tool and Workpiece in AISI304L Drilling Operations with Finite Element Method

Engin Unal[1]

Abstract

This study focuses on the drilling of AISI 304L stainless steel by using different parameters namely, drill point angle, rotational speed, and drill feed rate. Drilling temperature was used to evaluate the machinability. In order to minimize the problem of drill bit damage such as tool wear in the drilling operations, it is necessary to operate with optimum drilling parameters. In this paper, the drilling process parameters have been studied by finite element method with ANSYS software. The maximum drill temperatures were observed in the group of large drill point angles. On the other hand, the minimum temperatures were observed at the higher feed rate levels. As a result, it can be evaluated that the minimum drill bit tip angle, maximum feed rate and minimum rotational speed conditions were found the best choice for the minimum temperature in drilling of AISI 304L steel.

Keywords: *AISI 304L, ANSYS, Drill tip angle, Drilling Temperature, Finite Element Analysis.*

1.INTRODUCTION

The most significant and irreplaceable aspect of machining sector are the cutting tools. Cutting tools are used in all areas of manufacturing sector and they have a direct effect on manufacturing cost and production speed. Developments in machining manufacture, increase of cutting and feed rates, utilization of different materials for the manufacture and the development of machine tools have caused the improvement of cutting tools. Today, the cutting features of HSS tools are significantly improved. The perfect combinations of alloy elements and heat treatments have provided the perfect hardness, fine satiety and also characteristics of abrasion resistance to this material. As a result of technological developments, HSS tools manufactured as coated and by powder metallurgy, are intensely used [1].

Machinability plays an important role in the evaluation of cutting tools' performances. Quality of the machined surface, heat during the cutting, abrasion of tools and type of chips are among the parameters of machinability.

The mechanism of chip generation is a very complicated and multi-disciplinary (thermodynamic, plasticity, heat transfer) subject. Therefore, it is sometimes not possible to experimentally measure each parameter that occurs during cutting. The method of finite elements in particular is a frequently used numerical analysis method to assume various data during cutting (Speed of shape shifting, tool strain, tool-chip contact length and heat distribution in the tool). But, to obtain more realistic results closer with experimental data from the finite elements solution depends on the model of material used and having closer friction conditions with the friction conditions under cutting conditions [2]. When the studies on this subject are generally evaluated, it is seen that the cutting transaction from Johnson-Cook material model is used more properly in simulations [3-5]. Because Johnson-Cook material model can analytically state the material behavior under high shape shifting speeds and temperatures [6, 7].

This study examines the cutting parameters on tool strains, temperature in tool-chip interface and temperature distribution on tools. Therefore, HSS twist drills were used and drilling transactions were modeled under orthogonal conditions. The model results were agreement with the literature.

2.MATERIAL AND METHOD

In this study, the temperature of drill bit was analyzed using ANSYS/Workbench software for validation purpose. In drilling simulations, a cylindrical workpiece 20mm in diameter and 10mm length was used. Drill diameter was 11mm (Figure 1). The workpiece and drill bit material properties from the software material library was chosen particularly (Table 1).

[1] *Mechanical Engineering Department, Faculty of Technology, Firat University 23119 Elazig, Turkey enginunal@firat.edu.tr*

Table 1. Properties of AISI304L material

Property	Value	Unit
Density	7896	kg/m^3
Young's Modulus	193000	MPa
Poisson's Ratio	0,31	
Bulk Modulus	169298	MPa
Shear Modulus	77000	MPa
Yield Strength	210	MPa
Tangent Modulus	1800	MPa
Specific Heat	423	$J\ kg^{-1}C^{-1}$
Melting Temperature T_{melt}	2106,85	C
Initial Yield Stress Y	340	MPa
Maximum Yield Stress Y_{max}	2500	MPa
Hardening Constant	430	MPa
Hardening Exponent n	0,35	

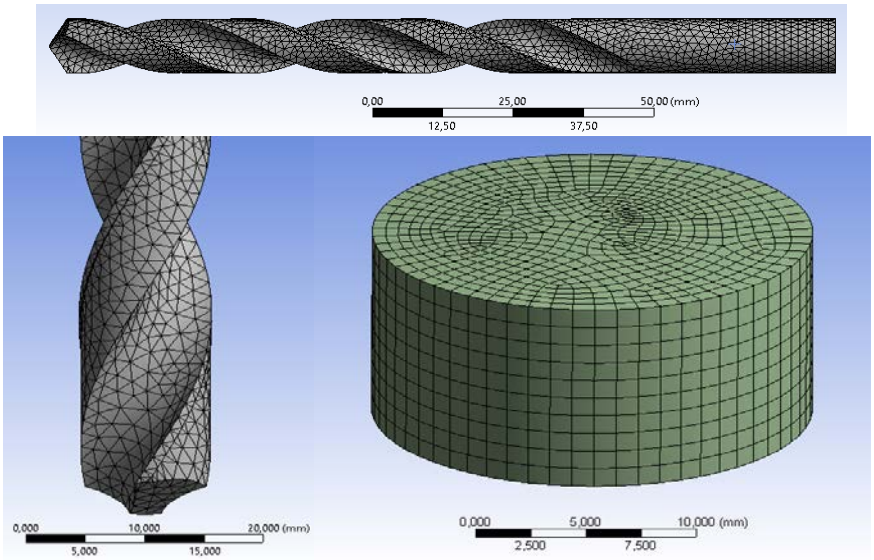

Figure 1. The mesh models of the workpiece and drill bit.

The ANSYS analyses were performed on the standard PC which has Intel Core 2 Duo 2800Mhz CPU, 4GB Ram and 2GB graphic processor. Calculations were performed using the explicit finite element code where the internal forces were balanced with the external forces through an iterative procedure, which gave the deformed state after a time increment. One of the advantage of this method is that the time increment can be relatively large because of conditional stability of the explicit time integrator and static solutions can be obtained by natural characteristics of the method. To solve the Explicit Dynamics iterations, the time step was controlled by ANSYS 15 automatic incrementation technique. The drill and work piece model consisted of 10116 nodes, 15604 elements and the analysis took more than 183 Minutes on Intel Core 2 Duo CPU time T9600 @ 2.80 GHz machine. The number of cycle used in computations was 247229, and double precision executable was used in the analysis. The drilling parameters used in the analyses are tabulated in Table 2, and modelling of the workpiece and drill bit is presented in Figure 2.

Table 2. Drilling Operations Parameters

Property	Values
Rotational Speed (rpm)	367 – 500 – 567
Feed Rate (mm/min.)	72 – 120 – 168
Drill Point Angle (°)	112 – 118 – 124 – 130 – 136

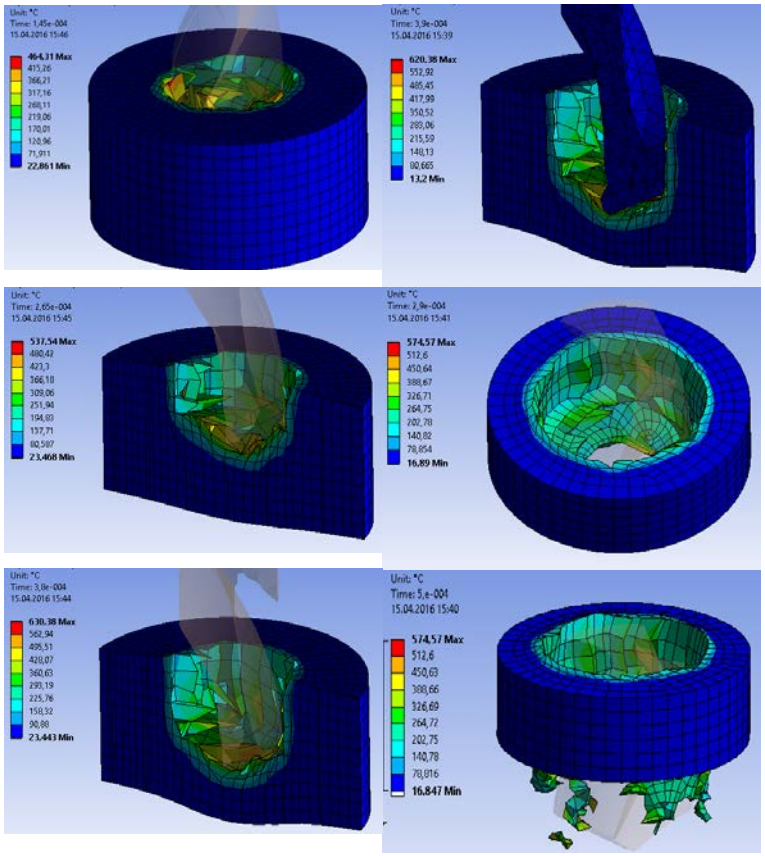

Figure 2. The modelling of workpiece and drill point.

3.RESULTS AND DISCUSSION

3.1.Effect of Cutting Speed on Temperature

Thermal features during metal cutting are important for tool life and abrasion. High temperatures during cutting, affect the tools and work piece surface quality. Temperature generated as a result of mechanic forces is dependent on cutting conditions. The cutting speed, feed rate, tool chip and relief angle should be refrained which might cause thermal load on tools. As a result of friction; heat is generated at the primary shear zone and tool chip interface and as a result of this, tool abrasion increases and its life time decreases [8]. One of the most important parameter temperature on the during cutting is the cutting speed. Change of tool temperature by cutting speed is indicated in Figure 3.

As seen from this figure, the temperature is tendency of increase with cutting speed at the constant feed rate and tool point angle levels. The max. temperature was calculated as 719°C. As it is known, cutting speed and change of temperature are directly proportional. As cutting speed increases, so does the temperature [9]. Because, the speed of material plastic deformation and tool – chip contact length and friction increase in the first deformation zone, depending on the increasing cutting speed. High plastic deformation speed causes the generation of high temperature during metal cutting and the temperature increases [9].

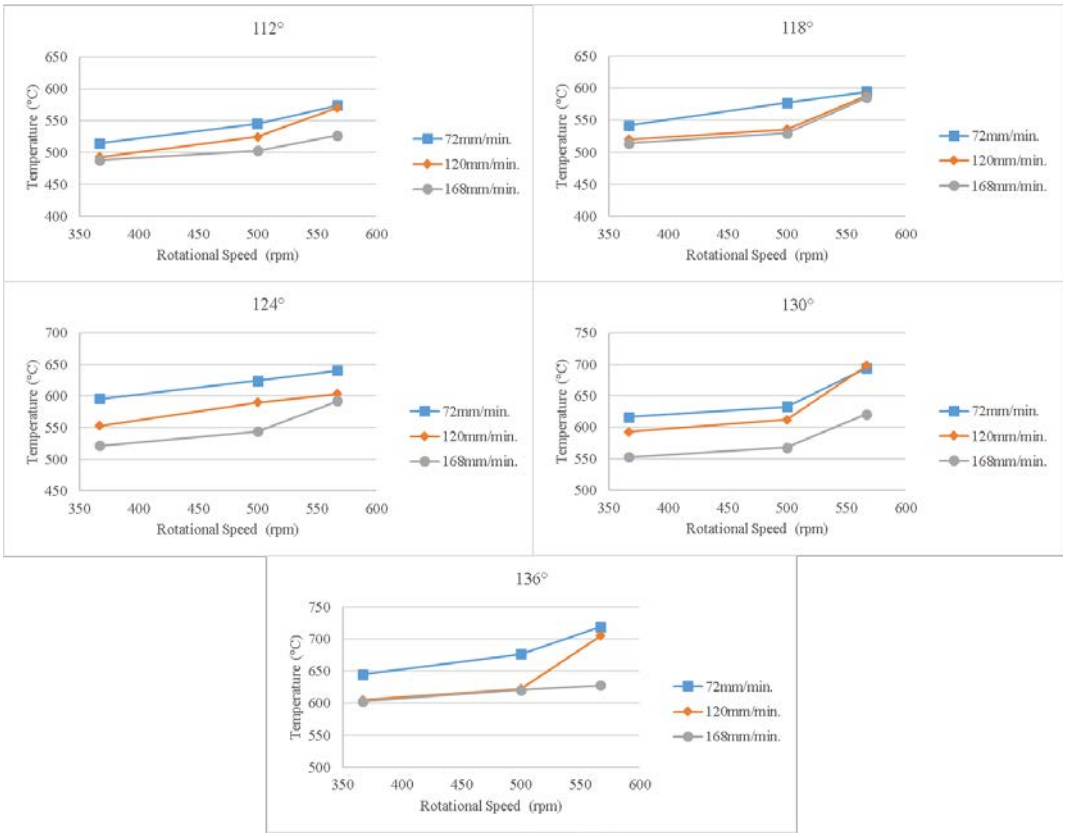

Figure 3. The temperature variations via rotational speed.

3.2.Effect of Feed Rate on Temperature

Figure 4 shows the effect of feed rate on the workpiece temperature. As seen from this figure, a slightly decrease in temperature was observed between 112 - 124° point angle levels and this tendency of decrease become sharpener at 130 - 136° especially at after 120 mm/min. The heat energy generated from frictional in the tool-chip contact interface was carried away with increasing feed rate [9]. Therefore, increasing feed rate leads to decrease in drill bit temperature due to higher material removal rates [10].

3.3.Effect of Drill Point Angle on Temperature

Change of temperature depending on drill end angle is indicated in Figure 3 and 4. It is observed in all analysis results that the generated temperature increases if the drill point does. When the figures are examined, it is seen that 136° point drill has a maximum temperature of 719°C. When all the figures are evaluated, it is observed that as drill end angle increases; temperature also tends to increase. Increasing end angle causes more friction on drilling surface and ends up with temperature increase. A similar case was observed in the study of Karaca et.al. [11]; and as the increasing point has decreased the cutting end of drill; more force was required in order to cut the material. Therefore, higher drill point angles have caused the generation of higher temperatures.

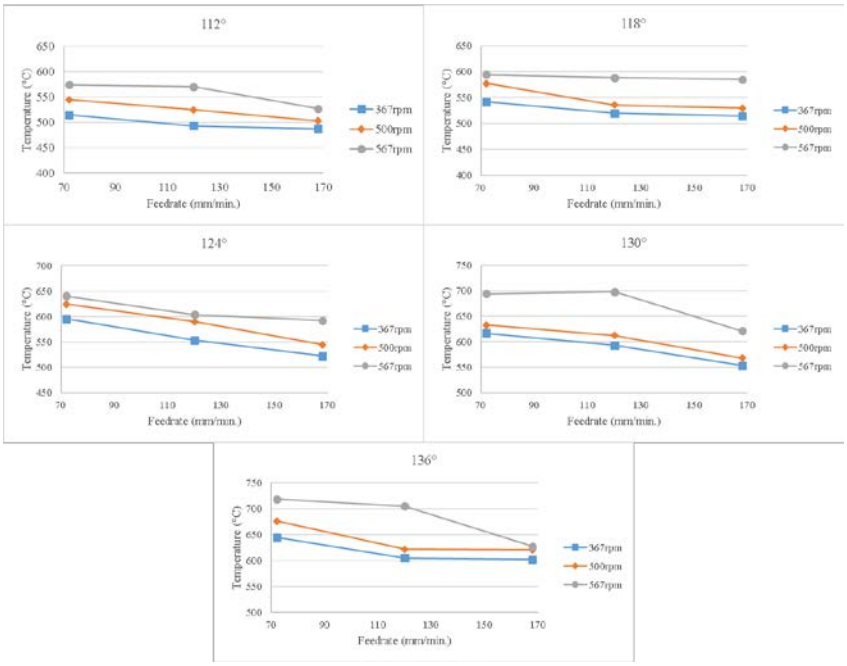

Figure 4. The temperature variations via feedrate.

4.CONCLUSION

- As the cutting speed increased, so did the generated temperature.
- As the feedrate increased, the generated temperature decreased.
- As the drill end increased, temperature increased too.
- It has been seen that cutting speed was the most important parameter for the increase of temperature.
- It has also been seen that feedrate did not have too much effect on the temperature change of selected values.
- The effect of drill end angle on temperature was obviously seen only at bigger values.

REFERENCES

[1]. F.J. Da silva, D.D. Franco, A.R. Machado, E.O. Ezugwu, and A.M. Souza Jr., "Performance of cryogenically treated HSS tools," *Wear.*, vol. 261,pp. 674-685, 2006.
[2]. T. Altan, I. Al-Zkeri, and P. Sartkulvanich, "Process Modeling of High Speed Cutting Using 2D-FEM," *Proceedings of the NIST-Machining Conference*, Washington, DC. 2007
[3]. A. P. Markopoulos, N. M. Vaxevanidis, and D. E. Manolakos. "Friction and Material Modelling in Finite Element Simulation of Orthogonal Cutting," *Tribology in Industry* vol. 37, pp. 440-448, 2015.
[4]. P.J. Arrazola,T. Özel, "Investigations on The Effects of Friction Modeling in Finite Element Simulation of Machining," *International Journal of Mechanical Sciences*, Vol. 52, pp. 31-42, 2010.
[5]. T. Ozel, E. Zeren, "Determination of Work Material Flow Stress and Friction for FEA Of Machining Using Orthogonal Cutting Tests," *Journal of Materials Processing Technology*, vol. 153-154, pp. 1019-1025, 2004.
[6]. H. Bil, S.E. Kılıç, and A.E. Tekkaya, "A comparison of orthogonal cutting data from experiments with three different finite element models," *International Journal of Machine Tools and Manufacture*, vol. 44, pp. 933-944, 2004.
[7]. S. Szabó and J. Kundrák, "Investigation of residual stresses in case of hard turning of case hardened 16MnCr5 Steel," *Key Engineering Materials*, vol. 581, pp. 501-504, 2014.
[8]. H. M. Şahin, and A. Acır, "Analysis of temperature distribution between tool and chip in metal cutting operations by using finite difference method", *Journal of Polytechnic*, vol. 6, pp. 541-549, 2003.
[9]. İ. Ucun, K. Aslantaş, and D. Apaydın, "Finite Element Modelling of Turning Process Using Cutting Tool with Multilayer Coatings", *Electronic Jornal of Machine Technologies*, vol. 7, pp. 69 – 82, 2010.

[10]. S. Sezek, B. Aksakal, and F. Karaca, "Ortopedik Operasyonlardaki Kemik Delme İşlemlerindeSıcaklık Dağılım Analizleri", *6th International Advanced Technologies Symposium (IATS'11)*,16 – 18 May 2011, Elazığ, Türkiye.
[11]. F.Karaca, B.Aksakal, M. Kom, "Influence of orthopaedic drilling parameters on temperature and histopathology of bovine tibia: An in vitro study", *Medical Engineering & Physics*, vol. 33, pp. 1221-1227, 2011.

Smart Cleaner Implementation for Solar Photovoltaic Panels

Mustafa Yagci[1], Serafettin Erel[2], Muciz Ozcan[1]

Abstract

Depending on the weather conditions, on the outside of the glass material of the photovoltaic (PV) panels where sunlight passes through, forms unwanted contamination with the time. This contamination occurred on the solar panels, blocks and prevents the essential sunlight passing through the glass material. This causes to the power output and efficiency reduction of the panels since the electricity production on the panels is closely related to the solar radiation. In this study, design and implementation of a mechanism which detects and cleans the possible contamination on the glass material of the photovoltaic panels was performed. To verify, the panel surface was contaminated artificially and after the determined dusting value is reached, the implemented mechanism starts to clean the undesired contamination. Consequently it was observed that, the former output values of the solar panels were achieved for the required electricity production after the cleaning process of the panels.

Keywords: *Efficiency, electricity production, solar panel, surface cleaning,*

1.INTRODUCTION

In recent years, the use of the photovoltaic (PV) systems has been expanded throughout the world. With the increasing use of the PV systems, the term of efficiency has become very important. Most of the applied solar panels output efficiency is between %15-%20 due to their semiconductor material characteristics. Besides, the installation design of the PV system such as orientation angle, optimum tilt angle and sun trackers are other important factors for the efficiency of the PV panels. On the other hand there are negative factors like dusting, bird droppings or water stains on the surface of solar cells that considered insignificant but effect in a negative way on the efficiency. It is a fact that PV efficiency decreases between %10-%25 due to the dusty solar panels, contaminated inverters or conductor materials [1].

There are many literature researches about this subject as follows: The low efficiency and high cost of the solar panels are the main factors for preventing the utilization of the PV systems in developing countries [2].

Besides the solar radiation, one of the most effective parameter related to the solar panel efficiency is dusting on the surfaces [3-4]. There are researches related to the effect of dust with different physical properties on the performance of photovoltaic cells, climate effects such as air pollution, raining intensity, humidity etc.[5-10]. With the increasing of the PV systems utilization on the flat roofs in many cities, scientists have been studying these parameters effects on the solar panel efficiency [11]. There are other scientists that investigate the effect of wind velocity and airborne dust concentration on the drop of photovoltaic (PV) cell performance caused by dust accumulation on such cells [12]. The solar panel tilting regarding the output efficiency has been compared for the same conditions [13]. In another study, solar panel surfaces were contaminated with different sand materials. After that the output power and efficiency were measured. It was observed that according to the materials on the solar surfaces the output power and efficiency were decreased [14-15]. 5 Solar panels were contaminated artificially. For two months it has been observed the output power and efficiency. When the dusty accumulation reaches 1 g/m^2 on the solar panel surface, the efficiency was decreased about % 6,5 [16]. In a study, the effect of the air pollution on the solar panel efficiency was observed. The efficiency reduction was changed between %33,5 and %65,8 for the 6 months period. It was recommended that the solar panel surfaces should be cleaned every week [17]. In the other study, the effect of the shading was reviewed. Shading is a big problem in PV modules since shading only one cell in the module can reduce the power output. The output of a cell declines when shaded by a tree branch, building or other objects. The output declines proportionally to the amount of shading [18]. Dust, humidity and wind speed affect the output power of the solar panels [19-20].

In this paper, design and implementation of a mechanism which detects and cleans the possible contamination on the surface of the photovoltaic panels was realized. To verify this, the panel surface was contaminated artificially and this has shown to result in the performance decrease of photovoltaic cells. After the threshold value is reached, the implemented mechanism cleans the dusting materials. It was found that the cleaning process has helped to increase the panel efficiency eminently for the electricity production.

2.MATERİAL AND METHOD

With the time on the glass material of the solar panels which protects the semiconductor material contained within the solar cells against external atmospheric effects forms contamination. This contamination prevents the necessary sunlight passes through the transparent part of the module. Since the performance of the solar panels is extremely related to the solar radiation, this causes to the decreasing of the generated DC (direct current) power and total efficiency of the solar panels. In order to prevent this, design and implementation of a controlled mechanism which automatically detects and eliminates the formed contamination on the solar panels was done. The implemented mechanism is mounted on the solar panels and the required energy for the operation of this mechanism is provided by the solar panel which is shown in Figure 1.

Figure 1. The implemented mechanism is mounted on the solar panel

Therefore there was no need for an extra power source. The most important part of this mechanism is the applied optical sensor which detects the possible contamination on the solar panels. This optical sensor is shown in Figure 2.

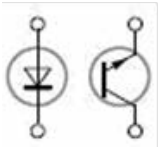

Figure 2. Electrical symbol of the optical sensor

Technical parameters of the optical sensor are:

- Sensing range: 2-9 mm.
- Supply power: 5VDC
- It can be used to sense the color of the line or to detect the possible obstacles.
- Output power 0-5 V.
- Sizes: 21mm x 11mm x 8mm.

The size of the applied optical sensor is suitable to mount inside the solar panels. The optical sensor consists of the infrared LED emitter and a couple of receiver that operate within the infrared spectrum. Dependent on the light which falls on the sensor kit, the output of the optical sensor varies between 0 and 5V. The block diagram of the implemented mechanism is shown in Figure 3. Operation of the system is explained briefly as follows:

With the help of the optical sensor mounted inside the solar panel, the light density can be detected. When the density of the light passing through the solar panels is under the determined value detected by the optical sensor, the mechanism starts to clean the surfaces of the dirty parts of the solar panels with the help of a wiper and water pump. This surface cleaning process is terminated with the related information obtained from the optical sensor.

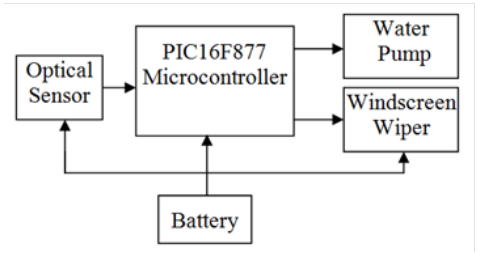

Figure 3. The block diagram of the circuit detecting solar panel contamination

The technical parameters of the applied solar panel used in this study are given in Table 1.Table 1. Parameters of the applied solar panel

Parameters	Values
Solar Cell Type Mono	125x125
Rated power (Pmpp)	50 W
Rated current (Impp)	2.64 A
Rated voltage (Vmpp)	47
Short circuit current (Isc)	19 V
Open circuit voltage (Voc)	2.96 A
Max. system voltage (V)	22.6 V

3. RESULTS AND DISCUSSION

For the tests of the smart surface cleaner are different soil and sand material used. The initial voltage and power values of the applied solar panel were measured and then solar surfaces were contaminated artificially. After the artificial contamination of the solar panel surfaces, the final voltage and power values were measured and compared to the initial values. The soil and sand material for the artificial contamination are filtered through a special sieve with 0,0631 mm. radius for getting all the materials in the same size. Before the artificial contamination, the solar panel surfaces were moistened with water equally in order to keep the soil and sand material on the surface. After that, the panel surfaces were contaminated dimensionally accurate as 1 gr to the 1 square meter and the test results were observed. Before the artificial contamination of the panels, the expected voltage and power values were registered. After the artificial contamination of the panels, the designed and implemented mechanism was detected the contamination and cleaned the surface. As a result the expected voltage and power values were obtained as before. With the help of this implemented mechanism the electricity generation capacity of the solar panels was not changed negatively depending on the external air conditions.

4. CONCLUSION

According to the performed test results, open circuit voltage value is different before and after the smart cleaner mechanism applied on the solar panels. The initial voltage values were achieved when the smart cleaner detects and eliminates the contamination on the solar panels. This implemented mechanism does not work periodically; it only works when the solar panels are not clean enough as it should be normally. If necessary, it should operate several times a day to get the clean surfaces. In this way, solar panels will be clean and uncontaminated regardless of the human control throughout the day. This will increase directly the annual amount of electricity generation capacity from the solar panels.

ACKNOWLEDGEMENT

This study was supported by Necmettin Erbakan University Scientific Research Projects Office.

REFERENCES

[1]. Lund PD, “Exploring past energy changes and their implications for the pace of penetration of new energy technologies,” Energy, vol. 35, pp. 647-656, 2010.
[2]. Johansson TB, Kelly H, Reddy AKN, Williams RH. Renewable energy-sources for fuels and electricity, 1st ed. Washington: Island Press, 1992.
[3]. Thevenard D. “Review and recommendations for improving the modeling of building integrated photovoltaic systems,” In: Proc. IBPSA’9 Conference, 2005, p. 112
[4]. El-Shobokshy MS, Hussein FM, “Effect of dust with different physical properties on the performance of photovoltaic cells,” Solar Energy, vol.51(6), pp.505-511,1993.

[5]. Tian W, Wang Y, Ren J, Zhu L, "Effect of urban climate on building integrated photovoltaics performance," Energy Conversion and Management, vol.48(1), pp.1-8, 2007.
[6]. Soleimani EA, Farhangi S, Zabihi MS, "The effect of tilt angle, air pollution on performance of photovoltaic systems in Tehran," Renewable Energy, vol.24, p.459-68, 2001.
[7]. Kappos L, Ntouros I, Palivos I. "Pollution effect on PV system efficiency," In Proc. 5th National Conference on Soft Energy Forms, 1996, Athens; Greek
[8]. Biryukov S, Faiman D, Goldfeld A, "An optical system for the quantitative study of particulate contamination on solar collector surfaces," Solar Energy, vol.66(5),pp.371-8, 1999.
[9]. Al-Hasan Ahmat Y, Ghoneim Adel A, "A new correlation between photovoltaic panel's efficiency and amount of sand dust accumulated on their surface," Sustainable Energy; vol.24(4),pp.187 -97, 2005.
[10]. Goossens D, Van Kerschaever E, "Aeolıan Dust Deposıtıon On Photovoltaıc Solar Cells: The Effects Of Wınd Velocıty And Aırborne Dust Concentratıon On Cell Performance," Solar Energy, vol.66(4),pp. 277–289,1999.
[11]. Kaldellis JK, Fragos P, Kapsali M, "Systematic experimental study of the pollution deposition impact on the energy yield of photovoltaic installations," Renewable Energy, vol.36(10),pp. 2717- 2724, 2011.
[12]. Nahar N. and Gupta J, "Effect of dust on transmittance of glazing materials for solar collectors under arid zone conditions of India," Solar and Wind Technology,vol. 7, pp. 237–243, 1990.
[13]. J.K. Kaldellis , P. Fragos, "Ash deposition impact on the energy performance of photovoltaic generators, "Journal of Cleaner Production" vol.19, pp. 311-317, 2011.
[14]. J.K. Kaldellis , A . Kokala, "Quantifying the decrease of the photovoltaic panels ' energy yield due to phenomena of natural air pollution disposal," Energy,vol. 35 pp.4862-4869, 2010 .
[15]. Hassan A, Rahoma U, Elminir H, Fathy A, " Effect of airborne dust concentration on the performance of PV modules" Journal of the Astronomical Society of Egypt, vol. 13,pp.24–38. 2005.
[16]. Elminir HK, Ghitas AE, Hamid RH, El-Hussainy F, Beheary MM, Abdel-Moneim KM, "Effect of dust on the transparent cover of solar collectors," Energy Conversion and Management,vol. 47(18),pp.3192–203, 2006.
[17]. A Ibrahim, "Effect of Shadow and Dust on the Performance of Silicon Solar Cell," Journal of Basic and Applied Scientific Research, vol.1(3), pp.222-230, 2011.
[18]. S Mekhilef , R Saidur , M Kamalisarvestani, "Effect of dust, humidity and air velocity on efficiency of photovoltaic cells," Renewable and Sustainable Energy Reviews, vol. 16,pp. 2920– 2925, 2012.
[19]. El-Nashar AM, "Effect of dust deposition on the performance of a solar desalination plant operating in arid desert area," Solar Energy, vol. 75,pp. 421-431, 2003.
[20]. Endiz, M. S., Erel, and S., Yagcı, M, "Comparative Study of Single Phase Power Inverters Based on Efficiency and Harmonic Analysis" i-manager's Journal on Instrumentation & Control Engineering, Vol. 4 pp. 1-9, November 2015.

The Effect of Resin Paper Coating on Some Particleboard Properties

Abdullah Istek[1], Ismail Ozlusoylu[1], Ufuk Aydın[2]

Abstract

In this study, the effects of resin impregnated decor paper and the lamination conditions on physical and mechanical properties of particleboard were thoroughly investigated. For coating material, 50% melamine and 50% urea formaldehyde resin were used in impregnation process of décor papers. The density of the boards were 630 kg/m3 and the lamination conditions were as follows; 30 kg/cm2 pressure, 180oC for 24 seconds, 200oC for 19 seconds and 205oC for 18 seconds as press temperatures and times. According to the results, coating with décor paper increased the bending strength and modulus of elasticity between 10 to 19%. However, internal bonding strength was decreased by 10 to 20%, and screw withdrawal by 1 to 4% and surface soundness by 1-9%. On the other hand, it was determined that water uptake and thickness swelling was improved by 5 to15%. It is stated that, pressure and heat application during the coating process is higher than the board production values and this affects the board properties negatively except bending strength and modulus of elasticity.

Keywords: *Décor paper, lamination, particleboard, mechanical properties, bending strength.*

1.INTRODUCTION

Wood composite panels are affected by biotic and abiotic factors at their utilization area. In order to reduce the damage caused by these factors, wood based panels are coated by solid and liquid overlaying materials depending on service conditions. Particleboard surface quality is an important physical property influencing different processes, including their finishing. Although particleboard panels are used for interior applications, their hygroscopic nature plays an important role on their performance due to long-term changes in relative humidity ([1], [2], [3]).

Decor paper is a special high-quality paper that is bonded to suitable substrates such as wood based panels using special synthetic resins. Papers impregnated with a resin have gained wide acceptance as facing materials for industrial grade particleboard. The base papers for the decorative films are alpha-cellulose papers, which are used exclusively. For impregnating, papers must have a high moisture resistance and the right porosity to accept the proper amount of resin. The surface print quality of the decor paper is essential for creating decorative designs by use of gravure printing process. Also, the paper shall be suitable for impregnation with applicable synthetic resins such as urea formaldehyde, melamine formaldehyde, acrylic and phenolic resins. The type of resin used for impregnation of decor paper influences the quality of substrate after the lamination. It is laminated under high pressure and heat with particleboard or other substrates. Quality of cauls, cleanliness, and temperature are key factors that influence coating or laminating quality ([4], [5], [6]).

According to Nemli et al. [7], coated panel surfaces exhibit improved physical and mechanical properties with a decreased formaldehyde emission of particleboard. İstek et al. [6] also stated that some physical and mechanical properties were significantly improved after the lamination process. It was reported in another study that the varnish type plays a very important role in the end use applications [8]. Bardak et al. [9] investigated the effect of décor paper properties and resin type on the particleboard properties. They found that the bending strength and modulus of elasticity values were improved with increasing paper grammage.

The objective of this study was to determine the effects of resin impregnated decor paper lamination conditions on some of the physical and mechanical properties of particleboard.

2.MATERIALS and METHODS

Laminated and un-laminated particleboards used in this study were produced in Kastamonu Integrated Forest Industry Inc. (Turkey). Three-layered particleboard panels were manufactured by using 40% softwood and 60% hardwood. Maximum press temperature, press time and pressure were used as 175 ^{0}C, 190 sec. and 28 kg/cm^2 for all particleboard (PB) manufacture, respectively. PBs were produced at the 630 kg/m3 density as P2 type [10]. PBs were laminated with resin impregnated décor papers. Base décor papers were impregnated with 50% urea formaldehyde and 50% melamine formaldehyde. Base decor paper at 90 g/m^2 was used as coating paper.

The conditions for the lamination process were as follows: press temperature 180-200-205 °C, pressure 30 kg/cm^2, and press time 24-19-18sec. These operations were carried out in a commercial plant production line. Thirty samples were prepared for each test to determine the physical and mechanical properties. Each test sample was conditioned at 20±2 °C and 65±5 relative

[1] *Corresponding author: Bartin University, Department of Forest Industry Engineering, 74100, Bartin, Turkey.* aistek@bartin.edu.tr

[2] *Kastamonu Integrated Wood Industry, Kastamonu, Turkey*

humidity for 2 weeks according to TS 642 (1997) [11] before testing. Lamination and particleboard production conditions are shown in Table 1.

Table 1. Particleboard production and lamination parameters

Board type	Lamination parameters		
	Pressure (kg/cm2)	**Temperature (°C)**	**Duration (sec.)**
L-PB 1	30	180	24
L-PB 2	30	200	19
L-PB 3	30	205	18
	Production parameters		
	Pressure (kg/cm2)	**Temperature (°C)**	**Duration (sec.)**
C-PB (Unlaminated Control Particle Board)	28	175	190

Physical and mechanical properties of un-laminated particleboard (C-PB) and laminated particleboard (L-PB) were determined according to relevant standards. Namely, test specimens and their dimensions were prepared in accordance with TS EN 325 (1999) [12] and TS EN 326-1 (1999) [13]. Physical properties of laminated particleboard such as water absorption (WA) (TS EN 317, 1999) [14], thickness swelling (TS) (TS EN 317, 1999), and from the mechanical properties such as modulus of elasticity in bending (MOE) (TS EN 310, 1999), bending strength (BS) (TS EN 310, 1999) [15], and internal bonding strength (IB) (TS EN 319, 1999) [16], screw withdrawal resistance (SW) (TS EN 320, 2011) [17] surface soundness (SS) (TS EN 311, 1999) [18] were tested. Data obtained in physical and mechanical tests were statistically analyzed, and ANOVA was performed ($p<0.05$) to determine the significance of differences among factors. Results were assessed by a DUNCAN test of whether there is a meaningful difference among the groups.

3. RESULTS AND DISCUSSION

The tests were carried out to evaluate the influence of lamination conditions on the physical and mechanical properties of PBs. The average values, standard deviation, and variation coefficient of some properties of PBs are given in Table 2.

Table 2. The Influence of lamination conditions on some properties of PB.

Properties	C-PB (Un-laminated)	(L-PB) Lamination conditions		
		L-PB1 (180 °C for 24 sec.)	**L-PB2 (200 °C for 19 sec.)**	**L-PB3 (205 °C for 18 sec.)**
Density (kg/m^3)	635±13 (a)	653±18 (b)	654±10 (b)	643±14 (a)
Thickness swelling (%)	14,92±1,49 (a)	12,71±0,41 (b)	12,56±0,79 (b)	12,64±0,58 (b)
Water absorption (%)	77,14±1,55 (a)	71,26±1,41 (b)	70,84±3,58 (b)	72,13±2,52 (b)
Internal bonding strength (N/mm^2)	0,52±0,04 (a)	0,46±0,05 (b)	0,46±0,04 (b)	0,43±0,04 (c)
Bending strength (N/mm^2)	13,45±0,85 (a)	15,66±1,19 (b)	15,38±1,75 (b)	14,89±0,43 (b)

Modulus of elasticity in bending (N/mm^2)	2614±152 (a)	3110±192 (c)	3118±220 (c)	2953±198 (b)
Surface soundness (N/mm^2)	1,20±0,08 (a)	1,12±0,12 (b)	1,19±0,09 (a)	1,08±0,13 (b)
Screw withdrawal (N)	753±29 (a)	750±65 (a)	741±48 (a)	722±52(a)

Means followed with the same letters a,b,c in the same row are not significantly ($p<0.05$) different.

As can be seen in Table 2 some of the physical and mechanical properties of the PBs changed after lamination process. The TS and WA values (2-h) were improved by lamination. The relationship between lamination and TS or WA were found statistically significant. However, these changes were not found to be associated with lamination duration and temperature. The results of the present study are in agreement with the results of a previous study on particleboards laminated with veneer Buyuksari, [19] in which TS and WA values decreased after lamination process. Figure 1 shows the changes in TS and WA values after submerging the test samples in water for a period of 2hours.

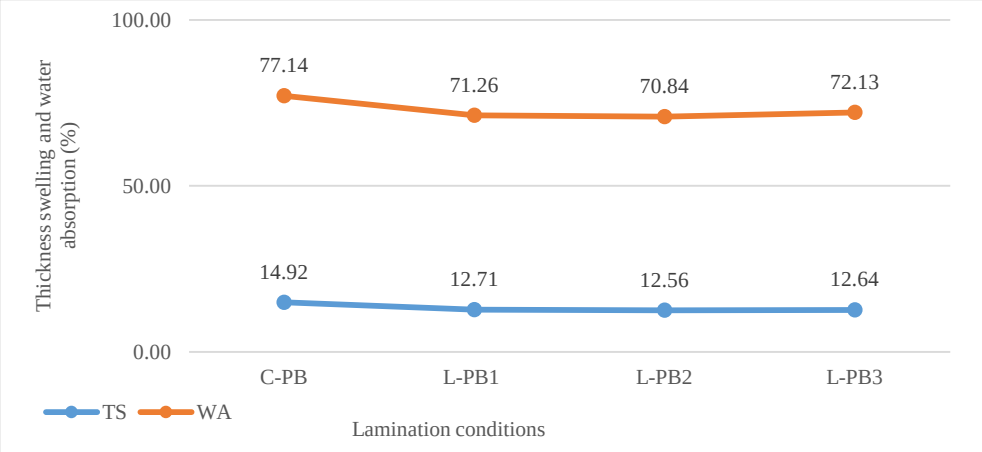

Figure 1. Thickness swelling and water absorption

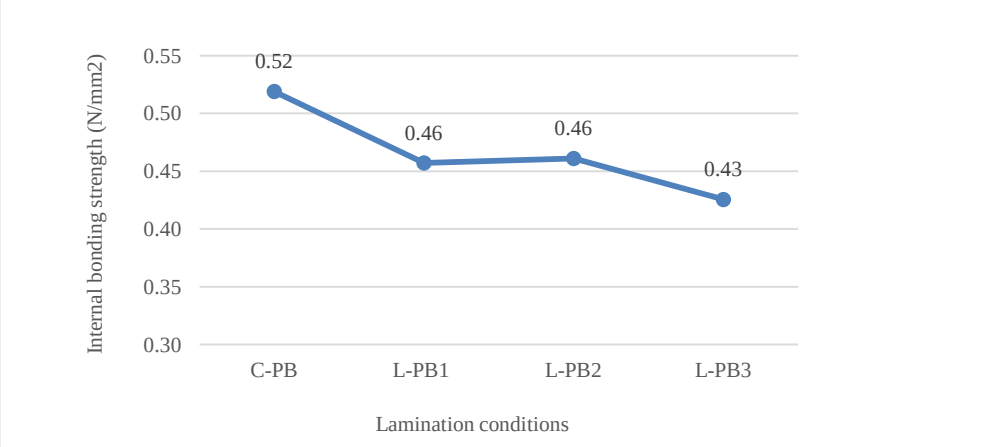

Figure 2. Internal bonding strength (N/mm2)

As shown in figure 2, IB strength of the laminated boards significantly decreased at 95 % confidence level. The lowest IB value was obtained as 0.43 N/mm2 in the L-PB3. The highest IB was found to be 0.52 N/mm2 in the control panel. The rates of decrease in IB strength were found to range from %11.53 to %17.30. The decrease in IB strength is attributed to the increase in press temperature and decrease in the press duration. High press temperatures during lamination process can lead to pyrolysis and de-condensation of the urea formaldehyde which is used as binder in the boards. In this study, the pressures were selected as 28 kg/cm2 in the board production and 30 kg/cm2 in the lamination. When lamination pressure is higher than the board production pressure, the IB strength is negatively affected. Hence, bonding among the chips is reduced and IB strength is decreased. Consequently, production conditions used in the lamination process should be in line with the board production conditions. The change in BS and MOE values are shown in Figures 3 and 4.

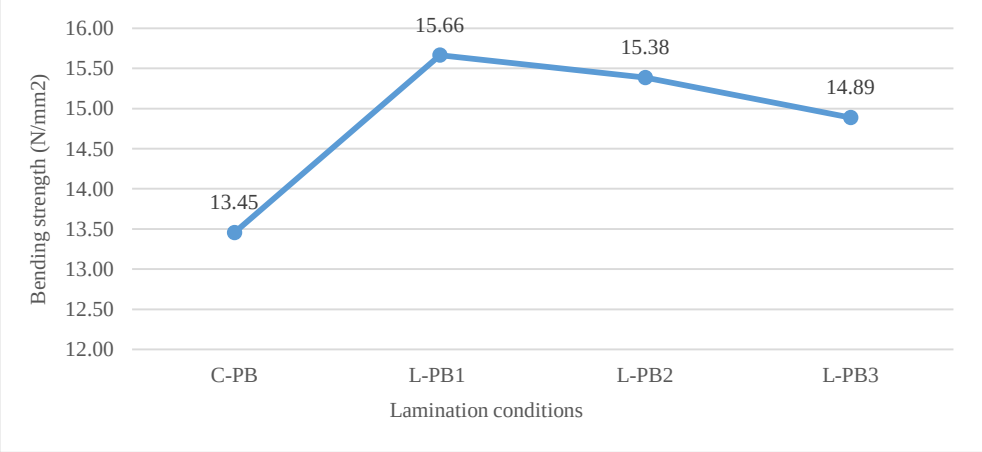

Figure 3. Bending strength (N/mm^2)

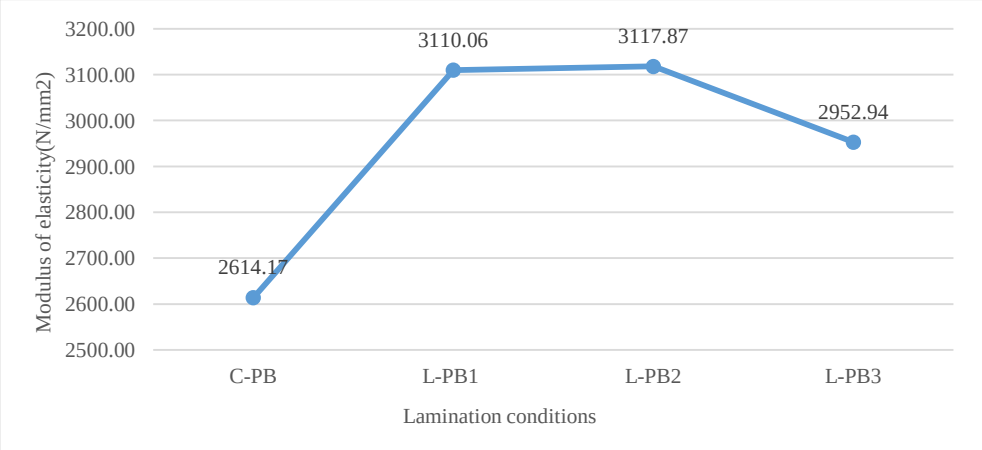

Figure 4. Modulus of elasticity in bending (N/mm^2)

As seen in Figures 3 and 4, the BS and MOE were improved with the lamination process. The increase in BS and MOE was found to be statistically significant when compared with the control board. The rates of increase in the BS were found to range from 10.70% to 24.05% according to control board. The higher BS value was found as 15.66 N/mm2 in the lamination condition at the 180 ^{o}C and 24 sec. Buyuksari, [19] reported that the bending strength values decreased with increasing temperature, especially after 150 ^{o}C. Another study Jamsa and Viitaniemi, [20] stated that wood starts to lose its strength properties at temperatures over 150 ^{o}C as a result of becoming more brittle at temperatures higher than this.

Similar rates of increase in the MOE were found to range from 12.96% to 19,28%. The best result of MOE in the laminated PB was obtained as 3118 N/mm2 in the 200 oC lamination press temperature and 24 sec. As a result, the BS and MOE were determined to be positively affected by lamination process. İstek et al. [6] found that after the lamination process, the mechanical properties of the particleboards laminated with impregnated décor papers were increased. It was determined that MOE and BS values of coated particleboards increased by statistically significant amounts compared to uncoated particleboards.

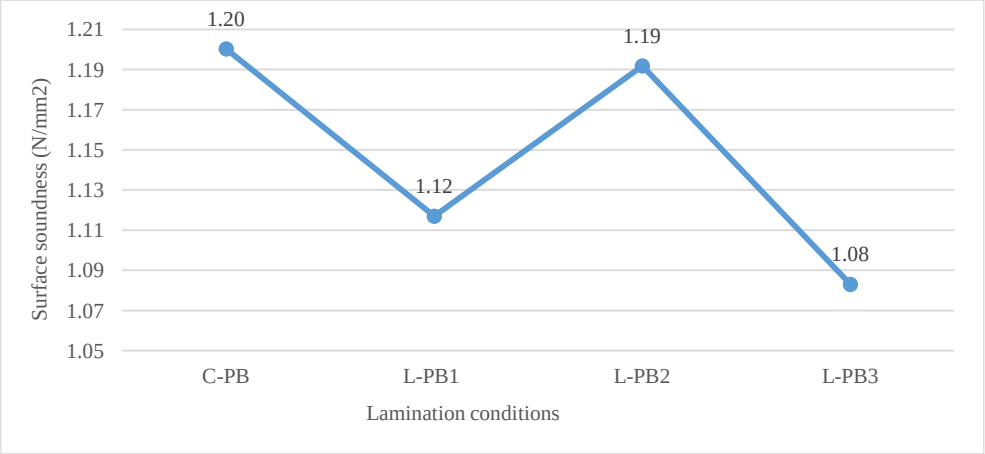

Figure 5. Surface soundness (N/mm2)

The surface soundness numerically decreased depending on the lamination process, but this decline was determined to vary. When compared to the control panels made in the coating process, Surface soundness of L-PB2 conditions was not statistically significant, whereas other lamination conditions were found to be statistically significant. The cause of varying decrease in the SS was not found. Similarly, after the coating process screw withdrawal slightly decreased, but this decrease was not statistically significant.

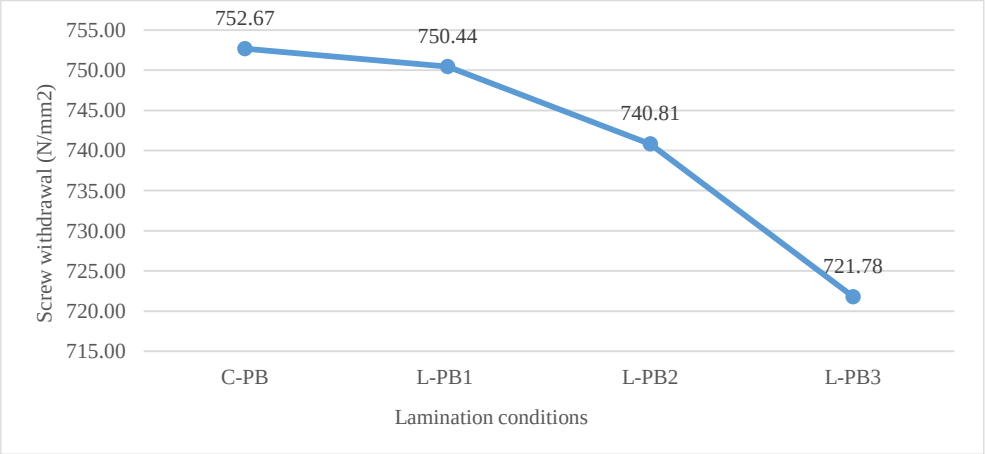

Figure 6. Screw withdrawal

4. CONCLUSION

It is known that during the lamination of wood based panels, similar or lower board production parameters affect the physical, mechanical and surface properties of the board. To obtain high gloss surface, temperature, pressure and duration should be kept at high levels in the lamination technique. Higher temperature, duration and pressure during the lamination lead to decrease in some of the physical and mechanical properties, while improving the surface properties. Higher temperatures and shorter pressing periods in the lamination are preferred to increase the production capacity. However, longer press time at higher temperature and pressure cause the capillary cracking due to the surface tension. In the case of high gloss surface, high pressure, higher amount of melamine resin, longer time of lamination under lower temperatures depending on board production press parameters are needed in the lamination process.

According to results obtained in the present study, internal bonding, surface soundness, withdrawal screw were significantly reduced by higher temperature and lower duration in the lamination process. Internal bonding strength, screw withdrawal and surface soundness were decreased by 10 to 20%, 1 to 4% and 1-9%, respectively. On the other hand, bending strength and modulus of elasticity in bending enhanced between 10 to 19% after lamination process. It was found that water absorption and thickness swelling were significantly improved at 95% confidence level. Water uptake and thickness swelling were improved by 5 to15%. Lamination conditions affected physical and mechanical properties of particleboard. In particular, bending strength and modulus of elasticity in bending of laminated boards were higher than those of unlaminated boards.

It was concluded that, press parameters in the lamination process should be selected in line with board production press parameters including pressure, temperature and duration. In addition, press conditions used in the lamination depend on the press technology and parameters, since high press temperatures in the lamination can lead to pyrolysis and de-condensation of

the resin which is used as binder in the boards. As a result, lamination process improved the mechanical and physical properties such as bending strength, modulus of elasticity in bending, water absorption and thickness swelling, and in turn decreased the internal bonding strength, screw withdrawal and surface soundness.

REFERENCES

[1]. Hiziroglu, S. "Surface roughness analysis of wood composites: A stylus method," *Forest Production Journal* 46(7/8), 67-72, 1999.
[2]. Kilic, M., Burdurlu, E., Aslan, S., Altun, A., and Tümerdem, Ö. "The effect of surface roughness on tensile strength of the medium density fiberboard (MDF) overlaid with polyvinyl chloride (PVC)," *Materials and Design* 30(10), 4580-4583, 2009.
[3]. Istek, A., Aydemir, D. and Eroglu, H. "Surface properties of MDF coated with calcite/clay and effects of fire retardants on these properties". *Maderas. Ciencia y Tecnología*, 14(2), 135-144, 2012.
[4]. Hiziroglu, S. "Surface roughness analysis of wood composites: a stylus method," *Forest Products Journal*, 46(7, 8), 67, 1996.
[5]. Nemli, G. "Factors affecting some quality properties of the decorative surface overlays," *Journal of Materials Processing Technology* 195, 218-223, 2008.
[6]. Istek, A., Aydemir, D. and Aksu, S. "The effect of décor paper and resin type on the physical, mechanical, and surface quality properties of particleboards coated with impregnated décor papers". *Bio Resources*, 5(2), 1074-1083, 2010.
[7]. Nemli, G., Gezer, E. D. and Hızıroğlu, S. "The changes in important quality properties of continuous pressed laminates (CPL) with some changes in thickness and press parameters". *Building and Environment*, 38(7), 913-917, 2003.
[8]. Aksu, S. "Effect of Décor paper and resin type on physical, mechanical and surface properties of particleboards," *Bartin University, Faculty of Forestry*, Bartin, Turkey, 80 p, 2009.
[9]. Bardak, S., Sarı, B., Nemli, G., Kırcı, H. and Baharoğlu, M. "The effect of decor paper properties and adhesive type on some properties of particleboard,".*International Journal of Adhesion and Adhesives*, *31*(6), 412-415, 2011.
[10]. *TS EN 312. Particleboards – Specifications*, Turkish Standards Institute, Ankara-Turkey; 2005.
[11]. *TS 642. Standard Atmospheres for Conditioning and/or Testing; Specifications*, Turkish Standards Institute, Ankara-Turkey, 1997.
[12]. *TS EN 325. Wood-based panels- Determination of dimensions of test pieces*, Turkish Standards Institute, Ankara-Turkey, 2005.
[13]. *TS EN 326. Wood-based panels- Sampling, cutting and inspection-sampling test pieces and expression of test results*, Turkish Standards Institute, Ankara-Turkey, 1995.
[14]. *TS EN 317. Particleboards and fiberboards- Determination of swelling in thickness after immersion in water*, Turkish Standards Institute, Ankara-Turkey, 2005.
[15]. *TS EN 310. Wood-based panels- Determination of modulus of elasticity in bending and of bending strength*, Turkish Standards Institute, Ankara-Turkey, 1999.
[16]. *TS EN 319. Particleboards and fiberboards - Determination of internal bonding strength*, Turkish Standards, Ankara-Turkey, 1999.
[17]. *TS EN 320. Particleboard and Fiberboard-Determination of resistance to axial withdrawal of screws*, Turkish Standards, Ankara-Turkey, 2011.
[18]. *TS EN 311. Wood-based panel- Surface Soundness-Test methods*, Turkish Standards, Ankara-Turkey, 2005.
[19]. Büyüksarı, Ü. "Physical and mechanical properties of particleboard laminated with thermally compressed veneer," Bio Resources, 7(1), 1084-1091.
[20]. Jämsä, S. and Viitaniemi, P. "Heat treatment of wood–Better durability without chemicals". In Proceedings of special seminar held in Antibes, 2001, France.

ICENS
INTERNATIONAL CONFERENCE ON ENGINEERING AND NATURAL SCIENCES
24-28 May 2016 /Sarajevo

Numerical and Experimental Investigation of Load-Settlement Behavior of Centrally Loaded Strip Footing on Sand

Erol Sadoglu[1], Ahmet Kuvat[2]

Abstract

Foundations are the elements that transfer the loads acting on them to the soil medium safely and economically. Safety condition expresses satisfaction of bearing capacity and settlement criteria at the same time. Bearing capacity can defined as the ultimate base pressure that foundation soil can sustain. Settlement criterion can be thought as level of vertical displacement occuring in foundation soil that does not cause any damage and trouble with the usage of the structure it supports. In this study, load-settlement behaviour of surface strip footing was investigated experimentally and numerically. For this purpose, ultimate load of a centrally loaded model shallow strip footing resting on sand were determined under plain strain conditions. The sand was placed in the tank at a relative density of 0.74. Numerical simulation of the experimental study was carried out by using Plaxis 2D finite element software. Different material models was used for the modeling of the sand and dependence of load-settlement behavior on cohesion was obtained numerically. The load-settlement relationships were investigated and compared between experimental and numerical results.

Keywords: *Strip Footing, Settlement, Bearing Capacity, Finite Element Method*

1.INTRODUCTION

Foundations are the structural elements transferring loads safely and economically from superstructure to soil medium and they can be classified into two main groups. First group is shallow foundations which are generally used in the case of strong shallow soil layers. Shallow foundations can be classified as spread footing, strip footing and mat according to their shape in the plan. Second group is deep foundations and preferred if foundation soil doesn't have necessary strength. Piles, piers, and caissons are the most common types of them.

Bearing capacity and settlement conditions are necessary safety criteria of foundations. Maximum base pressure of footing during failure can be defined as ultimate bearing capacity (q_{ult}) and safe bearing capacity (q_{safe}) of the footing is obtained by dividing ultimate bearing capacity by a factor of safety. Bearing capacity condition can be explained as maximum base pressure of footing should be smaller than safe bearing capacity. Settlement is defined as vertical movement of foundation hence superstructure. Main reason of settlement is the loads applied on footing from superstructure and then from footing to soil. Thus, the loads cause reduction in void ratio and compression in soil layers. Additionally, freezing and swelling are another reasons of settlement. Settlement conditions can be defined as actual or estimated settlement of foundations should be smaller than permissible settlement value.

Many researchers have made experimental, analytical and numerical investigations about bearing capacity and load-settlement relationship (Eastwood, 1955; Chummar, 1972; Ko ve Davidson, 1973; Uzuner, 1975; Kirkpatrick ve Uzuner, 1975; Pfeifle ve Das, 1979; Nova ve Montrasio, 1991; Andrawes vd., 1996; Briaud ve Gibbens, 1999; Lou ve Bolton, 2011; Taiebat ve Carter, 2000). In this study, the load-settlement relation of a model shallow strip footing was investigated experimentally. The footing was placed on dry sand at a relative density of 0.74. Bearing capacity tests were performed with a specific experimental setup satisfying plane strain conditions. From the experiments, load-settlement relation and bearing capacity of the model footing were obtained. The experimenal setup was simulated with different nonlinear material models by a finite element program namely Plaxis (2D). The material models used in numerical simulation are Mohr-Coulomb and hardening soil models.

2.EXPERIMENTAL STUDIES

The primary components of the experimental set-up include a tank, model strip footing, loading system, sand, etc. These primary components are explained below (Sadoglu et. al, 2009).

[1] *Corresponding author: Karadeniz Technical University, Department of Civil Engineering, 61080, Ortahisar/Trabzon, Turkey.* esadoglu@ktu.edu.tr

[2], *Karadeniz Technical University, Department of Civil Engineering, 61080, Ortahisar/Trabzon, Turkey.* ahmet.kuvat@gmail.com.tr

2.1.Tank

The strip footing case corresponds to a plane strain condition. The internal dimensions of the tank containing the sand are 0.9 m (length) × 0.10 m (width) × 0.65 m (height) (Fig. 1).

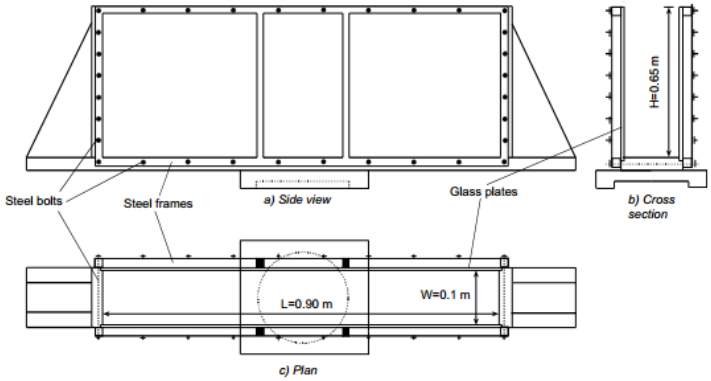

Figure 1. Three wiev of tank

The bottom and the sides of the tank were produced using hard wood. The front and back faces were constructed of 20 mm thick glass plates to observe failure surfaces. Two steel frames made of hollow sections were produced and connected to each other with steel bolts along the sides of the frames. Steel elements made of solid profiles were welded in the middle part of the frames to prevent deformation of the glass plates. The surface of the steel frame on which glass plates touch was produced to be almost perfect plane so that no glass plate was broken during tests. Two dial gauges were placed on the external faces of the glass plates to measure deformations. Measured and calculated strains of the sides were found to be well less than 0.1% in the tests. Thin latex sheets ideally should be placed on the internal faces of the lightly lubricated glass plates to achieve almost frictionless side faces. This application has the difficulties due to movements of the sand mass in different directions. The sand is in contact with glass faces directly in this experimental work. Kirkpatrick and Uzuner (1975) showed that the effect of side friction is less than 10% of the ultimate load in B/W = 1 (B: footing width, W: tank width), glass sides, medium dense sand and surface footing. The conditions of this experimental work are close to the conditions of the work done by Kirkpatrick and Uzuner (1975).

2.2. Model Footing

The model strip footing was produced by welding 8-mm thick steel plates to applying rigid footing condition (Fig. 2). The dimensions of the footing in the test set-up are 80 mm (width) × 100 mm (length) × 80 mm (height). V shaped grooves were opened along on the length of the base plate so that different eccentricities but in this study only center groove was used. The footing base was covered by coarse sandpaper to obtain a full frictional condition along the base of the footing.

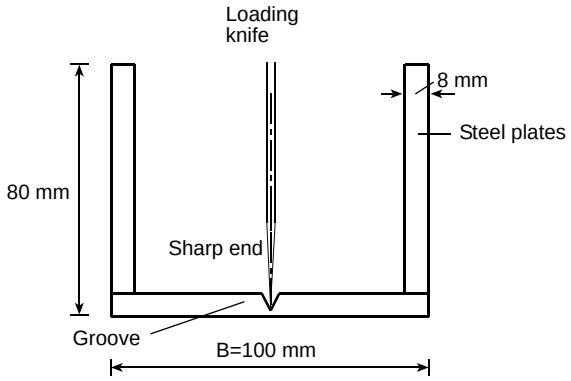

Figure 2. Model footing

2.3. Sand

The sand used in tests was local Black Sea coastal sand and it has a grain size distribution that ranges from about 0.2 to 4 mm (medium-coarse) and is classified as SP (poorly graded). Properties of the sand are summarized in Table 1.

Table 1. Properties of the sand used in test

Property	Quantity
Specific gravity, G_s (Mg/m^3)	2.66
Maximum dry density, ρ_{kmax} (Mg/m^3)	1.658
Minimum dry density, ρ_{kmin} (Mg/m^3)	1.395
Effective size, D_{10} (mm)	0.58
D_{30} (mm)	0.80
D_{60} (mm)	0.95
Coefficient of uniformity, C_u	1.64
Coefficient of curvature, C_r	1.16
Internal friction angle ϕ (Degree)	41

The internal friction angles of the sand were measured from triaxial test (D= 38 mm) at the relative density of 0.74. The sand was placed in the tank at sufficient density so that general shear failure can be obtained in the tests and its relative density (D_r) was kept constant throughout all the tests as 0.74 (γ_{dry}=1.581 Mg/m^3). Sand was placed in the tank in 50 mm thick layers. The quantity (7112 g) for a 50 mm thick layer was deposited in the tank loosely as a uniform thick (about 57 mm) layer. This loose sand layer was lightly compacted with a wooden hammer in the tank to about 50-mm thick layer. To confirm 50-mm thickness, horizontal lines at 50-mm intervals were drawn on the internal face of the glass plates. This process continued until sand mass height reached 0.50 m. (Fig 3).

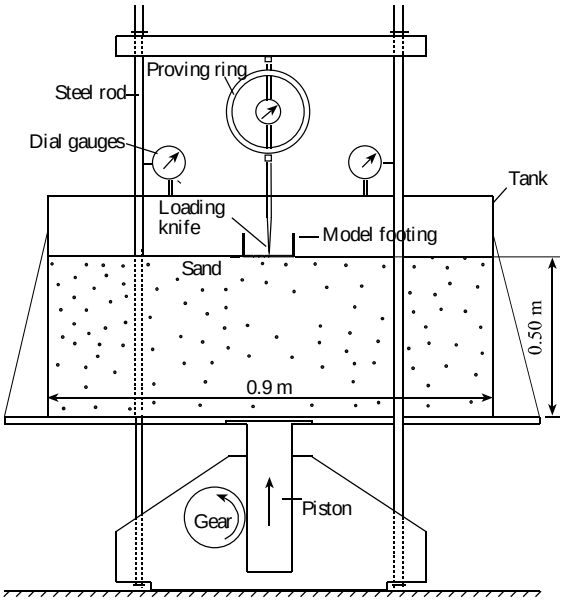

Figure 3. The loading mechanism for test

3.NUMERICAL STUDIES

In the numerical simulation studies, PLAXIS 2D FEM software was used and 15 noded triangular elements were used in analysis and the model was discreted totally into 1529 elements (Fig. 4).

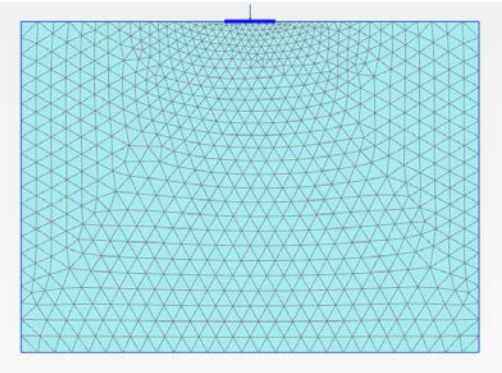

Figure 4. General wiev of numerical model

Experimental setup was analyzed with two different nonlinear material models for sand (Mohr-Coulomb, Hardening Soil) and the model footing was modelled as a plate element. Material input parameters are given in the Table 2, 3 and 4.

Table 2. Mohr-Coulumb input parameters

Properties	**Value**
Drainage	Undrained
Dry unit weight Mg/m^3	15.8
Saturated unit weight Mg/m^3	1.98
Coefficient of Permeability, (k_x=ky) m/day	10
Young Modulus (E) (kN/m^2)	25400
Poisson ratio	0.25
Effective internal friction angle (^{0})	43
Dilatancy angle (^{0})	13
Coefficient of lateral earth pressure at rest (K_0) (1-sinϕ)	0.318

Table 3. Hardening Soil input parameters

Properties	**Value**
Drainage	Undrained
Dry unit weight (kN/m^3)	15.8
Saturated unit weight (kN/m^3)	19.8
Coefficient of Permeability, (k_x=ky) m/day	10
E_{50} (kN/m^2)	25400
E_{oed} (kN/m^2)	15000
E_{ur} (kN/m^2)	55000
Poisson ratio	0.25
Effective internal friction angle (^{0})	43
Dilatancy angle (^{0})	13
P_{ref} (kN/m^2)	100
Coefficient of lateral earth pressure at rest (K_0) (1-sinϕ)	0.318

Table 4. Model footing input parameter

Model	EI (kNm^2/m)	EA (Nt/m)
Plate	102400	1600000

Different values (c=0-0,1-0,25-0,5-0,75-1,0-2,0-3,0 and 4,0 kN/m^2) were assigned to cohesion to investigate the effect of cohesion on load-settlement behavior and ultimate loads.

4.RESULTS AND DISCUSSIONS

4.1. Experimental Results

Bearing capacity tests were performed with the model strip footing placed on dry sand that has a relative density of 0.74. After filling the tank with sand at desired relative density, loading of footing was started with 0,15 mm/min. constant vertical deformation velocity. Load and settlement were measured periodically from starting of test and totally two experiments were made. The ultimate load was reached to 3.432 kN at the vertical displacement of 7.74 mm. Experimental results are shown in Fig. 5.

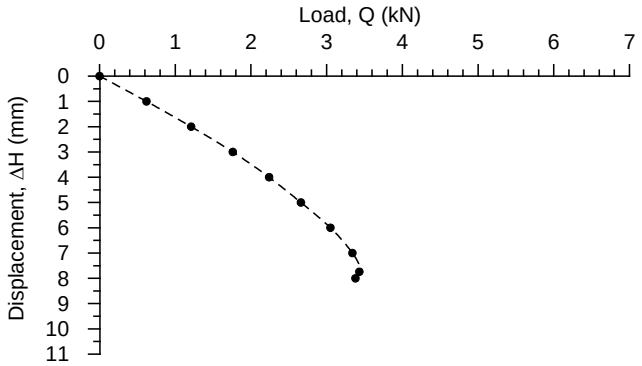

Figure 5. Experimental load-settlement result

4.2. Numerical Results

Ultimate loads and vertical displacements which were acquired from Hardening Soil and Mohr-Coulomb models for different cohessions are given Fig. 6 and Fig. 7. When numerical ultimate loads were compared with experimental measurement, numerical loads are much smaller than experimental loads in case of zero cohesion. Increasing cohesion causes an increase in the ultimate loads of numerical simulation. This increase is nearly three fold for c=1 kN/m^2 with respect to c=0. Beyond the cohesion of 1 kN/m^2, increase ratio of ultimate load decreases.

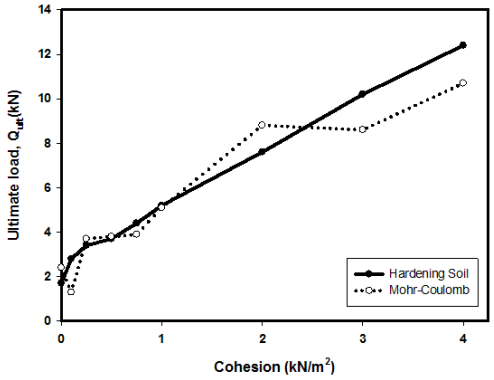

Figure 6. Variation of ultimate loads depending on cohesion

As it can be seen Fig. 7, increasing cohesion from 0 to 1 kN/m^2 has very important effect on vertical displacements obtained from hardening soil model. However, this effect of cohesion is negligible for Mohr-Coulomb model.

When numerical and experimental vertical displacements are compared, vertical displacements obtained from hardening soil model are close to experimental measurement (especially c=0,5-1 kN/m^2). However vertical settlements of Mohr-Coulomb model are very small (nearly ten percent of experimental measurement).

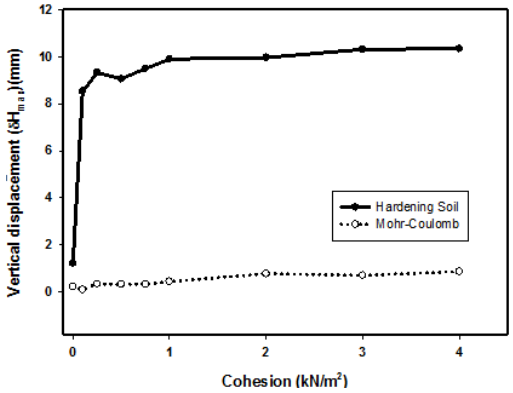

Figure 7. Variation of vertical displacement depending on cohesion

5. CONCLUSIONS

Experimental and numerical studies were carried out in order to determine load-settlement relationship of shallow strip footing placed on dense sand. Beside these, in the numerical studies effect of cohesion on the load-settlement relationship was determined parametrically. The following conclusions can be drawn from the numerical and experimental studies:

- According to numerical simulations, increase in cohesion leads to an increase in ultimate loads obtained both hardening soil and Mohr-Coulomb models. This effect is very noticeable for the cohesion between 0.5 and 1 kN/m^2.
- According to numerical simulations, increasing cohesion has very important effect on the vertical displacements of hardening soil model, however, this increase was not dinstictive for Mohr-Coulomb model.
- In terms of ultimate loads, experimental and numerical results are very close for the cohesion between 0.5 and 1 kN/m^2. On the other side, Mohr-Coulomb model gives misleading settlement results in these cohesion values and vertical displacement of hardening soil model is very close to experimental results.

REFERENCES

[1]. Andrawes, K. Z., Al-Omari, R. R. and Kirkpatrick, W. M., *Geotechnical and Geological Engineering*, 'Bearing Capacity of A Strip Foundation on a Sand Layer Overlying a Smooth Rigid Stratum', 14, 227-236, 1996.
[2]. Briaud, J.L. and Gibbens, R., *Journal of Geotechnical and Geoenviromental Engineering, ASCE*, 'Behaviour of Five Large Scale Spread Footings in Sand', 125, 9, 787-796, 1999.
[3]. Chummar, A.V., *Journal of the Soil Mechanics and Foundations Division, ASCE*, 'Bearing Capacity Theory From Experimental Results', 98, 12,1311–1324, 1972.
[4]. Das, B. M. , Shin, E. C. , Omar, M. T., *Geotechnical and Geological Engineering*, 'The bearing capacity of surface strip foundations on geogrid-reinforced sand and clay-A comparative study', 12, 15-33, 1994.
[5]. Eastwood, W., *The Structural Engineer*, 'The Bearing Capacity of Eccentrically Loaded Foundations on Sandy Soil', 29, 6, 181-187, 1955.
[6]. Khing, K. H., Das, B. M., Puri, V. K. , Cook, E. E., Yen, S. C., *Geotextiles and Geomembranes*, 'The bearing capacity of a strip foundation on geogrid-reinforced sand', 351-361, 1993.
[7]. Kirkpatrick, W. M., and Yanikian, H. A., *Proceedings of the Fourth South East Conference On Soil Engineering*, 'Side Friction in Plane Strain Tests', Kuala Lumpur, Malaysia 76-84, 1975.
[8]. Kirkpatrick, W. M. and Uzuner, B.A., *Istanbul Conference on Soil Mechanics*, 'Measurement Errors in Model Foundations Tests', Istanbul, Turkey, 98-106, 1975.
[9]. Ko, H., and Davidson, L. W.,, *Journal of the Soil Mechanics and Foundations Division, ASCE*, 'Bearing Capacity of Footings in Plane Strain', 99, 1, 1-23, 1973.
[10]. Lau, C. K. and Bolton, M. D., *Geotechnique*, 'The bearing capacity of footings on granular soils. I: Numerical analysis', 61, 8, 627–638, 2011.
[11]. Lade, P. V. and Lee, K. L., 'Engineering Properties of Soils', Report UCLA-ENG-7652, University of California, Los Angeles, 145 s.
[12]. Moroğlu, B., Uzuner, B. A., Sadoğlu, E., *Indian Journal of Engineering and Material Sciences*, 'Behaviour of the model surface strip footing on Reinforced sand', 12(5), 419-426, 2005.
[13]. Nova, R. and Montrasio, L., *Geotechnique*, 'Settlements of Shallow Foundations on Sand', 41, 2, 243-256, 1991.
[14]. Omar, M. T., Das, B. M., Puri, V. K. Yen, S. C., *Canadian Geotechnical Journal*, 'Ultimate bearing capacity of shallow foundations on sand with geogrid reinforcement', 545-549, 1993.
[15]. Pfeifle T. W., ve Das, B. M., *Soils and Foundation*, 'Bearing capacity of surface footings on sand layer resting on rigid rough base', 1, 1-11, 1989.
[16]. Sadoğlu, E., Cure E., Moroğlu, B., Uzuner, B. A., *Geotextiles and Geomembranes*, 'Ultimate loads for eccentrically loaded shallow strip footings on geotextile-reinforced sand', 27, 176-182, 2009.
[17]. Taiebat H.A. ve Carter, J.P., *Geotechnique*, 'Numerical studies of the bearing capacity of shallow foundations on cohesive soil subjected to combined loading', 50, 4, 409-418, 2000.
[18]. Uzuner, B. A.,. 'Centrally and Eccentrically Loaded Strip Foundations on Sand', PhD Thesis, Strathclyde University, Glosgow, Scotland, 149 p, 1975.

[19]. Wasti, Y., Bütün, M. D., *Geotextiles and Geomembranes*, 'Behaviour of model footings on sand reinforced with discrete inclusions', 14 (1), 575-584, 1996.

A Fuzzy Logic Approach for Prediction of Suspended Sediment in River

Fatih Unes[1], Bestami Tasar[2], Mustafa Demirci[3]

Abstract

Suspended sediment forecast is crucial to maintain of the water resources. In this paper, Fuzzy Logic (FL) and statistical approaches such as Sediment Rating Curves (SRC), Multiple Linear Regression (MLR) are used for forecasting daily suspended sediment concentration from daily temperature of water and streamflow in river. The daily data measured at Augusto station by the US Geological Survey. These aproaches are compared to each other according to three statistical criteria, namely, mean square errors (MSE), mean absolute relative error (MAE) and correlation coefficient (R). Statistical criteria were used to assess the performance of the approaches. Comparisons of modeling and measurements results demonstrate that FL approach have better forecasts than the other conventional techniques.

Keywords: *Forecasting,Fuzzy Logic, Sediment Rating Curves, Stream Flow, Suspended Sediment,*

1.INTRODUCTION

Sediment forecast is important to solve the problems and maintain of the water resources. Directly measuring sediment load of rivers is more time consuming and expensive. Although river flows have measured in field stations, there isn't enough measurement of Suspended Sediment. In the last years, studies have been made to develop sediment rating curve (SRC), regression methods and artificial intelligence techniques for simulation processes with limited knowledge of the physics. In most rivers, sediments are mainly transported as suspended sediment load [1]. Many models have been provided to simulate this phenomenon. However, traditional sediment rating curves are not able to provide sufficiently accurate results. A sediment rating curve is a relation between the sediment and river discharges. Such a relationship is usually established by a regression analysis, and the curves are generally expressed in the form of a power equation.

[2] examined suspended sediment rating curves and the practice of using sediment load versus discharge is shown to be misleading, since the goodness of fit implied by this relation is spurious.

Fuzzy logic has been used successfully for prediction of suspended sediment during recent years ([3]; [4]; [5]; [6]). [7] developed fuzzy models to forecast daily suspended sediments. He compared the fuzzy estimates with those of the sediment rating curves and found that the fuzzy models performed better than the rating curves.

[8] demonstrated that the NF model performs better than the SRC and other artificial intelligence techniques in daily suspended sediment concentration estimation.

[9] tried to forecast sediment suspended load of Khaivchay River And Comparison of the models' results, NF model results more reasonably forecast suspended sediment load than other techniques.

[10] studied suspended sediment concentration (SSC) in rivers and the performance Fuzzy and other models are analyzed for daily SSC prediction in two hydrometry gauging stations in the United States. They found that NF models were usually superior and performance of NF model gave accuracy results.

[1,2,3] *Corresponding author: Iskenderun Technical University Civil Engineering Faculty / Hydraulics Division. 31200, İskenderun / Hatay – TURKEY*

fatih.unes@iste.edu.tr ; bestami.tasar@iste.edu.tr; mustafa.demirci@iste.edu.tr

In this paper, SRC, MLR and FL modelling approaches are utilized for forecasting the sediment load of the Skunk River to compare their performances in modeling . So as to forecast sediment concentration, the daily streamflow, water temperature and suspended sediment time series data belonging to one station in USA are used.

2.APPLICATION

The time-series data of Skunk Augusto Station at Iowa (USGS Station No. 05474000, latitude 40°45'13, longitude 91°16'37"), operated by the US Geological Survey (USGS) were used in the study. The location of the station is shown in Figure 1. The gauge datum is 160 m. above sea level. For this station, daily time-series of river flow and suspended sediment concentration were downloaded from the Web server of the USGS.

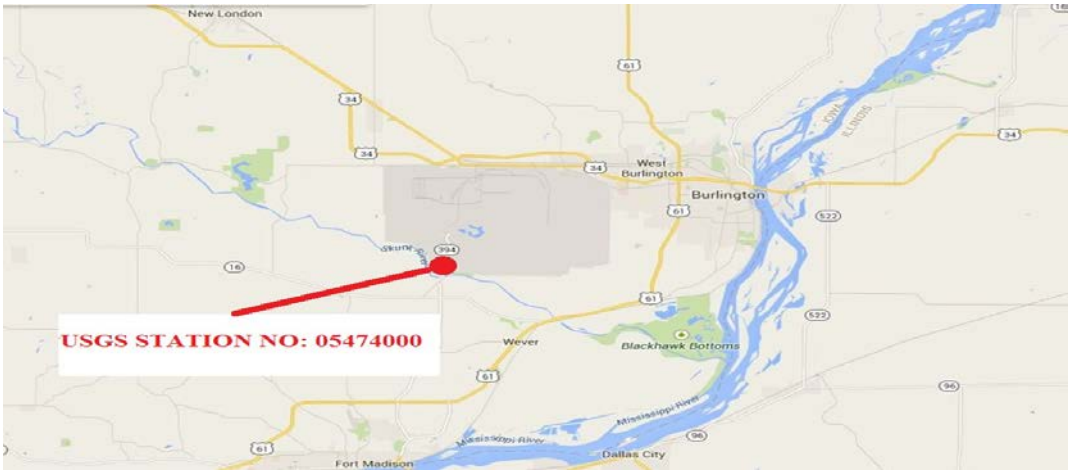

Figure 1. The location of the Skunk Augusto Station at Iowa

3. METHODS AND RESULTS

The statistical parameters of streamflow, river flow water temperature, suspended sediment concentration data of Skunk Augusto Station for 5 years (2009-2014) are shown in Table I. In this table, S_x, C_{sx}, X_{max}, X_{min}, X_{mean} denote the standard deviation, the skewness coefficient, and maximum, minimum and mean values.

In the executing of models, the observed data set are divided into two groups as the training and testing data. The inputs used in this study are average daily stream discharge (Q), river water temperature (T) and suspended sediment concentration recorded at time t-1 (St-1). The output indicates the suspended sediment concentration at time t (St).

Table 1. The statistical parameters of Augusto Station data

	Variables	T(° C)	Q(m^3/s)	S(Mg/L)
Training	X_{Max}	35,0	1217,6	3040,0
	X_{Min}	0,0	3,1	7,0
	X_{mean}	14,7	116,6	242,0
	s_x	9,7	159,5	345,2
	c_{sx}	0,1	2,7	3,4
Test	X_{Max}	30,0	1245,9	3410,0

X_{Min}	0,0	21,6	14,0
X_{mean}	16,6	289,1	348,1
s_x	8,8	253,5	392,3
c_{sx}	-0,3	1,4	3,4

3.1. Sediment Rating Curves (SRC) Results

The sediment rating curve generally represents a functional relationship of the form in which Q is stream discharge and S is either suspended sediment concentration or yield. Values of a and b for a particular stream are determined from data via a linear regression between (log S) and (log Q). In Sediment rating curve (SRC) model, 1100 of 1580 data for the training, 480 data are divided for testing. The obtained sediment concentration data are compared with testing data and scatter plot is shown in Figure 1. The correlation coefficient was obtained as R = 0.42. When distribution graph in Figure 2 for testing data are analyzed, SRC sediment concentration values are seen different for estimated value according to the actual values. Values of sediment rating curve are seen to be spaced out from the actual values.

$$S = aQ^b \quad (1)$$

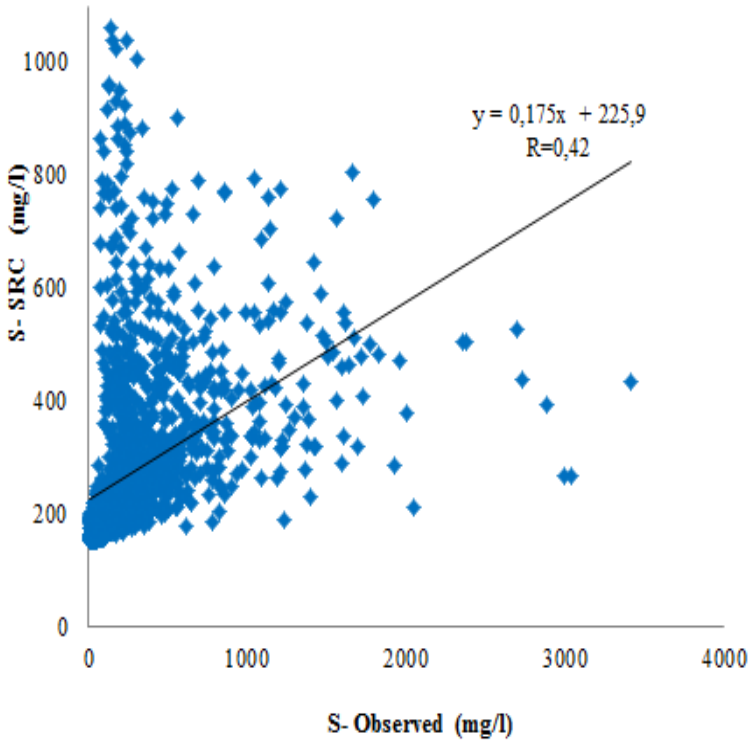

Figure. 1. Observed and SRC scatter graph for the testing data

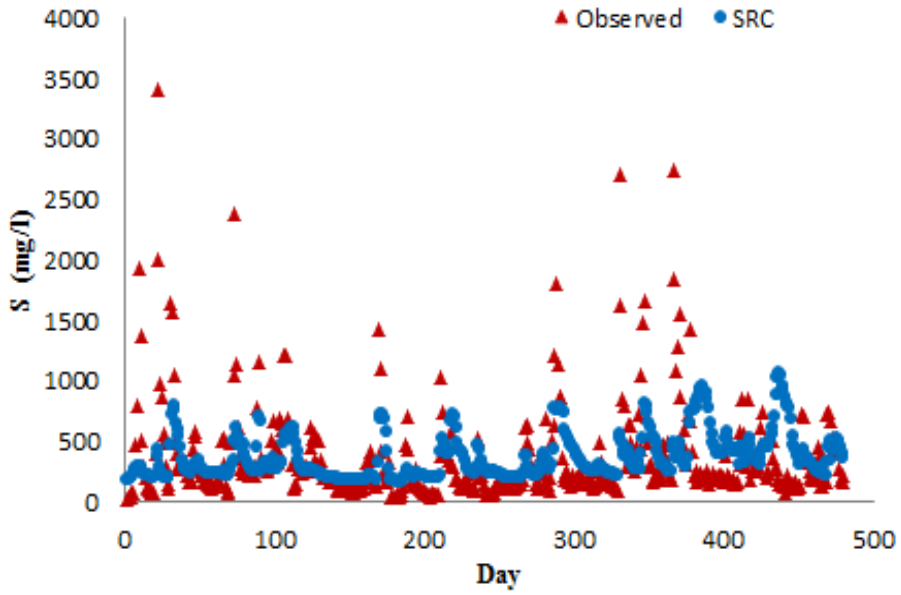

Figure. 2. Observed and SRC distribution graph for the testing data

3.2. Multilinear Regression (MLR) Model Results

For Multiple linear regressions (MLR), 5years data (2009-2014) are evaluated and the results are given in figures and the input combinations present the previously recorded daily lag time suspended sediments, discharge and water temperature. (S_{t-1} , Q, T).

Distribution and scatter plots are shown for testing data in figure 3 and 4. The correlation coefficient were obtained as R = 0.664 from the generated graphic. MLR estimation values in test phase are observed and although daily real-time suspension sediment concentration values is better results than SRC values, the worst estimated results are observed according to the actual values. In distribution and scatter charts, MLR values are smaller than the actual values.

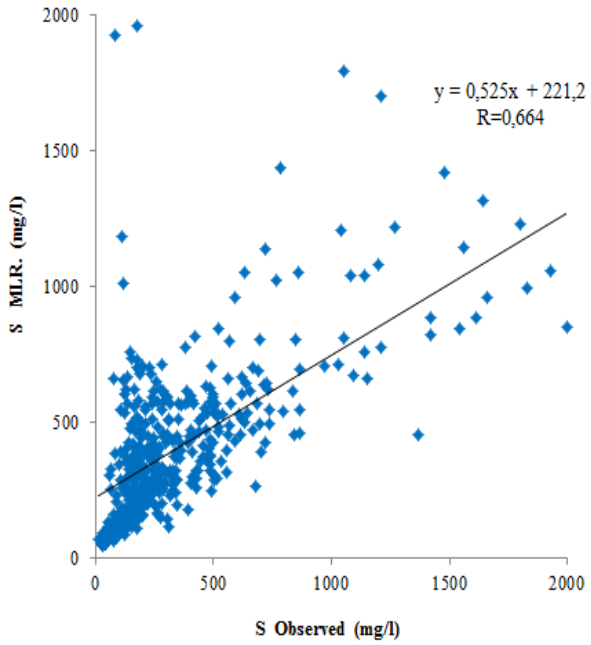

Figure 3. Observed and MLR scatter graph for the testing data

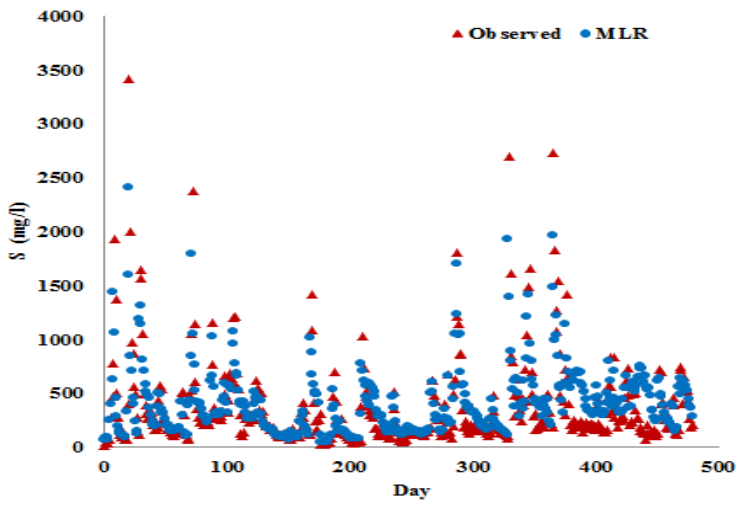

Figure 4. Observed and MLR distribution graph for the testing data

3.3. Fuzzy Logic Model (FL) Results

FL models are evaluated for five years data (2009-2014) created in Matlab fuzzy editor. For Fuzzy Logic approaches, the input combinations present the previously recorded daily lag time suspended sediments, discharge and water temperature. (S_{t-1} , Q, T).

Estimated testing results are shown in Figure 5 and Figure 6 as respectively the distribution and scatter plots.

In figure 5, the correlation coefficient were obtained as R = 0.782 from the generated graphic. The FL estimated values are observed in the test phase and gives better results than the SRC values. As can be seen from figures, the fit line of the FL closer to the exact line with a higher R value than those of the SRC model. As seen from the scatter plots, the FL model estimates are less scattered in relative to the other models

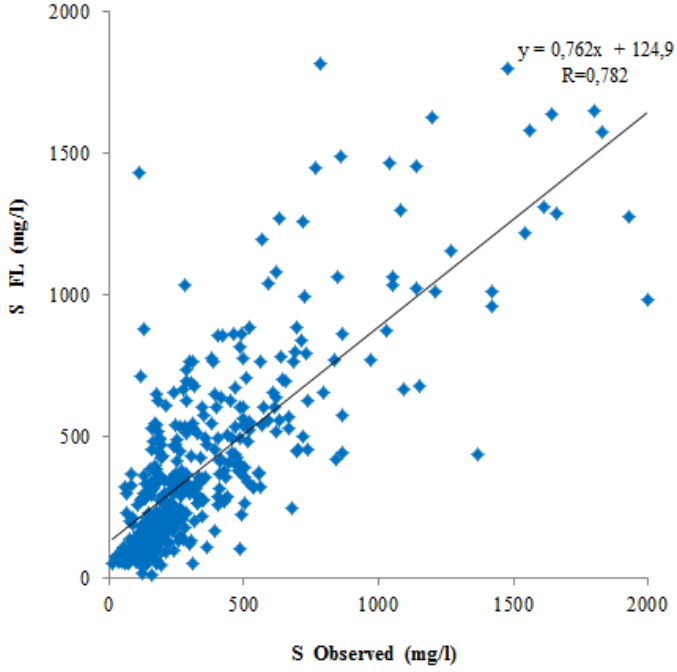

Figure 5. Observed and FL scatter graph for the testing data

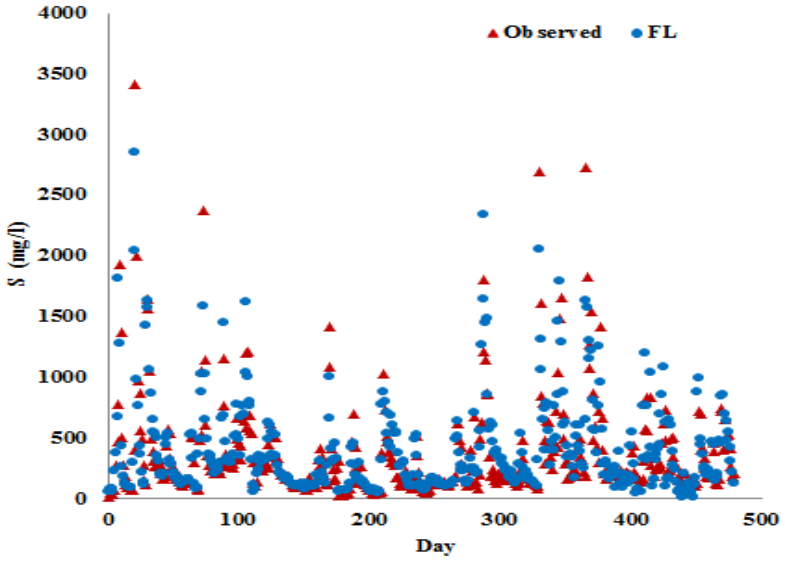

Figure 6. Observed and FL distribution graph for the testing data

For 5-year data (between 2009 and 2014) used to generated forecast aproaches in order of Suspended Sediment Rating Curve (SRC), Multi Linear Regression (MLR) and Fuzzy Logic (FL).And results of these aproaches given below. Using daily real-time stream flow and suspended sediment concentration data from Skunk River, Augusto station, correlation coefficient (R), the mean squared error (MSE), the mean absolute error (MAE) is calculated for performance evaluation of SRC, MLR and FL models. Results are used to compare the performance of model prediction and the observation data. MSE and MAE values were determined accarding to these equations ;

$$MSE = \frac{1}{N} * \left[\sum_{i=1}^{i=N} Yi_{observed} - Yi_{forecast} \right]^2 \quad (2)$$

$$MAE = \frac{1}{N} * \left[\sum_{i=1}^{i=N} Yi_{observed} - Yi_{forecast} \right] \quad (3)$$

Table2. Comparing performances of models created for the Skunk River, Augusto station

Method	MSE	MAE	R
SRC	148266	233,73	0,420
MLR	91526	171,955	0,664
FL	67063	142,29	0,782

MSE: Mean squared error; MAE: Mean absolute error R; Correlation coefficient

Comparing parameters of MSE, MAE and R obtained from testing data are shown in Table 2. When Table 2 is considered, FL model gives better results than the SRC model in all performance values.

4. CONCLUSIONS

In current study, NF, MLR and SRC models were investigated for simulation of suspended sediment concentration of Skunk River in USA. The daily real-time flow rate and sediment concentration of 5 year data in the Skunk river, Augusto station, were analyzed. Model comparisons were made using the research to see which model gave better results. For 5 year data, according to the MSE, MAE and R criteria max. R=0,782 (FL) , min MAE=142,29 (FL) and min MSE=67063(FL) ,the best results were obtained in FL models.

The accuracy of the FL approach in total sediment load forecasting was also investigated and results were compared with the SRC and MLR approaches. Comparison of approaches and measurements results demonstrate that FL approach have better forecasts than the other conventional techniques.

In total sediment load forecasting, comparisons revealed that the FL approach had the best accuracy.

REFERENCES

[1]. G.L. Morris and J. Fan, " Reservoir Sedimentation Handbook, McGraw-Hill", New York, 1997.
[2]. E.A. McBean and S. Al-Nassri, "Uncertainty in suspended sediment transport curves", Journal of Hydraulic Engineering, ASCE 114(1): 63–74,1988.
[3]. O. Kisi, "Modelling of suspended sediment yield in a river cross-section using fuzzy logic", PhD thesis, Istanbul Technical University Institute of Science and Technology, Istanbul, Turkey, 2003.
[4]. O. Kisi, "Daily river flow forecasting using artificial neural networks and autoregressive models", Turk J Eng Environ Sci ;29:9–20, 2005.
[5]. A.K. Lohani, N.K. Goel and K.K.S. Bhatia, "Deriving stage–discharge–sediment concentration relationships using fuzzy logic", Hydrol Sci J;52(4):793–807, 2007.
[6]. M. Demirci and A. Baltaci, "Prediction of suspended sediment in river using fuzzy logic and multilinear regression approaches",Neural Computing and Applications Sci. S145–S151, 2013.
[7]. O. Kisi, "Daily suspended sediment modelling using a fuzzy differential evolution approach". Hydrol Sci J;49(1):183–97, 2004.
[8]. M. Cobaner, B. Unal and O. Kisi, "Suspended sediment concentration estimation by an adaptive neuro-fuzzy and neural network approaches using hydro-meteorological data", Journal of Hydrology 367, 52–61, 2009.
[9]. V. Nourani, "Introducing a model to estimate sedimentary suspended load using fuzzy area and its comparison with classical methods and neural network", Case Study: Gharesou River located in Ardebil Province. 8th International Congress on Civil Engineering, 2009.
[10]. T. Rajaee, S.A. Mirbagher, M.Z. Kermani and V. Nourani, "Daily suspended sediment concentration simulation using ANN and neuro-fuzzy models", Science of the Total Environment 407; 4916–4927,2009.

Prediction of Dam Reservoir Volume Fluctuations Using Adaptive Neuro Fuzzy Approach

Fatih Unes[1], F Gokhan Gumuscan[2], Mustafa Demirci[3]

Abstract

Determination of reservoir volume fluctuations is important for the operation of dam reservoir, design of hydraulic structures, the hydropower for the energy production, flood damage reduction, navigation in the dam reservoirs, water quality management in reservoir and the safety of dam. In this study, reservoir volume variations were estimated using average monthly precipitation, monthly total volume of evaporation, dam discharge volume, and released irrigation water amount. In the present paper, adaptive-neuro-fuzzy inference system (ANFIS) was applied to estimating of reservoir volume fluctuations. ANFIS results are compared with conventional multi-linear regression (MLR) model. The results show that reservoir volume was successfully estimated using fuzzy logic model with low mean square error and high correlation coefficients.

Keywords: *Dam, Reservoir Volume, Prediction, Fuzzy Logic, Multi-linear Regression*

1.INTRODUCTION

A dam reservoir is an artificial lake, storage pond or impoundment from a dam which is used to store water. Water structures such as dams are very expensive to build, and therefore, they must be well planned and management. Dam reservoir water volume predicting for different time intervals using the records of past time series is an crucial issue in water resources planning and management. Since predicting reservoir volume variations in a dam is affected by many environmental factors such as precipitations, the influence of adjacent catchments, evaporation, air and water temperature variations in catchments and reservoir surface, it is difficult to prediction of reservoir volume. Determining accurate volume of reservoir is important due to the design and operation of the hydraulic structures, the water supply, the irrigation and drainage, the energy production, flood planning and management, navigation in the dam reservoirs, water quality management and modeling in the reservoir.Recently, the artificial intelligence techniques have been used in hydrology and water resources systems. Adaptive neuro-fuzzy inference system (ANFIS) which is one of them has been widely applied in water resources. ANFIS is a combination of an adaptive neural network and a fuzzy inference system. The parameters of the fuzzy inference system are determined by the NN learning algorithms. Since this system is based on the fuzzy inference system, reflecting amazing knowledge, an important aspect is that the system should be always interpretable in terms of fuzzy IF–THEN rules. ANFIS is capable of approximating any real continuous function on a compact set to any degree of accuracy [1]. ANFIS identifies a set of parameters through a hybrid learning rule combining backpropaga-tion gradient descent error digestion and a least-squared error method. There are two approaches for fuzzy inference systems, namely the approach of Mamdani [2] and the approach of Sugeno [3]. The neuro-fuzzy model used in this study implements Sugeno's fuzzy approach [3] to obtain the values for the output variable from those of input variables. Keskin et al. [4] used fuzzy models to estimate daily pan evaporation in Western Turkey. Kazeminezhad et al. [5] applied ANFIS to forecast wave parameters in Lake Ontario and found ANFIS superior to the Coastal Engineering Manual methods. Kisi [6] investigated the ability of ANFIS techniques to improve the accuracy of daily evaporation estimation. Kisi and Ozturk [7] used ANFIS computing techniques for evapotranspiration estimation. Demirci and Baltacı [8] estimated suspended sediment of Sacremento river in USA using fuzzy logic. Unes [9] predicted plunging depth of density flow in dam reservoir using the ANN technique. Unes [10], Unes at al. [11] used ANN model and Unes at al. [12] used generalized neural network (GRNN) model for predicting reservoir level fluctuation. Shiri et al. [13] used ANFIS for predicting short-term operational water levels.

The present study investigates the abilities of ANFIS and multi-linear regression (MLR) techniques to forecast daily reservoir volumes. Here, ANFIS has some daily input variables (basin rainfall, evaporation from reservoir, dam spillway release, and volume of irrigation water) and one output, reservoir volumes at the following day(s).

[1,2,3] *Corresponding author: Iskenderun Technical University Civil Engineering Faculty / Hydraulics Division. 31200, İskenderun / Hatay – TURKEY*

fatih.unes@iste.edu.tr ; mustafa.demirci@iste.edu.tr; fghan82@htomail.com

2. CASE STUDY

Yarseli Dam in Hatay region (Mediterranean part of Turkey) was selected for this study. Yarseli Dam was constructed Beyazçay river in Hatay, Turkey, and dam location can be seen in Figs. 1 and 2. The dam was built for the irrigation and the energy purpose and is located on the border of Hatay (Fig. 1). It is an earth fill dam having 55 million m^3 maximum reservoir volume, and 42 m height from the river bed. The data, which contains the time period between 2002 and 2012 on a daily basis, were obtained from Turkish General Directorate of State Hydraulic Works (DSI) and Turkish General Directorate of State Meteorology (MGM). The data sample consists of 10 years of daily records of basin rainfall (R), volumes of inflow river water (IR), evaporation from Reservoir (E), Dam Spillway Release (SR), volume of Irrigation water (IRGW) and change Reservoir Volume (CVO). These selected parameters are the most effective variables for reservoir volume fluctuation and measured in the field conditions and, therefore, are used in this work.

Based on these data both model development and validations are performed. Therefore, the first 3015 daily data are used for training the model, and the remaining 1004 daily data are used to test the model. Table 1 gives the statistical parameters of the used data set during the study period. In Table 1, x_{max}, x_{min}, and x_{avg} represent the maximum, minimum, and average values of the parameters within the time period, respectively. The values of s_x and c_{sx} are standard deviation and skewness coefficients respectively.

Table 1. Statistical summaries of all data of Yarseli Dam

Data	Statistical Parameters	**R** (mm)	**IR** (10^3m^3)	**E** (10^3m^3)	**SP** (10^3m^3)	**IRGW** (10^3m^3)	**CVO** (10^3m^3)
1	2	3	4	4	5	6	7
Whole Data	x_{max}	177	11883.0	50.00	9777.00	985.00	57104.0
	x_{min}	0.0	-2935.0	0.00	0.00	0.00	4960.0
	x_{avg}	2.11	167.56	9.87	10.87	132.46	26549.69
	s_x	7.96	346.00	12.21	163.39	199.15	17690.9
	c_{sx}	7.45	11.85	0.92	53.54	1.23	0.34

R: Average Daily Precipitation; **IR**: Total Daily inflow river water; ;**E**: Total Daily Evaporation **SP**: Total Daily Volume Released from Spillway; **IRGW**: Total Daily Irrigation Volume; **CVO**: Total Daily Reservoir Volume.

Since the range of the variables is large, all the variables were normalized between 0.1 and 0.9 using the Equation 2 before training and testing phases.

$$x_{min} = 0.1 + 0.8\left(\frac{x_i - x_{min}}{x_{max} - x_{min}}\right) \quad (1)$$

Fig.1 The location of Yarseli dam in Turkey.

Fig.2 General view of Yarseli dam

3. APPLICATION AND RESULTS

MLR Results

Conventional multiple linear regression (MLR) technique were also used to define reservoir volume. These techniques assume a linear relationship among variables. Although a nonlinear approach is needed for the solution of reservoir volume problem, a multi linear regression model was compared with field measurement and ANFIS model results. The MLR predicted and observed volumes are given for testing periods in Fig.3. A statistical analysis is performed between the estimated and the recorded test data to find out how well the ANFIS models perform. Performance evaluation measures, the mean square error

(MSE) and the coefficient of correlation (R) between estimated and observed volume values of this statistical analysis are given Table 2. It can be seen from Fig.3 and Table.2 that MLR performance for testing and training stages is not quite satisfactory although the performance criteria have moderate values. The model estimates were quite scattered. The correlation coefficient between the predicted and the observed testing data is 0.74. The general shape of the recorded reservoir volume is not captured by MLR.

Table.2 Performance of different methods in terms of MSE, MAE and R

Method	**MLR**	**ANFIS**
MSE (Test)	0.043	0.032
MAE (Test)	0.170	0.130
R (Test)	**0.74**	**0.83**

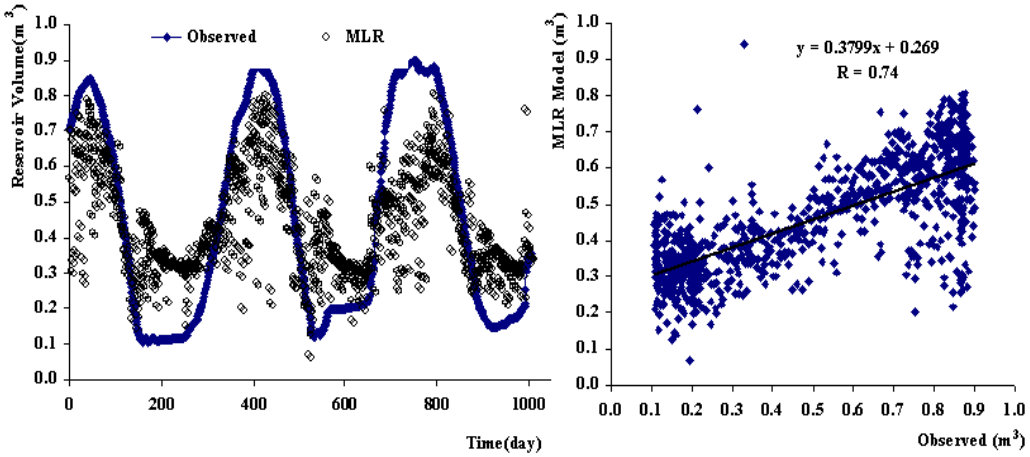

Fig 3. *Observed and MLR model predicted reservoir volumes for Yarseli Dam in the test period*

ANFIS Results

The back-propagation ANFIS network was applied in MATLAB code for forecasting reservoir volumes using the recorded aforementioned daily reservoir data. The testing statistics of ANFIS models in term of R, MAE and MSE are presented in Table 2. The results show that low MSE, MAE and high correlation coefficients (0.032 and 0.130 respectively) can be obtained using ANFIS. Fig. 4 shows model performance of the ANFIS. As it is seen Fig.4, ANFIS model performs better than the other MLR model in terms of the R in the test period. ANFIS model has also less scattered predictions than the other models and provided the highest R coefficient (0.83) for the input combination.

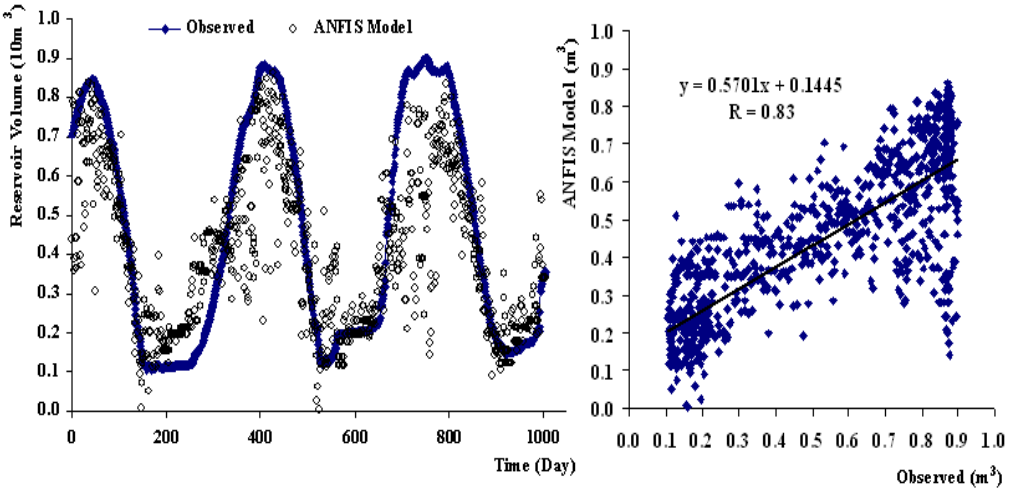

Fig 4. Observed and ANFIS model predicted reservoir volumes for Yarseli Dam in the test period

4. CONCLUSIONS

In this study, Yarseli dam reservoir volumes are predicted based on several parameters: the rainfall, the inflow river volume the spillways discharge, the irrigation, and the evaporation. The monthly reservoir volume estimations can be quite informative for the determination of the periodic water supply strategies, the hydroelectric energy computations and the flood management studies. ANFIS and MLR model used to estimate the dam reservoir volume. As a result of the study in this paper it is possible to derive the following conclusions.

- The presented ANFIS provides better estimates of the dam reservoir volume fluctuations than the conventional MLR model.

- MLR model describes empirical relations, but could not reach the desired accuracy in the same problem due to nonlinearity in the density flow behavior.

- Once an ANFIS model is developed for a specific region, the model can be quite helpful in the water resources management studies. The daily reservoir volume fluctuation prediction can be quite informative for the determination of the periodic water supply strategies, the hydroelectric energy computations and water resources management.

REFERENCES

[1]. J.S.R. Jang, C.T. Sun, and E. Mizutani, Neurofuzzy and Soft Computing: A Computa-tional Approach to Learning and Machine Intelligence. Prentice-Hall, New Jersey, 1997.
[2]. E.H. Mamdani, and S. Assilian, “An experiment in linguistic synthesis with a fuzzy logic controller”. International Journal of Man Machine Studies, 1–13, 1975, 7.
[3]. T. Takagi, and M. Sugeno, “Fuzzy identification of systems and its application to modeling and control”. IEEE Transactions on System, Man and Cybernetics, 116–132, 1985, vol. 15.
[4]. M.E. Keskin, O. Terzi, and D. Taylan, “Fuzzy logic model approaches to daily pan evaporation estimation in Western Turkey”. Hydrological Sciences Journal, 1001–1010, 2004,vol. 49.
[5]. M.H. Kazeminezhad, A. Etemad-shahidi, and S.J. Mousavi, “Application of fuzzy inference system in the prediction of wave parameters”. Ocean Engineering, 1709–1725, 2005 vol. 32.
[6]. O. Kisi, “Daily pan evaporation modeling using a neuro-fuzzy computing technique”. Journal of Hydrology , 636–646, 2006, vol. 329.
[7]. O. Kisi, and O. Ozturk, “Adaptive neurofuzzy computing technique for evapo-transpiration estimation”. Journal of Irrigation and Drainage Engineering, 368–379 , 2007, vol.133 .
[8]. A. Demirci, and A. Baltacı, ”Prediction of suspended sediment in river using fuzzy logic and multilinear regression approaches”. Neural Computing and Applications, 145-151, 2013, vol.23.
[9]. F. Üneş, “Dam reservoir level modelıng by neural network approach. A case study”. Neural Network World, 461-474, 2010a, vol. 4.
[10]. F. Üneş, ”Prediction of density flow plunging depth in dam reservoir: An artificial neural network approach”, Clean - Soil, Air, Water, 296 – 308, 2010b, vol.38.
[11]. F. Üneş, M. Demirci, and Ö. Kişi, “Prediction of millers ferry dam reservoir level in usa using artificial neural network” Periodica Polytechnica Civil Engineering, 309–318,2015a, vol.59.
[12]. F. Üneş, and M. Demirci, “Generalized Regression Neural Networks For Reservoir Level Modeling”, International Journal of Advanced Computational Engineering and Networking , 81-84, 2015b, vol. 3.

[13].J. Shiri, and O. Kisi, "Comparison of genetic programming with neuro-fuzzy systems for predicting short-term water table depth fluctuations. Computers & Geosciences. 1692-1701, 2011, vol.37.

Estimation of Dam Evaporation Level With Artificial Neural Network Method

Fatih Unes[1], *Mustafa Demirci*[1], *Koray Mazmancı*[1]

Abstract

Reservoir plays a vital function at various times and for different purposes such as the analysis and design of several water resources projects such dam construction, irrigation needs and flood control. Prediction of dam reservoir evaporation level is also important for operation, design of dam structure. In the present study, prediction of dam reservoir evaporation level is investigated using Artificial Neural Networks (ANN) method. Feasibility of ANN is evaluated using dam reservoir daily amount of evaporation data. The data was collected on daily basis measurements over 1095 days at the Çatalan Dam in the Mediterranean region of Turkey. A multi layer perception (MLP) is used as the ANN structure. The technique updates the weight and bias values according to Levenberg-Marquardt optimization. ANN results are compared with conventional multi-linear regression (MLR), and autoregressive (AR(p)) model. The models are analysed with statistics and graphs results. The results show that ANN model solution for dam reservoir level fluctuations can provide better performance prediction compared to those of the conventional statistical method.

***Keywords: Artificial** Neural Networks, Dam Reservoir, Evaporation, Regression, Prediction, Model*

1. INTRODUCTION

Reservoir is a physical structure such as pond or lake either natural or artificially developed to impound and regulate the water. It has been used as one of the structural approaches for flood defence and water storage. During both flood and drought situations, decision to open or close water gate is a critical action that need to be undertaken by dam operator as late decision will not only cause flood downstream but also will damage dam structure. The use of forecasting and warning system might improve the dam operation and decision. The modeling experience in using ANN for evaporation estimation is still limited in comparison with a wider application in other fields such as flood forecasting, reservoir inflow forecasting, rainfall-runoff forecasting, and water quality forecasting [1-5]. Dibike and Solomatine[6] forecasted river flow using Multi Perceptron Network (MLP) & Radial Basis Function Network (RBF) Coulibaly et al. [7] studied multivariate reservoir inflow forecasting using neural network. Coulibaly et al. [8] predicted daily reservoir Inflow using neural network. Chang and Chang [9] estimated reservoir water level using Adaptive Based Fuzzy Inference System (ANFIS) Lobbrecht and Solomatine [10] controlled the polder water levels using ANN and ANFIS.

In the present study, prediction of dam reservoir evaporation level is investigated using Artificial Neural Networks (ANN) method. Feasibility of ANN is evaluated using dam reservoir daily amount of evaporation data. The data was collected on daily basis measurements over 1095 days at the Çatalan Dam in the Mediterranean region of Turkey. ANN results are compared with conventional multi-linear regression (MLR) model.

2. ARTIFICIAL NEURAL NETWORKS MODEL (ANN)

The artificial neural network consists of nodes, also known as processing elements, which are distributed in the layers of the network by connections known as weights. All the processing nodes are arranged into layers, and each layer is fully interconnected to the following layer. There is no interconnection between the nodes of the same layer. In the model, there is an input layer that acts as a distribution structure for the meteorological data being presented to the network. After this layer, one processing layer follow, called the hidden layer. This type of ANN is called multilayer perceptron (MLP) [11]. In this study a multi layer perception (MLP) is used as the ANN structure. The technique updates the weight and bias values according to Levenberg-Marquardt optimization. In the executing of an ANN, the observed data set are divided into two groups as the training and testing data. Multilayer perceptrons (MLP) are feed-forward networks with one hidden layer and back-propagation algorithm (BPA) (see Fig. 2). The inputs used in this study are monthly evaporation reservoir level recorded at lag time (E_{t-1}. . . E_{t-6}). Fig. 2 shows the structure of the ANN model, which is adopted in this study.

[1] *Corresponding author: Iskenderun Technical University, Department of Civl Engineering, 31200, İskenderun//Hatay, Turkey.* *fatih.unes@iste.edu.tr ; mustafa.demirci@iste.edu.tr;*

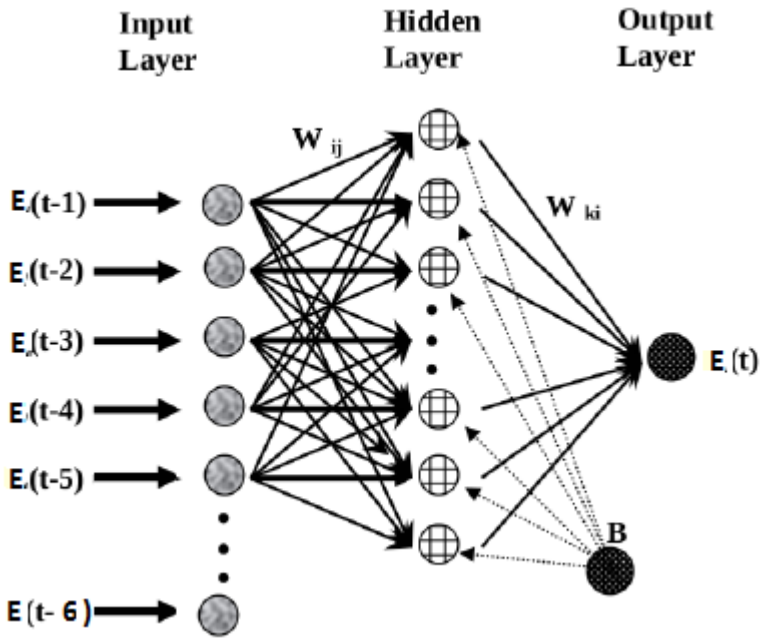

Fig. 1.Structure of ANN model

3. CASE STUDY: ÇATALAN DAM RESERVOIR

Çatalan Dam is an embankment dam on the Seyhan River dam in Adana Province, Turkey. It is 22 km (14 mi) north of the city of Adana. Constructed between 1982 and 1997, the development was backed by the Turkish State Hydraulic Works. Reservoir area at normal water surface elevation is 82 km^2. Çatalan Dam is an earth-fill dam and its drainage basin area is about 224 km^2. Maximum volume of reservoir is almost 14,5 million m^3 and height of the dam (from the river bed) is 70 m. Location of Çatalan Dam in Turkey and the map of Çatalan Dam map are presented in Fig. 2a, b

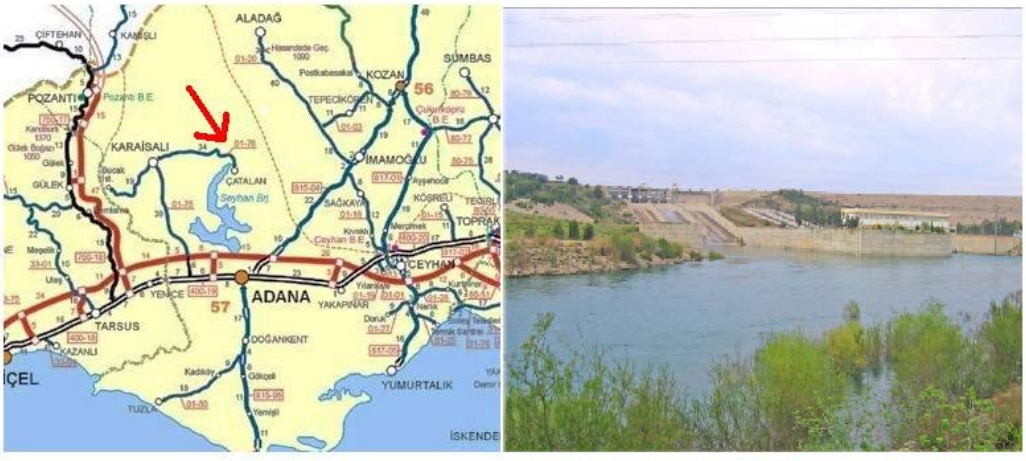

Fig. 2 a) Location of Çatalan Dam in Turkey; b) Çatalan Dam

Table 1. Comparison of models with MSE, MAE and R for testing period.

Models	Input Combinations	MSE (m)	MAE (m)	R^2
MLR	**E- 1,2,3,4,5,6**	**31,278x10^8**	**33700**	**0,81**
ANN	**E- 1,2,3,4,5,6**	**31,589 x10^8**	**34712**	**0,84**

E: Total Evoparition; MSE :Mean square error ; MAE: Mean absolute error R; Determination coefficient

4.PREDICTION OF ÇATALAN DAM EVAPORATION LEVEL FLUCTUATION

The data was collected on daily basis measurements over 1095 days at the Çatalan Dam in the south of Turkey. 739 of 1095 data are used for the training,356 data are divided for testing. A multi layer perception (MLP) is used as the ANN structure. Bayesian regularization technique is used in the training of the network. Bayesian regularization technique is used in the training of the network. The technique updates the weight and bias values according to Levenberg-Marquardt optimization. In all MLP models simulations during the training and testing stages, after trying various MLP structure, a network structure is taken with one hidden layer having four nodes and one output neuron. Tab. I. shows the MSE, MAE and coefficient of determination (R^2) for testing period and each combination. As seen from Tab.1, MLR model has the highest MSE (31,278x10^8*m*); MAE (33700*m*) and the smallest R^2(0.81) for input combination. ANN model has the smallest MSE (31,589 x10^8*m*); MAE (34712*m*) and the smallest R^2(0.84) for input combination. Distribution and scatter plots of MLR results are shown for testing data in Figs. 3 and Fig. 4. Estimated ANN testing results are shown in Figs. 5 and Fig. 6 as, respectively, the distribution and scatter plots. The correlation coefficient was obtained as R^2 = 0.84. The ANN estimated values are observed in the test phase and give better results than the MLR values.

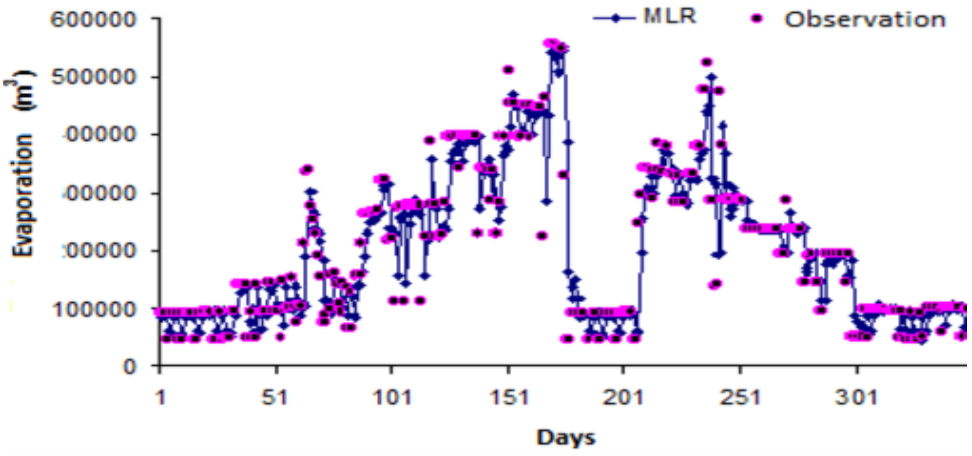

Fig 3. Observed and MLR distribution graph for Çatalan Dam in the test period

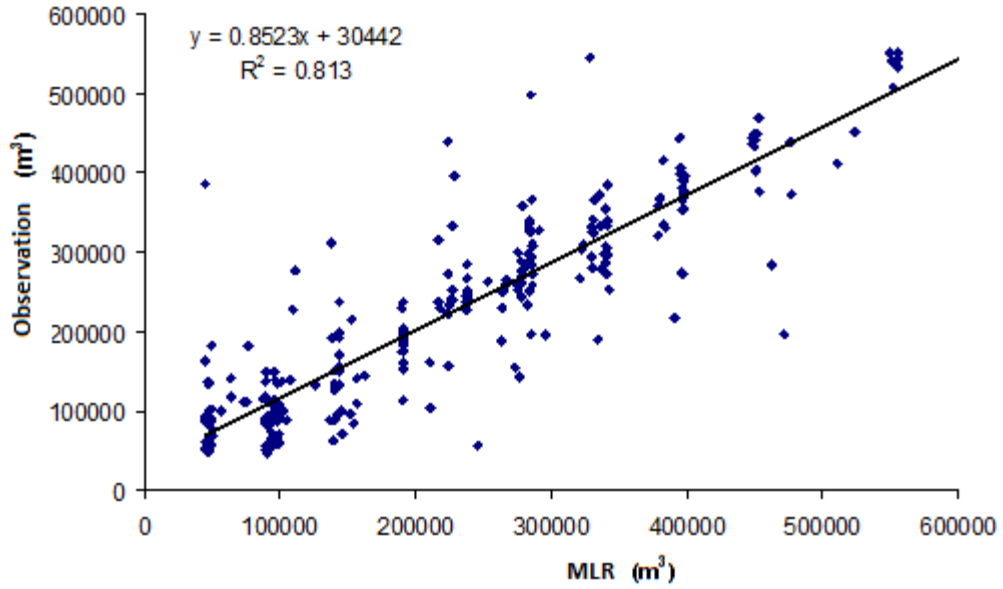

Fig 4. Observed and MLR scatter graph for the testing data

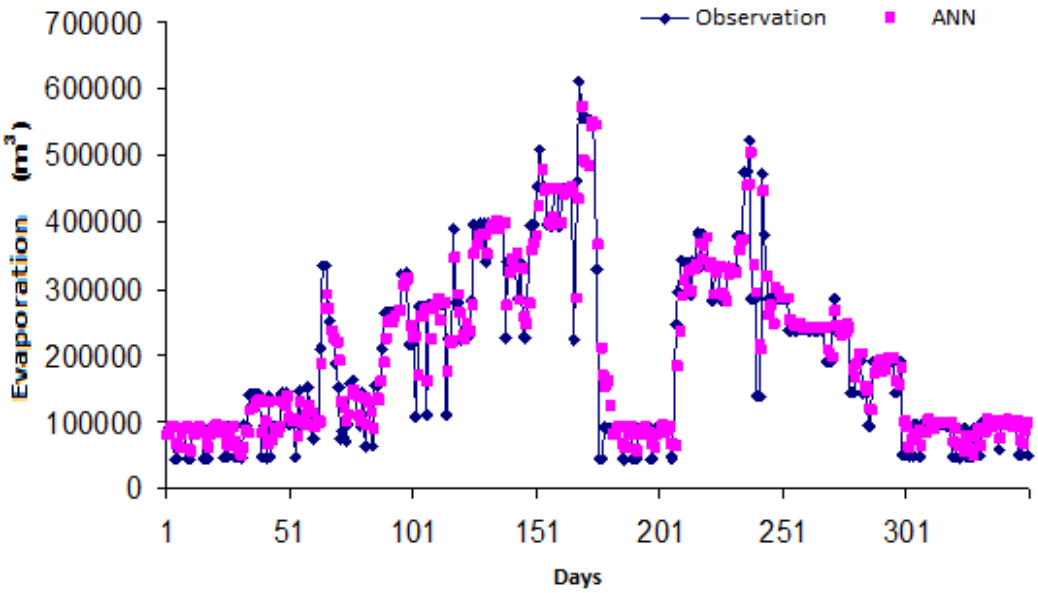

Fig 5. Observed and ANN distribution graph for Çatalan Dam in the test period

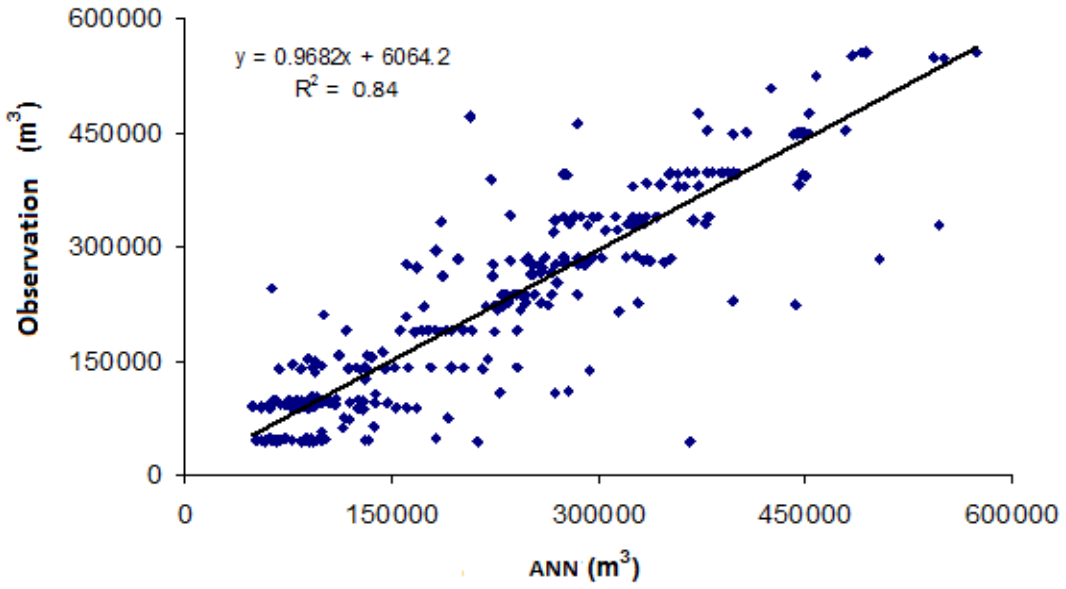

Fig 6. Observed and ANN scatter graph for the testing data

5.CONCLUSION

Artificial neural network and multi linear regression models for estimation of reservoir evaporation has been implemented in this paper. The study demonstrated the accuracy of the Artificial Neural Network technique (ANN) for evaporation modeling compared with MLR model using the Çatalan Reservoir as a test case.

The presented ANN model provides better estimates of the reservoir evaporation fluctuations than the MLR model. The multi-linear regression model (MLR), can provide a good prediction with the smallest mean square error (MSE), mean absolute error (MAE) for reservoir evaporation levels. However, ANN performance is preferably better than MLR model.

If an ANN model is developed for a specific region, the model can be quite helpful in water resources management studies. Monthly reservoir evaporation level estimations can be quite informative for the determination of the periodic water supply strategies, the hydroelectric energy computations and the food management studies.

REFERENCES

[1]. J.A. Ahmed, A.K. Sarma. "Artificial neural network model for synthetic stream flow generation". *Res. Water Manage*. vol 21: pp. 1015-1029, 2009
[2]. D.T. Han, L.0.S Kwong. "Uncertainties in real-time flood forecasting with neural networks". *Hydrolog.Process* :pp. 223-228, 2007
[3]. M. Singh, B. Datta. Artificial neural net work modeling for identification of unknown pollution sources in ground water with partially missing concentration observation data. *Water Res. Manage*, ;vol. 21:pp. 557-572. 2007
[4] K. Hsu , H.V. Gupta, S. Sorooshian, "Artificial neural network modeling of the rainfallrunoff process". *Water Resour. Res, vol.* 31(10), pp.59-169. 1995
[5] C.E. Imrie, S. Durucan, A Korre. "River flow prediction using neural networks: Generalization beyond the calibration range," *J. Hydrol. Eng*, vol. 233(3-4), pp. 138-154, 2000
[6] Y. B. Dibike, D. P Solomatine,. "River flow forecasting using artificial neural networks," *Physics and Chemistry of the Earth, Part B: Hydrology, Oceans and Atmosphere* vol. 26(1), pp. 1-7, 2001
[7] P. Coulibaly, F. Anctil,, B. Bobee, "Daily reservoir inflow forecasting using artificial neural networks with stopped training approach". *Journal of Hydrology* , vol. 230, pp. 244– 257, 2000.
[8] P. Coulibaly, F. Anctil,, B. Bobee,. "Multivariate Reservoir Inflow Forecasting using Temporal Neural Networks". *Journal of Hydrologic Engineering*. vol. 6(5), pp. 367-376, 2001.
[9] F.J., Chang, Y.T. Chang, "Adaptive neuro- fuzzy inference system for prediction of water level in reservoir". *Advances in Water Resources*, vol. 29, pp. 1-10, 2006.
[10] A.H. Lobbrecht, D.P. Solomatine,. "Control of water levels in polder areas using neural networks and fuzzy adaptive systems". Water Industry Systems: Modelling and Optimization Applications, vol. 1, pp: 509- 518, 1999.
[11] L.V. Fausset, "Fundamentals of Neural Networks: Architectures", Algorithms and
Applications. Upper Saddle River, NJ: Prentice Hall; 1994.

ICENS
INTERNATIONAL CONFERENCE ON ENGINEERING AND NATURAL SCIENCES
24-28 May 2016 /Sarajevo

Ottoman Cultural Heritages in Bursa: Structural Determination of Historical Minarets

Ramazan Livaoglu[1], Cavit Serhatoglu[2]

Abstract

The minarets were built in various forms by different civilizations throughout the history. In the Ottoman Period, geometric forms and construction techniques of these structures were progressively changed and improved. Therefore, the minarets were became indispensable components of a mosque as both symbol indicating the location of the mosque and the support member to the main building wall in the residential area of the Ottoman Empire. One of the area is Bursa, in which many examples of Ottoman architecture are seen due to the empire's first capital and reigned throughout six century. Thus, the minarets of the city have various geometric properties and construction techniques. The boot of each minaret was built using different cross-section, height, wall thickness, material properties and boundary conditions within the body wall. The shaft of the minarets were also design different heights and cross-sections as cylindrical. Even so, the components of the minarets were constructed with the specific sizes ratio between cross-sections and heights. However, some of these minarets experienced damage due to 1855 Bursa earthquakes and were repaired or reconstructed with altered sizes. In this study, the current rates are presented for the minarets. The construction techniques of boot, stairs and shaft of the minarets are also explained. Furthermore; common damage examples of the minarets are shown because of the earthquakes and storm.

Keywords: *Construction Techniques, Geometric Form, Historical Ottoman Minaret*

1.INTRODUCTION

Humans have built private structures such as church, synagogues for religion and beliefs since the past. Muslims have also adopted to mosques as a place of worship. Seeing mosque, one of the remarkable structure elements is minaret. The minarets is a historically used to recite the Adan, call for prayer [1]. These structures, had to different structural properties, are similar to tower structures. There are many reasons for these differences such as material resources of the region, architectural and engineering skills of the nations. The architecture and construction techniques of the minarets were considerably improved during the Seljuk and Ottoman State period. These techniques and architectural forms were used in many regions of the world and Anatolia while the minarets were built in the past.

Investigations about the ottoman minarets or historical minarets are seldom in the literature. Dogangun et al (2007) review the construction practices for historical and new masonry minarets in Turkey and discuss the seismic damage observed in those structures [2]. Ertek et al (2007) was also investigated to structural system of Ottoman minarets and submitted method of analysis. Four type model were occur by using finite element method and the results of analysis were compared with each other [3]. Another research is the seismic assessment of the Qutb Minar in Delhi, India [4]. After modal parameters of the minaret was determined from modal test; eigenvalue, seismic analyses were performed by using the finite element models by Peña at al (2010). Oliveira et al. (2012) carried out comprehensive study about historical minaret [5]. They performed ambient vibration tests to determine the dynamic characteristics of seven minarets with heights ranging from 23 to 67 m in Turkish city of Istanbul. The numerical models were constructed using surveyed geometric properties of the minarets and local ground conditions. Calibrated numerical models were used in earthquake analyses of these minarets. On the other hand, Hejazi at al (2015) studied the structural behavior of nine historical brick masonry minarets in Isfahan against weight, temperature, wind, and earthquakes [6].

The historical Turkish minarets generally have cylindrical and slender shafts in the Seljuk and Ottoman period. It is considered that these geometrical forms were get inspired from watchtower in Central Asia. Ottoman minarets can be evaluated dividing into three main periods. The early Ottoman period, is time interval from establishment of state until the conquest of Istanbul, is transition period from Seljuk minarets to Ottoman minarets. In this period, the shaft components of minarets were preferred thinner than Seljuk minarets and transition segments was used between boot and shaft component. However, the number and location of the minarets uncertain. They were constructed mostly adjacent to or next to the mosques. The classical Ottoman period was continued from the conquest to approximate 17th century. The most prominent architect of the period is Architect Sinan. After the start of the period, minarets were became indispensable components of a mosque as both symbol indicating the location of the mosque and the support member to the main building wall in the residential area of the Ottoman Empire. In the final period, it can be said that design of Turkish minaret is affected from the western architecture.

This study contains to minarets of the early and classical Ottoman period in Bursa (see Figure 1), where many examples of Ottoman architecture are seen due to the empire's first capital and reigned throughout six century. Today partially protected historical silhouette in Bursa appears as a living museum. The minarets that rise within the skyline of this historic city are

[1] *Corresponding author: Uludag University, Department of Civil Engineering, 16059, Nilüfer/Bursa, Turkey. rliva@uludag.edu.tr*

[2] *Uludag University, Department of Civil Engineering, 16059, Nilüfer/Bursa, Turkey. cserhatoglu@uludag.edu.tr*

undoubtedly a signature of past. However, the general area is located in an active seismic region. For the city, the most devastating earthquake occurred in 1855. This disaster has caused the destruction or damage of most of the minarets. Thus, some of these minarets and were repaired or reconstructed with altered sizes to be behaved more resistant. In this investigation, we target to reveal the specific sizes ratio between cross-sections and heights of some minarets in Bursa. In addition, it was explained that what type of damage may occur in the historical minarets.

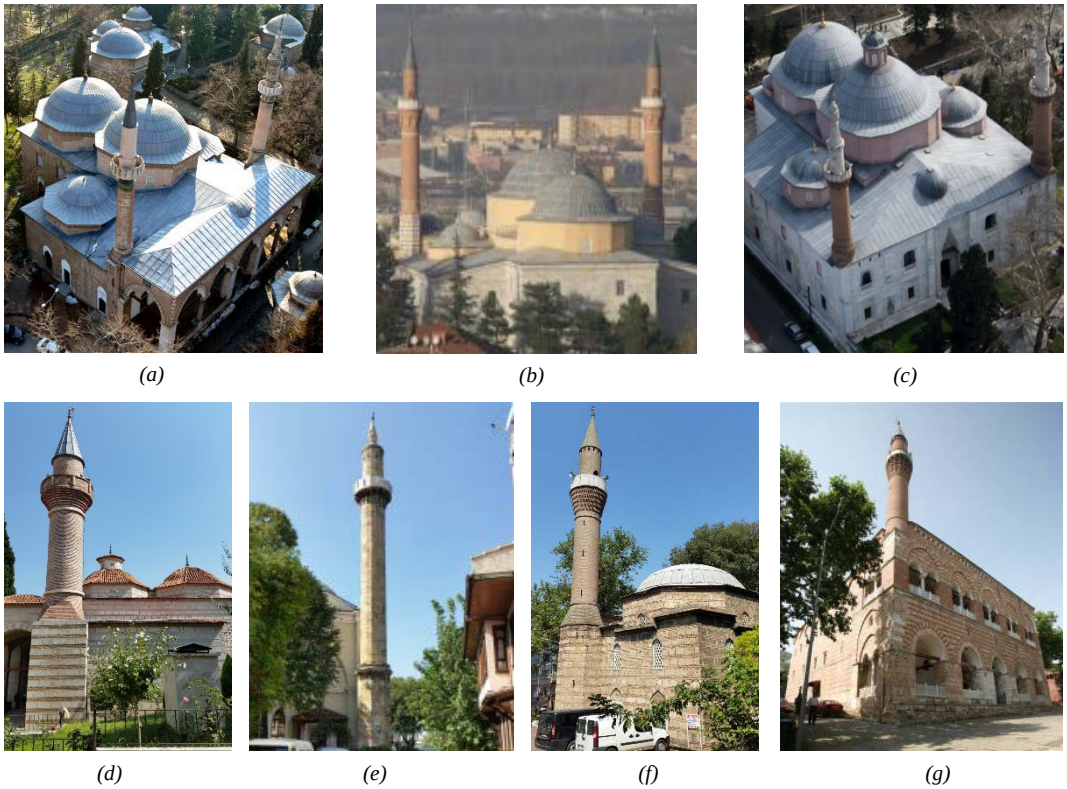

(a) *(b)* *(c)*

(d) *(e)* *(f)* *(g)*

Figure 1. (a) Minarets of Muradiye Mosque (b) Minarets of Yıldırım Beyazıt Mosque (c) Minarets of Yeşil Mosque (d) Minaret of Ali Paşa Mosque (e) Minaret of Şehadet Mosque (f) Minaret of Altıparmak Mosque (g) Minaret of 1. Murat Mosque

2.COMPONENTS AND CONSTRUCTION TECHNIQUES OF OTTOMAN MINARET

Ottoman minarets can be describe with nine structural elements or components as shown figure 2.

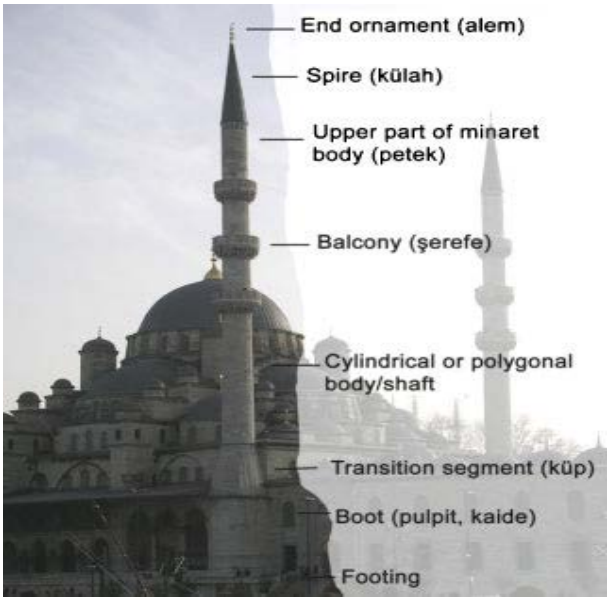

Figure 2. The Components of Ottoman minaret [5]

Footing: The part, provides the link between the structure and the ground. It could be built using stones and timbers.

Boot (Pulpit): It, could be design separate or adjacent from the main wall of mosque, the first part on the ground. In Bursa, the component was generally constructed using stone or stone+brick material as square, hexagon and octagonal plan. It was sometimes utilized to the main building wall as the support member.

Transition segment: This component obtains cross-section transition between the boot and body/shaft. It may be the different geometrical forms.

Body/Shaft: The section is the most slender and the longest component of the minaret. It is usually built using brick+khorassan mortar as cylindrical or polygonal in the early ottoman period. Rarely, limestone body/shaft may be seen such as minarets of Emir Sultan and Şehadet Mosque in Bursa.

Balcony: The component, built gradually expanding body wall, is console structure element. It was used to call for prayer reciting the Adan at a certain height. While minarets of early Ottoman period have usually one balcony, minarets of classical Ottoman period may have one, two or three balcony.

Stairs: The structural elements were built using stone or stone+brick material as helical, in order to reach to balcony at the certain height. Each step of the component was usually occurred from 90-120-150-degree slice.

Upper part of minaret body: It is cylindrical or polygonal wall element between balcony and spire. The component fixed to console balcony from the upper surface due to the self-weight. It is usually built using same material with material body/shaft.

Spire: Purpose of this component protect to inside of minaret from rainwater and snow. It was constructed using lead and timber or same material with upper part of minaret body in the era ottoman period. This part may have different shapes such as conical, dome.

End Ornament: It is the top component of the minaret. This element, was generally produced using copper material, is Islamic symbol.

Structural elements of the minaret was generally constructed using brick, khorassan mortar and limestone (küfeki) in the early Ottoman period. However, lateral resistances of these minarets are weak against earthquake and wind loads due to low tensile behavior. In order to reinforce to tensile strength of structural elements, a special technique was started to be used for linking adjacent stone blocks with iron pieces and clamps in the vertical and horizontal directions as shown in figure 3, [2]. It is considered that application of the technique begun for the minarets in the classical Ottoman period. Example of the application is seen on the repaired minarets after 1855 earthquake in Bursa.

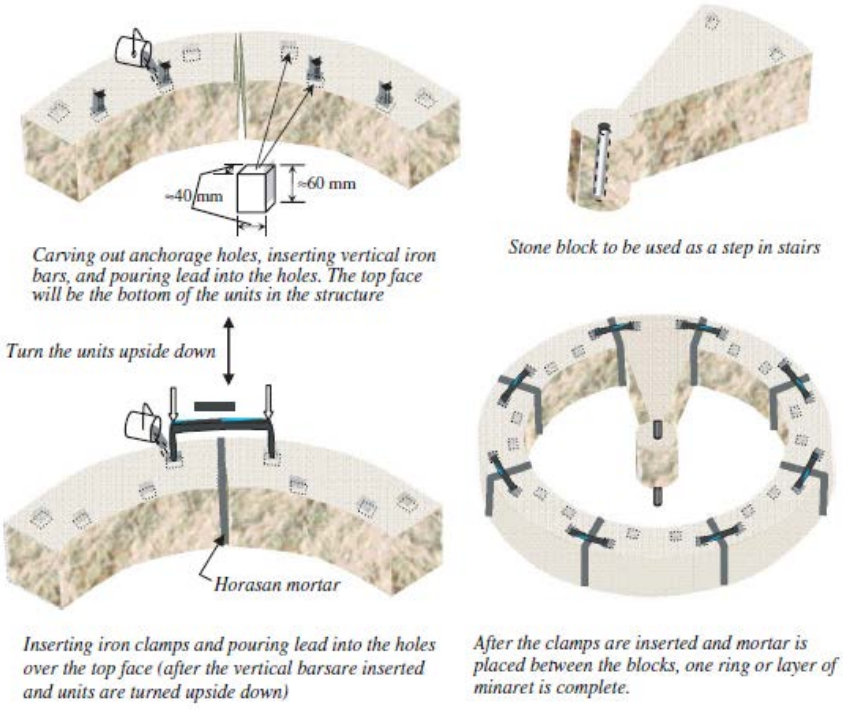

Figure 3. Schematic illustration of the construction of Ottoman minarets using stone blocks reinforced and anchored with iron bars and clamps [2]

3.THE SPECIFIC SIZES RATIO OF BURSA MINARET

The Ottoman wanted to create composition between the mosque and minaret in particularly classical Ottoman period. So, they determined specific design standards. For example, the balcony level of minaret could not higher than end ornament (alem) of mosque dome. In addition, component dimensions of Ottoman minarets were determine identifying specific ratio, so as to build a stable structure. The most critical and effective component of Ottoman minarets are Body/shaft. Thus, correct selection of dimensions of the component were important in ottoman period. In this study, the relationships were investigated between body sizes of twenty one Ottoman minarets in Bursa. However, since some of the minarets were destroyed by the earthquake in 1855, these minarets could be rebuilt different from the original size. Thus, the assessments were carried out using the present dimensions. Firstly, three relationships were occurred. These is:

(a) Thickness of body wall (t) - height of body (h_2)

(b) Thickness of body wall (t) - Height of transition segment (h_1)+ body (h_2)+ upper part of minaret body (h_3)

(c) Height of body (h_2) - Height of transition segment (h_1)+ body (h_2)+ upper part of minaret body (h_3)

Secondly, linear regression analysis were performed for the relationships (see Figure 4, 5, 6). Lastly, the arithmetic average values of ratio of the relationships were determined in the study. These rates are stated in below.

- Avg[h_2/t]=0,035876
- Avg[(h_1+h_2+h_3)/t]=0,02265
- Avg[h_2/(h_1+h_2+h_3)]= 0,63742

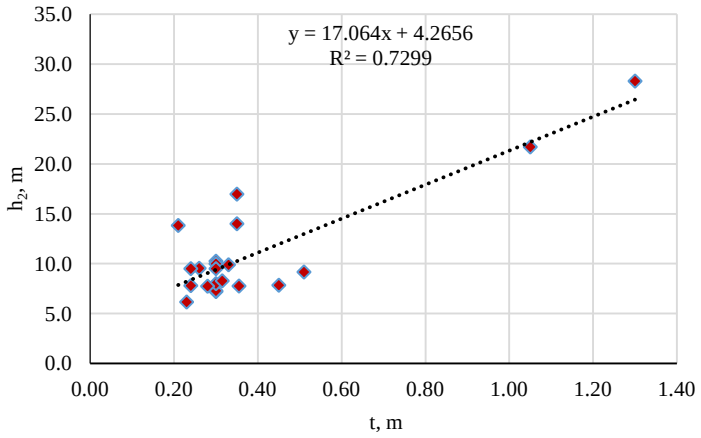

Figure 4. The relationship and results of the linear regression between t and h_2

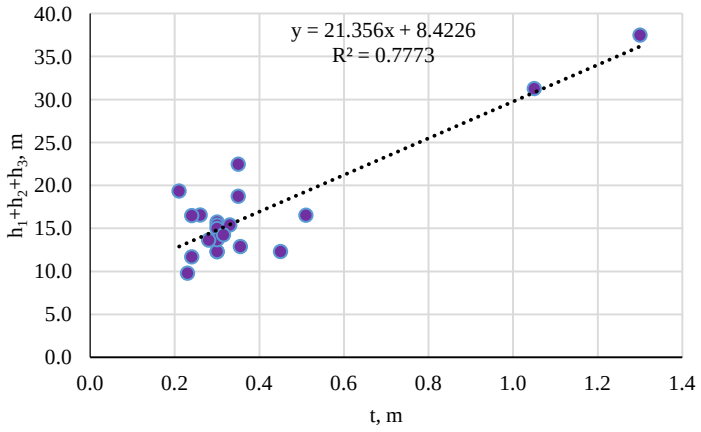

Figure 5. The relationship and results of the linear regression between t and h_1+h_2+h_3

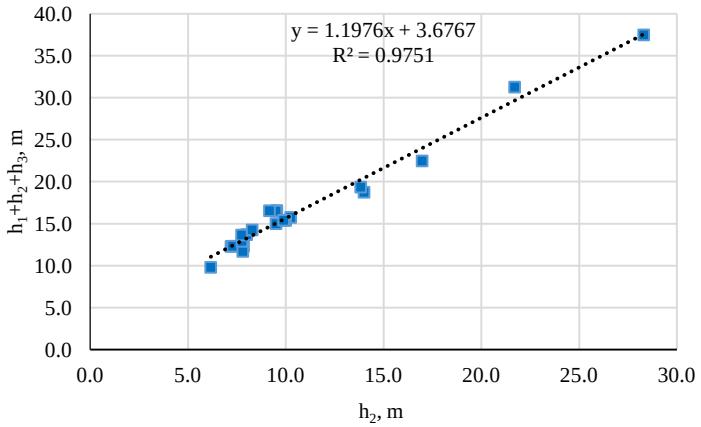

Figure 6. The relationship and results of the linear regression between h_2 and $h_1+h_2+h_3$

4.THE DAMAGE TYPES OF OTTOMAN MINARET

The ottoman minarets are tall and slender structures. Beside, tension and bending strength of minaret elements are low. The most critical sections of the minaret is usually between body and transient segment or upper body component, because cross-section and/or used material change in these areas of the minaret. Thus, the damages may occur in these sections of the minarets due to strong external loads such as earthquakes and storms (see figure 7).

(a) *(b)* *(c)*

(d) *(e)* *(f)*

Figure 7. (a) Collapsed minaret due to the storm, Konya/Bozkır, 2010, [7] (b) Collapsed minaret of Elmacık Mosque due to the storm, Elmacık/Aksaray,2013, [8] (c) Damaged minarets of Van Yolu Mosque due to the earthquake , Erciş/Van, 2011, [9] (d) Damaged minaret of Nasuh Ağa Mosque due to the earthquake, Simav/Kütahya,2009,[10] (e) Damaged minaret of Balaban Paşa Mosque due to the storm, Aliağa/İzmir,2015, [11] (f) Damaged minaret of Yavuz Sultan Selim Mosque due to the thunderbolt, Kilis, 2016, [12]

The historical minarets may be exposed to uncommon other damage types. For example, foundation of the minaret can be rotate and kocal axis of the minaret can be change due to soil problems (Figure 8a) or the minaret may be damaged from the fire (Figure 8b).

(a) (b)

Figure 8. (a) Minaret of Sultan Alaaddin Mosque, Eskişehir (b) Minaret of *Şeyh Hacı Ahmet Mosque, Yozgat, 2015, [13]*

5.CONCLUSIONS

This study is composed from three main research topics. Firstly, the construction techniques and components of Ottoman minarets were described. The techniques were improved in classical Ottoman period. After the starting of period, the minarets were generally built adjacent to the main building wall as the support member for the great mosques. Also, components and architectural of Ottoman minarets of the period still are preferred and used today.

Secondly, the relationships were investigated performing linear regression analyzes between component dimensions of twenty one Bursa minarets. As a result of analysis, R-squared of a., b., c. relationships were calculated as 0.7299, 0.7773, and 0.9751 respectively. These values show that there are meaningful specific relations between dimensions of the components. However, if some of the minarets hadn't been rebuilt different from the original sizes after the earthquake in 1855, the relationships could have been more powerful.

Thirdly, the damage types of ottoman minaret were demonstrate in the real life. In the future studies, sizes of the boot of the minarets can be attached to the relationships between dimensions of the components. In addition, to increase the resistance of the minarets against the damages, reinforcement methods can be investigated.

ACKNOWLEDGMENT

The present work is supported by Grant-in-Aid for Research Project (No.KUAP(MH)-2014/48) from the Uludag University, Turkey.

REFERENCES

[1]. Z. Sayar, "Does minaret lose its task ?," *Arkitekt*, No.368, pp. 154-157, 1977. (in Turkish)
[2]. A. Doğangün, H. Sezen, O.İ. Tuluk, R. Livaoğlu and R. Acar "Traditional Turkish masonry monumental structures and their earthquake response." *International Journal of Architectural Heritage*. 1:3: 251-271, 2007
[3]. E. Ertek, Y. Fahjan, "Osmanlı Minarelerinin Yapısal Sistemleri:Sınıflandırma, Modelleme ve Analizi," *Altıncı Ulusal Deprem Mühendisliği Konferansı*, İstanbul, 2007 (in Turkish).
[4]. *F*. Peña, P. B. Lourenço, N. Mendes, and D. V. Oliveira, "Numerical models for the seismic assessment of an old masonry tower," *Engineering Structures*, 32(5), 1466-1478, 2010.
[5]. C. S. Oliveira, E. Çaktı, D. Stengel, and M. Branco, "Minaret behavior under earthquake loading: The case of historical Istanbul," *Earthquake Engineering & Structural Dynamics*, 41(1), 19-39, 2012.
[6]. M. Hejazi, S. M. Moayedian, and Daei, M. "Structural analysis of Persian historical brick masonry minarets," *Journal of Performance of Constructed Facilities*, 04015009,2015.
[7]. (2010) [Online]. Available: http://www.iha.com.tr/haber-ruzgar-minareleri-yikti-109116/
[8]. (2013) [Online]. Available: http://www.iha.com.tr/haber-firtina-minareleri-yikti-267638/
[9]. (2011) [Online]. Available: http://www.haber7.com/guncel/haber/798559-bir-minaresi-dun-bir-minaresi-bugun-yikildi
[10]. (2009) [Online]. Available: http://haberciniz.biz/vakiflar-bolge-mudurlugu-depremde-hasar-goren-minarelerin-restorasyonunu-unuttu-kuta-745989h.htm
[11]. (2015) [Online]. Available: http://m.34volt.com/aliaga-da-695-yillik-cami-minaresi-kulahi-devrildi-haberi-107072/
[12]. (2016) [Online]. Available: http://www.gazetevahdet.com/kiliste-minareye-yildirim-dustu-46048h.htm
[13]. (2016) [Online]. Available: http://www.haberler.com/yozgat-ta-tarihi-seyh-haci-ahmet-efendi-camii-nde-7177322-haberi/

Dynamic Characteristics and Seismic Behavior of Historical Minaret of the Altıparmak Mosque

Cavit Serhatoglu[1], Ramazan Livaoglu[2]

Abstract

There are different procedure on the identification of dynamic characteristics of historical masonry minarets, the most common used procedure and so difficult one is Structural Health Monitoring. After collecting data from this procedure, evaluation of the performances is also complex. Because the historical masonry minarets have complex stiffness, high heterogeneity and shadowy boundary conditions as observational. Thus, ambient vibration test was performed with aim of defining modal parameters of the minaret. In order to achieve the modal analysis-frequency domain, peak-picking method was employed in derivation of modal data. Since the structural behavior of the minaret were also represented with mathematical model, solid model were implemented by using the finite element technique. For the determination of the seismic behavior of the minaret, non-linear static pushover analysis were carried out. As a result of analysis, demand/capacity curve of the minaret were computed and damage mechanism of the structure were investigated. The Altıparmak Mosque of Bursa, which was built in second half of 15th century, is selected as an example to understand of the dynamic performance of historical minarets. The result showed that most critical sections and deviation of the tensile stress value and plasticization level of the region.

Keywords: *Ambient Vibration Test, Historical Masonry Minaret, Modal Analysis, Pushover Analysis, Seismic Assessment*

1.INTRODUCTION

Historical structures are significant heritages because of their link to important periods in the past. Anatolia has a lot of the historical structures from different eras. Most of the historical structures are world heritages in this area. From all this historical structure, one of the most critical structure types is the masonry minaret. The minaret is indispensable part of a mosque, which is a historically used to recite the Adan, call for prayer [1]. Minarets, constructed mostly adjacent to or next to the mosques, are slender tower type structures. Unfortunately, most of the monuments are located in the highly active seismic regions of the Turkey. Therefore, seismic behavior of the historical heritages should be surveyed so as to be preserved from the possible earthquakes. In this study, dynamic parameters and the seismic behavior of minaret of the Altıparmak mosque is investigated in Bursa. The construction of Altıparmak Mosque, one of the primary specimens of Ottoman Period Architecture was completed in 1470. It is estimated that some parts of the mosque and the minarets were destroyed by earthquake in 1855 (Figure 1). Thus, these structural components and the minaret were repaired in 1967. No devastating earthquakes have occurred in the city since 1855 and the city was slightly affected from the recent large earthquakes such as 1999 Kocaeli and Düzce. However, an earthquake that may occur in the both side of the southern and northern Marmara region, which is a high probability, can induce significant damage in the city.

Investigations on the seismic behaviour and dynamic characteristics of the minarets are seldom in the literature. One of them were submitted by Dogangün et al [2]. In this study, in order to investigate the dynamic behavior of historical unreinforced masonry minarets, three representative minarets with 20, 25, and 30m height were modeled and analyzed using two ground motions recorded during the 1999 Kocaeli and Duzce., Turkey earthquakes. Another research is the seismic assessment of the Qutb Minar in Delhi, India [3]. After modal parameters of the minaret was determined from modal test; eigenvalue, seismic analyses were performed by using the finite element models. Three different numerical models were considered to evaluate the structural behavior of the minaret. Oliveira et al. (2012) carried out comprehensive study about historical minaret [4]. They performed ambient vibration tests to determine the dynamic characteristics of seven minarets with heights ranging from 23 to 67 m in Turkish city of Istanbul. The numerical models were constructed using surveyed geometric properties of the minarets and local ground conditions. Calibrated numerical models were used in earthquake analyses of these minarets. Resta at al. (2013) also investigated non-linear finite element analysis of masonry towers by adopting the damage plasticity constitutive model [5]. The damage plasticity constitutive law was adopted in four finite element modelling approaches.

In literature different studies have shown that new and powerful numerical methods have developed for static and dynamic analysis of the old masonry structures. The methods aimed to estimate the structural response the masonry buildings during the earthquake. One of the numerical methods is the finite element method (FEM), enabling to describe different geometrical properties and material modeling. However, using combination of different materials and the complexity of historical structures led engineers to ask for appropriate experimental tools so as to identify the most relevant structural properties, thus obtaining reliable data to support calibration and validation of numerical models [6]. The model updating is carried out thanks to modal analysis.

[1] *Corresponding author: Uludag University, Dept. of Civil Eng, 16059, Nilüfer/Bursa, Turkey. cserhatoglu@uludag.edu.tr*

[2] *Uludag University, Department of Civil Engineering, 16059, Nilüfer/Bursa, Turkey. rliva@uludag.edu.tr*

Modal analysis is the process of identify the specific dynamic characteristics of a structure in forms of natural frequencies, damping ratio, mode shapes, and utilizing them to formulate a mathematical model for determining the dynamic behavior. Modal analysis include both experimental and theoretical techniques in other words, consists of two parts: modal testing and modal modelling. Modal test is an experimental technique. Thanks to the techniques, impulse response function of a linear time-invariant dynamic system can be obtained. The function, which is called Frequency Response Function (FRF) in the modal analysis literature, helps to modal parameter identification. Frequency Response Function has different graphical displays which include different information [7]. Theoretical modal analysis is also based on a physical model of dynamic system comprising its mass, stiffness and damping properties. These properties may be occur in forms of different equations. However, investigated structures or systems may have a lot of unknown equations. Thus, finite element model should be generated by using numerical techniques in order to be solved accurate mathematical model and better understanding the behavior of the systems. Since structural analysis has always been a critical area, modal analysis has become using the inevitable technical in the civil engineering. Many applications are concerned with the estimation of response of a civil structure due to external loadings or ambient vibrations. Soil-structure, tower type structures, bridges and dam-foundation may be given as examples of the applications.

In this study, modal analysis and seismic assessment of the minaret has been performed as stated below by using a stepped strategy.

- **General information,** which include the materials, geometry and position description of the minaret.
- **Modal test,** we performed in situ testing for identification of at least the first six modes and corresponding frequencies in this section.
- **Modal modelling,** where the finite element model was occurred and modal updating was performed for the numerical model.
- **Structural response**, include that to make probability-based seismic assessments, pushover analysis was carried on the model.

2.GENERAL INFORMATION

In the pre-classical Ottoman era, minarets are positioned either away from the main structure of mosque or adjacent to or on top of the main body wall. Particularly in 14-15th century in Bursa, minarets are constructed such that they are positioned at one or both corners of north wall of a mosque. The minaret of the Altıparmak Mosque was also built adjacent to the main body wall by positioned at corner of west wall of the mosque (Figure 1).

Figure 2. Damaged the mosque due to the 1855 earthquake - current repaired the mosque and the location.

2.1.Geometrical Properties

Ottoman minarets have assembly of components as shown in Figure 2. The geometric properties of the components of the historical minarets under investigation are a very difficult task because we don't have existing detailed information and drawings about them. Thus, height and wall thickness of different components, the internal diameter changes throughout the structure, boundary conditions, and staircase details of the minaret were surveyed in situ (see Table 1). It was also examined that during the construction of the minaret, whether different special techniques unlike the common techniques could be used or not.

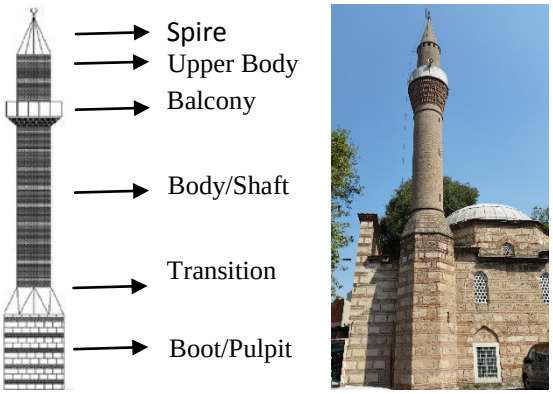

Figure 2. The components of ottoman minarets and Altıparmak minaret

Table 1. Geometric characteristics of the minaret components of Altıparmak Mosque

	Boot Pulpit	Transition Segment	Body Shaft	Upper Body	Spider
Wall Thickness	0.80 m	variable	0.30 m	0.23 m	variable
Outer Diameter	octagonal l=1.21 m	variable	1.85 m	1.70 m	variable
Total Height			25.65		

2.2.Material Properties

The transition segment, body and upper body components of the minaret was made of brick+mortar as masonry. The boot wall and the spire were also built by using brick+mortar and limestone (kufeki).

Strength of the limestone is higher despite lightweight stone. When first extracted, the stone can be cut easily and portable but the strength is low when comparing with the other rock types. As time passes, tensile-compressive stress, modulus of elasticity increase while spaces, water diffusion and permeability decrease in the stone. All these features of the coarse stone, which are similar to concrete properties, are desired behaviors. However, properties of the both material type are quite difficult to estimate, due to the anisotropy and composite of the masonry structure and construction techniques.

It is impossible to carry out intrusive techniques such a flat-jack and a shear-jack test on historical structures because it isn't permission. Therefore, average value of material properties, determined with ultrasound test and laboratory test in the previous studies [8], are given in this study. According to the tests; the limestone of young modulus (E=10000-13000 N/mm^2), bulk density (γ=2.10-2.30 t/m^3) and the brick of young modulus (E=2600-3700 N/mm^2) and bulk density (γ=1.40 t/m^3) were calculated. These values will be helpful so as to check the calibration of the model material properties.

3.MODAL TEST

Modal test is based on the fact that the vibration response of a linear-invariant dynamic system can be described as the linear combination of a set of simple harmonic motions called the natural modes of vibration. This concept is similar to the use of a Fourier combination of sine and cosine waves to represent a complicated waveform. The theoretical foundation of modal testing is secure upon establishing the relationship between the vibration response at one location and excitation at the same or another location as a function of excitation frequency. The complicated mathematical function is called frequency response function. The function is obtained by Fourier transforms of impulse response of the system. Afterwards, the function can be plotted different graphical display such as amplitude-phase plot and log-log plot, real and imaginary plot, nyquist plot, dynamic stiffness plot and etc. Finally, dynamic parameters of the system can be graphically determined.

Modal test can be adopted as both experimental modal analysis and ambient vibration test for identification of modal parameters of civil engineering structures. Though, their large size imposes additional challenges. In particular, the application of a controlled and measurable dynamic excitation requires the use of very heavy and expensive devices. However, in the case of civil engineering structures, Ambient Vibration Tests are much more practical, fast and cheap, since the heavy shakes are replaced by freely available ambient forces, like the wind, tectonic activity or the traffic circulating over or nearby the structure [9]. Ambient vibration test is called natural-excitation, or output-only modal analysis. Ambient vibration test techniques are based on random response that is to say on a stochastic approach. In Ambient vibration test input is assumed to be a Gaussian

white noise, characterized by a flat spectrum in frequency domain. Thus, all modes are assumed to be equally excited in the frequency range of interest and extracted by appropriate procedures.

In this study, Peak-peaking method was used a sub-method of ambient vibration test in frequency domain. The most fundamental method for modal parameter estimation from output-only data is the Basic Frequency Domain (BFD) technique [10]. The name of the method is related to the fact that natural frequencies are determined as the peaks of the power spectral density graphics, obtained by converting the recorded data to the frequency domain by the discrete Fourier transform. In Basic Frequency Domain (BFD), Frequency response spectrum (FRF) and when the input spectrum is assumed to be constant, the output spectrum matrix, which can be defined as follows:

$$[\mathrm{H}(\omega)] = \sum_{k=1}^{n} \left[\frac{[R]_k}{j\omega - \lambda_k} + \frac{[R]_k^*}{j\omega - \lambda_k^*} \right] \tag{1}$$

$$\left[G_{yy}(\omega) \right] = \left[H(\omega) \right]^* \left[G_{xx}(\omega) \right] \left[H(\omega) \right]^T \tag{2}$$

$$\left[G_{yy}(\omega) \right] \approx \sum_{k=1}^{n} \left[\frac{R_k}{j\omega - \lambda_k} + \frac{R_k^*}{j\omega - \lambda_k^*} \right] \tag{3}$$

where *[H(ω)]* is the l x r FRF matrix, $[A]_k$ is the residue matrix, λ_k is the kth eigenvalue, * and T represents complex conjugate and transpose respectively, $G_{yy}[\omega]$ si the *r x r* input PSD matrix, *r* is the number of inputs, $G_{yy}[\omega]$ is the *l x l* output PSD matrix, *l* is the number of outputs.

Ambient vibrations were determined using accelerometers for the minaret (see Figure 3). Since accelerometers are designed for a specific range of sensitivity and of frequency, selection of accelerometers is very important. Two of the four accelerometers were fixed to exterior wall from the level of balcony above 1.50-1.70 m (G3-G4) while the others were fixed to interior wall from level of the balcony beneath 0.50-1.00 m (G1-G2) perpendicular to each other. To convert the digital data to analog signals, Quattro four-channel data acquisition unit was used. The collected signals were transferred from the accelerometer to this unit, where they are formatted by a software, SignalCalc 240 by Dataphysics [11]. Measurements were performed in four different frequency ranges which are 0-10 Hz, 0-25 Hz, 0-50 Hz and 0-100 Hz. Our experience indicates that the lower frequency components (below 1 Hz) of these vibrations are contributed consistently by strong winds. Higher frequencies (above 25 Hz) are considered meaningless given the structure type and the range of frequencies where, modal characteristics of structures are sought. Therefore, the responses were expected at a low pass of 1 Hz and 25 Hz. On the other hand, because the data are obtained from accelerometers which include the unwanted effects like noise, Hamming Windowing Function was used to get more realistic results by removing such effects from the spectrum. Figures 4 shows power spectrum obtained from in-situ ambient test of minarets. The identical modal frequencies were obtained under all test setups which are conducted for different frequency ranges. However, only the results from 25 Hz range-setup are depicted. Furthermore, the values of modal frequencies were measured for the first six modes using these test and the results are given in Table 2. In figure 4, G1-G3 represent to record data in North-South (NS) direction while the others represent to record data in East-West (EW) direction.

Figure 3. The Ambient vibration test set up in the minaret

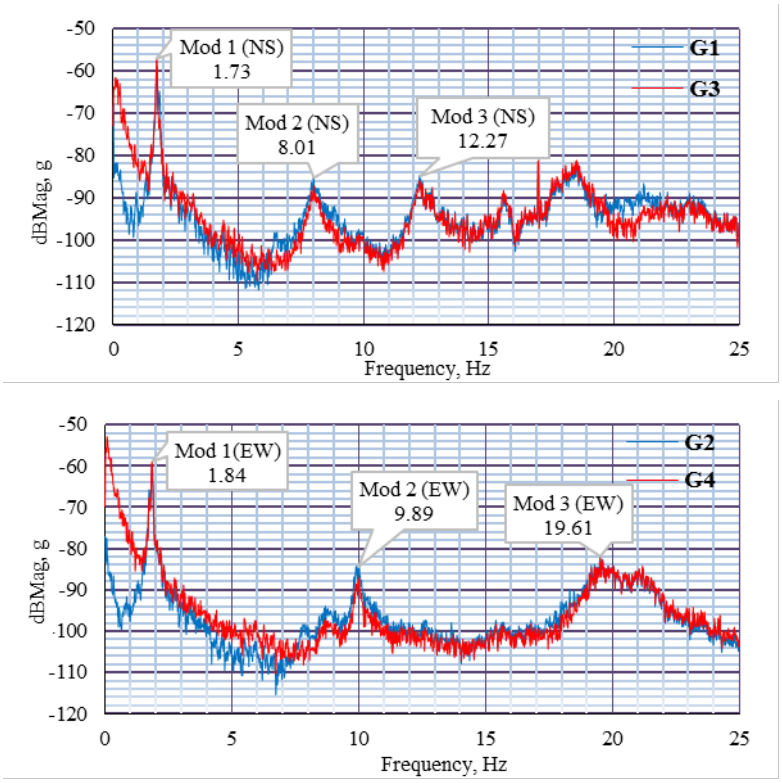

Figure 4. Power spectrum of the measured response for the minaret

4.MATHEMATICAL MODEL AND MODAL ANALYSIS

Many civil engineering problems for which we cannot obtain exact solutions. So as to deal with such problems, we prefer to numerical approximations. However, many applications of structural dynamics and static depend their achievement on having an accurate numerical model for a structural system. Such a model can be derived from the finite element (FE) modelling. Yet, historical structures have complex structural systems, uncertain material properties and boundary conditions. Therefore, modal analysis should be performed on the models of these structures so as to update the models by verifying results of modal test.

In this study, the numerical model was designed for the minaret using finite elements analysis program ABAQUS CAE (v13.1). After the finite element model was prepared using the structural dimensions from in-situ measurement, modal analysis were performed (see Figure 5). The structural elements were occurred with the solid elements having three degrees-of-freedom at every node. Element type was also selected an 8-node linear brick, reduced integration (C3D8R) with a view to obtaining proper and real analysis, although the model was occurred difficult due to a large number of different dimension parts. Linear elastic material was assumed for structural elements of the minaret, because the result from the in-situ test is in elastic range.

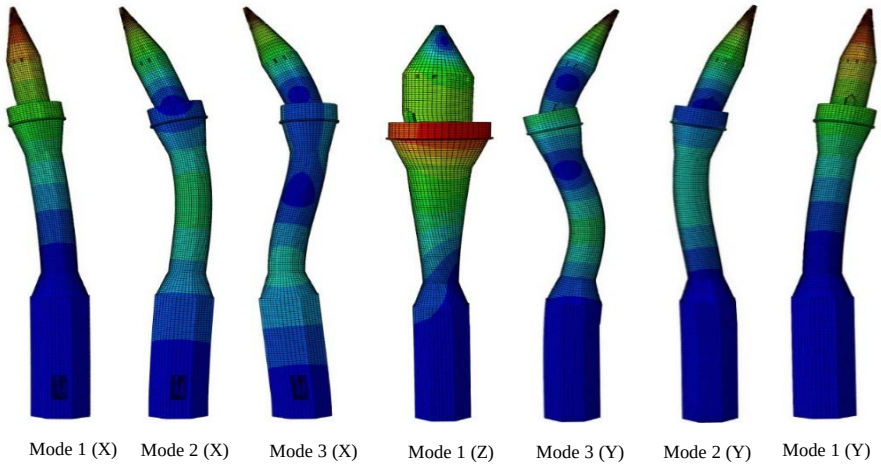

Figure 5. The first seven mode shapes and frequencies belongs to the minaret of Altıparmak Mosque

The natural vibration frequencies, the mass participation factors and mode shapes belonging to modes were obtained from the analysis (see Figure 5). Estimated natural vibration periods from the numerical model solutions were examined comparatively with those obtained from experimentally. As a result, the numerical model was calibrated such a way. The results of the numerical analysis were compared with modal testing in the Table 2. Besides, mass participation ratio of the first six modes were obtained from finite element model of the system. The ratio of the first mode is dominate in each direction. Table 2 also shows that percentage of error of modal model/FEM according to modal testing. The percentages are quite low. Therefore, the model represents to the realistic behavior of the minaret.

Table 2 Comparison of the first six modes between modal testing and finite element model results

Direction	Mode	Mass participation factors, %	Modal Model Frequency, Hz	Modal Testing Frequency, Hz	Error, %
NS	1. Mode	30	1.69	1.73	2
	2. Mode	30	7.46	8.01	7
	3. Mode	25	13.44	12.27	9
EW	1. Mode	49	1.80	1.84	2
	2. Mode	17	9.31	9.89	6
	3. Mode	15	21.05	19.61	7

5.SEISMIC ANALYSIS

Bursa is located on the North Anatolian Fault Line, has intense seismic activity. Therefore, seismic behavior of the historical heritages should be surveyed so as to be preserved from the possible earthquakes. Predicting seismic demands, requires determination of inelastic behavior of the heritages. In order to calculate seismic demand and the behavior, one of the preferred method is the non-linear static procedure or pushover analysis. In this study, for the determination of the seismic behavior of the minaret, pushover analysis were carried out considering displacement distribution of the first mode on the calibrated model. To occur demand curve, Turkish Earthquake Code (2007) was used. Due to location of the minaret, effective ground acceleration coefficient (A_o=0,4) and local site class (Z2) were selected from the code. Soil–structure interaction wasn't considered. Boundary condition of the minaret was designed as encastre at the foundation level. As a result of the analysis, demand/capacity curve of the minaret were computed (see Figure 6). In addition, stress and plastic strain value of critical sections evaluated for the seismic demand of the minaret (see Figure 7).

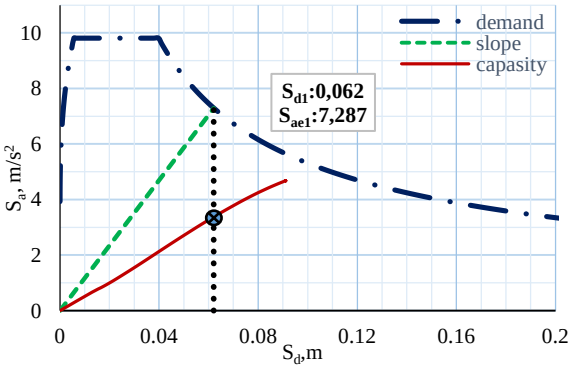

Figure 6. The first seven mode shapes and frequencies belongs to the minaret of Altıparmak Mosque

In order to evaluate to stress of the model elements, we considered the brick+mortar and the limestone+brick compression strengths as 3 Mpa and 5 Mpa, respectively. The tensile strengths were assumed as 10% of the compression strengths. These values were selected with a view to evaluating of analysis under the literature value. Capacity of tensile plastic strain value was also accepted as 0.005. For the masonry structure, the value can vary in the literature.

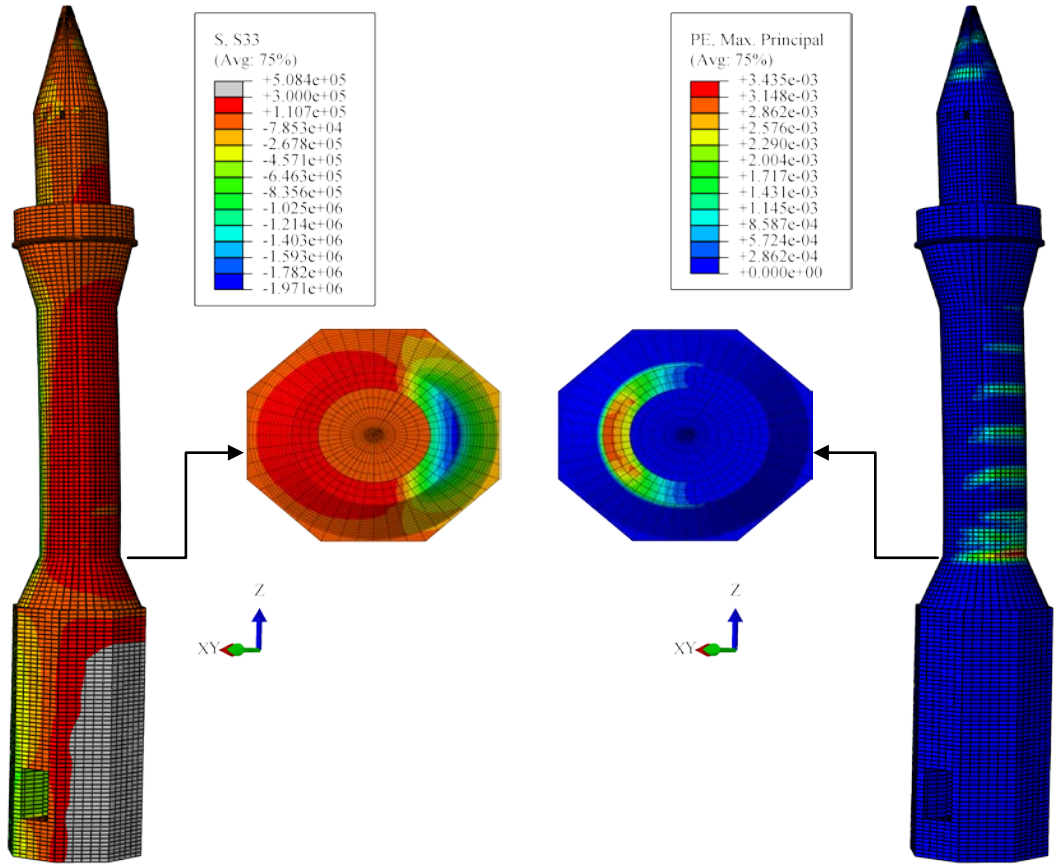

Figure 7. Stress S, S33 and plastic strain PE graphics of the minaret

6.CONCLUSIONS

Dynamic properties of the minaret of the Altıparmak Mosque were identified by means of ambient vibration test and numerical simulation. The results of the modal tests provide strong support for the finite element model presented in this study. A total of six mode frequencies and mode shapes were obtained from FEM of the structure under investigation. These modes which are extracted among a large number of modes can be evaluated as sufficient. Since their contributions to total response are approximately 85% or over this in each direction. Maximum percentage of error of modal model/FEM according to modal testing was calculated 9%. The percent value are quite low for such a historical masonry structure. Consequently, it can be easily stated that the calibrated finite element model can represent to the actual structural behavior. Whereby, the model is ready to use in the dynamic and static seismic analysis.

After modal updating; the limestone+brick of young modulus (E=8000 N/mm^2), bulk density (γ=2.1 t/m^3) and the brick of young modulus (E=3600 N/mm^2) and bulk density (γ=1.70 t/m^3) were calculated in the finite element model. When these values were compare with our test result on material of different minaret [8], it is understood that the results are close to each other. Therefore, we can be said that realistic results were obtained from the material tests.

For the evaluation of the seismic response of the minaret, pushover analysis were performed on the calibrated FE model. When capacity curve of the minaret obtained from analysis was examined at the figure 6, pseudo acceleration and the displacement values of minaret was seen under the peak level for the slope of the first period. To make a more detailed assessment, looking at the S33 and PE graphs will be more accurate. Since tension behaviors of the masonry structure such a historical minaret is more important than compression behaviors, tension stress and plastic strain value were considered in the graphs. The result showed that most critical section of the minaret is between body and transient segment, because the cross-section was changed in this area of the minaret. The average tension stress and plastic strain value were determined as 0.2-0.3 Mpa and 0.002-0.003, respectively in the half of the cross-section. These results can be supported with non-linear response history analysis in the future study.

ACKNOWLEDGMENT

The present work is supported by Grant-in-Aid for Research Project (No.KUAP(MH)-2014/48) from the Uludag University, Turkey.

REFERENCES

[1]. Z. Sayar, "Does minaret lose its task ?," *Arkitekt*, No.368, pp. 154-157, 1977. (in Turkish)
[2]. A. Dogangun, R. Acar, H. Sezen, and R. Livaoglu "Investigation of dynamic response of masonry minaret structures," *Bulletin of Earthquake Engineering.*, *6*(3), 505-517, 2008.
[3]. F. Peña, P. B. Lourenço, N. Mendes, and D. V. Oliveira, "Numerical models for the seismic assessment of an old masonry tower," *Engineering Structures*, *32*(5), 1466-1478, 2010.
[4]. C. S. Oliveira, E. Çaktı, D. Stengel, and M. Branco, "Minaret behavior under earthquake loading: The case of historical Istanbul," *Earthquake Engineering & Structural Dynamics*, *41*(1), 19-39, 2012.
[5]. Resta, A. Fiore, and P. Monaco, "Non-linear finite element analysis of masonry towers by adopting the damage plasticity constitutive model," *Advances in Structural Engineering*, *16*(5), 791-803, 2013.
[6]. Rainieri, "*Operational Modal Analysis for seismic protection of structures*," Doctoral dissertation, Università degli Studi di Napoli Federico II, 2008.
[7]. Z. F. Fu, and J. He, *Modal analysis*, 1st ed, Delhi, India: Butterworth-Heinemann, 2001.
[8]. C. Serhatoğlu, R. Livaoğlu, and B. Bağbancı, "Comparison Of Dynamic Characters Historical Minarets Of The Muradiye Mosque And Earthquake Safety," *5th International Earthquake Symposium* ID: CVLENC-1109 , 10-12 June 2015, Kocaeli-Turkey.
[9]. F. M. R. L. D. Magalhães, "Operational modal analysis for testing and monitoring of bridges and special structures," 2012.
[10]. J.S. Bendat, A.G. Piersol, *Engineering Applications of Correlation and Spectral Analysis*, Second Edition, John Wiley & Sons, New York, USA, 1993.
[11]. SignalCalc 240, *ACE Dynamic Signal Analyzer*, User Manual, Data Physics Cooperation, 1997.

Enrichment Of Tailings At Eti Mine-Hisarcık Waste Dam By Using Thermal Processing

Ahmet Aydin[1]

Abstract

In this study, the possibility of enrichment for the (-3 mm) waste product obtained after the enrichment process at Emet-Hisarcık concentrator plant of Eti Mine and stored in the tailings, causing both environmental problems and also economic loss, has been investigated. For this purpose, the chemical, physical and physicochemical characterization studies have been made on the representative samples taken. In this study, it was found out that the samples taken from the Hisarcık tailing dam include 19.10% B_2O_3 and minerals such as colemanite, calcite and illite minerals.

Thermal process (Microwave) experiments; the samples in the three different grain size such as +0.5, -0.5+0.125, -0.125 mm, were classified into concentrate and waste after being subjected to microwave energy at different times (10, 20, 30, 40, 50, 60 minutes) and microwave power levels (360, 600, 800 watt). As a result of this experimental work, 43.65% B_2O_3 grade was obtained with an efficiency of 93.48% by using the +0.5 mm grain size waste sample (at 600 watt power for 40 minutes) after they were exposed to microwave.

Keywords: *Thermal Processing, Colemanite Mineral*

1. INTRODUCTION

Turkey has 73% of the world's natural boron reserves which is strategically important (Eti Mine 2014,). The production, processing and marketing of the boron minerals which are generally found as tincal, colemanite and ulexite is done by a state company called Eti Mine Works General Directory (Frost, et al. 2013, Aydın et al. 2014).The total World boron reserves are estimated to be to 1.310,3 million tons of B_2O_3 The USA and Turkey are the world's two largest producer of boron minerals (Eti Mine 2014, Duydu at al 2015).

Borate mining in Turkey is generally done by open pit mining. Produced boron ore is then processed using simple processing techniques such as washing, dispersing and classifying according to size groups. After processing, boron products are used in many industrial fields (Oruç et al. 2004, Sönmez et all. 1996).

In modern technology boron minerals are used in wide variety of fields for example, from fertilizer to medicine, from detergent to nuclear industry (Aydın et al. 2009 and 2012). Fast production and consumption brings about many problems. Boron tailings nowadays represent a kind of secondary raw material, therefore, it is important to recover them (Oruç et al., 2004, Badruk et al., 1997, Aydin et al., 2014). In this study, microwave energy which has already been applied to food, chemistry and paper industries becomes important tool for mineral processing and metallurgical applications (Ozbayoglu and Depçi 2006, Aydin et al. 2012). Heating by microwave energy has some advantages such as fast reaching to process temperature, uniform distribution of temperature, environmental safety, better quality end product, fast processing and high automation (Aydın 2012, Uslu 2003). These advantages promote microwave energy to use in mineral processing and extractive metallurgy (Kingston and Jassie, 1985, Yıldız and Alp 2000). In this study, enrichment possibility of the sample taken from Hisarcık concentrator waste dam by microwave energy at different durations and different power levels was investigated.

2. EXPERIMENTAL STUDIES

The represantative samples taken from Hisarcık waste dam (-3mm) of Emet Boron Enterprise, were first dehumidified at laboratory and then used in the experimental studies

2.1. Characterization Tests

Some chemical, physical and physico-chemical characterization tests were applied to the samples.

2.2. Chemical tests

Chemical properties of samples used in characterization test were given in Table 1.

Table 1. Chemical analysis of Hisarcık Colemanite waste sample

Content	Amount (%)	Content	Amount (%)
B_2O_3	19,10	TiO_2	0,18
SiO_2	28,17	CaO	22,3
Fe	1,41	SrO	**1,43**
Na2O	0,78	Fe_2O_3	1,55
MgO	10,63	P_2O_5	10,63
Al_2O_3	3,274	SO_3	0,72
K_2O	1,41	Loss of Ignition	8,48

2.3 Analysis of Thermal Properties

Thermal properties of the sample were investigated by Perkin Elmer Diamond brand, TG/DTA device.

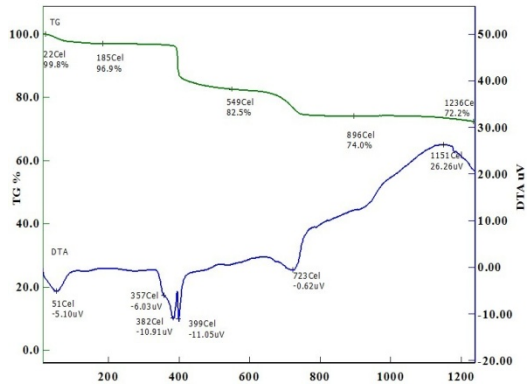

Figure 1: TGA and DTA graph of Hisarcık Waste Dam colemanite sample

The hydroscopic water was removed at 30-100°C at a mass flow rate of 2,56% as seen in Figure 1. As it is seen from TGA line, the weight did not almost change up to 380°C. The aim of the analysis is to investigate the amount of crystal water of the samples, decomposition nature and re-crystallization mechanism.

2.4 Mineralogical Investigation

Mineralogical content of the samples were studied by Rigaku Miniflex Brand XRD device with using Cu α(λ=1,54 A°) radiation rate by Material Science Engineering Department of Dumlupınar University.

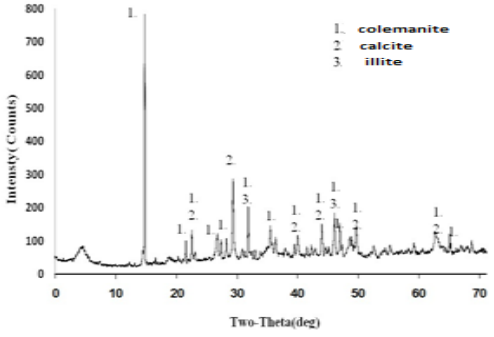

Figure 2: XRD graphs of Hisarcık waste dam colemanite samples

As it is seen from Figure 2, there are colemanite, calcite and illite minerals in the sample of Hisarcık waste dam.

2.5 Particle size Analysis

It was found that 80% of the sample was below 2 mm and the B_2O_3 distribution classified the samples into 3 different size groups. The grade distribution according to particle size groups is given below in Table 2.

Table 2. Grade Distributions according to particle sizes.

Particle Size (mm)	Weight (%)	ΣOS (%)	ΣUS (%)	B_2O_3 (%)
+0,5	53,73	53,73	100	20,95
-0,5 +0,125	38,59	92,32	46,27	16,4
-0,125	7,68	100	7,68	19,4
Total	100			

3. METHOD

Microwave energy which is one of thermal processing method was used to enrich waste products of Hisarcık concentrator of Emet Etimine Company. In the experiments, a Beko MD 1505 brand microwave owen working at a constant frequency of 2450 MHz and a maximum power of 800 watt was used. This equipment can be set to 5 different power levels (90-180-360-600-800) mechanically.

4. MICROWAVE EXPERIMENTS

To enrich tailings of Hisarcık concentrator; different microwave power levels were applied to the 3 particle size groups (+0,5, -0,5+0,125, -0,125 mm) for different durations.

4.1 Microwave experiments for 0,5 mm sized particles

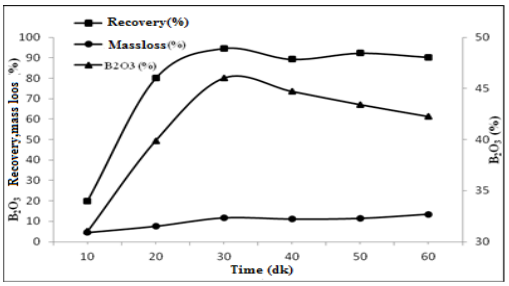

Figure 3: Experiment result of +0,5 mm sample at 800 watt microwave power

As seen from figure 3, when the waste sample was exposed to 800 watt microwave power, the following concentrates were obtained. For 10 minutes, the recovery was 20% with a grade of 31,01% B2O3; for 20 minutes, the recovery was 80% with a grade of 39,88% B2O3; for 30 minutes, the recovery was 94,62% with a grade of 46,00% B2O3; for 40 minutes, the recovery was 89% with a grade of 44,47% B2O3; for 50 minutes, the recovery was 92,30% with a grade of 43,41% B2O3; for 60 minutes, the recovery was 90,31% with a grade of 42,25% B2O3.

The recovery increased significantly until 30 minutes, but there was not a serious change after this period and the line went on almost horizontal. Similarly, until 30 minutes B2O3 grade increased, however, after 30 minutes, due to increasing exposure time, size distribution of clays (calcite, illite) was changed and B2O3 grade went a little down.

The amount of mass loss, on the other hand, increased until 30 minutes, but then there was not a significant change. Mass loss was 11,64 % at the end of 30 minutes. When associated this loss with TGA and DTA graphs; it was determined that the sample's capillary water was released when a temperature range of 380-400°C was reached and free crystalline water was removed from the structure. The highest grade and recovery rate was obtained from microwave experiments for +0,5 mm particle size, 800 watt power and 40 minutes time duration.

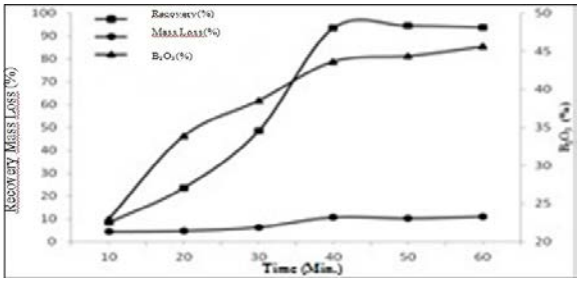

Figure 4: the experiment results for +0,5 mm particle sized sample at 600 watt.

As seen in figure 4, if the waste sample was exposed to 600 watt microwave power, the following concentrates were obtained. For 10 minutes, the recovery was 8,5% with a grade of 23,00% B_2O_3; for 20 minutes, the recovery was 23,60% with a grade of 33,87% B_2O_3; for 30 minutes, the recovery was 48,45% with a grade of 38,53% B_2O_3; for 40 minutes, the recovery was 93,48% with a grade of 43,65% B_2O_3; for 50 minutes, the recovery was 94,45% with a grade of 44,38% B_2O_3; for 60 minutes, the recovery was found as 93,78% with a grade of 45,62% B_2O_3.

The recovery increased until 40 minutes significantly. Similarly B_2O_3 grade also increased until 40 minutes continuously. The amount of mass loss on the other hand, increased till 40 minutes, but then there was not a significant change. Mass loss was 10,70% at the end of 40 minutes. When associated this loss with TGA and DTA graphs; it was determined that the sample's capillary water was released when a temperature range of 380-400°C was reached and free crystalline water was removed from the structure. The highest grade and recovery rate was obtained from microwave experiments for +0,5 mm particle size, 600 watt power and 40 minutes time duration. At this time point, the recovery rate and B_2O_3 grade was found as 93,48% and 43,65 %, respectively.

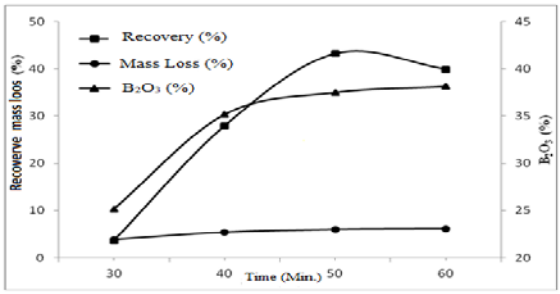

Figure 5: The experiment results for +0,5 mm particle sized sample at 360 watt

There was not enough enrichment at 360 watt microwave energy up to 30 minutes exposure. As seen from figure 5, if the waste sample was exposed to 360 watt microwave power for 30 minutes, the recovery was 3,6% with a grade of 25,14% B_2O_3; for 40 minutes, the recovery was 27,9% with a grade of 35,17% B_2O_3; for 50 minutes, the recovery was 94,45% with a grade of 44,38% B_2O_3; for 60 minutes, the recovery was 43,2% with a grade of 37,5% B_2O_3.

The recovery increased significantly until 50 minutes. Similarly, until 50 minutes B_2O_3 grade increased. The amount of mass loss on the other hand, increased till 50 minutes. Mass loss was 6,10% at the end of 50 minutes. When associated this loss with TGA and DTA graphs; it was determined that the sample removes its capillary water. The overall results of the experiments for +0,5 mm particle size is given in the Table 3.

Table3. Optimal Results of Microwave experiment for +0,5 mm particle size

Power (Watt)	Optimal Time (Min.)	Feeding		After Microvawe				Mass Loss (%)	Recovery (%)
		Weight (%)	B_2O_3 (%)	Weight (%)		B_2O_3 (%)			
				Conc.	Waste	Conc.	Waste		
360	50	100	20,95	25,2	74,8	37,5	16,6	6,1	43,2
600	40	100	20,95	49,26	50,74	43,65	3	10,7	93,48
800	30	100	20,95	46,9	53,1	46	2,31	11,64	94,62

From the result of the experiments, at 800 watt power, the following concentrates were obtained. For 30 minutes exposure time, the recovery was 94,62% with 46,00% B_2O_3 grade; for 40 minutes exposure time, the recovery was 93,48%, with 43,65% B_2O_3 grade; for 50 minutes exposure time, the recovery was 43,20%, with 37,50% B_2O_3. Microwave energy levels less than 360

watt were insufficient for the enrichment at this particle size. Since 40% B_2O_3 grade is sufficient for boric acid factories and considering energy saving, the results corresponding to 600 watt power for 40 minutes exposure time were considered as the optimal results.

4.2. Microwave experiments for -0,5+0,125 mm particle size

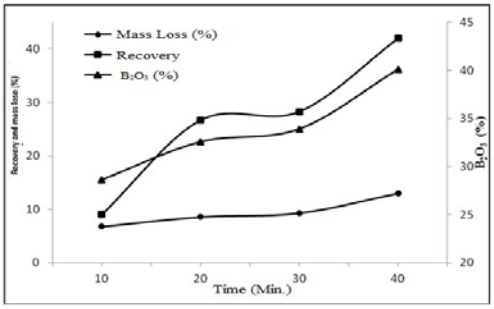

Figure 6 Experiment results of -0,5+0,125 mm sample at 800 watt microwave power

As seen from figure 6, if the waste sample was exposed to 800 watt microwave power, the following concentrates were obtained. For 10 minutes, the recovery was 9% with a grade of 28,62% B_2O_3; for 20 minutes, the recovery was 26,7% with a grade of 32,56% B_2O_3; for 30 minutes, the recovery was 28,3% with a grade of 33,90% B_2O_3, for 40 minutes, the recovery was 42% with a grade of 40,10% B_2O_3. Since more than 40 minute exposure time caused an increase of agglomeration, the sample was not experimented over 40 minute exposure times. The recovery increased significantly until 40 minutes. Similarly, B_2O_3 grade continuously increased until 40 minutes.

The amount of mass loss on the other hand, increased till 40 minutes. Mass loss was 10,70% at the end of 40 minutes. When associated this loss with TGA and DTA graphs, it was determined that the sample's capillary water was released when a temperature range of 380-400°C was reached and free crystalline water was removed from the structure. The highest grade (40,10%) and recovery rate (42,00%) from microwave experiments were obtained for -0,5+0,125 mm particle size, 800 watt power and 40 minutes duration.

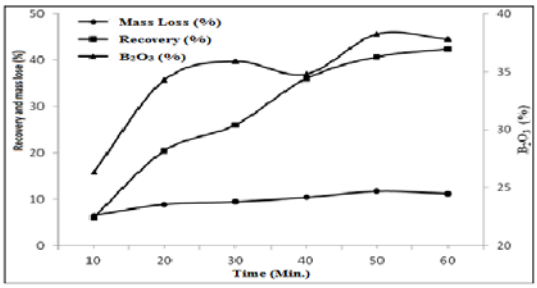

Figure 7. The experiment results for -0,5+0,125 mm particle sized sample at 600 watt

As seen in figure 7, if the waste sample was exposed to 600 watt microwave power, the following concentrates were obtained. For 10 minutes, the recovery was 6% with a grade of 26,33% B_2O_3; for 20 minutes, the recovery was 20,43% with a grade of 34,30% B_2O_3; for 30 minutes, the recovery was 36,00% with a grade of 35,90% B_2O_3; for 40 minutes, the recovery was 36,00% with a grade of 34,82% B_2O_3; for 50 minutes, the recovery was 40,70% with a grade of 38,27% B_2O_3; for 60 minutes, the recovery was 42,4% with a grade of 37,80% B_2O_3.

The recovery increased until 60 minutes significantly while B_2O_3 grade increased until 50 minutes. But after 50 minutes, due to increasing exposure time, the size distribution of clays (calcite, illite) was changed and B_2O_3 grade went a little down. The amount of mass loss on the other hand increases till to 50 minutes, but then there is not a significant change. Mass loss is 11,71% at the end of 50 minutes. When associated this loss with TGA and DTA graphs, it was determined that the sample removes self capillary water when at the temperature reaches at 380-400°C and free crystalline water leaves the structure. The highest recovery rate was obtained from microwave experiments for -0,5+0,125 mm particle size, 600 watt power and for 60 minutes duration. The overall results of the experiments for -0,5+0,125 mm particle size are given in Table 4.

Table 4. Optimal Results of Microwave experiment for -0,5+0,125 mm particle size

Power (Watt)	Optimal Time (Min.)	Feeding		After Microwave				Mass Loss (%)	Recovery (%)
		Weight (%)	B_2O_3 (%)	Weight (%)		B_2O_3 (%)			
				Conc.	Waste	Conc.	Waste		
600	50	100	16,4	19,17	80,3	38,27	13,7	11,71	40,7
800	40	100	16,4	19,6	80,4	40,1	13,43	10,7	42

From the experiments, the following concentrates were obtained. At 800 watt power and for 40 minutes exposure time, the recovery was 42% with 40,10% B_2O_3 grade; at 600 watt power and for 50 minutes exposure time, recovery was 40,70% with 38,27% B_2O_3 grade. Microwave energy levels of less than 600 watt were insufficient for the enrichment at that particle size. According to the results obtained, 600 watt power and 40 minutes exposure time were considered as the optimal parameters.

4.3.Microwave experiment for -0,125 mm particle size

For -0,125 mm size particles, any concentrate with sufficient recovery rate and concentrate grade could not be produced.

As seen from figure 8, if the waste sample was exposed to 800 watt microwave power, the following concentrates were obtained.

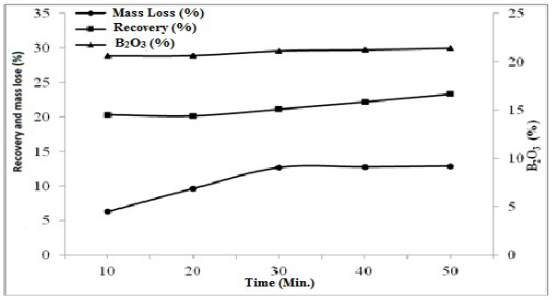

Figure 8: The experimental results for -0,125 mm particle sized sample at 800 watt

For 10 minutes, the recovery was 20,34% with a grade of 20,60% B_2O_3; for 20 minutes, the recovery was 20,17% with a grade of 20,63% B_2O_3; for 30 minutes, the recovery was 21,15% with a grade of 21,13% B_2O_3; for 40 minutes; the recovery was 22,21% with a grade of 21,23% B_2O_3; for 50 minutes; the recovery was 25,92% with a grade of 21,40% B_2O_3. Since more than 50 minute exposure time caused an increase in agglomeration, the sample was not experimented over 40 minute exposure time.

The amount of mass loss on the other hand, increases till 30 minutes, but then there is not a significant change. Mass loss is 12,67% at the end of 30 minutes. When associated this loss with TGA and DTA graphs, it was determined that the sample removed self capillary water when at the temperature reached at 380-400°C and free crystalline water left the structure.

5. RESULTS AND DISCUSSIONS

In this study, the samples taken from Hisarcık Concentrator Plant of Etimine waste dam was enriched by using microwave energy. The experimental results obtained are given below.

- Hisarcık waste dam samples contain 19,1% B_2O_3.
- According to XRD results, the samples consist of colemanite, calcite and illite minerals.
- From TGA and DTA graphs, it can be said that the samples remove its capillary, free crystal and (OH)-formed water as poly-anions at 179°C and 1232°C, respectively. Total mass loss reaches 24% at 1232°C.
- From the sieve analysis results, it was found that B_2O_3 distribution classifies the samples into 3 different size groups (+0,5 , -0,5+0,125, -0,125 mm).

- During the experiments, a constant frequency of 2450 MHz and a microwave device running at maximum 800 watt power were used.
- For +0,5 mm particle size group, a concentrate having a B_2O_3 grade of 43,65% and a recovery rate of 93,48% was obtained at 600 watt power and for 40 minutes.
- For -0,5 +0,125 mm particle size group, a concentrate having a B_2O_3 grade of 40,10% and a recovery rate of 42,00% was obtained at 800 watt power and for 40 minutes.
- For -0,125 mm particle size group, it was determined that enrichment by microwave energy was not suitable.

When all results were compared, the optimal result was found as the concentrate having 43,65% B_2O_3 with 93,48% recovery rate for -0,5 mm particle size, 600 watt microwave energy and for 40 minutes exposure time. Since there is a great amount of colemanite reserve at Emet mine, there is not a plant yet for tailing handling which causes an increased stockpiling of waste every year. If the tailings are enriched by microwave energy, not only it contributes to the national economy but also it decreases the cost of storage and dam maintenance. Moreover, environmental pollution caused by the waste dams and the surface and ground water contaminations will be prevented.

It is hoped that this research opens a window for the future handling of the boron wastes. It is also hoped that the proposed technique may be applied to the run of mine ores as an alternative method to wet processing techniques. This may be a topic for further researches. In this study, enrichment economy (process costs) by microwave power was not investigated. By preparing a feasibility study in terms of the comparative costs, this technique should then be considered an alternative to wet methods.

REFERENCES

[1]. Eti Mine Works General Management, 2014, Boron Sector Report, http://www.enerji.gov.tr/File/?path=ROOT%2F1%2FDocuments%2FSekt%C3%B6r+Raporu%2FBOR+SEKT%C3%96R+RAPORU+2013+docx.pdf, [accessed 04.20.2016], Ankara-Turkey

[2]. Frost, R.,I.,Xi, Y.,Scholz,R.,Belotti,F., M.,Filho,N.,C., 2013Infrared and Raman Spectroscopic Characterization of The Borate Mineral Colemanite CaB3O4(OH)3,H2O-Implications For Molecular Structure, Journal of Molecular Structure, 1037,23-28.

[3]. Aydin, A., Ayaz, S., Demir, U.,2014, Benefication of Tailing of Emet Hisarcık Boron Plant waste dam by flotation, 14th Mineral Processing Symposium,Turkey,569-577.

[4]. Duydu, Y., Başaran, N., Bolt, H., M., (2015), Risk Assesment Borates in Occuptaional Settings, Boron Separation Processes Eds.(Kabay N., Bryjak M., Hilal N.), Elsevier, P. 77 .

[5]. Oruç, F., Sabah E., Erkan Z., (2004) Evaluation Strategies of Boron Tailings according to Sector, II. International Boron Syposium, May 2013, Eskişehir Turkey

[6]. Sönmez, E., Özdag, H. ve Savas, M., 1996, Beneficiation of Emet Tailing by Water Absorbsion Mechanical Attrition Megnetic Separation , 6th International Mineral Processing Symposium , edt. Kemal, Arslan, Akar, Canbazoglu, İzmir, Türkiye, 143-149

[7]. Kingston H.M. ve Jassie, L.B., 1985, Introduction to Microwave Sample Preparation-Theory and Practise, Chapters 2 and 3, ACS Professional Reference Book, Am.Chem.Soc.

[8]. Aydın, A., Aykul, Ö, Demir, U., (2009), "Beneficiation With Decrepitation of Colemanite Tailings

[9]. In Eti Bor In Hisarcık, Emet, VII. International Industrial Mineral Symposium, 25-27 February Kusadası-Turkey

[10]. Aydın,A., Demir,U, AK, M, Bütüner,R.,(2012) "Research of The Enrichment In Hisarcik Concentrator Tailings At Emet Boron Works with Microwave Energy Using" Proceedings of XIIIth International Mineral Processing Symposium, 10-12 October, Bodrum, Turkey

[11]. Badruk, M., Yamik, A., Akçıl, A., (1997): " Compaction And Dissolutıion of The Concentrates And Tailings From Tincal Ore "15TH Mining Congress of Turkey, 6-9 May, Ankara,Turkey 1997, ISBN 975-395-216-3.

[12]. Kingston H.M. ve Jassie, L.B., 1985, Introduction to Microwave Sample Preparation-Theory And Practise, Chapters 2 and 3, ACS Professional Reference Book, Am.Chem.Soc.

[13]. Özbayoğlu, G., Depçi, T., 2006, The Grindability of The Coal to The Effect of The Microwave Energy 10TH International Energy Conference, Istanbul-Turkey, S. 5.

[14]. Aydın,A., Bütüner, R., Demir,U, Ak, M, (2012)" Enrichment of Low Grade (Espey -3 mm.) Colemanıte Stocks in Emet Regıon Usıng Decrepitation and Microwave Methods" Proceedings of XIIIth International Mineral Processing Symposium, 10-12 October, Bodrum, Kuşadası, Turkey

[15]. Uslu, T. ve Atalay, U., 2003, Microwave Heating Of Coal For Enhanced Magnetic Removal Of Pyrite, Fuel Processing Technology, Vol. 85, 21-29.

[16]. Yıldız, K. ve Alp, A., 2000, Metalurjik Proseslerde Mikrodalga Kullanımı, Metalurji Dergisi, Cilt 24, Sayı:125, 24-29

ICENS
INTERNATIONAL CONFERENCE ON ENGINEERING AND NATURAL SCIENCES
24-28 May 2016 /Sarajevo

Deblurring Images Taken by a Quadrotor Using Artificial Neural Networks

Harun Celik[1], Ilke Turkmen[2], Tugrul Oktay[3]

Abstract

Motion blur occurs when the camera mounted on quadrotor moves abruptly (i.e., adverse air conditions). In this study, an artificial neural network (ANN) is designed in order to deblur the images taken by our quadrotor. For deblurring or sharpening the blurred images, initially, sharp images of scenes that blur occurred before are taken from same altitudes and angles in various flights. The collected sharp and blurred images of same scenes are used to train the neural network (NN) to be capable of estimating the relationship between sharp and blurred images. The characteristics of NN such as number and transfer function of layers are selected experimentally. Finally, the performance of designed NN in deblurrig images taken by the quadrotor is measured and deblurrig results are illustrated by real experimental images. NN is proved to be used as an intelligent method to deblur the images.

Keywords: *quadrotor, image deblurring, artificial neural networks*

1.INTRODUCTION

Since quadrotors have the capability of taking off and landing vertically, they need a small landing field only. Therefore, quadrotors are very common used air vehicles [1]. One of the areas which are most commonly utilized is aerial photography [2]. Although high quality photos can be acquired by quadrotor, sharp movements such as vibration, oscillation or shake during exposure results to motion in the images.

Various studies in reducing the motion blur degradation have been collected. It is possible to divide the existent solutions in two groups based on whether they are aiming to remove blur from images or to prevent images from the motion blur degradation [3]. For the first group, it is necessary to estimate the motion or trajectory of the quadrotor that causes blur. When the motion occurred during exposure is known then the motion blur resulted from can be removed by applying deconvolution process [4]. In the first group, there are also methods to assess the motion of camera when it is unknown [5, 6].

An example for the second group is [7] in which internal sensors and CMOS are used to prevent images from motion blur by preventing the camera from vibrations. On the other hand, NN is a method which is among the first group as a modern solution that is applied to deblur images in recent years. Various NN researches in order to identify the type of blur [8], remove known blur from images [9, 10], identify blur and remove it from image simultaneously to obtain sharp images [11, 12] are collected. Moreover, several NN models have been utilized to deblur or denoise the images. One of them is convolutional neural network (CNN) which is a NN model with three key ideas: weight sharing, sub-sampling in the spatial domain, and local receptive fields. CNN is designed for the recognition of two-dimensional visual patterns [13] and used by [14] for image restoration. Another one is a multilayer neural network based on multivalued neurons that consist of multivalued neurons, it has complex-valued weights and an activation function as introduced in [15] and used by [16] for blur identification.

Figure 1. A photo of the operating quadrotor.

[1] *Corresponding author: Erciyes University (ERU), Department of Aircraft Electric and Electronic, 38039, Kayseri, Turkey. haruncelik@erciyes.edu.tr*

[2] *ERU, Department of Aircraft Electric and Electronic, 38039, Kayseri, Turkey. titi@erciyes.edu.tr*

[3] *ERU, Department of Aeronautical Engineering, 38039, Kayseri, Turkey. oktay@erciyes.edu.tr*

Appropriate adjustment of aperture and exposure time can also prevent images from motion blur when the camera is stable or moves smoothly. It is possible to get sharpener images by faster shutter speed means shorter exposure time, but faster shutter speed causes image noise due to increasing the sensitivity of imaging sensor. Also, designing a control system that protects the quadrotor from big vibrations and shakes can resist from motion blur. However, despite all these solutions, the images taken by quadrotor in turbulence or shakes suffer from motion blur. Since, especially for quadrotor, it is not possible to extinguish the shakes and turbulence, images exposed during sharp moves include somewhat blur.

In order to remove motion blur from images, a NN model is investigated in this study. For this purpose, sharp images of blurred images taken before are also taken from same altitudes and angles in various flights. These collected sharp and blurred images of same scenes are used to train the NN to be able to estimate the relationship between sharp and blurred images. The performance of designed NN in deblurrig images taken by the quadrotor is measured and deblurrig results are illustrated by real experimental images.

2.BLUR IN IMAGES

2.1.Motion Blur

When acquiring images, the most crucial factors affecting the quality and sharpness of the images are aperture, shutter speed (exposure time) and noise. Aperture with focal length determines the depth and so sharpness of the image by adjusting an opening through which light travels in optical system. Shutter speed controls the length of time that light is permitted to expose the camera. In other words, it is an indicator of the number of sampling. Noise originates from the sensitivity of sensors inside camera, but it is neglected to focus on motion blur in this study.

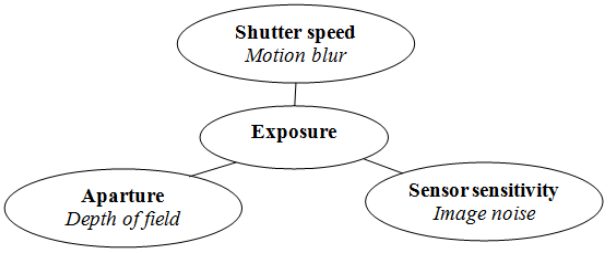

Figure 2. Factors affecting the quality and sharpness of the image.

Besides various image blur resulted from various sources, motion blur is caused by the relative motion between the camera and imaging scene. This motion can be modeled as a blur kernel added to images though convolution process. Thus, convolution can define the sampling process to obtain digital images from analog signals generated by imaging sensors. For 2D images, convolution is

$$(f * g)(x,y) = \int_{-\infty}^{\infty}\int_{-\infty}^{\infty} f(a,b)g(x-a,y-b)dadb \tag{1}$$

In this model, the motion of camera during exposure time cause blur as its effect is also convolved and added to the pixel values of latent image at quantization.

2.2.Motion Blur in Images Taken by Quadrotor

The blur, assumed to be uniform over a discrete spatial domain, $x \subset Z^2$, resulted from the motion of the quadrotor can be expressed as;

$$b(x) = f(x) * h(x) + n(x), \quad x \in X, \tag{2}$$

where $b(x)$ designates blurred image, $f(x)$ denotes underlying latent image, $h(x)$ is the blur kernel or point spread function that expresses how the effect of the motion spreads over the image and $n(x)$ denotes noise. The most important step in deblurring images is estimation of blur kernel, $h(x)$. Blur kernel is proportional to the motion of the camera. Blur increases as well as the motion of camera during exposure time increases. Estimation of blur kernel is very difficult and complex process if the latent image or the motion of camera is unknown. Thus, methods such as NN able to deblur images without estimation of blur kernel are vital methods in image deblurring.

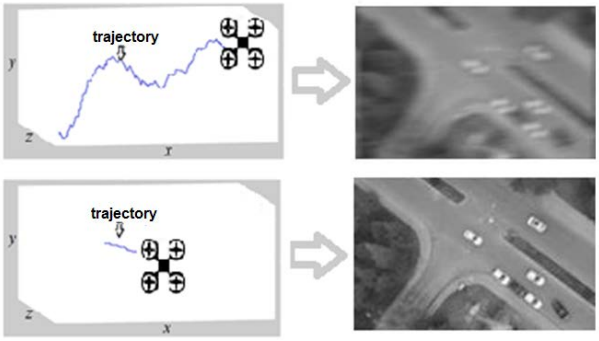

Figure 3. Examples for the blur occurred with respect to the motion of our quadrotor in same time interval.

3.NN FOR DEBLURRING

The designed NN architecture consists of 25 inputs, 2 hidden layers: there are 10 neurons in the first, and 6 neurons in the second layers, and an output. The relationship between the input size and blur kernel size which is identified by the motion of quadrotor is crucial for deblurring performance. Because the input size should include the exact blur kernel size as the NN is trained by the input. In other words, if the blur kernel size is bigger than the input size, the NN cannot learn the character of blur as the exact blur is not included by inputs. Since a designed NN model cannot be performed or evaluated for every level of blur, the interested blur size should be constrained.

In this study, as the input size is 5×5, the blur kernel sizes which are bigger than this input size, that means the images are blurred so much, are neglected owing to identify them by checking the motion of the quadrotor during relative exposure time. The blurred images resulted from large movements of quadrotor are excluded and similar motions cause similar blurs are chosen only by scanning the saved trajectory of quadrotor. For this paper, this step is not detailed.

The NN is trained to learn the functional mapping between the blurred and sharp images. Thus, the 25 inputs of the NN are the 5×5 patch in blurred image and the output is the center pixel of sharp image. Training and test images are the images of same scene taken by quadrotor as seen in Figure 4.

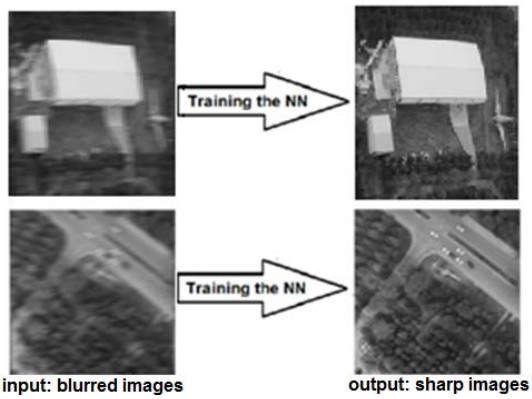

Figure 4. A pair of blurred and sharp images to train the NN.

For architecture of NN, a multilayer feedforward neural network [17] which is also called as a “multilayer perceptron” and proportional to the derivative of the activation function is designed and implemented. In addition, the activation functions are selected as linear and sigmoid for input and hidden layers, respectively.

4.RESULTS

The process steps followed in this paper are;

i. Load the exposure time of the camera and saved trajectory of the quadrotor during flight
ii. Define the limited size for the motion of quadrotor during exposure time
iii. Set the input size for NN with respect to the length of motion
iv. Choose the blurred images taken within limited length of motion
v. Divide chosen images into two parts for training and testing the NN
vi. Train and test the NN

vii. Depict the results.

With the Step 4, in this paper, only the blurry images that blurred by similar motion or certain size of blur kernel are taken account. Therefore, four pair of images (two for training and two for testing) taken by quadrotor are utilized. The size of all images is 256×256 pixels.

After implementing the NN, the result deblurred images are illustrated in Figure 5 and Figure 6. Figure 5 (a) and Figure 6(a), and Figure 5 (c) and Figure 6(c) are the blurred and sharp images taken by quadrotor, respectively. Figure 5 (b) and Figure 6 (b) are deblurred images by the designed NN.

In order to evaluate the performance of the NN for deblurring, the Peak Signal to Noise Ratio (PSNR) can be applied for quantitative comparison. In Figure 5(b) and Figure 6 (b), PSNRs of deblurring result images are 31,96 dB and 33,89 dB respectively. Since higher PSNR indicates that the deblurring is of higher quality, the designed NN is proved to be used in deblurring images taken by quadrotor.

5.CONCLUSIONS

In this study, blurred images taken by the quadrotor are deblurred by artificial neural networks. Initially, sharp images of the blurred images from almost same altitude and angle are taken. By using the blurred and sharp images of same scenes, the NN is trained to learn the functional mapping between the blurred and sharp images. The used blurred images are also constrained by choosing blurred images resulted from similar blur only. That means, blurred images degraded from under a certain blur kernel size are collected by scanning the trajectory of quadrotor and used in this paper. Aspects of the NN architecture such as number hidden layers and transfer functions are selected experimentally. 25 inputs are 5×5 pixels that consist of the neighbors of the center pixel. The output is the center pixel in sharp image. The designed NN model is applied to real blurred images, and results are illustrated. Furthermore, PSNR evaluated to show the performance of NN model are given. The results prove that the designed NN model is compatible to deblur the images taken by the quadrotor.

REFERENCES

[1]. T. S. Kim, K. Stol and V. Kecman, "*Control of 3 DOF quadrotor model*", London: Springer, 2007.
[2]. P. C. Garcia, R. Lozano and A. E. Dzul, "*Modelling and control of mini-flying machines*", London: Springer Science & Business Media, 2006.
[3]. M. Tico and M. Vehvilainen, "Image stabilization based on fusing the visual information in differently exposed images", in *IEEE International Conference on Image Processing, ICIP 2007*.
[4]. P. A. Jansson, "*Deconvolution of images and spectra*", Courier Corporation, 2014.
[5]. S. Oh, and G. Kim, "Robust estimation of motion blur kernel using a piecewise-linear model", *Image Processing, IEEE Transactions on*, vol. 23(3), pp. 1394-1407, 2014.
[6]. F. Xue and T. Blu, "A Novel SURE-Based Criterion for Parametric PSF Estimation", *Image Processing, IEEE Transactions on*, vol 24(2), pp. 595-607, 2015.
[7]. X. C. Liu, and A. E. Gamal, "Synthesis of high dynamic range motion blur free image from multiple captures", *Circuits and Systems I: Fundamental Theory and Applications, IEEE Transactions on*, vol. 50(4), pp. 530-539, 2003.
[8]. C. Khare, and K. K. Nagwanshi, "Image restoration in neural network domain using back propagation network approach", *Int. J. Computer Information Systems*, vol. 2(5), pp. 25-31, 2011.
[9]. U. Schmidt, C. Rother, S. Nowozin, J. Jancsary, and S. Roth, "Discriminative non-blind deblurring", *IEEE Conf. Computer Vision and Pattern Recognition*, 2010.
[10]. L. Xu, J. S. Ren, C. Liu, and J. Jia, "Deep convolutional neural network for image deconvolution", *Advances Neural Information Processing Systems*, pp. 1790–1798, 2014.
[11]. C. J. Schuler, M. Hirsch, S. Harmeling, and B. Schölkopf, "Learning to deblur", *arXiv:1406.7444*, 2014.
[12]. J. Sun, W. Cao, Z. Xu, and J. Ponce, "Learning a Convolutional Neural Network for Non-uniform Motion Blur Removal", *ArXiv e-prints*, 2015.
[13]. Y. LeCun, L. Bottou, Y. Bengio, and P. Haffner, "Gradient-based learning applied to document recognition", *Proceedings of the IEEE*, vol. 86(11), 2278-2324, 1998.
[14]. V. Jain, J. F. Murray, F. Roth, S. Turaga, V. Zhigulin, K. L. Briggman, ... and H. S. Seung, "Supervised learning of image restoration with convolutional networks" in *ICCV 2007*, pp. 1-8.
[15]. I. Aizenberg, C. Moraga, and D. Paliy, "A feedforward neural network based on multi-valued neurons" in *Computational Intelligence, Theory and Applications*, 2005, Springer Berlin Heidelberg, pp. 599-612.
[16]. I. Aizenberg, D. V. Paliy, J. M. Zurada, and J. T. Astola, "Blur identification by multilayer neural network based on multivalued neurons", *Neural Networks, IEEE Transactions on*, vol. 19(5), pp. 883-898, 2008.
[17]. D. E. Rumelhart, J. L. McClelland, "Parallel Distributed Processing: Explorations in the Microstructure of Cognition", Cambridge, MA, 1986.

ICENS
INTERNATIONAL CONFERENCE ON ENGINEERING AND NATURAL SCIENCES
24-28 May 2016 /Sarajevo

Airspeed Computation for Aircrafts with ANFIS Using Flight Parameters

Ilke Turkmen[1], Harun Celik[2]

Abstract

The airspeed is a fundamental parameter for accurate navigation of the aircrafts. Conventional pitot-static system consists of pressure sensors to measure total air pressure and static pressure as the aircraft moves through air mass. The measured pressure values are used by the Air Data Computer (ADC) to compute airspeed that shown to pilot by a conventional airspeed indicator. When ADC or pitot-static system is failed, there is no alternative way to compute airspeed. For this reason, it is very important to find alternative methods for computing the airspeed. In this paper, an alternative airspeed computation method based on adaptive neuro fuzzy inference system (ANFIS) is presented. The data set used to train proposed ANFIS model is obtained from the Digital Flight Data Acquisition Unit (DFDAU) records of a Boeing 737-82R type commercial aircraft. The proposed method uses the flight parameters as inputs of the ANFIS. As such, airspeed is calculated using flight parameters instead of the pitot-static system measurements. Simulation results clearly show that the proposed ANFIS method can be used as an alternative airspeed computation method when pitot-static probe or ADC failures.

Keywords: *Airspeed, flight parameters, ANFIS*

1.INTRODUCTION

The airspeed information of the aircrafts is measured using traditional airspeed measuring methods for over sixty years. Pitot-static systems are still commonly utilized because they offer simple and accurate solutions for measuring the airspeed. In this system, airspeed is obtained with the use of ADC by measuring the difference between the total pressure at the forward facing pitot probe and the static pressure measured at a static vent [1]-[3].

Because of the importance of the ADC, some aircrafts are installed more than one ADC for computing the basic flight parameters. Although these precautions have been taken, one or all of the pitot-static probes may ice up and provide incorrect data to ADC, or ADC itself can fail. In this situation, there isn't any alternative source to obtain airspeed information. For this reason, it is very important to develop an alternative airspeed computation method without using pitot-static system measurements.

The accuracy of the traditional pitot-static probes also decreases in a low airspeed environment [4]-[7]. The accurate low airspeed information is especially needed by helicopter pilots in order to maintain critical control authority. Because flight is required increased power in the low airspeed regime, accurate low airspeed data is needed to maintain control margins. In order to overcome this difficulty, there are several studies in the literature to calculate helicopter airspeed using alternative methods especially for low airspeed regime [4]-[6].

Over the last two decades, ANFIS [8], [9] has been popular and utilized by many researchers for solving difficult engineering problems. The ANFIS is a FIS implemented in the framework of an adaptive fuzzy neural network. It incorporates the advantages of artificial neural networks and FISs in a single model. It has accurate and fast learning, perfect explanation capability in the form of semantically meaningful fuzzy rules, the ability to accommodate both data and existing expert knowledge about the problem, and good generalization features. Because of these advantages, in this study, we proposed an ANFIS model which only uses the flight parameters to compute airspeed without requiring pitot-static system measurements. Totally, 960 data sets were obtained from the DFDAU records of a commercial aircraft.

The airspeed is conventionally computed by the ADC using complicated nonlinear equations. While the relationships to compute air data parameters may be readily derived, the relationship is extremely involved and electronic computation of air parameters from the relationship would be quite difficult. The proposed method also provides more simple alternative method for computing airspeed according to the traditional method. As such the ANFIS model provides simpler and efficient computation method and it can be used ADC failures.

[1] *Erciyes University, Faculty of Aviation and Space Sciences, Department of Aircraft Electric and Electronic, 38039, Kayseri, Turkey. titi@erciyes.edu.tr*

[2] *Corresponding author: Erciyes University, Faculty of Aviation and Space Sciences, Department of Aircraft Electric and Electronic, 38039, Kayseri, Turkey . haruncelik@erciyes.edu.tr*

2.PROPOSED METHOD

The calibrated airspeed (CAS) is indicated to pilot with airspeed indicator and it is used for critical flight management and control functions. For example, the pilot knows what thrust will maintain level flight or whether the aircraft is undergoing a stall using the CAS information. The CAS is computed using following equations:

$$\mathrm{CAS} = a_{SL}\left(5\left\{\left[\left(\frac{q_c}{P_{SL}}\right)+1\right]^{1/3.5}-1\right\}\right)^{0.5} \quad (1)$$

where a_{SL} is the speed of sound at sea level, P_{SL} is the standard sea level air pressure value, and q_c is the differential pressure which is given by:

$$q_c = P_T - P_a \quad (2)$$

In Equation (2), P_a is the ambient air pressure and P_T is the total air pressure.

In this study, CAS is calculated using an alternative ANFIS model instead of complicated nonlinear equation given by Equation (1).

The ANFIS model used to compute airspeed requires performing the following two important steps: (i) Preparing the data set including identifying the input and output parameters and generating the data set, (ii) selecting the most suitable membership function shape and number for the ANFIS.

2.1.Preparing the data set for the ANFIS

Identification of ANFIS model's input and output parameters is the first important step. There are a lot of flight parameters but in this study, ten flight parameters including heading, pitch attitude, roll attitude, rotor rotational speed (N1), captain control wheel position, present position lateral, present position longitudinal, elevator position-left, aileron position-left, and rudder position were selected as input parameters.

The data set used to train and test the ANFIS model were obtained from DFDAU records of a short-to-medium range, narrow body, and featured turbofan engines a Boeing 737-82R type commercial aircraft for three phase of the flight: take-off, cruise, and landing. The data set grouped into two sets: training data set and test data set. The training data set is utilized for training the ANFIS model. The size of the training data set has significant importance on generalization capabilities of the ANFIS. The size of the training data should be large enough to generalize of the ANFIS.

The test data set is used to analyze the final generalization and prediction performance of the trained ANFIS model. In this study, the total number of input/output pairs, obtained from DFDAU was 960. The size of the training and test data sets was 75% and 25% of the total input/output pairs, respectively.

2.2.ANFIS Architecture

The ANFIS utilized in this paper performs a first-order Sugeno fuzzy model. For this model, a characteristic rule set with two fuzzy if-then rules can be given as

Rule 1: If x is A_1 and y is B_1, then $z_1 = p_1x + q_1y + r_1$ (3a)

Rule 2: If x is A_2 and y is B_2, then $z_2 = p_2x + q_2y + r_2$ (3b)

where A_i and B_i are the fuzzy sets in the antecedent, and p_i, q_i, and r_i are the design parameters that are found during the training process. As in Figure 1, the ANFIS consists of five layers. The ANFIS has two adjustable parameters set named the premise and consequent parameters. During the learning process, the premise parameters in the layer 1 and the consequent parameters in the layer 4 are adapted until the desired response of the FIS is achieved. In this paper, the hybrid learning algorithm [8], [9], which combines the least square method (LSM) and the backpropagation (BP) algorithm, is used to rapidly train and adapt the FIS.

The number of membership functions (MF) for the input variables were 2 for all inputs. The number of rules is then 128 (2×2×2×2×2×2×2=128). Different membership functions were used for input variables. The best results were obtained when triangular MF was used for all input variables. The triangular MF is specified by three parameters. Therefore, the ANFIS used here contains a total of 1066 fitting parameters, of which 42 (2×3+2×3+2×3+2×3+2×3+2×3+2×3=42) are the premise parameters and 1024 (8×128=1024) are the consequent parameters for the triangular membership function.

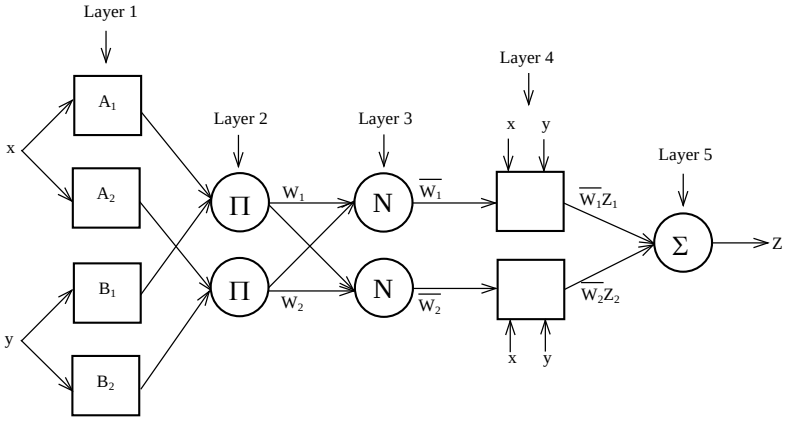

Figure 3. Architecture of ANFIS

2.3.Performance Evaluation

In order to quantitatively evaluate the prediction performances of the proposed ANFIS model, the root mean squared error (RMSE), coefficient of determination (R^2), and the percentage error (PE) are used.

The *RMSE* is stated by:

$$RMSE = \sqrt{\frac{1}{n}\sum_{i=1}^{n}(y_i - y_{d_i})^2} \tag{4}$$

where n is the number of points, y_i is the predicted value obtained from ANFIS model, and y_{d_i} is the actual value.

The R^2 indicates the degree of the fit for the ANFIS model. If the R^2 value is close to 1, it shows that the predicted values are a very close approximation to the actual values. The most general definition of the R^2 is given by:

$$R^2 = 1 - \frac{\sum_{i=1}^{n}\left(y_i - y_{d_i}\right)^2}{\sum_{i=1}^{n}\left(y_{d_i} - y_m\right)^2} \tag{5}$$

where y_m is the average actual values.

The PE is defined as:

$$PE = \left\{\left[\sum_{i=1}^{n}\left(\left|y_i - y_{d_i}\right|/y_{d_i}\right)\right]\right\} \times 100 \tag{6}$$

After several trials, the model which has minimum RMSE, minimum PE, and maximum R^2 is accepted as the best model.

3.RESULTS

The validity of the trained ANFIS model for computing the CAS was evaluated for the test data set. Figure 2 represents the comparison between measured and predicted airspeed results obtained from ANFIS model for testing data sets. It is clearly seen from Figure 3 that the predicted airspeed values obtained by ANFIS are in very good agreement with the measured airspeed values. The advantage of the ANFIS model according to the traditional computation method is that it is independent of the pitot-static measurements. For this reason, it is preferred as an alternative airspeed computation method especially pitot-static system or ADC failures.

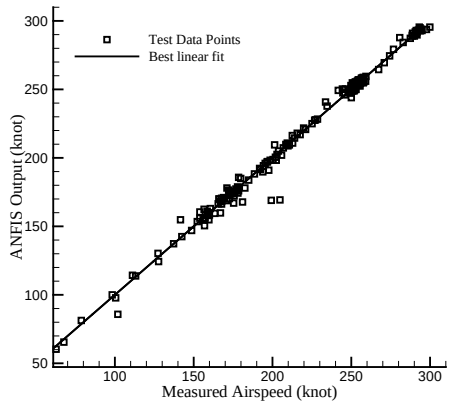

Figure 2. The correlation of the measured and predicted CAS values obtained from the ANFIS model for test data set

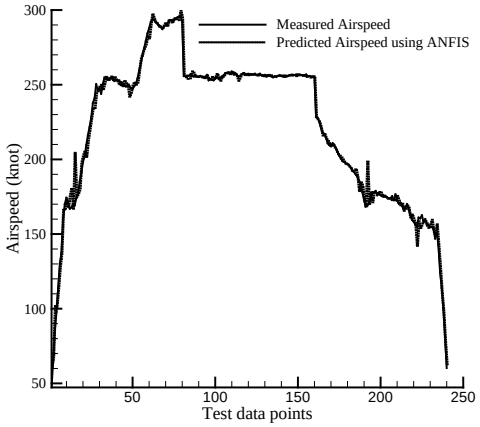

Figure 3. Measured and predicted airspeed values

The RMSE, R^2, and PE values for ANFIS model are summarized and presented in Table I using three different commonly used membership function types for test data set. It is seen from Table I that the best results are obtained when triangular membership functions was used. The R^2 is 0.996 for the triangular membership functions. The predicted airspeed values are very close to the measured values. The RMSE and PE values are 4.248 and 0.799 for the test data set, respectively. This results show that the predictive accuracy of the presented models are very high.

Table I. The performance comparison of the ANFIS model for different membership function type in terms of the RMSE, R^2, and PE

Membership Function	ANFIS Model		
	RMSE (knot)	R^2	PE (%)
Gaussian	4.759	0.995	1.254
Generalized Bell	4.903	0.995	1.380
Triangular	**4.248**	**0.996**	**0.799**

4.CONCLUSIONS

When ADC or pitot-static system is failed, it isn't possible to compute CAS for aircrafts because there is no alternative way of the aircraft other than this. Some aircraft crashes, especially passenger aircraft, have been occurred due to the failure of all ADCs or all pitot-static sensors. In this situation, the CAS information can't be obtained from the ADC by the pilot. In those extreme cases, it is very important to be provided the CAS information to pilots using an alternative method such as ANFIS model proposed in this study.

It is seen from comparison results of the proposed ANFIS model in terms of R^2, RMSE, and PE that the proposed ANFIS model is capable to predict suitable results for CAS. The most important advantages of the proposed model is that its simplicity and accuracy. The implementation of the proposed ANFIS model is very easy. Input parameters can be chosen as quantities, which are commonly measured on a DFDAU. The ANFIS model completely bypasses the repeated use of complex iterative processes for new cases presented to it after the training stage. Thus, the ANFIS computation is very fast after training stage.

The proposed method is low-cost and software-based approach according to traditional air data sensors which are costly and expensive to calibrate. The complicated nonlinear relationship to compute airspeed may be readily derived by the ADC. However, the electronic computation of air parameters from the relationship would be quite difficult. The proposed method provides more simple alternative method for computing airspeed according to the traditional computation method performed by the ADC.

REFERENCES

[1]. J. A. Lawford, K. R. Nippress, "Calibration of air-data systems and flow direction sensors", AGARD-AG-300, 1(300), 1983.
[2]. W**.** Wuest, "Pressure and flow measurement", AGARD-AG-160, 11, 1980.
[3]. W. Gracey, "Measurement of aircraft speed and altitude", NASA RP-1046, 1980.
[4]. K. M. McCool, D. J. Haas, "A NN based approach to helicopter low airspeed and sideslip angle estimation", in *Proceedings of the AIAA Flight Simulation Technologies Conference*, 1996, p. 91-101.
[5]. D.A. Goff, S.M. Thomas, R.P. Jones, and C.P. Massey, "A neural network approach to predicting airspeed in helicopters", *Neural Comput & Applic*., vol. 9, pp. 73–82, 2000.
[6]. O. Samlioglu, *A neural network approach for helicopter airspeed prediction*, Storming Media, 2002.
[7]. K. McCool, D.J. Haas, "Neural network system for estimation of aircraft flight data", U.S. Patent 6 466 888 B1, 2002.
[8]. J.S.R Jang, "ANFIS: Adaptive-network-based fuzzy inference system", *IEEE Trans. Systems, Man, and Cybernetics* vol. 23, pp. 665-685, 1993.
[9]. J.S.R Jang, C.T. Sun, E Mizutani, *Neuro-fuzzy and soft computing: A computational approach to learning and machine intelligence*, Prentice-Hall: Upper Saddle River, NJ, 1997.

ICENS
INTERNATIONAL CONFERENCE ON ENGINEERING AND NATURAL SCIENCES
24-28 May 2016 /Sarajevo

On the Influence of Elasticity Modulus of Concrete on Seismic Response of a Cantilever Wall

***Tufan Cakir*[1]**

Abstract

The problems relating to the vibration of soil and earth retaining structures have received great attention of geotechnical engineers in recent years, and significant advances have been made in this direction. New theoretical and experimental procedures have been developed for design of retaining walls due to the abundance and importance of them, and the complexity of their dynamic response. The behavior of earth retaining structures is a function of relative soil-structure displacements, structural rigidity, backfill and foundation soil properties and characteristics of applied ground motions. This paper presents a three dimensional finite element model of backfill-cantilever wall-soil/foundation interaction system, and investigates the influence of elasticity modulus of wall on seismic response of the cantilever retaining wall. The backfill and foundation soil is modelled as an elastoplastic medium considering the Drucker-Prager yield criterion, and the backfill-wall interface behavior is taken into consideration by using interface elements between the wall and soil to allow for de-bonding. Lysmer-Kuhlemeyer type viscous boundary elements are also used to simulate the wave energy absorption. Nonlinear time history analyses of the interaction system are carried out for three different values of modulus of elasticity. The response quantities examined include the lateral displacements of the wall relative to the moving base, and the stresses in the wall in all directions. The results show that the variation of elasticity modulus of concrete has a considerable effect on seismic behavior of cantilever retaining walls, and should be considered in design process of cantilever walls.

Keywords: *Earth retaining structures, elasticity modulus, seismic response, soil-structure interaction*

1.INTRODUCTION

Soil retaining walls are among the earliest and most common geotechnical structures for the protection of transportation facilities, building structures and ports [1]. In spite of the apparent simplicity of these structures, several aspects of their behavior are poorly understood, especially for conditions involving dynamic actions [2]. On the other hand, it is widely recognized that determination of their seismic response is an important component for their successful design in earthquake prone areas. The most common types of retaining walls are gravity concrete, cantilever T-type reinforced concrete, and cantilever and anchored sheet pile walls. A cantilever T-type retaining wall consists of a concrete stem and base slab which form an inverted T. The structural members are fully reinforced to resist applied moments and shears. The base is made as narrow as practicable, but must be wide enough to ensure that the wall does not slide, overturn, settle excessively, or exceed the bearing capacity of the foundation. The bottom of the base should be below the zone subject to freezing and thawing or other seasonal volume changes [3]. The T-type reinforced concrete retaining wall represents a popular type of retaining system, and is more widely used than any other type for common retaining wall heights. In this study, the T-type cantilever retaining wall is under investigation.

There are mainly three categories of methods for design and seismic analysis of retaining walls: (1) analytic limit-state analysis methods where the wall can displace and/or rotate sufficiently at its base to induce a limit or failure state in the backfill, (2) analytic linear elastic or viscoelastic methods where the wall remains fixed at its base and the backfill soil is considered to respond in a linear elastic or viscoelastic manner, (3) numerical methods of solution, mainly finite element methods under the assumption of linear elastic or nonlinear elastoplastic soil behavior [4]-[6]. The present paper belongs to the third category of methods to seismically analyze the cantilever retaining wall under consideration.

Literature investigation shows that a lot of research has been carried out concerning the dynamic behavior of retaining walls, and a number of methods of varying degrees of accuracy, efficiency and sophistication have been developed for its evaluation. However, limited research has been carried out on the effects of wall rigidity and soil–structure interaction. Evidence of earthquake-induced damages to retaining structures is widely documented in the literature and still stimulates the interest for solutions capable to embody the effect of seismic loading. Furthermore, numerical model studies have demonstrated that the soil stiffness and retaining wall rigidity/movement can substantially impact the seismic behavior of retaining walls. As such, the main purpose of this study is to shed light on the effect of elasticity modulus on dynamic response of a cantilever retaining wall subjected to backfill and subsoil interactions.

2.NUMERICAL MODEL AND SEISMIC ANALYSIS

The finite element method is a well-established technique that is used to solve problems in geotechnical earthquake engineering. For solving the problem of backfill-cantilever wall-soil/foundation system, the general purpose structural analysis

[1] *Corresponding author: Gümüşhane University, Department of Civil Engineering, 29100, Bağlarbaşı/Gümüşhane, Turkey.* cakirtufan@hotmail.com

program ANSYS was used [7]. Numerical analysis of the cantilever retaining wall problem with backfill and subsoil interactions and subjected to earthquake loading is a complex problem. Figure 1 shows the proposed finite element model for the problem of cantilever retaining wall under investigation, which contains different aspects of the model.

The heights of the wall and soil stratum are considered to be the same. The vertical stem height of the cantilever wall is H= 6 m, the wall stem has a constant thickness of 0.4 m, the thickness of base slab is 0.6 m, and the base slab width is 4.0 m. The cantilever wall system is founded on a deformable soil layer of thickness 2H. In the finite element modelling, the structural wall is modelled with 3-D reinforced concrete solid elements (SOLID65) defined by eight nodes having three translational degrees of freedom in each node. The SOLID65 is used for the 3-D modeling of solids with or without reinforcing bars. The solid is capable of cracking in tension and crushing in compression. The backfill and soil/foundation system are modelled with 3-D structural solid elements (SOLID185) with eight nodes having three degrees-of-freedom at each node: translations in the nodal x, y, z directions. The SOLID65 has plasticity, hyperelasticity, stress stiffening, creep, large deflection, and large strain capabilities. It also has mixed formulation capability for simulating deformations of nearly incompressible elastoplastic materials, and fully incompressible hyperelastic materials. Reasonable modelling of the wall-backfill interface requires using special interface elements between the wall and the adjacent soil to allow for separation. Hence, as a special interface element, nonlinear spring (COMBIN39) is used between the backfill and the wall allowing for the opening and closing of the gaps (i.e. de-bonding and bonding) to model backfill-wall interaction in this study. COMBIN39 is a unidirectional element with nonlinear generalized force-deflection capability that can be used in any analysis. The element has longitudinal or torsional capability in 1-D, 2-D, or 3-D applications. The longitudinal option is a uniaxial tension-compression element with up to three degrees of freedom at each node: translations in the nodal x, y, and z directions [8].

Another important consideration in the dynamic finite element analyses is the modeling of semi-infinite extent of the soil medium. The general approach of treating these problems is to divide the infinite medium into the near field (truncated layer), which includes the irregularity as well as the non-homogeneity of the soil adjacent to the structure, and the far field, which is simplified as an isotropic homogeneous elastic medium [9]. In this study, the viscous boundary model [10], which was successfully employed in the finite element modelling of the cantilever walls performed by [11]-[13], is used in three dimensions to consider radiative effect of the seismic waves through the soil medium. To represent the behavior of the semi-infinite backfill medium, the critical minimum distance from the face of the wall is taken as 10H, a value which is believed to approximate adequately the behavior of the semi-infinite layer [5], [14]. In this context, the dashpots were also placed 10H away from the wall in three dimensions to improve the accuracy of the simulation. Similarly, the artificial viscous boundaries have been placed in three dimensions on the boundaries of soil/foundation medium.

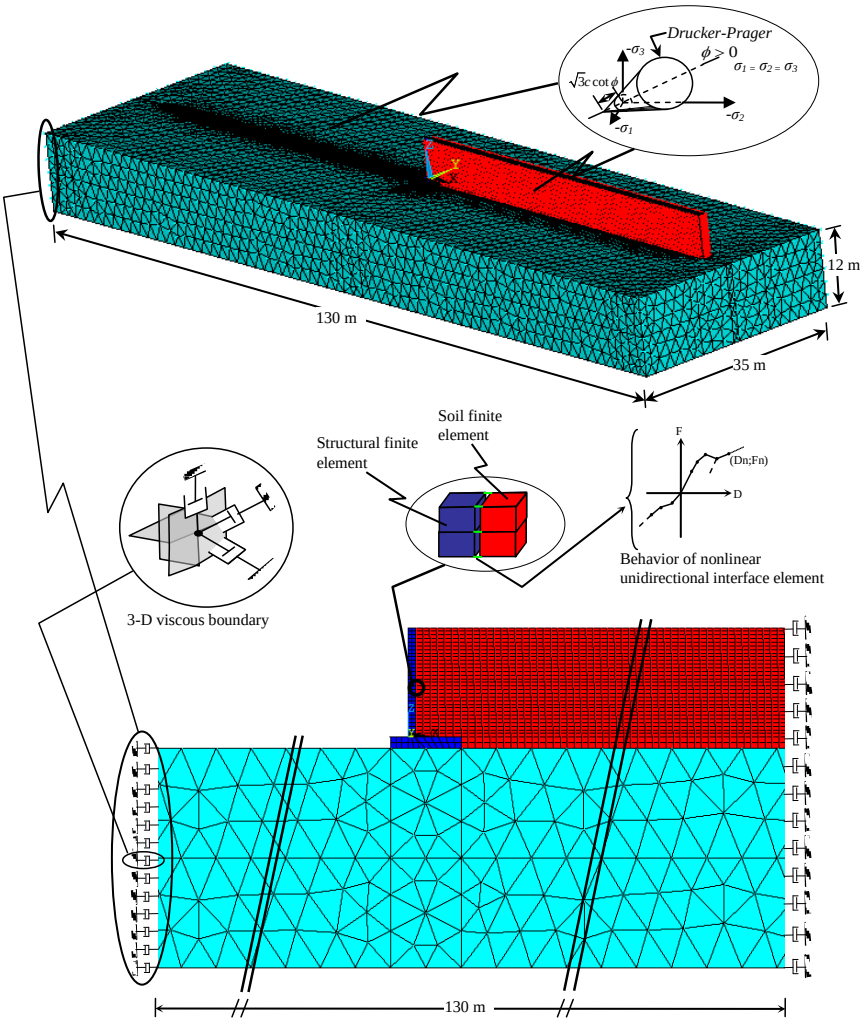

Figure 1. Finite element model of the interaction system

Three different dynamic analyses with variation of elasticity modulus of the cantilever retaining wall were carried out by using the suggested finite element model. As shown in Table 1, while three different elasticity modules of 24000, 28000 and 32000 MPa were selected in the nonlinear time history analyses, the other material properties were considered as constant for both soil and structure. In the seismic analyses, North-South component of the ground motion recorded during August 17, 1999 Kocaeli Earthquake in Yarimca station was used. In the FE procedure, Rayleigh damping was taken into consideration in the Newmark's direct step-by-step integration method [15]. The damping values for both structure and soil were taken as 5%.

Table 1. Material properties of wall and soil

Component	***Elasticity Modulus (MPa)***			***Poisson's Ratio***	***Mass Density (kg/m^3)***
Cantilever wall	E1	E2	E3	0.20	2400
	24000	28000	32000		
Foundation soil		150		0.30	1800
Backfill soil		50		0.30	1800

3.RESULTS AND DISCUSSIONS

Computational results, obtained by applying the proposed procedure, are presented in terms of the lateral displacements and stresses. Table 2 reports the maximum top displacements and the stress responses at the front and back faces of the cantilever wall and their occurrence times depending on the variation of elasticity modulus of wall. As can be seen from Table 2, while the lateral displacements are not practically affected by the variation of elasticity modulus of the wall, the stress responses change to a certain extent. The effects of elasticity modulus on seismic response of cantilever wall are shown graphically, and discussed comparatively below. It is important to note here that since all results obtained from the analyses cannot be illustrated, some comparisons were selected to describe the system behavior.

Table 2. Summary of the maximum seismic responses and their occurrence times

Maximum sponses	***Case***					
	E1		E2		E3	
	t(s)	Value	t(s)	Value	t(s)	Value
u_t (m)	4.8	0.0245	4.8	0.0242	4.8	0.0240
S_{zb} (MPa)	9.7	6.1246	9.7	6.5181	5.35	6.9420
S_{yb} (MPa)	9.7	0.8080	5.35	0.8582	5.35	0.9143
S_{xb} (MPa)	9.7	2.4918	9.7	2.6455	9.7	2.7693
S_{zf} (MPa)	9.7	-6.1998	9.7	-6.5996	5.35	-7.0213
S_{yf} (MPa)	5.35	-0.4834	5.35	-0.5156	5.35	-0.5482
S_{xf} (MPa)	5.3	-0.4330	5.3	-0.4548	5.3	-0.4775

u_t : Maximum lateral top displacement of cantilever wall; S_{zb}, S_{yb} and S_{xb} : Stresses estimated ı the back face (backfill side) of the cantilever wall in *z*, *y* and *x* directions, respectively; S_{zf}, S_{yf} ıd S_{xf} : Stresses estimated on the front face of the cantilever wall in *z*, *y* and *x* directions, spectively.

Figure 2 shows the height-wise variations of the lateral displacements of cantilever retaining wall for varying the elasticity modulus of the wall. It is worth noting here that these displacements represent the relative lateral displacements of the wall with respect to the ground. While the negative displacements refer to the movements away from the backfill, the positive ones refer to the movements toward the backfill. It is observed from this figure that as the elasticity modulus increases, the displacement response tends to decrease.

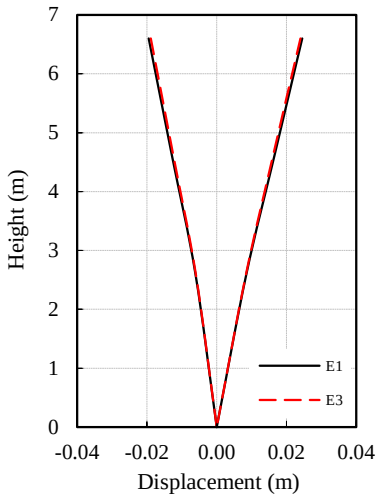

Figure 2. Height-wise variation of maximum calculated displacements of the exterior wall

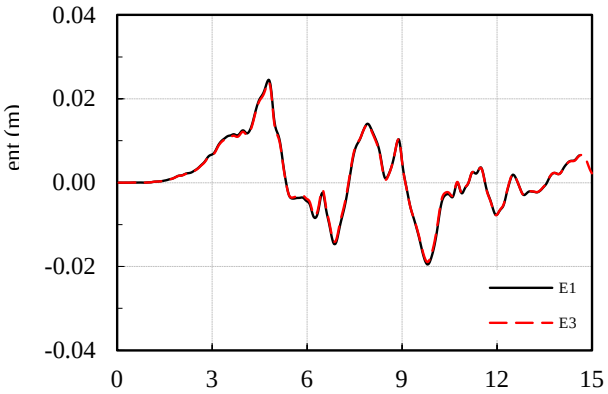

Figure 3. Time histories of lateral top displacement of the cantilever retaining wall

It is possible to evaluate the lateral displacements in terms of time history using the suggested model. Accordingly, the deviations of the displacements in time are illustrated and compared in Figure 3 in order to clarify the changes of the lateral top displacement values due to the variation of elasticity modulus. It can be noted from Figure 3 and Table 2 that while the maximum lateral displacement is estimated as 0.0245 m for E1, the same quantity is calculated as 0.0240 m for E3. Thus, it can be highlighted that the effect of the elasticity modulus of the wall on can be ignored in the evaluation of the seismic behavior of the system so that the decrement in the displacement response is at a level of only 2% between E1 and E3.

The estimated stress responses and their variations in time at the back and the front faces of the cantilever retaining wall can be compared with each other to introduce the modulus of elasticity effects. A comparison of stress time history responses in z direction for front face of the cantilever wall are shown in Figure 4. As this figure depicts, the maximum stresses obtained at the critical section of the wall change with varying the modulus of elasticity. For example, while the peak stress, as compression, has the value of 6.1998 MPa for E1, it is calculated as 7.0213 MPa for E2. This reflects a stress increment of about 13% between E1 and E3 due to the variation of modulus of elasticity. If similar comparisons are made in the other directions as seen in Table 2, the same trend can be clearly observed.

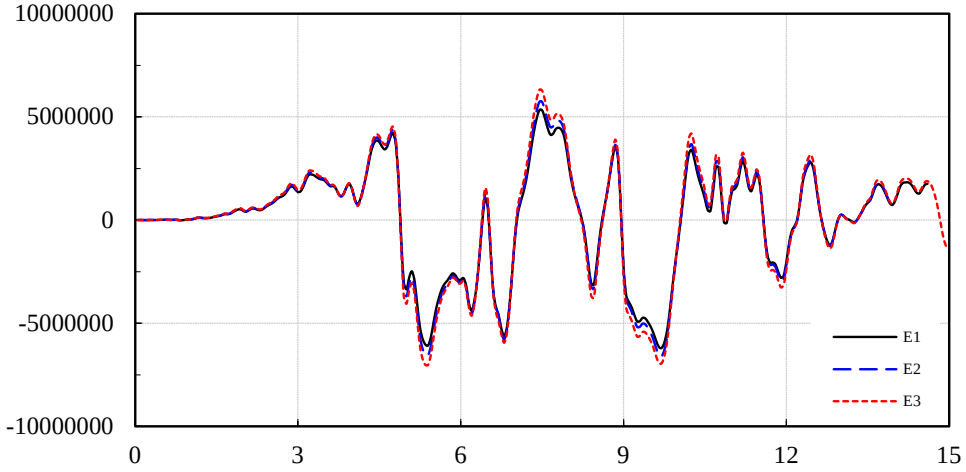

Figure 4. Time histories of stress in z direction at the front face of the cantilever wall

4.CONCLUSIONS

A series of dynamic analyses were conducted to determine the effects of elasticity modulus of the wall on seismic behavior of cantilever retaining wall by means of the finite element model developed in three dimensional space, considering soil-structure interaction. Three different values of elasticity modulus were taken into account in the analyses. The dynamic response of backfill-cantilever wall-soil/foundation system was assessed by using the time histories of calculated lateral displacements of the wall and stresses in the wall.

The lateral displacement response is not practically affected from the variation of elasticity modulus of the cantilever retaining wall considered in this study. Therefore, the effect of the modulus of elasticity on the lateral displacement can be ignored in the evaluation of the seismic behavior of the system. However, the stresses calculated at the critical sections of the cantilever retaining wall is affected from the modulus of elasticity, and the stress response is found to be sensitive to changes in value of elasticity modulus.

It is recommended that more numerical examples should be analyzed so that the results presented here can be generalized.

ACKNOWLEDGMENT

This research has been supported by Gümüşhane University Scientific Research Projects Coordination Department. Project Number: 15.F5110.02.02.

REFERENCES

[1]. G.A. Papagiannopoulos, D.E. Beskos, and T. Triantafyllidis, "Seismic pressures on rigid cantilever walls retaining linear poroelastic soil: An exact solution," *Soil Dynamics and Earthquake Engineering*, vol. 77, pp. 208-219, 2015.
[2]. P. Kloukinas, A.S. di Santolo, A. Penna, M. Dietz, A. Evangelista, A.L. Simonelli, C. Taylor, and G. Mylonakis, "Investigation of seismic response of cantilever retaining walls: Limit analysis vs shaking table testing," *Soil Dynamics and Earthquake Engineering*, vol. 77, pp. 432-445, 2015.
[3]. *Engineering Manual (EM 1110-2-2502)*, Retaining and Flood Walls, US Army Corps and Engineers, Washington, 1989.
[4]. H.N. Nazarian, and A.H. Hadjian, "Earthquake-induced lateral soil pressures on structures," *J. Geotech. Eng. Div., ASCE*, vol. 105(GT9), pp. 1049-1066, 1979.

[5]. A.S. Veletsos, and A.H. Younan, "Dynamic soil pressures on rigid vertical walls," *Earthquake Eng. Struct. Dyn.*, vol. 23(3), pp. 275-301, 1994.
[6]. C. Vrettos, D.E. Beskos, and T. Triantafyllidis, "Seismic pressures on rigid cantilever walls retaining elastic continuously non-homogeneous soil: An exact solution," *Soil Dynamics and Earthquake Engineering*, vol. 82, pp. 142-153, 2016.
[7]. *ANSYS 13.0*, ANSYS Inc., Canonsburg, PA, 2010.
[8]. T. Cakir, "Finite element based investigation of backfill effects on seismic behavior of a cantilever wall," *Procedia Earth and Planetary Science*, vol 15, pp. 231-236, 2015.
[9]. J.P. Wolf, and C. Song, "Finite element modelling of unbounded media," in *11th World Conference on Earthquake Engineering*, 1996, San Francisco, p.p. 1-8.
[10]. J. Lysmer, and R.L. Kuhlemeyer, "Finite dynamic model for infinite media," *J. Eng. Mech. Div., ASCE*, vol. 95, pp. 859-877, 1969.
[11]. T. Cakir, "Evaluation of the effect of earthquake frequency content on seismic behavior of cantilever retaining wall including soil-structure interaction," *Soil Dynamics and Earthquake Engineering*, vol. 45, pp. 96-111, 2013.
[12]. T. Cakir, "Influence of wall flexibility on dynamic response of cantilever retaining walls," *Structural Engineering and Mechanics*, vol. 49, pp. 1-22, 2014.
[13]. T. Cakir, "Backfill and subsoil interaction effects on seismic behavior of a cantilever wall", *Geomechanics and Engineering, An International Journal*, vol. 6, pp. 117-138, 2014.
[14]. P.N. Psarropoulos, G. Klonaris, and G. Gazetas, "Seismic earth pressures on rigid and flexible retaining walls," *Soil Dyn. Earthquake Eng*., vol. 25, pp. 795-809, 2005.
[15]. N.M. Newmark, "A method of computation for structural dynamics," *J. Eng. Mech. Div., ASCE*,vol. 85, pp. 67-84, 1959.

ICENS
INTERNATIONAL CONFERENCE ON ENGINEERING AND NATURAL SCIENCES
24-28 May 2016 /Sarajevo

Effects of Different Ground Motions on Seismic Response of a Cantilever Retaining Wall Considering Soil Structure Interaction

Tufan Cakir[1]

Abstract

It is a well-known fact that earthquake damage to retaining walls is strongly affected by the dynamic properties of local soil deposits and frequency content of the ground motion occurred. The magnitudes of wall movements and stresses in the wall depend on the response of the foundation soil, the response of the backfill, the inertial and flexural responses of the wall itself, and the nature of the ground motions. Major advances have been made for characterizing the seismic behavior of retaining walls over the years. Although researchers have developed a variety of analytical and numerical models to estimate the dynamic behavior of retaining walls or performed various types of experiments to study the mechanisms behind the development of seismic earth pressures on retaining structures, there has been relatively little work on understanding the effects of soil-structure interaction (SSI) and earthquake frequency content on seismic behavior of cantilever walls. In light of the foregoing, a better understanding of the effects of ground motions and SSI appears desirable. As such, the primary objective of this study is to shed light on the effect of the different ground motion records considering SSI on the behavior of cantilever walls. In line with this aim, considering two different ground motion records, nonlinear dynamic analyses of backfill-cantilever wall-soil/foundation interaction system were carried out in time domain using finite element method (FEM). The FEM of the system was constructed using the finite element package ANSYS. Radiation damping and wave reflection effects were considered by using artificial viscous boundaries in the FEM. Consequently, based on the response amplification/reduction pattern observed on the lateral displacements and stresses, it is concluded that the dynamic behavior of cantilever walls is highly sensitive to ground motion characteristics and SSI.

Keywords: *Finite element method, ground motion characteristics, soil-structure interaction, response amplification*

1.INTRODUCTION

Considering frequent occurrence of earthquakes all over the world, investigations on the response of retaining walls under earthquake loading are of critical importance. There are many parameters affecting the seismic response of retaining walls such as backfill soil properties, relative stiffness of the wall/soil system, wall fixity conditions, foundation stability, and characteristics of applied earthquake motions [1]. It is a well-known fact that earthquake damage to retaining walls is strongly affected by the dynamic properties of local soil deposits and frequency content of the ground motion occurred. The local soil conditions and interaction between soil and structure affect the dynamic behavior of a structure in three different ways such as soil amplification, kinematic interaction, and inertial interaction effects. The total interaction effect is generally termed as SSI [2].

There are generally two major methods for analyzing SSI [3]: the direct method and the substructure method. Accumulating experience indicates that while the direct method is a conceptually easier way to model the entire soil-structure system in a single step, the substructure method is computationally more efficient [4]. The direct method of analysis proceeds by applying a consistent free-field ground motion to the boundaries of a discrete model and computing the response of the combined soil-structure system. Hence, a direct method determines the response of the soil and structure simultaneously. In practice, the structural model used in a direct method of analysis represents only an overall dynamic response of the structure. A second stage structural analysis must be performed to obtain the detailed structural response, using the results of SSI analysis as input. Implementation of a direct method requires solution of the free-field ground motion problem, analysis of the coupled soil-structure system, and a detailed second-stage analysis of structural response [2]. On the other hand, in the substructure method, the soil-structure system is divided into two parts: one part is the generalized structure including a portion of adjacent soil with an irregular boundary, which can behave nonlinearly; the other part is the semi-infinite, unbounded linear soil medium. The generalized soil-structure interface separates the two parts [4], [5]. In this study, the direct method of analysis was adopted for SSI evaluation.

[1] *Corresponding author: Gümüşhane University, Department of Civil Engineering, 29100, Bağlarbaşı/Gümüşhane, Turkey.*
cakirtufan@hotmail.com

Seismic analysis and design of retaining walls constitute an important area in geotechnical earthquake engineering, which has received considerable attention, especially in recent years. The existing methods for seismically analyzing retaining walls (in almost all cases under plane strain conditions) can be grouped in the following three categories: (a) analytical limit-state analysis methods where the wall can displace and/or rotate sufficiently at its base to induce a limit or failure state in the backfill soil; (b) analytical linear elastic or viscoelastic methods where the wall remains fixed at its base and the backfill soil responds in a linearly elastic or viscoelastic manner ;(c) numerical methods of solution, mainly finite element methods (FEM),under the assumption of linear elastic or non-linear elastoplastic soil behavior [6]. An extensive list of papers for each one of the above three categories can be found in [6]-[9], and the details need not be repeated herein. A comparison between the results of the two first categories of methods and those from experiments has been conducted by Giarlelis and Mylonakis [10]. The present paper is in the third category of methods.

Considering previous studies on retaining walls, it is seen that most of them have concentrated on the determination of earthquake-induced earth pressures. However, limited research has been done on the effects of SSI and earthquake frequency content on seismic behavior of cantilever walls under three dimensional conditions. As such, the objective of this paper is to investigate the seismic response of a cantilever retaining wall considering the effects of different ground motions and SSI. In line with this aim, a series of seismic analyses were carried out taking two different ground motions and five different soil conditions into consideration in time domain.

Two different ground motions including 1966 Parkfield and 1986 N. Palm Springs are applied to consider the effect of frequency content. All records are scaled in such a way that the horizontal peak ground acceleration reaches 4.7 m/s^2. The frequency content characteristic of the ground motion is reflected in predominant period, bandwidth, central frequency, power spectrum intensity, the ratio of peak ground velocity to peak ground acceleration (PGV/PGA), response spectrum intensity, velocity spectrum intensity and acceleration spectrum intensity etc. [11]. Accordingly, consideration of the frequency content can be raised through different ways. Although PGA and PGV are very useful intensity measures for seismological studies, none can provide any information on the frequency content. PGA and PGV have to be supplemented by additional information for the proper characterization of a ground motion [12]. In this connection, the ratio of PGV to PGA is a ground motion parameter which provides information about frequency content. Because PGA and PGV are usually associated with motions of different frequency, the ratio should be related to the frequency content of the motion [13], [14]. Furthermore, Tso et al. [15] have shown that the ratio of PGA/PGV indicates the relative frequency content of the ground motion. So, a good indicator of the frequency content is the ratio of PGA which is expressed in units g to PGV expressed in units m/s. Earthquake records may be classified into three groups according to the frequency content ratio: (a) high PGA/PGV ratio when PGA/PGV > 1.2, (b) intermediate PGA/PGV ratio when $1.2 \geq PGA/PGV \geq 0.8$, (c) low PGA/PGV ratio when PGA/PGV < 0.8. [7]. So, the Parkfield record has low frequency content, and the N. Palm Springs record has high frequency content.

2.FEM OF THE INTERACTION SYSTEM

Numerical analysis is an important way to evaluate the seismic response of the cantilever retaining wall considering SSI. The main advantage of the FEM in analyzing a SSI problem is that it can accommodate easily for heterogeneity in the soil or structure medium and for nonlinearity in the materials, as well as in the geometry [7]. At this point, the backfill-cantilever wall-soil/foundation model is briefly described. The vertical stem height of the cantilever wall is H= 6 m, the wall stem has a constant thickness of 0.8 m, the thickness of base slab is 0.6 m, and the base slab width is 4.4 m. The cantilever wall system is founded on a deformable soil layer of thickness 2H. Dry-cohesionless soil is considered in the modelling. Furthermore, three-dimensional modelling of interaction system for a cantilever wall length of 1m is adopted in this study (Figure 1). It should be noted here that the finite element modelling and analyses were carried out by using general purpose finite element package ANSYS [16]. The cantilever wall itself is discretized by 3-D solid elements (SOLID 65) defined by eight nodes having three translational degrees of freedom in each node in the finite element procedure. The discretization of the soil medium is made by 3-D structural solid elements (SOLID 185) defined by eight nodes having three degrees of freedom at each node: translations in the nodal x, y, z directions. Moreover, as a special interface element, nonlinear spring is used between the backfill and the wall allowing for the opening and closing of the gaps (i.e. de-bonding and bonding) to model backfill-wall interaction.

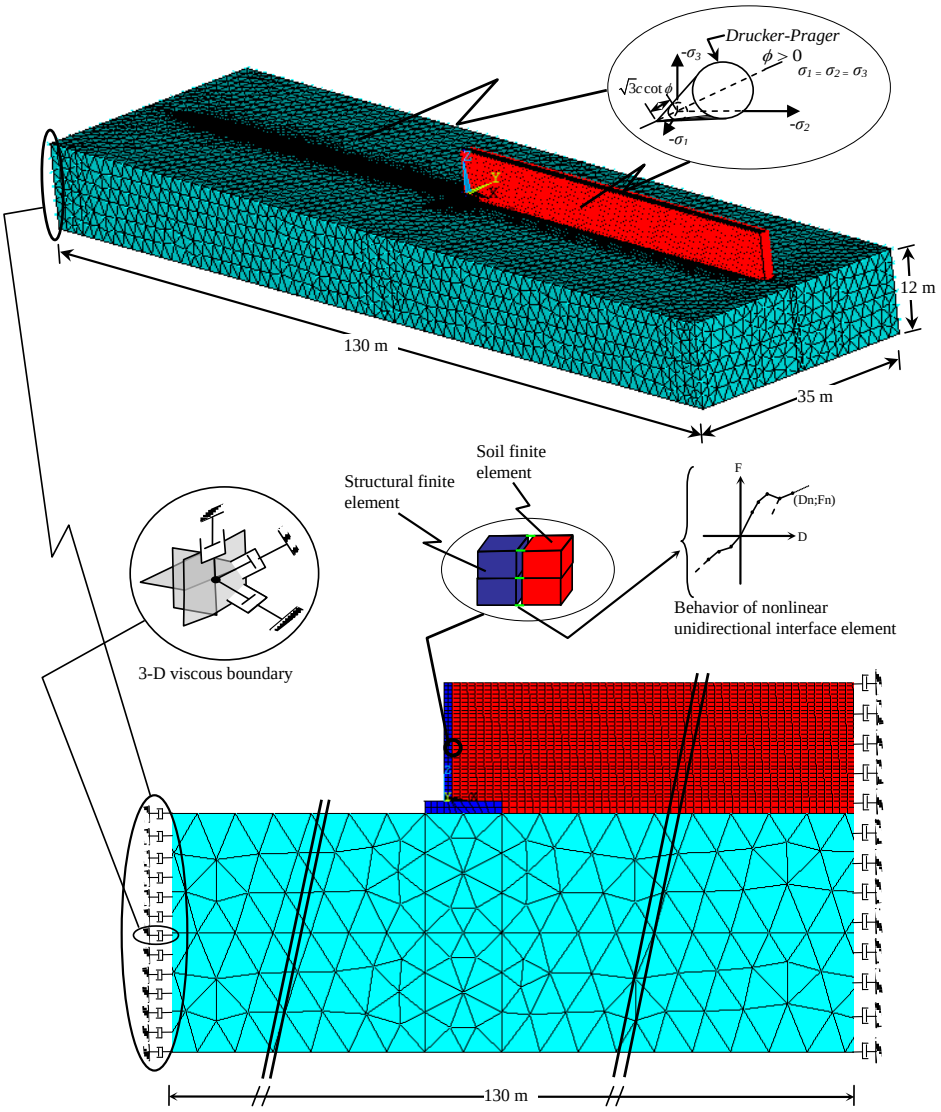

Figure 1. Finite element model of the backfill-cantilever wall-soil/foundation system

Analysis of the soil involves the solution of a wave propagation problem with the radiation condition imposed as a boundary condition at infinity. Therefore, particular attention must be given to the soil boundary conditions when modelling a dynamic problem including soil-structure interaction,. As the soil is modelled by a finite element grid which will be truncated by artificial grid boundaries, there is a need for using absorbing boundaries to simulate the radiation of energy away from the structure. The general approach of treating the problem is to divide the infinite medium into the near field (truncated layer), which includes the irregularity as well as the non-homogeneity of the soil adjacent to the structure, and the far field, which is simplified as an isotropic homogeneous elastic medium [17]. Thus, as an alternative to modelling very large soil volumes and to limit the model to a reasonable size, special artificial and/or transmitting boundaries must be introduced in the finite element analysis of dynamic soil-structure interaction problems. This not only avoids unrealistic wave reflections against the artificial boundaries introduced in the mathematical model but also provides the consideration of radiation effects, and thus, the results are not distorted. In this study, the viscous boundary model [18], which was successfully employed in the finite element models of liquid tank performed by Livaoglu and Dogangun [19], and of cantilever retaining walls carried out by Cakir [7]-[9], is used in three dimensions to consider radiational effect of the seismic waves through the soil medium. To represent the behavior of the semi-infinite backfill medium, the critical minimum distance from the face of the wall is taken as 10H, a value which is believed to approximate adequately the behavior of the semi-infinite layer [20], [21]. In this context, the dashpots were also placed 10H away from the wall in three dimensions to improve the accuracy of the simulation. Similarly, the artificial viscous boundaries have been placed in three dimensions on the boundaries of soil/foundation medium. The proposed finite element model of the backfill-cantilever wall-soil/foundation system is shown in Figure 1.

3.DYNAMIC ANALYSIS

To shed some light on the dynamic performance of cantilever walls, a series of dynamic analyses are conducted for the system. The Young's modulus, Poisson's ratio and unit weight of the wall are 28000 MPa, 0.2 and 25 kN/m^3, respectively. The

Young's Modulus, the Poisson's ratio and the unit weight of cohesionless backfill soil were taken to be 30 MPa, 0.35 and 18 kN/m^3, respectively. To evaluate the dynamic response of the cantilever wall supported on flexible foundation, five different foundation soil types were considered in the analyses, as shown in Table 1. C02065 component of 1966 Parkfield (Figure 2), and WWT-UP component of 1986 N. Palm Springs (Figure 3) earthquakes were used in time history analyses. The horizontal peak ground acceleration for this record reaches 4.7 m/s^2. Furthermore, Rayleigh damping was taken into consideration in the analyses. The damping values for both structure and soil were presumed to be 5%.

Table 1. Properties of the soil types considered in this study

Soil types	E (kN/m^2)	G (kN/m^2)	υ	γ (kg/m^3)	V_s (m/s)	V_p (m/s)
S1	2000000	769231	0.30	2000	620.17	1160.24
S2	500000	185185	0.35	1900	312.20	649.89
S3	150000	55556	0.35	1900	171.00	355.96
S4	75000	26786	0.40	1800	121.99	298.81
S5	35000	12500	0.40	1800	83.33	204.12

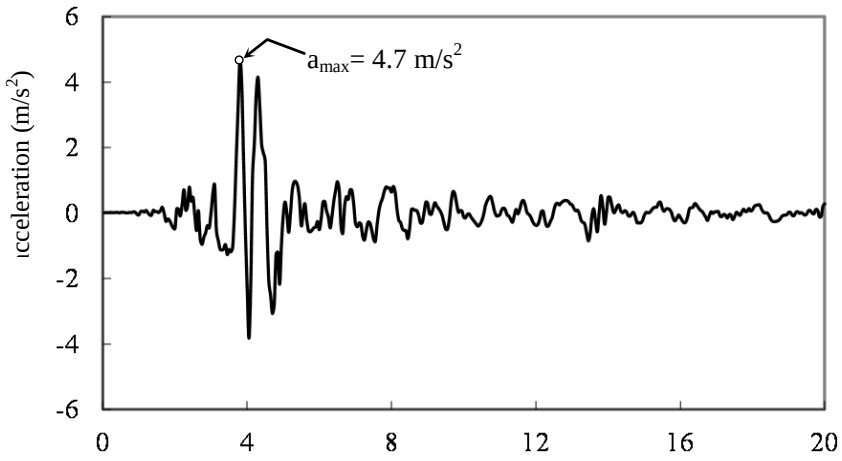

Figure 2. C02065 component of 1966 Parkfield earthquake

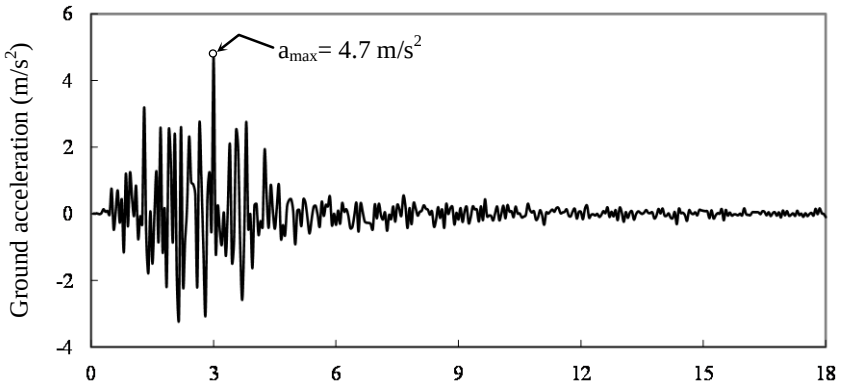

Figure 3. WWT-UP component of 1986 N. Palm Springs earthquake

4.RESULTS AND DISCUSSIONS

Results, obtained by applying the proposed methodology, are presented in terms of the lateral displacements and stresses in two parts. In the first part, a discussion on the effects of SSI on seismic behavior of cantilever wall is given. In the second part, the effects of earthquake frequency content on dynamic behavior of cantilever wall subjected to the combined effects of backfill and soil/foundation interactions are discussed. Tables 2-3 report the peak responses and the corresponding times calculated for

varying the soil types and the ground motions. The tables clearly indicate the effects of SSI and earthquake frequency content so that the maximum values of both lateral displacements and stresses changed significantly. These effects on seismic response of cantilever wall are discussed comparatively below, by performing some comparisons to describe the system behavior. It is worth emphasizing here that the displacements represent the relative lateral displacements of the wall with respect to the ground.

Table 2. Seismic analysis results for Parkfield earthquake

Maximum responses	Soil system									
	S1		S2		S3		S4		S5	
	t (s)	Value	t (s)	Value	t (s)	Value	t (s)	Value	t (s)	Value
u_t (m)	4.50	0.0003	4.50	0.0052	4.55	0.0196	4.55	0.0342	4.60	0.0566
S_{zb} (MPa)	4.40	-0.2508	4.40	-3.1192	3.90	-6.8083	4.45	-7.5214	4.50	-5.9910
S_{yb} (MPa)	4.45	-0.0366	4.40	-0.5212	3.90	-1.2343	3.90	-1.4456	4.45	-1.2396
S_{xb} (MPa)	4.50	-0.1683	4.45	-2.7459	4.45	-6.6222	4.45	-7.8632	4.50	-6.8476
S_{zf} (MPa)	4.40	0.2546	4.40	3.0047	3.90	6.3823	4.45	6.8750	4.50	5.3224
S_{yf} (MPa)	3.90	0.0222	3.90	0.2380	3.90	0.4585	3.90	0.4977	4.45	0.3756
S_{xf} (MPa)	3.90	0.0917	3.90	0.8908	3.90	1.5024	3.90	1.5186	4.45	1.0248

u_t : Maximum lateral top displacement of cantilever wall; S_{zb}, S_{yb} and S_{xb} : Stresses estimated on the back face (backfill side) of the cantilever wall in *z*, *y* and *x* directions, respectively; S_{zf}, S_{yf} and S_{xf} : Stresses estimated on the front face of the cantilever wall in *z*, *y* and *x* directions, respectively.

It is observed from Tables 2 and 3 that as the soil stiffness decreases, the displacement response generally tends to increase for all conditions, and this reflects a significant SSI influence on the response. For example, while the maximum lateral displacement is estimated as 0.0196 m for S3 soil type, the same quantity is calculated as 0.0566 m for S5 soil type under Parkfield earthquake. Thus, it can be highlighted that SSI affects the wall behavior so that the dramatic increment in the displacement response is almost at a level of 189% between S3 and S5 soil types. A similar comparison can be made from Table 3 for N. Palm Springs earthquake.

The computed stress responses can also be compared to introduce the SSI effects. As seen from Tables 2-3, the maximum stresses obtained at the critical sections of the wall change with varying soil conditions. For example, under the N. Palm Springs earthquake, while the peak stress, as compression, has the value of 1.3667 MPa for S2 soil type, it is calculated as 2.6914 MPa for S4 soil type at the back face of the cantilever retaining wall in z direction. This reflects a stress increment of about 97% between S2 and S4 soil types due to the variation of soil conditions. A similar trend can be observed for Parkfield earthquake as well, the maximum stress responses due to the SSI are highly magnified.

Table 3. Seismic analysis results for N. Palm Springs earthquake

Maximum responses	Soil system									
	S1		S2		S3		S4		S5	
	t (s)	Value	t (s)	Value	t (s)	Value	t (s)	Value	t (s)	Value
u_t (m)	3.05	0.0002	3.65	0.0030	3.65	0.0136	3.70	0.0244	4.7	0.0432
S_{zb} (MPa)	3.05	-0.1215	3.05	-1.3667	3.05	-2.4896	3.10	-2.6914	3.10	-1.8464
S_{yb} (MPa)	3.05	-0.0184	3.05	-0.2239	3.05	-0.4661	3.10	-0.5310	3.10	-0.4080

S_{xb} (MPa)	3.05	-0.0766	3.05	-1.1169	3.10	-2.4693	3.10	-2.9148	3.10	-2.2556
S_{zf} (MPa)	3.05	0.1221	3.05	1.3393	3.05	2.3384	3.10	2.4548	3.10	1.6224
S_{yf} (MPa)	3.05	0.0104	3.05	0.1088	3.05	0.1829	3.10	0.1788	3.10	0.1242
S_{xf} (MPa)	3.05	0.0396	3.05	0.4046	3.05	0.6213	3.10	0.5422	3.10	0.3454

u_t : Maximum lateral top displacement of cantilever wall; S_{zb}, S_{yb} and S_{xb} : Stresses estimated on the back face (backfill side) of the cantilever wall in *z*, *y* and *x* directions, respectively; S_{zf}, S_{yf} and S_{xf} : Stresses estimated on the front face of the cantilever wall in *z*, *y* and *x* directions, respectively.

As mentioned before, to assess the effects of earthquake record on structural behavior, two different ground motions are used in the analyses. Accordingly, Tables 2-3 indicate that effect of earthquake characteristics is fairly significant on the structural response of the wall so that the peak responses are different from each other depending on the variation of the ground motion. Another sign of this influence is the differences in occurrence times of responses. Furthermore, maximum responses are smaller for N. Palm Springs earthquake with high frequency content in comparison to the Parkfield earthquake with low frequency content, and this is valid for all soil types.

As Tables 2-3 demonstrates, while the maximum lateral top displacement is calculated as 0.0030 m at 3.65 s for N. Palm Springs earthquake with high frequency content, the same quantity is computed as 0.0052 m at 4.50 s for Parkfield earthquake with low frequency content. Hence, it can be noted that input earthquake motion affects the system behavior so that the increment in the displacement response is almost at a level of 73%. If similar comparison is made for S5 soil type, a similar trend of an increase in the response can be seen (see Tables 2-3). For instance, the value of maximum lateral displacement is 0.0432 m for N. Palm Springs earthquake, while the displacements are estimated as 0.0566 m for Parkfield earthquake. It is clear that the variation of the ground motion leads to an increment of about 31% in peak displacement response. It is found that the effect of earthquake frequency content is quite significant on the displacement response, and may cause a considerable increase in time domain peak response values.

In addition to the lateral displacement response, stress behavior of the cantilever wall is can be examined in this section. As the tables show, the maximum stress responses obtained at the critical sections of the wall generally tend to increase in absolute value with decrement in the frequency content. For example, at the back face of the wall in *z* direction for S4 soil type, while the maximum stress, as compression, has the value of 2.6914 MPa for N. Palm Springs record with high frequency content, its value is 7.5214 MPa for Parkfield earthquake with low frequency content. This reflects an increase of about 180% in stress value due to the variation of the ground motion. The same tendency can be observed for the other soil types, as seen in Tables 2-3.

It is clear that the response amplification or reduction pattern due to deformable foundation is highly dependent on the nature of the earthquake.

5.CONCLUSIONS

A series of dynamic analyses were conducted to determine seismic behavior of cantilever retaining walls by means of the FEM developed in three dimensional space, considering the effects of SSI and different ground motions. Five different soil types and two different ground motions with low and high frequency contents were taken into account in the analyses. It is concluded that the seismic response of cantilever retaining structures is a complex SSI problem, and the magnitudes of wall movements and stresses in the wall induced by horizontal ground shaking are quite sensitive to the response of the soil underlying the wall and the nature of the ground motions.

The computational results include the lateral displacements and stresses in the wall obtained from nonlinear time history analyses of the considered system. It is found that SSI has a significant effect on the seismic behavior of cantilever wall. Therefore, accurate determination of local soil properties is of critical importance to establish a reliable seismic design of cantilever retaining walls. Furthermore, it is found that effect of earthquake characteristics is significant on structural response, and may cause a considerable increase in time domain peak response values. The ground motion with higher PGV/PGA value has larger damage potential on the cantilever retaining wall.

It is clear that the dynamic behavior of cantilever walls depends on a wide range of parameters such as nature of earthquakes, backfill interaction and soil/foundation interaction which should be taken into consideration in current codes of practice. Accordingly, this research provides an important addition to the available knowledge database of the earthquake analysis of cantilever walls. However, it is recommended that more numerical examples should be analyzed so that the results presented here can be generalized.

ACKNOWLEDGMENT

This research has been supported by Gümüşhane University Scientific Research Projects Coordination Department. Project Number: 15.F5110.02.02.

REFERENCES

[1]. M. M. Dewoolkar, H. Y. Ko, and R. Y. S. Pak, "Seismic behavior of cantilever retaining walls with liquefiable backfills," *Journal of Geotechnical and Geoenvironmental Engineering*, vol. 127(5), pp. 424-435, 2001.
[2]. K. P. Jaya and A. M. Prasad, "Embedded foundation in layered soil under dynamic excitations," *Soil Dynamics and Earthquake Engineering*, vol. 22, pp. 485-498, 2002.
[3]. J. P. Wolf, *Soil-Structure Interaction Analysis in Time Domain*, Englewoods Cliffs, NJ:Prentice-Hall, 1988.
[4]. J. B. Li, J. Yang, and G. Lin, "A stepwise damping-solvent extraction method for large-scale dynamic soil-structure interaction analysis in time domain," *International Journal for Numerical and Analytical Methods in Geomechanics*, vol. 32(4), pp. 415-438, 2008.
[5]. R. Livaoglu, "Investigation of seismic behavior of fluid-rectangular tank-soil/foundation systems in frequency domain," *Soil Dynamics and Earthquake Engineering*, vol. 28, pp. 132-146, 2008.
[6]. C. Vrettos, D.E. Beskos, and T. Triantafyllidis, "Seismic pressures on rigid cantilever walls retaining elastic continuously non-homogeneous soil: An exact solution," *Soil Dynamics and Earthquake Engineering*, vol. 82, pp. 142-153, 2016.
[7]. T. Cakir, "Evaluation of the effect of earthquake frequency content on seismic behavior of cantilever retaining wall including soil-structure interaction," *Soil Dynamics and Earthquake Engineering*, vol. 45, pp. 96-111, 2013.
[8]. T. Cakir, "Influence of wall flexibility on dynamic response of cantilever retaining walls," *Structural Engineering and Mechanics*, vol. 49, pp. 1-22, 2014.
[9]. T. Cakir, "Backfill and subsoil interaction effects on seismic behavior of a cantilever wall", *Geomechanics and Engineering, An International Journal*, vol. 6, pp. 117-138, 2014.
[10]. C. Giarlelis and G. Mylonakis, "Interpretation of dynamic retaining wall model tests in light of elastic and plastic solutions," *Soil Dynamics and Earthquake Engineering*, vol. 31, pp. 16-24, 2011.
[11]. S. L. Kramer, *Geotechnical Earthquake Engineering*, New Jersey: Prentice-Hall; 1996.
[12]. E. Kermani, Y. Jafarian, and M.H. Baziar, "New predictive models for the v_{max}/a_{max} ratio of strong ground motions using genetic programming," *International Journal of Civil Engineering*, vol. 7(4), pp. 236-247, 2009.
[13]. N. M. Newmark, "A study of vertical and horizontal earthquake spectra," NM Newmark Consulting Engineering Services. Directorate of Licencing, US Atomic Energy Commission, Washington, DC, 1973.
[14]. R. K. McGuire, "Seismic ground motion parameter relations," *ASCE Journal of the Geotechnical Engineering Division*, vol. 104(GT4), pp. 481-490, 1978.
[15]. W. K. Tso, T. J. Zhu, and A.C. Heidebrecht, "Engineering implications of ground motion A/V ratio," *Soil Dynamics and Earthquake Engineering*, vol. 11(3), pp. 133-144, 1992.
[16]. *ANSYS 13.0*, ANSYS Inc., Canonsburg, PA, 2010.
[17]. J.P. Wolf, and C. Song, "Finite element modelling of unbounded media," in *11th World Conference on Earthquake Engineering*, 1996, San Francisco, pp. 1-8.
[18]. J. Lysmer, and R.L. Kuhlemeyer, "Finite dynamic model for infinite media," *J. Eng. Mech. Div., ASCE*, vol. 95, pp. 859-877, 1969.
[19]. R. Livaoglu and A. Dogangun, "Effect of foundation embedment on seismic behavior of elevated tanks considering fluid-structure-soil interaction," *Soil Dynamics and Earthquake Engineering*, vol. 27, pp. 855-863, 2007.
[20]. A.S. Veletsos, and A.H. Younan, "Dynamic soil pressures on rigid vertical walls," *Earthquake Eng. Struct. Dyn.*, vol. 23(3), pp. 275-301, 1994.
[21]. P.N. Psarropoulos, G. Klonaris, and G. Gazetas, "Seismic earth pressures on rigid and flexible retaining walls," *Soil Dyn. Earthquake Eng.*, vol. 25, pp. 795-809, 2005.

Simulation and Investigation of Two Dimensional MHD Laminar Flow in Parallel Plate Channels for Different Surface Structures

*Cigdem Susantez *[1], Aysegul Ozturk[1], Kamil Kahveci[1]*

Abstract

In this study, steady laminar flow and heat transfer of an electrically conducting viscous fluid in parallel plate channels with uniform but not equal wall temperatures is investigated numerically in the presence of a transverse magnetic field. Numerical results are obtained for the cases of smooth and sinusoidal wall surfaces respectively for Br = 0, 0.05 and 0.1 and Ha = 0, 1, 2, 3, 4, 5. Effects of the Brinkman number and Hartmann number on the temperature and velocity distribution and local Nusselt numbers has been discussed.

Keywords: *MHD, Viscous dissipation, Parallel plate flow, Comsol Multiphysics*

1.INTRODUCTION

Magnetohydrodynamics (MHD) is a field about hydrodynamics under the effect of electromagnetic field.

It deals with the fluid flow of an electrically conducting fluid through a magnetic field. MHD has many applications especially in microfluid pumping, power generation nuclear reactors and metallurgy. It gives humans the ability to control the flow without mechanical influence [1]. There have been numerous studies about MHD flow and heat transfer. Wu and Cheng [2] made a theoretical study about the thermal entrance region heat transfer problem for MHD laminar flow in parallel plate channels with unequal wall temperatures.

In their study, they consider viscous dissipation and Joule heating and used the eigenfunction expansion method. They showed that viscous heating effect is appreciable near the upper and lower walls and dissipation effects increase by the Joule heating. Witt and Schwarz [3] numerically investigated the two and three dimensional flow of a conducting fluid in a duct under the influence of transverse magnetic and electric fields. They showed that the predicted velocity profiles for the two dimensional investigation match the analytic solution with high accuracy. Regarding their three dimensional analysis they also showed that, high velocity regions appear near the insulated side walls due to smaller Lorentz force. Kiema et al. [4] numerically investigated the steady MHD poiseuille flow between two infinite parallel porous plates with transverse magnetic field. They showed that increasing the Hartmann number leads to a decrease in velocity distribution due to Lorentz force. Hunt and Leibovich [5] made a theoretical, two dimensional analysis on steady, incompressible, MHD flow through ducts with arbitrarily varying cross section. They examined the flow for three different flow regions called as core region, Hartmann boundary layers and thin layers parallel to the magnetic field in which pressure gradient, inertial and electromagnetic forces balance each other. Mhone and Makinde [6] studied unsteady MHD flow in an exponentially diverging symmetrical channel. They obtain analytical expressions of stream function, vorticity and temperature distribution. Attia and Kotb [7] made a numerical investigation on steady, MHD flow of a viscous, electrically conducting and incompressible fluid between two parallel infinite insulated horizontal plates with constant but unequal temperatures. In their study the viscosity of the fluid was assumed to vary exponentially with temperature, the upper plate was given a horizontal velocity. They showed that the magnetic field has a significant restraining effect on the reversed flow and flow recirculation depth. Umavathi et al. [8] made a flow and heat transfer analysis on the Poiseuille-Couette flow of two immiscible fluids between parallel plates. They assumed that only one fluid is electrically conducting. They not only obtain numerical results but also analytically solved the governing equations for small values of PrEc. They presented the velocity profiles in the channel for different values of Hartmann number. They also compared numerical and analytical solutions and detected significant difference on the flow and rate of heat transfer for the high values of Pr Ec. Sreekala and Reddy [9] studied steady MHD three dimensional couette flow of an incompressible viscous fluid through a porous medium between two infinite parallel plates. In their study, inclined magnetic field has been applied to parallel plates, stationary plate was subjected to sinusoidal surface temperature and sinusoidal suction velocity, moving plate was isothermal and subjected to uniform injection velocity. They obtain velocity and temperature distributions for different values of Reynolds number, suction parameter, Hartmann number and Darcy parameter by using perturbation technique.

[1] *Corresponding author: Trakya University, Department of Mechanical Engineering, 22180, Center/Edirne, Turkey.*
cigdemsusantez@trakya.edu.tr

In this study, steady laminar flow and heat transfer of an electrically conducting viscous fluid in parallel plate channels investigated numerically in the presence of a transverse magnetic field. Viscous dissipation and joule heating effects have been considered for each channel geometry examined.

2.MATERIAL AND METHOD

*2.1.*Mathematical Method

Governing equations has been performed for incompressible fluid with constant physical properties. Upper and lower walls have constant temperature as shown in Fig.1. Inlet velocity is u_m , inlet temperature is T_2. Dimension of the sinusoidal wall has also been presented in Fig. 2.

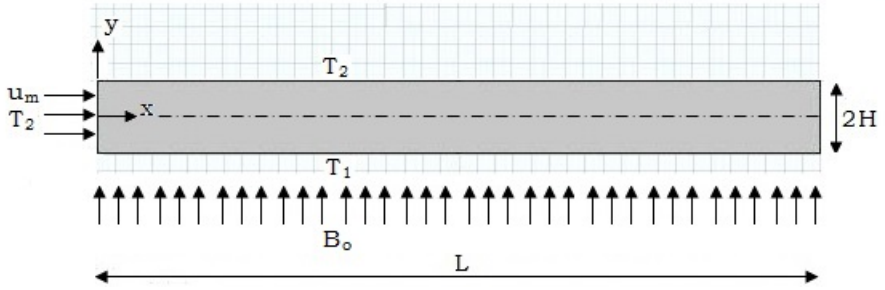

a) Straight wall configuration

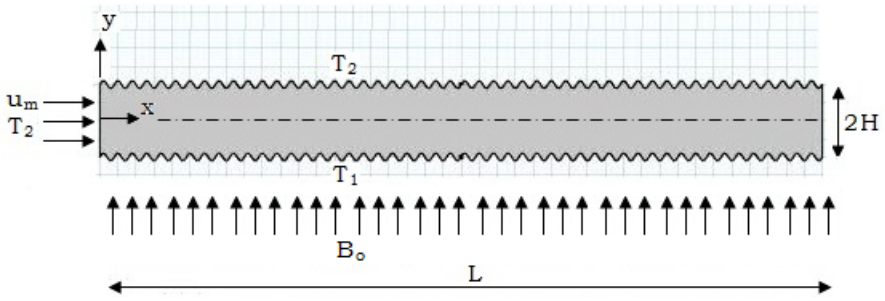

b) Sinusoidal wall configuration

Figure 1. Geometry of the problem

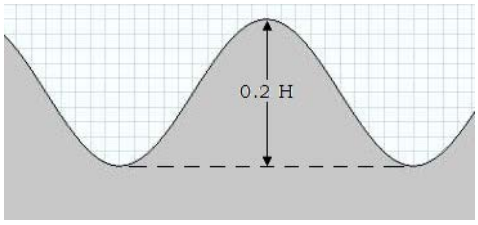

Figure 2. Dimension of the sinusoidal wall structure

The governing equations for the problem under consideration are continuity, momentum, energy equations and Ohm's law with Maxwell's equations. General forms of these equations are given below.

Continuity equation:

$$\vec{\nabla} \cdot \vec{V} = 0 \tag{1}$$

Momentum equation:

$$(\vec{V} \cdot \vec{\nabla})\vec{V} = -\frac{1}{\rho}\vec{\nabla}p + \nu\nabla^2\vec{V} + \frac{1}{\rho}\vec{J} \times \vec{B} \tag{2}$$

Energy equation:

$$\rho c_p(\vec{V}\cdot\vec{\nabla})T = k\nabla^2 T + \mu\emptyset + \frac{1}{\sigma}(\vec{J}\cdot\vec{J}) \quad (3)$$

Ohm's law:

$$\vec{J} = \sigma(\vec{E} + \vec{\mathrm{V}}\times\vec{B}) \quad (4)$$

Maxwell's equations:

$$\vec{\nabla}\cdot\vec{\mathrm{B}} = 0\,,\ \vec{\nabla}\times\vec{B} = \mu_e\vec{J}\,,\ \vec{\nabla}\cdot\vec{\mathrm{E}} = 0\,,\ \vec{\nabla}\times\vec{E} = 0 \quad (5)$$

where $\mu\emptyset$ is viscous dissipation term, $\vec{V}$ is velocity vector, $\vec{J}$ is electric current density vector, $\vec{E}$ is electric field intensity vector and $\vec{B}$ is magnetic field induction vector. In these analysis $\vec{\nabla}\cdot\vec{\mathrm{E}} = 0$ shows that there is no excess charge density. On the other hand, the effect of the induced magnetic field is assumed to be negligible in comparison with the applied magnetic field B_o.

The nondimensional form of the following governing equations has been solved in Comsol Multiphysics program for two dimensional geometry in the case of $\vec{V} = (u, v, 0)$, $\vec{J} = (0,0,J_z)$, $\vec{E} = (0,0,-E_o)$ and $\vec{B} = (0, B_o, 0)$.

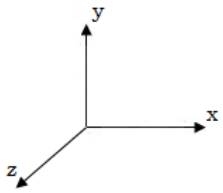

Figure 3. Coordinate axis

Continuity equation:

$$\frac{\partial u}{\partial x} + \frac{\partial v}{\partial y} = 0 \quad (6)$$

x momentum equation:

$$u\frac{\partial u}{\partial x} + v\frac{\partial u}{\partial y} = -\frac{1}{\rho}\frac{\partial p}{\partial x} + \nu\left(\frac{\partial^2 u}{\partial x^2} + \frac{\partial^2 u}{\partial y^2}\right) - \frac{1}{\rho}B_o\sigma(uB_o - E_o) \quad (7)$$

y momentum equation:

$$u\frac{\partial v}{\partial x} + v\frac{\partial v}{\partial y} = -\frac{1}{\rho}\frac{\partial p}{\partial y} + \nu\left(\frac{\partial^2 v}{\partial x^2} + \frac{\partial^2 v}{\partial y^2}\right) \quad (8)$$

Energy equation:

$$\rho c_p\left(u\frac{\partial T}{\partial x} + v\frac{\partial T}{\partial y}\right) = k\left(\frac{\partial^2 T}{\partial x^2} + \frac{\partial^2 T}{\partial y^2}\right) + \mu\emptyset + \sigma(uB_o - E_o)^2 \quad (9)$$

$$\mu\emptyset = \mu\left[\left(\frac{\partial u}{\partial y} + \frac{\partial v}{\partial x}\right)^2 + 2\left(\left(\frac{\partial u}{\partial x}\right)^2 + \left(\frac{\partial v}{\partial y}\right)^2\right) - \frac{2}{3}\left(\frac{\partial u}{\partial x} + \frac{\partial v}{\partial y}\right)^2\right]$$

Dimensionless variables and numbers have been defined as follows:

$$X = \frac{x}{H}\,,Y = \frac{y}{H}\,,\theta = \frac{T - T_m}{T_2 - T_m}\,,U = \frac{u}{u_m}\,,V = \frac{v}{u_m}\,,\mathrm{P} = \frac{pH}{\mu\, u_m}\,, \quad (10)$$

$$Ha = B_o H\left(\frac{\sigma}{\mu}\right)^{1/2}\,,Br = \frac{\mu\, {u_m}^2}{k\,\theta_c}\,,Re = \frac{\rho u_m H}{\mu}\,,K = \frac{E_o}{B_o u_m}$$

where θ_c is characteristic temperature difference and defined as $T_2 - T_m$. T_m is mean temperature, it is also defined as $\frac{T_1+T_2}{2}$.

The nondimensional forms of the continuity, x and y momentum and energy equation have been obtained as given in equation (11), (12), (13) and (14) respectively.

$$\frac{\partial U}{\partial X} + \frac{\partial V}{\partial Y} = 0 \quad (11)$$

$$Re\left(U\frac{\partial U}{\partial X} + V\frac{\partial U}{\partial Y}\right) = -\frac{\partial P}{\partial X} + \left(\frac{\partial^2 U}{\partial X^2} + \frac{\partial^2 U}{\partial Y^2}\right) - Ha^2(U - K) \quad (12)$$

$$Re\left(U\frac{\partial V}{\partial X} + V\frac{\partial V}{\partial Y}\right) = -\frac{\partial P}{\partial Y} + \left(\frac{\partial^2 V}{\partial X^2} + \frac{\partial^2 V}{\partial Y^2}\right) \quad (13)$$

$$Re\left(U\frac{\partial\theta}{\partial X}+V\frac{\partial\theta}{\partial Y}\right)=\frac{1}{Pr}\left(\frac{\partial^2\theta}{\partial X^2}+\frac{\partial^2\theta}{\partial Y^2}\right)+\frac{Br}{Pr}\left[\left(\frac{\partial U}{\partial Y}+\frac{\partial V}{\partial X}\right)^2+2\left(\left(\frac{\partial U}{\partial X}\right)^2+\left(\frac{\partial V}{\partial Y}\right)^2\right)\right] \quad (14)$$
$$+\frac{Ha^2Br}{Pr}(U-K)^2$$

Nondimensional forms of the boundary conditions have been defined as:

$$\begin{aligned}&U|_{X=0}=1\,,V|_{X=0}=0\,,\\&U,V|_{upper\ and\ lower\ walls}=0 \quad \text{(for straight wall } U,V|_{Y=\pm1}=0)\\&P|_{X=L/H}=0\\&\theta|_{X=0}=1\end{aligned} \quad (15)$$

$$\begin{aligned}&\theta|_{upper\ wall}=1 \quad \text{(for straight wall } \theta|_{Y=1}=1)\\&\theta|_{lower\ wall}=-1 \quad \text{(for straight wall } \theta|_{Y=-1}=-1)\\&\left.\frac{\partial\theta}{\partial X}\right|_{X=L/H}=0 \quad \text{(comes from outflow boundary condition)}\end{aligned} \quad (16)$$

Length of the channels L is equal to 20H and local Nusselt numbers at the upper and lower walls has been determined at the middle of the walls (X=10). The expressions for the local Nusselt numbers Nu_1 and Nu_2 at the lower and upper plates are defined respectively as:

$$Nu_1=\frac{h_1H}{k}=\frac{1}{1+\theta_b}\left.\frac{\partial\theta}{\partial Y}\right|_{Y=-1} \quad (17)$$

$$Nu_2=\frac{h_2H}{k}=\frac{1}{1-\theta_b}\left.\frac{\partial\theta}{\partial Y}\right|_{Y=1} \quad (18)$$

where the dimensionless bulk temperature is

$$\theta_b=\frac{\int_{-1}^{1}\theta U dY}{\int_{-1}^{1}U dY} \quad (19)$$

3.CONCLUSION

The working fluid is sea water with salinity of 20 g/kg. The value of the Prandtl number of this working fluid is taken as 3.66 under the assumption of the mean value of the bulk temperature is around 50^{o}C [10]. Numerical result obtained for Re=100 and K=1 (lowest current case). Extra fine mesh and physics-controlled mesh has been used for the geometry. While maximum element size is 0.4, minimum element size is 0.015.

Simulations of the velocity profiles for the each investigated channel geometry have been presented in Fig. 4 and 5 respectively. Hartmann number is the ratio of the Lorentz force to the viscous forces. As it is seen form Fig. 4 and 5, increasing magnetic field decreases the velocity due to retarding effect of the Lorentz force. Larger Hartman number means stronger retarding effect on the velocity field. On the other hand, as expected Brinkman number has no effect on the velocity profiles.

In this study it has been also observed that the effects of the Brinkman and Hartmann number on temperature profiles is not significant and temperature profile only for Br = 0.1 Ha = 5 has been presented in Fig.6.

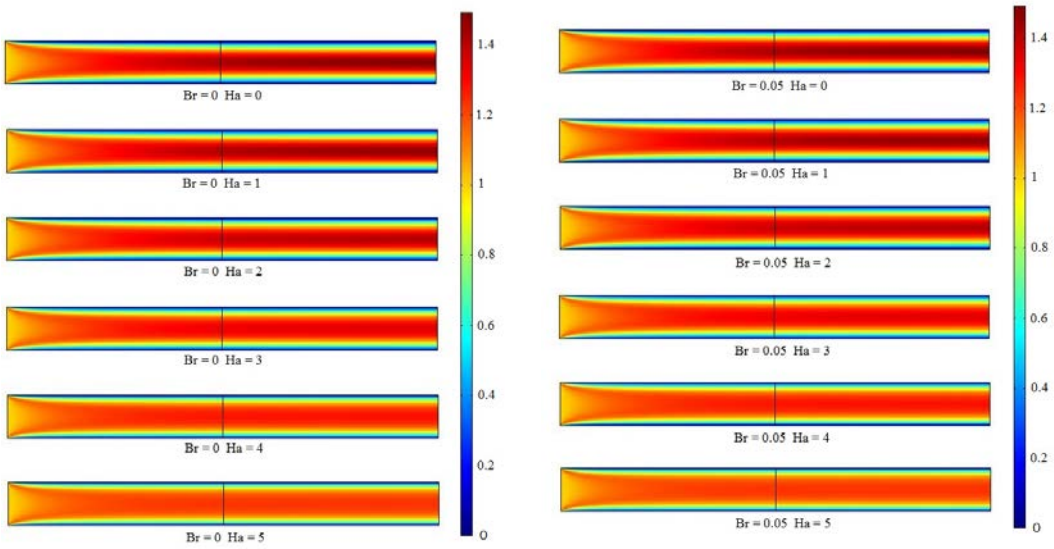

a) Br=0 *b) Br=0.05*

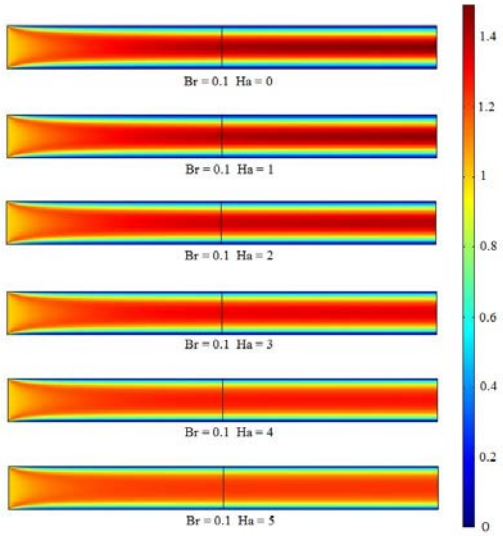

c) Br=0.1

Figure 4. Velocity profile inside the channel with smooth surfaces

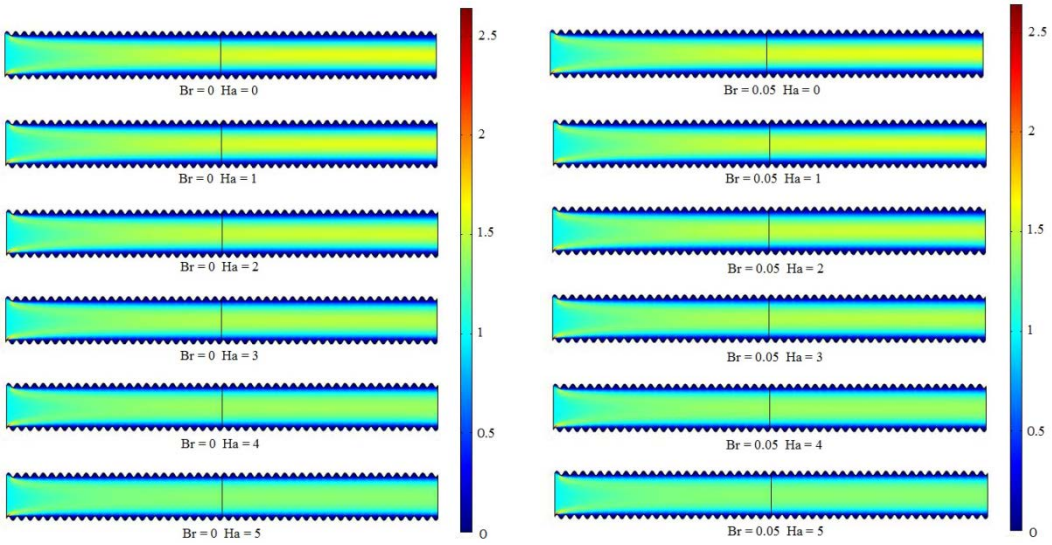

a) Br=0 *b) Br=0.05*

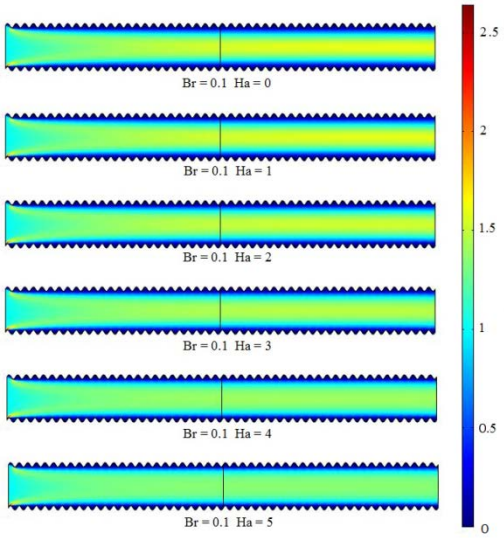

c) Br=0.1

Figure 5. Velocity profile inside the channel with sinusoidal surfaces

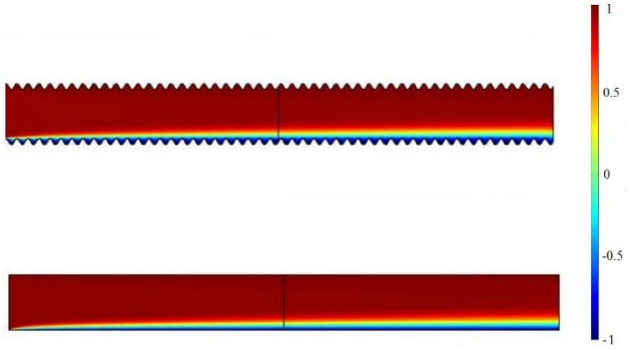

Figure 6. Temperature profile inside the channels for Br=0.1 Ha=5

Local Nusselt numbers at the lower (Nu_1) and upper (Nu_2) walls have been presented in Fig. 7. The negative values of Nu imply that the temperature of the fluid is higher than that of the upper plate due to heating effects of viscous dissipation and joule heating. It has been also shown that local Nusselt number at the lower wall is always positive. This means heat always transfers from the fluid to the lower plate.

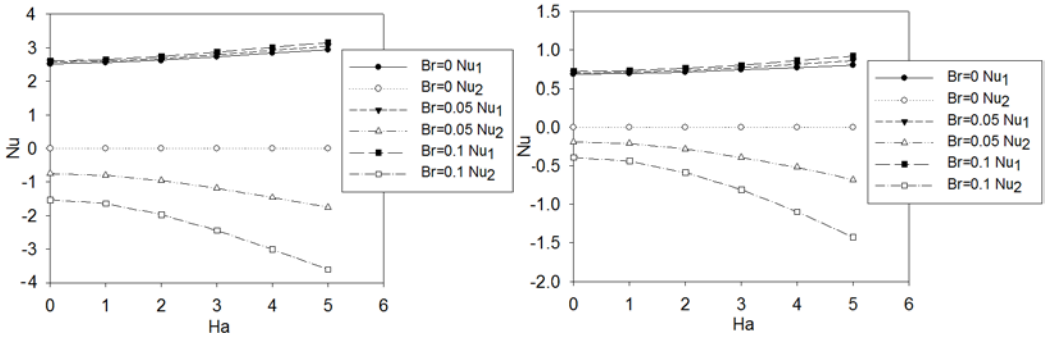

a) on smooth surfaces *b) on sinusoidal surfaces*

Figure 7. Local Nusselt numbers for the channel

It is known that Brinkman number is the ratio of the heat production due to viscous forces to the heat transferred from the wall to the fluid [11]. The second and third terms on the right hand side in equation (14) indicates the thermal energy generation due to viscous dissipation and Joule heating, in dimensionless form respectively. In respect to this fact, the increase of the local Nusselt number at the lower wall (Nu_1) and decrease of the local Nusselt number at the upper wall (Nu_2) with Br and Ha numbers are expected results. It has been also observed that the absolute values of the local Nusselt numbers at the walls of the channel with smooth walls are greater than that of the channel with sinusoidal walls for the investigated point. But is should be noted that the values of the local Nusselt numbers at the upper and lower walls are significantly depend to the position of the point on the sinusoidal wall especially in the case of viscous dissipation.

Nomenclature

$\vec{B}$, B_o	magnetic field induction vector and magnitude of the applied magnetic field
Br	Brinkman number
c_p	specific heat at constant pressure
$\vec{E}$, E_o	electric field intensity vector and component
H	one-half of the channel height
Ha	Hartman number
h_1, h_2	local heat transfer coefficients at the lower and upper plates
$\vec{J}$, J_z	electric current density vector and component
K	external loading parameter
k	thermal conductivity
L	length of the channel
Nu	local Nusselt number
Nu_1, Nu_2	local Nusselt number at the lower and upper plates
P	dimensionless pressure
p	pressure
Re	Reynolds number
T_1	temperature of the lower wall
T_2	inlet temperature, temperature of the upper wall
U	dimesionless velocity in x direction
u_m	inlet velocity, mean velocity
u	velocity in x direction
$\vec{V}$	velocity vector
V	dimesionless velocity in y direction
v	velocity in y direction
T	temperature
T_m	mean temperature
X	dimesionless x coordinate
Y	dimesionless y coordinate

Greek letters

ρ density
μ dynamic viscosity
μ_e magnetic permeability
$\mu\emptyset$ viscous dissipation term
$\vec{\nabla}$ vector differential operator

ν kinematic viscosity

σ electric conductivity
θ dimensionless temperature
θ_b dimensionless bulk temperature
θ_c characteristic temperature difference

REFERENCES

[1]. T. R. DePuy, "Fluid dynamics and heat transfer in a Hartmann flow," *An Engineering Project*, Rensselaer Polytechnic Institute, Hartford, Connecticut, USA, December, 2010.
[2]. Ray-Shing Wu and K. C. Cheng, "Thermal entrance region heat transfer for MHD laminar flow in parallel-plate channels with unequal wall temperatures, " *Wärme- und Stoffübertragung*, vol. 9, pp. 273-280, 1976.
[3]. P. J. Witt and M. P. Schwarz, "Numerical magnetohydrodynamic modelling of a conducting fluid in a rectangular duct," *13th Australasian Fluid Mechanics Conference*, Monash University, Melbourne, Australia, 13-18 December 1998.
[4]. D. W. Kiema, W. A. Manyonge and J. K. Bitok, "On the steady MHD poiseuille fluid flow between two infinite parallel porous plates, " *International Journal of Scientific Research and Innovative Technology*, vol. 2, no. 2, pp. 100-108, February 2015.
[5]. J. C. R. Hunt and S. Leibovich, "Magnetohydrodynamic flow in channels of variable cross-section with strong transverse magnetic fields, " *J. Fluid Mech.*, vol. 28, part. 2, pp. 241-260, 1967.
[6]. P. Y. Mhone and O. D. Makinde, **"Unsteady** MHD flow with heat transfer in a diverging channel," *Rom. Journ. Phys.*, vol. 51, nos. 9-10, pp. 967-979, 2006.
[7]. H. A. Attia and N. A. Kotb, **"MHD flow between two parallel plates with heat transfer,**" *Acta Mechanica*, vol. 117, pp. 215-220, 1996.
[8]. J. C. Umavathi, I-C. Liu and J. P. Kumar, **"Magnetohydrodynamic poiseuille-couette flow and heat transfer in an inclined channel,**" *Journal of Mechanics*, vol. 26, no. 4, pp. 525-532, December 2010.
[9]. L. Sreekala and E. Kesave Reddy, **"Steady MHD Couette Flow of an incompressible viscous fluid through a porous medium between two infinite parallel plates under effect of inclined magnetic field,**" *The International Journal of Engineering and Science*, vol. 3, no. 9, pp. 18-37, 2014.
[10]. http://web.mit.edu/seawater/Seawater_Property_Tables_8March16.pdf
[11]. L. P. Yarin, A. Mosyak and G. Hetsroni, **"**Fluid Flow, Heat Transfer and Boiling in Micro-Channels**,**" *Heat and Mass Transfer*, pp.161, 2009.

BIOGRAPHY

Çiğdem Susantez was born in Istanbul, Turkey in 1982. She received the Bachelor degree from Trakya University, Edirne, Turkey, in 2007. She worked as a research assistant at Trakya University between 2009-2016 years. She pursued her PhD in 2015. She has been working as Assistant Professor from at the beginning of 2016. Her main areas of research are heat and mass transfer, drying phenomena, fluid mechanics, analysis of the thermodynamic systems, genetic algorithm.

Comparison of the Borehole Logs Drilled in Çağlayan Dam Reservoir Area and In-Situ Seismic Velocities

Tumay Koca[2], Aykut Tuncel[1], Mehmet Yalcın Koca[2]

Abstract

The investigation of relationship between seismic velocities and geological units, variation of seismic velocities with depth in order to estimate the underground geological structures are commonly performed in dam reservoir area surveys. In this context, the relationship between seismic data derived from MASW method on 6 profiles and the data derived from core drillings located in Çağlayan Dam upstream and downstream areas was investigated. This study aims; a) To obtain the seismic velocities of geological units and to compare the geophysical profiles to borehole logs b) To estimate the depth and size of the embedded rock blocks which were moved towards the stream bed by landslides occurred beforehand on left and right banks of the dam site and afterwards were covered by stream sediments. Thus, the presence of rock blocks which fell into the stream bed from the slopes where landslides were occurred in the past will be verified.

As a consequence of geophysical survey, the shear velocities of geological units are found to be between 300 and 1200 m/s. According to the velocity-depth graph, shear velocities are between 300 and 400 m/s for the first 10 m from the ground surface level whereas alluvial units are intersected in the first 6 m in drill holes. Therefore, the mean shear velocities of alluvial units are 350 m/s. The Vs values of 400-1200 m/s are well matching with the borehole logs and local geological units consisting of Neocene aged conglomerate, sandstone, siltstone and limestone intercalations. The highly heterogeneous rock units are the reason for deriving wide variety of seismic velocities.

Keywords: *Çağlayan dam, heterogeneous rock units, MASW method, landslide*

1.INTRODUCTION

Çağlayan Dam is a project which is still being planned by DSI (The General Directorate of State Hydraulic Works). It is estimated that 26 hm^3 water per year will be provided for the use of drinking and industrial purposes to İzmir city (Figure 1). The study area is located in Manisa city at western part of Turkey (Figure 1). The active and passive landslide zones in the study area indicate the necessity of detailed investigation of the rock units in the reservoir area.

Core drilling in dam sites are commonly performed in order to specify the subsurface lithological units and to compare and control the geological knowledge obtained from surface mapping and geophysical survey. Other main objectives of core drilling are determining the groundwater table level, permeability by in-situ tests and some geotechnical properties of geological units by borehole logs. Nevertheless core drilling is expensive and slow subsurface investigation method. In this case, the cooperation of geophysical techniques and drilling will be an alternative that allow coverage of wide areas at reduced time and cost of investigation.

In-situ geophysical methods are increasingly used for investigation of near surface landslides. Most of the researchers were studied landslides via electrical methods ([1]-[6]). On the other hand, reference [7] investigated a dam site by combination of methods Multichannel Analysis of Surface Waves (MASW) and P- and SH- wave tomography; reference [8] studied landslides on quick clays by correlating stratigraphical data with geophysical data obtained by MASW.

MASW is a geophysical technique that can be used for geotechnical characterization of near surface geological units by obtaining seismic shear wave velocity (Vs) ([9], [10], [11]). Measurement or estimation of the Vs profile of sediments overlying geological basement is a vital part of site zonation studies for earthquake hazard prediction, and more generally for geotechnical studies. Boreholes drilled in the Çağlayan dam site provide opportunity for the comparison of geophysical methods with known geological data. This paper compares the shear-wave velocity profiles obtained from six profiles and two boreholes with changing depths.

[1] *Corresponding author: Dokuz Eylul University, Department of Geophysical Engineering, 35160, Buca/Izmir, Turkey.* aykut.tuncel@deu.edu.tr

[2] *Dokuz Eylul University, Department of Geological Engineering, 35160, Buca/Izmir, Turkey.*

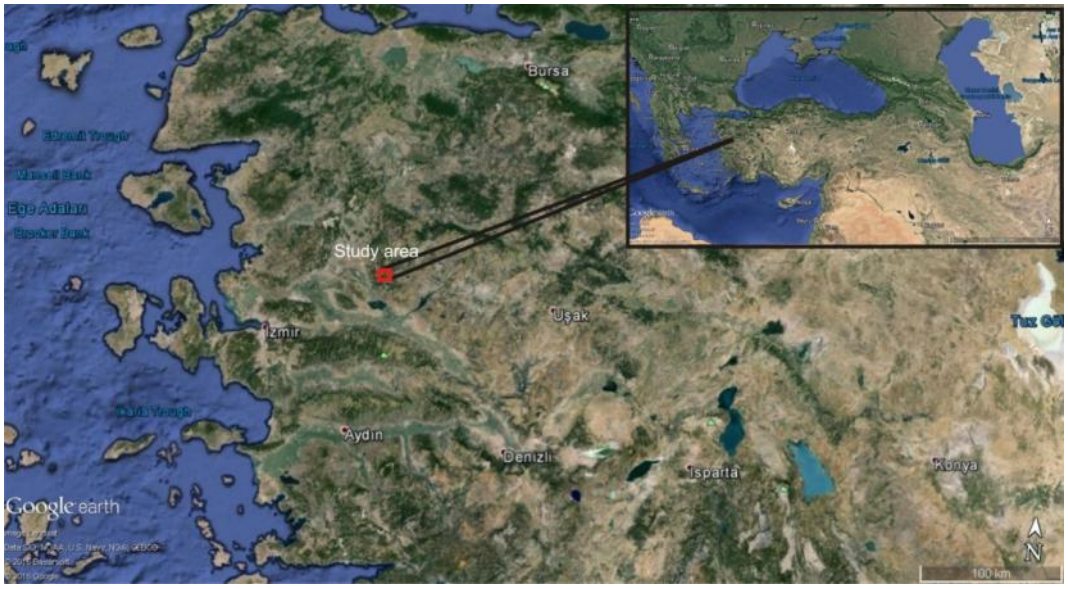

Figure 1. Location of the study area.

2.GEOLOGY

The oldest geological unit in the study area is the Paleozoic aged Keçidağ Formation consisting of marble, limestone and schist which form a basement under the Cenozoic rocks and alluvium ([12]-[14]) (Figure 2). Schist are highly weathered and including several, thin siltstone bands. Thickness of schistosity is between 0.5 and 1 cm and inclines to southeast. This geological unit mostly outcrops as grey colored, recrystallized limestone around the dam axis and includes numerous joint sets. Miocene aged sedimentary rocks are unconformably overlying the Keçidağ Formation. Göcek Formation which consists of poorly sorted carbonate-cemented, well rounded conglomerate; beige-yellow colored sandstone; siltstone interfingered with locally algal limestone accumulated in alluvial fan ([15]-[17]). The maximum water level for the dam is in the limits of Göcek Formation. Most of the landslides are also formed in this formation (Figure 2).

Yeniköy Formation unconformably overlies the Göcek Formation. It consists of cross-bedded sandstone indicating fluvial deposition; sandy limestone, mudstone, coarse grained conglomerate and siltstone intercalations. Lacustrine deposits of Küçükderbent Formation which overlies the Yeniköy Formation are composed of clayey limestone, claystone, sandstone, marl interfingered with mudstone and tuff. The youngest geological units are Quaternary aged alluvium, terrace and talus ([12], [13], [18]). Alluvium is composed of blocks up to 22 cm diameter, pebbles, sand and silt. Grain size of pebbles is 3-5 cm and originated from limestone and schist.

E-W trending normal faults with dip direction to north which forms the valley were identified. Similarly to the tectonics of Aegean region, NE-SW trending thrust faults and NW-SE trending normal faults were determined as well.

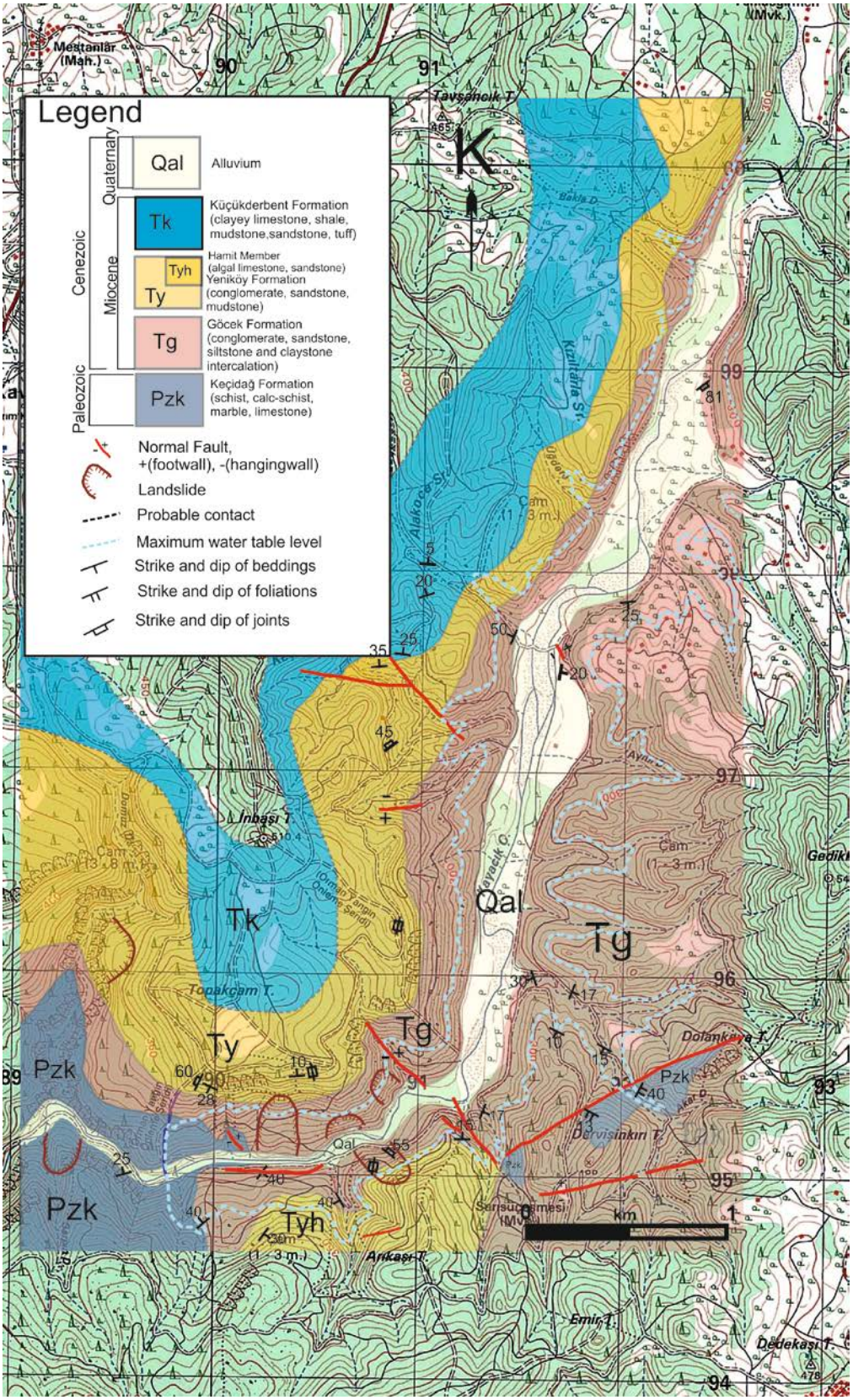

Figure 2. Geological map scaled 1/5000 of the study area

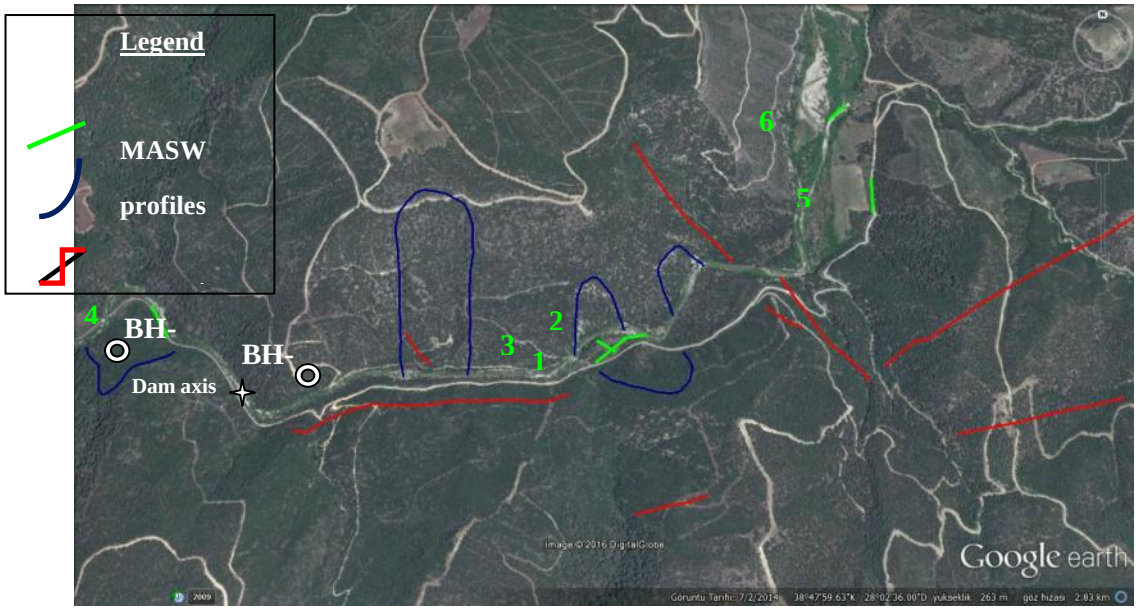

Figure 3. Illustration of MASW profiles, pre-failed slopes, faults, dam axis and boreholes on Google Earth screenshot

3.METHODS

In this study, geophysical methods accompanying drilling methods were utilized in order to define the dynamic and stratigraphic variety of the field. Six profiles of MASW method and two boreholes were performed in both upstream and downstream of the dam site (Figure 3).

3.1. MASW Method

Geophysical methods are used to determine the geological sequence and the structure of sub surface rocks by the measurement of certain physical properties. MASW method is commonly employed like as electrical resistivity and seismic refraction methods in subsurface investigations. MASW is an active-source technique requiring an impulsive signal, such as from a sledgehammer or weight drop, or swept vibratory signal, such as vibroseis, to generate surface waves. Vs structure is typically derived from the fundamental mode Rayleigh wave field generated by the source. The MASW method was introduced by [10]. In their method, phase velocities were directly determined from MASW data after transforming seismic data to the phase velocity–frequency domain.

MASW field study was performed along six profiles as shown in Figure 4. For profile 1, 4 and 5, 24 geophones were employed with a geophone spacing of 5 m. For the rest profiles geophone spacing is 3 m. due to the convenient spaces in the study area. The data sets were created using a Geometrics Geode Seismic receiver, 24 geophones of 4.5Hz resonant frequency and a 100 lb hydraulic hammer as the energy source. During the field studies, the sample interval was utilized as 0.5 ms and the recording time was 2 s.

Figure 4. MASW field setup.

3.2. Drilling Method

There are no given rules regarding the location of boreholes or the depth to which they should be sunk. Core borings were made to recover rock cores by using the rotary system. In this work, borehole depths were determined as a result of the geophysical and geological surveys. This depends upon; geological conditions, shape, load and extent of the structure. On the other hand, the smaller diameters were used in exploratory borings for rock identification (NX cores). In fractured rock and breccia zone, core recovery improves with larger diameters. HX size was used in these zones along the profiles.

Within the study area, 38 boreholes (coded BH-1 through BH-38) were drilled; they reached depths between 15 and 50 m. Eleven boreholes revealed groundwater close to the surface. Two of them (BH-11 and BH-36) are only considered in this work, because the locations of them are agree with the site that the geophysical works were performed.

4. ENGINEERING GEOLOGY

A dam is simply a barrier placed across a water-course to prevent or retard the normal flow of water therein. In addition, dams depend on the environmental conditions, particularly on the geology of the site. Engineering geological investigations involve the assessment of material and mass characteristics of geological units as well as the evaluation of stability of natural slopes and cuts. These investigations mentioned above and subsurface investigations in dam site were performed with the help of the borings, and geophysical measurements. In addition, subsurface investigations also involve the production of detailed geological map scaled 1/5000 (Fig. 2) and geophysical sections showing the succession and structures, depth of weathering and/or breccias zone.

Two vertical core drillings were performed in the study area (Figure 3). 20 m deep BH-11 and 26 m deep BH-36 were drilled in alluvium in downstream and upstream areas. Ground water table levels in the boreholes are 18.12 m and 1.7 m, respectively. The thickness of alluvium in the stream bed is 4.5 and 6 m. In BH-36, 6.2 m thick, fractured but impermeable Göcek Formation consisting conglomerate, sandstone, siltstone and limestone intercalation was encountered below the alluvium. BH-36 is located near to intersection of a two normal fault trending in E-W and NW-SE direction. As a consequence, highly fractured breccia and karstic limestone with clay fills, highly fractured and slightly weathered limestone units were intersected in the following depths (Figure 5). In BH-11 which was drilled in downstream area, Neogene aged sedimentary rocks were not intersected, disintegrated and highly fractured, slightly to moderately weathered limestone were intersected instead along the depths 6 m to 19 m. Paleozoic aged calcschist (belonging to the Menderes Massif) was intersected in the last 1 m. of drilling depth (Figure 5).

Core recovery of 100% was obtained from the limestone unit with hard and sound. However, very poor core recovery was acquired in heavily fractured and/or breccia zone through the profile of BH-36 (Fig. 6). The first unit encountered during drilling consisted of alluvium, and is a medium-dense to dense, particularly cohesionless material.

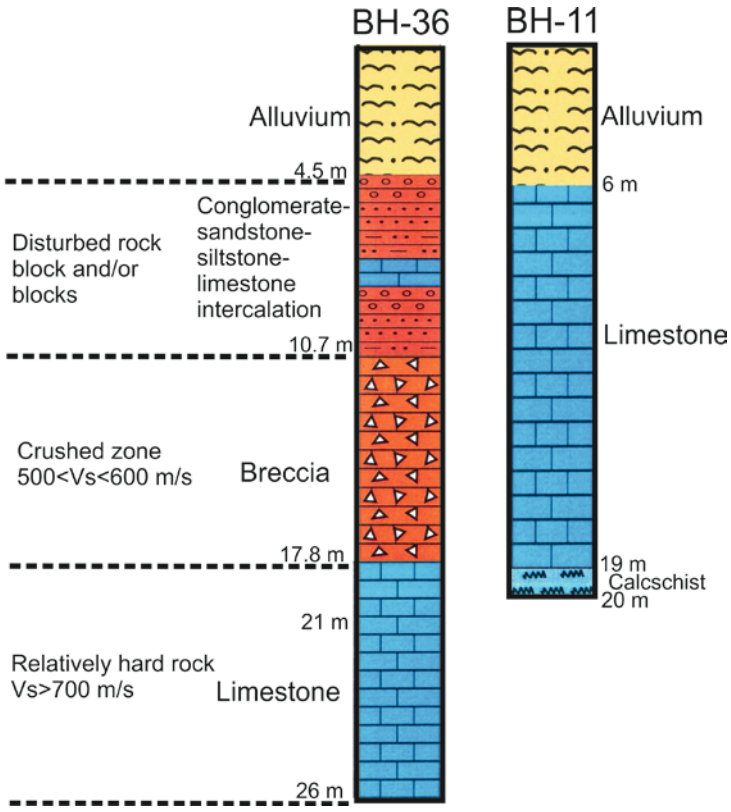

Figure 5. Sub-surface profiles of boreholes BH-11 and BH-36

In order to investigate the Vs-depth changes in a 1D cross-section in the study area, MASW method was applied along six profiles. As a consequence of geophysical survey, the shear wave velocities of geological units are found to be between 300 and 1200 m/s. According to the velocity-depth graph, shear velocities are between 300 and 400 m/s for the first 10 m from the ground surface level whereas alluvial units are intersected in the first 6 m in drill holes. Therefore, the mean shear velocities of alluvial units are 350 m/s. The Vs values of 400-1200 m/s are well matching with the borehole logs and local geological units consisting of Neogene aged conglomerate, sandstone, siltstone and limestone intercalations.

After evaluation of the MASW data, Vs-depth model is graphed for 6 profiles. For longer profiles (1,4 and 5) the research depth is 50 meters but the depth is lower (35 m.) at the profiles (2,3 and 6) which the profile length is shorter (Figure 6).

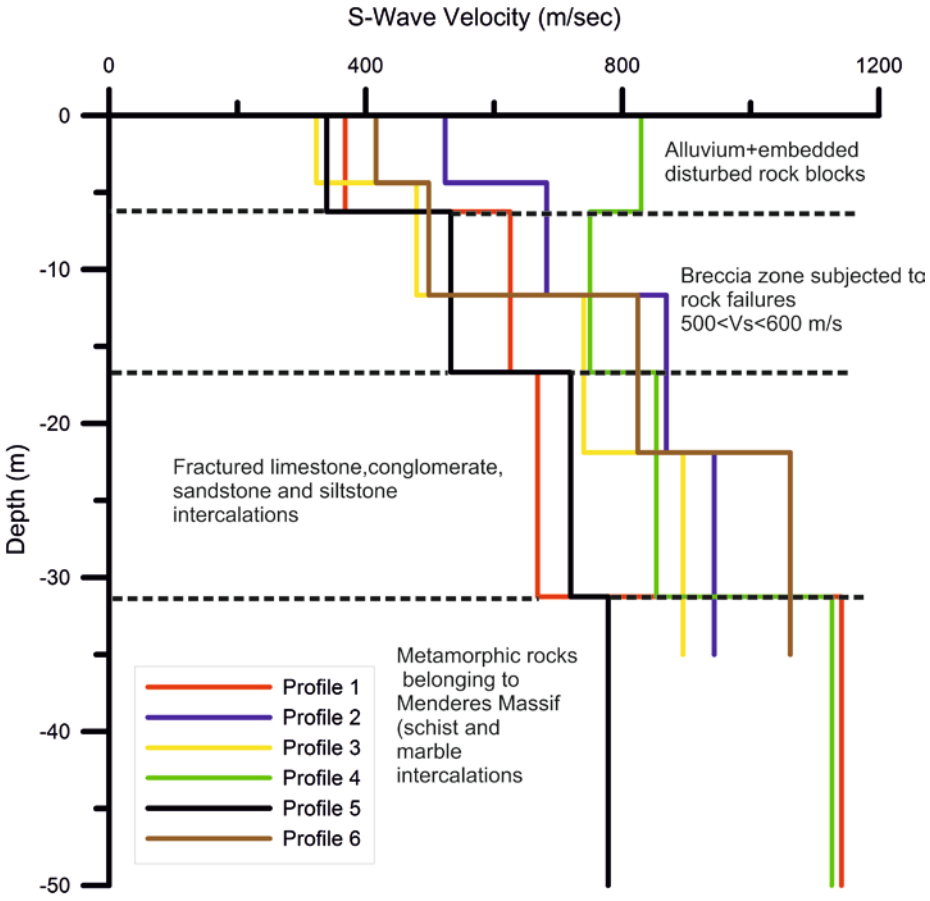

Figure 6. Vs-depth model at the midpoint of the profiles obtained using MASW method

5. DISCUSSION AND CONCLUSIONS

The MASW method was performed to estimate the shear and compressive velocities of sub-surface soil profile. According to the obtained Vs depth graph, Vs values of the soil changes both laterally and vertically. In profile 4, it was determined that the first 8 m. from the ground surface, shear velocity values are higher (Vs >700 m/s) due to the rock block embedded in alluvium (Figure 7). Alluvium is represented by dense sand and pebbles (400< Vs< 700 m/s) in left and right sides of the embedded rock blocks. The transition zone from rock blocks to basement rock has shear velocities ranging between 750 m/s and 900 m/s (Figure 7). These shear velocity values represent granular soil consisting many, relatively smaller rock blocks. Nevertheless, in MASW profiles 1, 2 and 3 located in front of the pre-failed slopes in upstream, rock blocks embedded in alluvium were not detected. Instead, several limestone and conglomerate blocks were encountered in the stream bed during field studies on the toe of the pre-failed slopes. Therefore, pre-failed slopes and on-going failure of the slopes in the dam reservoir area were verified.

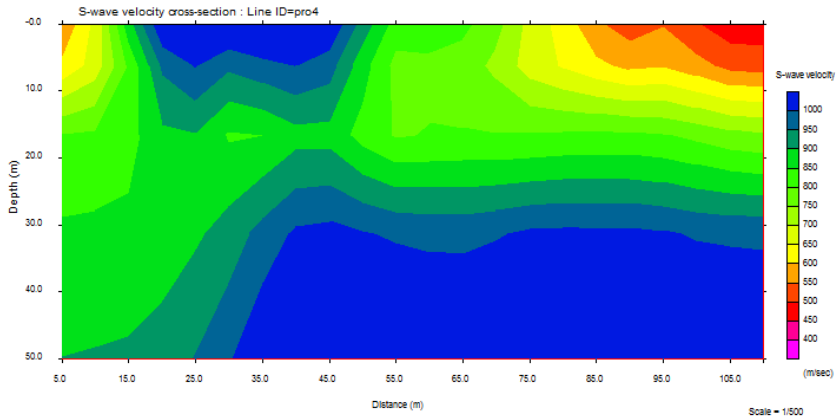

Figure 7. 2D Vs-depth graph for profile 4

Except for the profile 4, the Vs values are increasing with depth (Figure 6). It is clearly seen on Figure 6 that there is a low velocity zone for the first 10 m. depth. Shear velocities are between 300 and 400 m/s for the first 10 m from the ground surface level whereas alluvial units are intersected in the first 6 m in drill holes. According to this harmony, mean shear velocities of alluvial units were determined to be 350 m/s. The Vs values of 400-1200 m/s are well matching with the borehole logs and local geological units consisting of Neogene aged conglomerate, sandstone, siltstone and limestone intercalations. The highly heterogeneous rock units are the reason for deriving wide variety of seismic velocities. Following the depth of 30 m, more homogeneous, moderately fractured Palaeozoic rocks were verified.

The blocky structures and disturbed zone/zones such as breccia zone are undesirable for dam sites. These rock masses are allochthon and embedded into alluvium and/or also placed in the breccia zone. Disturbed materials and masses are generally permeable and the reservoir from which a considerable quantity of leakage may occur should be avoided.

REFERENCES

[1]. McCann, D.M., Forster, A., "Reconnaissance geophysical methods in landslide investigations", *Engineering Geology*, vol. 29, pp. 59 –78, 1990.
[2]. Hack, R., "Geophysics for slope stability", *Surv. Geophys*., Vol. 21, pp. 423 –448, 2000.
[3]. Jongmans, D., Garambois, S., "Geophysical investigation of landslides: a review", *Bull. Soc. Geol. Fr.*, vol. 178 (2), pp.101–112, 2007.
[4]. Godio, A., Bottino, G., "Electrical and Electromagnetic Investigation for Landslide Characterization", *Phys. Chem. Earth (C).*, vol. 26 (9), pp. 705-710, 200l.
[5]. Perrone, A., Lapenna, V., Piscitell, S., "Electrical resistivity tomography technique for landslide investigation: A review", *Earth-Science Reviews*, vol. 135, pp. 65 –82, 2014.
[6]. Le Roux, O., Jongmans, D., Kasperski, J., Schwartz, S., Potherat, P., Lebrouc, V., Lagabrielle, R., Meric, O., "Deep geophysical investigation of the large Séchilienne landslide (Western Alps, France) and calibration with geological data", *Eng. Geo.*, vol. 120, pp.18 – 3, 2011.
[7]. Cardarelli, E., Cercato, M., De Donno, G., "Characterization of an earth- filled dam through the combined use of electrical resistivity tomography, P- and SH-wave seismic tomography and surface wave data", *Journal of Applied Geophysics*, vol. 106, pp. 87 –95, 2014.
[8]. Donohue, S., Long, M., O'Connor, P., Helle, T.E., Pfaffhuber, A.A., Romoen, M., "Multi-method geophysical mapping of quick clay", *Near Surf. Geophys*., vol. 10, pp. 207–219, 2012.
[9]. Miller R.D., Xia J., Park C.B., and Ivanovo J.M., "Multichannel analysis of surface waves to map bedrock", *The Leading Edge*, vol. 18(12), pp. 1392-1396, 1999.
[10]. Park C. B., Miller R. D. and Xia J., "Multi-channel analysis of surface waves", *Geophysics*, vol. 64, pp. 800–808, 1999.
[11]. Xia, J., Miller, R. D., and Park, C. B., "Estimation of near-surface shear-wave velocity by inversion of Rayleigh wave", *Geophysics*, 64, 691-700, 1999.
[12]. Akdeniz, N., "Geology of Akhisar-Gölmarmara-Gördes-Sındırgı" PhD Thesis, İstanbul University, pp.254, İstanbul, 1985, (in Turkish).
[13]. Kılıç, A.M., "Stratigraphy of Lower Mesozoic sediments of Akhisar (Manisa) region", MSc Thesis, Cumhuriyet University, pp.70, Sivas, 1997, (in Turkish).
[14]. Konak, N., "A general review of Menderes Massif Menderes", 47. Turkey Geological Congress, Ankara, pp. 126, 1994, (in Turkish).
[15]. Yağmurlu, F., "Geology and coal potential of the Neogene sediments in the east of Akhisar", PhD Thesis, Dokuz Eylül University, Institute of Natural and Applied Sciences, pp.217, İzmir, 1983, (in Turkish).
[16]. Yağmurlu, F., Baykal, H., "Fundamental geological properties of Gördes Dam and its surrounding", Geological Bulletin of Turkey, vol. 32/1-2, pp. 1-7, Ankara, 1989, (in Turkish).
[17]. Yağmurlu, F., Karayiğit, A.İ., "Petrographical properties of Çıtak (Akhisar) lignites", Turkey 4. Coal Congress, TMMOB, pp. 111-122, 1984, (in Turkish).
[18]. Emre,T., "Geology and tectonics of Gediz Graben", Turkish Journal of Earth Sciences, vol. 5,pp. 171-185, 1996.

The Comparison of Some Physical and Mechanical Properties of Damaged and Undamaged Calabrian Pine Woods in Forest Fires

Ibrahim Bektas[1], *Aysenur Kılıç Ak**[1], *Gonca Duzkale Sozbir*[1]

Abstract

The forest fires, nowadays progressively increasing, cause a significant loss in the Mediterranean belt, where especially the Calabrian Pine is widely grown. In here, usage of damaged woods productively is important because of raw material shortage in forest products industry. Thus, the aim of this study is to compare some physical and mechanical properties of forest fire damaged and undamaged Calabrian pine. For this purpose, air-dried density, oven-dried density, shrinkage, swelling, compressive strength parallel to grain, dynamic bending strength and janka hardness tests were carried out. The results showed that wood properties of undamaged samples were higher than the damaged samples, except for the shrinkage percentage. This might probably caused by the higher density of the damaged woods. This research will contribute to utilize damaged samples more profitable.

Keywords: *Calabrian pine, forest fire, physical properties, mechanical properties, Turkey.*

1.INTRODUCTION

Calabrian pine, which has an extended distribution area in Turkey especially in regions where the Mediterranean climate prevails, is vulnerable to the danger of fire in most days of the years. Ecologically and economically, it is one of the most important forest tree species of the country [1].

The most important factor in the formation of forest ecosystems are forest fires. Although forest fires are inseparable part of many ecosystems, they can be cause burning of thousand of hectares every year and they may have very devastating effects of disasters which waste a lot of value attached to forest utilized sufficiently. By the reason of to take place in the Mediterraneon geography and climate zone, Turkey is severely under fire threat especially in summer so because of forest fires that occur every year, significant amount of forest area have been damaged [2], [3].

Fire can be beneficial if used by men in a controlled way and with well-defined guidelines. However, in situations where there is no prescribed burn the resulting negative effects will cause losses of different intensities and magnitudes on diverse forest aspects. Among these aspects, the effect of fire on tree survival and their technological wood potential should be highlighted [4].

Survival of trees during forest fires depends on several factors such as bark thickness, moisture content, chemical composition, density and type; root depth; age; species; fire intensity, duration and type whether a crown or superficial burning [5].

Trees may not exhibit significant damage as a result of the interaction of these factors; however, they can undergo partial damage, which eventually cause increment reduction, vulnerability to fungi and insects attacks, scars in the trunks and decrease of wood value; or they can die [6]. Furthermore, in extraordinary circumstances trees can be totally transformed into ashes by fire, which obviously results in a total loss of wood [4].

In Turkey, *P. brutia* forms extensive forests, especially in regions where the Mediterranean climate prevails. Ecologically and economically, it is one of the most important forest tree species of the country.

The general objective of this study was to assess wood properties of *Pinus brutia* Ten., using trees affected by a forest fire and using as control wood of trees of the same species, planting area that were not affected by fire. The specific objectives were (a) assessment of wood physical properties: air- and oven-dried density and volumetric shrinkage and swelling (tangential, radial, longitudinal and volumetric);(b) assessment of wood mechanical properties: compressive strength parallel to grain, static quality, dynamic bending strength, dynamic quality and janka hardness.

2. MATERIAL AND METHOD

2.1. Test Trees

[1] *Kahramanmaraş Sütçü İmam University, Department of Forest Industry Engineering, 46100, Kahramanmaraş, Turkey. ibtas@ksu.edu.tr*

Test trees were randomly collected from the Calabrian pine (*Pinus brutia* Ten) forests damaged partially by fire of the Baskonus district within the borders of K.Maras province located in the East Mediterranean region of Turkey. The ages of damaged trees are between 10-20 years and undamaged trees are over 30 years. Later, from these selected logs, the test specimens were prepared for some physical and mechanical properties explained in detail as follows.

2.2. Determination of Physical Properties

The specimens with a dimension of 20 × 20 ×30 mm were prepared from 15-cm parts taken from logs as described in TS 2470 [14] for determination of air- and oven-dry densities of the pine wood. The pine wood specimens were first conditioned at 20 ± 2°C and under 65 ± 5% relative humidity (RH) in a humidity chamber equipped with a fan for 30 days to the moisture content of about 12% [7]. Later, the specimens were weighed to the nearest 0.01 g, and the dimensions of the specimens were measured by a digital micrometer to an accuracy of 0.001 mm.

On the other hand, since it is practically impossible to make the moisture content of all the samples 12%, the air-dry densities of the specimens, the moisture of which deviated from 12%, were corrected by using JANKA Equation [12]:

$$d_{12} = d_m + p_1 (m_2 - m_1) \ (g/cm^3) \quad (1)$$

where, d_{12} is air-dry density of the specimen at the moisture content of l2% (g/cm^3), d_m is air-dry density of the specimen at the moisture content deviated from 12% (g/cm^3), p_1 is the factor showing a relationship between moisture and density, m_l is the oven-dry moisture content and m_2 is the moisture content of the specimen.

For the measurement of oven-dry density, the wood specimens were first oven dried at the temperatures of 50°C, 75°C and 103± 2°C, respectively in order to not affect that specimens negatively by the high temperatures. The weight and dimensions of the specimens were measured as described above. Eventually, the densities of the specimens were calculated by the conventional equation as described in relevant standard above.

Besides, from 1-m trunk parts taken from 2-4 m parts of trees, specimens having a dimension of 20 × 20 × 30 mm were prepared for swellings and shrinkages in tangential and radial, and longitudinal directions, respectively, based upon TS 4083-4084-4085-4086 [17], [18], [19], [20].

2.3. Determination of Mechanical Properties

Specimens of all mechanical tests were conditioned at 20±2°C and 65±5 percent relative humidity (RH) to a moisture content (MC) of about 12 percent.

The compressive strength parallel to grain was measured on by following TS 2595 [13]. The dimensions of the specimens were 30 (T) by 30 (R) by 45 (L) mm and crosshead motion or rate of loading was 0.6 mm/min. The test was performed on a universal testing machine. Later, compressive strength was determined by using Equation (2):

$$\sigma_{B//} = P_{max}/(a \times b) \ (N/mm^2) \quad (2)$$

where, $\sigma_{B//}$ is compressive strenght parallel to grain (N/mm^2), P_{max} is Maximum force (N), a and b are cross-sectional area of sample (mm^2).

And static quality value of compressive strength specimens calculated by following formula (3);

$$I_{st} = \sigma_{B//} / (100 \times D_{12}) \quad (3)$$

where, $\sigma_{B//}$ is compressive strenght parallel to grain (N/mm^2), D_{12} is air-dry density (g/cm^3).

Dynamic bending strenghts were measured by following TS 2477 [15]. The test specimens were prepared as 20 (T) by 20 (R) by 300 (L) mm. Then, dynamic bending strength of the specimens was tested on an impact tester (Model HPSW 10) and calculated according to formula (4);

$$\sigma DE = 1000 \times Q / b \times h \ (kgm/cm2) \quad (4)$$

where, Q is required amount of work (kgm) for breaking the sample, b and h is radial and tangent directive sizes of the sample (b×h, cm^2).

Then, dynamic quality value for wood specimens was determined by equation (5) as follow:

$$I_d = \sigma_{DE} / D_{12}^2 \quad (5)$$

where Id is dynamic quality value, σDE is dynamic bending strenghts (kgm/cm2), D12, air-dry density (g/cm3).

Janka hardness specimens, 50 mm × 50 mm × 50 mm were tested using a universal tester (Losenhausen) according to TS 2479 [16]. In this test, a hemispherical head with a diameter of 10 mm was forced into the center of the specimens to a depth of 25

mm with a head speed of 0.63 cm/minute [8]. The load required was recorded in kgf and reported as N. The hardness was performed on cross, radial, and tangential sections of the wood specimens.

3. RESULTS AND DISCUSSION

Table 1 demonstrates the mean values of air dry density, oven dry density, shrinkage and swelling properties of Calabrian pine wood damaged by forest fire obtained from tests.

Table 1.The analyses results of air dry density, oven dry density, shrinkage and swelling values for damaged wood.

Calabrian pine tree		Number of sample	Mean	Standard deviation	Coefficient of variation (%)	Range
Air dry density (g/cm^3)		235	0.540	0.049	9.08	0.260
Oven dry density (g/cm^3)		235	0.519	0.050	6.63	0.269
Shrinkage (%)	radial	235	5.26	1.198	22.78	5.87
	tangential	235	4.14	1.054	25.47	7.32
	longitudinal	235	1.36	0.811	59.64	3.56
	volumetric	235	10.64	1.586	14.90	9.36
Swelling (%)	radial	235	5.11	1.221	23.87	6.10
	tangential	235	4.26	1.202	28.16	6.89
	longitudinal	235	1.34	0.880	65.67	4.90
	volumetric	235	10.60	1.781	16.79	10.0

When Table 1 analyzed, it was found that avarage air density value was 0.540 g/cm^3 for partially damaged test material in fire and oven-dried density was 0.519 g/cm^3. From the same table it was understood that volumetric shrinkage (%10.64) and swelling (%10.60) percentage is very close to one.

Table 2. The values of compressive strength, dynamic bending strength and Janka hardness obtained from damaged woods.

Calabrian pine tree		N	Mean	Standard deviation	COV (%)	Range
Compressive	Strength (N/mm^2)	66	42.7	3.179	6.94	13.9
(parallel to grain)	Static quality value	-	7.8	-	-	-
	Specific quality value	-	14.6	-	-	-
Dynamic bending	Strength (kgm/cm^2)	30	0.27	0.022	8.15	0.80
	Dynamic quality value	-	0.93	-	-	-
Janka hardness	cross	50	36.7	2.470	6.73	11.6
(N/mm^2)	radial	50	21.8	2.156	9.89	8.7
	tangential	50	19.6	2.697	13.76	13.0
	average	50	26.0	3.045	11.71	18.7

N: Number of sample, COV: Coefficient of variation (%)

Data obtained from some mechanical tests of the partial damaged Calabrian pine wood were presented in Table 2. Calabrian pine, is considered as a medium-hard wood [9], according to the static quality value that can be evaluable as 'medium' quality material. It also made the same assessment for the specific quality value. Based on the dynamic quality value (0.93) ,for this value is less than 1, it can be said that burnt calabrian pine, has brittle structure and “poor” quality.

Table 3.The Comparison of some physical and mechanical properties of damaged and undamaged calabrian pine woods in forest fires.

Calabrian pine tree		Mean		Variation(*)
		Undamaged	**Damaged**	(%)
Air dry density (g/cm^3)		0.546	0.540	−1
Oven dry density (g/cm^3)		0.519	0.509	−2
Volumetric shrinkage (%)		9.81	10.64	+8
Volumetric swelling (%)		10.82	10.60	−2
Compressive strength grain to parallel (N/mm^2)		45.4	42.7	− 6
Static quality value		8.3	7.8	− 6
Spesific quality value		15.2	14.6	− 4
Dynamic bending strength (kgm/cm^2)		0.37	0.27	−27
Dynamic quality value		1.4	1.0	−28
Janka hardness (N/mm^2)	cross	45.7	36.7	− 20
	radial	23.6	21.8	− 7
	tangential	22.3	19.6	− 13
	average	30.5	26.0	− 13

(*)(undamaged mean−damaged mean)/undamaged mean×100.

The data in Table 3 show the variation between values of some physical and mechanical properties obtained from partially damaged and undamaged calabrian pine logs by forest fires.

In Table 3, the calculation difference evaluation in general, it can be deduced that physical properties except volumetric shrinkage have an average decrease %1.6, while volumetric shrinkage has increase %8 to damaged and undamaged test materials. As is known, increase of shrinkage percent is undesirable property in terms of dimensional stability of wood materials [10].

On the other hand, it was obtained that in all measurements of mechanical properties affected by fire test samples had lower values. The comparison of calculated results avarage decrease amount is %13.5. Comparing to the physical properties, mechanical properties had a higher decrease value. The reason for this can be thought of the changes in woods chemical compositions and samples dimensions. In literature, the studies by Aydın et al. 2007 [11], Bortoletto and Moreschi 2003 [5] prove the evaluations carried out in this study.

Tree ages, distance from the fire and time, habitat and ecological differences can be given as reasons for decrease in properties of damaged woods compared to the other woods.

4. CONCLUSIONS

In this research, air-dried density, oven-dried density, shrinkage, swelling, compressive strength parallel to grain, dynamic bending strength and janka hardness of calabrian pine were tested and analyzed to compare some physical and mechanical properties of forest fire damaged and undamaged wood. The results showed that wood properties of undamaged samples were higher than the damaged samples, except for the shrinkage percentage. This might probably caused by the higher density of the damaged woods. This research will contribute to utilize damaged samples more profitable.

REFERENCES

[1]. M. Boydak, *Silvicultural Characteristics and Natural Regeneration of Pinus Brutia Ten.* -a review. Plant Ecology 171: 153-163, 2004.
[2]. J.G. Pausas and V.R. Vallejo, *The Role of Fire in European Mediterranean Ecosystems*, Springer-Verlag, 3-16, 1999
[3]. A. Tutuş, M. Çiçekler, İ. Deniz, *Yanmış Kızılçam Odunlarının Kağıt Hamuru ve Kağıt Üretiminde Kullanılması*, KSÜ Mühendislik Bil. Der., Özel Sayı, 90-95, 2012.
[4]. G.J. Bortoletto, *Estudo da qualidade da madeira de Pinustaeda L. proveniente dearvores adultas atingidas por incendio florestal*. Ph.D. thesis, SCA/DETR/Federal University of Parana, Brazil, 1999.
[5]. G.J. Bortoletto, and J.C. Moreschi, *Physical-Mechanical Properties and Chemical Composition of Pinus taeda Mature Wood Following a Forest Fire*, Bioresource Technology, 87, 3, 231-238, 2003.
[6]. R.V. Soares, *Os incendios florestais no Brasil: problemas e perspectivas. In: Proc. Annual Course of Atualizacao em controle de incendios florestais.* FUPEF/Federal University of Parana, Curitiba, Brazil, pp. 1–11, 1994.
[7]. S. Korkut and İ. Bektas, *The effects of heat treatment on physical properties of Uludağ fir (Abies bornmuellerinana Mattf.) and Scots pine (Pinus sylvestris L.) wood*. Forest Products Journal, 58(3): 95-99, ISSN: 0015-7473, 2008.
[8]. İ. Bektaş and M.H. Alma, *Determination of Brinell and Janka hardness of eastern beech and relationship between two hardness.* Forest Prod. J. 51(11/12):84-88, 2001.
[9]. İ. Bektaş, A. Tutuş, *The Cleavage strength of calabrian pine (Pinus brutia Ten.) woods growing naturally in different ecological regions of Turkey*. Turkish Journal of Agriculture and Forestry, Vol:23, No 3, ISSN 1300-011X, Ankara-Turkey, pp. 549-557, 1999.
[10]. İ. Bektaş and C. Güler, *Determination of Some Physical Properties of Eastern Beech Wood in Andırın Region.* Turkish Journal of Agriculture and Forestry (in Turkish), Vol:25, No: 4, Ankara-Turkey, pp. 209-217, 2001.
[11]. A. Aydın, N. Ay, Y. Aydın, *Effects of the Forest Fires on the Mechanical Properties of Turkish Red Pine (Pinus brutia Ten.)*. SAFRI publications no:35, ISSN: 1300-8579, Issue: 8, volume: I, Page: 55-68, Antalya, 2007.
[12]. N. As, *The effect of different origins on the physical, mechanical properties of Pinus Pinaster*. Ph.D. thesis. Istanbul Univ., Istanbul, Turkey. pp. 293-398, 1992.
[13]. TS 2595, Wood-Determination of Ultimate Stress In Compression Parallel to Grain (Turkish Standards). Ankara, Turkey, 1977.
[14]. TS 2470, Wood - Sampling Methods and General Requirements for Physical and Mechanical Tests (Turkish Standards). Ankara, Turkey, 1976.
[15]. TS 2477, Wood-Determination of Impact Bending Strength (Turkish Standards). Ankara, Turkey, 1976.
[16]. TS 2479, Wood-Determination of Static Hardness (Turkish Standards). Ankara, Turkey, 1976.
[17]. TS 4083, Wood - Determination of Radial and Tangential Shrinkage (Turkish Standards). Ankara, Turkey, 1998.
[18]. TS 4084, Wood- Determination of Radial and Tangential Swelling (Turkish Standards). Ankara, Turkey, 1983.
[19]. TS 4085, Wood - Determination of Volumetric Shrinkage (Turkish Standards). Ankara, Turkey, 1983.
[20]. TS 4086, Wood - Determination of Volumetric Swelling (Turkish Standards). Ankara, Turkey, 1983.

ICENS
INTERNATIONAL CONFERENCE ON ENGINEERING AND NATURAL SCIENCES
24-28 May 2016 /Sarajevo

The Effects of Habitat on Calabrian Pine Fiber Dimensions

Ibrahim Bektas[1], *Aysenur Kılıc Ak**[1]

Abstract

The aim of this study was to indicate the effect of growing areas on the fiber dimensions of Calabrian pine (Pinus brutia Ten.) woods. For this reason, test materials were cut from four different habitat of Turkey. In tests, the fiber diameter, fiber length, wall thickness and lumen diameters were measured on samples obtained from 2 to 4 meters of the logs taken from each of the growing areas. It was determined that the effect of habitat on the cell wall thickness, the fiber diameter, the lumen width and the fiber length are significant at probability levels of $p<0.001$, $p<0.05$, $p<0.05$ and $p<0.001$, respectively. The results were demonstrated that the highest fiber dimensions were obtained in Onikişubat and Bucak habitat located in semi-arid climates.

Keywords: *Climatic type, fiber dimensions, habitat, pine wood.*

1.INTRODUCTION

Most of the researchers has focused on the effect of position within the stem and distance from pith on the length of wood fibers. The variations in the wood properties of the same species are a result of different growth factors, such as growth and ecological conditions. In addition, altitude, soil and climate are also very effective factors. Besides, tree age, sample size, ring properties (e.g. ring width, ring orientation), and the test procedure may also affect the test results [1],[2].

According to Bozkurt and Erdin [8], the lengths of tracheids or fiber in the sunny sides, can be shorter than in the shadow sides.

Due to the abovementioned reasons, the habitat is important in the formation of the physical and technological properties of trees. Consequently, the properties of Calabrian pine, just as for other tree species, vary according to growth regions [3].

According to Krib's, when comparing various cross-sections, it is apparent that fiber length is more related to the position of the ring with regard to the pith than to the age at which the ring is laid down [7], [6].

Similar studies were undertaken by Gerry (1915, 1916) with white pine, longleaf pine and Douglas-fir found that the fiber length increased outwards from the pith at both the bottom and top of an 82-foot-tall, 250-year-old white pine, and that at a distance of two and one-half to three inches from the pith, the increase in fiber length was apparent for approximately two-thirds the height of the tree [4], [5], [6].

The general objectives of this study were to evaluate the effect of habitat on fiber dimensions of Calabrian pine wood.

2.MATERIAL AND METHOD

2.1.Test Specimens

Firstly, the test material was collected from four different growth regions of Turkey Onikişubat (Kahramanmaras), Bucak (Burdur), Muğla and Kemalpaşa (İzmir) according to Turkish Standards TS 4176 [9] as shown in Figure 1. Then logs about 1 m, were obtained from the each tree's heights of between 2−4 m from the base. Afterwards, specimens used in this study were prepared from these logs (10×10×20 mm).

[1] *Kahramanmaras Sutcu Imam Unıversıty, Department of Forest Industry Engineering, 46100, Kahramanmaras, Turkey.*

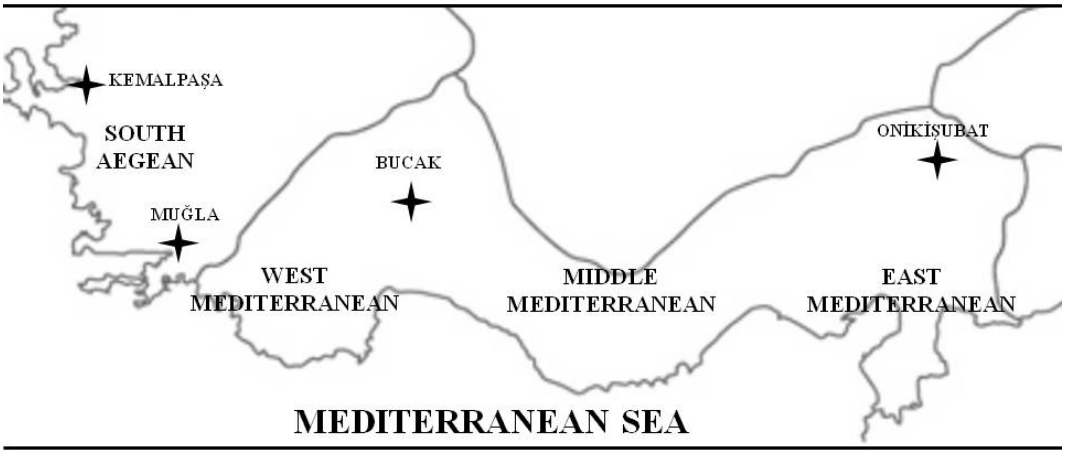

Figure 1: The location of growing areas in the Mediterranean region on the map of Turkey

3.MEASUREMENT OF SPECIMENS DIMENSIONS

After microscopic sections are easily obtained, these specimens were boiled into water till they sink into water and then, sections were placed on microscope slide. The fiber diameters, lumen diameters and cell wall thicknesses of test materials were measured with the microscope in radial and tangential directions on the cross-sections of specimens.

Finally, 0.5-mm thickness and 2 cm-long in parallel to grain specimens were used to measure fiber lengths. After they were defibered, fiber lengths were measured with the microscope.

4.RESULTS AND DISCUSSIONS

The analyses results of Anova and Duncan's mean separation test for cell wall thickness were shown in Table 1.

Table 1: Cell wall thicknesses.

	Cell wall thickness (µm)							
Areas	**N**	**Mean**	**SD**	**SE**	**COV**	**Min**	**Max**	**P**
Onikişubat	80	6.8A	0.660	0.074	9.74	5.5	8.6	***
Bucak	80	6.5B	0.665	0.074	10.31	4.5	8.1	***
Muğla	80	6.4B	0.520	0.058	8.06	5.2	7.6	***
Kemalpaşa	80	6.2C	0.587	0,066	9.43	4.5	7.4	***
Total	320	6.5	0.639	0.036	9.87	4.5	8.6	-

N: Number of sample, SD: Standard deviation, SE: Standard error, COV: Coefficient of variation, means with the same capital letter are not significantly different in Duncan's mean separation test, P: Probability level in ANOVA (***P < 0.001).

A review of the values in Table 1, it will be seen that decrease of the cell wall thickness towards from the east to the west of the Mediterranean. The reason for this decrease can be explained due to the geographical location. Measured cell wall thickness, has created significant differences P <0.001 among testing sites. On these differences, as well as geographical location, the other factors are given in Table 5 are certainly to be effective.

The statistical analysis values of fiber diameters for growing areas were presented in Table 2.

Table 2: The test values of fiber diameters.

	Fiber diameter (µm)							
Areas	**N**	**Mean**	**SD**	**SE**	**COV**	**Min**	**Max**	**P**
Onikişubat	80	27.1A	3.156	0.353	11.66	22.8	38.0	*
Bucak	80	26.7AB	3.110	0.348	11.63	18.1	34.7	*
Muğla	80	25.9B	2.694	0.301	10.41	20.0	31.4	*
Kemalpaşa	80	26.1B	3.037	0.340	11.65	20.0	33.7	*
Total	320	26.4	3.030	0.169	11.46	18.1	38.0	-

N: Number of sample, SD: Standard deviation, SE: Standard error, COV: Coefficient of variation, means with the same capital letter are not significantly different in Duncan's mean separation test, P: Probability level in ANOVA (*P < 0.05).

If Kemalpaşa test area which is located in the Aegean region does not taken into account, there is also similar situation to the wall thicknesses like fiber diameters. While the highest fiber diameter were measured in the Onikişubat test area (27.1 µm)

located in the most east of the Mediterranean, the minimum value of the specimens were obtained from the Western Mediterranean area (Muğla, 25.9 µm). By evaluation of fiber diameters test areas on the basis of statistically, it was seen that significant differences P < 0.05 among them as shown Table 2.

The statistical analyses values of the lumen diameters for four growing areas are given in Table 3.

Table 3: Lumen diameters.

	Lumen diameter (µm)							
Regions	**N**	**Mean**	**SD**	**SE**	**COV**	**Min**	**Max**	**P**
Onikişubat	80	23.3A	2.929	0.328	12.55	18.5	30.9	*
Bucak	80	22.4B	2.600	0.291	11.61	16.2	30.4	*
Muğla	80	22.9AB	3.131	0.350	13.69	16.6	32.3	*
Kemalpaşa	80	22.8AB	2.567	0.287	11.24	17.1	27.6	*
Total	320	22.9	2.824	0.158	12.35	16.2	32.3	-

N: Number of sample, SD: Standard deviation, SE: Standard error, COV: Coefficient of variation, means with the same capital letter are not significantly different in Duncan's mean separation test, P: Probability level in ANOVA (**P < 0.05).

The results of Anova and Duncan's mean separation test presented in Table 3 revealed that there is a significant difference in the level of P < 0.05 among the lumen diameters of the four test areas. The maximum lumen diameter value (23.3 µm), parallelly cell wall thicknesses and fiber diameters, was also reached in Onikişubat test area. However the lowest lumen diameter (23.3 µm) was measured in Bucak testing area located in the Central Mediterranean. Table 4 proves the results of ANOVA and Turkey's mean separation test for fiber lengths totally.

Table 4: Fiber lengths.

	Fiber lengths (mm)							
Regions	**N**	**Mean**	**SD**	**SE**	**COV**	**Min**	**Max**	**P**
Onikişubat	360	4.3AB	1.998	4.051	46.47	1.1	10.9	***
Bucak	360	4.6C	1.751	4.414	38.07	2.4	11.3	***
Muğla	360	4.5BC	2.170	4.307	48.22	2.2	16.2	***
Kemalpaşa	360	4.0A	2.111	3.806	52.78	1.2	13.2	***
Total	1440	4.4	2.025	0.053	46.52	1.1	16.2	-

N: Number of sample, SD: Standard deviation, SE: Standard error, COV: Coefficient of variation, means with the same capital letter are not significantly different in Duncan's mean separation test, P: Probability level in ANOVA (***P < 0.001).

When analyzed Table 4 where the results of measurement and statistical analysis of fiber lenght and statistical analysis is observed that the occurrence of significant differences in the level of P < 0.001 among fiber lengths in the test areas. Among the factors that affect this situation, the area's ecological and topographical structure can be counted [10].

On the other hand, the fiber lengths compared on the basis of test areas were quite a different situation from other measurement issues in this study. Because the first maximum value (4.6 mm) was obtained from the Bucak test area. However minimum value was also measured in Kemalpaşa test area as in wall thickness.

Some of the parameters considered to influence on the fiber dimensions are listed in Table 5.

Table 5. Some parameters influenced on fiber dimensions.

	Onikişubat	**Bucak**	**Muğla**	**Kemalpaşa**
Altitude (m)	800	800	700	350
Slope (%)	47.5	30	24	30
Aspect	south	south	south	north
Stand type	pure	pure	pure	pure
Closeness	1.5	2	2	2
Site index	2-3	1	1	2
Annual rainfall (kg/m^2)	708	744	1221	701
Annual temperature (^{o}C)	16.5	14	15	17.6
Relative humidity (%)	58	58	64	68
Climatic type	MMC[a]	TCM[b]	MMCH[c]	MAC[d]
Tree age	72	89	81	61
Soil type	Clay-loam	Clay-loam	Clay-loam	Clay-loam

[a]Mediterranean near mountain climate (Semi-arid); [b]The transition zone terrestrial climate from Mediterranean region (Semi-arid); [c]Mediterranean mountain climate (Humid); [d]The Mediterranean (Aegean type) climatic type (Semi-arid).

The parameters listed in Table 5 were evaluated collectively in absolute terms given in Table1-4 could be thought that effect on habitat such as altitude, aspect, closure, relative humidity, climatic type, and geographical position influence on the fiber dimensions. Fiber lengths increase from North to South and up from a low altitude. Similarly, closure (from 1.5 to 2) and relative humidity (from % 58 to % 64'e) increase, fiber dimensions have also improved. Both the geographical position and

climate type were considered, it is observed that deteriorates the fiber properties from East to West. This was also confirmed by Bektaş 2015 [2].

Table 6: An evaluation of mean values for growing areas according to success ratings.

Fiber dimension	Test areas							
	Onikişubat		Bucak		Muğla		Kemalpaşa	
	Mean	SR	Mean	SR	Mean	SR	Mean	SR
Cell wall thickness (µm)	6.8	1	6.5	2	6.4	3	6.2	4
Fiber diameter (µm)	27.1	1	26.7	2	25.9	4	26.1	3
Lumen diameter (µm)	23.3	1	22.4	4	22.9	2	22.8	3
Fiber length (mm)	4.3	3	4.6	1	4.5	2	4.0	4
The average of SR(*)	-	1.5	-	2.25	-	2.75	-	3.5
The total of SR	-	6.0	-	9.0	-	11.0	-	14.0

(*)Success rating is created from ranked in descending order of means.

When Table 5 and 6 were handled, mean values of fiber dimensions has improved from West to South in Mediterranean shown in Figure 1. Thus, where the fiber dimensions are effective, especially usage areas such as papermaking, considering of this determination can provide an important contribution to users for evaluation of calabrian pine.

4.CONCLUSION

In this study, effect of growing areas on the fiber dimensions of Calabrian pine logs were researched. It was determined in the tests that the effect of habitat on the cell wall thickness, the fiber diameter, the lumen width and the fiber length are significant at probability levels of $p<0.001$, $p<0.05$, $p<0.05$ and $p<0.001$, respectively. The results were demonstrated that the highest fiber dimensions were obtained in Onikişubat and Bucak habitat located in semi-arid climates. When evaluate the results, it can be said that the effect on habitat such as altitude, aspect, closure, relative humidity, climatic type, and geographical position influence on the fiber dimensions. Finally, fiber dimensions have improved from West to South in Mediterranean according to analyses.

REFERENCES

[1]. N.S. Abasali, M. Kiaei and A. Samariha, *Experimental Characterization of Shrinkage and Density of Tamarix aphylla Wood.* Cellulose Chemistry and Technology, 46: 369–373, 2012.
[2]. İ. Bektas, *The effect of Some Climate factors on Dimensional Stability in Pinus brutia*, Journal of Forest Science 61, (8): 352–358, 2015.
[3]. İ. Bektaş, M.H. Alma, N. As and R. Gundogan, *Relationship Between Site Index and Several Mechanical Properties of Turkish Calabrian pine (Pinus brutia Ten.).* For. Prod. J. 53(2):27-31, 2003.
[4]. G. Eloise, *Fiber measurement studies; lenght variations: Where they occur and their relation to the strenght and uses of wood.* Science 41 (1048):179, 1915.
[5]. G. Eloise, A *comparison of traheid dimension in longleaf pine and douglar fir. With data on the strenght and length, mean diameter and thickness of wall of the tracheids*. Science 43 (1106): 360, 1916.
[6]. S. Spurr, M. J. Hyvarinen.*Wood Fıber Length as Related to Position in tree and Growth*. Bot Rev 20: 561-575, 1954.
[7]. D. Kribs, *Length of tracheids in jack pine in relation to their position in the vertical and horizontal axis of the tree.* Minn Agr. Exp. Sta., Bul. 54.14 pp. 1928
[8]. A.Y. Bozkurt and N.Erdin, *Ağaç Teknolojisi,* İ.Ü. Yayın No: 3998, Orm. Fak. Yayın No: 445, ISBN 975-404-449-X İ.Ü. Basımevi ve Film Merkezi, 1997.
[9]. TS 4176, Wood - Sampling Sample Trees and Long for Determination of Physical and Mechanical Properties of Wood in Homogeneous Stands
[10]. T. Bozlar, V. Gerçek, S. Yilmaz and A. Usta, *Kızılağaç Plantasyonlarında Odunun Anatomik Özellikleri Üzerine Yetişme Ortamının Etkileri*. II. Ulusal Akdeniz Orman ve Çevre Sempozyumu "Akdeniz ormanlarının geleceği: Sürdürülebilir toplum ve çevre" ss.729-737, 2014.

ICENS
INTERNATIONAL CONFERENCE ON ENGINEERING AND NATURAL SCIENCES
24-28 May 2016 /Sarajevo

A Case Study for Decision Making and Valuation of Contract Flexibility in Manufacturing Industry

Mehmet Aktan [1]

Abstract

An investment decision is rarely a now-or-never decision and rarely a decision that cannot be abandoned or changed. In most instances, the decision can be delayed or accelerated, and often it comes in sequential steps with various decision points, including "go" and "no-go" alternatives. All of these choices are real managerial options and they affect the value of the investment opportunity. The real option at each step in the decision-making process is the freedom of choice to embark on the next step in the climb, or to choose against doing so based on the examination of additional information. Managers are very conscious of preserving a certain freedom of choice to respond to future uncertainties. In this study, the real options approach to evaluate the flexibility to contract a project is presented using a case study for an electric car manufacturing firm that is unsure of the technological efficacy and market demand of its new cars. Valuation of the option is demonstrated using binomial trees. Optimal decisions for each state are shown on the tree.

Keywords: *flexibility, manufacturing, real options, stochastic optimization*

1.INTRODUCTION

An initial investment related to an asset buys the potential opportunities such as to continue, expand, abandon or contract the use of the asset when it is favorable to do so, but does not carry the obligation to realize some losses when unfavorable conditions prevail. Managerial decisions lead to strategic and financial goals and they can follow different paths. They usually come in incremental steps. The real option at each step in the decision-making process is the freedom of choice to embark on the next step in the climb, or to choose against doing so based on the examination of additional information. An investment decision is rarely a now-or-never decision and rarely a decision that cannot be abandoned or changed. In most instances, the decision can be delayed or accelerated, and often it comes in sequential steps with various decision points, including "go" and "no-go" alternatives. All of these choices are real managerial options and have impact on the value of the investment opportunity. Further, managers are very conscious of preserving a certain freedom of choice to respond to future uncertainties [1], [2].

Financial options are defined on financial assets whereas real options are related with real assets. The application of real options valuation concepts for valuing real assets is a growing area in the theory and practice of finance and economics. Over the last years, many studies have presented the real options valuation method as a promising technique for valuing natural resource investments under conditions of uncertainty [3].

A firm may have the right to delay, expand, contract, switch or abandon a manufacturing project for a given cost or salvage value at some future date, which are real options. The value of the project may be increased if it is optimal to exercise the project's embedded option. Whether or not it is optimal depends on market conditions. The option need not be exercised if conditions are not optimal [4].

Thinking about investment projects in option terms encourages managers to decompose an investment into its component options and risks, which can lead to valuable insights about sources of uncertainty and how uncertainty will resolve over time [5]. Options thinking also encourages managers to consider how to enhance the value of their investments by building in more flexibility where possible. Real options analysis has the potential to allow companies to examine programs of capital expenditures as multi-year investments, rather than as individual projects [6]. If real options parameters can be estimated, any method used to value financial options can potentially be used to value real options [7]. Guidelines for analyzing real options can be found in several resources [8], [9], [10], [11].

The most commonly used method for evaluation of possible investment opportunities is the net present value approach (NPV). However, for situations in which flexibility plays a role, NPV method systematically underestimates the investment value since some management options such as contracting or expanding a project or company are not taken into account [12]. The real options approach overcomes these shortcomings considering that the investor's choice is subject to flexibility, i.e., the investor has the option to postpone his decision on investments [13]. Mainly used to evaluate real assets, real options approach factors in operational and managerial flexibilities over the project lifetime, differentiating itself from traditional methods like NPV. Indeed, real options give flexibility to investors when making decisions about real assets, revealing uncertainty associated with cash-flows and allowing investors to make decisions that positively influence the final project value [14].

[1] *Necmettin Erbakan University, Industrial Engineering Department, Konya, Turkey,* maktan@konya.edu.tr

2.MATERIALS AND METHODS

Suppose that an electric car manufacturing firm is unsure of the technological efficacy and market demand of its new cars. The firm decides to hedge itself through the use of strategic options, specifically an option to contract 80% of its manufacturing facilities at any time within the next 8 years. Suppose that the present value of the expected future cash flows discounted at an appropriate market risk-adjusted discount rate is S=$1 billion for the firm's current operating structure. Volatility of the logarithmic returns on the projected future cash flows is σ=0.15. The risk-free rate on a riskless asset for the next 8 years is found to be yielding r=1%. Suppose the firm has the option to contract 80% of its current operations at any time over the next 8 years, thereby creating an additional $300 million in savings after this contraction [11]. Figure 1 shows the binomial asset lattice for the following 8 years for the electric car manufacturing firm in billion dollars.

1,00	1,16	1,35	1,57	1,82	2,12	2,46	2,86	3,32
	0,86	1,00	1,16	1,35	1,57	1,82	2,12	2,46
		0,74	0,86	1,00	1,16	1,35	1,57	1,82
			0,64	0,74	0,86	1,00	1,16	1,35
				0,55	0,64	0,74	0,86	1,00
					0,47	0,55	0,64	0,74
						0,41	0,47	0,55
							0,35	0,41
								0,30

Figure 1. Binomial lattice that shows the asset value for the following 8 years

3.RESULTS AND DISCUSSION

Using a binomial lattice approach to calculate the contraction option and to find the optimal decisions, the real options value of the option is estimated to be nearly $100 million, as shown in the option valuation lattice of Figure 2. Lattices in Figures 1 and 2 were obtained using Real Options Valuation SLS software [15].

Management will choose the strategy that maximizes profitability. The calculations are made moving backwards, beginning from the last column in the asset price lattice. Maximum profit in a node of the asset price lattice can be found as

$$\text{Max}\ [\ (\ pS_{(i+1,j)} + (1-p)S_{(i+1,j+1)}\ )e^{-r}\ ,\ 0.8S + \$300\ \text{million}\ ] \qquad (1)$$

where p is the risk-neutral probability of asset value increase, i is the column number and j is the row number of the node, and $S_{i,j}$ is the asset price in node$_{i,j}$. The profit maximizing decision is to "continue" if the value of the first element in brackets is larger than the second element, and it is to "contract" if the value of the second element in brackets is larger than the first element in Equation 1.

The value of continuing is simply the discounted weighted average of potential future option values using the risk-neutral probability. Using the backward induction technique, the lattice is back-calculated to the starting point to obtain the value of $1.1 billion. Because the value obtained through discounted cash flows (DCF) is $1 billion for current existing operations, the option value of being able to contract 80 percent of its operations is $100 million. $1 billion is the static NPV without flexibility, $100 million is the real options value, and the combined value of $1.1 billion is the ENPV (Expanded NPV or NPV with real options flexibility value), the correct total value of this manufacturing initiative. If a real options approach is not used, the manufacturing initiative will be undervalued [11].

1,10	1,24	1,40	1,60	1,84	2,12	2,46	2,86	3,32
Continue	Continue	Continue	Continue	Continue	Continue	Continue	Continue	End
	0,99	1,10	1,23	1,40	1,59	1,83	2,12	2,46
	Contract	Contract	Continue	Continue	Continue	Continue	Continue	End
		0,89	0,99	1,10	1,23	1,39	1,58	1,82
		Contract	Contract	Contract	Continue	Continue	Continue	End
			0,81	0,89	0,99	1,10	1,23	1,38
			Contract	Contract	Contract	Contract	Contract	Contract
				0,74	0,81	0,89	0,99	1,10
				Contract	Contract	Contract	Contract	Contract
					0,68	0,74	0,81	0,89
					Contract	Contract	Contract	Contract
						0,63	0,68	0,74
						Contract	Contract	Contract
							0,58	0,63
							Contract	Contract
								0,54
								Contract

Figure 2. Binomial lattice that shows the optimal decisions for the following 8 years

4.CONCLUSIONS

By using the real options approach, managers can value the flexibility that exists in the system, or is planned to be added to the system. In addition, they can get idea about the optimal strategic decisions for future possible levels of prices. Real options approach reveals the additional value of uncertainty which cannot be found by static NPV analysis. Real options valuation also enables sensitivity analysis of its inputs, i.e., impacts of input parameter differences on profitability can be estimated [2].

The scenario covered shows that real options analysis can be used to support managerial decision making for manufacturing related operations such as contracting the operations.

REFERENCES

[1]. M. A. Brach, *Real Options in Practice*, Hoboken, New Jersey: John Wiley & Sons, Inc., 2003.
[2]. H. B. Nembhard, M. Aktan, and L. Shi, Real Options in Manufacturing Operations, Chapter 4, *Real Options in Engineering Design, Operations, and Management*, Boca Raton, FL: CRC Press, Taylor & Francis Group, 2010.
[3]. M. A. Haque, E. Topal, E. Lilford, "A numerical study for a mining project using real options valuation under commodity price uncertainty," *Resources Policy*, 2014, Vol. 39, pp. 115-123.
[4]. C. Agar, *Capital Investment & Financing. A Practical Guide to Financial Evaluation*, Elsevier Finance, 2005.
[5]. T. Brabazon, "Real options: valuing flexibility in capital investment decisions," *Accountancy Ireland*, 1999, Vol. 31, No. 6, pp. 16–18.
[6]. T. Copeland, "The real options approach to capital allocation", *Strategic Finance*, 2001, Vol. 83, No. 4, pp. 33–37.
[7]. J. Charnes, *Financial Modeling with Crystal Ball and Excel*, Hoboken, New Jersey: John Wiley & Sons, Inc, 2007.
[8]. M. Amram, and N. Kulatilaka, *Real options: Managing Strategic Investment in an Uncertain World*, Boston, Harvard: Business School Press, 1999.
[9]. T. Copeland, and V. Antikarov, *Real Options: A Practitioner's Guide*, NewYork: Texere Publishing Limited, 2001.
[10]. J. Mun, *Real Options Analysis: Tools and Techniques for Valuing Strategic Investments and Decisions*, Hoboken, New Jersey: John Wiley & Sons, Inc., 2002.
[11]. J. Mun, *Real Options Analysis Course: Business Cases and Software Applications*, Hoboken, New Jersey: John Wiley & Sons, Inc., 2003.
[12]. E. Johansson, *Real Options in Energy Investments*, 2010.
[13]. G. Kumbaroğlu, R. Madlener, and M. Demirel, "A real options evaluation model for the diffusion prospects of new renewable power generation technologies," *Energy Economics*, 2008, Vol. 30, No. 4, pp. 1882-1908.
[14]. L. Santos, I. Soares, C. Mendes, and P. Ferreira, "Real options versus traditional methods to assess renewable energy projects", *Renewable Energy*, 2014, Vol. 68, pp. 588-594.
[15]. Real Options Super Lattice Solver (SLS) software 2010, Real options Valuation, Inc.

Biography

Prof. Mehmet Aktan is the head of Industrial Engineering Department at Necmettin Erbakan University, Faculty of Engineering and Architecture. His BS degree is from Boğaziçi University, Industrial Engineering Department. He received MS and PhD degrees from The University of Iowa and University of Wisconsin-Madison, respectively. He has been a visiting professor in Industrial and Manufacturing Engineering Department of Penn State University. His research interests are quality engineering, financial engineering, artificial intelligence and statistics.

Characterization and Desulfurization Possibilities of High Sulfur Gediz-Turkey Coal

Ugur Demir[1]

Abstract

Coal is one of the important energy sources but it causes serious environmental problems such as air pollution, acid rain and greenhouse effects. Sulfur in coal is one of the responsible of these negative effects. Coal includes two types sulfur; organic and inorganic. While inorganic sulfur can be completely removal with physical desulfurization methods, organic sulfur can be removed only by chemical desulfurization methods. But chemical methods are not only expensive but also difficult process. Firstly in desulfurization, types of the sulfur content in coal should be well characterized. High sulfur Gediz-Turkey coal has been chosen to this study. This coal basin is located in the central of the Turkey. In this study, characterization and desulfurization possibilities of high sulfur Gediz coal were investigated. For this purpose several physical and chemical characterization methods such as proximate and ultimate coal analysis (ash, calorific value, volatile matter, moisture, sulfur analysis), mineralogical and petrographic analysis, fourier transform infrared spectroscopy, scanning electron microscope were used. Results of these analysis shown that Gediz coals include 3,15% pyritic sulfur and 2,89% organic sulfur. Removed of pyritic sulfur from Gediz-Turkey coal with physical methods such as gravity and sink-float separation is not possible because pyrite particle has 1-2 micron liberation size in coal.

Keywords: *Characterization, Desulfurization, High Sulfur, Gediz Coal*

1.INTRODUCTION

Coal is one of the most important sources of energy. It's around the world use will continue to expand during the next several decades. Unfortunately, the use of coal causes several kinds of environmental and health hazard problems. The control of pollutants such as SO_2, NO_2 and particle matter after burning such low quality coals will require low cost new technologies. Combustion of high sulfur coal produces SO_2 which is toxic and corrosive. Sulfur dioxide is subsequently converted to SO_3, which in contact with water forms sulfuric acid. In weathered coal, acidic mine water percolates into the round and makes the groundwater highly acidic. SO_3 leads to formation of acid rain, and corrosion of boilers, underground pipelines, metallic installations, mine machinery ect. [1][2].

Until recently, Turkish economy was growing rapidly and demand for electrical energy has increased approximately 8% per year on average. Total installed electric capacity of Turkey reached 71800 MW by end of 2015 [3]. Over half of this capacity is thermal energy which is derived from coal and natural gas, and remaining capacity comes from other sources [4]. Coal is clearly important to the Turkish economy. Turkish lignite reserves has been estimated to be over 13 billion metric tons. Low quality lignitic these coals are characterized by high moisture, ash, volatile matter and sulfur contents. Almost 75% of the total reserves have a calorific value below 2500 kcal/kg, while only 8% is in between 3000-5000 kcal/kg [5][6].

Sulfur in coal is present in both inorganic and organic. The inorganic sulfur in coal consist predominantly of sulfides (pyrite, sphalerite, galena, arsenopyrite, and others) and sulfates (barite, gypsum, anhydrite, and a number of iron sulfates) [2][7][8][9][10]. The pyrite is generally the predominant inorganic sulfur in coal. Particles of pyrite randomly distributed as crystals throughout the coal but are not bound to it. The organic sulfur in coal is covalently bound into its large complex structure and is difficult to remove physically or chemically, in contrast to pyritic or inorganic sulfur [11][12]. Organic sulfur in coal occurs in both aliphatic and aromatic networks. These include thiol, sulphide, disulphide, thioether, thioketonic and thiophene. Thiophene is resistant to oxidation when high sulfur coals are heated at 180 ^oC. Thiophene even reacts slowly with water at 300 ^oC, the reaction proceeds readly at 240 ^oC at pH 1 [13].

Combustion of high sulfur and ash coal leads to serious environmental pollution and other hazardous effects. Therefore, removal of the sulfur from a coal prior to its utilization has attracted interest of all concerned. To determine the suitability of any particular coal desulfurization method, knowledge of the distribution of different forms of sulfur within the coal is required [14]. Desulfurization of coal may be achieved by physical, chemical and biological methods. The physical methods are based on the differences in the physical properties of the sulfur and the carbonaceous part of the coal. In the physical processes coal is crushed, ground and washed. This allows for up to 90% of pyrite to be removed. However, depending on the type of coal, a considerable amount of finely distributed pyrite as well as organic sulfur can remain in and attach to the coal particles. The inability of physical methods to completely remove even the inorganic sulfur has led to the development of many chemical desulfurization processes. Desulfurization by chemical means involves solubilization of the inorganic constituents or their converted forms in various solvents [2]. These include carbonization in different atmospheres, air oxidation, wet oxidation, Mayer process, chlorination and extraction with sodium hydroxide, copper chloride and ethanol solutions [12][15][16]. The

[1] *Corresponding author: Dumlupınar University, Department of Mining Engineering, 43100, Kütahya, Turkey.* ugur.demir@dpu.edu.tr

biological methods are performed under mild conditions with no harmful reaction products and the value of coal is not affected. Several microorganisms such as Thiobacillus ferrooxidans and Thiobacillus tiooxidans are used in these processes [12].

In this study, characterization and desulfurization possibilities of high sulfur Gediz-Turkey coal samples were investigated. For this purpose physical and chemical analysis methods were used.

2.CHARACTERIZATION AND DESULFURIZATION POSSIBILITIES

Coal used in this study was provided from Kütahya-Gediz, Turkey. The coalfield is located to Gediz in the middle of the western of Turkey (Fig. 1). This coalfield has 15 million tons reserves. Two coal seams, the upper and the lower are located at the base of the Gediz formation. They are separated by about 3m thick black claystone and brown to dark brown clayey dolomitic limestone in the center of the coalfield. The average thickness of the upper seam is 1,7 m and lower seam 1.2 m [17].

Figure 4. Location of Küthay-Gediz coalfield map.

2.1.Characterization

2.1.1 Proximate and Ultimate Analysis

Coal samples air-dried were crushed and milled to less than 0,25 mm particle size by laboratory type crusher and grinder before characterization studies. Proximate, elemental and sulfur forms of Gediz coal sample analyses were given in Table 1. The ash, sulfur and its forms in the samples were determined by ASTM D 3173, ASTM D 3177 and ASTM D 2492 respectively. IKA c7000 calorimeter was used to determine the calorific value of sample.

Table 2. Proximate, elemental analysis and sulfur forms of Gediz coal

Proximate	**%**	**Ultimate**	**%**
Moisture	3,3	Carbon	78,41
Ash	25,99	Hydrogen	5,12
Volatile Matter	32,81	Nitrogen	1,61
Fixed Carbon	37,9	Oxygen (dif.)	7,8
		Total Sulfur	7,06
Calorific Value	5607 (kcal/kg)	Organic Sulfur	2,89
		Pyritic Sulfur	3,55
		Sulfatic Sulfur	0,62

As seen from Table 1, Gediz coal includes very high total sulfur (7,06%) and organic sulfur constitutes an important part of total sulfur. The forms of sulfur in coal are pyritic sulfur (3,55%), organic sulfur (2,98%) and sulfate sulfur (0,62%). Pyritic and organic sulfur generally account for the bulk of sulfur in coal. There are two forms of pyrites: 1- diagenetic framboidal pyrite which is distributed in the organic matrix; 2- epigenetic crystals and massive grains occurring mainly infills within microfractures of the organic matrix. Liberation size of pyritic sulfur in Gediz coal was determined as 1-5 micrometer.

2.1.2 Chemical Analysis

The chemical composition of Gediz coal was given in Table 2. Spectro X-Lab 2000 XRF device was used in this analysis. As seen in Table 2 important part of coal mineral matters are silicates and ferrous minerals.

Table 2. Chemical analysis of Gediz coal

	SiO_2	Al_2O_3	Fe_2O_3	CaO	MgO	Na_2O	K_2O	SO_3
%	4,15	0,014	3,75	0,25	0,16	2,26	0,14	22,07

2.1.3 Mineralogical and Petrographic Analysis

Mineralogical analysis of Gediz coal was given in Fig 2 and made with XRD device (Rigaku MiniFlex). XRD analysis was applied to raw coal sample to identify key mineral matter compounds. Fig. 2 shows that the major mineral phases are pyrite, melnicovite, quartz and calcite. However, trace of other minerals like kaolinite, illite, dolomite, gypsum and marcasite, and mixed clays minerals, feldspar and opal are also observed in coal. Petrographic analysis of the Gediz coal samples are in general composition by higher amounts of macerals of the vitrinite group (87%) than exinite (2%) and inertinite group (2%).

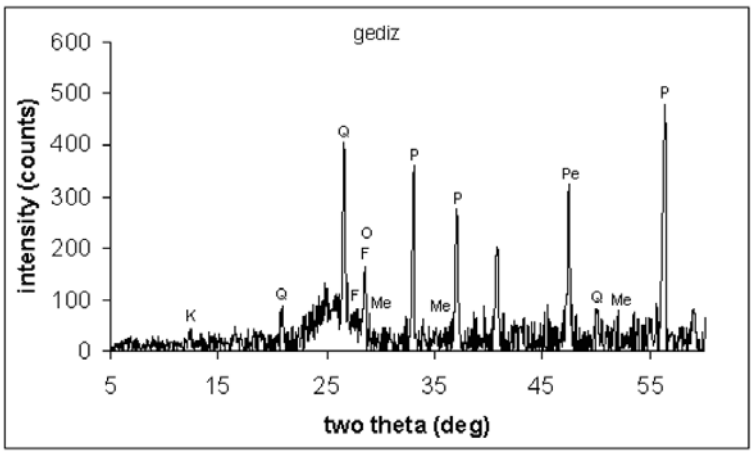

Figure 2. XRD pattern of Gediz Coal(K, Kaoline; Q, Quartz; P, Pyrite; Me, Melnicovite; F, Feldispar)

2.1.4 FTIR Analysis

FT-IR spectra of coal sample in the range 4000-400 cm^{-1} was run in a Perkin Elmer BX FTIR device on KBr pellets (Fig. 3). To permit measurements in the aromatic C-H out of plane zone (900-700 cm^{-1}). Spectra were recorded by co-adding 124 scans at a resolution of 2 cm^{-1}. Software facilities were used for baseline corrections of spectra, which were scaled to 1 mg sample cm^{-2}. The aromatic (H_{ar}) and aliphatic (H_{al}) hydrogen distribution in the solid samples was calculated from the integrated absorbance of the bands at 900-700 and 3000-2800 cm^{-1} respectively. The extinction coefficients used for converting integrated absorbance areas to concentration units were 541 and 710 abs cm^{-1} $mgcm^{-2}$ for aromatic and aliphatic bands, respectively, for the lignite and subbituminous coal. As shown in Figure 3, the mineral matter peaks is observed in the 536, 667, 694 and 1099 cm^{-1}wavelength. At 914, 1033, 3620 and 3694 cm^{-1} wavelength shows the kaolin conclusion. Quartz, pyrite and jibs are seeing in 779, 1164 and 470 cm^{-1} wavelength respectively. Carboxyl C=O groups at 1700 cm^{-1}, O-H strongly bonds at 3300-3400 cm^{-1} wavelengths are seen. Strong aliphatic C-H bonds were observed intensively at 2850 cm^{-1}. At 1033-1100 cm^{-1} wavelength C_{al}-O-C_{al} and C_{ar}-O-C_{al} bonds are observed in association with the minerals.

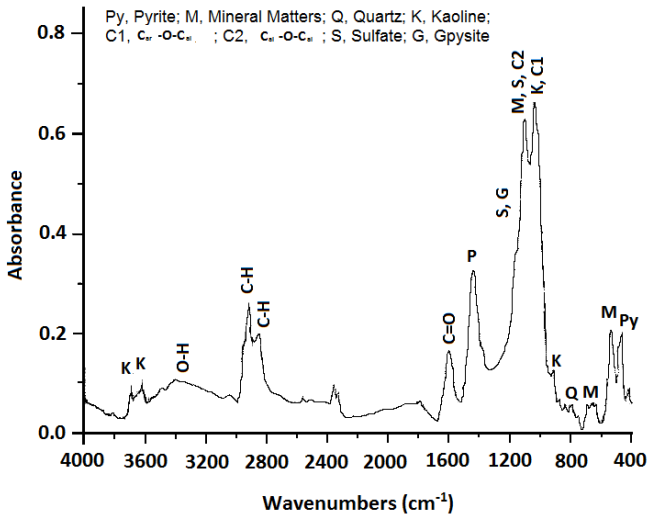

Figure 3. FTIR analysis of Gediz Coal.

2.1.5 SEM Analysis

The optical microscopy investigations shows that pyrite is present in the form of discrete grains, fracture and cavity filling, regular and irregular framboidal with particle size ranging from 1-5 micrometer. Scanning electron microscopy (SEM) studies show that pyrite is distributed even finer than 2 micrometer. Fine grinding is needed for the removal of this finely distributed sulfur from coal and is impossible using the conventional methods in practice.

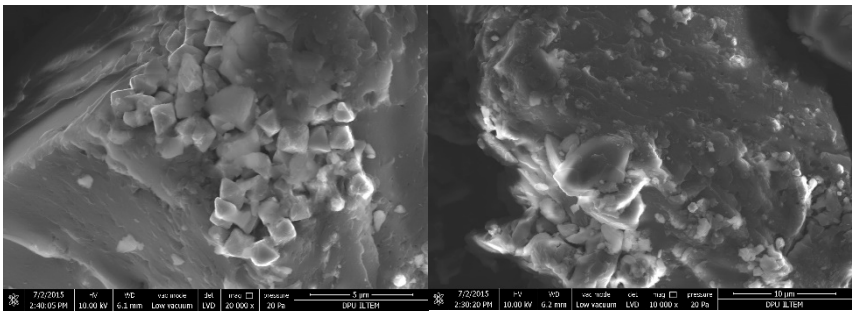

Figure 4. SEM images of Gediz-Turkey coal (mag. 20000x).

2.2 Desulfurization Possibilities

The processes of sulfur removal from coal prior to combustion can be subdivided into physical and chemical methods. Of these, physical methods can remove soluble sulfates and a considerable portion of the coarse pyrite, but the fine pyrite and organic sulfur remain largely untouched [18][19]. A number of chemical methods are under development with the intent to remove all of the pyrite and at least a portion of the organic sulfur. In general there are three chemical coal desulfurization strategies: 1- oxidation of sulfur in the coal to form soluble sulfates; 2- conversion of the sulfur to elemental sulfur in which form it can be vaporized or removes by organic solvents; 3- reaction with hydrogen to form gaseous hydrogen sulfide [18].

In this section, inorganic and organic sulfur removal facilities in Gediz coal will be examined. Properties of inorganic and organic sulfur content of the coal will be studied and research for suitable sulfur removal methods.

2.2.1 Physical Desulfurization

Basically, physical desulfurization can be divided into four broad categories based on the physical properties that are used to affect a separation: specific gravity, surface properties, magnetic susceptibility and electrical conductivity. Gravity separation depends on the specific gravity difference between coal and sulfurs. The specific gravity of clean coal is usually between 1,3 and 1,7 g/cm^3 whereas the specific gravity of mineral matter is between 2,5 and 5,0 g/cm^3 [20][21]. Gravity separation processes are relatively simple and include most conventional coal cleaning methods such as jigging, shaking tables, heavy medium, hydrocyclone and air classification. Several sulfur removing methods including froth flotation, oil agglomeration and solvent partitioning make use of the difference in surface properties to separate both sulfur and ash-forming mineral matter

from coal. In one commonly used process (dense medium cyclone) the coal particles sink or float in a medium of controlled density according to their densities. The heavier coal particles contain a large amount of minerals (including pyrites), so that the float product results purer than the original coal [20]. Generally, the coal minerals except pyrite tend to be quite hydrophilic (water attracting), whereas the coal macerals are either hydrophobic (water repelling) or at least less hydrophilic than the minerals. In the froth flotation process, the hydrophobic coal particles cling to air bubbles and rise to the top of a liquid suspension where the clean coal is recovered in froth. A frothing reactive is normally added to facilitate the flotation of the coal. The hydrophilic minerals are left behind in the aqueous suspension. In oil agglomeration a small amount of fuel oil is added to agitated slurry of coal and water, causing the hydrophobic coal particles to become oil-coated and agglomerated into larger clumps of coal and oil. The large agglomerates can be separated from the unagglomerated mineral particles by screening the suspension [21]. Magnetic separation relies on the difference in magnetic susceptibility of coal and mineral matter, either in air or aqueous slurries. Electrical methods employ electrical charges and magnetic forces to effect separation. Electrostatic separation depends on the difference in electrical change of various particles produced by one of several mechanisms in air [20][21].

The chemical composition, physical size and mode of distribution of the ash-forming mineral matter and sulfur types in coal greatly affect the way in which it can be removed from coal. Certain physical cleaning methods are well-developed, inexpensive, and trouble-free when applied to the separation of large discrete mineral particle from coal. However, finely disseminated pyrite and mineral particles cannot be removed efficiently and economically by physical methods. Also, physical methods do not remove the impurities which are bonded chemically to the organic matrix of the coal.

It is shown that in characterization studies of Gediz-Turkey coal, coal samples included high sulfur which is 3,55% pyritic, 2,89% organic and 0,62% sulfatic sulfur. Sulfur content of Gediz coal is high both in inorganic sulfur and organic sulfur. Pyritic sulfur liberation particle size is very fine (1-2 micron) and disseminated in coal matrix. It is also concluded from this study, entire removal of inorganic sulfur from Gediz coal is not possible by physical desulfurization methods.

2.2.2 Chemical Desulfurization

The organic sulfur form is about 50% of the total sulfur that cannot be removed by physical methods. Removal of organic sulfur requires chemical desulfurization techniques that can remove inorganic sulfur and ash-forming minerals, too. Although chemical desulfurization of coal is not profitable in the current economic conditions, it may become economical in the future, as SO_2 emission regulations are tightened and low sulfur coal reserves are depleted [22][23]. A number of chemical processes are under development which varies substantially in their approach. Basically, these processes can be classified into four general types: oxidative, reductive, caustic and miscellaneous treatments [21].

Several oxidizing chemical/agents as air, oxygen, chlorine, nitrogen oxide, and ferric salts are sufficiently strong (at elevated temperatures) to convert the pyritic and part of the organic sulfur in coal to water soluble sulfate. Oxydesulfurization processes employ oxygen or air in an aqueous solution at an elevated temperature and pressure. Caustic treatments; ıt has long been known that caustic, either in the form of a hot melt or a hot aqueous solution, is an effective chemical for removing sulfur and ash-forming mineral matter from coal [21].

The chemical desulfurization methods are based on solubilization of the sulfur in different chemicals. Well known desulfurization processes include; caustic treatment (NaOH, KOH, CaOH vs), acidic treatment (HCl, HNO_3, H_2SO_4, HF, H_2O_2 vs) and thermal treatment [1][18][22][24][25][26][27][28]. Thermal treatment can be used efficiently for desulfurization of coals by both removal of organic sulfur species and pyrite decomposition prior to combustion. In this process, while the raw coal is desulfurized some useful gaseous and liquid produce and residual char are also obtained. Thermal treatment combined with char combustion appears to be the most efficient technology for the utilization of high sulfur coals [29][30]. The extent of sulfur removal from coal by thermal treatment depends on many factors, such as temperature, nature of the atmosphere and residence time, as well as coal type [31]. Pyrite decomposes to pyrrhotite, H_2S, and some pyrrhotite reduction to iron is observed during thermal treatment. Pyrite begins to decompose to FeS_x around 350 ^oC, this reaction is finished at 750-950 ^oC [32][30].

An important part of inorganic sulfur forms in Gediz-Turkey coal is pyritic sulfur therefore removal of pyritic sulfur from coal can achieved by acidic or alkaline chemical. During this chemical treatments while pyritic sulfur is converted to soluble forms between organic sulfur and coal matrix weak bonds (C-S, S-S, H-S) is broken or strong bonds are weaked. As it can be seen, all of the characterization studies for both fine pyritic sulfur and organic sulfur can be removed only chemical desulfurization methods.

3 CONCUSION

The Gediz coalfield in the western part of Turkey mainly contains high sulfur (7,06% S) subbituminous coal old Middle Miocene age. The coalfield is in general characterized by higher amounts of macerals of the vitrinite group than liptinite and inertinite contens. Minerals identified by XRD in the coal include major quartz, pyrite and calcite with subsidiary amounts of kaolinite, illite, dolomite, gypsum, marcasite, rarely mixed layer clay minerals, feldspar and opal. Ash content are relatively high and detrital minerals are an important component in the coal samples. As an inorganic sulfur pyrite and marcasite were detected by SEM, these iron sulfides with in microfractures and micropores and syngenetic framboidal pyrites dispersed in the coal matrix.

This study concludes that as investigated for all identified properties of Gediz-Turkey coal, removal of sulfur types from coal by physical desulfurization methods are not possible. Nowadays, applications of chemical desulfurization methods are difficult in current economical conditions. Therefore, Gediz-Turkey coal must not be used as a fuel but alternative usage areas should be investigated.

REFERENCES

[1]. Liu G., Zheng L., Gao L., Zhang H., Peng Z., 2005 "The characterization of coal quality the Jining coalfield" Energy, vol: 30, 1903-1914
[2]. Mukherjee, S., Mahjuddin, S., Borthakur, P.,C., 2001a, "Demineralization and desulfurization of subbituminous coal with hydrogen peroxide" Energy & Fuels, vol: 15, 1418-1424
[3]. Euas.gov.tr, 2016
[4]. Palmer, S., R., Hippo, E., J., and Dorai, X., A., 1994, Chemical coal cleaning using selective oxidation, Fuel 1994 Volume 73 Number 2, 161-170
[5]. Ateşok, G., Perek, K.,T., Dinçer, H., Çelik, M.,S., 1999, "Reduction of ash and sulfur contents of low-rank Turkish semicoked lignite by high intesity dry magnetic separation" Coal Preparation, vol: 20, 179-190
[6]. TKİ, 2014 Kömür Sektör Raporu (linyit), Enerji ve Tabii Kaynaklar Bakanlığı.
[7]. Chalkins W. H., 1994 "The chemical forms of sulfur in coal: a review" Fuel, vol: 73, number 4, 475-484
[8]. Jorjani, E,. Rezai, B., Vossoughi, M., Osanloo, M., Abdollahi, M., 2004, "Oxidation pretreatment for enhancing desulfurization of coal with sodium butoxide" Minerals Engineering, vol: 17, 545-552
[9]. Pietrizak, R., Wachowska, H., 2006,"The influence of oxidation with HNO3 on the surface composition of high-sulphur coald: XPS study" Fuel processing technology, vol:87, 1021-1029
[10]. Uzun, D., Özdoğan, S., 2006, "Sulfur removal from original and acid treated lignites by pyrolysis" Fuel, vol: 85, 315-322
[11]. Constanti M., Giralt J., and Bordons A., 1994 "Desulphurization of dibenzothiophene by bacteria" World journal of Microbiology & Biotechnology, vol: 10, 510-516
[12]. Prayuenyong, P., 2002, "Coal biodesulfurization processes" Songklanakarin J. Sci. Technology, vol:24, No: 3, 493-507
[13]. Borah, D., Baruah, M.,K., Haque, I., 2001, "Oxidation of high sulphur coal. Part 1. Desulphurization and evidance of the formation of oxidised organic sulphur species" Fuel, vol: 80, 501-507
[14]. Jorjani, E., Yperman, J., Carleer, R., Rezai, B. 2006 "Reductive pyrolysis study of sulfur compounds in different Tabas coal samples (Iran)" Fuel, vol: 84, 114-120
[15]. Yaman S., and Küçükbayrak S., 1996 "Oxydesulfurization of a Turkish hard lignite with ammonia solution" Energy Sources, vol: 18, 677-683
[16]. Klein, J., 1998, "Technological and economical aspects of coal biodesulfurization" Biodegradation, vol: 9, 293-300
[17]. Karayiğit, A. I. Spears, D.A. Booth, C.A. 2000, "Antimony and arsenic anomalies in the coal seams from the Goker coalfield, Gediz, Turkey" İnt. Journal of Coal Geology, vol: 44, 1-17
[18]. Karaca, S., Akyürek, M.., Bayrakçeken, S. 2003, " The removal of pyritic sulfur from Aşkale lignite in aqueous suspention by nitric acid" Fuel processing Technology, vol: 80, 1-8
[19]. Mukherjee, S., Borthakur, P.,C., 2003b, "Demineralization of subbitumious high sulphur coal using mineral acids" Fuel processing Technology, vol: 85, 157-164
[20]. Trindade, S., C., Kolm, H., H., 1973, "Magnetic desulfurization of coal" IEEE Transactions on magnetics, vol: mag-9, No:3, 310-313
[21]. Fan C.W., 1984, "Coal desulfurization and demineralization by chemical/physical treatments" PhD Teases , Iowa State Universtiy, Ames, Iowa, USA
[22]. Jorjani, E,. Rezai, B., Vossoughi, M., Osanloo, M., Abdollahi, M., 2004a, "Oxidation pretreatment for enhancing desulfurization of coal with sodium butoxide" Minerals Engineering, vol: 17, 545-552
[23]. Kawatra ve 2001 Kawatra, S.K., ve Eisele, T.C. 2001, Coal desulfurization, high-efficiency preparation methods, Printed by Edwards Brothers, Ann Arbor, Taylor & Francis Inc. 349p.
[24]. Alam, H.,G., Moghaddam, A.,Z,. Omidkhah, M.,R., 2008, " The influence of process parameters on desulfuruzation of Mezino caol by HNO3/HCl leaching" Fuel Processing Technology, vol:90, 1-7
[25]. Mukherjee, S., Borthakur, P., C., 2003a, " Effect of leaching high sulphur subbituminous coal by potassium hydroxide and acid on removal of mineral matter and sulphur" Fuel, vol: 82, 783-788
[26]. Mukherjee, S., Borthakur, P.,C., 2003c "Effect of alkali treatment on ash and sulphur removal from Assm coal" Fuel processing Technology, , vol: 85, 93-101
[27]. Ceylan, K., Karaca, H., Önal, Y. 1999, "Thermogravimetric analysis of pretreated Turkish lignites" Fuel, vol: 78, 1109-1116
[28]. Karaca, H., Ceylan, K. 1997, "Chemical cleaning of Turkish lignite by leaching with aqueous hydrogen peroxide" Fuel processing Technology, vol: 50, 19-33
[29]. Erşahin, H., Şara, O., N., Boncukoğlu, R., 1997, " Desulphurizaiton of two Turkish lignite in an entrained flow reactor" Journal of analytical and applied pyrolysis, vol: 44, 65-74
[30]. Koca, H., Kockar, O.,M., Koca, S,. 2007, "Desulphurizaiton of lignites by slow, fast and flash pyrolysis and high intensity dry magnetic separation" Energy Sources Part A, vol: 29, 1457-1470
[31]. Xu, L., Yang, J., Li, Y., Liu, Z., 2003, "Effect of organic gaseous additives on desulfurization of coal during pyrolysis" Energy Sources part A, vol: 25, 1033-1042
[32]. Uzun, D., Özdoğan, S., 2006, "Sulfur removal from original and acid treated lignites by pyrolysis" Fuel, vol: 85, 315-322

ICENS
INTERNATIONAL CONFERENCE ON ENGINEERING AND NATURAL SCIENCES
24-28 May 2016 /Sarajevo

Accuracy and Precision Analysis of Precise Point Positioning (PPP) using Online-PPP Services

Serkan Doganalp[1], Salih Alcay[1], Sermet Ogutcu[1]

Abstract

Precise Point Positioning (PPP) is a Global Positioning System (GPS) based positioning technique which enables high positioning accuracy for static and kinematic applications using precise orbit and clock information. Combining the precise satellite positions and clock information with a dual frequency geodetic GNSS receiver, centimeter level accuracy is possible for three-dimensional positioning. Several online PPP services are available which provides reliable positioning. These services become ubiquitous thanks to the continuing improvement and user friendly interface from organizations and universities. Among these services, CSRS-PPP (Canadian Spatial Reference System), magicGNSS, APPS (Automatic Precise Positioning Service) and GAPS (GPS Analysis and Positioning Software) have an important place in the literature in terms of accuracy. In this study, 6 IGS (International GNSS Service) stations in different latitudes were used in order to investigate positioning performance of CSRS-PPP, magicGNSS, APPS and GAPS. The results were examined in terms of both accuracy and precision. The accuracy analysis was performed by comparing the estimated coordinates of the stations with the published true ones (ITRF 2008).

Keywords: *Precise Point Positioning (PPP), GPS, online-PPP service, International GNSS service (IGS)*

1.INTRODUCTION

Recently Precise Point Positioning (PPP) became a powerful technique with applications in surveying. Based on accurate GPS satellite orbit and clock information, PPP enables adequate (cm level) positioning accuracy using single receiver unit [1]. Despite the great potential of the method, PPP suffers a number of deficiencies. The most important is the requirement of long convergence time in order to ensure reliable position solution [2]. For nearly 20 years, most researchers have focused on the theory and applications of the PPP technique [2], [3-5], [6]. [2], 2014 performed a comprehensive statistical assessment of static PPP technique using GPS-only, GLONASS-only and GPS/GLONASS data. According to the results, the superiority of the combine GPS/GLONASS solutions is apparent for 1^h and 2^h observation period. A number of institutions and organizations developed online processing services (APPS, CSRS-PPP, GAPS, magicGNSS) in order to estimate coordinates using PPP techniques. Among the most recent researches, [6] investigated the performance of PPP technique in urban areas using online PPP services based on GPS and GPS+GLONASS data. The results exhibited an increase in the number of satellites may not bring any significant contribution to the solution when the sufficient numbers of GPS satellites were available.

This study attempts an investigation analysis and assessment of high precision PPP performance in terms of accuracy and precision using online services. Testing employs GPS datasets obtained from 6 IGS stations in different region.

2.MATERIAL AND METHOD

In order to examine the performance of the web based PPP services (APPS, CSRS-PPP, GAPS, magicGNSS), observation data of 6 IGS sites, located in different region, were used (Figure 1). Details of the used IGS sites, including location, antenna, receiver information, are given in Table 1.

[1] *Corresponding author: Necmettin Erbakan University, Department of Geomatics Engineering, 42090, Konya /Turkey.*
sdoganalp@konya.edu.tr

Figure 1: Location of the stations and baselines

Table 1: Details of used IGS stations

Site ID	Network	Country	Latitude	Longitude	Height(m)	Receiver	Antenna	Radome
AUCK	IGS	New Zealand	-36.6028	174.8342	132.711	TRIMBLE NETR9	TRM57971.00	NONE
CKIS	IGS	Cook Islands	-21.2008	-159.801	18.4	TRIMBLE NETR9	TRM59800.00	NONE
CRO1	IGS	Virgin Islands	17.75667	-64.5842	-31.4974	ASHTECH UZ-12	JAVRINGANT_DM	SCIS
GLSV	IGS	Ukraine	50.36417	30.49667	226.8	NOV OEMV3	NOV702GG	NONE
HLFX	IGS	Canada	44.68333	-63.6111	3.1	TPS NET-G3A	TPSCR.G3	NONE
HYDE	IGS	India	17.41722	78.55083	441.68	LEICA GRX1200GGPRO	LEIAT504GG	NONE

Observation data were downloaded from the SOPAC website [7]. 15 daily observation data, from 16.01.2015 to 30.01.2015, were employed. Although CSRS-PPP and MagicGNSS have ability for processing both GPS and GLONASS data, GAPS and APPS can only process GPS data. For this reason, in order to provide same conditions, GLONASS observations were removed from each observation files. Thus, all observations files corresponding to 6 IGS sites contained only GPS observations. Processes were performed using static positioning modes of each PPP services. For the details of the web based PPP services authors refer to [8].

3.RESULTS

In this study, results of PPP services including 15 daily solutions, were examined in terms of both accuracy and precision. Accuracy of the estimated coordinates corresponding to PPP services were tested based on ITRF 2008 coordinates of IGS sites. For doing this, measurement epoch coordinates of 6 IGS sites were obtained based on ITRF 2008 reference epoch coordinates and velocities. These coordinates were used as true coordinates. Then differences between true coordinates and the estimated ones, based on APPS, CSRS-PPP, GAPS, magicGNSS, were computed and given in Figures 2-7.

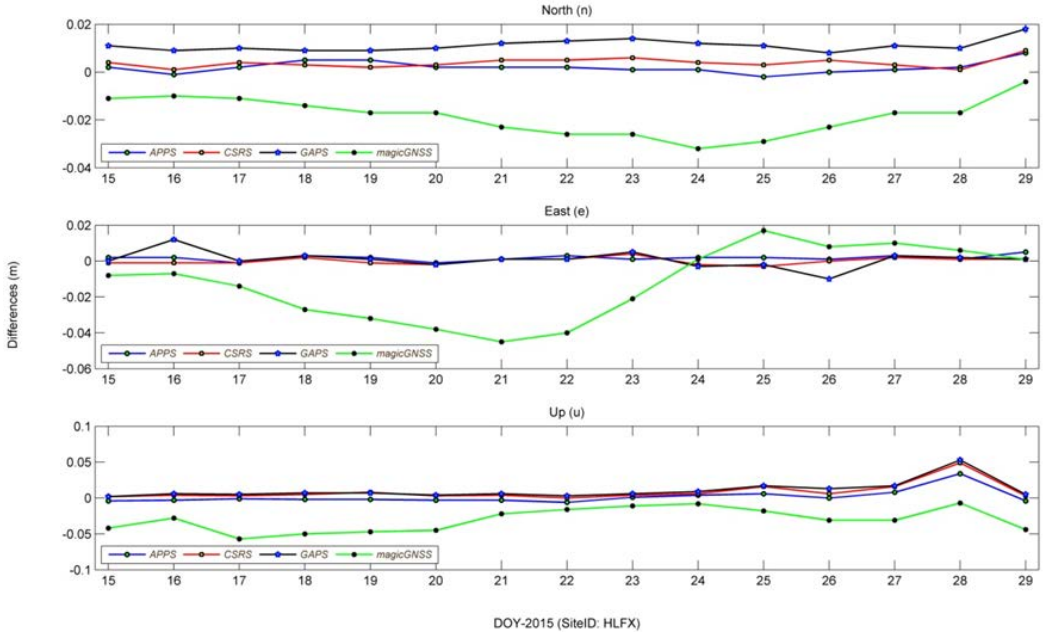

Figure 2. Differences between true and estimated coordinates of HLFX site

Figure 2 exhibits the differences for the mid-latitude station (HLFX) of the northern hemisphere. While the differences corresponding to APPS, CSRS-PPP and GAPS are close to each other and reaching less than 2 cm for "n" and "e" components, magicGNSS results are a little larger. However in the "up" component, magicGNSS results are closer to the others, reaching maximum 5 cm.

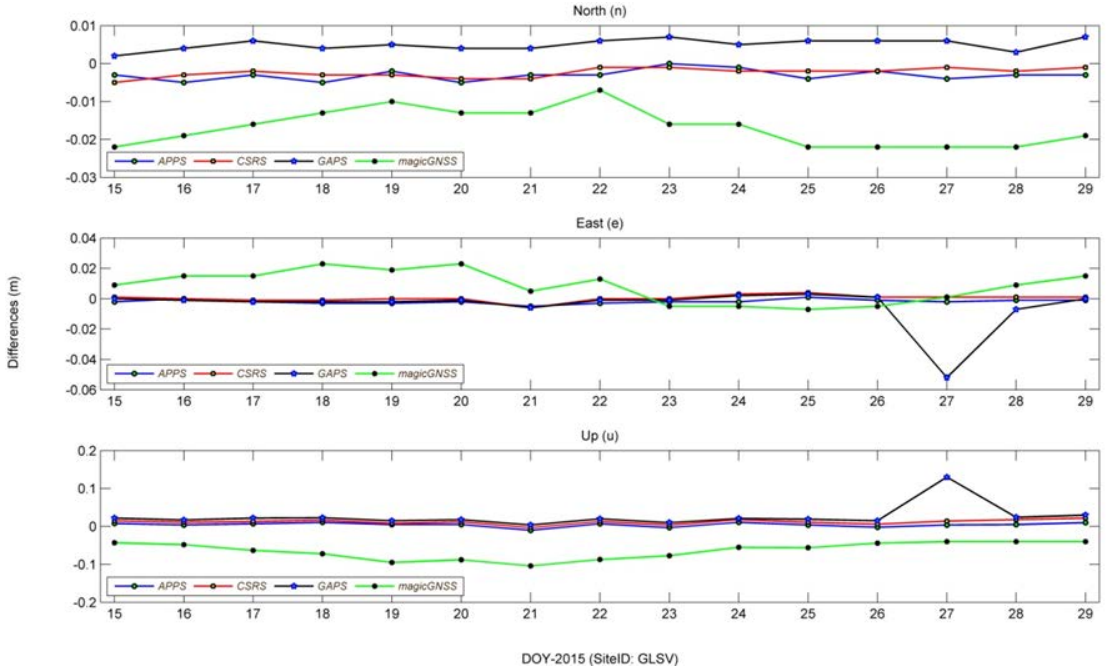

Figure 3. Differences between true and estimated coordinates of GLSV site

Differences corresponding to the other northern hemisphere station (GLSV) are given in Figure 3. Although results are generally similar, inconsistent results in the east and up components were detected one of the GAPS solutions (DOY 27).

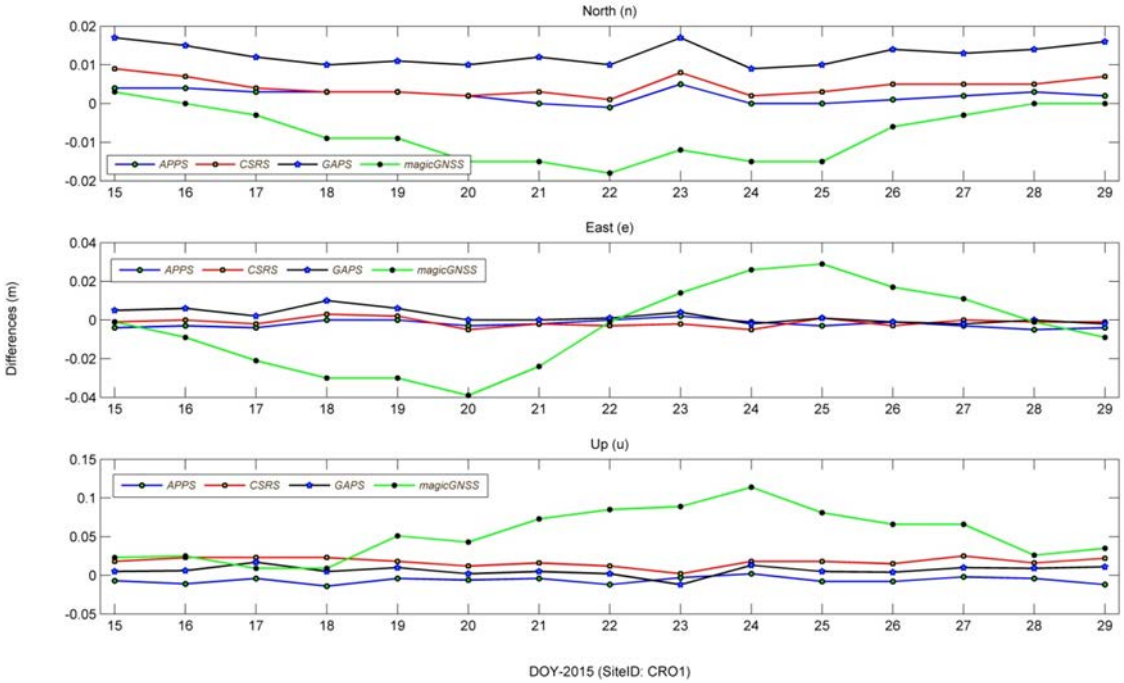

Figure 4. Differences between true and estimated coordinates of CRO1 site

Figure 4 shows the differences for the CRO1 station in equatorial region. While the differences corresponding APPS, CSRS and GAPS are highly consistent for all components, magicGNSS results are a little different. Although, differences of magicGNSS are negative for the "n" component and positive for the "u" component, they are negative between DOY 15 and 22 and also positive after DOY 22 for the "e" component.

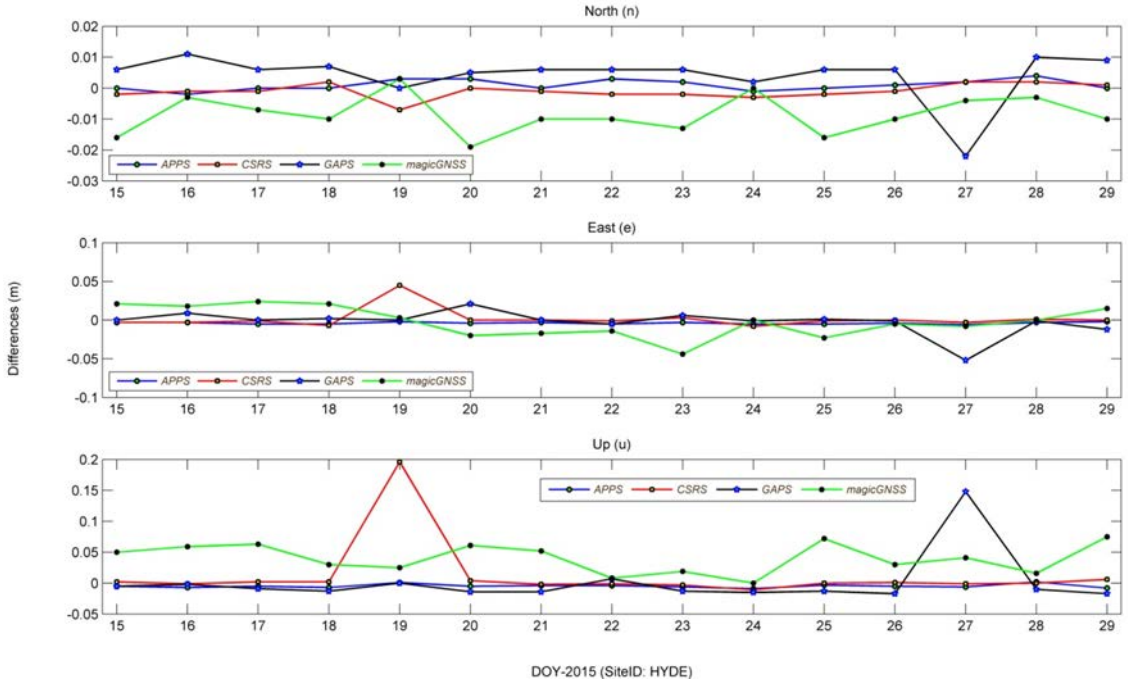

Figure 5. Differences between true and estimated coordinates of HYDE site

For another equatorial station (HYDE), results illustrate that differences based on services are similar level (Figure 5). However in DOY 19 and 27, there are some inconsistent results are depicted, reaching 2 cm.

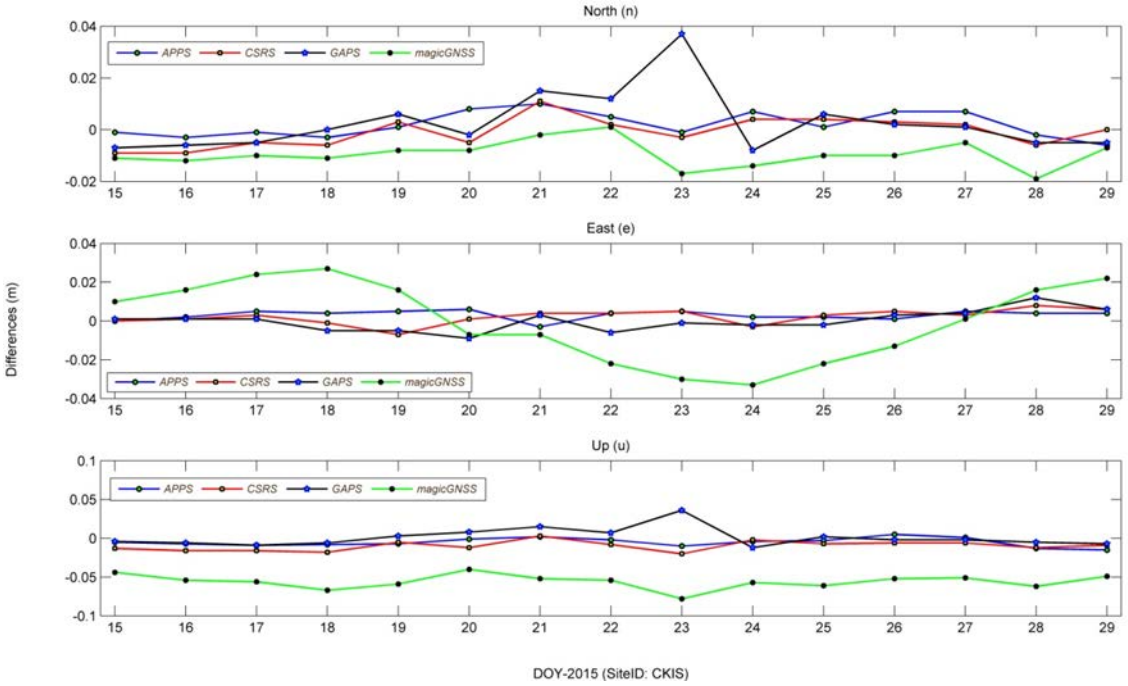

Figure 6. Differences between true and estimated coordinates of CKIS site

In the southern mid-latitude station (CKIS), differences are generally less than 3 cm for the horizontal components for all services. However in the vertical component, while the magicGNSS results are at the 5 cm level, others are generally less than 2 cm (Figure 6).

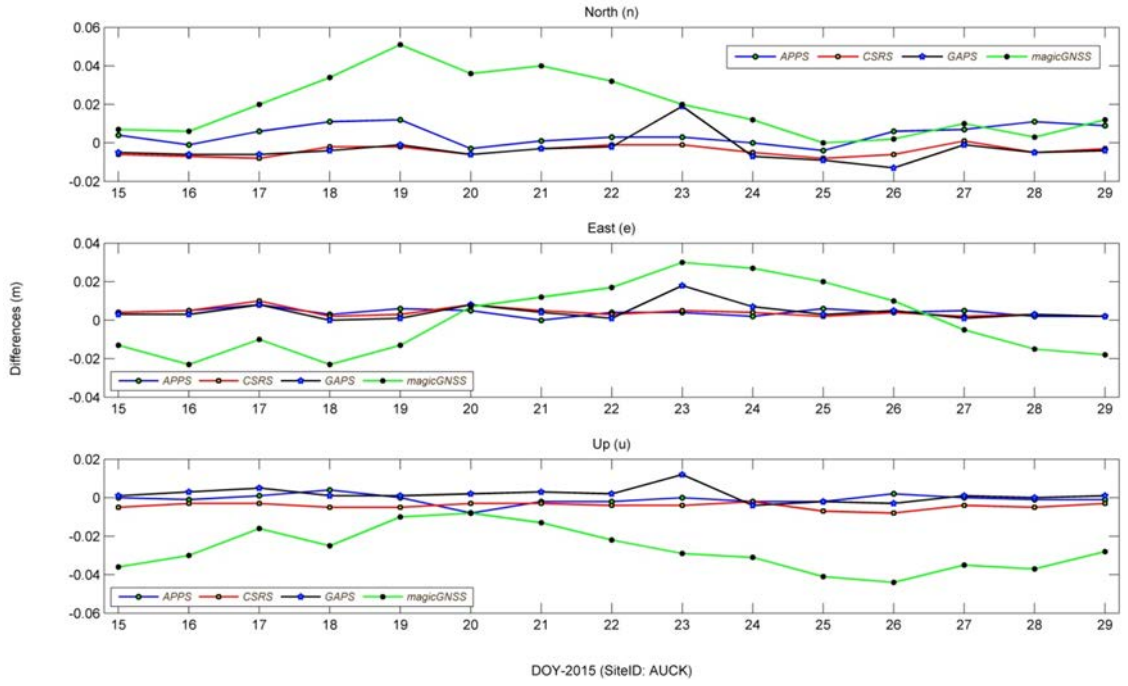

Figure 7. Differences between true and estimated coordinates of AUCK site

For the AUCK station in the southern mid-latitude, differences are in the same level comparing to the other stations (Figure 7).

Besides the accuracy analysis, precision of the results which gives the internal consistency were also tested. For this purpose standard deviations (std) corresponding to the differences were calculated. Besides the std, some statistical values of the differences including minimum, maximum, range, mean values were also computed and given in Table 2.

Table 2 Statistical value of the differences

Site	Service	North (cm)					East (cm)					Up (cm)				
		Min	**Max**	**Range**	**Mean**	**Std**	**Min**	**Max**	**Range**	**Mean**	**Std**	**Min**	**Max**	**Range**	**Mean**	**Std**
HLFX	APPS	-0.2	0.8	1.0	0.2	0.2	-0.1	0.5	0.6	0.2	0.2	-0.6	3.4	4.0	0.2	1.0
	CSRS-PPP	0.1	0.9	0.8	0.4	0.2	-0.3	0.4	0.7	0.0	0.2	0.0	4.9	4.9	0.9	1.2
	GAPS	0.8	1.8	1.0	1.1	0.3	-1.0	1.2	2.2	0.1	0.5	0.2	5.3	5.1	1.1	1.3
	MagicGNSS	-3.2	-0.4	2.8	-1.8	0.8	-4.5	1.7	6.2	-1.3	2.0	-5.7	-0.7	5.0	-3.0	1.6
GLSV	APPS	-0.5	0.0	0.5	-0.3	0.1	-0.5	0.1	0.6	-0.2	0.1	-1.0	1.1	2.1	0.4	0.6
	CSRS-PPP	-0.5	-0.1	0.4	-0.2	0.1	-0.6	0.4	1.0	0.0	0.2	-0.3	2.2	2.5	1.2	0.6
	GAPS	0.2	0.7	0.5	0.5	0.1	-5.2	0.3	5.5	-0.5	1.3	0.4	13.0	12.6	2.6	2.9
	MagicGNSS	-2.2	-0.7	1.5	-1.7	0.5	-0.7	2.3	3.0	0.8	1.0	-10.4	-4.0	6.4	-6.3	2.2
CRO1	APPS	-0.1	0.5	0.6	0.2	0.2	-0.5	0.2	0.7	-0.2	0.2	-1.4	0.2	1.6	-0.6	0.4
	CSRS-PPP	0.1	0.9	0.8	0.4	0.2	-0.5	0.3	0.8	-0.1	0.2	0.2	2.5	2.3	1.7	0.6
	GAPS	0.9	1.7	0.8	1.3	0.3	-0.2	1.0	1.2	0.2	0.4	-1.2	1.7	2.9	0.6	0.7
	MagicGNSS	-1.8	0.3	2.1	-0.8	0.7	-3.9	2.9	6.8	-0.5	2.1	0.9	11.4	10.5	5.3	3.2
HYDE	APPS	-0.2	0.4	0.6	0.1	0.2	-0.6	-0.2	0.4	-0.4	0.1	-0.9	0.2	1.1	-0.5	0.3
	CSRS-PPP	-0.7	0.2	0.9	-0.1	0.2	-0.8	4.5	5.3	0.1	1.2	-1.1	19.6	20.7	1.3	5.1
	GAPS	-2.2	1.1	3.3	0.4	0.8	-5.2	2.1	7.3	-0.2	1.6	-1.7	14.8	16.5	0.1	4.1
	MagicGNSS	-1.9	0.3	2.2	-0.9	0.6	-4.4	2.4	6.8	-0.2	2.0	0.0	7.5	7.5	4.0	2.4
CKIS	APPS	-0.6	1.0	1.6	0.2	0.5	-0.3	0.6	0.9	0.3	0.2	-1.5	0.5	2.0	-0.5	0.6
	CSRS-PPP	-0.9	1.1	2.0	-0.1	0.6	-0.7	0.8	1.5	0.2	0.4	-2.0	0.3	2.3	-1.0	0.6
	GAPS	-0.8	3.7	4.5	0.3	1.2	-0.9	1.2	2.1	0.0	0.5	-1.2	3.6	4.8	0.1	1.2
	MagicGNSS	-1.9	0.1	2.0	-1.0	0.5	-3.3	2.7	6.0	0.0	2.0	-7.8	-4.0	3.8	-5.6	0.9
AUCK	APPS	-0.4	1.2	1.6	0.4	0.5	0.0	0.8	0.8	0.4	0.2	-0.8	0.4	1.2	-0.1	0.3
	CSRS-PPP	-0.8	0.1	0.9	-0.4	0.3	0.2	1.0	0.8	0.4	0.2	-0.8	-0.2	0.6	-0.4	0.2
	GAPS	-1.3	1.9	3.2	-0.4	0.7	0.0	1.8	1.8	0.4	0.5	-0.4	1.2	1.6	0.2	0.4
	MagicGNSS	0.0	5.1	5.1	1.9	1.6	-2.3	3.0	5.3	0.0	1.8	-4.4	-0.8	3.6	-2.7	1.1

As depicted in Table 2, according to the standard deviations which indicate the precision of the differences, APPS results are better than the others for all components. They are reaching maximum 0.5 cm and 1.0 cm for the horizontal and the vertical components respectively. In addition according to the range values, “up” components are usually at the larger level when compared to the horizontal components for all results.

4.CONCLUSION

In order to investigate the performance of web based PPP services, observation data corresponding to three set of IGS sites (6) in different latitude regions, were used. In terms of the accuracy analysis, PPP results corresponding to the web based services were given based on the true coordinates (ITRF 2008) of the IGS sites. Results exhibited that APPS, CSRS-PPP and GAPS results are close to each other for all stations. However magicGNSS results are generally a little worse than the others. Besides the accuracy analysis, precision of the results were also tested. Standard deviations corresponding to the differences of services illustrated that APPS, CSRS-PPP and GAPS results were highly consistent.

ACKNOWLEDGMENT

The authors are thankful to SOPAC for providing observation data. Authors also thankful to the APPS, CSRS-PPP, GAPS and magisGNSS web based services for the PPP analysis. This work is supported by Coordinatorship of Necmettin Erbakan University Scientific Research Projects.

REFERENCES

[1]. Rizos. C, Janssen. V. Roberts, C. Grinter. T, "GNSS: Precise Point Positioning PPP versus DGNSS," *Geomatics World*., Oct, pp. 18-20, 2012.
[2]. Yigit C.O, Gikas V, Alcay. S, Ceylan. A, "Performance evaluation of short to long term GPS, GLONASS and GPS/GLONASS post-processed PPP," *Survey Review*., vol. 46(3), pp. 155-166, 2014.
[3]. Zumberge, J.F, Heflin. M.B, Jefferson. D.C, Watkins. M.M, Webb. F.H, "Precise Point Positioning for the efficient and robust analysis of GPS data from large networks," *J. Geophys. Res.*, vol. 102 (B3), pp. 5005– 5017, 1997.
[4]. Gao, Y, Shen. X, "A new method for carrier-phase–based Precise Point Positioning," *Navigation*., vol. 49 (2), pp. 109–116, 2002.
[5]. Alkan. R.M, Ocalan. T, "Usability of the GPS Precise Point Positioning (PPP) technique in marine applications," *J. Navig.*, vol. 66 (4), pp. 579–588, 2013.
[6]. Alkan. R.M, Ilci. V, Ozulu. I.M and Saka. M.H, "Two-quartic tropospheric refractivity profile for correcting satellite data A Comparative Study for Accuracy Assessment of PPP Technique Using GPS and GLONASS in Urban Areas," *Measurement*., vol. 69, pp. 1-8, 2015.
[7]. [Online]. Available: http://sopac.ucsd.edu/dataBrowser.shtml
[8]. Ocalan. T, Erdogan. B, Tunalioglu, N, "Analysis of web-based online services for GPS relative and precise point positioning techniques," *Boletim de Ciências Geodésicas*., vol. 19(2), pp. 191-207, 2013.

Spatial Variability of Eroded Soils on Different Shaped Slopes: A Field Study in Turkey

Huseyin Sensoy[1], Omer Kara[2]

Abstract

This study was carried out for two years from September 2007 to September 2009 in straight, concave and convex shaped slopes under natural rainfall conditions. The aim of this study is to monitor eroded soil variation and spatial variability behaviour along the slope. For this purpose, a total of nine field plots were located on complex hillslope, including straight, concave and convex slope forms, three plots for each slope forms. Metal level sticks were used to monitor variations, such as transport or deposition of soil on ground surfaces on plots. When evaluating the results, plots that were located on slopes were divided into three sections, such as top (Section 1= S1), middle (Section 2= S2) and bottom (Section 3= S3) for better understanding transported and deposited soil variations on plots.
The assessment was conducted by taking the average of the three plots for each slope forms. As a result, eroded soil was transported in the plots S1 and S2 on straight slope while it was deposited in S3. For concave slope, eroded soil was transported in the plots S1 and half part of S2, but a clear deposition occurred in S3. On convex slope, eroded soil was transported in S1 and lower part of S2 and upper part of S3, but a clear deposition occurred in lower part of S3.

Keywords*: Eroded soil, spatial variability, slope shape*

1. INTRODUCTION

Many studies have been carried out to have information about the nature of soil erosion and investigate various parameters affecting soil erosion such as soil characteristics, precipitation, and vegetation. One of the important factors affecting soil erosion is slope. The basic slope parameters affecting soil erosion are steepness, length, and shape. The slope steepness and slope length compared to other factors are more effective in runoff and soil loss [1]. When the previous studies are viewed from this perspective, it is observed that most of the research studying the relations between slope and soil loss mostly consist of the ones researching steepness and length. Some researchers have stated that previous studies on the relation between slope length and soil loss are fewer than the studies on slope steepness and soil loss relations ([2], [3]). It may conveniently be referred that early studies about slope shape and soil loss relations are also fewer than the other two slope factors, steepness and length.
Slopes may have straight, concave, convex or complex forms, and they are usually not in a regular placement in natural conditions. Although a small number of studies were made about slope forms and soil loss relations, it was clearly understood that slope form affects soil loss, runoff and soil erosion ([4], [5], [6], [7], [8], [9]). It must be added that most of the studies about slope forms were carried out on flat slopes ([7], [10]). So, problems and inaccurate estimates may occur for soil loss or erosion forecast in complex slopes.
At this point, this study is performed to determine the spatial variation on the slopes with three different slope forms such as straight, concave and convex shaped. The aim of this study is to monitor eroded soil variation and spatial variability behaviour of soil along the different formed slopes. It was not aimed to measure the amount of soil loss or soil erosion for slope forms in this study. So, spatial variation was limited to soil transportation or deposition in plot scale.

2. MATERIALS and METHODS

This study was conducted in the Dallıca experimental area in Bartın City in northwestern part of Turkey as part of a comprehensive research from September 2007 to September 2009. Nine experimental plots were established on a 30 per cent complex hillslope, including straight, convex and concave slope forms, three plots for each slope forms. Land use type of experimental area was uncontrolled pasture during the study period and before. Plots were 11 meters in length, oriented parallel to main slope and metal level sticks are placed in it with one meter intervals. It was not allowed to plant growth inside the plots during the study period. Plots were enclosed by metal sheets in order to prevent sediment from outside. Sticks are placed firmly on the surface ground in plots and all sticks are numbered and also height from the ground of the sticks are measured and recorded before starting research. Metal sticks were used to measure spatial variations, such as transport or deposition of soil on ground surfaces on plots for two years. Heights of metal sticks were measured from the ground surface and spatial variation was determined.

Plots that were placed on slopes were divided into three sections, such as top (Section 1= S1), middle (Section 2= S2) and bottom (Section 3= S3) for better understanding transported and deposited soil variations on plots.

[1] [1] *Corresponding author: University of Bartın, Department of Watershed Management, Faculty of Forestry, 74100 Bartın, Turkey, hsensoy@bartin.edu.tr*

2 Karadeniz Technical University, Department of Watershed Management, Faculty of Forestry, 61080 Trabzon, Turkey, okara@ktu.edu.tr

3. RESULTS

3.1 Soil Properties

Some topsoil (0-8 cm) properties were determined for plots that were placed on straight, concave and convex slope forms. Data consist of mean values of transported and deposited soil variations occurred in three plots for each slope form. It is observed that the soil texture type is clay. It is understood that the numerical values of physical soil characteristics such as hydraulic conductivity and surface stoniness are more freely scattered than those regarding chemical characteristics of slope forms. Hydraulic conductivity of concave slope was quite low than other two slope forms with the value 37, 19 cm h^{-1}. Surface stoniness values of straight, convex and concave slope forms, were 23, 83%, 33, 84%, and 41, 21%, respectively, very different from each other. The same situation can be seen for bulk density values, with 1, 35, 1, 41, and 1, 51 g cm^{-3}, respectively. Chemical soil properties such as pH, $CaCO_3$, and electrical conductivity have closer values for each of the slope forms (Table 1).

3.2 Rainfall and Runoff

The average annual rainfall amount was measured 1194, 80 mm during two years of study in experimental area under natural rainfall conditions. The average annual runoff amount was recorded 270, 81 mm m^{-2} for straight plots; 265, 46 mm m^{-2} convex plots, while it was 271, 11 mm m^{-2} for concave plots. Runoff coefficient was recorded as 22, 63 %, 22, 22 %, and 22, 69 % for straight, convex, and concave plots, respectively.

Table 1 Description of some average topsoil properties of the slope forms

Physical and chemical properties	Slope forms		
	Straight	Concave	Convex
Sand %	35,98	33,78	31,38
Silt %	18,74	19,92	20,35
Clay %	45,28	46,30	48,27
Bulk density g cm^{-3}	1,35	1,51	1,41
Particle density g cm^{-3}	2,62	2,66	2,59
Porosity %	48,28	43,13	45,44
pH H_2O	8,03	8,09	8,10
Hydraulic conductivity cm h^{-1}	53,84	37,19	61,90
Electrical conductivity dS m^{-1}	0,21	0,18	0,18
Organic matter %	6,01	5,02	6,20
Surface stoniness %	23,83	41,21	33,84
$CaCO_3$ %	39,83	38,91	39,21

3.3 Spatial Variations

Eroded soil was transported in S1 and S2 of straight form while it was deposited in S3. A significant soil loss occurred between the 5^{th} and 7^{th} meters in S2. Soil loss reached a peak of 3 cm in depth at the end of study at the 6^{th} meter of straight plot. Eroded soil deposited between the 0^{th} and 2^{nd} meters in S3. Transported and deposited soil reached the highest level with 2, 5 cm at the 1^{st} meter (Figure 1).

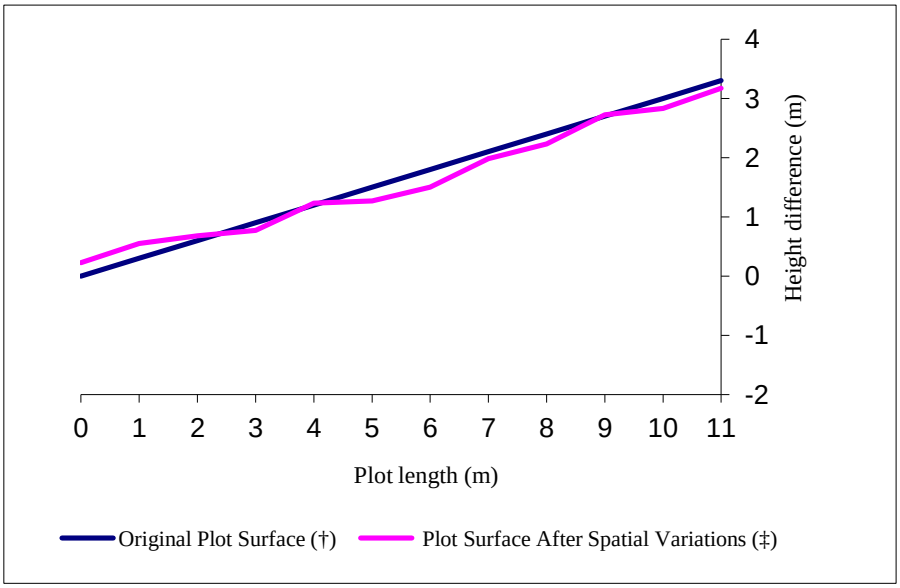

Figure 1. Spatial variations of the transportation or deposition of the soil in straight plot. († shows the longitudinal slope profile of original slope surface. ‡ shows the longitudinal slope profile of the slope surface after two years.)

Spatial variations for concave form show close similarities with straight form when evaluating sections. Eroded soil was transported in S1 and partly S2. Eroded soil deposited in S3 as is the case with the straight slope form. Soil is eroded between the 6th and 11th meters and a clear deposit is occurred between 0th and 2nd meters exactly like the straight slope form (Figure 2).

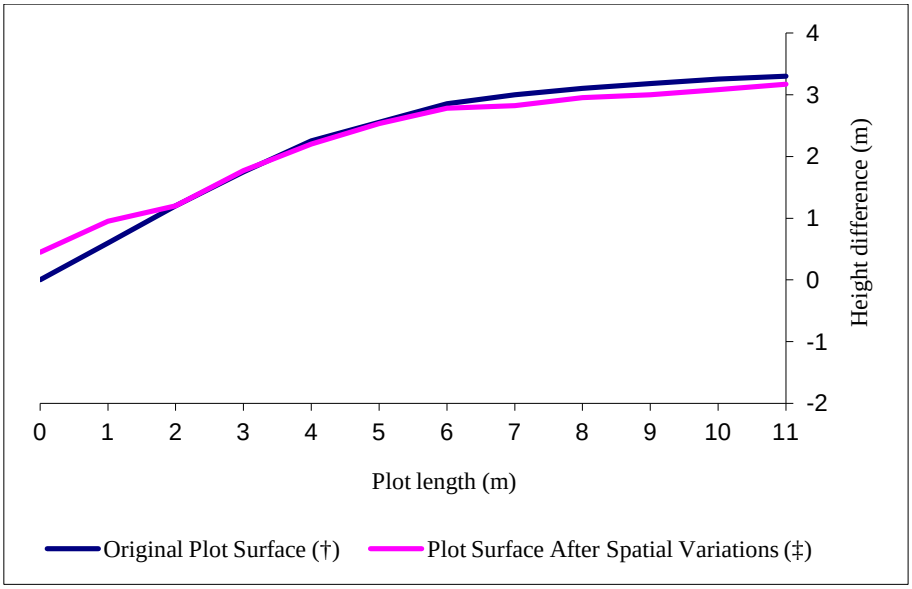

Figure 2. Spatial variations of the transportation or deposition of the soil in convex plot. († shows the longitudinal slope profile of original slope surface. ‡ shows the longitudinal slope profile of the slope surface after two years.)

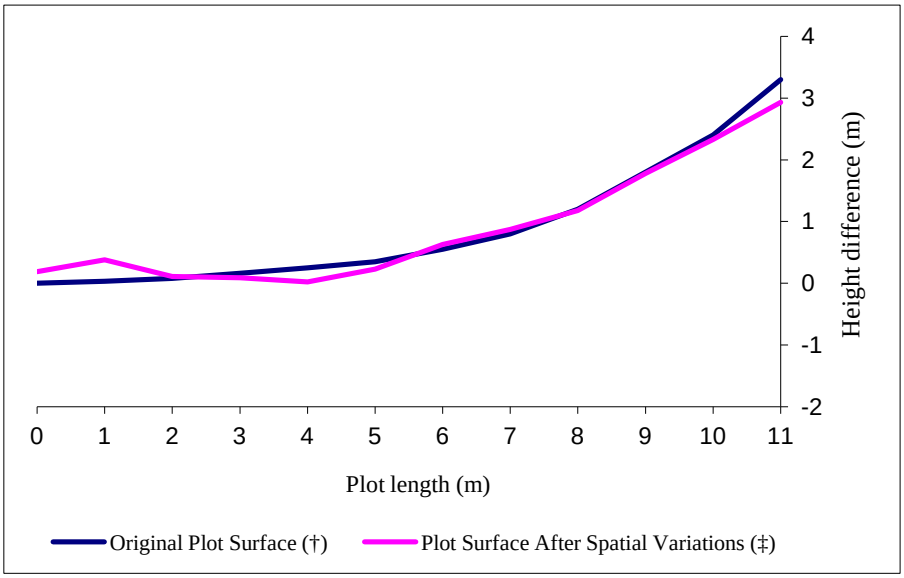

Figure 3. Spatial variations of the transportation or deposition of the soil in concave plot. († shows the longitudinal slope profile of original slope surface. ‡ shows the longitudinal slope profile of the slope surface after two years.)

For convex slope form, the soil is entirely eroded in S1. There is a clear transportation between 10th and 11th meters, but in lower parts from the 10th meter in S1 transport rate decreased. A small amount of eroded soil deposited on the upper part of S2 while a large amount of eroded soil was transported on lower part of S2. For S3, it was observed that a conspicuous deposition occurred between 0th and 2nd meters (Figure 3).

4. DISCUSSION

It is observed that spatial variations took place as in the form of transportation in S1 and S2 in all three slope forms. For concave plots, eroded soil depth reached 3, 7 cm in S1 (Figure 3), and for convex plots, it reached 1, 3 cm (Figure 2). One of the early studies about slope forms was performed by Reference [6] and they have reported similar results indicating that soil loss from upper part of concave slopes was observed more than twice compared to convex slopes. There are some differences between the results of this study and Reference [6] results in S3, for convex and concave slopes. In both convex and concave slope forms, close deposition values were measured in S3, with 3, 5 cm in this study. It can be incorporated easily for straight slope with 2, 5 cm deposition values. However, Reference [5] reported that a small amount of eroded soil deposited in downslope part for concave plots but it was a considerable soil loss for convex plots. Experimental field area was not specifically established for this study, but it was designed for a comprehensive study and therefore plots were bordered from the bottom part forming an enclosed plot. This has created a deposition on bottom part of all plots apart from the natural generation of eroded soil in S3 for all slope forms. In studies that used closed plots, especially concave slopes, eroded soil deposited in bottom part and didn't reach out of plot. This effect is called plot end effect Reference [7] and created by the bottom part of plot due to deposited soil. In this study, clearer plot end effect could be observed, if an open plot type was used. Reference [8] reported that eroded soil quantity was lower in upper part of convex slope forms than the other parts due to low slope steepness. This statement is confirmed partially with the results obtained from this study. Although eroded soil quantity in S1 from convex plots was less than that in concave plots, an equal quantity of soil was lost in straight plots.

Undoubtedly, the number of such studies should be increased and diversified in terms of spatial and temporal dimensions for more detailed assessment to be made. The number of studies carried out in such slope forms under natural rainfall conditions is quite few.

5. CONCLUSIONS

Using enclosed plots, the lower part closed, for this study prevented the study from reaching its aims in all aspects. Deposition zone is composed anywhere along the downslope in convex or concave plots while eroded soil was transported along the downslope completely without intervals for straight plots. In order to determine spatial variations in plot scale, level sticks can be used to carry out simple studies.

REFERENCES

[1]. W.H. Wischmeier and D.D. Smith, *Predicting rainfall erosion losses. A guide to conservation planning. USDA Agricultural Handbook 537*, U.S. Department of Agriculture. Washington DC, 58 p, 1978.

[2]. R.B. Bryan and J. Poesen, **"**Laboratory experiments on the influence of slope length on runoff, percolation and rill development," *Earth Surface Processes and Landforms*, vol.14, pp. 211-231, 1989

[3]. S.A. El-Swaify, "Factors affecting soil erosion hazards and conservation needs for tropical steeplands," *Soil Technology*, vol.11, pp. 3-16, 1997
[4]. D.L. Meyer and A.L. Kramer, "Erosion equations predict land slope development," *Agricultural Engineering*, vol.50, pp. 522-523, 1969
[5]. R.A. Young and C.K. Mutchler, "Effect of slope shape on erosion and runoff," *Transactions of the American Society of Agricultural Engineers*, vol.12, pp. 231-233 and 239, 1969a
[6]. R.A. Young and C.K. Mutchler, "Soil movement on irregular slopes," *Water Resourches Research*, vol.5, pp. 1084-1089, 1969b
[7]. D.H. Rieke-Zapp and M.A. Nearing, "Slope shape effects on erosion: a laboratory study," *Soil Science Society of America Journal*, vol.69, pp. 1463-1471, 2005
[8]. H. J. Schor and D.H. Gray, *Landforming: An environmental approach to hillside development, mine reclamation and watershed restoration.* John Wiley and Sons, Inc. 368 p, 2007
[9]. H. Sensoy and O. Kara, "Slope shape effect on runoff and soil erosion under natural rainfall conditions," *iforest Biogeosciences and Forestry*, vol.7, pp. 110-114, 2014
[10]. P.I.A. Kinnell, "Sediment delivery from hillslopes and the universal soil loss equation: some perceptions and misconceptions," *Hydrological Processes*, vol.22 pp. 3168-3175, 2008

ICENS
INTERNATIONAL CONFERENCE ON ENGINEERING AND NATURAL SCIENCES
24-28 May 2016 /Sarajevo

Estimation of Earthquake Occurrences by Using Markov Chain Approach in Turkey

Kaan Hakan Coban [1]***, Nilgun Sayil*** [2]

Abstract

It is necessary to investigate earthquake risks because Turkey is located in an active earthquake zone that caused large earthquakes. According statistical study, earthquake predictions are obtained with using earthquakes occurred in the past. 3 regions were selected in Turkey according to the scope of study. Two of these regions are located on the North Anatolian Fault Zone and 3rd region is located around Van Lake. The data sets were created for the magnitude of earthquakes $M_s \geq 5.0$ *between1900-2015. Region-transition probabilities were calculated from the created data sets with Markov Chain approach. There are cases for selected 3 regions. According to earthquake may occurred or not, all cases are numbered between 0-7. In this study, "0" indicates that any earthquakes is occurred in 3 regions, on the other hand "7" indicates that there are earthquakes in 3 regions. Transition matrix (P) was generated from number of earthquakes between1900-2015 by Markov statistical method. In selected regions, it has tried to estimate the probability of earthquake may occur within 5 years by generated transition matrix and defined initial distribution values. According to the results, in case of "0" probability for 5 years; 1st year: %16.8, 2nd year % 18.5, 3rd year % 19.0, 4th year %19.0, 5th year % 19.0, respectively.*

Key Words*: Markov Chain approach, Earthquake prediction, North Anatolian Fault Zone.*

1.INTRODUCTION

Turkey has high earthquake risk because it is located in Alpine-Himalayan seismic belt and involve North Anatolian Fault Zone. Therefore, detailed researches should be done in Turkey. So, it is important that necessary precautions should be taken, appropriate structures must be designed and safe living areas should be determined.

One of the most important methods about earthquake research is statistical method which predicts earthquake risk from occurred earthquake data. The precautions against earthquakes can be obtained with the help of these estimates. Living areas can be built with less risky zones according to the probability of earthquakes. Also, disaster management plan can be prepared according to calculated risk of earthquakes.

Many statistical methods are used to predict earthquakes. One of the well-known and reliable methods is Poisson model [1]. However, this model assumes that earthquakes occur independently to each other. According to researches, Poisson model has been found to give no reliable results in small areas [2]. For these reasons, researchers have used different statistical models. Markov is one of these models [3]. Markov model uses in different research subjects and it can be described as the events are linked to previous events. Therefore, it is a more appropriate model for earthquake prediction studies.

In the present study, 3 sub-regions were selected in Turkey. The region to region earthquake transition probabilities have been determined by using Markov chain method from occurred earthquakes (Ms ≥ 5.0). Applied methods and calculated results are described in the following sections according to generated regions.

2. METHODS AND MATERIALS

Modern probability theory studies are based on stochastic processes, which is affect future experiments the results of the tests carried out in the past. Results of the past data affect the future results. In such a situation, estimation the probability of the future will be very difficult [4].

On the basis of these developments; Markov has begun study on a new stochastic process as known by his name. His studies are based on how current result affect future outcomes. After that Markov method has been applied in many fields and has achieved impressive results. On the other hand, if the all values are known, the sequential process are affected past values with conditionally independent [5]. Markov Chain method can predict the state when the system was at a certain time. Also, system has an ability to predict the equilibrium state as well.

X_n is the case in i ; $X_{n+1}$is the case in j called as single-step transition probabilities [6] and defined as;

$$P^{n,n+1}\ ij = \mathrm{P}\ \{X_{n+1}=j \mid X_n = i\} \qquad (1)$$

[1] *Corresponding author: Karadeniz Technical University, 61080, Trabzon, Turkey, h.coban@ktu.edu.tr*

[2] *Karadeniz Technical University, 61080, Trabzon, Turkey, sayil@ktu.edu.tr*

Single-step transition probability is independent from the time parameter. So, Markov chain is called stable transition probability and described as;

$$P\{X_n=j \mid X_{n-1}=i\}=p_{ij} \quad \forall i,j \in S, n \geq 1 \tag{2}$$

While t is independent and i,j letters are described all state, the assumption of $P\{X_{t+1}=j \mid X_t=i\}$ would be correct. Assumption of P can be described as $\{X_{t+1}=j \mid X_t=i\}=p_{ij}$; the possibility of current system transition state i at time t to state j at time $t + 1$, is referred to p_{ij}. Therefore p_{ij} are defined as the transition probabilities of Markov chain. p_{ij} transition probabilities are expressed as a single-step transition probabilities.

Another assumption is that the transition probability isn't affected by the time. Therefore, p_{ij} can be indicated stable. The probabilities are defined as n x n dimensional transition matrix P.

$$P=\begin{bmatrix} p_{11} & p_{12} & \cdots & p_{1s} \\ \vdots & & \ddots & \vdots \\ p_{s1} & p_{s2} & \cdots & p_{ss} \end{bmatrix} \tag{3}$$

π_o initial value is determined to predict the future state of the system and F_n is calculated by multiplying P transition matrix with π_o [7].

$$F_n=\pi_o * P^n \qquad n=1.2.\ldots.. \tag{4}$$

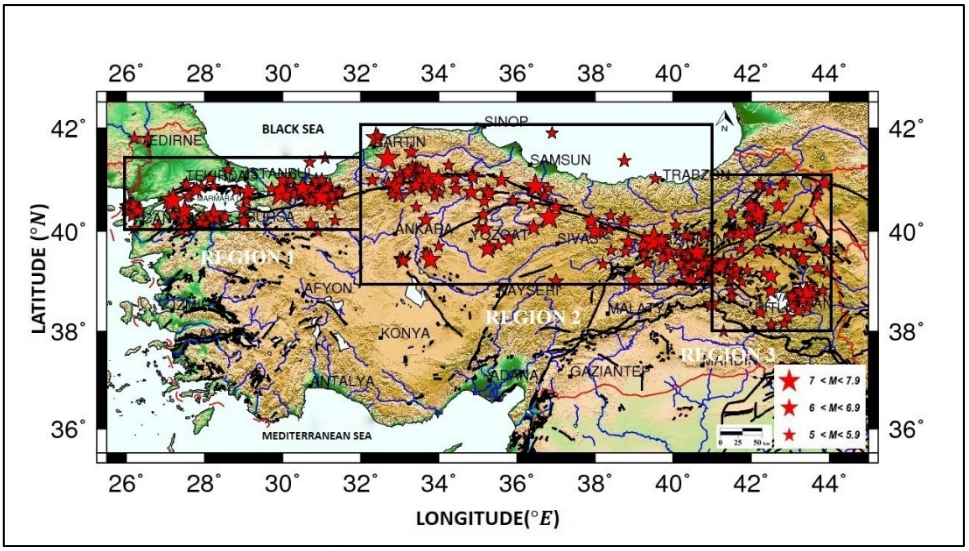

Figure1. Epicentral distribution of earthquakes (Ms ≥ 5.0) according to all generated region. [9], [10]

All data were taken from Kandilli Observatory and Earthquake Research Institute [11] and were converted to surface wave magnitude (*Ms*) for applying statistical method. These conversions are estimated with relations [8], which calculated from all the instrumental period earthquakes in Turkey. Thus, earthquake magnitude has become homogeneous. All earthquakes (Ms ≥ 5.0, between 1900-2015) used in the analysis are shown in Fig. 1.

Data was primarily put into chronological order for all regions. After that, $2^3=8$ state are generated condition of earthquakes may occur or not. So, '0' indicates that an earthquake hasn't occurred, on the other hand '1' earthquakes occurred. 8 states with condition of earthquake occurred or not are shown in Table 1.

Table 1. 8 state for all region

STATE	1.REGION	2.REGION	3.REGION
0	0	0	0
1	1	0	0

2	0	1	0
3	0	0	1
4	1	1	0
5	1	0	1
6	0	1	1
7	1	1	1

Earthquake numbers are calculated according to interval $\Delta t = 1\text{year}$ for each region and are shown in Table2.

Table 2. Number of earthquake magnitude (Ms ≥ 5.0) according to state and interval $\Delta t = 1$ year,

STATE	0	1	2	3	4	5	6	7
0	8	3	2	5	2	1	0	0
1	1	0	2	3	0	0	1	1
2	5	3	10	2	3	2	2	0
3	2	0	6	3	2	1	1	3
4	1	1	1	1	2	1	1	3
5	1	0	3	1	1	0	0	1
6	2	1	3	1	0	1	1	1
7	1	0	1	1	1	1	4	1

The earthquake transition probability matrix *P* is calculated from earthquake number according to states.

$$P = \begin{bmatrix} 0.38 & 0.14 & 0.10 & 0.24 & 0.10 & 0.05 & 0 & 0 \\ 0.13 & 0 & 0.25 & 0.38 & 0 & 0 & 0.13 & 0.13 \\ 0.19 & 0.11 & 0.37 & 0.07 & 0.11 & 0.07 & 0.07 & 0 \\ 0.11 & 0 & 0.33 & 0.17 & 0.11 & 0.06 & 0.06 & 0.17 \\ 0.09 & 0.09 & 0.09 & 0.09 & 0.18 & 0.09 & 0.09 & 0.27 \\ 0.14 & 0 & 0.43 & 0.14 & 0.14 & 0 & 0 & 0.14 \\ 0.20 & 0.10 & 0.30 & 0.10 & 0 & 0.10 & 0.10 & 0.10 \\ 0.10 & 0 & 0.10 & 0.10 & 0.10 & 0.10 & 0.40 & 0.10 \end{bmatrix} \quad (5)$$

In order to get state in the future, Markov chain's initial distribution shown as below.

$$\pi_0 = [0.125\ 0.125\ 0.125\ 0.125\ 0.125\ 0.125\ 0.125\ 0.125] \quad (6)$$

Final step the earthquake transition probabilities were estimated with Equation (4) for the next 5 years.

3. CONCLUSIONS

In the present study, Markov Chain method is used to calculate the earthquake state-transition probabilities for next 5-years period in all study regions by the reason of the high earthquakes risk in Turkey. Results of the study are shown below in Table 3 and Fig. 3.

Table 3 State-transition probabilities for next 5-years period

	0	1	2	3	4	5	6	7
F(1)	0.168	0.055	0.246	0.161	0.093	0.059	0.106	0.114
F(2)	0.185	0.069	0.252	0.144	0.098	0.066	0.099	0.090
F(3)	0.190	0.072	0.252	0.150	0.098	0.063	0.090	0.088
F(4)	0.190	0.072	0.251	0.151	0.098	0.063	0.089	0.088
F(5)	0.190	0.072	0.251	0.152	0.099	0.063	0.089	0.088

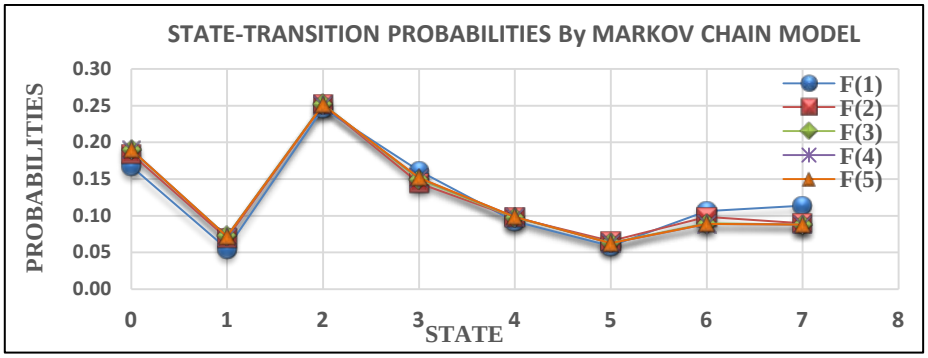

Figure 3. Results of Markov Chain Model according to state-transition probabilities

The probabilities show the close value according to years and in the state 2 which they have reached max. values. This means the probabilities of earthquake have high risk in region 2 and 3 in the same time.

REFERENCES

[1]. Lloyd, C. J., Statistical Analysis of Categorical Data, New York, s. 306, 1999.
[2]. Oliveria, C.S., Seismic Risk Analysis, Report No. EERC 74-1, Univ. of California, Berkeley, 1974.
[3]. Markov, A. A., Extension of the limit theorems of probability theory to a sum of variables connected in a chain. The Notes of the Imperial Academy of Sciences of St. Petersburg, VIII Series, 1907.
[4]. Grinstead, C. ve Snell, M.J.,. Introduction to the Probability. United States of America,American Mathematical Society 1997.
[5]. Çınlar, E., Introduction to Stochastic Processes,, *Englewood Cliffs*, New Jersey, 106-277,1997.
[6]. Taylor, H.M. and Karlin, S., An Introduction To Stochastic Modeling, Orlando:Academic Press 1984.
[7]. Özel, G and Solmaz, A., Prediction of the Turkey Earthquake Recurrence Time and Investigation of Neotectonic District Seismicity by Markov Chain, Cankaya University Journal of Science and Engineering, Volume 9 No. 2, 125-138, 2012.
[8]. Aydın, Y., Long Term Earthquake Prediction with Time and Magnitude Predictable Model, Msc.Thesis, Karadeniz Technical University, Turkey, 2016.
[9]. Wessel, P., and W. H. F. Smith, New improved version of Generic Mapping Tools released, EOS Trans. Amer. Geophys. U., vol. 79 (47), pp. 579, 1998.
[10]. Wessel, P., and W. H. F. Smith, New version of the Generic Mapping Tools released, EOS Trans. Amer. Geophys. U., vol. 76 (33), pp. 329, 1995.
[11]. http://www.koeri.boun.edu.tr/sismo/zeqdb

ICENS
INTERNATIONAL CONFERENCE ON ENGINEERING AND NATURAL SCIENCES
24-28 May 2016 /Sarajevo

Determination of Earthquake Probability by Using Statistical Methods in Turkey

Kaan Hakan Coban [1]***, Nilgun Sayil*** [2]

Abstract

Many studies are performed on earthquakes because of the loss of life and property as a result of the major earthquakes, which was located worldwide. The most important one of these studies is statistical study which estimates the earthquakes will be occurred in the future by using the earthquake data in the past. The aim of this study is estimated the return period and the probability of earthquakes by Poisson distribution and Exponential distribution methods, which widely used in seismology. Therefore, it was used the earthquakes between 1900 and 2015, Ms ≥ 4. 0 occurred in Turkey. From these data it was estimated the earthquakes occurrence probability for Ms ≥ 5.0. 3 regions in the study area is determined to taking into consideration on the epicentral distribution, seismicity, the type of faulting and geomorphological features. 2 of these regions are located on the North Anatolian Fault Zone, the third region is selected around Van Lake. In the result of the calculations made in region 1, annual earthquake occurrence number for Ms=5.2 was determined 0.62 and recurrence interval was estimated as 1.6 years according to the exponential distribution method. On the other hand, annual earthquake occurrence number to Ms=5.2 was calculated 0.48 and recurrence interval was estimated as 2.23 years for Poisson model. Used statistical methods were applied separately to each region. Also, seismic risk for each region with the Poisson distribution model was calculated in the next 10 years.

Keywords*: Poisson distribution method, Exponential distribution method, Earthquake occurrence probability, Turkey*

1.INTRODUCTION

Statistical earthquake occurrence models have get more importance while amount of the available earthquake data increase. These models allow ones to reduce the large data sets of earthquake occurrences to statistical parameters for any region.

The most common model is Poisson model, which assumes spatial and temporal independence of all earthquakes including great earthquakes: i.e. the occurrence of an earthquake does not affect the likelihood of a similar earthquake at the same location in the next time unit [1], [2]. Other models consider the clustering of earthquakes in time [3], [4].

The subject of the present study is to estimate the probability of earthquake occurrences and recurrence periods by using Poisson model and exponential distribution model from instrumental data for selected three characteristic sub-regions in Turkey.

2.DEFINITION OF THE STATISTICAL METHODS

Since magnitude-frequency relations are formed as the basis of the earthquake occurrence, it is used for the criterion of earthquake activity as times ago. Distribution of earthquakes with respect to magnitudes exhibits scale constancy**,** appears to be self-similar and follow a power law. [5] relation defines the distribution of earthquakes with respect to the magnitude:

$$LogN = a - bM \tag{1}$$

where N (cumulative frequency), is the number of earthquakes equal or larger than M magnitude. For a certain region and time interval, Eq. (1), provides the number of earthquakes, N, with magnitude, M, where a- and b-value are positive, real constants. a-value describes the seismic activity. b-value is a tectonic parameter describing the relative abundance of large to smaller shocks. It seems to represent properties of the seismic medium in some respect, like stress and/or material conditions in the focal region [6]. For (M, $LogN$) dataset, a- and b-values are commonly computed by using the linear least square approximation. According to this method, a- and b-value are found by Eq. (2);

$$\sum_{i=1}^{n} LogN_i = an - b\sum_{i=1}^{n} M_i$$

[1] *Corresponding author: Karadeniz Technical University, Department of Geophysical Engineering, 61080, Trabzon, Turkey.* h.coban@ktu.edu.tr

[2] *Karadeniz Technical University, Department of Geophysical Engineering, 61080, Trabzon, Turkey.* sayil@ktu.edu.tr

$$\sum_{i=1}^{n} M_i.LogN_i = a\sum_{i=1}^{n} M_i - b\sum_{i=1}^{n} M_i^2 \quad (2)$$

where n is the number of group. Other parameters are as described in Eq. (1). The earthquake occurrence probability with the specific magnitude in a specific period could be determined by using a- and b-values obtained from Eq. (2). Eq. (3) could be obtained from the relation between cumulative and normal frequency. Eqs. (4) and (5) are obtained for the specified time-period (T_1).

$$a' = a - Log(b\ln 10) \quad (3)$$

$$a_1^{'} = a' - LogT_1 \quad (4)$$

$$n(M) = 10^{a_1^{'} - bM} \quad (5)$$

According to the Poisson model, the annual mean number n of earthquakes ($M \geq M_1$) with specific magnitude equal and larger than M_1 value in a specific time can be estimated by using these relations. In any regions, $R(M)$, occurrence risk in T years of an earthquake with any magnitude M for observation interval of T_1 year is calculated by Eq. (6) and Q, recurrence period of an earthquake is estimated by Eq. (7) [7].

$$R(M) = 1 - e^{-n(M)T} \quad (6)$$

$$Q = \frac{1}{n(M)} \quad (7)$$

In identification of seismic risk using exponential distribution model, x is assumed to be a random variable having the magnitude of M. The probability density function of x random variable in the form of exponential function is given in Eq. (8) [8].

$$f_M(x) = \lambda e^{-\lambda(x-\theta)} \quad \lambda > 0 \quad \theta \leq x < +\infty \quad (\lambda = (\bar{x} - \theta)^{-1}) \quad (8)$$

where, $\bar{x}$ is the mean magnitude value obtained from many earthquake data and θ stands for the smallest magnitude value. The distribution function of x random variable is found as in Eq. (9) by utilizing exponential probability density function [9].

$$F_M(x) = \int_0^x \lambda e^{-\lambda(U-\theta)} dU = 1 - e^{-\lambda(x-\theta)} \quad \theta \leq x < +\infty \quad (9)$$

3. DATA

Data ($M_s \geq 4.0$, the earthquakes occurred between 1900 and 2015) obtained from the catalogue of Bogazici University Kandilli Observatory Earthquake Research Institute (KOERI) has been used in this study [10]. Three regions in Turkey have been selected to taking into consideration on the epicentral distribution, seismicity, the type of faulting and geomorphological features. Two regions are located on the North Anatolian Fault Zone, the third region is selected around Van Lake (Figure 1). In order to ensure homogeneity, magnitude scales of all events were converted to surface wave magnitude (M_S) through a set of empirical equations derived based on regional earthquakes by [11].

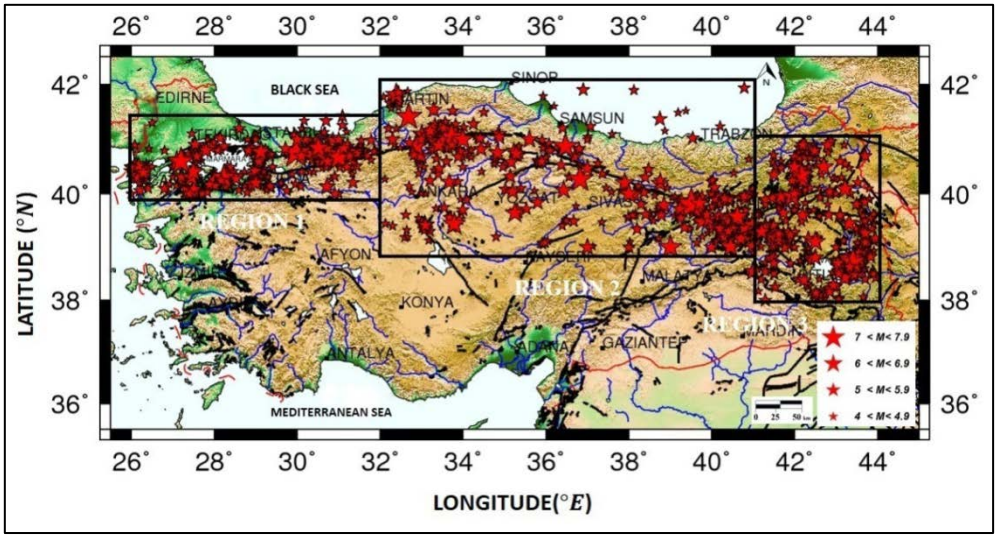

Figure 1. Epicentral map and selected 3 sub-regions of Turkey [12] ,[13].

4 . DISCUSSIONS AND CONCLUSIONS

In this study, the Gutenberg-Richter relationships (Eq. (1)) have been obtained for each sub-region shown in Fig. 1. Magnitude-frequency relations computed by the linear least square method are shown in Fig.2. Seismic risk and recurrence period values according to the Poisson model have been estimated by using a- and b-parameters shown in Fig 2. In the computations, magnitudes of $M_S \geq 5.0$ and increment interval of 0.5 were chosen, and Eq. (6) for seismic risk and Eq. (7) for recurrence period are used. Observational time interval (115 year) has been determined by the completeness condition of each sub-region. Computations have been done for years in the next 10 years. The results are given in Table 1**.**

Furthermore, earthquake occurrence number per year (F_i) and recurrence period values (Eqs. (8) and (9)) have been estimated according to exponential distribution model for each sub-region. Earthquake occurrence numbers per year according to the Poisson and exponential distribution models for each sub-region are shown in Fig. 3. Recurrence period graphics for different earthquake magnitudes (in the same magnitude range) according to the Poisson and exponential distribution models are shown in Fig. 4.

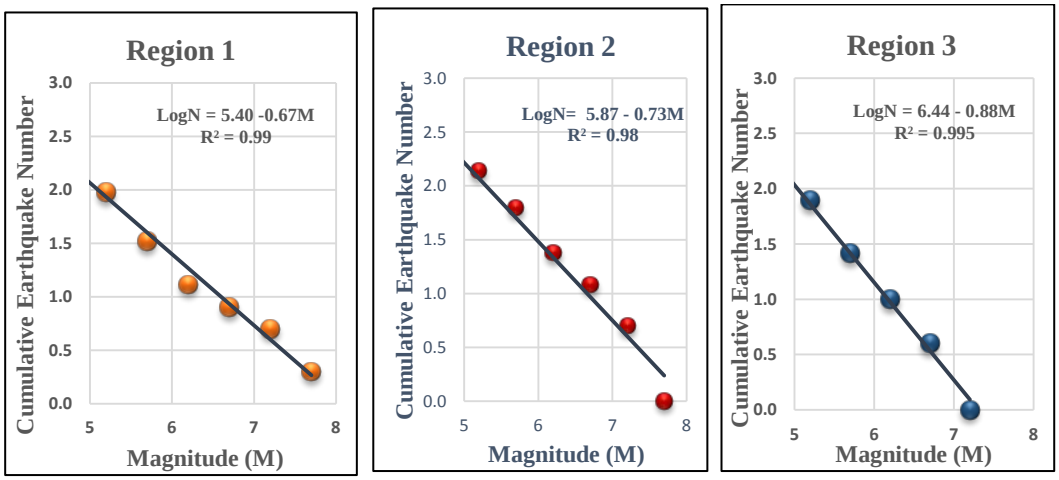

Figure 2. Magnitude-frequency relations computed by the linear least square method. R is correlation coefficient.

Table 1. Seismic risk and recurrence period values estimated by using a- and b-values for the earthquakes of $5.0 \leq M_S \leq M_{max}$ with the magnitude increment of 0.5 in observation interval (T_1 =115 year) of each sub-region.

Sub Regions	Magnitudes (M_S)	Seismic risk R(%) Period (year)										Recur. period Q (year)
		1	2	3	4	5	6	7	8	9	10	
Region 1	5.0	48.2	73.2	86.1	92.0	96.3	98.1	99.0	99.5	99.7	99.9	1.5
	5.5	26.3	45.7	60.0	70.5	78.3	84.0	88.2	91.3	93.6	95.3	3.3
	6.0	13.2	24.7	34.7	43.3	50.8	57.3	63.0	67.9	72.1	75.8	7.1
	6.5	6.4	12.4	17.9	23.2	28.1	32.7	37.0	41.0	44.7	48.3	15.2
	7.0	3.0	5.9	8.8	11.5	14.2	16.8	19.3	21.7	24.1	26.4	32.7
	7.5	1.4	2.8	4.2	5.5	6.9	8.2	9.5	10.8	12.0	13.3	70.4
Region 2	5.0	57.1	81.7	92.1	96.6	98.6	99.4	99.7	99.9	100	100	1.2
	5.5	30.6	51.8	66.6	76.8	83.9	88.8	92.2	94.6	96.3	97.4	2.7
	6.0	14.6	27.0	37.6	46.7	54.5	61.1	66.7	71.6	75.7	79.3	6.4
	6.5	6.6	12.7	18.4	23.7	28.7	33.4	37.8	41.8	45.7	49.2	14.8
	7.0	2.9	5.7	8.4	11.0	13.6	16.1	18.5	20.8	23.1	25.3	34.3
	7.5	1.3	2.5	3.7	4.9	6.1	7.3	8.4	9.6	10.7	11.8	79.5
Region 3	5.0	37.0	60.3	75.0	84.3	90.1	93.8	96.1	97.5	98.4	99.0	2.2
	5.5	15.4	28.5	39.5	48.9	56.8	63.4	69.1	73.8	77.9	81.3	6.0
	6.0	5.9	11.5	16.7	21.6	26.2	30.6	34.7	38.5	42.1	45.5	16.5
	6.5	2.2	4.3	6.4	8.4	10.4	12.4	14.3	16.2	18.0	19.8	45.4
	7.0	0.8	1.6	2.4	3.2	3.9	4.7	5.4	6.2	6.9	7.7	125.2
	7.5	0.3	0.6	0.9	1.2	1.4	1.7	2.0	2.3	2.6	2.9	345.2

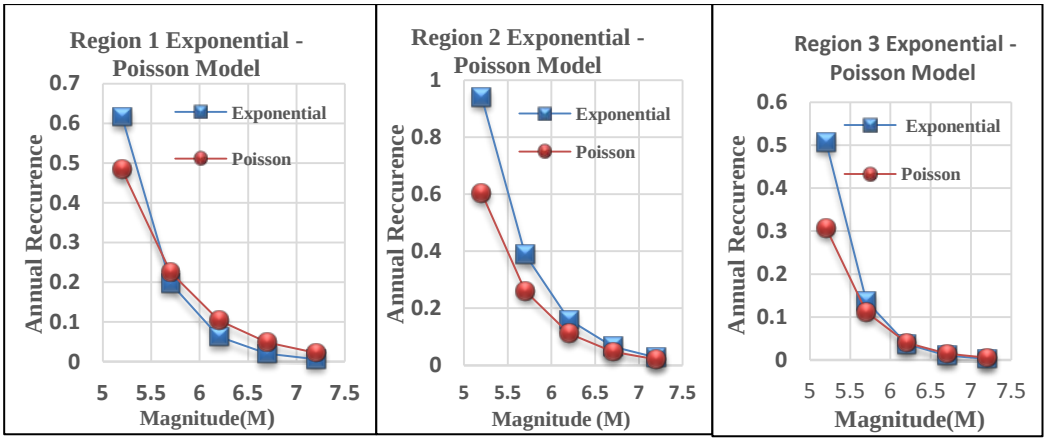

Figure 3. Earthquake occurrence numbers per year according to the Poisson and exponential distribution models for each sub-region.

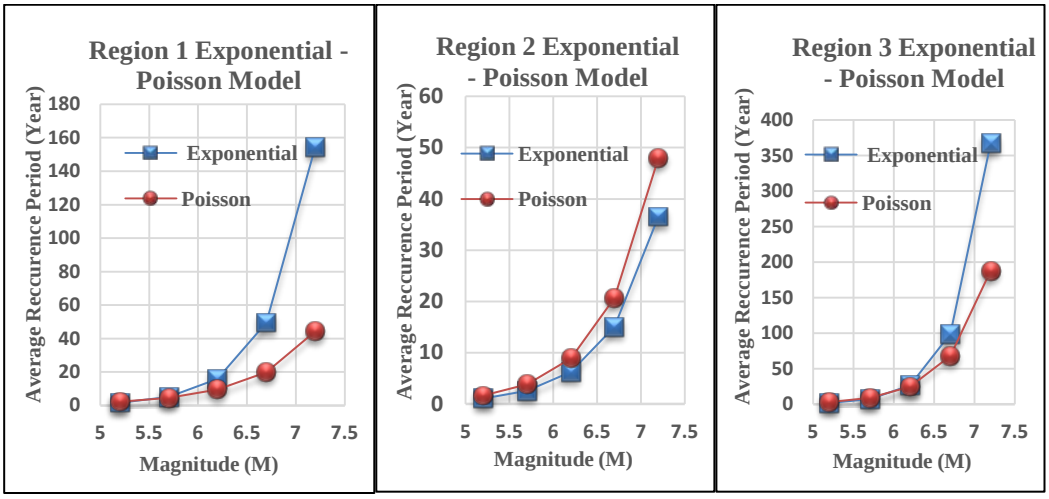

Figure 4. Recurrence periods graphics for different earthquake magnitudes according to the Poisson and exponential distribution models for each sub-region

The lowest and highest b-values were determined as 0.67±0.03 for sub-region 1 and as 0.88±0.02 for sub-region 3. As it well known, the high b value implies that the high seismic activity had rolled in that region. According to the seismic risk estimations for Poisson model, the highest earthquake occurrence probability of $M_S \geq 7.0$ in the next 10 years is %26.4 for sub-region 1.

5. REFERENCES

[1]. Caputo, M., *Analysis of Seismic Risk*. Nato Advanced Study Institutes Series, Applied Sciences 3, Noordhoff-Leiden, 1974.
[2]. Shah, H.C. and Movassate, M., *Seismic Risk Analysis of California State*, Water Project Proc of Fifth European Conf. on Earthquake Engineering, 2:156, 1975.
[3]. Sykes, L.R. and Quittmeyer, R.C., *Repeat Times of Great Earthquakes along Simple Plate Boundaries*, Maurice Ewing Series 4:297-332, 1981.
[4]. Coral, A., Dependence of earthquake recurrence times and independence of magnitudes on seismicity history. *Tectonophysics*, 424:177–193, 2006.
[5]. Gutenberg, B. and Richter, C.F., *Seismicity of the Earth and Related Phenomena*. Second Printed, Princeton University Press, Princeton, 1954.
[6]. Miyamura, S., Magnitude-frequency relations and its bearing to Geotectonics. *Proc. Japan. Ac.*, 38:27-30, 1962.
[7]. Tabban, A. and Gencoglu, S., Earthquake and its parameters. *Bull. Earthq. Res. Inst.* Turkey 11:7–83, 1975.
[8]. Ramachandran, G., *Extreme Values Theory And Earthquake Insurance*, Transactions of 21st International
[9]. Congress of Actuaries, Switzerland 1, 337-353, 1980.
[10]. Hahn, G.J., and S.S. Shapiro, *Statistical Models in Engineering*, (Third Edition, John Wiley & Sons, New York,
[11]. 1994.
[12]. Aydın, Y., Long Term Earthquake Prediction with Time and Magnitude Predictable Model, Msc.Thesis, Karadeniz Technical University, Turkey, 2016.
[13]. http://www.koeri.boun.edu.tr/sismo/zeqdb/

[14]. Wessel, P., and W. H. F. Smith, New improved version of Generic Mapping Tools released, EOS Trans. Amer. Geophys. U., vol. 79 (47), pp. 579, 1998.
[15]. Wessel, P., and W. H. F. Smith, New version of the Generic Mapping Tools released, EOS Trans. Amer. Geophys. U., vol. 76 (33), pp. 329, 1995.

Drying Model of Rough Rice Based on Genetic Algorithm

Oktay Hacıhafızoglu[1], Cigdem Susantez[2], Kamil Kahveci[3]

Abstract

In this study, drying of rough rice has been investigated by the method of genetic algorithm. An Arrhenius type diffusion coefficient has been defined with three parameters. The optimum values of this parameters for each drying condition was investigated with genetic algorithm. It has been shown that the results of the theoretical model are convenient with the experimental results.

Keywords: *Rough Rice, Drying, Diffusion Coefficient, Genetic Algorithm*

1.INTRODUCTION

Rice is the world's second most grown cereal after wheat. Since rough rice is usually harvested at high moisture content (24-25% db), it should be reduced below 14% (db) to prevent it from deterioration during storage. Drying process is generally performed by heating the ambient air and then sending it by forced convection over the crops to be dried. The drying rate of rough rice is affected by a number of factors such as initial moisture content, drying air temperature, relative humidity, and airflow rate.

Multi-pass drying systems are used in industry to gradually bring moisture content to desired levels. Three main kinds of operations can be involved in a pass: drying, cooling, and tempering. Drying units remove the moisture content within a rice grain; cooling or sometimes known as air ventilation units lower the temperature of the grain to prevent moisture accumulation on the grain surface and remove some amount of moisture content at low temperature, and finally tempering units equalize the moisture gradient that has developed during the drying processes [1]. Because of the importance of rice for human consumption, and the drying of rice is an important process of the food production, there are many studies in the literature dealing with the drying characteristics of rough rice [2,3,4]. A thin-layer drying model was developed to investigate the effect of particle size distribution on the drying characteristics of crushed feed rice by *Tanaka et al* [5]. Erenturk and Erenturk investigated experimentally thin layer drying kinetic of carrot and performed a comparative study between regression analysis, genetic algorithm based optimization, and FNN (*Feedforward Neural Networks*) to estimate dynamic drying behaviour of carrots [6]. Cakmak and Yildiz investigated the thin-layer drying kinetics of seedy grapes by developing an FNN model. They found that FNN model is more useful than regression models for analyzing nonlinear behaviour of drying [7]. The genetic algorithm method has been used for estimating the moisture content of grain drying process by *Liu et al*. By combining the BP (back-propagation) neurons and the RBF (radial basis function) neurons at the hidden layer, structural modular neural network was proposed to predict the moisture content of grain drying process [8].

2.MATERIAL AND METHOD

*2.1.*Mathematical Method

In this study drying of rough rice has been modelled based on diffusion equation and a new Arrhenius type diffusion coefficient has been determined by using genetic algorithm. The governing equations with boundary and initial conditions are given as follows.

$$\vec{\nabla}\cdot\left(D_{eff}\vec{\nabla}m\right)=\frac{\partial m}{\partial t} \quad (1)$$

$$m|_s = m_e \quad (2)$$

$$m|_{t=0} = m_o \quad (3)$$

Arrhenius type diffusion coefficient of rough rice is given in equation (4) where T is in ^oC. The convenient coefficients K_1, K_2 and K_3 is also determined by using genetic operators and considering experimental drying results.

[1] *Corresponding author: Trakya University, Department of Mechanical Engineering, 22180, Merkez/Edirne, Turkey. oktayh@trakya.edu.tr*

[2] *Trakya University, Department of Mechanical Engineering, 22180, Merkez/Edirne, Turkey, cigdemsusantez@trakya.edu.tr*

[3] *Trakya University, Department of Mechanical Engineering, 22180, Merkez/Edirne, Turkey, kamilk@trakya.edu.tr*

$$D_{eff} = \boldsymbol{K_1} \exp\left(\boldsymbol{K_2} m - \frac{\boldsymbol{K_3}}{T + 273.15}\right) 10^{-13}\ m^2/s \quad (4)$$

It can be seen from equation (4) that diffusion coefficient of rough rice not only depends on temperature but also it depends on local dry basis moisture content m. Average moisture content of a single rough rice and moisture ratio are also determined by using equation (5) and (6) respectively. The values of m_o and m_e are also represented in Table 1. The experiments has been carried out for different drying air temperature (40°C–60°C) and 1.5 ms^{-1} velocity. The progress of the drying process is followed by weighting the sieves containing rough rice grains at regular time intervals on a digital scale, with an accuracy of ± 0.0001g. The model has been performed by using Comsol Multiphysics software The length of semi-axis and the radius of prolate elipsoid shaped rough rice are 4.605 mm and 1.25 mm respectively [9].

$$m_{ave} = \frac{1}{V}\int_V m dV \quad (5)$$

$$mr_{theo} = (m_{ave} - m_e)/(m_o - m_e) \quad (6)$$

Table 1. Initial and equilibrium moisture contents [2]

T (°C)	m_o	m_e
40	0.2409	0.0720
45	0.2409	0.0630
50	0.2424	0.0570
55	0.2395	0.0435
60	0.2320	0.0352

Fitness function for each member of the population is determined according to experimental and calculated moisture ratios.

$$mr_{exp} = (m_{exp} - m_e)/(m_o - m_e) \quad (7)$$

$$f = 1/\sqrt{\sum_{t=0}^{t=5h}\left[mr_{exp} - mr_{theo}\right]^2} \quad (8)$$

2.2. Genetic Algorithm Method

Genetic Algorithm is a kind of optimization method. It imitates nature by selection, crossover and mutation. In this study K_1, K_2 and K_3 parameters are represented on a single chromosome which is in the form of binary string and consisting from 60 genes. Maximum values of K_1, K_2 and K_3 parameters are 50, 15 and 10 respectively. The first population of chromosomes is randomly generated. Tournament selection process has been performed based on the fitness values. While a population consisting 10 individuals (candidate solution), generation numbers is set to 40. The reason of chosing mutation probability as 0.025 is not only to satisfy the variability of the population but also recall lost information during the process. Settings for the genetic algorithm has been given in Table 2. In this study, tournament selection parameter selected as 1. This means, according to program written in Matlab, the best one of randomly selected two individuals in tournament to go foward and have change to have crossover.

Table 2. Genetic Algorithm Settings

Number of Generations	40
Population Size	10
Number of Genes	60 (20 per one parameter)
Selection Method	Tournament Selection
Tournament Selection Parameter	1
Crossover probability	0.8
Crossover type	Triple crossover (1 per one parameter)
Mutation probability	0.025

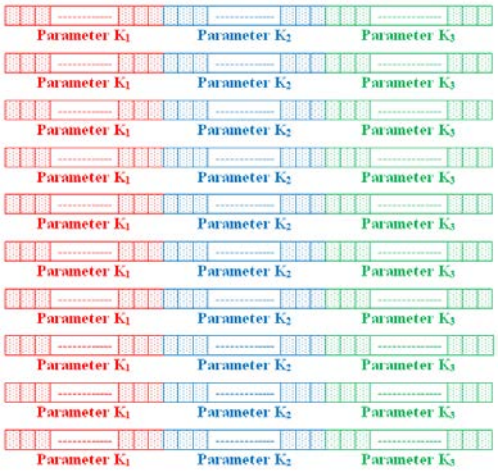

Figure 1. Representation of a Population Consisting from 10 individuals

Selection method determines which individuals to go foward and produce offspring. It is important to save the best candidate solution for each population. This has been satisfied by applying elitism. In this study the best individual of each population has been transferred into to next generation.

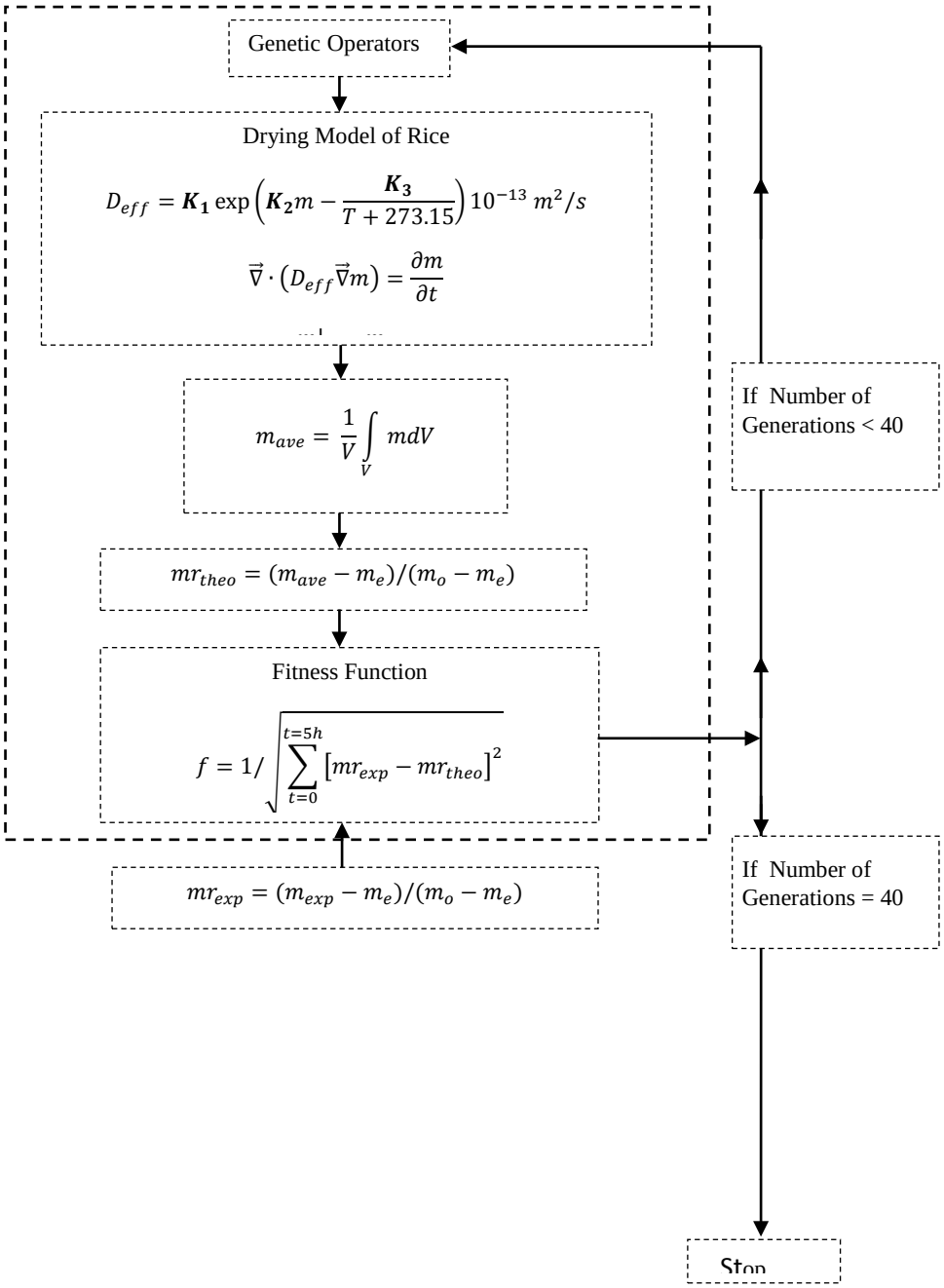

Figure 2. Algorithm structure

3.CONCLUSION

The parameters giving the best fit in the diffusion expression are presented on Table 3. At the beginning of the drying, moisture transfers easily and drying rate is high. After a period of time drying rate decreases due to difficulty of moisture transfer from the inner parts of the rough rice. As it has been shown figures 3-7, theoretical and experimental results are close to each other. This means the method of genetic algorithm is useful for the drying phenomena of rough rice. On the other hand in this study, population size was chosen as 10, by applying mutation genetic diversity was increased.

Table 3. Coefficients in D_{eff}

T (°C)	K_1	K_2	K_3	Fitness
40	43.3279	4.1915	0.0482	9.8977
45	45.7029	4.7755	0.0107	11.7773
50	38.8391	7.7353	5.0217	12.0832
55	46.4064	7.5042	1.5006	13.5058
60	41.0206	11.7262	9.9355	10.9108

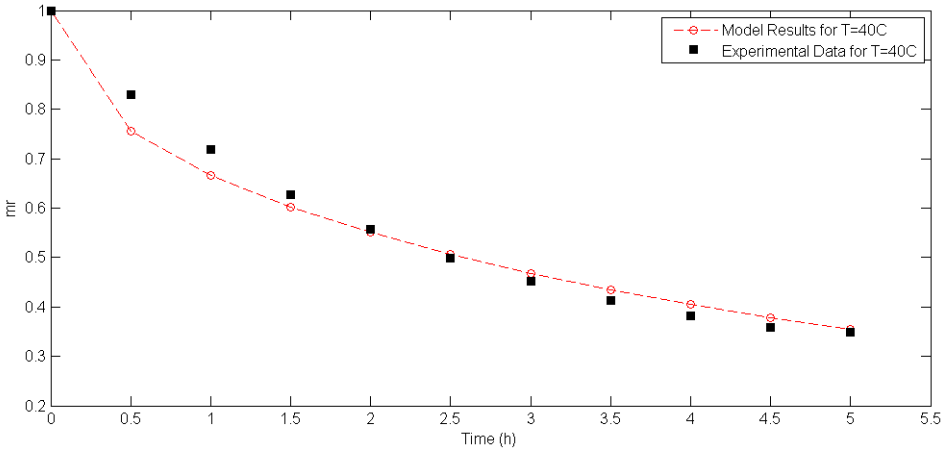

Figure 3. Drying Results for T = 40°C (Fitness = 9.8977)

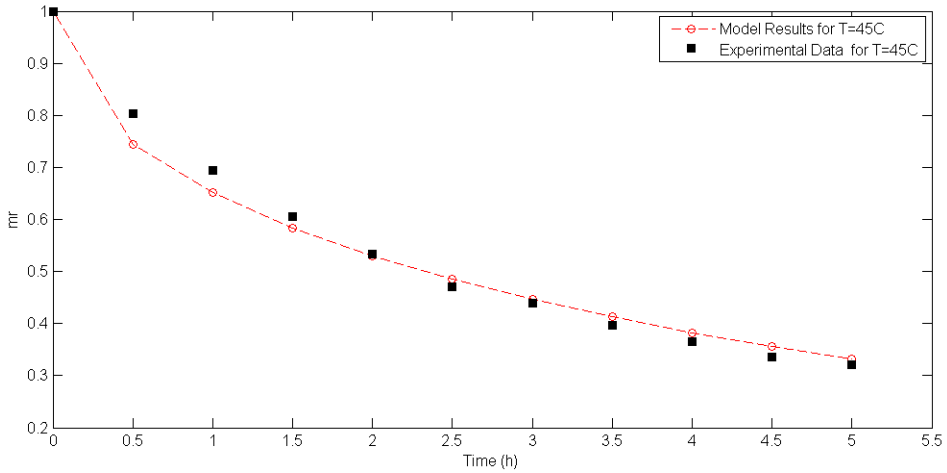

Figure 4. Drying Results for T = 45°C (Fitness = 11.7773)

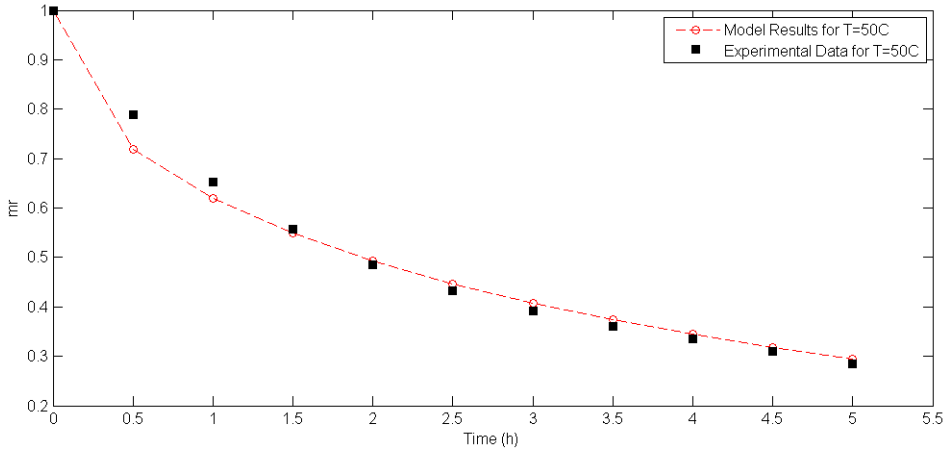

Figure 5. Drying Results for T = 50°C (Fitness = 12.0832)

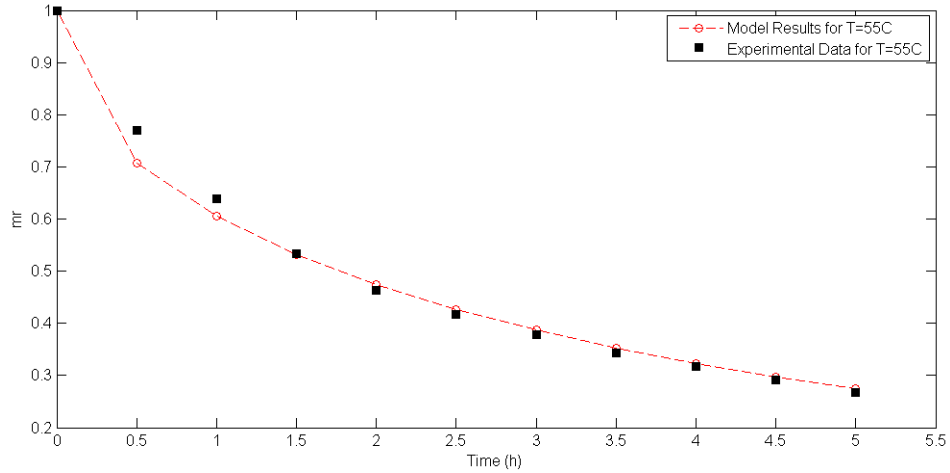

Figure 6. Drying Results for T = 55°C (Fitness = 13.5058)

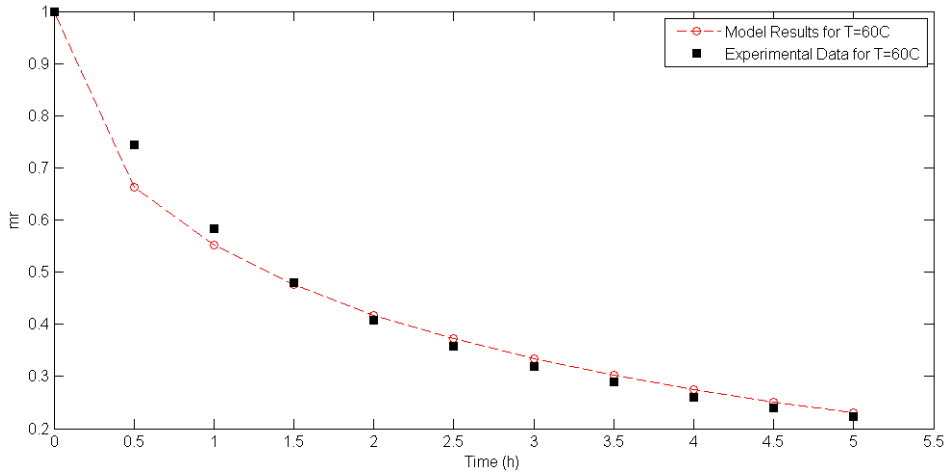

Figure 7. Drying Results for T = 60°C (Fitness = 10.9108)

Figure 8 shows the performance of the genetic algorithm. After 5 or 6 generations average fitness values oscillates around a mean value and the increase of the maximum fitness value is negligible. According to these results one can conclude that 10 generations is sufficient for the algorithm.

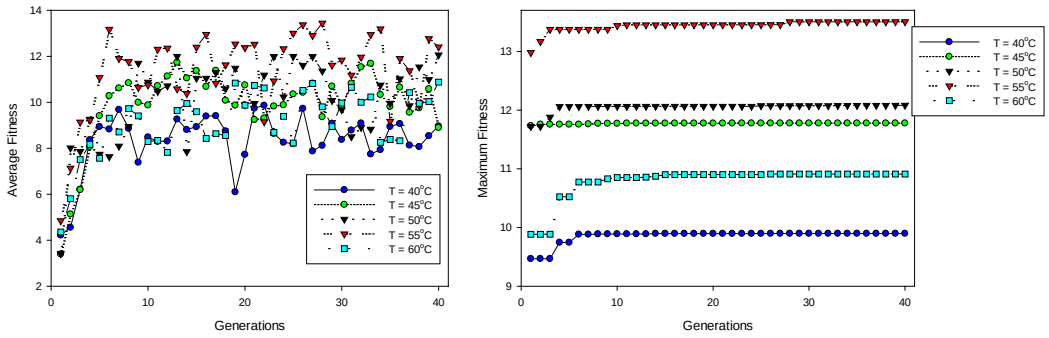

Figure 8. Average and Maximum Fitness Values for Each Drying Air Temperature

Nomenclature

Deff	effective diffusion coefficient, m2h-1
T	drying air temperature,°C
t	time, s
V	volume, mm3
R	radius of a rough rice grain, mm
K	convenient coefficient
L	half-length of a rough rice grain, mm
m	moisture content in dry basis, kg/kg
mr	dimensionless moisture ratio

Greek letters

$\vec{\nabla}$	Nabla operator

Subscripts

e	equilibrium condition
exp	experimental
o	initial condition
s	surface
theo	theoretical

REFERENCES

[1]. W. Wongrat, A. Younes, A. Elkamel, P. L. Douglas and A. Lohi, "Control vector optimization and genetic algorithms for mixed-integer dynamic optimization in the synthesis of rice drying processes," *Journal of the Franklin Institute*, vol. 348, pp. 1318-1338, 2011.

[2]. O. Hacıhafızoğlu, A. Cihan and K. Kahveci, **"**Mathematical modelling of drying of thin layer rough rice," *Food and Bioproducts Processing*, vol. 86, no. C4, pp. 268-275, 2008.

[3]. A. Cihan, K. Kahveci and O. Hacıhafızoğlu, "Modelling of intermittet drying of thin layer rough rice," *Journal of Food Engineering*, vol. 79, no.1, pp. 293-298, 2007.

[4]. M. A. Basunia and T. Abe, "Thin-layer solar drying characteristics of rough rice under natural convection," *Journal of Food Engineering*, vol. 47, pp. 295-301, 2001.
[5]. F. Tanaka, F. Tanaka, A. Tanaka and T. Uchino, "Mathematical modelling of thin-layer drying according to particle size distribution in crushed feed rice," *Biosystems Engineering*, vol. 136, pp. 87-91, 2015.
[6]. S. Erenturk and K. Erenturk, "Comparison of genetic algorithm and neural network approaches for the drying process of carrot," *Journal of Food Engineering*, vol. 78, pp. 905-912, 2007.
[7]. G. Cakmak and C. Yildiz, "The prediction of seedy grape drying rate using a neural network method," *Computers and Electronics in Agriculture*, vol. 75, pp. 132-138, 2011.
[8]. X. Liu, X. Chen, W. Wu and G. Peng, "A neural network for predicting moisture content of grain drying process using genetic algorithm," *Food Control*, vol. 18, pp. 928-933, 2007.
[9]. O. Hacıhafızoğlu, A. Cihan, K. Kahveci and A. G. B. de Lima, **"**A Liquid Diffusion Model for Thin-Layer Drying of Rough Rice," *European Food Research and Technology*, vol. 226, no. 4, pp. 787-793, 2008.

Analysis of a Novel Desiccant Cooling System

Osman Kara[1], Ertac Hurdogan, Orhan Buyukalaca[1]

Abstract

A desiccant based air-conditioning system is suitable especially for hygienic applications. In this study, Desiccant cooling technology with conventional vapor compression air conditioner is considered for hot and humid climate. In this system, the moisture of supply air is reduced with a solid desiccant wheel and its temperature is decreased by "dry coil" of a vapor-compression refrigeration cycle. To enhance the performance of the system, some technologies such as "pre-cooling with outdoor air", "waste cool recovery", "pre-cooling of waste air with evaporative cooling" and "use of a cheap thermal energy source such as solar energy to remove the moisture from the desiccant" are utilized. Analysis of the system considered is carried out using a program written in FORTRAN language and suitability of the system is investigated for the health care facilities in which hygiene is crucially important.

Keywords: *Air-conditioning, desiccant cooling, dehumidification, hygiene*

1.INTRODUCTION

Nowadays, solid desiccant air-conditioning system has been proposed as an alternative to the conventional vapor compression refrigeration air-conditioning systems for efficient control over humidity of conditioned air especially in hot and humid areas. The solid desiccant cooling can be more favorable over the traditional vapor compression refrigeration air conditioners, because it assures more accessible, economical and cleaner air conditioning. It is still more important when it is powered by free energy sources like solar energy and waste heat with temperatures of between 60 °C and 80 °C. In addition, it can significantly reduce the operating cost as well as save energy [1]. La et al. [2] investigated rotary desiccant air conditioning system, which combines the technologies of desiccant dehumidification and evaporative cooling, is advantageous in being free from CFCs, using low grade thermal energy and controlling humidity and temperature separately. Compared with conventional vapor compression air conditioning system, it preserves the merits of environment-friendly, energy saving, healthy, comfortable, etc. Ongoing research and development works suggest that new desiccant materials and novel system configurations have significant potential for improving the performance and reliability and reducing the cost and size of rotary desiccant dehumidification and air conditioning system.

The literature search showed that different types of rotary desiccant cooling systems were studied by several researchers [3, 4]. Elgendy et al. [5] proposed, simulated and compared three novel desiccant evaporative cooling system configurations with the conventional system under a wide range of ambient air temperature. In configuration-I, a direct/indirect evaporative cooling is inserted before the rotating heat exchanger. However, it is inserted after the rotating heat exchanger for system configuration-II. In configuration-III, an extra direct/indirect evaporative cooling is added in an opposite manner. Validation results confirm that, simulation and experimental results are in a good agreement with average errors of 2.23 and 3.87% for ambient air temperature and humidity ratio, respectively. Energetic analysis revealed that configuration-I has the highest cooling capacity while configuration-III has the highest thermal COP and air handling COP. Cejudo at al. [6] presented physical and neural network models for modeling a solid desiccant wheel. Experimental values are used to validate the physical model and to calculate the parameters of the neural network model. An important conclusion of this work was that special attention must be paid when calculating moisture content from measured values of dry bulb temperature and relative humidity.

It was also seen that desiccant based air-conditioning systems are a suitable way to improve indoor air quality. In this study, a novel desiccant based air conditioning system was designed to improve the indoor air quality. In this study, analysis of the system considered is carried out using a program written in FORTRAN language and suitability of the system is investigated for the health care facilities in which hygiene is crucially important.

2.MATERIAL AND METHOD

Figure 1 shows the desiccant cooling system studied [3, 7]. Since the system is considered for the health care facilities, 100 % fresh air will be used. Fresh air duct is used to supply fresh air for the air-conditioned room. The waste air sucked from the air-conditioned room is sent to outside via waste air duct. Regeneration air duct is used to remove moisture of desiccant unit. Various components (dehumidifier, heat exchangers, fans, heaters, temperature and relative humidity sensors) were located into these channels to control and adjust the conditions of the air streams. Psychrometric diagram of the system considered for the design day of Adana, Turkey for summer air conditioning is shown in Figure 2.

[1]*Corresponding author: Osmaniye Korkut Ata University, Department of Energy Systems Engineering, 80000, Osmaniye, Turkey.*
osmankara@osmaniye.edu.tr

The fresh air enters the rotary desiccant wheel (RD) in which moisture is absorbed by the desiccant materials of a wheel (process 1–2). The dry fresh air is pre-cooled first by the regeneration air in heat exchanger-1 (HE1) (process 2–3) and then enters into heat exchanger-2 (HE2) (process 3–4) where it is further pre-cooled by evaporatively cooled waste air. The fresh air finally enters cooling coil (HE3) (process 4–5), in which it is cooled down to blowing conditions and supplied to the conditioned room (state 6).

Air which is sucked from the indoor (7) into the waste air duct is evaporatively cooled in an evaporative cooler (8→9) before entering into the second heat exchanger in order to increase the saving. In the second heat exchanger, due to heat transfer from the fresh air to the waste air, temperature of the fresh air decreases (3-4) and that of the waste air increases (9-10). The waste air leaving the heat exchanger is rejected to the outdoors. At the desiccant wheel, hot regeneration air which is outdoor air is used for removing moisture. Firstly, ambient air is sent into HE1. Because of heat transfer from the fresh air in HE1, temperature of the regeneration air increases (process 11–12) and that of the fresh air decreases (process 2–3). The regeneration air is sent into rotary generator for further pre-heating (process 12–13). Electric heaters (EH) are used for heating regeneration air before entering into rotary dehumidifier (state 14). The regeneration air is pre-heated first by recuperative HE1 and then by rotary generator heat exchanger. The heat required for the further heating of regeneration air to the desired regeneration temperature is supplied with the electric heater unit. Subsequently the regeneration air passes through the desiccant wheel (process 14–15), where its moisture content increases and then it is sent into into rotary generator heat exchanger (process 15–16). Finally, the regeneration air is discharged to the atmosphere (state 17).

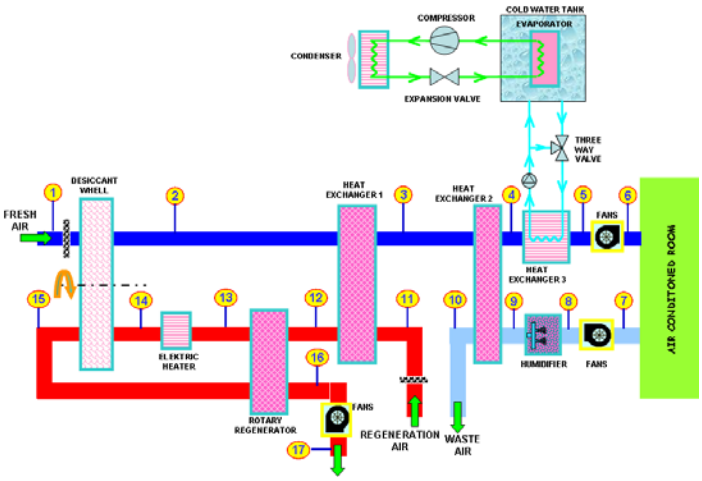

Figure 5. Schematic view of desiccant cooling system

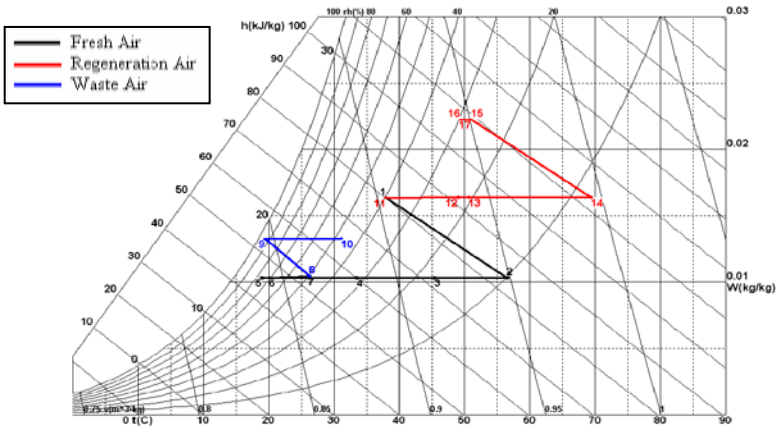

Figure 2. Psychrometric diagram of the system considered for the design day of Adana

2.1. Description of Computer Program Written

Psychrometric analyses were carried out using the design day parameters of Adana (38 ºC dry and 26 ºC wet bulb temperature). The preliminary design of the system was based on the results of these parameters. When the number of the states (17 states) in the system considered, and number of the hours in a cooling season (5000 hours) are thought together, it is clear that analysis

cannot be carried out manually. Therefore, it was decided to develop a computer program for the hourly analysis of the system. FORTRAN programming language was selected for the programming [7].

The parameters below are used as input for the program:

- Flow rate of the fresh air supplied to the air-conditioned room (V_{fresh})
- Flow rate of the exhaust air (V_{waste})
- Flow rate of the regeneration air (V_{regen})
- Dry bulb temperature of the outside air (T_{dbo})
- Humidity ratio of the outside air (W_o)
- Design dry bulb temperature of the air-conditioned room (T_{dbi})
- Design relative humidity of the air-conditioned room (φ_i)
- Sensible heat ratio of the air-conditioned room (SHR)
- Total cooling load of the air-conditioned room (Q_{total})
- Effectiveness of the heat exchangers (η_{heatex})
- Effectiveness of evaporative cooler (η_{hum})
- Efficiency of the fans (η_{fan})
- Powers of the fans (W_{fan})

Using these inputs, the psychrometric features given bellow are calculated separately for every state on the system; Dry bulb temperature (^oC), Wet bulb temperature (^oC), Enthalpy (kJ/kg), Humidity ratio (kg/kg dry air), Relative humidity (%), Dew point temperature (^oC), Density (kg/m^3), Specific heat (kJ/kg K). These psychrometric properties can be calculated using psychrometric equations given by [8].

2.2. Psychrometric Equations

Knowledge of psychrometric properties is the basic requirement for environmental measurements. An understanding of physical and thermodynamic properties of an air-water vapor mixture is called psychrometric. It is fundamental to the design of environmental control systems for plants, crops, animals and human beings. The equations presented in this study enable someone to calculate all or some of the psychrometric properties, if any two independent psychrometric properties of an air-water vapor mixture are known in addition to the atmospheric pressure [9].

Relative humidity (φ) is the ratio of the actual water vapor pressure to the saturation water vapor pressure at the same temperature [8]:

$$\varphi = \frac{P_w}{P_{ws}} \tag{1}$$

where P_{ws} is the water vapor saturation pressure [kPa], P_w is partial pressure of water vapor [kPa].

The amount of water vapor in moist air varies from zero to a maximum that depends on temperature and pressure. The wet-bulb temperature (t_{wb}) can be determined using Equation (2) [8], where W_s is Saturation humidity ratio.

$$t_{wb} = \frac{1.006 \times t_{db} + W \times (2501 + 1.805 \times t_{db}) - 2501 \times W_s}{4.186 \times W - 2.381 \times W_s + 1.006} \tag{2}$$

Dry-bulb temperature (t_{db}) can be calculated using the Equation (3) if wet-bulb temperature and humidity ratio are known [8]:

$$t_{db} = \frac{W_s \times [2501 - (2.381 \times t_{wb})] + t_{wb} \times [1.006 + (4.186 \times W)] - (2501 \times W)}{[1.006 + (1.805 \times W)]} \tag{3}$$

Humidity ratio (W) of a given moist air sample is defined as the ratio of the mass of water vapor (m_w) to mass of dry air (m_a) contained in the sample [8]:

$$W = \frac{m_w}{m_a} \tag{4}$$

Dew point temperature is defined as the temperature to which the air would have to cool (at constant pressure and constant water vapor content) in order to reach saturation. A state of saturation exists when the air is holding the maximum amount of water vapor possible at the existing temperature and pressure. The dew point temperature range of 0 to 93°C is given by [8], where C_{14}= 6.54, C_{15}=14.526, C_{16}=0.7389, C_{17}=0.09486 and C_{18}=0.4569 are coefficients:

$$t_{dp} = C_{14} + C_{15} \times \ln(P_w) + C_{16} \times (\ln(P_w))^2 + C_{17} \times (\ln(P_w))^3 + C_{18} \times (P_w)^{0.1984} \tag{5}$$

Enthalpy is the heat energy content of an air-water vapor mixture. The enthalpy of moist air can be given as for (-50 °C ≤ t_{db} ≤ 110 °C):

$$h = 1.006 \times t_{db} + W \times (2501 + 1.805 \times t_{db}) \quad (6)$$

The equations from (1) to (6) are used for the determination of psychrometric properties, if any two psychrometric properties of an air-water mixture are known. Four subroutines in FORTRAN program were written to find the psychrometric properties of moist air at different states of the system considered.

The effectiveness of humidifier (η_{hum}) is defined as the dry-bulb temperature depression divided by the difference between the entering dry and wet bulb temperatures [10]:

$$\eta_{hum} = \frac{T_{d,i} - T_{d,o}}{T_{d,i} - T_{w,i}} \quad (7)$$

The fans that circulate air in the system cause a temperature rise in air, because fan motors are located inside the air channels. This temperature rise (T_o-T_i) can be calculated using the equations below [8]:

$$Q_{gain} = \left(1 - \frac{\eta_{fan}}{100}\right) \times W_{fan} \quad (8)$$

$$T_o - T_i = \left(\frac{\dot{Q}_{gain}}{c_p \times \dot{m}}\right) \quad (9)$$

By using the data received from the rotary wheel manufacturer, an equation of regeneration temperature (treg.temp.) which depends on the humidity ratio of the fresh air at the inlet (W_1) and outlet (W_2) of the rotary wheel dehumidifier was composed:

$$t_{reg.\,temp.} = 114.78 \times \left(W_1^{0.65419 \times W_2^{-0.099848}}\right) - 149.77 \times \text{Alog}(W_1) \quad (10)$$

The effectiveness of heat exchanger (η_{heatex}) is the ratio of actual ($\dot{Q}$) to maximum ($\dot{Q}_{max}$) possible heat transfer rates (Equation 11,12). C_{min} is minimum fluid capacitance rate of fluids, [W/K], $t_{h,i}$ and $t_{c,i}$ is dry bulb temperature of the hot air and cold air at the inlet of heat exchanger [^oC].

$$\eta_{heatex} = \frac{\dot{Q}}{\dot{Q}_{max}} \quad (11)$$

$$\dot{Q}_{max} = C_{min} \times (t_{h,i} - t_{c,i}) \quad (12)$$

The equations which were used in the calculation of the amount of heat transfer that take place in heat exchangers are presented in Table 1.

Table 1. Equations used for the calculation of heat transfer

No	Calculated Parameter	Equations Used
1	$Q_{2\rightarrow3}$	$\dot{m}_{fresh} * (h_2 - h_3)$
2	$Q_{3\rightarrow4}$	$\dot{m}_{fresh} * (h_3 - h_4)$
3	$Q_{4\rightarrow5}$	$\dot{m}_{fresh} * (h_4 - h_5)$
4	$Q_{14\rightarrow13}$	$\dot{m}_{reac} * (h_{14} - h_{13})$
5	$Q_{15\rightarrow16}$	$\dot{m}_{reac} * (h_{15} - h_{16})$

3.RESULTS AND DISCUSSION

In this study, the performance of the system designed under the conditions of Adana is analyzed using the hourly climate data (dry bulb temperature and relative humidity), which were measured by DMI (Turkish State Meteorological Service) for the period 1983-2006. In order to analyze the performance of the system under summer conditions, the climate data, which were measured between the months June and September for the hours 07:00, 14:00 and 21:00 (relative humidity is measured terdiurnal by DMI), are used in the calculations. The psychrometric properties of the each state of the system are calculated using the equations which are given above (Equations 1-12) and the values given in Table 2.

Table 2. The values used in the calculations

Parameter	**Value**
Total cooling load of the air-conditioned room (kW)	10
Design dry bulb temperature (^{o}C) and relative humidity (%) of the air-conditioned room	26 - 50
Flow rate of the fresh air (m^3/h)	4000
Flow rate of the exhaust air (m^3/h)	4000
Flow rate of the regeneration air (m^3/h)	4000
Effectiveness of the recuperators (%)	65
Effectiveness of the regenerator (%)	85
Sensible heat ratio of the air-conditioned room	0.9
Effectiveness of the evaporative cooler (%)	90
Efficiency of the fans (%)	60
Powers of the fans (kW) (Fresh-Waste-Regeneration)	3-1-4

Figures 3 to 5 shows the amount of heat transferred in the heat exchangers during summer season (from June to September). Heat load required for removing moisture (State 13-14) on desiccant wheel is between 8 to 42 kW at 07:00 h, between 3 to 30 kW at 14:00 h, between 13 to 43 kW at 21:00 h. It can also be seen from these figures that the amount of heat transferred in the heat exchangers starts to increase in June, reaches to the maximum level in July and August and decreases in September. If the daily period is considered, the amount of heat transfers in each heat exchanger at 07:00 h and 21:00 h are greater than at 14:00 h.

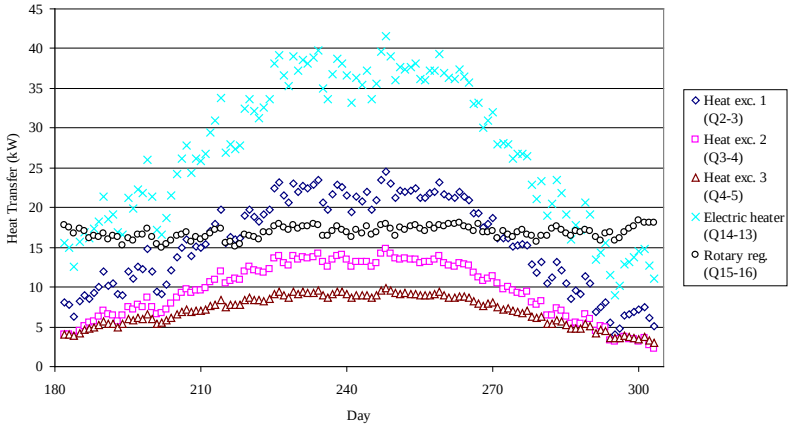

Figure 3. Distribution of the heat transfer at each heat exchanger for 4 months (from June to September) at 07^{00}h

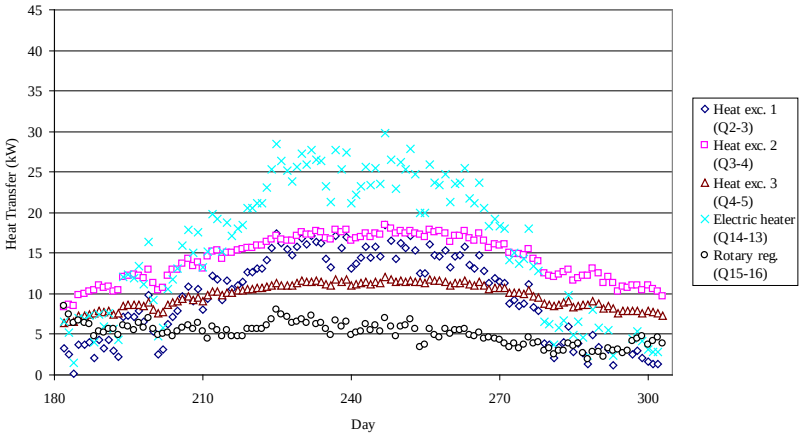

Figure 4. Distribution of the heat transfer at each heat exchanger for 4 months (from June to September) at 14^{00} h

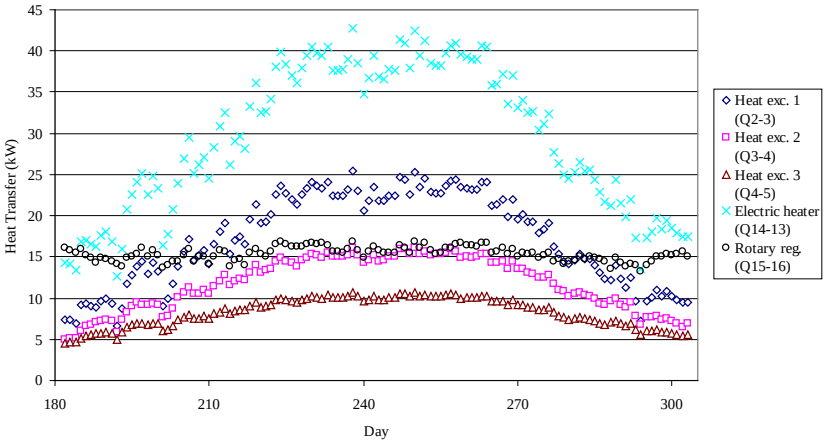

Figure 5. Distribution of the heat transfer at each heat exchanger for 4 months (from June to September) at 21^{00} h

4.CONCLUSION

This study aimed to identify the role of desiccant systems to reduce the infection risks of intensive care patients in the hospital. Using desiccant cooling systems, the humidity of the hospitals can be controlled.

In this study, a computer program was written in order to simulate hourly operating of the air-conditioning system considered with desiccant wheel. The program calculates the parameters for each state and the amount of heat transferred in each heat exchanger.

The amount of heat transfer with the values given in Table 1 for the design day during summer season were analyzed by the program developed for variable outdoor conditions (variable dry bulb temperature, relative humidity). Hourly psychometric properties of each state in the system and hourly amount of heat transfer were calculated using computer program.

The results of the analysis shown that the heat load required at state 13-14 during summer period in Adana is between 8 to 42 kW at 07:00 h, between 3 to 30 kW at 14:00 h, between 13 to 43 kW at 21:00 h.

The results shown that heating energy of electric heater for removing moisture on desiccant wheel is very important parameter for the economic operation of the desiccant systems. If the system can be used by cheap thermal energy sources such as natural gas, waste heat, solar energy, operating cost can be decreased.

REFERENCES

[1]. D.B. Jani, Manish Mishra, P.K. Sahoo, Solid desiccant air conditioning – A state of the art review, Renewable and Sustainable Energy Reviews vol.60, pp. 1451–1469, 2016.
[2]. D. La, Y.J. Dai, Y. Li, R.Z. Wang, T.S. Ge, Technical development of rotary desiccant dehumidification and air conditioning: a review, Renewable and Sustainable Energy Reviews vol.14, pp. 130 – 147, 2010.
[3]. E. Hürdoğan, O. Büyükalaca, T. Yılmaz, A. Hepbaşlı, Experimental investigation of a novel desiccant cooling system, Energy and Buildings, vol. 42, pp. 2049-2060, 2010.
[4]. K. Daou, R.Z. Wang, Z.Z. Xia, Desiccant cooling air conditioning: a review, Renewable and Sustainable Energy Reviews, vol. 10, pp. 55-77, 2006.
[5]. E. Elgendy, A. Mostafa , M. Fatouh, Performance enhancement of a desiccant evaporative cooling system using direct/indirect evaporative cooler, International journal of refirigeration, vol 51, pp 77-87, 2015
[6]. J.M. Cejudo, R. Moreno, and A. Carrillo, Physical and Neural Network Models of A Silica-Gel Desiccant Wheel, Energy and Building, Vol. 34, pp. 837-844. 2002.
[7]. O. Kara, Design of Air-conditioning system with dehumidification, MSc Thesis, Cukurova University Institute of natural and applied sciences, 2009.
[8]. ASHRAE, Handbook of Fundamentals, American Society of Heating, Refrigerating and Air Conditioning Engineers, Inc, Atlanta, USA, 2001.
[9]. A.K Singh, H. Singh, S.P. Singh, R.L. Sawhney, Numerical Calculation of psychrometric Properties on A Calculator, Building and Environment, Vol. 37, pp. 415-419, 2002.
[10]. J.F. Kreider and A. Rabl, Heating and Cooling of Buildings, McGraw Hill, 1994.

Use of Waterjets in Mining and Natural Stone Cutting

Cagatay Pamukcu[1]

Abstract

It is a known fact that Earth contains all the minerals required for the development of civilizations and industrial utilization. Open pit mining technique and especially natural stone quarrying, which has a significant importance for Turkey, is the two extraction methods which are mostly employed in the exploitation of these natural resources. Water jets comprising high-volume but low-pressure had been experienced for the excavation of unconsolidated rock formations for many years in the past and still finds application opportunities on special occasions even today. However, the usage of high-pressure, high-velocity and low-volume water jets has become a major issue in rock cutting for the last two decades. In this study, first of all, a brief summary of high-energy liquid jets (mostly the water jets) in mining applications is presented. In the first stage, the use of liquid jets in underground applications associated with mechanical excavation tools are explained, and then its utilization in the areas of rock quarrying and precise shaping of particularly natural stones are explained in more detail. Their practical use in rock quarrying and advantages particularly in the field of rock shaping are given and general recommendations and further research attempts for their efficient work are presented as well. In addition, the state-of-the- art improvements in water jet-assisted rock cutting both at laboratory and field scale is discussed and possible future enhancements in this area are evaluated.

Keywords: *Water jet, mining, excavation, stone cutting, rock shaping.*

1.INTRODUCTION

Earth contains all the minerals required for the development of civilizations and industrial utilization. Open pit mining technique and especially natural stone quarrying, which has a significant importance for Turkey, is the two extraction methods which are mostly employed in the exploitation of these natural resources. In this study, waterjet applications experienced in both open pit quarrying and underground mining are investigated. Another important usage area of waterjets is the smooth and precise shaping of natural stones. This submission deals rather with applications of waterjet technology in natural stone quarrying and also mentions its general applications in the mining sector and tries to suggest alternatives for the technical problems it has to cope with.

2.APPLICATION OF WATERJETS IN MINING

The water jets are not usually utilized as direct excavator medium in underground but they mostly aid mechanical excavation tools such as drill bit and cutter tips. In both open pit mining and underground mining methods, waterjets serve as an assistant means that lengthen the lifetime of excavator tools rather than taking part in direct excavation process. They general help the machinery to increase their working capacity and lifetime. However, in order to achieve this function, they should be directed in such a way within the rock formation which will be excavated and also they should be energetic enough to take away the fragments that had been broken off. It is known that waterjets are used for the purposes of cooling the cutter bits and creating discontinuities within the formation beforehand within the rock formation which will be excavated [1]. These types of applications are elaborately studied and evaluated by the research groups who develop designs on tunnel boring machines, new drilling machines and shearer-loaders. And then, various research institutes and universities work on these research programs to come up with novel ideas over the efficient extraction of mineral deposits.

The use of waterjets actively in underground mining in combination with excavations tools or their usages in natural stone quarrying are experienced in the following forms:

- Directed towards the center of the profile that had been opened by the excavator tool and deployed in front of the excavator tool,
- Directed towards the center of the profile that had been opened by the excavator tool and deployed behind the excavator tool,

[1] *Dokuz Eylul University, Engineering Faculty, Department Of Mining Engineering, Tinaztepe Campus, 35160, Buca/Izmir, Turkey. Cagatay.Pamukcu@Deu.Edu.Tr*

- Embedded within the mechanized tool, located in front of the cutter bit and directed towards the very center of the profile or slit,
- Embedded within the mechanized tool, located at the very tip of the cutter bit and directed towards the very center of the profile or slit,
- Embedded within the mechanized tool, located behind the cutter bit and directed towards the very center of the profile or slit,
- Located on one side of the mechanical tool and directed towards the center of the profile,
- Located on both sides of the mechanical tool and directed towards the center of the profile,
- Located on both sides of the mechanical tool and directed parallel to the profile axis.
- Located on one side of the mechanical tool and directed out from the center of the profile,

The most common combinations of excavator tools with waterjets are shown in Figure 1.

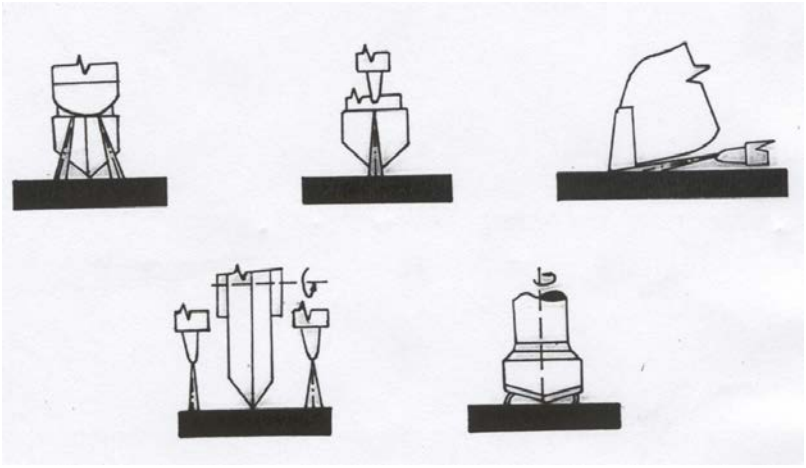

Figure 1. Most Common Combinations of Excavator Tools and Waterjets [2]

Another important operation, in which waterjets are applied underground is hydraulicking. Hydraulicking is an underground mining method in which high pressure water jets (50-400 atm) are utilized at high velocities such as (2-6 m^3/min). The principle of this method seems very similar to the drilling-blasting operation applied underground. First of all, a drillhole is bored within the formation and then several slits are formed to increase the fluid energy. Then, the drill hole is covered with a waterproof material tightly and pressure is applied until the rock breakage (Figure 2). This hydraulic method is widely used in underground mines that are located in Russia.

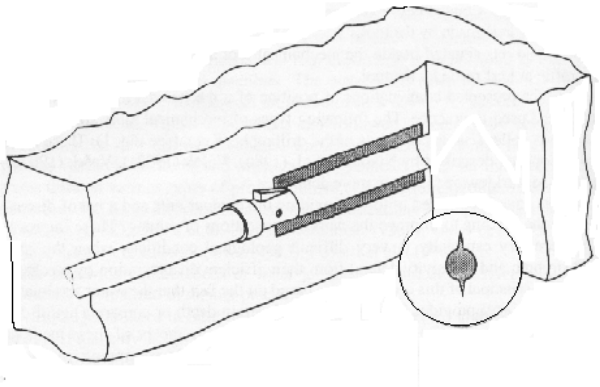

Figure 2. Operation of Fracturing by Means of Threaded Drillhole [2]

On the other hand, in regards to open pit mining; waterjets play an important role in precise contour cutting of faces and ensuring a web of discontinuities in the front part of the face for improving working conditions. These developments are important in open pit mines especially in hard geologic conditions, where it is not possible to break off fragments by mechanical excavators due to the strength values of the formation [3]. The principle of this application depends on the fact that

waterjet makes precise boundary cuttings on the face until a specific depth and creates a web of discontinuities as discussed before. By this means, the rock formation weakens so as to be excavated more easily by the mining machinery.

3.USE OF WATERJETS IN NATURAL STONE QUARRYING

The extraction of natural stones for decorative and building purposes are met mostly from the open pit marble and granite quarries. The use of waterjets in open pit mining, especially in natural stone quarrying, has earned himself an important place especially when blasting is not desired. With respect to blasting operation, the basic problem lies in occupational health and safety concerns that pose a threat to human life. The other problems that would be induced by blasting in open pit mines are dust generation, air shocks and ground vibrations [4].

Especially in natural stone quarrying blasting is not a desired and preferred operation because it creates structural weakness within the blocks that affect the block efficiency adversely. These internal problems that would be encountered within marble blocks lead to several damages in the efficiency of marble processing machines and also loss of labor. A global view of the cutting of blocks in a natural stone quarry is illustrated in Figure 3.

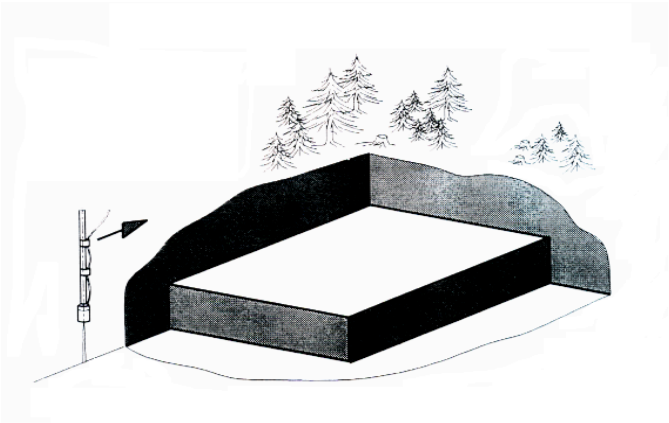

Figure 3. Quarrying Conducted With the Help of Waterjets [5]

4.PRECISE SHAPING OF NATURAL STONES BY WATERJET TECHNOLOGY

The use of waterjet technique in this specific industrial area is a widespread application in our time. The energy required for cutting natural stones is transferred to the cutting point by pressurized water which flows through a synthetic diamond material which has a very tiny cross-section. The pressure of this water is about 3800 bars and its velocity at the tip of the injector is 800 m/s [6]. In this manner, pressure energy is converted into kinetic energy. The water jets which contain abrasive sands that are made up of various minerals, are gradually replacing other shaping methods in our day because the products which had been shaped that way comprise smoother and more precise shape and also higher quality. In addition, the use of waterjet technology in this field is much less complicated and difficult when compared to those decorative stone, glass and ceramic shaping conducted by means of metals. Waterjets do not directly insert pressure effect on the surface which is being cut. The mechanical reaction formed during cutting process occurs at micro-molecular scale and thanks to this, in spite of the high kinetic energy of waterjet, it does not cause any deformation on the material that is being cut and a smooth cutting operation that does not leave and burred part on the material is ensured. Besides, the material loss is minimized by forming a considerably small cutting trace on the material (0.12-1.1 mm) [7]. Waterjet technology presents great advantages especially in complicated form cuttings. The starting points of the cutting operation does not have to be on the edge of the material and thus it is possible to commence cutting process in any part of the material by making holes in it. It is an environmental-friendly technique since it does not release any effluent gas into the atmosphere or require any water filtration process and it does not cause any dust or chips around [8]. Waterjets alone or waterjets containing abrasive material is capable of shaping stones in the third dimension as well with the help of robotic equipment but it is not widely used as three-dimension shaping requires extra time and qualification. Nevertheless, some research groups in the world are making great effort to facilitate this process.

5.CONCLUSIONS AND RECOMMENDATIONS

In this paper, the waterjet applications in both open pit and underground mining were investigated but special emphasis was given in their usage in natural stone quarrying. The practical problems that would arise during these operations were also discussed. The use of waterjets in these fields could be found convenient in spite of their relatively high energy costs. Additionally, seek for ensuring the use of waterjet technology in every possible area of mining in an efficient and cost-effective way is still underway. The usage of high-pressure, high-velocity and low-volume water jets has become a major issue in rock cutting for the last two decades.

Within these searches for improvement, the first advance was observed in the field of developing a well coordination between excavator tools and waterjets. For instance, the flow of high-pressure fluid was achieved through the inner part of the mechanical tools and various tools were developed to provide multiple movement of jets (vibrating, oscillating and rotary). Besides, in order to increase the efficiency of waterjets which contain abrasive material, special types of abrasives and novel mixing techniques were developed. In addition, in order to optimize the shapes of abrasive grains and to mitigate transmission of energy and momentum to abrasive material, studies are continuing. With respect to the processing of natural stones; marble, granite and ceramic material is easily deformed due to their fragile structure when processed by conventional processing machinery and a great deal of material loss occurs. The greatest advantage of waterjet technology over natural stone cutting is that they reduce the material deformation and also material disposal by decreasing the shear forces acting on the material itself and provides smoother and more precise surfaces and edges.

In order to transfer jet energy to the fragmented material, several modifications were tried and conclusively, modular type water jets that operate interruptedly were preferred to the ones that operate on a continuous basis. The waterjets operation in compliance with this principle were started to be preferred in excavation processes which require higher capacity and more precision at the same time.

REFERENCES

[1] Chynkin, B.F., 1989; “Rock Disintegration by Hydraulic Monitor Jts in Open Pit Mines”, Moscow, Russia, pp. 27-35.
[2] Bergman, S.E., 1998; “New Developments in Drill and Blast Methods”, Tunneling and Underground Space Technology 3, pp. 159-161.
[3] Vijay, M.M., 1994; “Power of Pulsed Liquid Jets”, Proc. Of Int. Conf. Geomechanics ’93, Rotterdam, pp. 265-274.
[4] Hlavac, L., Sitek, L. & Vasek, J., 1994; “Using of Physical Model to the Evaluation of an Efficiency of the Tools Creating Multiple-Motion of the Nozzles”, Proc. Of 12th Int. Conf. On Jet Cutting Technology, London, UK, pp. 255-263.
[5] Ciccu, R., Fornaro M. & Russo, C., 1994; “Waterjet in Granite Quarrying- The Italian Experience”, Proc. Of 12th Int. Conf. On Jet Cutting Technology, London, UK, pp. 281-288.
[6] Waterjet Italiana S.R.L. Catalogue, 1998, Milano, Italy.
[7] “Catalogue of Cutting Technology by Waterjets (in Turkish)”, MA-KON Inc., 1999, Istanbul, Turkey.
[8] Kose, H. & Tatar, C., 1997; “Underground Mining Methods (in Turkish) - 4th Edition” DEU Faculty of Engineering Publications, No: 014, Izmir, Turkey, pp. 132-135.

Assessment of Wind Speed Forecasting Models for Wind Energy Conversion System

Emrah Dokur*[1], Salim Ceyhan[1], Mehmet Kurban[1]

Abstract

In recent years wind power generation has experienced a very fast development in the whole world. The wind speed and wind generation forecasting are of extreme importance to aid in the planning studies and scheduled operation of wind energy conversion systems. Consequently, the wind speed forecast for the wind energy sector is essential due to the following reasons, wind farms unit maintenance , for electricity bidding, to schedule the power generators, to plan and schedule energy reserves and storages. Several methods have been proposed for wind speed prediction. One them is statistical models concentrate on capturing the relationship between historical measurements and future outputs with statistical models, whose parameters have to be estimated from available data. These models rely on the previous wind patterns over time and extrapolate the future patterns. Many statistical models have been proposed in recent years, such as autoregressive, moving average, and autoregressive moving average algorithms, and the persistence approach, time series analysis, artificial neural networks, hybrid models which are wavelet artificial neural network and emprical mode decomposition-artificial neural network. In this paper, time series analysis, artificial intelligent methods and hybrid methods for wind speed forecasting are explained.

Keywords: *Wind Speed, Forecast, Wind Energy*

1.INTRODUCTION

The reason that fossil fuels used for meeting the energy need shall run short together with the fact that they are harmful for the environment leaded the path for a search of new energy sources worldwide and renewable energy sources have gained importance in this respect. The energy generated from the wind has been well recognized as environmentally friendly, socially beneficial, and economically competitive for many applications.

Wind speed forecasting is important for wind energy conversation system. Accurately wind speed forecasting provides precision production planning of electrical energy systems. Besides, it is import to schedule the power generators, plan and schedule energy reserves, wind farms unit maintenance and electricity bidding.

Wind speed can be forecasted for short term and long term periods. Several methods for wind speed forecasting have been developed in literature. Time series analysis [1-5], Artificial neural networks [6-10] ,hybrid approaches [11-15] and other techniques [16-17] use to forecast wind speed for different time periods.

In this paper, time series analysis, artificial intelligent methods and hybrid methods for wind speed forecasting are explained over the previous our studies. In Section 2, SARIMA models are given for monthly wind speed analysis. Wavelet Decomposition-Artificial Neural Networks (WT-ANN) and Empirical Mode Decomposition- Artificial Neural Networks (EMD-ANN) which are hybrid models and Artificial Neural Networks are explained with sample wind speed data in Section 3. Finally conclusion is given in Section 4.

2.TIME SERIES ANALYSIS

For time series, commonly adopted models include the auto-regression process (AR), moving-average process (MA), auto-regression and moving-average process (ARMA) and integrated auto-regression and moving-average process (ARIMA). Among them, ARMA model is the combination of AR process and MA process; ARIMA model is available to be converted to ARMA model by difference operation. Thus, AR model, MA model and ARMA model are always considered as a specific case of ARIMA model.

Several variations of ARMA models can be found in the literature. A general expression of the seasonal ARIMA (p,d,q)(P,D,Q)s (SARIMA) model is shown in Equation (1).

[1] *Corresponding author: Bilecik S.E. University, Department of Electrical and Electronics Engineering,11210, Bilecik, Turkey.*
emrah.dokur@bilecik.edu.tr

$$(1-\phi_1 \mathrm{B}-\phi_2 \mathrm{B}^2-....-\phi_p \mathrm{B}^p)(1-\Phi_1 \mathrm{B}^s-\Phi_2 \mathrm{B}^{2s}-...-\Phi_p \mathrm{B}^{Ps})(1-\mathrm{B})^d(1-\mathrm{B}^s)^D Y_t = (1-\theta_1 \mathrm{B}-\theta_2 \mathrm{B}^2-...-\theta_q \mathrm{B}^q)(1-\Theta_1 \mathrm{B}-\Theta_2 \mathrm{B}^2-...-\Theta_Q \mathrm{B}^{Qs})\varepsilon_t \quad (1)$$

Where Y_t is the time series variable, ε_t is the residual series at the current time, where *AR(p)* is a p^{th} order of the autoregressive component, *MA(q)* is a q^{th} order of moving average component, *I(d)* is a d^{th} non-seasonal difference, $AR_S(P)$ is a P^{th} order of seasonal autoregressive component, $MA_S(Q)$ is a Q^{th} order of seasonal moving average component, $I_s(D)$ is a D^{th} seasonal difference, s is a period of the seasonal pattern, B^i is an i^{th} order of backshift operator, and $\phi, \Phi, \theta, \Theta$ are the parameters of the SARIMA model.

Monthly wind speed data was analyzed using SARIMA models by [5]. The ARIMA(1,0,0)(0,1,1)$_{12}$ model was better than other models for the selected area. Their models structure is given Equation [2-3].

$$Y_t = \phi Y_{t-1} + \mathrm{Y}_{t-12} + \phi Y_{t-13} + \varepsilon_t - \Theta \varepsilon_{t-12} \quad (2)$$

$$Y_t = -0.00706 + 0.169978 Y_{t-1} + \mathrm{Y}_{t-12} - 0.169978 Y_{t-13} + \varepsilon_t - 0.794957 \varepsilon_{t-12} \quad (3)$$

Figure 4 outlines the consistency between the original and estimating series obtained by SARIMA model for the selected region wind speed data sets.

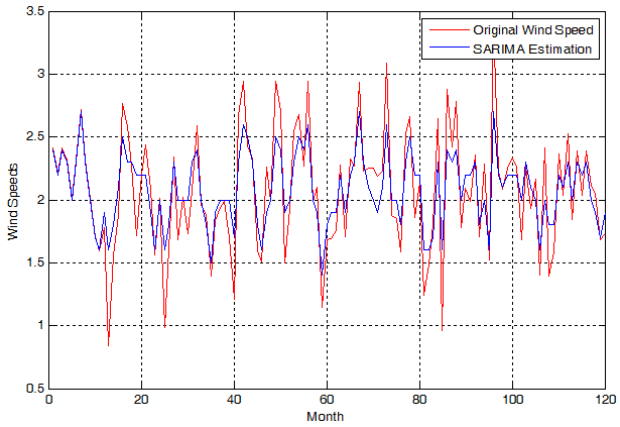

Fig. 4. Original and Estimating Series of Wind Speeds.

The mean squares error (MSE), root mean squares error (RMSE) and mean absolute percentage error (MAPE), sum squares error (SSE), mean absolute error (MAE) and other different criterions can be used to compare methods about performance criteria.

The MSE,RMSE and MAPE criterion is given by Equation (4-6):

$$\mathrm{MSE}(\mathrm{x},\mathrm{y}) = \frac{1}{N}\sum_{i=1}^{N}(\mathrm{x}_i - \mathrm{y}_i)^2 \quad (4)$$

$$\mathrm{RMSE}(\mathrm{x},\mathrm{y}) = \sqrt{\frac{1}{N}\sum_{i=1}^{N}(\mathrm{x}_i - \mathrm{y}_i)^2} \quad (5)$$

$$\mathrm{MAPE}(\mathrm{x},\mathrm{y}) = \frac{1}{N}\sqrt{\sum_{i=1}^{N}\frac{(\mathrm{x}_i - \mathrm{y}_i)}{x_i}}100 \quad (6)$$

Where N is the number of samples, x_i and y_i are measured and predicted values respectively.

Figure 2 shows the forecasting series of wind speed data for selected region. SARIMA(1,0,0)(0,1,1)$_{12}$ wind speed model provides better accuracy by comparison with other SARIMA modeling parameters. Table 1 shows the performance metrics for different parameters of the model.

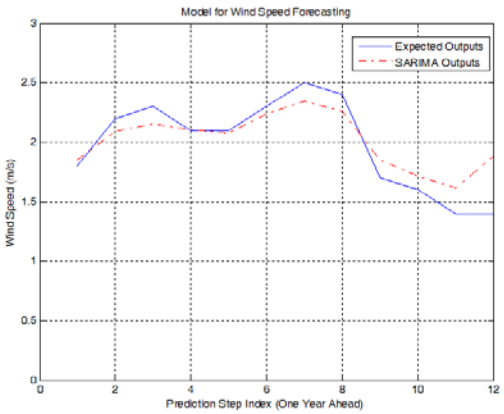

Fig. 2. Monthly Average Wind Speed Forecasting Outputs.

Table 3. Performance Metrics of Different Parameters for SARIMA Models.

Models	RMSE	MSE	MAPE
$(0,0,2)(1,1,0)_{24}$	1.2990	1.6875	15.2170
$(0,0,1)(1,1,0)_{24}$	1.2950	1.6770	15.1143
$(0,0,1)(1,1,0)_{36}$	1.0998	1.2095	14.7953
$(1,0,0)(0,1,1)_{36}$	0.8929	0.7973	12.0242
$(1,0,0)(0,1,1)_{24}$	0.8797	0.7739	11.8160
$(1,0,1)(1,1,2)_{12}$	0.8564	0.7335	10.8725
$(1,0,1)(1,1,1)_{12}$	0.8514	0.7249	10.8209
$(1,0,1)(0,1,2)_{12}$	0.6453	0.4165	8.1982
$(1,0,0)(0,1,1)_{12}$	**0.6335**	**0.4014**	**8.0003**

It is known that value of 10% MAPE is acceptable therefore 8.00% will be suitable for analyzed model. As a result **$(1,0,0)(0,1,1)_{12}$** is acceptable SARIMA model.

3.ANN AND HYBRID APPROACHES

ANNs are highly interconnected simple processing units designed in a way to model how the human brain performs a particular task [18].

Each of those units, also called neurons, forms a weighted sum of its inputs, to which a constant term called bias is added. This sum is then passed through a transfer function: linear, sigmoid or hyperbolic tangent (Figure 3).

[7] presents wind speeds models with the aim of developing suitable models for hourly, daily, weekly and monthly forecasting. Artificial Neural Networks (ANN) implemented in a software are used to perform the forecasts. Three main types of artificial neural network are built, namely: Feed forward neural networks (FFNN), Jordan/Elman neural networks (JENN) and cascade forward neural networks (CFNN).

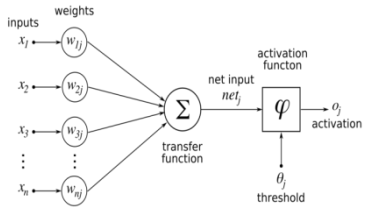

Fig. 3. A Single Neuron Model

Table I is given forecast The ANN architectures and activation functions for different time periods. All models have same activation function for hidden layer and output layer. In this study, FFNN was better results than other neural networks models.

Table I. The ANN architectures and activation functions used for each model

Model	Time	ANN Arthitectures	Activation Functions	
			Hidden Layer	Output Layer
FFNN, JENN, CFNN	Hourly	2 inputs+1 hidden layer 2 neurons+output layer 1 neuron	Tansig	Purelin
	Daily	24 inputs+2 hidden layer 2 neurons+output layer 12 neurons	Tansig	Purelin
	Weekly	14 inputs+1 hidden layer 2 neurons+output layer 7 neurons	Tansig	Purelin
	Monthly	60 input+1 hidden layer 20 neurons+output layer 30 neurons	Tansig	Purelin

The other approach is hybrid models which are WT-ANN and EMD-ANN. Figure 4 shows hybrid approaches flow chart for wind speed forecasting.

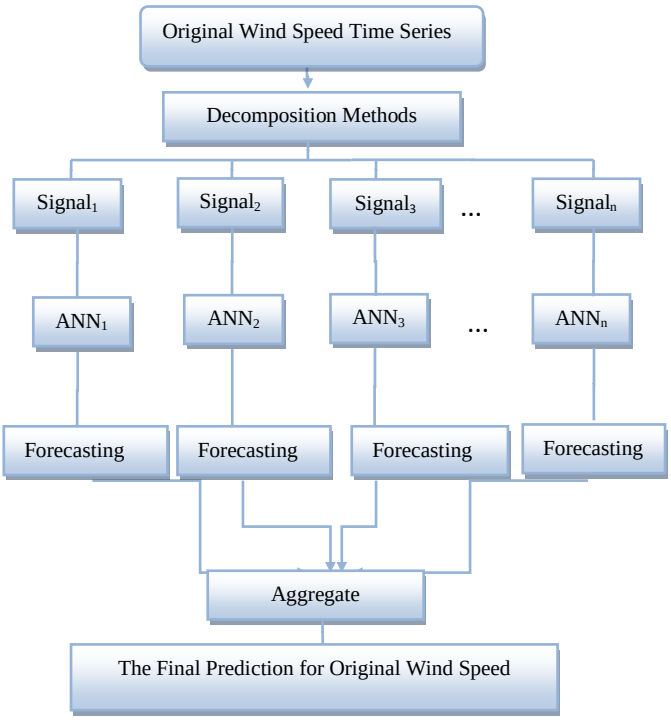

Fig. 4. Flow Chart of Hybrid Approaches

In EMD hybrid method, firstly the original wind speed datasets are decomposed into a collection of intrinsic mode functions (IMF) and a residue by EMD, which are relatively stationary subseries and can be modeled. Second, both the IMF components and the residue are used to establish the corresponding ANN models. Finally, the prediction values of the original wind speed datasets are calculated by summing the forecasting values of every subseries. Decomposition of wind speed sample data is presented in Figure 5.

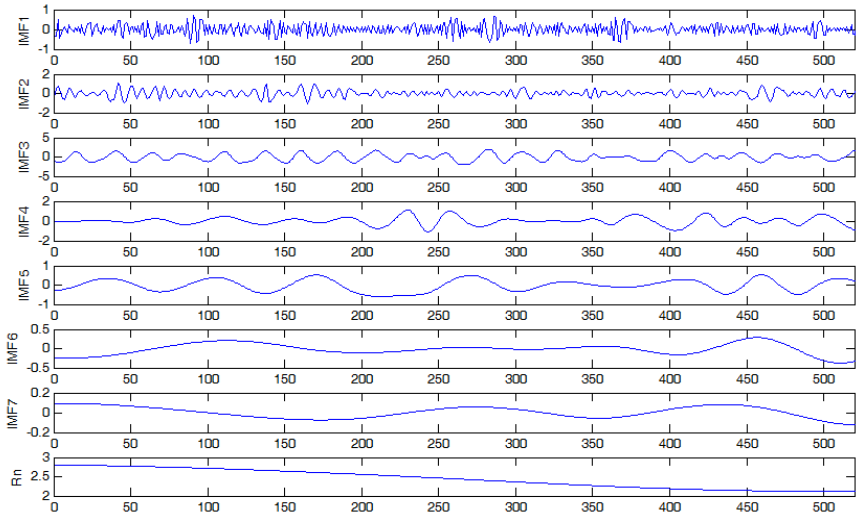

Fig 5: Decomposition Wind Speed Series by EMD

[12] and [14] used hyrid approaches EMD-ANN and WT-ANN, respective hybrid models provides better accuracy by comparison with ANN model. Figure 6 shows sample results of ANN and hybrid model which is EMD-ANN. According to performance criteria, MSE of ANN is 0.2871 while MSE of EMD-ANN is 0.0879.

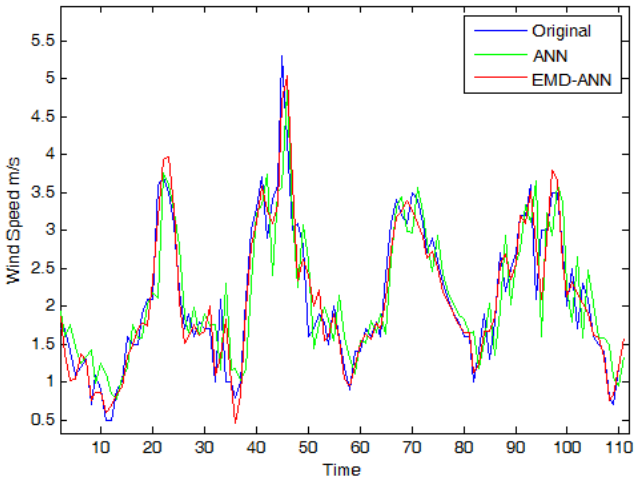

Fig. 6. EMD-ANN and ANN Comparative Analysis

In WT-ANN model, the original wind speed data sets are decomposed into high and low frequencies by WT, which are relatively stationary subseries and can be readily modeled. Second, both the subseries are used to establish the corresponding ANN models. Then, each subseries is predicted by the corresponding ANN. Finally, the prediction values of the original wind speed datasets are calculated by summing the forecasting values of every subseries. At the same time according to performance criteria, RMSE of ANN is 0.5239 while MSE of WT-ANN is 0.2253.

4.CONCLUSION

Wind power is one of the cleanest renewable energy sources that produce no greenhouse gases, has no effect on climate change, and produces little environmental impacts. The energy generated from the wind has been well recognized as environmentally friendly, socially beneficial, and economically competitive for many applications. Wind speed forecasting is important for wind energy conversation system. Accurately wind speed forecasting provides precision production planning of electrical energy systems. Besides, it is import to schedule the power generators, plan and schedule energy reserves, wind farms unit maintenance and electricity bidding. This paper has presented time series analysis, artificial intelligent methods and hybrid methods for wind speed forecasting over the previous our studies. Some forecasting models cannot do this very well, because wind, with some complicated characteristics, is so complex that it is difficult to handle. Therefore, results of hybrid approaches are better than other methods

REFERENCES

[1]. Kavasseri, Rajesh G., and Krithika Seetharaman. "Day-ahead wind speed forecasting using f-ARIMA models." *Renewable Energy* vol.34.5, pp.1388-1393, 2009.
[2]. Cadenas, Erasmo, and Wilfrido Rivera. "Wind speed forecasting in three different regions of Mexico, using a hybrid ARIMA–ANN model." Renewable Energy vol.35.12, pp.2732-2738,2010.
[3]. Chen, Peiyuan, et al. "ARIMA-based time series model of stochastic wind power generation." *Power Systems, IEEE Transactions* on vol.25.2, pp. 667-676,2010.
[4]. Shi, Jing, Xiuli Qu, and Songtao Zeng. "Short-term wind power generation forecasting: Direct versus indirect ARIMA-based approaches." *International Journal of Green Energy* vol.8, pp.100-112, 2011.
[5]. Dokur E., Kurban M., Ceyhan S., 2016, Short Term Forecasting of Wind Speed Using SARIMA Models with Statistical Tests, *8th International Ege Energy Symposıum and Exhibition*, 11-13 May 2016, Afyon, Turkey
[6]. Li, Gong, and Jing Shi. "On comparing three artificial neural networks for wind speed forecasting." *Applied Energy* vol.87 2313-2320, 2010.
[7]. Dokur E., Kurban M., Karakuzu C., 2016, Artificial Neural Network Models for Different Time Periods of Wind Speed Prediction, *The International Conference on Engineering Technology and Applied Sciences* (ICETAS2016),21-22 April 2016, Afyon, Turkey
[8]. Cadenas, Erasmo, and Wilfrido Rivera. "Short term wind speed forecasting in La Venta, Oaxaca, México, using artificial neural networks." *Renewable Energy* vol.34, pp.274-278, 2009.
[9]. Sfetsos, A. "A novel approach for the forecasting of mean hourly wind speed time series." *Renewable Energy* vol.27, 163-174, 2002.
[10]. Methaprayoon, K., et al. "An integration of ANN wind power estimation into UC considering the forecasting uncertainty." *Industrial and Commercial Power Systems Technical Conference*, 2005 IEEE. IEEE, 2005.
[11]. Guo, Zhenhai, et al. "Multi-step forecasting for wind speed using a modified EMD-based artificial neural network model." *Renewable Energy* 37.1 241-249, 2012.
[12]. Dokur E., Kurban M., Ceyhan S., 2016, Hybrid Forecasting Model for Wind Speed Using Wavelet and Artificial Neural Network, *8th International Ege Energy Symposıum and Exhibition*,11-13 May 2016, Afyon, Turkey
[13]. Xiaolan, Wang, and Li Hui. "One-month ahead prediction of wind speed and output power based on EMD and LSSVM." *Energy and Environment Technology*, ICEET'09. International Conference on. vol. 3. IEEE, 2009.
[14]. Dokur E., Kurban M., Ceyhan S., 2015, Hybrid Model for Short Term Wind Speed Forecasting Using Empirical Mode Decomposition and Artificial Neural Network, *International Conference on Electrical and Electronics Engineering* (ELECO 2015) ,26-28 November 2015, Bursa,Turkey
[15]. Hu, Jianming, Jianzhou Wang, and Guowei Zeng. "A hybrid forecasting approach applied to wind speed time series." *Renewable Energy* vol.60, 185-194, 2013.
[16]. Kani, SA Pourmousavi, and M. M. Ardehali. "Very short-term wind speed prediction: a new artificial neural network–Markov chain model." *Energy Conversion and Management*, vol. 52, pp.738-745, 2011.
[17]. Hocaoğlu, Fatih O., Mehmet Fidan, and Ömer N. Gerek. "Mycielski approach for wind speed prediction." Energy Conversion and Management 50.6 (2009): 1436-1443.
[18]. S. Haykin, *Neural Networks: A Comprehensive Foundation*, New Jersey: Prentice-Hall, 1999.

Wind Speed Modeling Using Two-Parameter Weibull Distribution for Potential Analysis

Emrah Dokur*[1], Salim Ceyhan[1], Mehmet Kurban[1]

Abstract

Globally fossil resources have very wide application area. The reason that fossil fuels used for meeting the energy need shall run short together with the fact that they are harmful for the environment leaded the path for a search of new energy sources worldwide and renewable energy sources have gained importance in this respect. Wind energy conversion systems are chosen based on wind speed potential analysis of a region. Wind speed modeling plays a critical role in wind related engineering studies. Frequency distribution of wind speed can be displayed different distributions such as Gamma, lognormal, Rayleigh and Weibull. Two-parameter Weibull distribution is used to model of many regions of the world wind speed in recent year. The reason of using this method is very good fit wind distribution. In this paper is presented assessment of wind speed modeling for wind energy conversion system based on two parameter Weibull distribution. Fitting of wind distribution is shown sample wind speed data.

Keywords: *Wind Speed, Weibull Distribution, Parameter Estimation.*

1.INTRODUCTION

Wind energy has been the most expeditious growing renewable energy technology in the last years. In recent years along with the development of wind industry, wind turbines capacity reached approximately to 370 GW by the end of 2014 [1].

The potential of wind energy of a certain region can be determined before a wind conversion system is installed. The determination of wind energy potential depends on accurately modeling wind speed. Statistical properties of the wind speed are important to predict the output energy of a wind conversion system [2]. There are several distribution functions for wind speed and power density analysis in literature. The log-normal distribution [3-6], the inverse Gaussian distribution [7], the wake by [8,9], three-parameter log normal [10], the gamma distribution [11,12], two-parameter gamma distribution [13], hybrid distributions [14–16], the three parameter generalized gamma distribution [6,17-18], and similar distribution functions were used about energy and other research areas. Two-parameter Weibull density function [19] is commonly used in wind resource assessment to describe wind speed as a stochastic quantity. There are many different methods for estimating the shape (k) and scale (c) parameters of Weibull wind speed distribution function [19-23].

In this paper, seasonal modeling of wind speed realized using Two-parameter weibull distribution for Bilecik, Turkey. Different parameter estimation methods such as maximum likelihood method, graphical method, method of Justus, method of Lysen used for seasonal modeling of wind speed. This paper is structured as follows: Two-parameter Weibull distribution methods is explained by Section 2. Section 3 contains parameter estimation methods for two-parameter weibull distribution. Modeling results is presented in Section 4. Finally, conclusion is given in Section 5.

2.TWO-PARAMETER WEIBULL DISTRUBITION

In the literature, the two parameters Weibull distribution is often used in the statistical analysis of data. The Weibull distribution function is given by Equation (1).

$$f(\mathrm{v}) = \frac{k}{c}\left(\frac{v}{c}\right)^{k-1} e^{-\left(\frac{v}{c}\right)^{k}} \tag{1}$$

where f(v) is the frequency or probability of occurrence of wind speed v, c is the Weibull scale parameter with unit equals to the wind speed unit (m/s) and k is the unitless Weibull shape parameter.

Function F(V) gives the probability of the wind speed exceeding the value V. It is expressed by Equation (2):

$$\mathrm{F(v)} = 1 - e^{-\left(\frac{v}{c}\right)^{k}} \tag{2}$$

[1] *Corresponding author: Bilecik S.E. University, Department of Electrical and Electronics Engineering,11210, Bilecik, Turkey.* emrah.dokur@bilecik.edu.tr

Maximum frequency of wind speed is determined by formula (3):

$$v_{mod} = c(1-\frac{1}{k})^{1/k} \quad (3)$$

Maximum wind speed can be calculated formula (4) [24] :

$$v_{maks} = c(\frac{k+2}{k})^{1/k} \quad (4)$$

Wind power is found commonly by formula (5) :

$$P = \frac{1}{2}\rho A v^3 \quad (5)$$

Where ρ (kg/m3) is air density, A (m^2) is swept area. Mean power density for Weibull distribution is given by Equation (6):

$$P_w = \frac{1}{2}\rho c^3 \Gamma(1+\frac{3}{k}) \quad (6)$$

Where Γ is gamma function. Here, taking into account, the density of the air at sea level, 1 atmosphere pressure and 16.6. Celsius degree ρ_0 =1.225 kg/m3 value; the corrected air density in reference to the height of the sea level (H_m) and other location information can be found according to Equation (7) [25].

$$\rho = \rho_0 - 1{,}194.10^{-4} H_m \quad (7)$$

3.PARAMETER ESTIMATION METHODS

3.1.Graphical Method

Graphic method (GM) is derived by a logarithmic function of the cumulative Weibull distribution expressed in Eq. (2). By taking the logarithm twice of Equation (2), following equation can be obtained [26]

$$ln[-ln[1-F(v)]] = klnv - klnc \quad (8)$$

The left side of the Equation (8) according to the lnv graph shows in the line at the space and k parameter is slope of the line. Firstly, calculation of the frequency distribution and cumulative frequency distribution for calculating the correct value of the ordinate is required. Least squares problem with the calculated values are found by solving these parameters k and c.

3.2.Maximum Likelihood Method

Maximum likelihood method (MLM) is proposed by Steven and Smulders [19]. This method requires large scale numerical iterations. The shape (k) and scale parameter (c) are calculated by Equation (9,10), respectively.

$$k = \left[\frac{\sum_{i=1}^{n} v_i^k \ln(v_i)}{\sum_{i=1}^{n} v_i^k} - \frac{\sum_{i=1}^{n} \ln(v_i)}{n}\right]^{-1} \quad (9)$$

$$c = \left(\frac{1}{n}\sum_{i=1}^{n} (v_i)^k\right)^{1/k} \quad (10)$$

where, vi is the observed wind speed and n is the total number of observations for non-zero wind speed values.

3.3. Methods of Justus and Lysen

Emprical methods are proposed by Justus [20] and Lysen [22].According to emprical method of Justus, shape (k) and scale (c) parameters are calculated, respectively by Equation (11,12).

$$k = \left(\frac{\sigma}{\overline{v}} \right)^{-1.086} \tag{11}$$

$$c = \frac{\overline{v}}{\Gamma(1+1/\mathrm{k})}. \tag{12}$$

Same shape parameter (k) Equation (11) in emprical method of Justus (MJ) is used by Lysen. In empirical method of Lysen (ML), scale parameter equation (13) is obtained by [22]:

$$c = \overline{v}\left(0.568 + \frac{0.433}{k} \right)^{\frac{1}{k}} \tag{13}$$

4.SEASONAL WIND SPEED MODELLING

Wind speed modeling is important to wind energy conversion systems. Modeling of wind speed can be analysis as monthly, yearly and seasonal. In this paper, wind speeds are modeled for seasonal data using different parameter estimation methods. Hourly wind speed data for 2014 year in Bilecik, Turkey are modeled seasonality analysis by Matlab software. Figure 1 illustrates probability and cumulative probability densities of seasonal wind speed at 10 m height for Bilecik, Turkey.

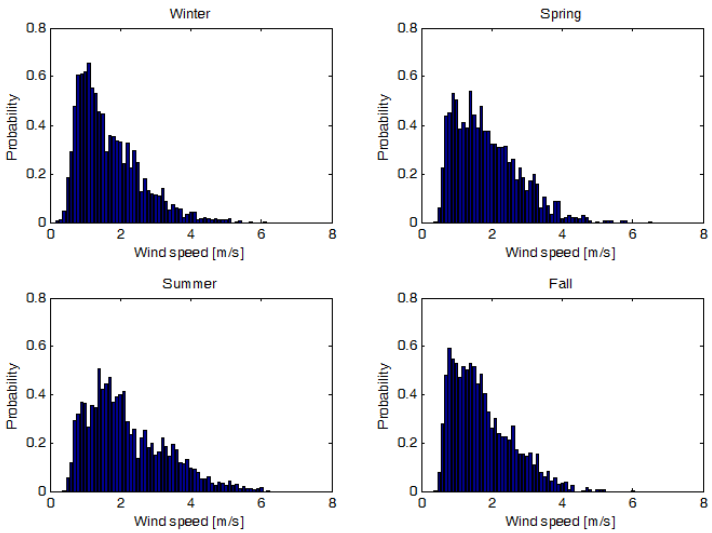

Figure 1.Probability and cumulative probability densities of seasonal wind speeds

Different estimation methods which are MLM,GM, MJ and ML for two-parameter weibull distrubition are analyzed for seasonal periods of 2014 wind speed data. Performance criteria of analysis is shown Root Mean Square Error (RMSE) by Equation (14).

$$RMSE = \sqrt{\frac{1}{n}\sum_{i=1}^{n}(\mathrm{y}_i - \mathrm{x}_i)^2} \tag{14}$$

Where, y_i is the actual wind speed probability value, x_i is the probability value calculated from Weibull distribution and n is the number of observationsTable1 shows seasonal wind speed data modeling results which consist of different estimation methods and error values.

Table 3. Two-Parameters Weibull Distrubition and Performance Criteria

Seasons	Methods	k	c	RMSE
Winter	MLM	2.0142	1.8916	0.0331
	GM	2.4506	2.0790	0.0791
	MJ	1.9867	1.8815	0.0311
	ML	1.9867	1.4773	0.0710
Spring	MLM	2.1417	2.1153	0.0269
	GM	2.5044	2.2630	0.0648
	MJ	2.1288	2.1067	0.0252
	ML	2.1288	1.6516	0.0833
Fall	MLM	2.1590	1.9547	0.0336
	GM	2.5612	2.0595	0.0669
	MJ	2.1423	1.9459	0.0318
	ML	2.1423	1.5255	0.0825
Summer	MLM	2.1131	2.4549	0.0290
	GM	2.5628	2.5602	0.0613
	MJ	2.0949	2.4443	0.0271
	ML	2.0949	1.9165	0.0863

Probability density and cumulative probability density functions of wind speed are illustrated in Figure 2.

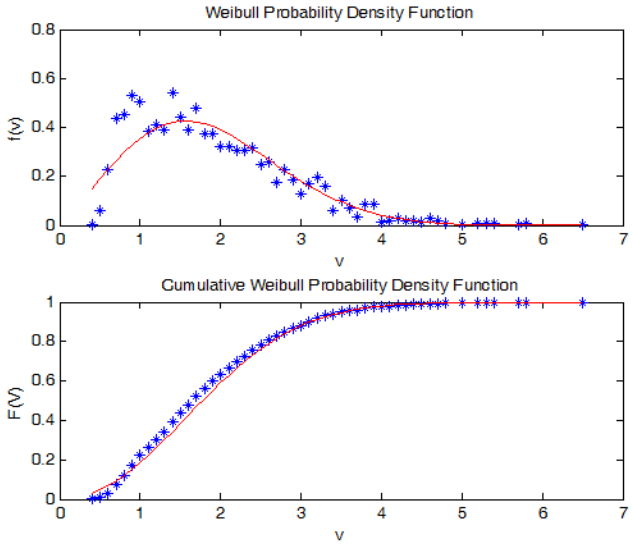

Figure 2. Probability density and cumulative probability density function for spring

5.CONCLUSION

Two parameter Weibull distribution is widely used to model variation of wind speed. Many different numerical methods can be used to estimate the shape and scale parameters of the Weibull distribution.

In this paper, different parameter estimation methods which are maximum likelihood method, graphical method, method of Justus and method of Lysen has been presented for seasonal wind speed data modeling. Accuracy results, measured in terms of RMSE indicate that method of Justus predictions are with high predictive accuracy for all seasons. The study presented the way to apply Two-parameter Weibull distribution for seasonal wind data analysis.

ACKNOWLEDGMENT

We are thankful to Turkish State Meteorological Service, for the support in the accomplishment of the present study.

REFERENCES

[1]. (2014) GWEC. Global Wind Energy Council. Global wind statistics The IEEE website. [Online]. Available: http://www.gwec.net
[2]. Pishgar-Komleh S H, Keyhani A, Sefeedpari, P. "Wind speed and power density analysis based on Weibull and Rayleigh distributions (a case study: Firouzkooh county of Iran)". *Renewable and Sustainable Energy Reviews* vol.42, pp.313-322, 2015;.
[3]. Garcia A, Torres J L, Prieto E, Francisco A D. Fitting wind speed distributions:a case study.*Sol Energy* vol.62 (2),pp.139–44,1998;.
[4]. Luna R E ,Church H W." Estimation of long-term concentrations using a universal wind speed distribution."J *Appl Meteorol* 1974; 13: 910–6.
[5]. Justus C G, Hargraves W R,Yalcin A. "Nation wide assessment of potential output from wind powered generators."*J Appl Meteorol* vol.15 pp.673–8, 1976;.
[6]. Kiss P, JanosiI M. "Comprehensive empirical analysis of ERA-40 surface wind speed distribution over Europe." *Energy Convers Manage* vol.49(8), pp.2142–51, 2008;.
[7]. Bardsley W E. "Note on the use of the inverse Gaussian distribution for wind energy applications." *J Appl Meteorol* vol.19, pp.1126–30, 1980;.
[8]. Vogel R M, Mcmahon T A, Chiew F H S. "Flood flow frequency model selectionin Australia." *J Hydrol* vol.146(1-4), pp.421–49, 1993;.
[9]. Guttman N B, Hosking J R M, Wallis J R. "Regional precipitation quantile values for the continental United States computed from L-moments ."*J Clim* vol.6, pp.2326–40, 1993;.
[10]. Stedinger J R." Fitting log normal-distributions to hydrologic data." *Water Resour Res* vol.16, pp.481–90, 1980.
[11]. Kaminsky F C. "Four probability densities (log-normal, gamma, Weibull, and Rayleigh) and their application to modelling average hourly wind speed." *Proc Int Sol Energy Soc* vol.19, pp.6-10, 1977.
[12]. Sherlock R H. "Analyzing winds for frequency and duration." *Meteorol Monogr* vol.1, pp.42–9, 1951.
[13]. Morgan E C ,Lackner M, Vogel R M , Baise L G. "Probability distributions for offshore wind speeds." *Energy Convers Manage* vol.52, pp.15–26, 2011.
[14]. Takle E S, Brown J M. "Note on the use of Weibull statistic stocharacterise wind- speed data. "*J Appl Meteorol* vol.17, pp.556–9, 1978;.
[15]. Jaramillo O A, Borja M A." Wind speed analysis in La Ventosa, Mexico: a bi modal probability distribution case." *Renewable Energy* vol.29, pp.1613–30, 2004;.
[16]. Rosen K, Buskirk Van R, Garbesi K. "Wind energy potential of coastal Eritrea: ananalysis of sparse wind data." *Sol Energy vol.*66, pp. 201–13; 1999;.
[17]. Carta J A, Ramirez P, Velazquez S. "A review of wind speed probability distributions used in wind energy analysis case studies in the Canary Islands." *Renewable Sustainable Energy Rev* vol.13(5), pp.933–55 2009.
[18]. Auwera V, Meyer L F, Malet L M." Theuse of the Weibull three parameter model forestimating mean wind power densities." *J Appl Meteoral* vol.19, pp.819–25, 1980.
[19]. Stevens M J, Smulders P T. "The estimation of the parameters of the Weibull wind speed distribution for wind energy utilization purposes." *Wind Eng* vol.3(2), pp.132–45,1979;.
[20]. Justus C G, Hargraves W R, Mikhail A, Graber D." Methods for estimating wind speed frequency distributions." *J Appl Meteorol vol.*17, pp.350–3, 1978.
[21]. Akdag S A, Dinler A. "A new method to estimate Weibull parameters for wind energy applications." *Energy Convers Manage* vol.50, pp.1761–6, 2009.
[22]. Lysen E H. "Introduction to wind energy." *The Netherlands: SWD Publication SWD* 82-1; 1983.
[23]. Carneiro T C, Melo S P, Carvalho P C, Braga A P D S. "Particle Swarm Optimization method for estimation of Weibull parameters: A case study for the Brazilian northeast region." *Renewable Energy* vol.86, pp.751-759,2016.
[24]. Cheng, R. C. H., & Amin, N. A. K. "Estimating parameters in continuous univariate distributions with a shifted origin." *Journal of the Royal Statistical Society. Series B (Methodological)*, pp.394-403, 1983.
[25]. Patel, M. R. *Wind and solar power systems: design, analysis, and operation.* CRC press, 2005.
[26]. Akdağ, Seyit Ahmet, and Önder Güler. "A novel energy pattern factor method for wind speed distribution parameter estimation." *Energy Conversion and Management* vol.106 pp.1124-1133,2015.

ICENS
INTERNATIONAL CONFERENCE ON ENGINEERING AND NATURAL SCIENCES
24-28 May 2016 /Sarajevo

A Numerical Study on Rock Barriers in Uzungöl Region.

Mehmet T. Seferoglu[1],S.Istemihan Cosgun[1], Muhammet Celik[1], Aysegul G.Seferoglu[2], Muhammet V.Akpınar[1]

Abstract

Uzungöl which is located on the Eastern Black Sea Region, is one of Turkey's most important tourism centers. Due to the mountainous nature of the region, rock falls occur during transportation line between. Thus, it consists of a variety of risks on the way to the tourism region. In this study, the detailed dimensional drawing has been done in a risky area between Trabzon and Uzungöl. The maximum speed and energy of rock that could fall on the road is calculated by Rocfall program. Based on analysis, the highest energy was found to be 100 KJoule and the jump height of rock was found as 0.85 m and the maximum bounce speed was calculated as the 8 m/sec. in the most critical cross-section. In the second part of study, rock barriers were modeled using ABAQUS finite element (FE) software. Absorbed energy for varying shaped barrier was computed using the F.E. models. As a result a rock barrier system was designed to carry safely falling rocks with maximum speed and energy. The designed rock barriers were expected to be applied in disaster risk zones of highway between Trabzon and Uzungöl.

Keywords: *Disaster, Finite Element, Highway, Rock Barrier, Rock Fall*

1.INTRODUCTION

The potential existence of rockfall, constitutes a serious problem in residential areas. Especially, rockfalls create a major hazard in numerous rock cuts transportation systems such as highways and railways cause to casualties, as well as a large amount of damage and injuries [1]. Also, rockfalls cause the road closed to traffic for a while. This problem is being handled with several developed rock reclamation techniques and people are able to continue live and travel safely in their residential areas. Rock reclamation is established with the collaborative work of detailed engineering service, project design stages and interdisciplinary engineering studies [2].

The main causes of rockfall are rainfall, frost, discontinuities, differential erosion, animal dens etc. whereas minor causes are tree roots, springs, vehicle vibrations [3].The topography, geology and climate of the areas being conducted of rock reclamation aggravate the work. East Black sea Region is an area where various challenges exist together. Therefore, the works should be conducted by considering these challenges.

Volume of falling rock blocks in the source area depends on the discontinuity and stability. The size of the block of rock is very important and must be a detailed study of topographies when making project. Micro-topography is also a need to work in a particular region. The topography data received from the field are entered into the statistical computer program. The rocks bounce and energy accounts vary considerably unless handled with precision.

After determined the potential of falling rocks stopped by various methods (steel nets, bolts or steel ropes etc.) . Another method is the use of energy damping with steel rock barrier. Nowadays, several manufacturers produce different models of falling rock protection barriers which cover a wide range of energy absorption capacities, from less than 100 kJ to more than 5000 kJ [4].Traditionally, these structures are designed using the results of full-scale tests in which prototypes are subjected to the impact of blocks having known mass and velocity. Since 2008, the testing methods and procedures have been provided by the European Guideline for the Technical Approval of Falling Rock Protection Kits – ETAG 27 [5].

In the last 10 years, the results of full-scale tests were also employed to develop numerical models of falling rock protection, using finite element models. A recently developed, two-dimensional, dynamic finite element (FE) model was proved to be able to reproduce the essential features of the barrier response in a full-scale impact test [6,7,8].Due to its basic implementation and remarkably low computational cost, the model can provide a preliminary assessment of barrier's on-site behavior [6].

[1]*Corresponding author:Karadeniz Technical University, Department of Civil Engineering, 61080, Ortahisar/Trabzon,Turkey.*
mtseferoglu@gmail.com

2. MATERIALS and METHODS

2.1. Site Description

In this study, the detailed dimensional drawing has been done in a risky area between Trabzon and Uzungöl. The area located in the route of falling rocks is covered with medium frequency pine trees. But, tree frequency in some particular areas diminishes due to various rock falls over the years. It is seen from the reports of Trabzon Provincial Disaster & Emergency Management Authority (AFAD), these fallen rocks blocked the roads repeatedly. Also, according to these reports, the rocks presenting danger of falling, threatens 28 housings, 2 workplaces, 1 mosque and some public buildings and outbuildings such as stables and coops (Fig. 1).

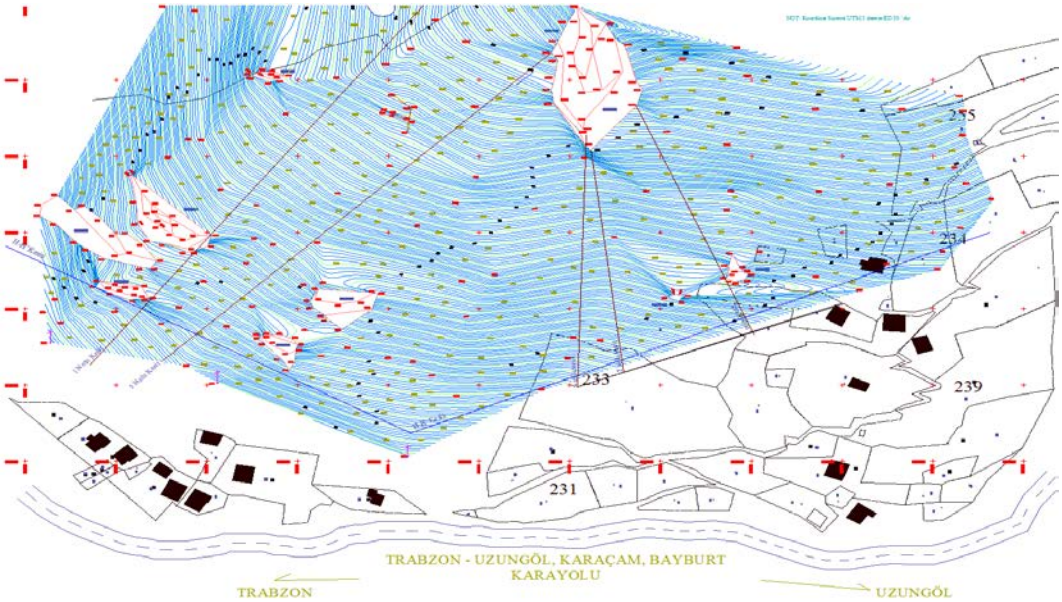

Figure 1. The region between Trabzon and Uzungöl

In this study, the primary conduct is literature research about the falling rocks in the field. After the field works are completed, the cross sections considered critical in the field and established maps are entered as input data into the Rocfall program. As the details of the cross sections increase, the more simulated the data of the program becomes [2]. The data entered into the program are based on the length of cross sections which correspond to each 1 meter of grade elevation. No ground information is defined specifically for the program, the source rock section is entered as “bedrock” and the falling routes are entered as talus with vegetable.

Rock weights are entered as 500 and 1000 kg into the programs stated in Trabzon AFAD reports. The initial speed of the rocks is entered as 1m/s and angular initial velocity is accepted as zero. The program is executed with approximately 500 different falling combinations and the most critical result are tabularized (Table 1).

Table 1. Rocfall software analysis result

UZUNGÖL region sections					
	Section 1	Section 2	Section 3	Section 4	Section 5
Height difference (m)	209	123,01	112,99	139,38	187
Length (m)	304,87	146,17	163,14	160	279,61
Average slope (%)	68,55	84,16	69,26	87,11	66,88
500 Kilogram,the first movement:5 m/s					
Hmax (m)	**2,67**	1,13	0,71	1,56	0,21
Vmax (m/s)	13,02	13,84	9,75	15,02	8,17
Emax (Kjoule)	42,33	47,88	23,76	56,4	16,68
1000 Kilogram,the first movement:5 m/s					

Hmax (m)	2,43	0,98	0,43	1,13	0,43
Vmax (m/s)	13,85	13,42	10,03	**14,78**	6,95
Emax (Kjoule)	95,91	90	25,15	**109,22**	24,15

As a result, the analysis conducted according to Rocfall program, the bouncing height of the rocks are observed higher in the scour rock areas where the incline is usually upright. In addition to this, it is seen that the energy and speed levels are usually higher in lower grades.

2.2. Numerical Modeling

In the second part of study, rock barriers were modeled using ABAQUS finite element (FE) software. The modeling of rock barrier was created three different mesh geometries (Fig. 2a,2b,2c).

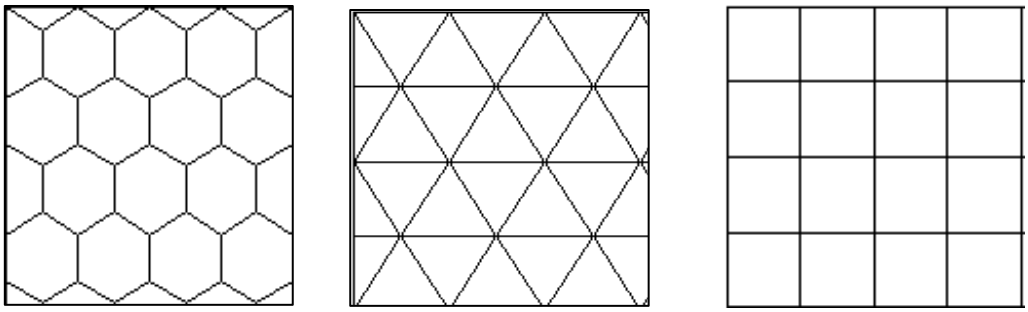

Figure 2a. B1, Hexagon *2b.B2, Triangle* *2c.B3, Square*

The Classical Metal Plasticity (CMP) material model was used for modeling of rock barriers. The T3D2 truss finite element was preferred for steel mesh of rock barriers. Because, these type of finite element is suitable for modeling rope and cable. The velocity and mass of rock were selected 20 m/s, 500 kg. All rock barriers model was simulated same dimensions, rope diameter and area of single mesh. Impact force-time, mid-span displacement-time and kinetic energy history of rock curves were obtained for varying shaped barrier.

3. RESULT AND DISCUSSION

Results at maximum impact force, maximum mid-span displacement were summarized in Table 2. The impact force-time curves were given in Figure 3. Furthermore, deformation shapes of rock barriers were given in Figure 4.

Table 2. Result summary

Barriers type	**Maximum impact force, kN**	**Maximum mid-span displacement, mm**
B1-Hexagon	337.15	405.8
B2-Triangle	474.83	359.6
B3-Square	240.55	701.3

As it is shown in the figure 3 and table 2, max impact force was obtained from the triangle geometry. Effect on impact force of the triangle geometry is positive and more than hexagon (40%), square (97%) respectively.

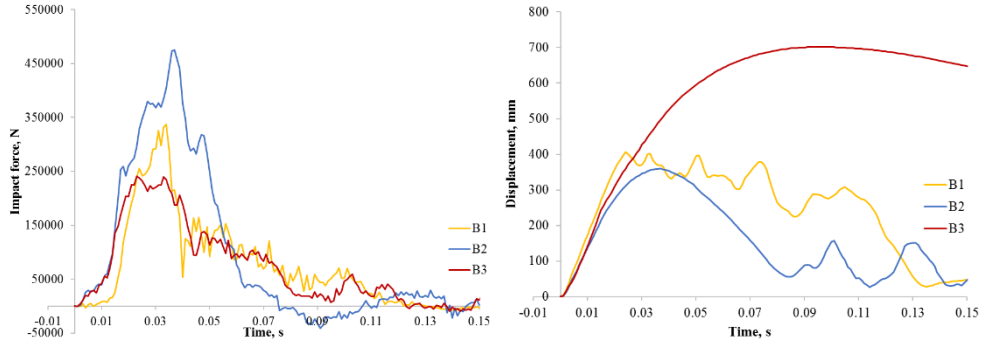

Figure 3a.Impact force-time curves *Figure 3b. Displacement-time curves*

Given the displacement values of square geometry, displacement was about 2 times more than the others geometry. The effect on the displacement value of the geometry is seen to be important.

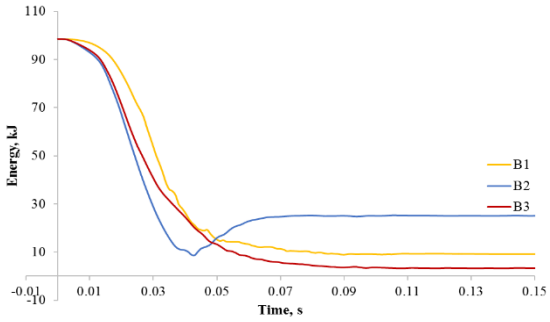

Figure 4. Energy-time curves of rock

Within 40 ms time period, the initial energy of rock was dissipated by B2 approximately 90%. The same time period, B1 and B3 dissipated similar energy 80%, 81% respectively. These results show that the mesh geometry is important parameter for absorbed impact energy value. After the 40 ms times, B1 and B3 continue to absorb energy. However, the rock was rebounded by B1 rock barrier.

4. CONCLUSION

A reliable numerical procedure for dynamic analysis of falling rock protection barriers has been presented. The triangle mesh geometry showed suitable result for Uzungöl region. Because, the maximum impact resistance was obtained from B2. Numerical results helped to understand impact behavior of rock barriers under falling rock. When the changes energy of rock were examined, in the certain time period (the first 40 ms), B1 and B3 barriers have same dissipated energy. As a result a rock barrier system was designed to carry safely falling rocks with maximum speed and energy. The designed rock barriers were expected to be applied in disaster risk zones of highway between Trabzon and Uzungöl.

ACKNOWLEDGEMENTS

The authors are grateful to Trabzon Provincial Disaster & Emergency Management Authority (AFAD) for allowing them to use the data presented in the paper.

REFERANCES

[1] P. Budetta. Assessment of rockfall risk along roads. Natural Hazards and Earth System Sciences (2004) 4: 71–81.

[2] M. Çelik, M. T. Seferoğlu, A. G. Seferoğlu, M. V. Akpınar. "Rehabilitation Methods, Challenges, Cost Benefit Analysis of Disaster Area Exposed due to Rockfalls in Trabzon Province",Doğal Afet ve Afet Yönetimi Sempozyumu (DAAYS'16), 2-4 Mart 2016, Karabük, Türkiye.

[3] M. Ahmad, R. K. Umrao, M. K. Ansari, Rajesh Singh, T. N. Singh. Assessment of Rockfall Hazard along the Road Cut Slopes of State Highway-72, Maharashtra, India.*Geomaterials*, 2013, 3, 15-23.

[4] C. Gentilini, G. Gottardi, L. Govoni, A. Mentani, F. Ubertini.Design of falling rock protection barriers using numerical models.Engineering Structures 50 (2013) 96–106.

[5] EOTA. Guideline for European technical approval of falling rock protection kits(ETAG 027), Febbraio 2008, Brussels.

[6] C. Gentilini, L. Govoni, Stefano de Miranda, G. Gottardi, F. Ubertini. Three-dimensional numerical modelling of falling rock protection barriers. Computers and Geotechnics 44 (2012) 58–72.

[7] de Miranda S, Gentilini C, Gottardi G, Govoni L, Ubertini F. A simple model tosimulate the full-scale behaviour of falling rock protection barriers. In:Springman S, Laue J, Seward L. (Eds.), Proceedings 7th international conference on physical modelling in geotechnics (ICPMG 2010), ETH, SwissFederal Institute of Technology, Zurich, Swizerland, 28 June–1 July, 2010, vol.2. CRC Press, Taylor & Francis Group: London, UK; June 2010. p. 1247–52 [ISBN978-0-415-59288-8].

[8] Govoni L, de Miranda S, Gentilini C, Gottardi G, Ubertini F. Modelling of fallingrock protection barriers. Int J Phys Model Geotech 2011;11(4):126–37.

ICENS
INTERNATIONAL CONFERENCE ON ENGINEERING AND NATURAL SCIENCES
24-28 May 2016 /Sarajevo

A Study for Developing a Gravity Based Trip Distribution Model for Interprovincial Bus Travels in Turkey

Yasar Vitosoglu[1]

Abstract

Although there are many Origin-Destination (O-D) estimation models in the literature, using conventional methods based on home surveys or roadside interviews for estimating O-D matrices are generally costly and time consuming. Since rapid changes in land use and demographic structure occur in developing countries, this situation shortens validity of data for these countries. Therefore, it is necessary to revise frequently the data obtained by using inexpensive methods. For this purpose, various methods that are cheaper have been developed to form and revise O-D matrices. Thus, since the early 1980s, the idea of determining trip matrices from traffic counts has attracted attention of the researchers, and various methods have been suggested on this subject. The model developed by Bell in 1983 is also one of these methods, and it has been used for determining the daily interprovincial bus travel matrix in Turkey. After the daily interprovincial bus travel matrix was determined, a multivariate regression analysis was performed to develop a gravity based trip distribution model for the interprovincial bus travels by using O-D information obtained from this matrix. In this analysis, as the interprovincial bus travels were used as the dependent variable, the populations of the provinces and the distances between them were taken as the independent variables. The coefficients of independent variables obtained from this regression analysis were then used as the calibration constants of the trip distribution model. Finally, by placing these constants in the equation of the trip distribution model, the gravity based trip distribution model was developed.

Keywords: *Gravity model, interprovincial bus travels, O-D matrix estimation, trip distribution models.*

1.INTRODUCTION

Using conventional methods based on home surveys or roadside interviews to estimate origin - destination (O-D) matrices are generally costly and time consuming. The life of data is very short in developing countries where rapid changes occur in land use and demographic structure, and it is necessary to revise frequently the data obtained by using relatively inexpensive methods. Therefore, various methods which are cheaper and do not require intensive labour have been developed in order to form and revise present and future O-D matrices.

Vehicle counts on highways are in reality a function of a trip matrix and a route-choice pattern of drivers. Therefore, they provide information about all O-D pairs that use the counted links. In addition, traffic counts are very attractive data sources because they could be obtained in a relatively inexpensive and automatic way without disrupting traffic. As a result, since the beginning of 1980s, the idea of estimating trip matrices and developing demand models from traffic counts has attracted serious attention of researchers, and various methods have been suggested on this subject. The model used for estimating the O-D matrix related to interprovincial bus travels in Turkey for the year of 2013 is also one of these methods, and was developed by Bell in 1983 [1, 2].

2.THE MODEL DEVELOPED BY BELL

If it is assumed that N zones are interconnected by a road network which consists of a series of nodes and links, it will be clear that the trip matrix is made up of N^2 cells. The number of cells in the trip matrix is N^2 - N if intra-zonal trips can be disregarded. In order to find out these N^2 cells constituting an O-D matrix from traffic counts, it is necessary first to identify paths followed by trips from each origin to each destination. If p_{ij}^a is defined as the probability or proportions of trips from zone i to zone j travelling through link a, the flow in this link (V_a) will be the summation of portions of all trips between zones using link a. This expression can be summarized mathematically as follows:

$$V_a = \sum_{ij} T_{ij}\, p_{ij}^a \qquad (1)$$

The probability of p_{ij}^a can be obtained by using various trip assignment techniques of which their degree of complexity increases from all-or-nothing assignment to equilibrium assignment. As a result, when all the p_{ij}^a proportions and all the

[1] *Corresponding author: Dumlupinar University, Department of Civil Engineering, 43100, Kutahya, Turkey.* yasar.vitosoglu@dpu.edu.tr

observed traffic counts (V_a) are given, there will be N^2 unknown T_{ij}'s of the problem to be estimated from a set of L simultaneous linear equations, where L is the total number of traffic counts.

In principle, N^2 independent and consistent traffic counts are necessary in order to determine the trip matrix **T** uniquely. On the other hand, in practice, the number of traffic counts is much less than the number of unknown T_{ij}'s. Therefore, it is impossible to find out a unique solution for the problem of estimating an O-D matrix. In general, more than one trip matrix that are consistent with the observed traffic counts will be found when they are assigned onto the network. Two basic approaches can be utilized in order to resolve this problem. In the first approach, the set of feasible solutions for the matrix to be estimated can be restricted by imposing a particular structure, which is provided by gravity or a direct demand model. In the second approach, general principles like maximum likelihood or entropy maximization are utilized in order to provide the minimum additional information required for estimating an O-D matrix.

Assignment methods used for estimating trip matrix from traffic counts are classified under two main groups. In the assignment methods belonging to the first group, it is assumed that the proportion of drivers choosing each route does not depend on flow levels in links. The most common example of assignment methods in this group is all-or-nothing assignment, and the probabilities of p_{ij}^a are defined in this case as follows:

$$p_{ij}^a = \begin{cases} 1, & if\ trips\ from\ origin\ i\ to\ destination\ j\ use\ link\ a \\ 0, & otherwise \end{cases} \quad (2)$$

Pure stochastic methods are also included in the first group. However, the probabilities of p_{ij}^a can take values between 0 and 1 in these cases.

Assignment methods in the second group, on the other hand, take account of congestion effects. Therefore, the probability of trips made between each O-D pair using any link also depends on traffic flow in that link. Equilibrium and stochastic user equilibrium assignment methods are included in this group [3].

The model developed by Bell is fundamentally based on the principle of maximum likelihood. In this method, the equation to be solved for estimating O-D matrices from traffic counts is given in the following equality:

$$V_a = \sum_{ij} t_{ij}^o \tau \left(\prod_a X_a^{p_{ij}^a} \right) p_{ij}^a \quad (3)$$

where

V_a : the observed flow at count site a,

t_{ij}^o : the initial estimate of trips made between zones i and j,

τ : an overall scaling factor,

X_a : the vector of parameters to be estimated,

p_{ij}^a : the probability that trips made between zones i and j pass through count site a.

The vector of parameters X_a is initially set to unity, and unless other values for τ have been defined by the user, the value of τ is calculated by using the following formula:

$$\tau = \frac{\sum_a V_a}{\sum_a \sum_{ij} p_{ij}^a} \quad (4)$$

The value of τ remains set at the level defined or calculated by the formula above during later phases. As for the solution procedure, it involves improving upon the initial estimated values of X_a by carrying out more iteration.

For every count site, an adjustment factor h_a is calculated in each iteration. This adjustment factor is then added to the prior estimate of X_a in order to obtain the value of X_a' as shown in the following formula:

$$X_a' = X_a + h \quad (5)$$

The formula used to calculate the value of h_a is also as follows:

$$h_a = \frac{V_a - \sum_{ij} t_{ij}^o \tau \left(\prod_a X_a^{p_{ij}^a} \right) p_{ij}^a}{\sum_{ij} t_{ij}^o \tau p_{ij}^{a^2} \left(\prod_{b \neq a} X_b^{p_{ij}^b} \right) X_a^{\left(p_{ij}^b - 1\right)}} \quad (6)$$

The process of iteratively calculating the values of h_a for each count site continues until the difference between observed and estimated traffic flows will remain the limits specified by the user. After the final values of X_a are determined for every link, the cells of trip matrix are calculated by the following formula:

$$T_{ij} = \tau t_{ij}^{o} \prod_{a} (X_a)^{p_{ij}^{a}} \quad (7)$$

Finally, the trip matrix has been formed by determining all its T_{ij} elements [1-3].

3.DETERMINATION OF THE INTERPROVINCIAL BUS TRAVEL MATRIX IN TURKEY

In determining the interprovincial bus travel matrix for the year of 2013 in Turkey, all the provinces in Turkey were considered although border crossing gates were not included. As a result, the study was carried out for 81 provinces. The highway network constructed for determining the interprovincial bus travel matrix is fairly detailed, and it consists of 714 links, 268 nodes and 81 regions. Then, this highway network was coded by using the Transport Program [4].

All or nothing assignment algorithm was employed for estimating trip matrix from traffic counts. Thus, all or nothing trees and shortest paths were built, taking into account the distances among the centroids of the regions as transportation cost. As a result, the probabilities of p_{ij}^{a} were obtained from these all or nothing trees. The speeds were assumed to be same for all the links, and the value of 70 km/h was used.

In order to estimate the interprovincial bus travel matrix for the year of 2013 in Turkey, Vmat Subprogram, which is a part of Transport Software and can determine O-D matrices from traffic counts, was utilized. The working principle of this subprogram is based on the model developed by Bell. This program consists of three subprograms. Vmat1 is the first of two programs used to produce the data files required for input to Vmat3. The main purpose of program Vmat1 is to define the probability of a trip between each origin-destination pair passing through each count site. Program Vmat2 is the second of the two programs used to produce the data files required for input to Vmat3. The purpose of this second program is to create a data file of traffic counts. Program Vmat3 creates trip matrix consistent with input traffic counts and route probabilities and also with input trip length distribution if it is required. The main purpose of this program is to identify the most likely trip matrix from input files of traffic counts at individual sites or groups of sites, and from route probabilities, using Newton-Raphson Technique [4].

As mentioned before, in order to determine the interprovincial bus travel matrix for the year of 2013, the model developed by Bell was used. As it is known, using a well-defined initial matrix ensures that the estimated matrix is more realistic. The initial matrix is generally constituted based on the matrices obtained from the previous studies. However, since any study on this subject was not carried out in Turkey during previous years, the principles of Gravity Model were used to form the initial matrix related to interprovincial bus travels. Thus, it has been assumed that the bus travel made from province i to province j is proportional to the multiplication of the power functions of the populations of provinces i and j, and inversely proportional to the power function of the distance between these two provinces. This statement can be summarized by the following equation:

$$t_{ij}^{o} = k \frac{P_i^{\alpha} P_j^{\beta}}{d_{ij}^{\gamma}} \quad (8)$$

where

t_{ij}^{o} : the initial daily bus travels made from province i to province j,

P_i : the population of province i,

P_j : the population of province j,

k : a coefficient,

d_{ij}^{γ} : the distance between province i and province j,

α, β and γ : the calibration constants.

The calibration constants of α, β and γ were obtained from the multiple regression analysis carried out based on the daily bus runs that were made from Istanbul and Ankara to some provinces reciprocally. This daily bus runs are given in Table 1 [5]. Furthermore, the populations of the provinces considered in this study are given in Table 2 [6]. In order to carry out the analysis, the number of interprovincial bus travels is firstly found by multiplying the number of interprovincial bus rides made reciprocally with the number of 30 passengers per bus that is the average bus occupancy rate given by the General Directorate of Highways (KGM). This approach is very rough and does not take into account the case that buses embark and drop off passengers in the settlement centres on their routes. Nevertheless, since the more detailed data could not be found on this subject, it is thought that this approach is sufficient for forming the initial matrix. In addition, the equation given above has been made linear by taking the logarithm of both sides in order to carry out the multiple linear regression analysis. This procedure is summarized in Eqs. (9) – (11).

$$log(t_{ij}^{o}) = log\left(k \frac{P_i^{\alpha} P_j^{\beta}}{d_{ij}^{\gamma}}\right) \quad (9)$$

$$log(t_{ij}^{o}) = log(k) + \alpha . log(P_i) + \beta . log(P_j) - \gamma . log(d_{ij}) \quad (10)$$

$$Y = A + \alpha . X_1 + \beta . X_2 - \gamma . X_3 \quad (11)$$

The multiple regression analysis carried out gave the goodness of fit value (r square value) as 0,759643. In addition, with this regression analysis performed, the calibration constants of α, β and γ were obtained as 0,635516, 0,635516 and 1,08475, respectively. The constant of k was also found as 0,0030408 from this analysis. By placing these constants into the equation which is given above and estimates the number of bus travels made among provinces depending on their populations and the distances between them, the initial matrix was obtained for the bus journeys.

Table 1. The daily bus runs that were made from Istanbul and Ankara to some provinces reciprocally

Origin Province Name	Destination Province Name	Daily Bus Runs	Origin Province Name	Destination Province Name	Daily Bus Runs	Origin Province Name	Destination Province Name	Daily Bus Runs
Istanbul	Ankara	95	Ankara	Karabuk	33	Ankara	Corum	45
Istanbul	Izmir	104	Ankara	Kutahya	12	Ankara	Ardahan	1
Istanbul	Adana	13	Ankara	Malatya	6	Ankara	Aksaray	53
Istanbul	Antalya	30	Ankara	Mardin	4	Ankara	K.Maras	9
Istanbul	Trabzon	20	Ankara	Nevsehir	15	Ankara	Kayseri	48
Istanbul	Erzurum	15	Ankara	Samsun	26	Ankara	Diyarbakir	8
Istanbul	Kars	10	Ankara	Sanliurfa	4	Ankara	Canakkale	13
Istanbul	Igdir	5	Ankara	Tekirdag	5	Ankara	Gaziantep	13
Istanbul	Edirne	30	Ankara	Yozgat	32	Ankara	Amasya	11
Istanbul	Çanakkale	35	Ankara	Trabzon	14	Ankara	Aydin	31
Istanbul	Mersin	12	Ankara	Sinop	3	Ankara	Batman	3
Istanbul	Tekirdag	80	Ankara	Sivas	17	Ankara	Bayburt	2
Istanbul	Bursa	57	Ankara	Eskisehir	32	Ankara	Bingol	2
Istanbul	Diyarbakir	13	Ankara	Van	7	Ankara	Karaman	3
Istanbul	Van	10	Ankara	Yalova	6	Ankara	Isparta	11
Istanbul	Konya	27	Ankara	Adana	21	Ankara	Konya	69
Istanbul	Malatya	15	Ankara	Sakarya	16	Ankara	Hatay	18
Istanbul	Kayseri	23	Ankara	Adiyaman	2	Ankara	Bursa	39
Istanbul	Elazig	7	Ankara	Agri	4	Ankara	Balikesir	21
Istanbul	Samsun	30	Ankara	Rize	4	Ankara	Giresun	7
Istanbul	Sivas	26	Ankara	Edirne	6	Ankara	Kocaeli	21
Istanbul	Gaziantep	20	Ankara	Siirt	2	Ankara	Sirnak	1
Istanbul	Sakarya	57	Ankara	Ordu	9	Ankara	Kirklareli	2
Istanbul	Izmit	104	Ankara	Nigde	14	Ankara	Erzincan	4
Istanbul	Zonguldak	28	Ankara	Kirsehir	40	Ankara	Erzurum	5
Istanbul	Yalova	10	Ankara	Kastamonu	26			

Thus, by entering the aforementioned initial matrix generated by the Gravity Model and the number of passengers travelling by bus on highway and motorway links into Vmat subprogram, the daily interprovincial bus travel matrix for the year of 2013 was obtained in terms of number of passengers. The number of passengers travelling by bus on highway links was found by multiplying the bus Average Annual Daily Traffic (AADT) values with the number of 30 passengers per bus that is the average bus occupancy rate. On the other hand, in addition to bus, there is another vehicle group used for commercial interprovincial passenger transportation in vehicle classification scheme of the General Directorate of Highways (KGM). This vehicle group is Medium Loaded Commercial Vehicle and includes vehicles with 14-25 person passenger capacity and trucks with 3,5-10 tons loaded weight. Even though the percentages of small buses and small trucks in this vehicle group change among highway sections, it has been learned from KGM that the 30 percent of medium loaded commercial vehicles consists of small buses with 14-25 person passenger capacity in average. Thus, in order to find the number of small buses on highway links, the number of medium loaded commercial vehicles was multiplied by the value of 0,30. Furthermore, it was assumed in this study that small buses carry 18 passengers per bus in average. Therefore, in order to find the number of passengers travelling by small buses on

highway links, the number of small buses was multiplied with the number of 18 passengers per bus. Then, this number was added into the number found for normal bus in every highway section. Finally, since AADT values given for the bus in Traffic and Transportation Statistics were the sum of the two sides and it was thought that the daily intercity bus journey matrix should be symmetrical, half of these values were taken [7].

Table 2. The populations of provinces for the year of 2013

Prov. Traf. Code	Province Name	Province Population	Prov. Traf. Code	Province Name	Province Population	Prov. Traf. Code	Province Name	Province Population
1	Adana	2.149.260	28	Giresun	425.007	55	Samsun	1.261.810
2	Adiyaman	597.184	29	Gumushane	141.412	56	Siirt	314.153
3	Afyon	707.123	30	Hakkari	273.041	57	Sinop	204.568
4	Agri	551.177	31	Hatay	1.503.066	58	Sivas	623.824
5	Amasya	321.977	32	Isparta	417.774	59	Tekirdag	874.475
6	Ankara	5.045.083	33	Icel	1.705.774	60	Tokat	598.708
7	Antalya	2.158.265	34	Istanbul	14.160.467	61	Trabzon	758.237
8	Artvin	169.334	35	Izmir	4.061.074	62	Tunceli	85.428
9	Aydin	1.020.957	36	Kars	300.874	63	Sanlıurfa	1.801.980
10	Balikesir	1.162.761	37	Kastamonu	368.093	64	Usak	346.508
11	Bilecik	208.888	38	Kayseri	1.295.355	65	Van	1.070.113
12	Bingol	265.514	39	Kirklareli	340.559	66	Yozgat	444.211
13	Bitlis	337.156	40	Kirşehir	223.498	67	Zonguldak	601.567
14	Bolu	283.496	41	Kocaeli	1.676.202	68	Aksaray	382.806
15	Burdur	257.267	42	Konya	2.079.225	69	Bayburt	75.620
16	Bursa	2.740.970	43	Kutahya	572.059	70	Karaman	237.939
17	Canakkale	502.328	44	Malatya	762.538	71	Kirikkale	274.658
18	Cankiri	190.909	45	Manisa	1.359.463	72	Batman	547.581
19	Corum	532.080	46	K.Maras	1.075.706	73	Sirnak	475.255
20	Denizli	963.464	47	Mardin	779.738	74	Bartin	189.139
21	Diyarbakir	1.607.437	48	Mugla	866.665	75	Ardahan	102.782
22	Edirne	398.582	49	Muş	412.553	76	Igdir	190.424
23	Elazig	568.239	50	Nevsehir	285.460	77	Yalova	220.122
24	Erzincan	219.996	51	Nigde	343.658	78	Karabuk	230.251
25	Erzurum	766.729	52	Ordu	731.452	79	Kilis	128.586
26	Eskisehir	799.724	53	Rize	328.205	80	Osmaniye	498.981
27	G.Antep	1.844.438	54	Sakarya	917.373	81	Duzce	351.509

In the case that two provinces are connected to each other by both highway and motorway, the sum of the bus AADT values on highway and motorway has been taken as the bus AADT value of highway section between these two provinces. Because vehicles on motorway sections were divided into two classes as the light and heavy vehicles, 13 percent of the heavy vehicles were assumed to be bus in determining the bus AADT value on motorway links. For calculating this percentage, at first, the number of buses and small buses on all significant highway sections was divided into the sum of the number of buses, small buses, trucks and trailers on these sections, and then, the arithmetic average of these ratios was taken. From here, it has been reached the result that buses compose approximately 13 percent of the heavy vehicle traffic on highways. With a rough approach, it has been assumed that this ratio is the same on motorways. Then, the number of heavy vehicles on motorway sections was multiplied by this ratio in order to find the number of buses and small buses on these sections. For motorways, the number of buses and small buses on motorway links was also divided by two because AADT values given for motorway sections were the sum of the two sides. On the other hand, in order to find the average bus occupancy rate for motorway links, a similar approach has also been followed. To this end, at first, the number of small buses on all significant highway sections was divided into the sum of the number of buses and small buses on these sections, and then, the arithmetic average of these ratios

were taken. From this analysis, it has been found that 48 percent of buses are small buses. From here, it has been also determined that normal buses compose 52 percent of buses. As a result, by multiplying these percentages with the average bus occupancy rates of small and normal buses and by summing up these values, the average bus occupancy rate for motorway links was found as 24 passengers per bus. Finally, this number was multiplied by the bus AADT values for motorway links in order to find the number of passengers travelling by bus on motorway links.

Thus, using the initial matrix constructed by the gravity model mentioned before and the numbers of passengers travelling by bus on highway sections for the year of 2013 given as average annual daily passenger number, the interprovincial bus travel matrix for the year of 2013 was obtained. The numbers of passengers travelling by bus on highway sections for the year of 2013 that have been used to determine the O-D matrix are summarized in Table 3 [7].

Table 3. The numbers of passengers traveling by bus on highway sections as the sum of both directions

Sec. No.	Highway Section	Number of Passen.	Sec. No.	Highway Section	Number of Passen.	Sec. No.	Highway Section	Number of Passen.
1	Burdur-Isparta A.	13.396	43	Erzurum-Tortum	3.178	85	Antalya-Burdur	9.430
2	Marmara E.-Tekirdag	26.980	44	Ordu-Samsun	20.499	86	Antalya-Isparta	5.236
3	Babaeski-Luleburgaz	34.942	45	Agri-Patnos	1.843	87	Konya-Manavgat	5.663
4	Gelibolu-Kesan	9.155	46	Igdir-D.Beyazit	2.196	88	Havsa-Babaeski	12.588
5	Lapseki-Bandırma	6.473	47	Elazig-Kovancilar	4.785	89	Tarsus-Adana	59.130
6	Izmit-Istanbul	140.747	48	Aksehir-Isparta	3.953	90	Adana-Toprakkale	34.697
7	Izmir-Manisa	38.162	49	Bayburt-Gumushane	2.613	91	T.Kale-Iskenderun	32.620
8	Izmit-Adapazarı	65.376	50	Gumushane-Trabzon	5.807	92	Osmaniye-Nurdagi	34.674
9	Duzce-Bolu	43.545	51	Usak-Salihli	15.955	93	Bingöl-Mermer	1.135
10	Duzce-Zonguldak	8.171	52	Afyon-Usak	17.837	94	Narli-K.Maras	6.953
11	Duzce-Adapazari	44.068	53	Afyon-Kutahya	17.306	95	Horasan-Agri	3.106
12	Narli-Golbaşi	6.685	54	Kutahya-Eskişehir A.	20.890	96	Mardin-Midyat	1.747
13	Karabuk-Bartin	2.078	55	İnegol-Bozuyuk	23.074	97	Tanyeri-Tunceli	718
14	Caycuma-Bartin	6.955	56	Cay-Aksehir	13.614	98	Ardahan-Kars	1.723
15	Ilgaz-Kastamonu	2.617	57	Konya-Aksaray	9.478	99	Kalecik-Cankiri	4.754
16	Bayburt-Askale	2.233	58	Konya-Cakmak	9.502	100	Cankiri-Iskilip	887
17	Gerede-Eskipazar	24.625	59	Karaman-Çakmak	1.855	101	Merzifon-Corum	11.095
18	Karabuk-Kastamonu	5.430	60	Konya-Karaman	4.082	102	Tokat-Turhal	9.620
19	Kastamonu-Boyabat	2.984	61	Ulukisla-Nigde	6.766	103	Kirikkale-Kirsehir	14.342
20	Sinop-Samsun	1.493	62	Nigde-Kayseri	5.825	104	Aksaray-Cakmak	14.715
21	Havsa-Samsun	22.366	63	Aksaray-Nevsehir	10.016	105	Kayseri-Pinarbasi	10.261
22	Ordu-Giresun	18.172	64	Nigde-Nevsehir	2.930	106	Mus-Haskoy	3.085
23	Giresun-Trabzon	14.491	65	Kayseri-Yozgat	3.925	107	Refahiye-Erzincan	8.003
24	Trabzon-Rize	13.748	66	Malatya-Dogansehir	5.054	108	Usak-Civril	2.372
25	Rize-Hopa	8.737	67	Gaziantep-Sanliurfa	28.794	109	Erzincan-Kose	1.291
26	Artvin-Ardahan	1.070	68	Adiyaman-Sanliurfa	1.934	110	Tercan-Askale	6.706
27	Igdir-Kars	2.335	69	Sanliurfa-Senyurt	5.388	111	Ankara-Kulu	24.161
28	Koprukoy-Horasan	6.781	70	Siverek-Diyarbakir	6.664	112	Denizli-Dinar	14.329
29	Canakkale-Edremit	6.575	71	Mersin-Erdemli	7.870	113	Sivrihisar-Ankara	23.515
30	Akhisar-Balikesir	17.003	72	Diyarbakir-Çinar	10.027	114	Dinar-Afyon	17.244
31	Balikesir-Susurluk	27.137	73	Sirnak-Siirt	1.018	115	Gaziantep-Kilis	3.497
32	Bursa-Yalova	38.425	74	Batman-Kurtalan	2.314	116	Sivas-Yildizeli	7.809

33	Bilecik-Adapazarı	15.632	75	Bitlis-Baykan	4.367	117	Delice-Ankara	33.203
34	Ankara-Gerede	19.867	76	Bitlis-Gevas	3.370	118	Kirsehir-Mucur	11.060
35	Delice-Corum	14.561	77	Gevas-Hakkari	1.797	119	Bozuyuk-Eskisehir	21.551
36	Kayseri-Sarkişla	5.673	78	Izmir-Aydin	33.868	120	Yerkoy-Yozgat	5.682
37	Sivas-Kangal	2.047	79	Aydin-Denizli	18.705	121	Yalova-Izmit	44.677
38	Malatya-Elazig	8.181	80	Denizli-Salihli	3.551	122	Hakkari-Sirnak	491
39	Elazig-Diyarbakır	3.057	81	Boyabat-Havsa	1.234	123	Denizli-Mugla	2.438
40	Silvan-Mermer	1.358	82	Aydin-Muğla	15.304	124	Karabuk-Eskipazar	7.333
41	Bingol-Mus	3.178	83	Altinyayla-Muğla	5.155	125	Nevsehir-Kayseri	9.203
42	Bingol-Erzurum	2.200	84	Altinyayla-Denizli	6.859			

4.DEVELOPING A GRAVITY BASED TRIP DISTRIBUTION MODEL FOR INTERPROVINCIAL BUS TRAVELS IN TURKEY

After the interprovincial bus travel matrix was found by using Vmat subprogram, the statistical analysis was also performed for the O-D information derived from this matrix. In order to model the interprovincial bus travels, the multivariate statistical analysis was carried out by using Microsoft Excel. The correlation coefficient between variables was determined by Pearson method. For the significance levels of the parameters, it was assumed that p must be smaller than 0,05 ($p < 0,05$). In this regression analysis, as the interprovincial bus travels were used as the dependent variable, the populations of the provinces and the distances between them were taken as the independent variables. Before performing the multivariate statistical analysis, the relationship between variables was determined by carrying out the analysis of variance-covariance. As a result of this analysis, it was determined that the relationship between the parameters is not linear as in the initial matrix and is as follows:

$$T_{ij} = k\frac{P_i^{\alpha} P_j^{\beta}}{d_{ij}^{\gamma}} \qquad (12)$$

where

T_{ij} :the daily bus travels made from province i to province j,

P_i : the population of province i,

P_j : the population of province j,

k : a coefficient,

d_{ij}^{γ} : the distance between province i and province j,

α, β and γ : the calibration constants.

The equation given above was linearized by taking the logarithm of both sides. All the parameters used in the analysis are quantitative. In order to identify the interprovincial bus travels, the multivariate statistical analysis was performed by using Microsoft Excel, and the coefficients of the independent variables were determined. First, by performing analysis of variance, it was tested whether or not there is a linear relationship between the dependent variable and the set of dependent variables [8]. For this analysis, F test was carried out, and it was found that the result is meaningful. The significance levels of the parameters were tested by the student t-test, and the significance levels were found to be smaller than 0,05. The results of this analysis are given in Table 4 below.

The coefficients of independent variables obtained from this regression analysis were then used as the calibration constants of the trip distribution model. Finally, by placing these constants in the equation of the trip distribution model, the gravity based trip distribution model was developed, and a second matrix for bus travels was obtained. The cells of this matrix show the number of interprovincial bus travels that the gravity based trip distribution model estimate ($\overline{T_{ij}}$).

Table 4. The results of the multivariate regression analysis

Independent Variables	b_i	p (<0,05)	R^2
Origin Population	0,678478	0,00	
Destination Population	0,678684	0,00	0,582039
Distance	1,47925	0,00	
Constant ($1/10^{bi}$)	0,003833	0,00	

The results obtained from the model developed by using the multiple regression method to predict the bus travels made between provinces are given in Table 5 for comparison with the observed daily bus journeys found by Vmat Subprogram for some province pairs. In addition, these results obtained from the model developed by using the multiple regression method were evaluated by using the statistics of the root mean square error (RMSE). As it is known, the statistics of RMSE is defined as follows: $RMSE = \sqrt{\frac{1}{n}\sum_{i=1}^{n}\left(T_{ij} - \overline{T_{ij}}\right)^2}$ (13)

where

T_{ij} : the observed daily bus travels made from province i to province j, that was found by Vmat Subprogram, $\overline{T_{ij}}$: the daily bus travels made from province i to province j, that was estimated by the gravity based trip distribution model.

Table 5. The bus travels obtained from the gravity based trip distribution model and the observed bus travels for some pairs of provinces

		1	6	16	25	34	35	38	42	44	55
Adana (1)	**Observed**	0	945	173	5	469	210	418	367	31	59
	Regression Model	0	282	84	37	216	100	192	254	114	59
Ankara (6)	**Observed**	947	0	664	55	809	551	491	1.561	107	227
	Regression Model	281	0	484	59	1.111	347	393	745	94	246
	Observed	175	673	0	5	6.191	287	141	302	45	21
Bursa (16)	**Regression Model**	84	484	0	23	1.810	538	80	182	31	68
	Observed	5	56	6	0	113	28	41	40	28	92
Erzurum (25)	**Regression Model**	37	59	23	0	72	24	38	30	45	36
	Observed	461	794	6.070	108	0	1.318	183	358	60	430
Istanbul (34)	**Regression Model**	216	1.111	1.809	72	0	717	210	349	85	219
	Observed	210	551	284	27	1.328	0	183	347	63	78
Izmir (35)	**Regression Model**	100	347	538	24	717	0	78	206	33	60
	Observed	420	493	140	40	187	183	0	354	98	48
Kayseri (38)	**Regression Model**	192	393	80	38	210	78	0	226	99	88
	Observed	369	1.566	300	39	359	349	355	0	76	138
Konya (42)	**Regression Model**	254	745	182	30	349	206	226	0	53	68
	Observed	32	107	45	28	61	63	98	75	0	31
Malatya (44)	**Regression Model**	114	94	31	45	85	33	99	53	0	41
	Observed	59	227	21	91	441	78	48	137	31	0
Samsun (55)	**Regression Model**	59	246	68	36	219	60	88	68	41	0

As it will be understood from the above expression, the daily bus travels made between provinces were taken as the observed values, and the journeys estimated by the gravity based trip distribution model were checked in terms how close to these values. The RMSE statistics of the gravity based trip distribution model was found as 311,10. As it can be seen from Table 5, through the model developed by the multiple regression method, the results that were far from the observed values have been found in estimating the large number of bus travels made between provinces that are especially located in Western Turkey.

5.CONCLUSION

In this study, the model that is one of the methods proposed for estimating travel matrix from traffic counts and developed by Bell in 1983 has been used in finding the O-D matrix related to interprovincial bus travels in Turkey for the year of 2013. After the matrix related to interprovincial bus travels was found, the multiple regression analysis was performed by using the O-D information obtained from this matrix. In this analysis, as the interprovincial bus travels were used as the dependent variable, the populations of the provinces and the distances between them were taken as the independent variables. The coefficients of independent variables obtained from this regression analysis were then used as the calibration constants of the trip distribution model. Finally, by placing these constants in the equation of the trip distribution model, the gravity based trip distribution model was developed.

The results obtained from the model developed by using the multiple regression method were evaluated by using the statistics of RMSE. The RMSE statistics of the gravity based trip distribution model was found as 302,36. In addition, it was seen that the model developed by the multiple regression method could not estimate well the large number of bus travels made between provinces that are especially located in Western Turkey. On the other hand, the multiple regression methods allow incidents occurred to be expressed mathematically. They also make it possible to examine the cause-effect relationships in detail.

REFERENCES

[1]. M. G. H. Bell, "The Estimation of Origin-Destination Flows and their Confidence Intervals from Measurements Link Volumes: a Computer Program," Traffic and Engineering Control 24, pp.202 – 205, 1983.
[2]. M. G. H. Bell, "The Estimation of an Origin-Destination Matrix from Traffic Counts," Transportation Science 17, pp. 198-217, 1983.
[3]. J. de D Ortuzar and L. G. Willumsen, Modelling Transport, 1st ed., New York, USA: John Wiley and Sons Inc., 1990.
[4]. Transport User Guide, Micro Computer Transportation Planning Package, Halcrow Fox and Associates, London, England, 1986.
[5]. "The data sheet of the daily bus runs made from Istanbul and Ankara to some provinces," Coacher Federation of Turkey, Istanbul, Turkey.
[6]. (2016) Turkish Statistical Institute website. [Online]. Available: www.tuik.gov.tr

[7]. Traffic and Transportation Survey (2013), Transportation Studies Directorate, Republic of Turkey General Directorate of Highways, Ankara, Turkey, 2014.
[8]. N. R. Draper and H. Smith, Applied Regression Analysis, 2nd ed., New York, USA: John Wiley and Sons Inc., 1981.

BIYOGRAPY

Yasar Vitosoglu was born in Eskisehir in 1969. He completed his primary and secondary education in the same city. In 1986, he entered Istanbul Technical University in order to study Civil Engineering. He completed his undergraduate education here in 1990. He was sent to the United States by the Ministry of National Education in 1995 to get a master's degree. He returned to Turkey after completing his master's degree at University of Wisconsin in 1997. In the same year, he was appointed to Dumlupinar University as a research assistant.

He began his doctoral studies in Transportation Engineering program at Istanbul Technical University in 1998. He got his PhD degree in 2006. Since 2007, he has been working as an assistant professor at Dumlupinar University.

Prediction of Chronic Kidney Disease Using an Artificial Neural Network

Ilker Ali Ozkan[1]

Abstract

Chronic renal failure is a long-term disease which inflicts damages on kidneys and prevents the normal duties of kidneys. This disease can result in serious complications such as high blood pressure, anemia, bone disease and cardiovascular diseases. In this study, a prediction model is developed for a common disease; chronic renal failure by using an artificial neural network which is a computer-based technology and recognizes the relationship between the output variable and input variables with non-linear statistics. The patients age, their blood and biochemical values, and 24 input data which consists of various chronic diseases are used for the estimation process. The input data have been subjected to preprocessing because they contain both missing values and nominal values. 147 patient data which was obtained from the preprocessing have been divided into as 70% training and 30% testing data. As a result of the study, artificial neural network model with 25 neurons in the hidden layer has been found as the model with the lowest error value. Chronic kidney failure disease has been able to be estimated accurately at the rate of 99.3% using this artificial neural network model. The developed artificial neural network has been found successful for the estimation of chronic kidney failure disease using clinical data.

Keywords: *Prediction, Artificial neural Network, chronic Kidney disease, disease diagnosis*

1.INTRODUCTION

Chronic renal failure (CRF) can be defined as advancing and chronic degradation state in kidney's metabolical and endocrine functions and its ability to adjust liquid solution balance resulting from decrease in glomerular filtration values [1, 2]. CRF, a long run disease, hinders the normal functions of kidneys and damages the kidneys [2-5]. The diagnosis of the disease is made by long run monitoring (more than three months) of urine albumin discharge and/or considerable decrease in kidney functionality. The disease also may also cause hypertension, anemia, bone diseases and heart and vascular diseases [6-8].

CRF is caused by diabetes, hypertension, nephritises, urological dysfunctionalities and cystic kidney diseases. Until the last phased of CRF, illness generally does not give any open and characteristic clues about the problem. For this reasons, diagnose can only be made by blood and urine tests containing measurement of creatine in blood, and calculation of glomerular filtration ratio (GFR), and observation of protein and albumin in the blood. Additionally with ultrasonographic surveys, structural kidney anomalies can be located [1-3].

Lately, the use different classification techniques in biomedical disease diagnosis become a common practice. With computer-based classification techniques near correct results are obtained. However, speed, accuracy and definitive diagnosis classification methods are became necessity. In the diagnosis of CRF, expert systems, fuzzy logic and artificial neural networks and similar methods are used in the literature studies [9-11].

Artificial Neural Networks (ANN) are developed a computer system aiming to simulate a human brain's capabilities of inventing and deriving new information, producing new understanding by means of learning and realizing it automatically without getting any outside help. To realize these abilities by using traditional programming techniques are either impossible or extremely difficult. For this reason, about artificial neural networks, it can be said that ANN is a scientific sub-field of computer science which is developed for impossible or extremely hard programming circumstances and interested in adaptive data processing [12, 13].

In this study, a chronic kidney disease (CKD) diagnose system based on artificial neural networks which is the most preferred soft computing method in the literature is developed. With the help of the system by using CRF related data gathered from various people, chronic kidney failure disease is estimated.

2.MATERIAL METHODS

In the realized study, an estimation of chronic renal failure diseases by using an ANN-based method. Data used for the estimation of the chronic kidney failure is gathered from UCI Machine Learning Repository database of "Early stage of Indians Chronic Kidney Disease" data set [14].

2.1.Dataset

As the data used in this study, CRF disease data set of the UCI machine learning Repository database is used. In this data set, data belongs to 250 CRF patients and 150 non-CRF patients total of 400 real experimental subjects. In the data set there are 24

[1] *Corresponding author: Selcuk University, Department of Computer Engineering, 42030, Konya, Turkey. ilkerozkan@selcuk.edu.tr*

different patient property are collected and laboratory work is performed and these properties are given in detail in Table 1 [14].

Table 4. CRF Data Set Properties

Attribute	Description
Age(numerical)	age in years
Blood Pressure(numerical)	bp in mm/Hg
Specific Gravity(nominal)	sg - (1.005,1.010,1.015,1.020,1.025)
Albumin(nominal)	al - (0,1,2,3,4,5)
Sugar(nominal)	su - (0,1,2,3,4,5)
Red Blood Cells(nominal)	rbc - (normal,abnormal)
Pus Cell (nominal)	pc - (normal,abnormal)
Pus Cell clumps(nominal)	pcc - (present,notpresent)
Bacteria(nominal)	ba - (present,notpresent)
Blood Glucose Random(numerical)	bgr in mgs/dl
Blood Urea(numerical)	bu in mgs/dl
Serum Creatinine(numerical)	sc in mgs/dl
Sodium(numerical)	sod in mEq/L
Potassium(numerical)	pot in mEq/L
Hemoglobin(numerical)	hemo in gms
Packed Cell Volume(numerical)	
White Blood Cell Count(numerical)	wc in cells/cumm
Red Blood Cell Count(numerical)	rc in millions/cmm
Hypertension(nominal)	htn - (yes,no)
Diabetes Mellitus(nominal)	dm - (yes,no)
Coronary Artery Disease(nominal)	cad - (yes,no)
Appetite(nominal)	appet - (good,poor)
Pedal Edema(nominal)	pe - (yes,no)
Anemia(nominal)	ane - (yes,no)
Class (nominal)	class - (ckd,notckd)

2.2.Artificial Neural Networks

Artificial Neural Networks is an artificial intelligence approach which aims to simulate to work of the human brain. It is one of the most preferred methods to use in classification problems. The biological structure of the human brain cells are the basis of the constructed ANN structure. In ANN, like our brain there are learning mechanism and decision-making mechanism based on learned knowledge [15-17].

In today's artificial intelligence networks, there are networks and learning models like Perceptron, Adaline, Multi-Layered Perceptron Model (Error Back Propagation), Vector Quantization Problem, Hopfield Networks and Elman Network [15]. Generally, in ANN network structures, according to the input values and corresponding output values, weight values are automatically changed by using the rules determined by chosen training method. After completion of training data, trained network can estimate the result of the given input data according to lastly set network weight values. In this study, Multi-Layered Perceptron Model is used. Forward feed, back propagated a Multi-Layered Network Model can be seen in Figure 1.

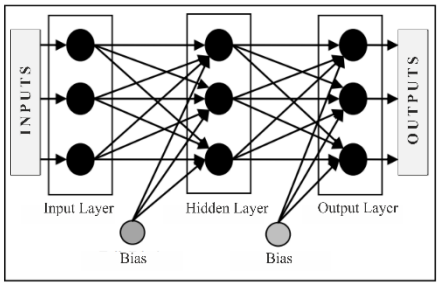

Figure 6. Multi-Layered Perceptron ANN Model

ANN developed in the content of the study is used for classification of CRF disease. In some of the records, some data are missing in the dataset. Because there is enough number of recorded data and some missing data includes categorized data, data is pre-processed before utilization. Data cleaning process are performed on the data to delete records with missing data. After preprocessing, ANN training is completed by using 147 patient records.

Classification process is realized by Artificial Neural Networks by using MATLAB software. By using Heuristic Research techniques 25 neuron hidden layer formation is used in ANN study structure. Levenberg-Marquart algorithm is used as training technique. Performance of the network is measured by applying mean square error (MSE) and regression rules.

Dataset consisting of 147 CRF patients is grouped into two sets, 70% of the set is used in ANN training phase and 30% of the set is used as the performance test data. Information about the developed network structure for the system is given in the Figure 2.

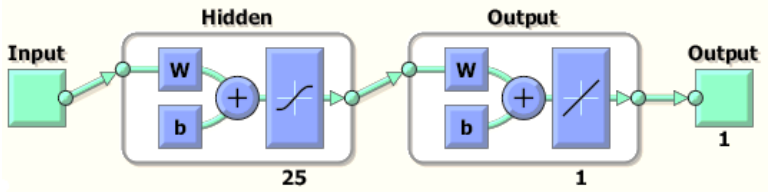

Figure 7. ANN structure used in this study

Most successful results are obtained for epoch 1000. To realize performance analysis after the test process accuracy percentage and percentage error criterion is taken as basis. Used ANN is determined to classify incorrectly only one patient in 147 patients. If all patient data is considered, correct classification percentage is 99.3 and incorrect classification percentage is 0.07%.

3.CONCLUSION AND SUGGESTIONS

The realized ANN by using the data is obtained by preprocessing is applied to full data set and estimated results are obtained for all patients. The ANN that was devised classified in total 380 of the 400 data as successful. The confusion matrix obtained through all of the training and test datasets is given in Table 2.

Table 5. Confusion matrix

	Data of reference		
Classification	**Sick**	**Healthy**	**Sum of rows**
Sick	222 (A)	11 (B)	233
Healthy	9 (C)	158 (D)	167
Sum of columns	231	169	**400**

When the diagnostic test conducted on all of the data in Table 2 is examined, the following results are reached: Sensitivity is the ability to distinguish the sick from the true ill.

$$Sensitivity = \frac{A}{A+C} \quad (1)$$

From Eq. 1, sensitivity was found to be = 0.9610. Specificity is the ability to distinguish the healthy from the true healthy.

$$\text{Specificity} = \frac{D}{D+B} \quad (2)$$

From Eq.2, specificity was found to be = 0.9349. Accuracy is the test's total accurate diagnoses of the sick and the healthy

$$\text{Accuracy} = \frac{A+D}{A+B+C+D} \tag{3}$$

From Eq. 3, accuracy was found to be = 0.9500. The positive predictive value of the result (PPV) is the probability of being truly sick when the diagnostic test passes the judgment of sick.

$$PPV = \frac{A}{A+B} \tag{4}$$

From Eq. 4, PPV was found to be= 0.9527. The negative predictive value of the result (NPV) is the probability of being really sick when the diagnostic test passes the judgment of healthy.

$$NPV = \frac{D}{D+C} \tag{5}$$

From Eq. 5, NPV was found to be= 0.9461. The achievement of the test can be determined by examining the ROC curves. In a successful test, the area that remains under the curves is expected to be large. The ROC curve for the dataset for all patients is given in Figure 3.

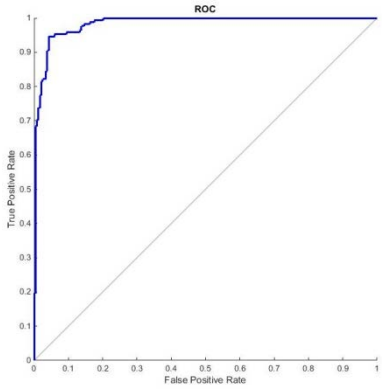

Figure 8. Graph for the ROC analysis of all patients' data

According to the results of Confusion matrix analysis, it is observed that the rate of distinguishing the sick from the true sick is 96.10 %, the ability to distinguish the healthy from the true healthy is 93.49% and the rate of total accurate diagnoses of sick and healthy is 95.00 %. Accordingly, when the ANN predictive value passes the judgment of sick, the probability of being truly sick is 95.27 %. Likewise, when the ANN predictive value passes the judgment of healthy, the probability of being truly healthy is 94.61 %.

According to ROC analysis, the area that remains under the ROC curve is 0.9833 for the ANN all dataset (Figure 3). The fact that these areas are large (close to 1) indicates that the study that was conducted was successful in predicting CKD.

When above analysis results are examined, obtained ANN model can successfully estimate CKD using both preprocessed patient data and incomplete patient data set. Clinical Decision Support System by using the obtained model CKD can be diagnosed quickly and with high accuracy.

Moreover increase the CKD estimation rate of the success, different preprocessing techniques and different classification can be developed for this study.

ACKNOWLEDGMENT

I thank Prof. Dr. Ünal SERT of Necmettin Erbakan University, Faculty of Medicine, and Department of Urology of the faculty for help and assistance for this study.

REFERENCES

[1]. M. H. Tanriverdi, A. Karadag, and E. Hatipoglu, "Chronic Kidney Failure," *Konuralp Tip Dergisi*, vol. 2, pp. 27-32, 2010.
[2]. M. S. Parmar, "Chronic renal disease," *British Medical Journal*, vol. 325, p. 85, 2002.
[3]. (2016). *Böbrek yetmezliği başlangıcı, belirtileri, nedenleri ve tedavisi*. Available: https://www.medikalakademi.com.tr/kronik-bobrek-yetmezligi-baslangic-belirtileri-tani-tedavisi/
[4]. R. G. Luke "Chronic Renal Failure — A Vasculopathic State," *New England Journal of Medicine*, vol. 339, pp. 841-843, 1998.
[5]. G. Grassi, F. Quarti-Trevano, G. Seravalle, F. Arenare, M. Volpe, S. Furiani, *et al.*, "Early sympathetic activation in the initial clinical stages of chronic renal failure," *Hypertension*, vol. 57, pp. 846-851, 2011.
[6]. V. M. Campese and E. Kogosov, "Renal afferent denervation prevents hypertension in rats with chronic renal failure," *Hypertension*, vol. 25, pp. 878-882, 1995.
[7]. J. W. Eschbach, M. H. Abdulhadi, J. K. Browne, B. G. Delano, M. R. Downing, J. C. Egrie, *et al.*, "Recombinant human erythropoietin in anemic patients with end-stage renal disease: results of a phase III multicenter clinical trial," *Annals of internal medicine*, vol. 111, pp. 992-1000, 1989.

[8]. P. S. Parfrey and R. N. Foley, "The clinical epidemiology of cardiac disease in chronic renal failure," *Journal of the American Society of Nephrology*, vol. 10, pp. 1606-1615, 1999.
[9]. A. E. Gaweda, A. A. Jacobs, M. E. Brier, and J. M. Zurada, "Pharmacodynamic population analysis in chronic renal failure using artificial neural networks—a comparative study," *Neural networks*, vol. 16, pp. 841-845, 2003.
[10]. J. D. M. n. Guerrero, E. S. Olivas, G. C. Valls, A. J. S. López, J. J. P. Ruixo, and N. V. c. J. Torres, "Use of neural networks for dosage individualisation of erythropoietin in patients with secondary anemia to chronic renal failure," *Computers in biology and medicine*, vol. 33, pp. 361-373, 2003.
[11]. A. Akgundogdu, S. Kurt, N. Kilic, O. N. Ucan, and N. Akalin, "Diagnosis of renal failure disease using adaptive neuro-fuzzy inference system," *Journal of medical systems*, vol. 34, pp. 1003-1009, 2010.
[12]. S. Agatonovic-Kustrin and R. Beresford, "Basic concepts of artificial neural network (ANN) modeling and its application in pharmaceutical research," *Journal of pharmaceutical and biomedical analysis*, vol. 22, pp. 717-727, 2000.
[13]. D. F. Specht, "A general regression neural network," *Neural Networks, IEEE Transactions on*, vol. 2, pp. 568-576, 1991.
[14]. P.Soundarapandian.M.D., "Chronic Kidney Disease Dataset," ed. UCI Machine Learning Repository, 2015.
[15]. E. ÖZTEMEL, *Yapay Sinir Ağlari*. İstanbul: Papatya 2003.
[16]. K. K. Çevık and E. Dandil, "Yapay Sinir Ağları İçin Net Platformunda Görsel Bir Eğitim Yazılımının Gelistirilmesi," *International Journal of InformaticsTechnologies*, vol. 5, 2012.
[17]. D. Karaboğa, "YAPAY ZEKÂ OPTİMİZASYON ALGORİTMALARI," 2014.

ICENS
INTERNATIONAL CONFERENCE ON ENGINEERING AND NATURAL SCIENCES
24-28 May 2016 /Sarajevo

Implementation of Special Cases for RSA Algorithm Where Plaintext is Equal to Ciphertext in Java

Mustafa Kocakulak[1], Turgay Temel[2]

Abstract

RSA is an asymmetric key cryptographic algorithm which is named after its inventors, Rivest, Shamir and Adleman. It is widely in use and it has an indisputable importance in cryptography. The security of this algorithm depends on the difficulty of factoring a big composite number where this composite number is the multiplication of two or more prime numbers. In this study, RSA Algorithm is introduced. The special cases, where plaintext is equal to ciphertext despite the enciphering process, are examined and implemented in Java by using graphical user interface. Thus, the unexpected cases, where RSA Algorithm cannot provide expected confidentiality of enciphering, are clearly indicated for the set of chosen prime number couples. With Java implementation of the cases of equality of plaintext and ciphertext, the importance of working with long prime numbers is also seen and the need for padding in such cases is proven Java.

Keywords: *Ciphertext, Enciphering, Equality, Plaintext, Prime Number, RSA.*

1.INTRODUCTION

Cryptography is a way of providing security to any communication between the sender and the receiver in any insecure channel [1]. In the communication channel, one of the sides, who sends the message into the channel, is known as a sender and the other side, who receives the message, is known as a receiver. The sender and the receiver want to exchange information among themselves securely and secretly. Up to this point, there is no need to benefit from cryptography. However, when eavesdroppers start listening to this insecure channel to reach the shared information between the sender and the receiver, the confidentiality of the communication becomes vulnerable. In order to provide security features such as confidentiality and integrity etc. to the channel against the attacks of eavesdroppers, cryptography should be used [2]. Up to now, humankind always wanted to send messages which can only be understood by the intended receivers. Until 1980s, any message between the sender and the receiver was carried by using symmetric key cryptography where the sender and the receiver use the same key [3]. With the usage of personal computers, people started to use computers to send and to receiver their private data [4]. By using personal computers and mobile devices, people started to realize how important cryptography is for more secure communication. At this point, RSA Algorithm has arisen as one of the leading examples of asymmetric key cryptography where the sender and the receiver has two different keys each, as a public key and a private key [5]. RSA is an asymmetric key cryptographic algorithm that is named after its inventors, Rivest, Shamir and Adleman [6]. RSA Algorithm's security depends on the difficulty of factoring any big composite into its multipliers [7]. In this study, RSA Algorithm is analyzed in detail. Although RSA requires working on big composite numbers, this study focuses on the cases where multipliers of the composite numbers are chosen from a limited set and

elements of this set are small prime numbers. Thus, the importance of working with long prime numbers for the sake of cryptographic security is proven. In this study, special cases for RSA, where plaintext is equal to ciphertext despite the enciphering process, are examined. By using Java and its graphical user interface, the list of unexpected cases, where RSA cannot provide expected confidentiality of enciphering, are analyzed.

2. RSA ALGORITHM

In order to understand the mathematical ideas underlying RSA Algorithm and the special cases for RSA which is examined throughout this study, it is necessary to explain RSA Algorithm by using pseudo-code and a numeric example.

2.1.Pseudo-code of RSA

The steps of RSA Algorithm are listed below [8].

- Firstly, the sender and the receiver should agree on two different prime numbers, p and q.
- Secondly, encryption and decryption modulo, N, should be calculated by using Equation 1 given below.

$$N = p \times q \qquad (1)$$

[1] *Corresponding author: Bursa Technical University, Department of Mechatronics Engineering, 16330, Yıldırım/Bursa, Turkey.* mustafa.kocakulak@btu.edu.tr

[2] *Previously, Bursa Technical University, Department of Mechatronics Engineering .* turgaytemel@hotmail.com

- After that $Phi(N)$ should be calculated where $Phi(N)$ is used to find public key (N, e) and private key (N, d). It is calculated by using Equation 2.

$$Phi(N) = (p-1) \times (q-1) \quad (2)$$

- By using $Phi(N)$, d, the component of private key (N, d), is chosen where d is relatively prime with $Phi(N)$.
- After deciding on d value, the component of public key (N, e), e, is calculated by using Equation 3.

$$e \times d = 1 \pmod{Phi(N)} \quad (3)$$

- In order to encrypt any given message, M, in RSA, M should be between the values 0 and $N-1$.
- M is encrypted by using Equation 4 given below where C is a ciphertext.

$$C = M^e \pmod{N} \quad (4)$$

- Similarly, any ciphertext, C, is decrypted by using Equation 5 where M is plaintext.

$$M = C^d \pmod{N} \quad (5)$$

2.2.A numeric example

Here are the steps of a numeric RSA example:

- Suppose $p = 11$ and $q = 5$ which are prime numbers.
- $N = p \times q = 11 \times 5 = 55$ which is a composite number.
- $Phi(N) = (p-1) \times (q-1) = (11-1) \times (5-1) = 10 \times 4 = 40$.
- Suppose d is chosen as 23 where d and $Phi(N)$ are relatively prime. 23 and 40 do not have any common multiple except 1.
- Since $d = 23$ and it is relatively prime with $Phi(N) = 40$, Equation 3, which states $e \times d = 1 \pmod{Phi(N)}$, should be satisfied.
- Therefore, e is found as 7 where $7 \times 23 = 161 = 1 \pmod{40}$.
- As it is seen, the resulting e is relatively prime with $Phi(N) = 40$.
- Since message values can get values from 0 to $N-1 = 55-1 = 54$, we can choose any message value from this interval to encrypt.
- Suppose $M = 13$. It is chosen as 13 and it will be encrypted.
- $M = 13$ is encrypted as C where $C = 13^7 \pmod{55} = 7$.
- $C = 7$ is decrypted as M where $M = 7^{23} \pmod{55} = 13$.

3.SPECIAL CASES FOR RSA WHERE PLAINTEXT EQUALS TO CIPHERTEXT

It is known and expected that in any insecure channel, cryptography is used for converting any plaintext into a ciphertext. By this conversion, the security and the secrecy of plaintext should be provided since the ciphertext is expected to contain no relevant data with plaintext. However, for some cases in RSA encryption, plaintext can be equals to ciphertext [9]. These cases can be named as special cases for RSA because in such cases RSA does not provide secrecy to a communication despite encryption process. These special cases are against the spirit of encryption [9]. Therefore, it is necessary to focus on and analyze these cases in detail.

3.1.Implementation of special cases in Java

In this study, Java is used to implement RSA Algorithm. The PQ set, which is defined as $PQ = \{2, 3, 5, 7, 11, 13, 17, 19, 23, 29, 31, 37, 41, 43, 47\}$, is used to choose p and q values. Since PQ set contains 15 different small prime numbers, the resulting N values are also small composite numbers. The list of possible (p, q) couples are shown in Figure 1 below and this list contains 225 different (p, q) couples.

p,q	p,q	p,q	p,q	p,q	p,q	p,q	p,q	p,q	p,q	p,q	p,q	p,q	p,q	p,q
2,2	3,2	5,2	7,2	11,2	13,2	17,2	19,2	23,2	29,2	31,2	37,2	41,2	43,2	47,2
2,3	3,3	5,3	7,3	11,3	13,3	17,3	19,3	23,3	29,3	31,3	37,3	41,3	43,3	47,3
2,5	3,5	5,5	7,5	11,5	13,5	17,5	19,5	23,5	29,5	31,5	37,5	41,5	43,5	47,5
2,7	3,7	5,7	7,7	11,7	13,7	17,7	19,7	23,7	29,7	31,7	37,7	41,7	43,7	47,7
2,11	3,11	5,11	7,11	11,11	13,11	17,11	19,11	23,11	29,11	31,11	37,11	41,11	43,11	47,11
2,13	3,13	5,13	7,13	11,13	13,13	17,13	19,13	23,13	29,13	31,13	37,13	41,13	43,13	47,13
2,17	3,17	5,17	7,17	11,17	13,17	17,17	19,17	23,17	29,17	31,17	37,17	41,17	43,17	47,17
2,19	3,19	5,19	7,19	11,19	13,19	17,19	19,19	23,19	29,19	31,19	37,19	41,19	43,19	47,19
2,23	3,23	5,23	7,23	11,23	13,23	17,23	19,23	23,23	29,23	31,23	37,23	41,23	43,23	47,23
2,29	3,29	5,29	7,29	11,29	13,29	17,29	19,29	23,29	29,29	31,29	37,29	41,29	43,29	47,29
2,31	3,31	5,31	7,31	11,31	13,31	17,31	19,31	23,31	29,31	31,31	37,31	41,31	43,31	47,31
2,37	3,37	5,37	7,37	11,37	13,37	17,37	19,37	23,37	29,37	31,37	37,37	41,37	43,37	47,37
2,41	3,41	5,41	7,41	11,41	13,41	17,41	19,41	23,41	29,41	31,41	37,41	41,41	43,41	47,41
2,43	3,43	5,43	7,43	11,43	13,43	17,43	19,43	23,43	29,43	31,43	37,43	41,43	43,43	47,43
2,47	3,47	5,47	7,47	11,47	13,47	17,47	19,47	23,47	29,47	31,47	37,47	41,47	43,47	47,47

Figure 1. (p, q) couples chosen from PQ set

In order to understand and visualize what special cases for RSA means, the couple $(p, q) = (5,7)$ is chosen among 225 couples. As a result, N becomes 35 and $Phi(N)$ becomes 24. In this case, the ED set, which is the set of relatively prime numbers with $Phi(N)$, contains $5, 7, 11, 13, 17, 19$ and 23. By using ED set, (e, d) couples are calculated and they are found as (5,5), (7,7), (11,11), (13,13), (17,17), (19, 19) and (23,23) where Equation 3 is satisfied.

In the following figures, N values are the last numbers shown by blue. The special cases, where plaintext is equal to ciphertext despite the enciphering process, are shown by dark gray. Normal RSA cases are shown by light gray.

1	2	3	4	5
6	7	8	9	10
11	12	13	14	15
16	17	18	19	20
21	22	23	24	25
26	27	28	29	30
31	32	33	34	35

Figure 2. Special cases for RSA where $(p, q) = (5,7)$ and $(e, d) = (5,5)$

If RSA encryption is applied to the plaintexts $1, 6, 7, 8, 13, 14, 15, 20, 21, 22, 27, 28, 29,34$, the resulting ciphertexts become equal to plaintexts, where $(p, q) = (5,7)$ and $(e, d) = (5,5)$, as shown in Figure 2.

1	2	3	4	5
6	7	8	9	10
11	12	13	14	15
16	17	18	19	20
21	22	23	24	25
26	27	28	29	30
31	32	33	34	35

Figure 3. Special cases for RSA where $(p, q) = (5,7)$ and $(e, d) = (7,7)$

If the plaintexts $1, 4, 5, 6, 9, 10, 11, 14, 15, 16, 19, 20, 21, 24, 25, 26,29, 30, 31, 34$ are encrypted by RSA, the resulting ciphertexts become equal to plaintexts, where $(p, q) = (5,7)$ and $(e, d) = (7,7)$, as shown in Figure 3.

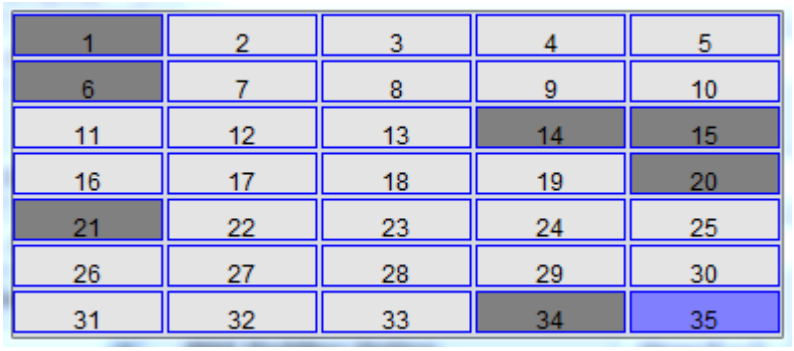

Figure 4. Special cases for RSA where $(p, q) = (5,7)$ and $(e, d) = (11,11)$

If the plaintexts $1, 6, 14, 15, 20, 21, 34$ are encrypted by RSA, the resulting ciphertexts become equal to plaintexts, where $(p, q) = (5,7)$ and $(e, d) = (11,11)$ as indicated in Figure 4.

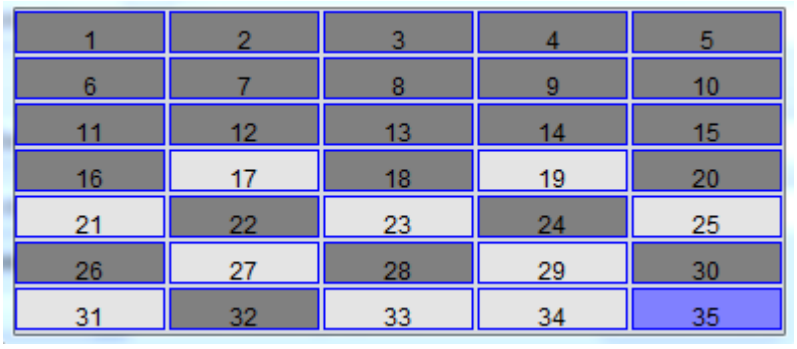

Figure 5. Special cases for RSA where $(p, q) = (5,7)$ and $(e, d) = (13,13)$

If the plaintexts $1, 2, 3, 4, 5, 6, 7, 8, 9, 10, 11, 12, 13, 14, 15, 16, 18, 20, 22, 24, 26, 28, 30, 32$ are encrypted by RSA, the resulting ciphertexts become equal to plaintexts, where $(p, q) = (5,7)$ and $(13,13)$ as shown in Figure 5.

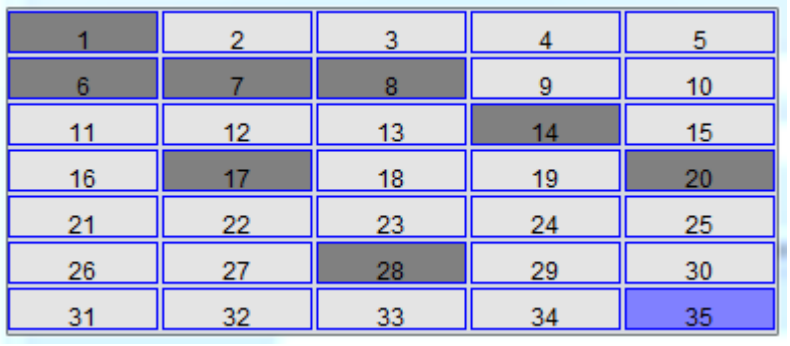

Figure 6. Special cases for RSA where $(p, q) = (5,7)$ and $(e, d) = (17,17)$

If RSA encryption is applied to the plaintexts $1, 6, 7, 8, 14, 17, 20, 28$, the resulting ciphertexts become equal to plaintexts where $(p, q) = (5,7)$ and $(e, d) = (17,17)$ as shown in Figure 6.

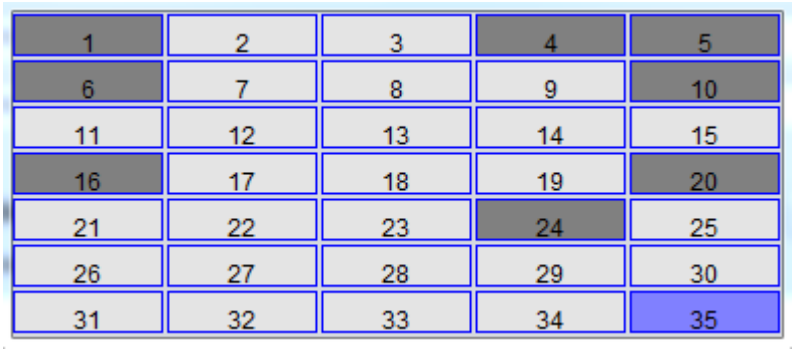

Figure 7. Special cases for RSA where $(p, q) = (5,7)$ and $(e, d) = (19,19)$

If the plaintexts $1, 4, 5, 6, 10, 16, 24$ are encrypted by RSA, the resulting ciphertexts become equal to plaintexts, where $(p, q) = (5,7)$ and $(e, d) = (19,19)$ as shown in Figure 7.

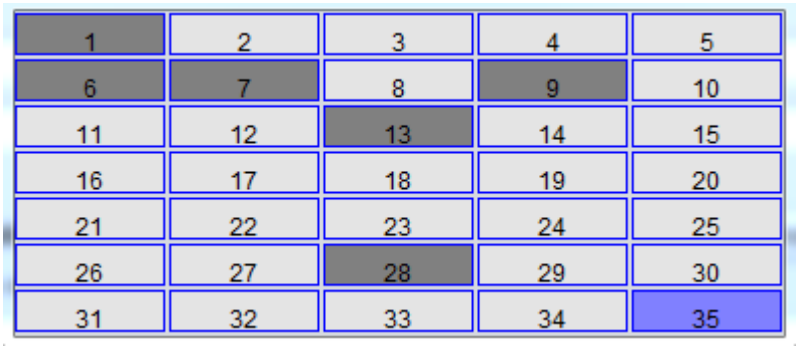

Figure 8. Special cases for RSA where $(p, q) = (5,7)$ and $(e, d) = (23,23)$

Lastly, if the plaintexts $1, 6, 7, 9, 13, 28$ are encrypted by RSA, the resulting ciphertexts become equal to plaintexts, where $(p, q) = (5,7)$ and $(e, d) = (23,23)$ as indicated in Figure 8. As it is seen in these figures, the number of special cases in RSA varies with the change in p and q values.

In order to understand the effect of p and q on the occurrence of special cases for RSA, 225 different (p, q) couples shown in Figure 1, are used. The ratio of special cases of RSA to the normal cases of RSA is abbreviated as $RSC2NC$.

For example, $RSC2NC$ value for the case shown in Figure 8, is calculated as $\frac{6}{28} \cong 0{,}214$ where the number of special cases is 6 and the number of normal cases is $34 - 6 = 28$. Equation 6 is used for finding this ratio.

$$RSC2NC = \frac{(Number\ of\ Special\ Cases)}{(Number\ of\ Total\ Cases - Number\ of\ Special\ Cases)} \quad (6)$$

By using the 225 different (p, q) couples shown in Figure 1, $RSC2NC$ values for 3 bit long (e, d) couples are calculated for some p values. For example, for $p = 5$, where special cases and normal cases of RSA were examined for $(5, q)$ values, $RSC2NC$ is found as 0,277515. For $p = 7$, where special cases and normal cases of RSA were examined for $(7, q)$ values, $RSC2NC$ is found as 0,239673. For $p = 19$, where special cases and normal cases of RSA were examined for $(19, q)$ values, $RSC2NC$ is found as 0,067662. For $p = 23$, where special cases and normal cases of RSA were examined for $(23, q)$ values, $RSC2NC$ is found as 0,041931. For $p = 41$, where special cases and normal cases of RSA were examined for $(41, q)$ values, $RSC2NC$ is found as 0,011749. The comparison of $RSC2NC$ values of changing p values indicates that $RSC2NC$ decreases when bigger p value is used.

4.RESULTS AND DISCUSSIONS

The secrecy of the relation between plaintext and ciphertext, is vital for the security of RSA Algorithm. The usage of small p and q values in RSA encryption, makes encryption process useless in some cases. These cases can be named as special cases where plaintext is equal to ciphertext. Since encryption aims to hide the relation between the plaintext and ciphertext, in these special cases, the relation cannot be hidden. By the increase in p and q values, the frequency of occurrence of these problematic cases decreases and RSA can provide secure communication although any padding algorithm is not used to provide security features to the channel.

5.CONCLUSIONS

This study explains RSA Algorithm in detail and examines the special cases for RSA Algorithm in Java where the plaintext is equal to the ciphertext. Although encryption is already done, the equality of ciphertext and plaintext makes encryption process useless for these special cases. The reason behind these unexpected cases is shown as the usage of small p and q values in RSA encryption. When p and q values are chosen as relatively big numbers, the frequency of occurrence of special cases decreases. The results show that, for secure communication in an insecure channel, N values should be as big as possible in RSA.

REFERENCES

[1] C. Paar and J. Pelzl, Understanding Cryptography, 1st ed. Berlin, Germany: Springer-Verlag, pp. 4-5, 2010.
[2] B. A. Forouzan, Cryptography & Network Security, 1st ed. NewYork, USA: McGraw-Hill, p. 2, 2007.
[3] C. Paar and J. Pelzl, Understanding Cryptography, 1st ed. Berlin, Germany: Springer-Verlag, pp. 3-4, 2010.
[4] C. Paar and J. Pelzl, Understanding Cryptography, 1st ed. Berlin, Germany: Springer-Verlag, pp. 56-57, 2010.
[5] B. A. Forouzan, Data Communications and Networking, 4th ed. Berlin, NewYork, USA: McGraw-Hill, p. 933-934, 2007.
[6] B. A. Forouzan, Data Communications and Networking, 4th ed. Berlin, NewYork, USA: McGraw-Hill, p. 949-950, 2007.
[7] C. Paar and J. Pelzl, Understanding Cryptography, 1st ed. Berlin, Germany: Springer-Verlag, p. 174, 2010.
[8] A. Shamir. R.L. Rivest, and L. Adleman, "A method for obtaining digital signatures and public-key cryptosystems." *CACM21,2*, pp. 120-126, 1978
B. Sadr, "Finding cases of ciphertext equal to plaintext in the RSA algorithm" , M. Eng. Thesis, Oklahoma State University, Stillwater, USA, July 2011.

BIOGRAPHY

Mustafa Kocakulak was born in Bursa, Turkey. He received his Bachelor's Degree from Electrical & Electronics Engineering Department of Ihsan Dogramaci Bilkent University, Ankara, Turkey, in 2012. Mr. Kocakulak's major fields of study are cryptology and signal processing. He is currently is a research and teaching assistant at Bursa Technical University.

Turgay Temel was a Assoc. Professor in the Department of Mechatronics Engineering at Bursa Technical University, Turkey. He received his Ph.D. degree from Electrical & Electronics Engineering Department of Bogazici University, Istanbul, Turkey in 2002.

ICENS
INTERNATIONAL CONFERENCE ON ENGINEERING AND NATURAL SCIENCES
24-28 May 2016 /Sarajevo

Thermodynamic Analysis of Waste Heat Recovery of Coal Drying Section in Cement Fabric Using Organic Rankine Cycles (Orc)

Sedat Ertas[1], Mustafa Alptekin[2,3], Abid Ustaoglu[1]

Abstract

One of the most energy consuming industries in the world is cement industry and it composes 12-15 % of the total industrial energy consumption. The coal drying section is one of the most energy consuming sections in a cement factory. Before the coal enters the rotary kiln, it first goes to the coal drying section to reduce the moisture in it. About exhausted heat of 2.5MW is wasted from the chimney of this section. In order to utilize this heat and evaluate the heat recovery capacity, an organic Rankine cycle (ORC) was adapted to system. Energy and exergy analyses were carried out using various organic working fluids as a function of condenser temperature and evaporator pressure. The optimum operation conditions and the best working fluid were determined.

Keywords: *Organic Rankine Cycle, Coal Drying Section, Exergy Analysis, Cement Fabric*

1.INTRODUCTION

Energy is one the most important factor for the development of many countries. World's energy consumption is continuously rising while energy sources are running out. Using the energy efficiently is a very important issue for all kinds of sectors. Industrial sector has a bigger share of consuming energy in the world. Cement industry's energy consumption composes 12-15 %of the total industrial energy consumption and %2-6 of the countries [1]. The cement sector is an industrial sector with energy-intensity and highly wasted heat recovery potential. In a cement production process it is estimated that about 40 % of the total energy consumption is transferred as waste heat to the environment [2].Because of this waste heat cement sector is one of the major industrial emitters of greenhouse gases. [3]. Therefore, there have been many studies about the sections of the cement factories in terms of the first and the second law of the thermodynamic. One of the most energy consuming sections in a cement factory is coal drying section. Before the coal enters the rotary kiln, it first goes to the coal drying section to reduce the moisture in it. The moisture requires being 0.5-1.5 % in order the coal to get the first flame. The excess moisture needs to be removed from the coal. Therefore, about 6.4MW energy is required for coal drying section. Bigger share of this energy is wasted by exhausted gasses. This wasted heat can be recovered with a waste heat recovery steam generator. Beyond the ORC, researchers have submitted various thermodynamic cycles, such as Kalina cycle, Goswami cycle, and trilateral flash cycle which can convert heat sources into electricity. Moreover, there is more power output for the same heat input with Kalina cycles compared to ORCs, but the ORC system is less complex and needs less maintenance [4,5]. Conversion of low heat into power has been demonstrated by Organic Rankine Cycle(ORC)[6]. The main objective of this study is to analyze the energy and exergy efficiencies of a coal drying section by applying an Organic Rankine Cycle for dry and isentropic working fluids for different operational conditions in order to decide the recovery capacity of the exhausted heat through the exhausted gasses of coal drying section. Energy and exergy analyses were carried out using various organic working fluids as a function of condenser temperature and evaporator pressure.
In this study in the coal drying section exhausted gas temperature is about 366 K and this type of energy is recovered and utilized by a proposed Organic Rankine Cycle. The optimum operation conditions and the best working fluid were determined.

2.MATERIAL and METHODS

2.1. System Description

Cement production has a long process and great amount of energy is required. Coal drying section is a part of consuming this energy. Before getting a new coal mixture the coal which comes from different places to the factory is analyzed in the laboratory to determine moisture, ash, volatile matter, combustive sulfur content, lower heating value and higher heating value and this mixture is sent to the coal bunker. The heated air in hanging oven is used to reduce moisture rate of entering coals to this section by means of suction fan. In order to use the mixture in the rotary kiln the coal is transported to the coal mill. Schematic diagram of the coal drying section is illustrated in Fig. 1

[1] *Corresponding author: Bartin University, Department of Mechanical Engineering, 74100, Merkez/Bartın, Turkey.* sertas@bartin.edu.tr
[2] *Hakkari University, Department of Mechanical Engineering, 30000, Hakkari, Turkey.* mustafaalptekin@sdu.edu.tr
[3] *Isparta University, Department of Mechanical Engineering, 30000, Hakkari, Turkey.* mustafaalptekin@sdu.edu.tr
[4] *Bartin University, Department of Mechanical Engineering, 74100, Merkez/Bartın, Turkey.*austaoglu@bartin.edu.tr

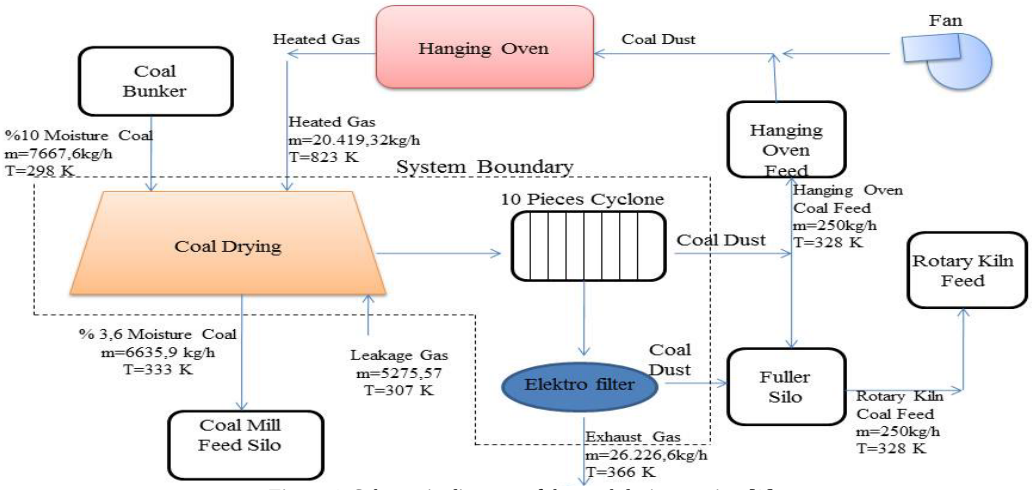

Figure 1. Schamatic diagram of the coal drying section [9].

2.2 System Analysis

In terms of thermodynamic laws coal drying section is analyzed and the results are obtained. Because of energy conservation input and output energy must be equal. Energy balance is applied to the coal drying section based on the measured real operation data. Under steady state conditions energy balance can be defined as:

$$\sum \dot{E}_{in} = \sum \dot{E}_{out} \tag{1}$$

$$\dot{Q} + \sum \dot{m}_{in} h_{in} = \dot{W} + \sum \dot{m}_{in} h_{in} \tag{2}$$

Where Ėin and Ėout are the rate of input and output energy transfer by heat, mass and work. Q̇ is heat transfer rate, Ẇ is work rate and h is enthalpy. The energy efficiency is defined:

$$\eta_{th} = \frac{\sum \dot{E}_{out}}{\sum \dot{E}_{in}} = \frac{\sum m_{out} e_{out}}{\sum m_{in} e_{in}} \tag{3}$$

In terms of this equations input and output energy were estimated. The system is assumed an open system. No heat transfer occurs. Potential and kinetic energy were neglected. All heat losses in the junctions were neglected. Input energy rate is 23,259,229 kJ/h to the coal drying section and output energy rate is 12,628,050 kJ/h. About 45 % of the input energy is lost during this proces.Exhaust gases consist the biggest share of this heat loses. About 9,065,775 kJ/h rate of energy is emitted by exhaust gasses. Energy efficiency of coal drying section is 54, 29 %. Input exergy to the coal drying section is 5,011,395 kJ/h and output exergy is 191,990 kJ/h were calculated.Exergy efficiency of the coal drying section is 3, 83 % and this result shows great amount of energy is wasted.This energy source can be recovered to the system and the system efficiency can be increased.Exergy analysis of coal drying section can be calculated as the following equation:

$$\eta_{Ex} = \frac{Ex_{out}}{Ex_{in}} \tag{4}$$

2.3 Organic Rankine Cycle Description

Organic Rankine cycle is a form of Rankine cycle uses low boiling organic working fluids to generate electricity or power from low heat source such as geothermal,solar,waste heat from industry.Organic Rankine cycle is a leading technology for low temperature waste heat recovery[7].As seen in Figure 2. basic organic Rankine cycle(ORC),mainly consists of turbine(expander),condenser,circulating pump and evaporator.This thermodynamic cycle includes an expansion process,a condensation process,a pumping process and an evaporation process.To simplify the process following assumptions are made:

1. System works under steady state conditions, 2. Saturated vapor at outlet of evaporator, 3. Saturated liquid at outlet of condenser, 4. No heat transfer from the ORC to the environment, 5. No pressure drops in pipelines.

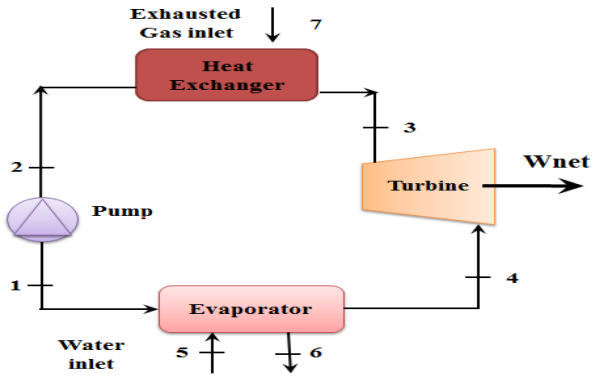

Figure 2. Organic Rankine Cycle Figure Schema

2.4 Thermodynamic Analysis of ORC

Coal drying section thermodynamic analysis is determined via Engineering Equation Solver (EES) program. Coal drying section exhaust gas temperature is about 366 K and energy output rate 2518 kJ/s. This energy can be recovered using a basic organic Rankine cycle. Input variables are listed in Table 1.

Table 1. Organic Rankine cycle accepted parameters

Parameters	**Values**
Turbine isentropic efficiency	85%
Pump isentropic efficiency	85%
Condenser temperature	300 K
Pump inlet temperature	303 K
Pump outlet temperature	304.5 K
Heat transfer rate of exhausted gas	2518 kW
Evaporator pressure	900 kPa
Evaporator effectiveness	85%
Mass flow rate of working fluid in ORC	45 kg/s
Ambient pressure	101.325 kPa
Ambient temperature	298 K
Exhaust gas temperature in coal drying section	366 K

Organic Rankine cycle working performance is strongly related to organic fluids [9].Before selection the working fluids what kind fluids are suitable for organic Rankine cycle is identified. Working fluids are defined wet, dry and isentropic. Wet type fluid can be undesirable for turbine blade. Dry and isentropic fluid types are chosen in this study.The properties of selected fluids are listed in Table 2.

Table 2. Properties of the selected working fluids

Substance	**Fluid type**	**Molecular mass(g/mol)**	**Tcrit (K)**	**Pcrit (MPa)**	**Boiling temp.(K)**
R236fa	Dry	152.04	398.1	3.2	271.7
R113	Dry	187.4	487.2	3.39	315.1
R245fa	Isentropic	134.05	427.2	3.64	288.15
R123	Isentropic	152.93	456.8	3.66	300.75

There has been a lot of factor to chose the working fluids. Most research focus on optimum working condition according heat source. Listed organic Rankine cycle fluids are selected because of low boiling and critical temperature

3.ENERGY and EXERGY ANALYSIS of ORC

The thermal efficiency, exergy efficiency, network output and total exergy destruction rate were calculated for different working fluids applying the thermodynamic laws to each component of ORC. Cycle mass flow rate was calculated 45 kg/s and cooling water mass flow rates were calculated 111,9 kg/s for R113, 112,4 kg/s for R123,114 kg/s for R236fa, 114,4 kg/s for R245fa at same condenser temperature.

3.1.Variation of Condenser Temperature Results on ORC

Condenser temperature variations effect on energy and exergy efficiency performance was calculated for R113, R123, R236fa, R245fa working fluids. The evaporator pressure is constant and taken 900 kPa. Increasing in condenser temperature is results decreasing network output for all working fluids. Under this working conditions best working fluid is R113 which is produced 180 Kw output power and respectively R123 is 164,5kw , R236fa is 134 kw and R245fa is 124,6 kw. Figure 3. a) shows the network output as a function of condenser temperature changes.

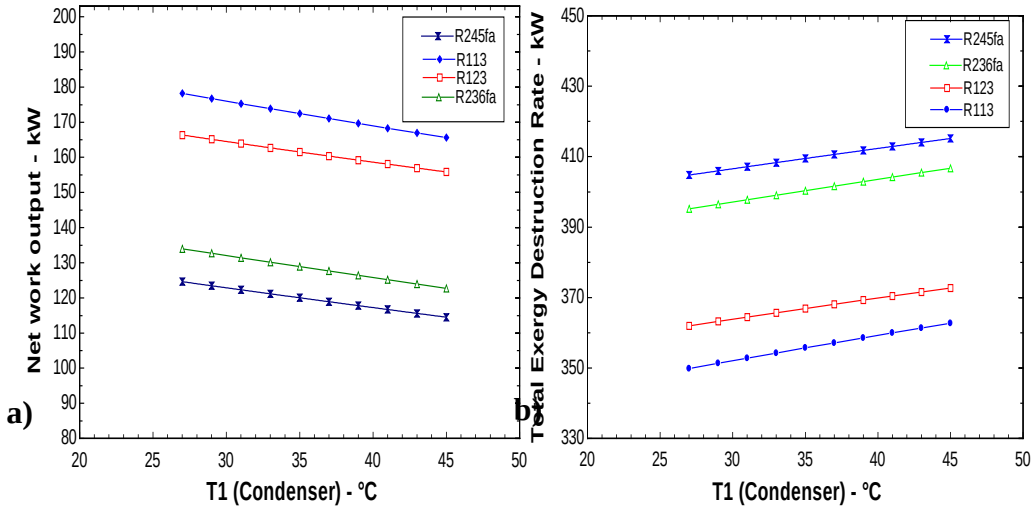

Figure 3. a) Net work output and b) Total exergy destruction rate for different working fluids as a function of condenser temperature.

Total exergy destruction rate as a function of condenser temperature changes is illustrated Figure 3. b) Total exergy destruction increases with increasing the condenser temperature.R245fa has the highest total exergy destruction rate and R113 lowest. Exergy destruction rate for R113 working fluid is 350 kW and respectively R123 is 360 kW , R236fa is 395 kW and R245fa is 405 kW. Decreasing the condenser temperature results decreasing the total exergy destruction rate and decreasing the total exergy destruction rate is increasing the thermal efficiency of the organic Rankine cycle.Thermal efficiency as a function of condenser temperature is illustrated in Figure 4 a).thermal efficiency is decreasing with increasing condenser temperature. The thermal efficiency rate of R113 is 7,1% respectively R123 is 6,6 %,R236fa is 5,3 % and R245fa is 4,9 %.R113 working fluid has the highest efficiency and R245fa has the lowest efficiency at 300 K. All working fluids efficiency decrease with increasing condenser temperature. Same as the thermal efficiency, the exergy efficiency decreases with increasing condenser temperature. Changes of exergy efficiency as a function of condenser temperature is illustrated in Figure 4 b).Exergy efficiency is decreasing with increasing condenser temperature.R113 working fluid is the highest exergy efficiency and R245fa is the lowest at 300 K condenser temperature.

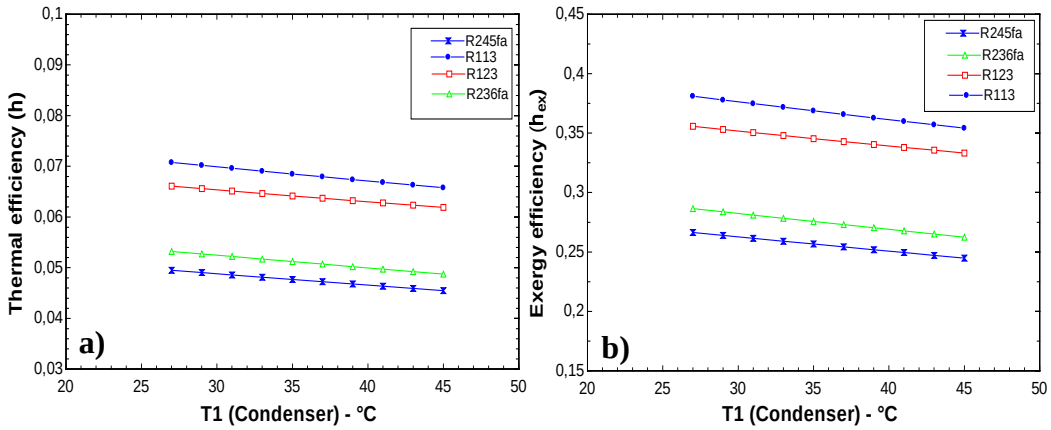

Figure 4. a) Thermal efficiency and b) Exergy efficiency for different working fluids as a function of condenser temperature.

3.2.Variation of Evaporator Pressure Results on ORC

As a function of evaporator pressure changes; thermal efficiency, network output, exergy efficiency and total exergy destruction rates were determined. Isentropic efficiencies of turbine and pump were assumed 85 %.Condenser temperature remained constant at 300K. Thermal efficiency of all working fluids is increasing as a function of evaporator pressure up to 400 kPa and after this pressure thermal efficiency is decreasing slightly. Optimum working evaporator pressure for all working fluids 900 kPa as seen in figure 5. a)

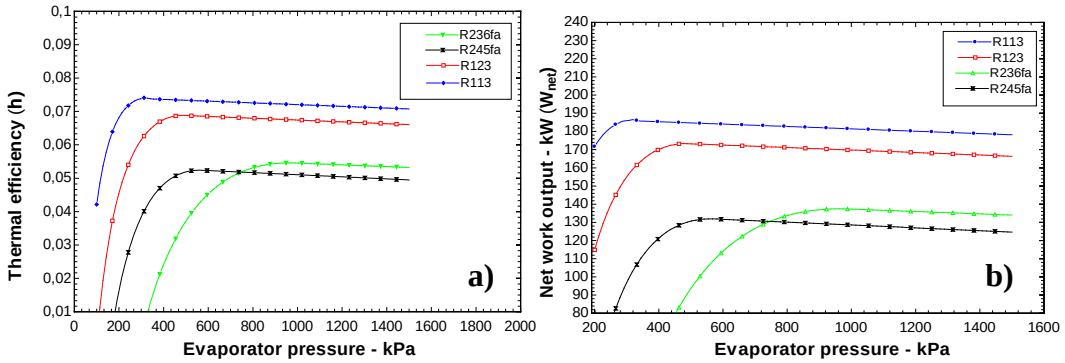

Figure 5. a) Thermal efficiency and b) Network output for different working fluids as a function of Evaporator pressure.

R113 working fluid is the highest efficiency and R245fa is the lowest one in this working conditions. The network output changes seen Figure 5. b).R113 working fluid is highest network output and respectively R123, R236fa, R245fa. Exergy efficiency and total exergy destruction are illustrated in Figure 6.a) and Figure 6.b). Exergy efficiency of all working fluids are increasing up to 400 kPa after this pressure exergy efficiency is decreasing slightly. By contrast with exergy destruction rates are decreasing up to 400 kPa and after this pressure exergy destruction rates are increasing more slightly. As a function of evaporator pressure exergy efficiency of R113 is the highest and R245fa is the lowest. Additionally, as seen in Figure 6. a) exergy destruction rate of R113 is the lowest and R24fa is the highest. This means R113 working fluid is the most effective to recover exhausted wasted heat in coal drying section. Exergy efficiency rate of R113 is 38 % and respectively R123, R236fa and 245fa are 35 %, 28 %, 25 %.Exergy destruction rate of R113 is 345kW, R123 is 358 kW, R236fa is 395 kW and 245fa is 403 kW.

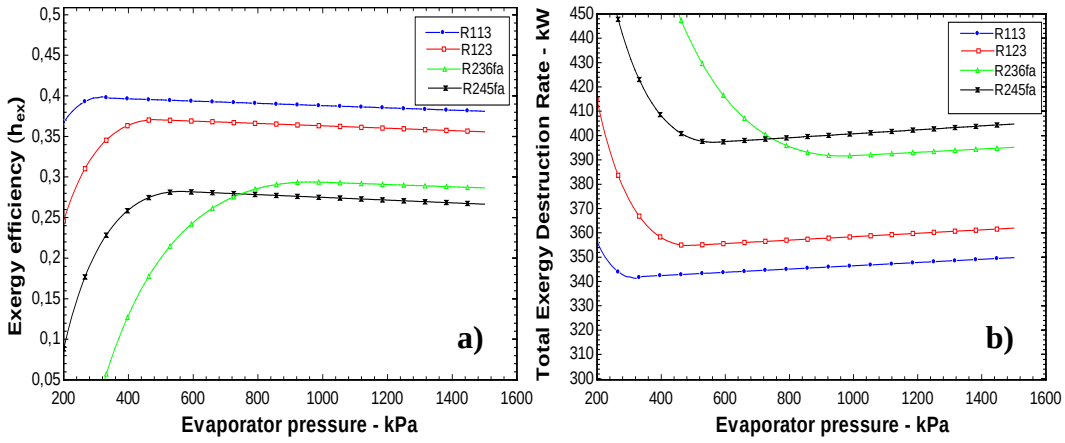

Figure 6. a) Exergy efficiency and b) Total exergy destruction rate for different working fluids as a function of Evaporator pressure.

4. RESULTS AND DISCUSSIONS

Cement production process consist of several parts. Coal drying section is one the these parts. The coal which is used in cement production has to 1-1, 5 % moisture in it.To reduce the moisture for this percentage coal drying section is built into Bartın cement factory. This section consumes 23,259,229 kJ/h rate of energy and 9,065,775 kJ/h rate of energy is wasted by exhaust gases. Energy efficiency of coal drying section is 54, 29 % and exergy efficiency is 3, 83 %. This big difference means that the great amount of wasted energy can be reused in the coal drying section to increase the total efficiency of the system .To utilize this wasted energy an Organic Rankine Cycle is adapted to coal drying section. Exhausted gas temperature is 366 K and four different working fluids which can work in this temperature are chosen. The chosen fluids are R113, R123, R236fa and R245fa. In this study an organic Rankine cycle is adapted to the coal drying section and using the Engineering Equation

Solver (EES) for R113, R123, R236fa and R245fa working fluids are analysied energy and exergy efficiency, network output, total exergy destruction as a function of condenser temperature and evaporator pressure.Optimum mass flow rate is 45kg/s was determined using the Engineering Equation Solver for R113, R123, R236fa and R245fa working fluids. As a function of condenser temperature thermal efficiency, exergy efficiency and network output decrease with increasing condenser temperature however, total exergy destruction is increased. The Best working fluid in this working condition is R113 and the others are respectively R123, R236fa and R245fa.As a function of evaporator pressure thermal efficiency, exergy efficiency and network output increase up to 400 kPa and after this point decrease slightly. Optimum working pressure is 900 kPa as seen figure-7 and figure-8 for all working fluids. At 900 kPa evaporator pressure best working fluid is R113 and and the others are respectively R123, R236fa and R245fa.As a function of condenser temperature and evaporator pressure R113 working fluid is the best working fluid. At 400 kPa the efficiency of R113 working fluid is 7.23 % but at 900 kPa is 7.1 %. Under this working conditions best working fluid is R113 which is produced 180 kW output power and respectively R123 is 164,5kW , R236fa is 134 kW and R245fa is 124,6 kW. an organic Rankine cycle can be adapted using R123 working fluid to the coal drying section and 180 kW energy recover to the system. Recovering this energy will increase the utility of total energy consumption, most strong for international competition and decrease the greenhouse gas emission in to the environment.

REFERENCES

[1]. S. Kaustubhu, K. V. Mujumdar, S. B. Ganesh Kulkarni, V. V. Ranade, " Rotary cement kiln simulatero(RoCKS): intergread modeling of pre-heater,calciner,kiln and clinker cooler," *Chem. Eng. Sci.*, vol. 62, pp. 2590-2607, 2007.
[2]. S. Karellas, A. D. Leontaritis, G. Panousis, E. Bellos, E. Kakaras, "Energetic and Exergetic analysis of waste heat recovery systems in the cement industry," *Energy*, vol. 58, pp. 56-147, 2013.
[3]. P. K. Mehta, "Greening of the concrete industry for sustainable development.", *Concr. Int.*, vol. 24, pp. 8–23, 2002.
[4]. R. D. Pippo, "Second law assessment of binary plants generating power from low-temperature geothermal fluids," *Geothermics*, vol. 33, pp. 565–586, 2004.
[5]. O. Badr, P. W. O'Callaghan, "Thermodynamic and thermophysical properties of organic working fluids for Rankine cycle engines," *Appl. Energy*, vol. 19, pp. 1–40, 1985.
[6]. Ö. Kaska, "Energy and exergy analysis of an organic Rankine for power generation from waste heat recovery in steel industry," *Energy Convers. Manage.*, vol. 77, pp. 17–108, 2014.
[7] S. Quoilin, M. V. D. Broek, S. Declaye, S. Dewallef, V. Lemort, "Thermo-economic optimization of waste heat recovery organic Rankine cycles," *Appl. Therm. Eng.*, vol. 31, pp. 288-93, 2011.
[8] A. A. Lakew, O. Bolland, "Working fluids for low-temperature heat source," *Appl. Therm. Eng.*, 2010 vol. 30, pp. 8-126.
[9]. A. Ustaoglu, S. Ertaş, M. E. Akay, *Energy and exergy analysis of the coal drying section in cement factory using wet method*, 8th Int. Ege Energy Symp. Exhib. 2016.

ICENS
INTERNATIONAL CONFERENCE ON ENGINEERING AND NATURAL SCIENCES
24-28 May 2016 /Sarajevo

A Numerical Investigation of Cyclic Behavior of Coupled Wall Systems

Hasan Sesli[1]*, S. Istemihan Cosgun[1], Metin Husem[1]

Abstract

RC (reinforced concrete) shear core walls preferred to depend on height of them form lateral-load resisting system for modern and high-rise building construction are divided into smaller wall units and coupling beams formed between openings due to the architectural requirements such as door, window, stairway and elevation. When the buildings are subjected to strong lateral loads, coupling beams act as fuses and exposed to inelastic rotation and deformation. Moreover, if units are properly detailed, behaviors of two independent shear wall piers will turn into a coupled system and their lateral stiffness will be greater than sum of individual wall piers and so the desired degree of coupling will be achieved. These groups of RC shear core walls are named RC coupled shear wall systems. Historically, the most of researches have focused on the coupling beam response but the studies on the behavior of coupled RC coupled shear wall systems are not prevalent. In this study, the behaviors of the RC coupled shear walls with different type coupling beams were numerically investigated under the cyclic loading.

Keywords: *RC Coupled Shear Wall Systems, Coupling Beams, ABAQUS*

1. INTRODUCTION

Reinforced concrete (RC) coupled-wall systems are mostly used in high rise buildings. RC shear coupled walls are divided into smaller wall units and coupling beams formed between openings due to the architectural requirements such as door, window, stairway and elevation. Coupling beams transfer shear forces acted on them between wall units as vertical force or normal force. This coupling action reduces overturning moments resisted by the individual walls and provides energy dissipation capacity for entire systems as the coupling beams undergo inelastic deformations. If coupling beams are properly designed and detailed as stiffness, strength and energy dissipation, coupling beams provide more efficient and economical structural system than individual shear walls.

Coupling beams and coupling action having importance on the coupled wall systems subjected to lateral loads have been main research subject ever since 1970. Firstly, test results for short and relatively deep coupling beams reinforced with conventional longitudinal bars and sufficient transverse reinforcement were presented in 1971 [1]. Test results showed that conventionally reinforced coupling beams to prevent diagonal tension failure are susceptible to sliding shear failure. Diagonally reinforced coupling beams were proposed as an alternative reinforcement to prevent diagonal tension failure and sliding shear failure [2]. Diagonal reinforcement design provisions have been included American Concrete Institu (ACI) Building Code since 2011 [3]. Since diagonal reinforcement creates construction difficulties due to the reinforcement congestion problems arised out of diagonal bar, rhombic type reinforcement which provides unconfined diagonal bars through the plastic hinge region was proposed [4].

Web shear plate coupling beams were investigated an alternative to the use of transverse reinforcement of conventionally reinforced coupling beam [5]. Harries et al. showed that steel coupling beams designed as steel link beams in an eccentrically-braced frame exhibited significant ductility and energy dissipation characteristics under cyclic loading [6]. The design provisions and detailing requirements have been provided in the Seismic Provisions for Structural Steel Buildings [7]. Concrete-steel composite coupling beams in which a steel coupling beam was encased in reinforced concrete core investigated [8]. Canbolat et al. developed a new type of coupling beam constructed with high-performance fiber-reinforced cement composites to simplify current reinforcement in RC coupling beams [9]. For difficulties and complexities in construction of beam-wall joints and difficulties and high cost in post-damage repair, researchers have been focused on alternative coupling dampers and replicable fuse systems ([10], [11], [12], [13], [14]).

When all researches are historically viewed, most of the researches have been developed on the coupling beam response, variation in configuration, coupling beam detail, reinforcement material, degree of coupling beam. Researches on coupled wall systems are not popular. The gap in the literature on the coupled wall systems have been filled yet. Lehman et al. investigated the response of a midrise coupled wall designed to meet current codes [15]. Cheng et al. investigated the cyclic behaviors of RC and hybrid coupled shear wall systems [16]. Research results indicate that a ductile coupling beam design does not guarantee a ductile behavior of a coupled shear wall systems.

In the literature, all studies are performed on behavior of the coupling beam specimens. Since it is quite difficult and expensive, excessive studies could not been developed on the RC coupled shear wall systems. In this study, the effects of different type

[1] *Corresponding author: Karadeniz Technical University, Department of Civil Engineering, 61080, Ortahisar/Trabzon, Turkey.* hasan_sesli@hotmail.com

coupling beams having same design shear strength and aspect ratio on the behavior of the RC coupled shear walls are numerically investigated.

2. DESIGN OF COUPLED WALL SYSTEM AND COUPLING BEAMS

The study investigates the cyclic behaviors of RC coupled shear walls with different types of coupling beams. Three full-scaled 4-storey coupled shear wall systems were modeled in The ABAQUS Finite Element Analysis (FEA) Software [17]. Since analyses take a long time, only the lower 4-storey coupled shear wall systems which represent 10-storey coupled shear wall systems considered in analysis.

Wall piers were designed using procedures in ACI 318-11 (2011) shown in Figure 1. The boundary elements were 800 mm long and had longitudinal reinforcement ratios of 1%. The transverse ratio in the boundary elements was 1.5%. In the web, transverse ratio was 0.5% and vertical reinforcement was 0.77%. The shear strength of each wall pier was 0.42 $\sqrt{\mathbf{f_c'}}\ \mathbf{A_{cv}}$ MPa, where $\mathbf{A_{cv}}$ is the gross wall cross sectional area. Vertical load was applied to the specimen at the upper level that was equivalent to 4% of $\mathbf{A_g f_c'}$. For shear wall piers and RC coupling beams, specified concrete strength ($\mathbf{f_c'}$) and specified yield strength ($\mathbf{f_y}$) of reinforcement steel rebar are 28 MPa and 420 MPa, respectively.

The conventionally (CR) shown in Figure 2a and diagonally reinforced (DR) shown in Figure 2b coupling beams are 1200 mm length and 800 mm height and 300 mm thickness. The longitudinal and transverse reinforcement detailing of both coupling beams detailing is represented in Figure 2. Nominal shear strength capacity of both coupling beams is $0.61\sqrt{\mathbf{f_c'}}\ \mathbf{A_{cw}}$ where $\mathbf{A_{cw}}$ is the cross-sectional area of the coupling beam and design forces in flexure were considered as $0.30\ \sqrt{\mathbf{f_c'}}\ \mathbf{A_{cw}l}$ where $\mathbf{l}$ is the length of the coupling beams. Longitudinal reinforcement ratio of the CR coupling beams was determined based flexural members design in the ACI 318-11. For DR coupling beams, the area of diagonal rebars ($\mathbf{A_{vd}}$) was calculated based on Equation 1 per the ACI 318-11.

$$\mathbf{V_n = 2A_{vd} f_y \sin\alpha} \tag{1}$$

The steel coupling beams shown in Figure 2c were designed to provide a shear capacity ($\mathbf{t_w}$) of about 800 kN according to Equation 2 per AISC-2011.

$$\mathbf{V_P = 0.6 F_y (d - 2t_f) t_w} \tag{2}$$

where $\mathbf{F_y, d, t_f}$ and $\mathbf{t_w}$ are the specified yield strength of steel (235 MPa), depth of the beam, thickness of the flange (30 mm)and thickness of the web (8 mm). Width of the flange of the beams ($\mathbf{b_f}$) which provides an embedment between steel rebar in the wall boundary was chosen as 200 mm. To prevent local flange and web buckling were limited respectively, by

$$\mathbf{b_f/t_f \le 0.31\sqrt{E_s/F_y}} \tag{3}$$

$$\mathbf{h/t_w \le 3.05\sqrt{E_s/F_y}} \tag{4}$$

where $\mathbf{E_s}$ **and** $\mathbf{h}$ are modulus of elasticity of the steel (210000 MPa) and depth of the web. The embedment length of the steel beam section in the wall boundary ($\mathbf{l_e}$) was 750 mm. The embedment length was checked using Equation 5 (Shahrooz, 2005).

$$\mathbf{V_u = f_b \beta_1 b_f l_e [(0.58 - 0.22\beta_1)]/[0.88 + \left(\frac{a}{l_e}\right)]} \tag{5}$$

$$\mathbf{f_b = 4.05\sqrt{f_c'}\left(\frac{t_{wall}}{b_f}\right)^{0.66}} \tag{6}$$

In Equation (5), $\mathbf{f_b}$ is stress over the embedded region of the beam, $\boldsymbol{\beta_1}$ is factor relating depth of the equivalent rectangular stress block to neutral axis depth,$\mathbf{b_f}$ is width of the flange of the beam and $\mathbf{a}$ is one-half of the clear span of the beam. $\mathbf{V_u}$ should be taken as 1.5 times the shear capacity of the beam ($\mathbf{V_p}$) to account for strain hardening and material overstrength. In Equation 6, $\mathbf{t_{wall}}$ is the thickness of the wall in which the steel beam is embedded.

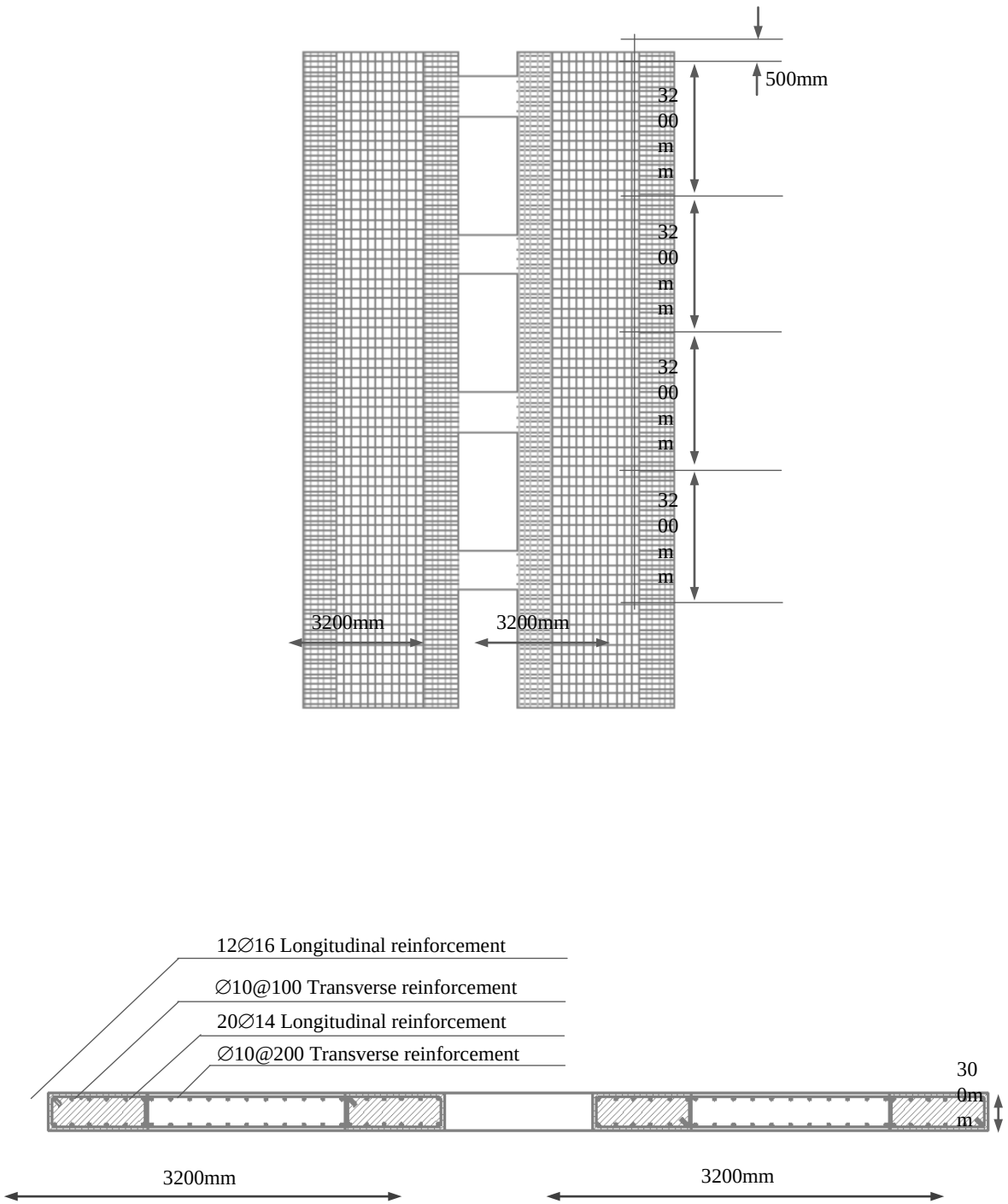

Figure 1. Detailed reinforcement layout of shear wall piers

To determine the thickness and spacing and web stiffeners named as face-bearing plates, the provisions in AISC-2011 were considered. The thickness of the stiffeners was chosen as 10 mm which is larger than $\mathbf{0.75}\boldsymbol{t_w}$ and minimum thickness in the AISC-2011. The required spacing of the stiffeners is dependent on the rotation demand on the beam in the AISC-2011. According to the AISC-2011, stiffener spacing shall be less than or equal $\mathbf{30}\boldsymbol{t_w} - \left(\frac{\boldsymbol{d}}{\mathbf{5}}\right)$ for a rotation angle equal to 0.08 radians and stiffener spacing shall be less than or equal $52\boldsymbol{t_w} - \left(\frac{\boldsymbol{d}}{\mathbf{5}}\right)$ for a rotation angle equal to 0.02 radians. For the assumed rotation angle 0.04 radians, 10 mm thick stiffener was chosen for each side of the web.

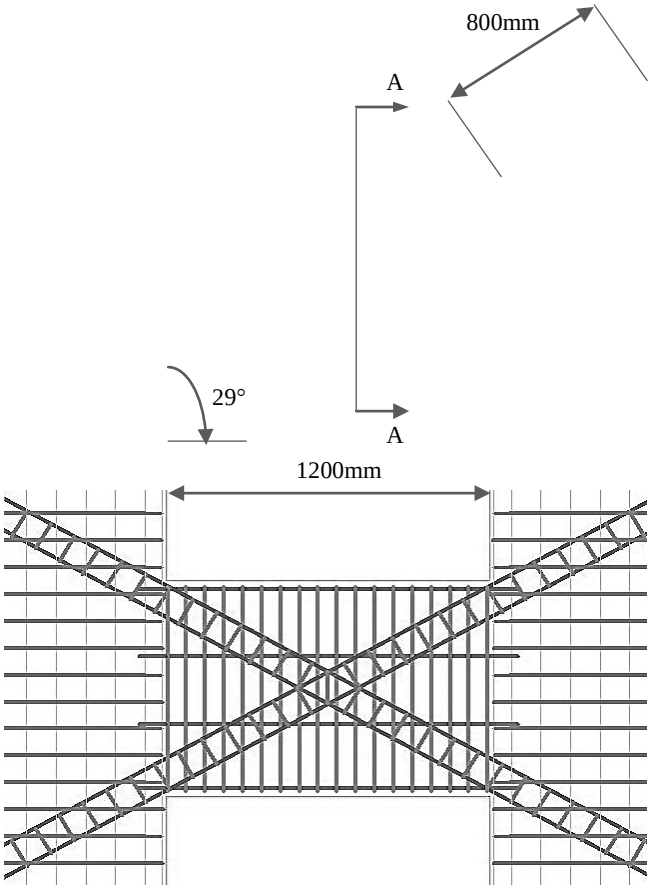
800mm
A
29°
A
1200mm

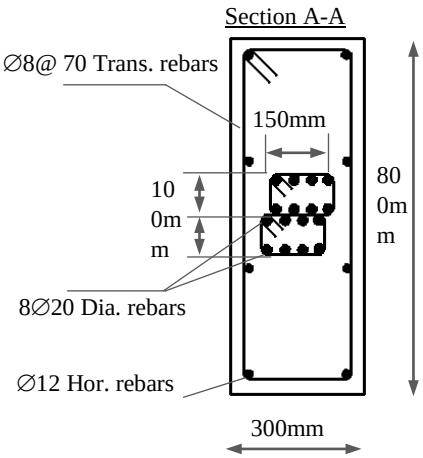
Section A-A
∅8@ 70 Trans. rebars
150mm
10
0m
m
80
0m
m
8∅20 Dia. rebars
∅12 Hor. rebars
300mm

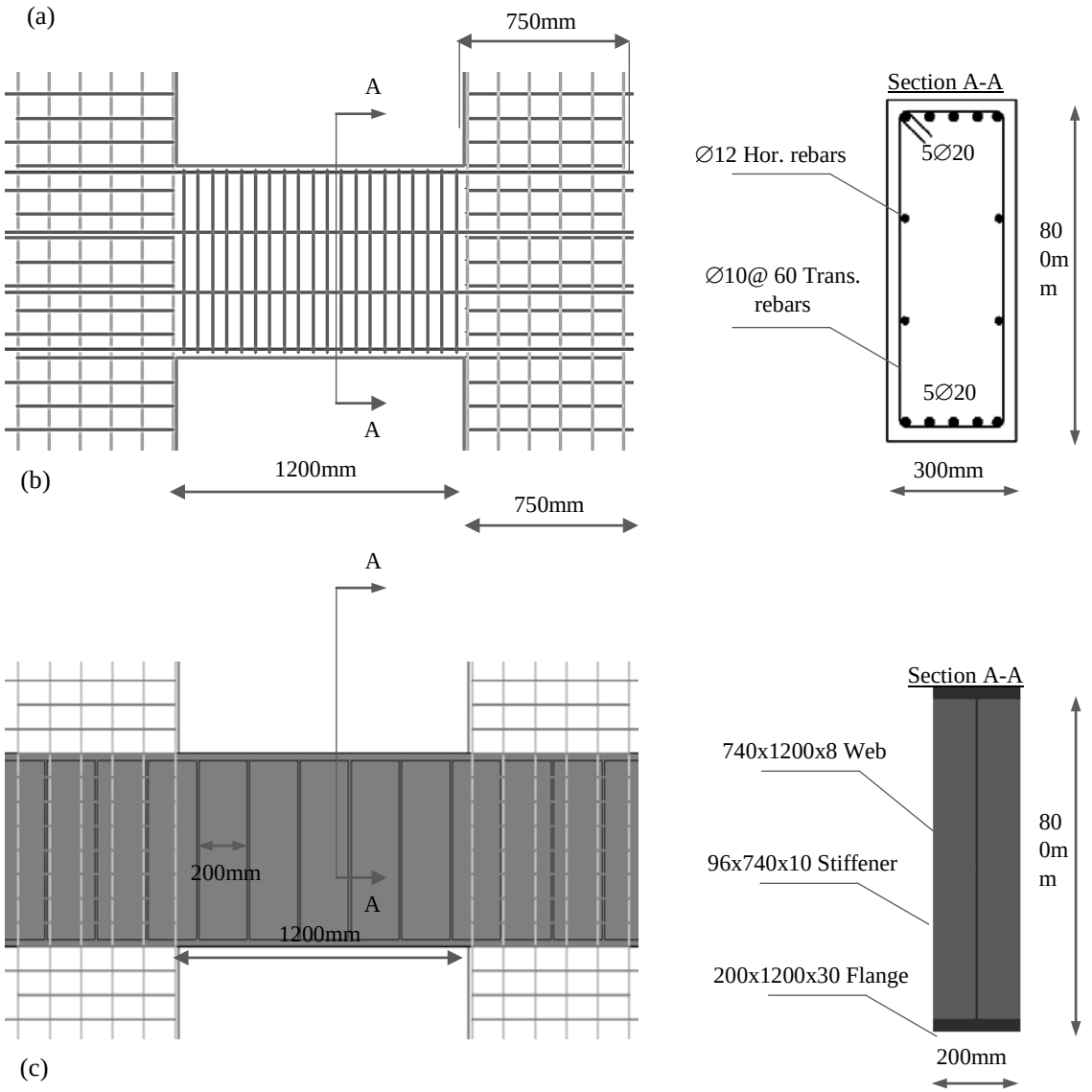

Figure 2. Detailing of coupling beams: (a) CR coupling beams, (b) DR coupling beams, (c) steel coupling beams

3. NUMERICAL STUDY

This study numerically investigates behaviors of the RC coupled shear walls with different type coupling beams under the cyclic loading. CR coupling beams, DR coupling beams and uncased steel coupling beams were chosen for investigation of behaviors of the RC coupled shear walls. In order to attain the numerical behavior of the systems, finite element computer program (ABAQUS) was used in this study. Finite element models of three RC coupled shear wall systems were only presented in Figure 3 for fourth story as they were represent all system in terms of mesh sizes . The concrete were modeled with Concrete Damage Plasticity Model (CDP) and reinforcing steel bars and steel beams were modeled with Classical Metal Plasticity Model (CMP). Loading history set up according to loading history prescribed in AISC (2011) for beam-to-column connection tests was used for the analyses (Figure 4). First displacement value in the cycle was chosen as 0.55mm.

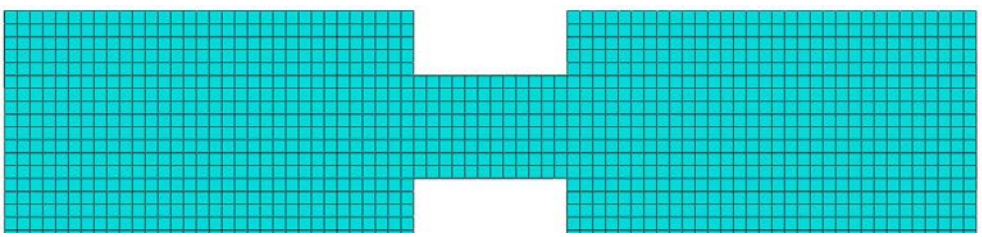

(a)

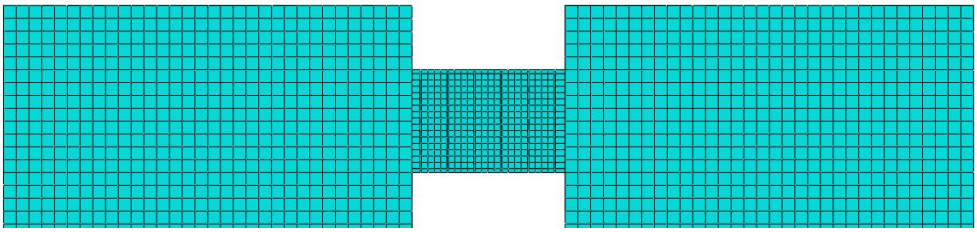

(b)

Figure 3. Finite element models: (a) with CR and DR coupling beams, (b) with steel coupling beams

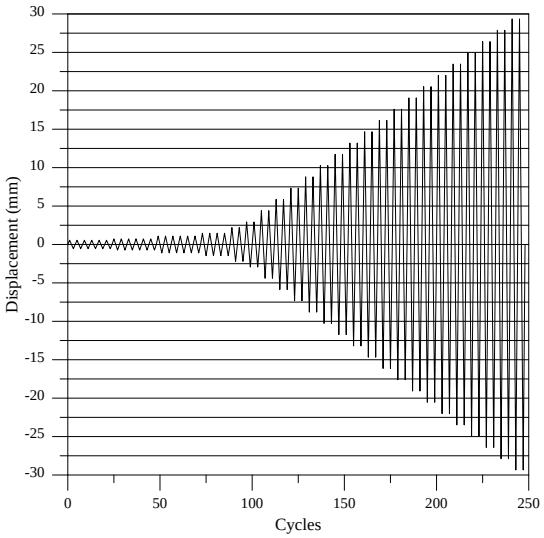

Figure 4. Cyclic loading sequence

Analyses are cut in the same damage level of the coupled shear wall piers at the compression zones although the numerical investigation and analyses are in the progress. Figure 5 compares the applied load versus displacement for the response of the systems according to available results. As can be seen, yielding load is 442 kN at 1.98 mm at a deflection, 489 kN at a deflection 2.20 mm and 546 kN at 2.64 mm for the models with CR coupling beams, DR coupling beams and steel coupling beams, respectively.

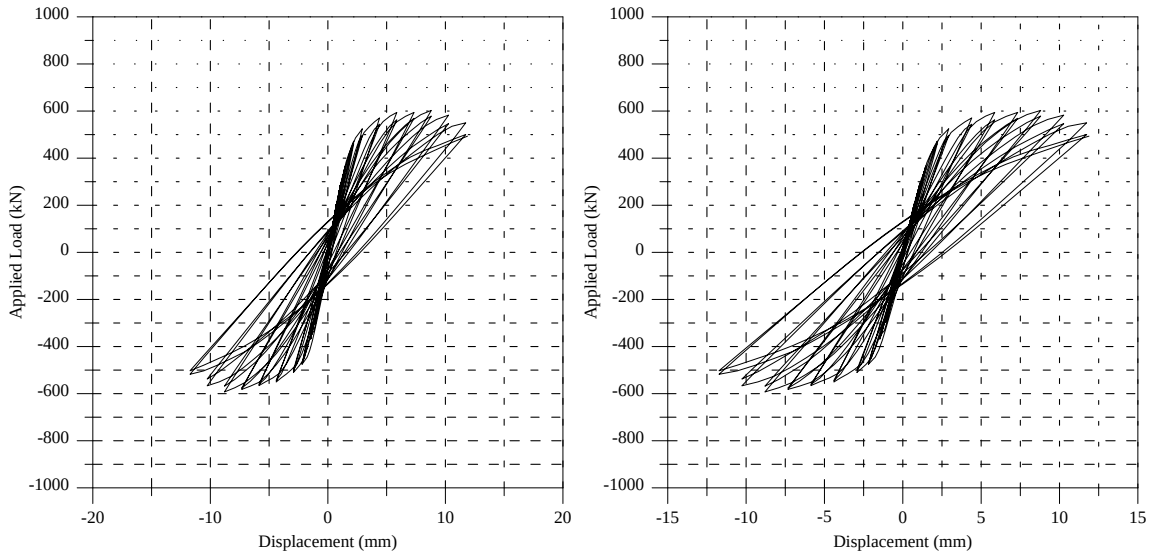

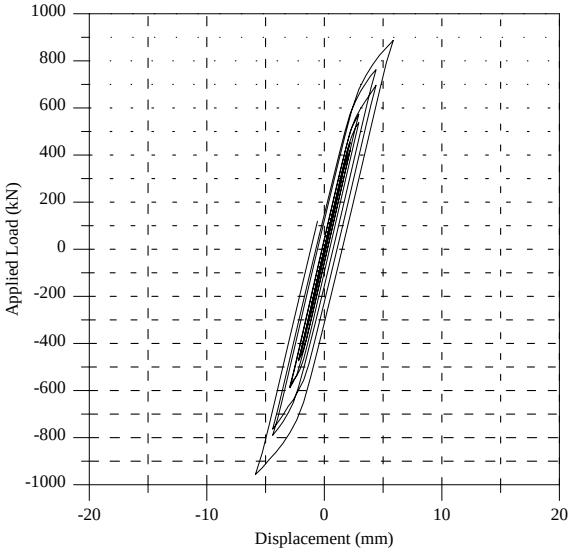

Figure 5. Hysteretic responses of the RC shear coupled wall systems

The variation of effective stiffness against to displacement is plotted in Figure 6. The initial stiffness for model with CR and DR coupling beams are about same level but the initial stiffness for model with steel coupling beams is 31% less than the other. At the yielding level, stiffness degradations of the systems are 20%, 22% and 5% for systems with CR, DR and steel coupling beams, respectively.

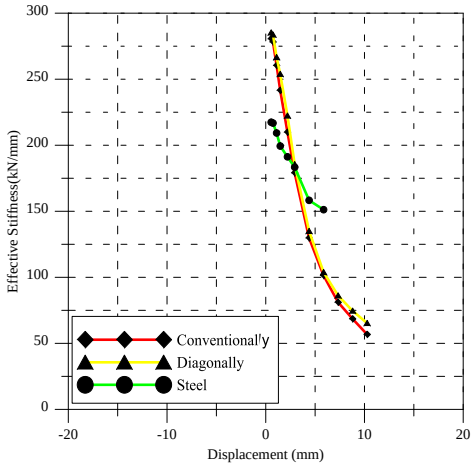

Figure 6. Stiffness degradation of the RC shear coupled wall systems

4. CONCLUSIONS

In this study, the effects of different type coupling beams having same design shear strength and aspect ratio on the behavior of the RC coupled shear walls were numerically investigated. In line with this purpose, behavior of three RC coupled shear wall systems consist of CR, DR and steel coupling beams under cyclic loading was presented. Several observations and conclusions can be drawn based on the numerical results. The coupled shear wall systems with CR and DR coupling beams showed poor hysteretic response with pinching effect but the coupled shear wall systems with steel coupling beams exhibited stable hysteretic response. Even if it has a less stiffness, the wall system with steel coupling beams brought on less stiffness degradation than the others.

REFERENCES

[1]. Pualay, T. (1971). Coupling beams of reinforced concrete shear walls. Journal of Structural Division, ASCE, Vol. 97, pp. 843-862.
[2]. Paulay, T. and Binney, J.R. (1974). Diagonally reinforced coupling beams of shear walls. Shear in Reinforced Concrete, American Concrete Institu (ACI), Vol. 42, pp. 579-598.
[3]. ACI 318-11 (2011). Building code requirements for structural concrete and commentary. American Concrete Institute, Farmington Hills, MI.
[4]. Galano, L. and Vignoli, A. (2000). Seismic behavior of short coupling beams with different reinforcement layouts. ACI Structural Journal, Vol. 97, pp. 876-885.

[5]. Subedi, N.K. (1989). Reinforced concrete beams with plate plate reinforcement for shear. Proceedings Institution Civil Engineers, Vol. 87, pp. 377-399.
[6]. Harries, K.A., Mitchell, D., Cook, W.D. and Redwood, R.G. (1993). Seismic response of steel beams coupling concrete walls. Journal of Structural Engineering, Vol. 119, pp. 3611-3629.
[7]. AISC 341-10 (2011). Seismic provisions for structural steel buildings. American Institute of Steel Construction, Chicago, Illinois, USA.
[8]. Shahrooz, B.M., Remmetter, M.E. and Qin, F. (1993). Seismic design and performance of composite coupled walls, Journal of the Structural Division, ASCE, Vol. 119, pp. 2858-2896.
[9]. Canpolat, B.A., Parra-Montesinos, G.J. and Wight, J.K. (2005). Experimental study on seismic behavior of high-performance fiber-reinforced cement composite coupling beams. ACI Structural Journal, Vol. 102, pp. 159-166.
[10]. Fortney, P.J. (2005). The next generation of coupling beams. Dissertation, University of Cincinnati, Cincinnati.
[11]. Ahn, T.A., Kim, Y., Kim, S.D. and Hwang, I. (2011). Seismic performance of coupling beam damper system. CTBUH 2011 World Conference, October 10-12, pp. 710-715.
[12]. Kim, H.J., Choi, K.S., Oh., S.H. and Kang, C.H. (2012). Comparative study on seismic performance of conventional RC coupling beams and hybrid energy dissipative coupling beams used for RC shear walls. 15TH World Conference on Earthquake Engineering, September 24-28, Vol. 17, pp. 13335-13343.
[13]. Chen, Y. and Lu. (2012). New replaceable coupling beams for shear wall structures. 15TH World Conference on Earthquake Engineering, September 24-28, Vol. 19, pp. 15364-15374.
[14]. Montgomery, M. and Christopoulos, C. (2015). Experimental validation of viscoelastic coupling dampers for enhanced dynamic performance of high-rise buildings. Journal of Structural Engineering, Vol. 141, 04014145:1-11.
[15]. .Lehman, D., Turgeon, J.A., Birely, A.C., Hart, C.R., Marley, K.P., Kuchma, D.A. and Lowes, L.N. (2013). Seismic behavior of modern concrete coupled wall. Journal of Structural Engineering, Vol. 139, pp. 1371-1381.
[16]. .Cheng, M.Y., Fikri, R. and Chen, C.C. (2015). Experimental study of reinforced concrete and hybrid coupled shear wall systems. Engineering Structures, Vol. 82, pp. 214-225.
[17]. ABAQUS/CAE v6.12 Programme, Dassault Systemes Simulia Corp. Providence, RI, USA.

ICENS
INTERNATIONAL CONFERENCE ON ENGINEERING AND NATURAL SCIENCES
24-28 May 2016 /Sarajevo

The Comparison of Pullout Strength of Square, Triangle and Circular Screw Threads

Faruk Karaca[1]

Abstract

The screw threads are used for various types of fastening applications. Especially, nonmetal materials such as plastics, polymers are fastened with screw threads because of non weldability. The screw threads are subjected to various type of loading conditions in these applications. Generally, the loading conditions are included tension, compression, shear, bending and torsion. In this study, the pullout test is used for the tensile strength of the three types of screw threads. The scope of the present study is, comparing the maximum tensile loading performances of square, circular and triangle screw threads with numerically by ANSYS software. The square, circular and triangle screw threads are tested for the directional deformation and von-mises stress. Among these three type of screw threads, the best pullout stress with triangle profile and the worst pullout stress have been obtained with square and circular profile. The circular profile has presented closer values to the square thread profile.

Keywords: *Screw thread, pullout strength, tensile loading, finite element analysis, ANSYS*

1.INTRODUCTION

The bolt and nut joints are widely used for assembling of various machine elements. The bolts are especially used in assemblies when a load-bearing connection that can be disassembled without destructive methods is required in a design. Also threaded components are applied in non weldability materials such as plastics and composites successfully. The bolts are subjected various loading conditions such as tension, shear, bending and torsion in many assemble applications. In order to determine the strength of the bolts, the tensile test is performed. The threaded part of the bolt is the weakest part on the body of the bolt. The cross sectional area of the longitudinal bolt is changed; thus the strength is reduced via the surface of the bolt is become unsteady.

In view of above results, the thread profile is an important factor for the strength of the screw threads. Every thread profiles are used for each threaded applications. But most of the threaded fasteners are subjected tensile loading applications. The experimental tensile test is only measured the maximum and/or average strength of the screw thread but not informed how this effect the tooth of the thread. For instance, where the maximum strained region of the screw thread is existed. In order to solve this problem, the numerical methods are very useful. The finite element method is the most common and strongest method for this applications. Nowadays finite element method is successfully subjected several mechanical engineering problems by improved powerful computers [1,2,3].

Therefore, the finite element method by ANSYS software was used in the present study. Three different thread profiles such as square, triangle and circular were subjected to pullout analysis in ANSYS. Thus, the most successful thread for tensile loading was determined. Furthermore, the most sensitive regions of the threads were identified from the ANSYS stress images in this study.

2MATERIAL & METHOD

2.1.Designing of the threads

The designed screw threads profiles are created according to ISO standards as shown in Figure 1. Where P is pitch, D_{maj} is major diameter, D_p is pitch diameter, D_{min} is minor diameter and H is depth/height of fundamental triangle of the screw thread are considered during the designing. For the standardization purpose, all the designed threads were designed geometrically at the same thread heights of 2,5mm.

[1] *Corresponding author: Firat University, Department of Mechanical Engineering, 23119, Elazığ, Turkey.* fkaraca@firat.edu.tr

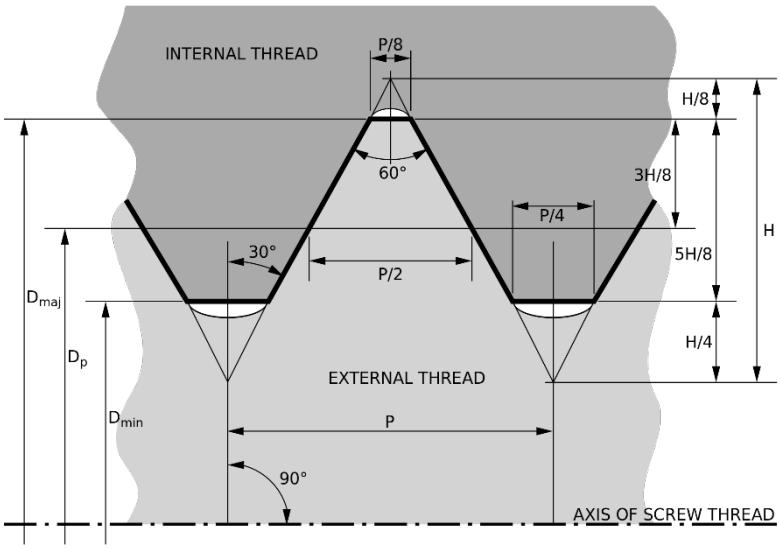

Figure 1. The parameters of a metric screw thread [4]

The designed screw thread models by ANSYS are seen in Figure 2.

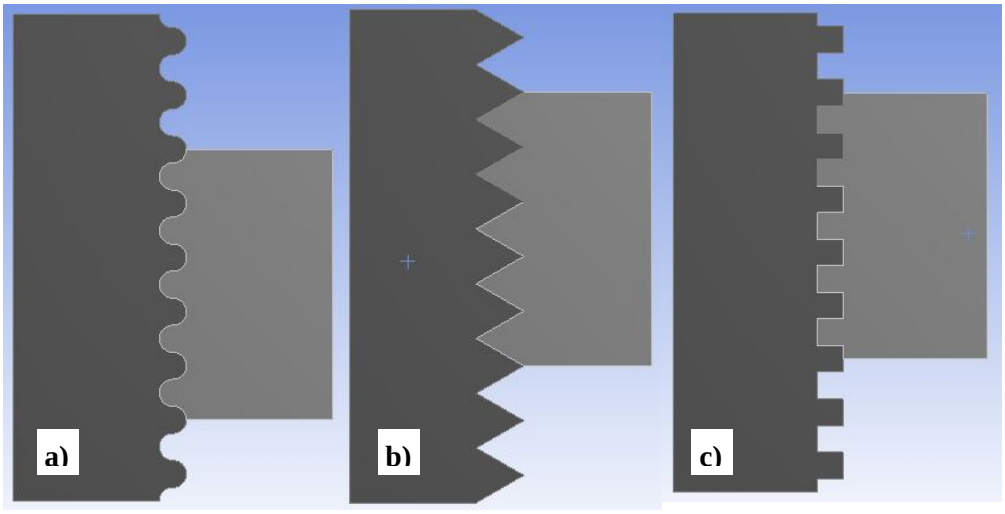

Figure 2. The designed screw thread models by ANSYS. a) circular b) triangular c) square

2.2.Designing of the model

The screw thread models are subjected the pullout simulation by ANSYS. The three threaded bolts are assembled with appropriate nuts. Each bolts are mated with its nuts. The material properties of the sample models were chosen as AISI 1010 steel. The default values of the material properties have been used in the analysis. The pitch of the screw threads was specified 2,5mm for all three types of the model.

In order to verify the load transferring between contact region conditions of the bolt and nuts, the contact region under "Connections Tool" is used. Then the edges of the screw threads are selected. Also the frictional contact interface of the bolt and nut is chosen from the Connections Tool and set 0,2.

The ANSYS Workbench has been used for meshing the bolt and nut mates. The Hex Dominant Method has been selected from the Mesh Tool of the ANSYS for each of the three thread models. In order to develop the performance of analysis of the three thread models, the mesh element size was reduced from default to 0,2mm at the connection edge regions of the bolt-nut assemblies. There were 20071 nodes and 5885 elements in square profile, 30219 nodes and 5828 elements in triangle profile and 24618 nodes and 74707 elements in circular profile of the models. Figure3 illustrates the meshing of all three types of screw threads models.

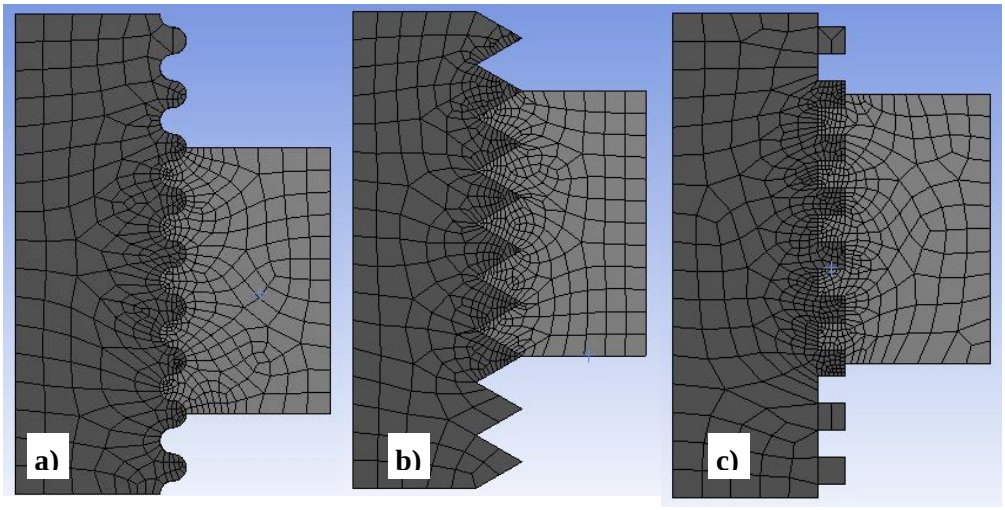

Figure 3. The mesh models of the screw threads. a) circular b) triangular c) square

The force form has been applied for loading of the models. The force was applied on the bottom of the bolt. The magnitude of the force was 100000N and it was applied in the positive direction of Y-axis (Figure 4).

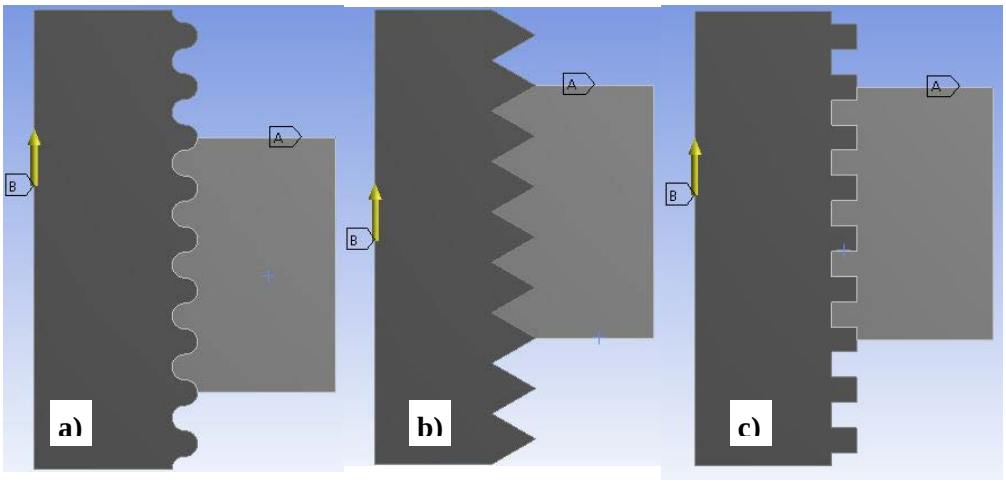

Figure 4. The direction of the applied force and supports

On the other hand, the frictionless supports were applied on the above of the nuts (Figure 4). Therefore, the directional deformation and Von-mises stress were measured for all three types of screw thread models.

3.RESULTS

The pullout tests are applied in the Y-axis and the directional deformation and Von-mises stress are determined (Figure 5 and Figure 6). The directional deformations and Von-mises stress of the models are tabulated in Table1.

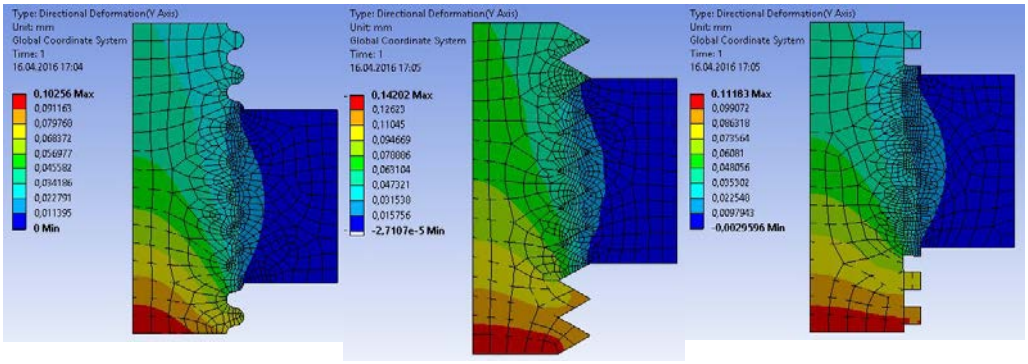

Figure 5. The directional deformation variation of the screw threads via pullout loading

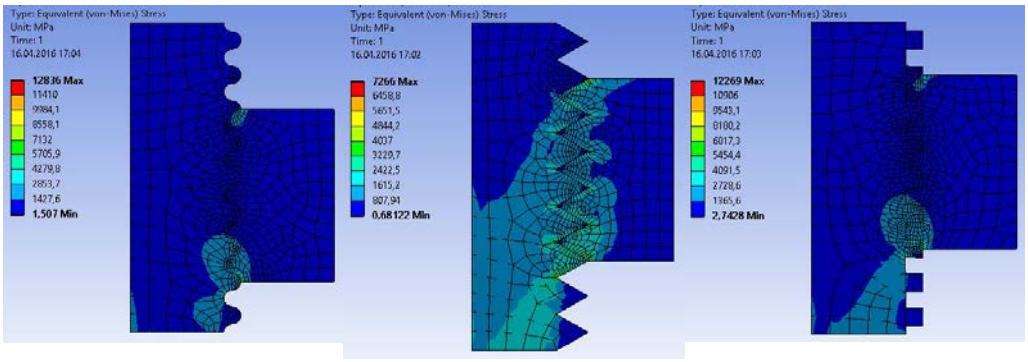

Figure 6. The Von-mises stress variation of screw threads via pullout loading

Table 1. The directional deformations and Von-mises stresses of the screw threads

SCREW THREAD	DIRECTIONAL DEFORMATION (mm)		VON – MISES STRESS (MPa)	
	Minimum	Maximum	Minimum	Maximum
Square Thread	-2,9596e-4	0,11183	2,7428	12269
Triangle Thread	-2,7107e-5	0,14202	0,68122	7266
Circular Thread	0	0,10256	1,507	12836

The maximum directional deformation is obtained in triangle screw threads as indicated Table 1. The square and circular profiles are presented closer directional deformations. On the other hand, the minimum Von-mises stress is obtained in triangular profile. The maximum Von-mises stress is existed in both square and circular screw threads. The Von-mises stresses are so close in square and circular screw threads.

The triangle screw threads could take more load than the other two screw models as evaluated the analyses results. But triangle profile is weak in terms of directional deformation. The square and circular screw threads are taken less load than the triangle screw threads. But they are strong in terms of directional deformation. Since the triangle threads have greater thread surface area, it showed higher mechanical strength than the other two selected type. The triangle threads are not preferred for axial pullout loadings because it could not tolerate screw stripping.

4.CONLUSIONS

In this study, the following conclusions may be drawn;

- The triangle screw threads are taken more load than square and circular screw threads
- The triangle screw threads are more deformed than the other screw threads
- The directional deformation and Von – mises stress of the square and circular screw threads are closer
- The square and circular screw threads are preferred for axial pullout loadings.

REFERENCES

[1]. S. Darshith, K. Ramesh Babu, "The pullout performance of square and DSR screw threads," *International Journal of Research in Engineering and Technology*., vol. 03, pp. 310 – 314, June 2014.

[2]. Purvi S.D. Patel, Duncan E.T. Shepherd, DavidW.L. Hukins, "The effect of screw insertion angle and thread type on the pullout strength of bone screws in normal and osteoporotic cancellous bone models," *Medical Engineering & Physics.*, vol. 32, pp. 822 – 828, May 2010.

[3]. R. L. Burguete, E. A. Patterson, "The effect of bending on the normalized stress at roots of threaded connectors," *Journal of Offshore Mechanics and Arctic Engineering.*, vol. 116, pp. 164 – 166, Aug. 1994

[4]. Inductiveload (2016), IEEEtran webpage on ISO and UTS Thread Dimensions.svg. [Online]. Available: https://commons.wikimedia.org/wiki/File:ISO_and_UTS_Thread_Dimensions.svg

Corrosion Behaviour of AlSi12/B_4C Composites

E. Cevik[1],Y. Sun [1],Y. Turen [1],H. Ahlatci,[1] H Cug[1]

Abstract

In this study, the effects of matrix compounds on the corrosion behaviour of AlSi12-XMg matrix composites reinforced by 60 % B_4C particles were analysed. The microstructure analysis of the composite materials showed that the porosities accumulated around B_4C reinforcement particles. By increasing Mg addition, there was considerable decrease in the porosity volume ratios. Corrosive properties showed two different attitudes in two different solutions. In NaCl solution, there was an increase in corrosion resistance with Mg addition, while in H_2SO_4 solution there was a decrease.

Keywords: *AlSi12-XMg/B_4C, corrosion behaviour.*

1.INTRODUCTION

In metal matrix composites, Al and Al alloys stand out with their advantages such as low density, high corrosion resistance and low production costs among light metals used as matrix.

In aluminium matrix composites local corrosion starts with physical and chemical heterogenics such as reinforcement/matrix interface, intermetallics, mechanic damages, grain boundary, inclusion or dislocation [1]. However, many researchers reported that reinforcements and intermetallic phases increased the corrosion resistance functioning as a barrier in some cases [2-6].

Zakaria added SiC particles in different sizes (3, 6, 11 µm) and different ratios (%5, 10, 15) to pure aluminium alloy. He determined that while the effects of particle grain size on corrosion is in low ratios, corrosion resistance increased with the increase in particle reinforcement volume ratio. The author related the increasing corrosion resistance with inert SiC particles in NaCl solution [7].

In this study, the effects of matrix compounds on the corrosion of AlSi12 matrix composites reinforced by 60 % B_4C particles were analysed.

2.MATERIALS AND METHODS

50x7 mm cylindrical preforms were produced by using B_4C particles that have 48 µm average grain sizes. AlSi12 aluminium matrixes with various Mg amounts (0-4 %) were infiltrated into the preforms by pressure infiltration technique. The infiltration process was held at 800^o C and 8 bar pressure.

The microstructure analysis of the composite materials was carried out by light optical microscope (LOM) and scanning electron microscope (SEM). The calculations of matrix-reinforcement material volume ratio and porosities were made by Clemex software integrated into the light optical microscope. In determination of the matrix element and structural differences, X-Ray diffraction was used.

Corrosion experiments were carried out in two different solutions (3,5 % NaCl and 3,5 % H_2SO_4) according to the weight loss measurement methods in determination of the corrosion attitudes.

3.RESULTS AND DISCUSSION

The (LOM) and (SEM) analyses of AlSi12-XMg matrix composites produced with Mg addition in different ratios and reinforced with 48 µm grain size B_4C particle are given below.

3.1.Microstructural analysis

In Fig 1, LOM figures of AlSi12 matrix composites produced with Mg addition in different ratios (%0-4) and reinforced with 48 µm grain size B_4C particle. In microstructural analysis it is clearly seen that agglomeration of particles does not occur and homogenization of particle distribution is achieved. Porosities are seen around reinforcement particle though in low amounts.

[1]*Corresponding author: Karabük University, Department of Metallurgical and Materials Engineering, 78150, Karabük, Turkey.*
engincevik@karabuk.edu.tr

Particle, matrix and porosity amounts gathered by image analysis are given in Table 1. The porosity amount decreased to 0,68 % with 4 % Mg addition to AlSi12 matrix composite with 1,59% porosity amount. The average volume ratio of the reinforcement is determined %58±2.

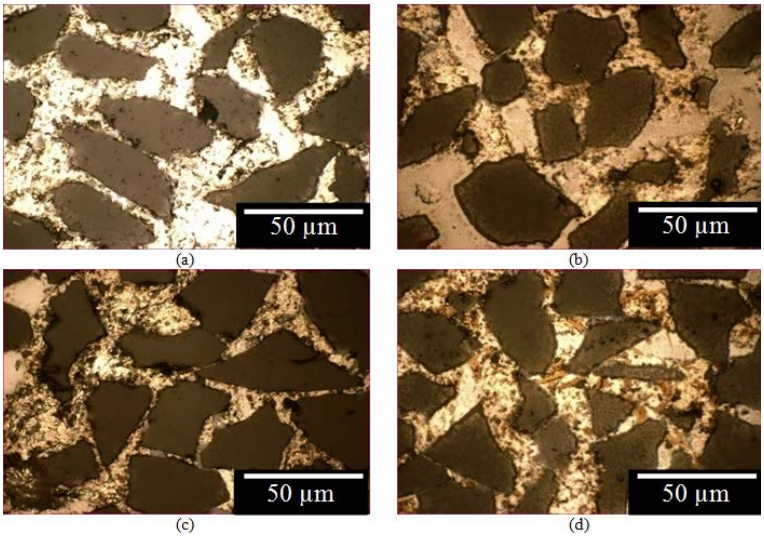

Fig 1. Microstructure of a) AlSi12-B_4C, b) AlSi12-1Mg-B_4C, c) AlSi12-2Mg-B_4C and d) AlSi12-4Mg-B_4C.

Table 1. Image analysis results of the investigated composites.

Matrix	***Mg Content (%)***	***Volume ratios (%)***		
		B_4C	***Matrix***	***Porosity***
AlSi12	0	56,59	41,82	1,59
	1	54,21	44,47	1,32
	2	57,65	41,59	0,76
	4	59,90	39,42	0,68

When the SEM images in Figure 2 is examined, according to the EDX analysis taken from region number 2, free eutectic Si formation is determined, with SEM analysis with higher magnification these results are supported. The arrows show the porosities in the structure.

XRD analysis of composites is shown in Fig 3. According to XRD analysis $Al_{99}Si$, Al_3BC, AlB_2 and AlB_{10} occurred as a result of interface reactions. Eutectic Si formations determined with SEM analysis was determined with XRD analysis as well. It can be clearly seen that with Mg addition Mg_2Si intermetallic phase occurred in addition to these phases.

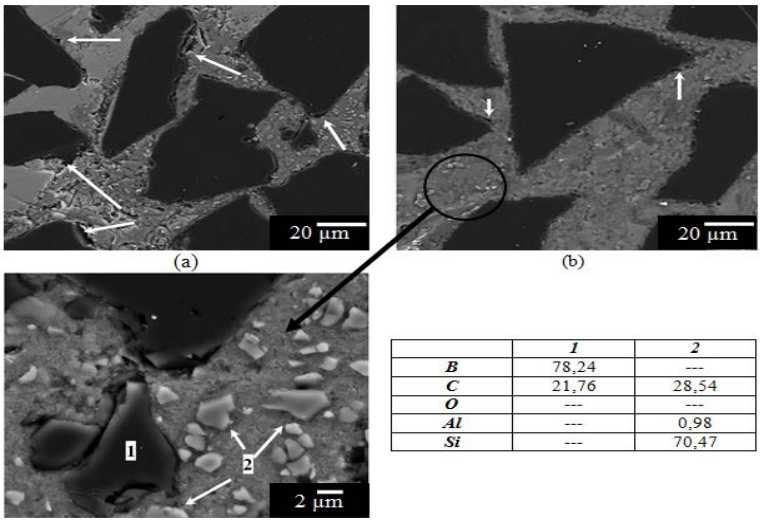

	1	2
B	78,24	---
C	21,76	28,54
O	---	---
Al	---	0,98
Si	---	70,47

Figure 2. SEM micrographs and EDX analysis result of the microstructure a) AlSi12-B_4C and b) AlSi12-4Mg-B_4C.

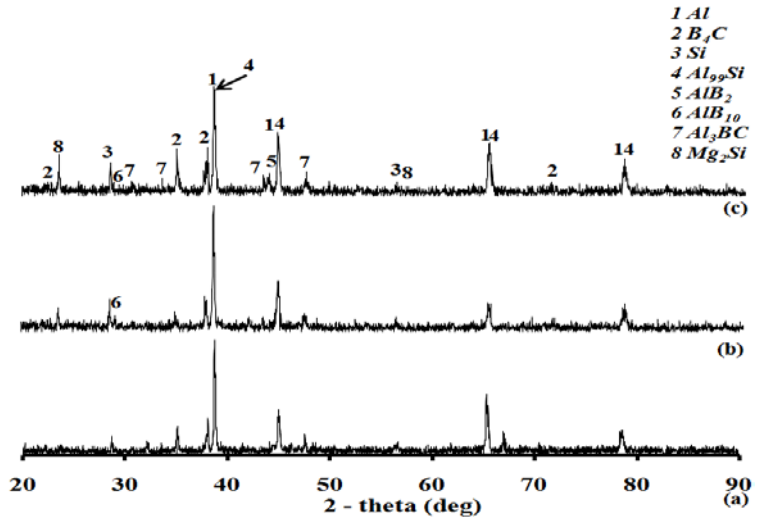

Figure 3. XRD patterns of a) AlSi12-B_4C, b) AlSi12-2Mg-B_4C and c) AlSi12-4Mg-B_4C.

3.2.Corrosion Behaviour

The effect of Mg addition on corrosion resistance of composites is plotted as the change of mass loss according to time in Fig 4.

The decrease in mass loss with increasing Mg addition in AlSi12-XMg alloy matrix composites is thought to be a result of the discontinuity of matrix channels inside the composites in 3,5% NaCl solution [4, 6, 8]. It is strongly possible that the intermetallics formed restrained the corrosion moving into inner regions of the composite.

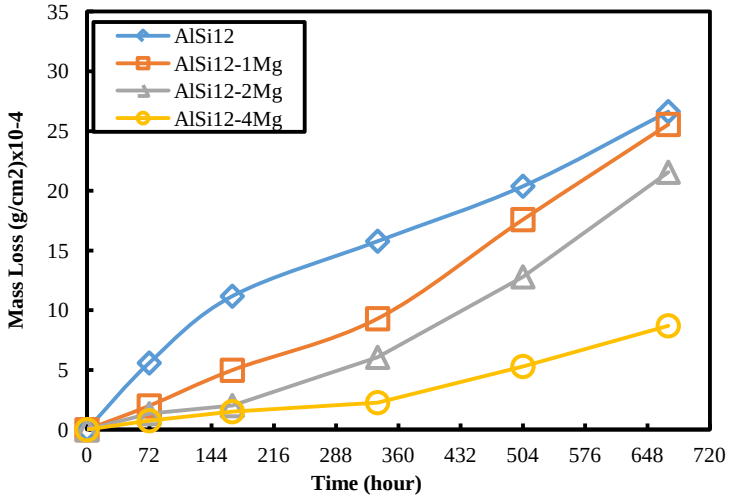

Figure 4. AlSi12-XMg-B_4C immersion corrosion test results in NaCl solution.

However, according mass loss method the primary reason for the increase of corrosion resistance with Mg addition is the formation of $Mg(OH)_2$ with $Al(OH)_3$ because of the reactions on the surface [8]. Therefore, when we look at the SEM images (Figure 5) composites with Mg addition is covered with a denser oxide layer than Mg free composites at the end of 28 days. Additionally, wider cavities occurred in the reinforcement-matrix interface in Mg free composites. With Mg addition cavities are narrower by means of oxide layer. These analyses support the mass loss results.

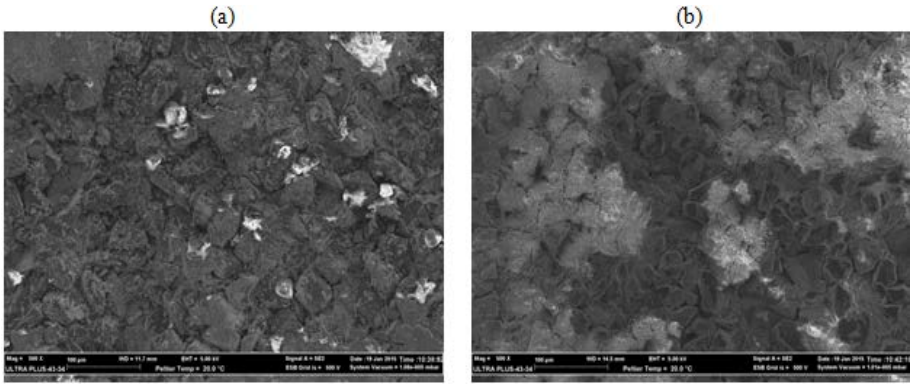

Figure 5. SEM micrographs showing surface of a) AlSi12-B_4C and b) AlSi12-4Mg-B_4C in NaCl solution.

An important point to pay attention to in the composites produced is that porosities were decreased substantially with Mg addition. The strong bonding between the matrix and reinforcements enabled the possible pitting corrosion in the early steps.

The effect of Mg addition on corrosion resistance of composites in 3,5% H_2SO_4 solution is plotted as the change of mass loss according to time (24 hours) in Figure 6.

When we look at Fig 6, in the first 4 hours the mass losses are closer to each other but after this period Mg addition to the matrix increased the mass loss considerably. The reason for this is thought to be the intermetallics formed after the addition of alloying elements to the matrix [9-11]. Because the intermetallics in the structure forms a galvanic couple with the matrix and act as cathode, matrix element acts as anode. The matrix is dissolved in 3,5% H_2SO_4 solution which is an aggressive environment and increases the mass loss. In addition to this, with the dissolution of the matrix, stable B_4C particles splits from the structure and sinks to the bottom and this increases the mass loss more than estimated. The study of Kumari et. al. supports our results and mentions the negative effects of the intermetallics on corrosion resistance [12].

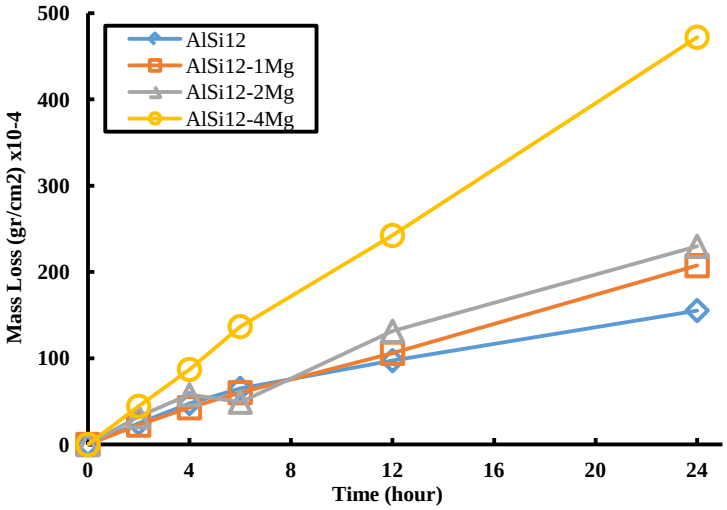

Figure 6. AlSi12-XMg-B_4C immersion corrosion test results in H_2SO_4 solution.

Surface images of studied composites are shown in Figure 7. When the SEM images of the surface are examined, as a result of 4% Mg addition to AlSi12 matrix composites pitting potential increased, the aggressive environment (%3,5 H_2SO_4) prevents oxide layer on the surface and causes higher amounts of mass loss.

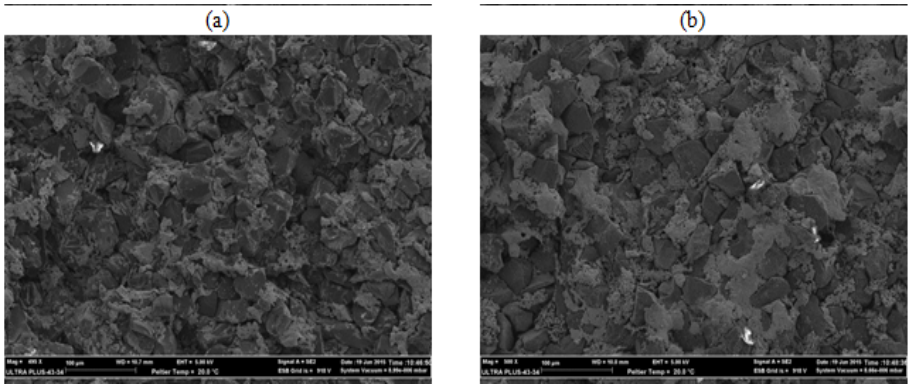

Figure 7. SEM micrographs showing surface of a) AlSi12-B_4C and b) AlSi12-4Mg-B_4C in H_2SO_4solution.

4.CONCLUSIONS

The microstructural analyses and corrosion experiments of AlSi12 matrix composites produced with Mg addition in different ratios (%0-4) and reinforced with 48 um grain size B_4C particle gives us the following results.

1. Porosities are seen around reinforcement particles. The porosity amount decreased by approximately 58% with 4% Mg addition to AlSi12 matrix composite with 1,59% porosity amount to 0,68%.
2. In AlSi12 matrix composites $Al_{99}Si$, Al_3BC, AlB_2 and AlB_{10} occurred as a result of interface reactions. Eutectic Si formations determined with SEM and XRD analysis. With Mg addition Mg_2Si intermetallic phase occurred in addition to these phases.
3. After the corrosion tests in 3,5% NaCl solution, while mass loss decreases with Mg addition to AlSi12 matrix, it is increased in 3,5% H_2SO_4 solution.
4. In the corrosion tests of NaCl solution while a denser oxide layer is observed in the surface SEM images, in H_2SO_4 solution oxide formation was almost non-existent in the samples exposed to corrosion.

ACKNOWLEDGMENT

This study is a part of project which has been supported by Karabük University.

REFERENCES

[1]. K. K. Alaneme, T. M. Adewale and P. A. Olubambi "Corrosion and wear behaviour of Al–Mg–Si alloy matrix hybrid composites reinforced with rice husk ash and silicon carbide", *Journal of Materials Research and Technology*, 3(1): 9–16, 2014.
[2]. A. Lekatou, , A. E. Karantzalis, , A. Evangelou, , V. Gousia, , G. Kaptay, , Z. Gácsi, , P. Baumli, and A. Simon "Aluminium reinforced by WC and TiC nanoparticles (ex-situ) and aluminide particles (in-situ), Microstructure, wear and corrosion behaviour", *Materials and Design*, 65, 1121–1135, 2015.
[3]. S. L.Winkler, M. P. Ryan and H. M. Flower "Pitting corrosion in cast 7XXX aluminium alloys and fibre reinforced MMCs", *Corrosion Science*, 46, 893–902, 2004.
[4]. F. Toptan, , A. C. Alves, , I. Kerti, , E. Ariza, and L. A. Rocha "Corrosion and tribocorrosion behaviour of Al–Si–Cu–Mg alloy and its composites rein forced with B_4C particles in 0.05 NaCl solution", *Wear*, 306: 27–35, 2013.
[5]. S.Candan "Effect of SiC particle size on corrosion behavior of pressure infiltrated Al matrix composites in a NaCl solution", *Materials Letters*, 58, 3601–3605, 2004.
[6]. S. Candan, and E. Bilgic "Corrosion behavior of Al–60 vol.%SiC_p composites in NaCl solution" *Materials Letters*, 58, 2787– 2790, 2004.
[7]. H. M. Zakaria "Microstructural and corrosion behavior of Al/SiC metal matrix composites" *Ain Shams Engineering Journal*, 5, 831–838, 2014.
[8]. S. Candan "An investigation on corrosion behaviour of pressure infiltrated Al–Mg alloy/SiCp composites" *Corrosion Science*, 51, 1392–1398, 2009.
[9]. B. Dikici, C. Tekmen, O. Yigit, M. Gavgali and U. Cocen "Detrimental effect of particle sol–gel coating on the corrosion behavior of A380–SiC composite" *Corrosion Science*, 51, 469–476, 2009.
[10]. J. Zhu and L. H. Hihara "Corrosion of continuous alumina-fibre reinforced Al–2 wt.%Cu–T6 metal–matrix composite in 3.15 wt.%NaCl solution" *Corrosion Science*, 52, 406–415, 2010.
[11]. S. Payan, Y. L. Petitcorps, J. M. Olive and H. Saadaoui "Experimental procedure to analyse the corrosion mechanisms at the carbon/aluminium interface in composite materials" *Composites Part A*, 32, 585–589, 2001.
[12]. P. D. R. Kumari J. Nayak and A. N. Shetty "Corrosion behavior of 6061/Al-15 vol. pct. SiC(p) composite and the base alloy in sodium hydroxide solution" *Arabian Journal of Chemistry*, 1-11, 2012.

Investigation of Service Quality in E-commerce Websites with Structural Equation Model

Mehmet Cabir Akkoyunlu[1], Merve Tutuncu[2], Zeynep Demirkol[2], Coskun Ozkan[2]

Abstract

This study examines the relationship between service quality and customer loyalty in electronic commerce sites. Perceived service quality of customer who uses electronic commerce sites was determined according to the SERVQUAL scale. The purpose of the study is sorting the perceived quality factors and examining the relationship between perceived quality factors and customer loyalty related to the usage of electronic commerce sites. Therefore, a survey consisting of 40 questions with four dimensions (activity, system compliance, operation realization and privacy) was applied to electronic commerce clients. 9 hypotheses are established on service quality and customer loyalty. Hypotheses were tested in SPSS. The model that indicates the impact of the survey's four dimensions on customer loyalty and customer satisfaction has been established in AMOS. The model has been improved four times to achieve the optimum result. A factor of commitment intention and activity dimensions was removed. The factors of activities have the covariance.

Keywords: *Customer loyalty, customer satisfaction, e-commerce, service quality.*

1.INTRODUCTION

Customer satisfaction has been an important topic in marketing and it is a major aim of all business activities. Nowadays, companies are in a tough competition. Therefore, they move from the product and sales strategy to the marketing strategy, which gives a company a better chance of outperforming competition.

In today's competitive business environment, meeting the demand for customer satisfaction is very important especially for managers. Every organization must explain customer satisfaction portfolio of their market. Because of this customer satisfaction could not be defined only standard or quality of product. Customer satisfaction is about relationships between "the customer of good or service" and "the provider of a good or service".

Customer loyalty has been perceived to be a behavioral concept entailing repeat buying of product or service evaluated as the series or share of purchases, leads, magnitude of relationship or all of the above mingled together. Lots of researches on the subject of loyalty have been measured by behavioral direction of brand loyalty, such as repeat purchase without considering cognitive directions of brand loyalty.

Electronic commerce, in a broad sense, is the use of computer networks to improve organizational performance. SERVQUAL is designed to measure service quality as perceived by the customer.

Structural Equation Modelling (SEM) techniques are considered today to be a major component of applied multivariate statistical analyses and are used by biologists, economists, educational researchers, marketing researchers, medical researchers and a variety of other social and behavioral scientists. Although the statistical theory that underlines the techniques appeared decades ago, a considerable number of years passed before SEM received the widespread attention it holds today. One reason for the recent attention is the availability of specialized SEM programs.

2.SERVICE QUALITY

Different definitions from different sources were made about the service. Especially in the early 1980s with the end of the 1970s compiled from studies, a group of property was listed [1]. So the service is intangible as a different from a product, heterogeneous and simultaneously because of production and consumption occur simultaneously [2]. The service is an intangible concept. Inventory cannot be held in any way, cannot hide, cannot be standardized, passing directly from the manufacturer to the consumer and there is no visual objectivity and property relations [3]. Because service has the number of unique features. These features [4]:

Services are intangible: Services that cannot be detected by the five senses and physical dimensions without product. Service is an activity that put forth with a performance.

Heterogeneity: Although a standard to ensure the production of goods, services show variety according to the production time and people. Because consumers' experiences directly effect on perceptions of service. When consumers receive existing

[1] *Corresponding author: Yildiz Technical University, Mechanical Engineering Faculty, Department of Industrial Engineering, Besiktas/İstanbul, Turkey.* mcabir@yildiz.edu.tr

[2] *Yildiz Technical University, Mechanical Engineering Faculty, Department of Industrial Engineering, Besiktas/İstanbul, Turkey.*

services, to compare them with similar services received before and decide. The success of the service shows changes with the power and type of the interaction between service offering and services bought [3].

Synchronism: When the product is produced it can be stored not consumed, although they can be transferred to another place, as soon as the service is consumed produced.

Crosby was defined the quality as a comply with the requirements, and Gryna "be suitable for use or purpose". Quality, market share and in terms of return on investment have an undeniable importance [5].

Before the emergence of the concept of quality of service, quality was associated with the quality of product. According to the famous Japanese philosophy of quality "zero defect - the first time to make the right" shape was defined. Carried out by research, quality began to be expressed as a comparison performance with expectations [1].

In today, service and quality has become an integral concept. In terms of services offered the concept of quality which carries has an importance, is began to perceive as an important element that determines preferences by consumers [3].

Depending on the given definition of quality, the quality of service is defined as "A resulting from a long-term performance evaluation approach" [6]. Zeithalm is defined the quality of service as "the customer is a general judgment about the superiority or excellence of a product or service" [3]. It reached the following conclusions for the service quality [7].

2.1.User Expectations and Perceived Service Quality

Customer satisfaction is directly related to compliance with the quality dimension. Perceived quality, users perceive revealed by comparing the performance with expectations [8].

Perceived quality of service, previous expectations of customers receiving services and actual service experience which benefit (performance) is the result of benchmarking. Morever, between the perceived performance and customers expectations are considered as the degree and direction of the difference [9].

Figure 1. Customer satisfaction index

2.2.Measuring the Quality of Service

Parasuraman used five core dimensions to measure service quality, but tangibility, reliability, responsiveness, empathy, and assurance, consisting of a total of 22 doubles of components. These are;

Reliability: The ability to execute the promised service dependably and exactly.

Assurance: The knowledge and kindness of employees and their ability to transmit trust and reliance.

Tangibles: The appearance of physical facilities, equipment, personnel and communication materials

Empathy: The provision of caring, personalized attention to customers.

Responsiveness: The willingness to help customers and to provide quick service [10].

SERVQUAL is designed to measure service quality as perceived by the customer. Relying on information from focus group interviews, Parasuraman identified basic dimensions that reflect service attributes used by consumers in evaluating the quality of service provided by service businesses.

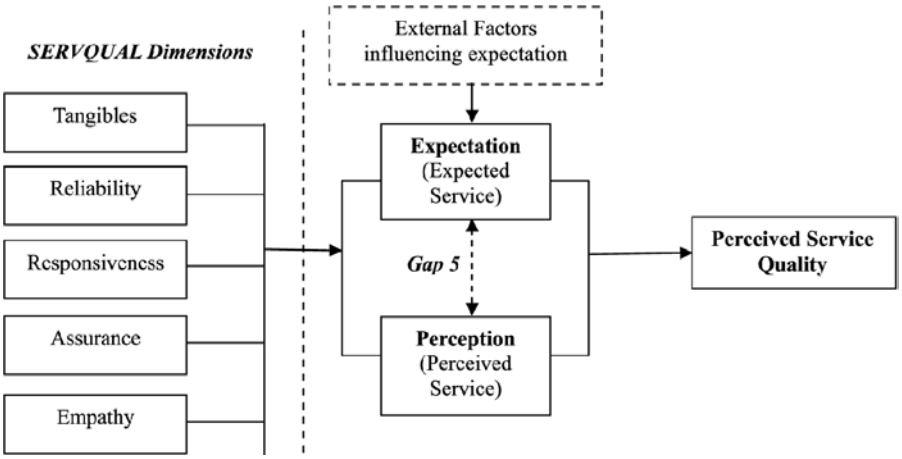

Figure 2. SERVQUAL dimensions

3.STRUCTURAL EQUATION MODELING

Structural Equation Modeling or SEM is a very general statistical modeling technique which is widely used in the behavioral sciences. It can be viewed as a combination of factor analysis and regression or path analysis. The interest in SEM is often on theoretical constructs, which are represented by regression or path coefficients between the factors. The Structural Equation Model implies a structure for the covariances between the observed variables, which provides the alternative name covariances structure modeling. However, the model can be extended to include means of observed variables or factors in the model, which makes covariance structure modeling a less accurate name [11].

3.1.Case Study

In this section of the research, information about the materials and methods used in the research are given. Sampling and sampling size, survey methodology and distribution, research questions, hypotheses and analysis techniques are located. Hypotheses have been tested and the test results are included in this section. The results of the relationship between service quality and customer loyalty are offered. Demographic information is presented with descriptive statistics.The theoretical basis of the analysis results have been created with secondary research data. In the study needed primary data were collected by a survey.

Nowadays, many companies promote their products not only via the Internet. At the same time, they allow also to make purchases over the Internet. Customer loyalty is the subject of this investigation. Studies in this area is important due to the fact that the new field and to be a turning point in the transition to a modern structure from a traditional structure. In this respect; the research is important because of the research toward a new phenomenon and to create a resource for the future.

In this research, within the framework of the identified problems and hypotheses, giving general information on electronic commerce system, it aimed to elucidate the factors that affect customer loyalty in e-commerce.

The research focuses on two interrelated objectives for theoretical and practical. The quality of service perceived by customers and if there is a relationship between loyalty and perceived service quality dimensions have examined by theoretical and practical. SERVQUAL Scale samples are seen too much to examine the quality of services in the services sector.

It has sought answers to the following questions:

- What are the dimensions of service quality in the electronic commerce website?
- How does it affect your satisfaction Customer electronic service quality dimensions of electronic commerce site?
- Is there a relationship between electronic service quality and customer loyalty?
- Is customer loyalty affected directly by demographic variables?
- What factors do determine the customer loyalty among Turkish consumers?

This research model focuses on the perceived quality of service and customer loyalty. Re-use web-based services for customers based on perceived service quality, price, demographics, and company image and customer satisfaction. Perceived quality of service is comprised of four electronic service quality dimensions. These dimensions affect customer loyalty are activity, system suitability, and perform operations consists of privacy. These four dimensions explain customer requests for re-use web-based electronic services. If electronic commerce sites are providing a high level of service quality, customer requests of re-use and level of customer loyalty will be high. Demographic characteristics include such as age, sex, marital status, education and income level. Age is associated with the use of Internet technology.

Research model is summarized in Figure 3 [12].

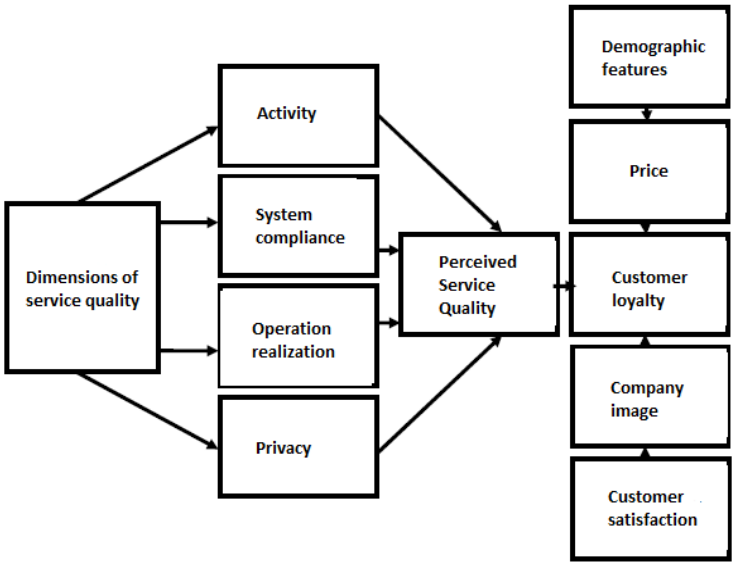

Figure 3. The model of the research.

3.2. Hypotheses of the Research

The research is mainly focused on the following hypotheses.

H1: Customer satisfaction is not recognized as a key qualification of the service quality for e-commerce sites.

H2: Price is not recognized as a key qualification of the service quality for e-commerce sites.

H3: Company image is not recognized as a key qualification of the service quality for e-commerce sites.

H4: The gender of the participants does not affect on customer loyalty.

H5: Price category does not affect on customer loyalty.

H6: Service quality and customer loyalty is not certainly related.

H7: Customer satisfaction and customer loyalty is not certainly related.

H8: Customer loyalty and company image is not certainly related.

H9: Customer loyalty and price category is not related.

To determine the reliability of research group questions for each factor the value recognized in the literature $\alpha = 0.70$ level reliability (Reliability) analysis. Analysis results are given in the Table 1 below.

Table 1. Reliability table.

Scale	The number of questions	Factor	Reliability alpha
Activity	8	The average value	0,839
System compliance	4	The average value	0,765
Operation realization	7	The average value	0,879
Privacy	3	The average value	0,731
Customer loyalty	5	The average value	0,755
Customer satisfaction	2	The average value	0,700

Reliability values measured for each scale and questions as will be seen from the table above the values accepted in the literature. This indicates that each scale is reliable and can be used. Skew value and standard deviation are given in the following Table 2 for measuring the uniformity of response to the research group questions.

Table 2. Skew values of research scale, standard deviation and reliability values

Scale	Skew value	Standard deviation	Reliability Alpha
Activity	0,632	3.747	0,839
System compliance	0,322	2.350	0,765
Operation realization	0,559	4.083	0,879
Privacy	0,554	0.931	0,731
Customer loyalty	1,517	2.157	0,755
Customer satisfaction	6,126	1.385	0,700

The relationship between service quality and customer satisfaction was investigated with Structural Equation Modeling. Model is shown below Figure 4:

As mentioned in the previous sections, activity, system compliance, operation realization and privacy are dimensions of the survey. These dimensions influence customer loyalty. The relationship between customer loyalty and customer satisfaction was examined.

Observed variables: e1, e2, e3, e4, e5, e6, e7, e8 are observed variables of activity. ig1, ig2, ig3, ig4, ig5, ig6, ig7 are observed variables of operation realization. su1, su2, su3, su4 are observed variables of system compliance. g1, g2, g3 are observed variables of privacy. bn1, bn2, bn3, bn4, bn5 are observed variables of customer loyalty. mm1, mm2 are observed variables of customer satisfaction.

Unobservable variables: activity, system compliance, operation realization, privacy, customer loyalty, customer satisfaction.

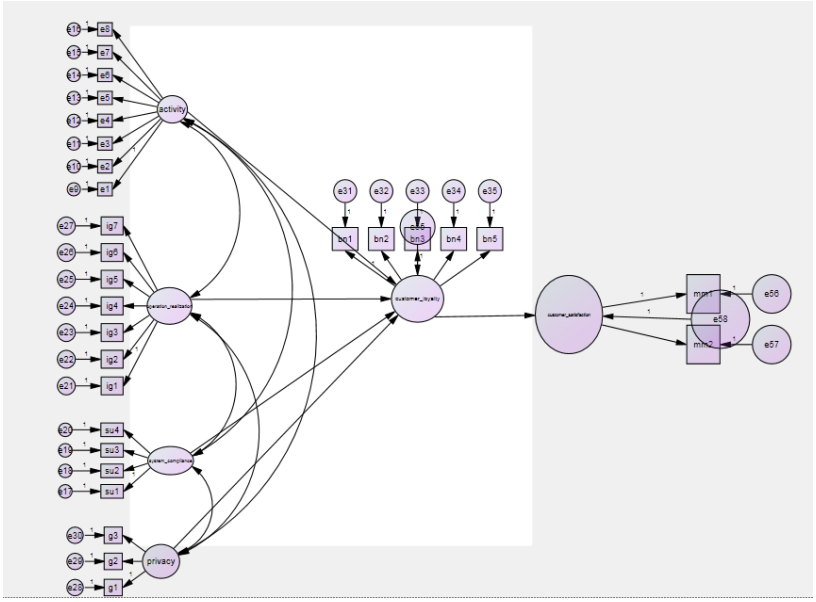

Figure 4. Structural equation modeling

Four steps were applied in improvement the model. First, bn5 which is observed variable was removed. e24 and e25 are connected to each other. Then, e2 is removed and e9 and e11 are connected to each other. The final model is as follows.

Table 3. Improved steps

	CMIN/DF	CFI	GFI	RMSEA
Step 1	2,0851	0,751	0,827	0,084
Step 2	1,986	0,760	0,838	0,081
Step 3	1,966	0,772	0,849	0,081
Step 4	1,910	0,777	0,858	0,078

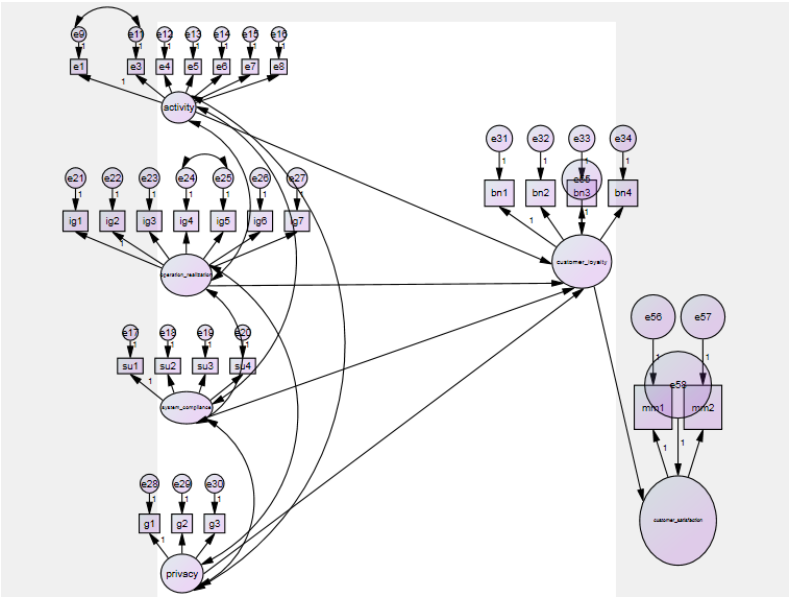

Figure 5. İmproved model

4.CONCLUSION

In this research, the relationship between service quality and customer loyalty in e-commerce was examined. Service quality and customer satisfaction in the e-commerce system depends on factors such as customer loyalty, price category and price perception. Contrary to expectations, company image related analysis is negative. The majority are based on data obtained from male customers.

There is a positive correlation between service quality and customer satisfaction (SQE). Customer satisfaction is called a key of service quality in electronic commerce sites (r=,354 and p<0,01). There is a significant relationship between service quality and customer satisfaction. The first hypothesis of the research is rejected. Service quality affects customer satisfaction.

There is a negative correlation between service quality and price (SQE). This situation indicates that price has a opposite perception with quality of service (r=-,163 and p>0,01). The hypothesis is not rejected. Monetary value of products or services received through e- commerce site is not a key qualification of the service quality.

There is a negative correlation between service quality and company image (SQE). This situation indicates that price has a opposite perception with quality of service (r=-,076 and p>0,01). At this point, expected situation is increasing quality of service by the increasing availability of the company's image. The results are interesting and worth considering. We can be interpreted as follows; big and famous companies being more comfortable think that to make a name is more sufficient than higher service quality.

Correlation analysis results showed that, there is no relationship between gender and customer loyalty (r=,047 and p>0,01). So, the hypothesis of research is not rejected.

There is a negative correlation between price and customer loyalty (r=-,092 and p>0,01). So, the hypothesis of research is not rejected.

There is a positive correlation between service quality and customer loyalty (r=,736 and p<0,01). The increase of service quality means to raise the customer loyalty. Hypothesis is rejected.

There is a positive correlation between customer satisfaction and customer loyalty (r=,283 and p<0,01). This situation, customer select firm which satisfied them.

There is a negative correlation between customer image and customer loyalty (r=-,036 and p>0,01). So, the hypothesis of research is not rejected.

There is a negative correlation between price and customer loyalty (r=-,092 and p>0,01). So, the hypothesis of research is not rejected.

The result of improvement making in AMOS shows that there is a relationship between customer loyalty and customer satisfaction. Expected results were obtained in step 4. CMIN/DF shows the ratio as a measure of fit. The ratio should be close to one for correct models. At the end of the study, we concluded 1,910. CFI is the comparative fit index. The model can be accepted when CFI Value is between 0,8-0,9 and we concluded 0,777. The GFI is goodness of fit index and the model can be accepted when GFI value is between 0,8 - 0,9. We concluded 0,858. 0.08 or less for the RMSEA would indicate a reasonable error of approximation and would not want to employ a model with a RMSEA greater than 0,1. In this study RMSEA value is 0,078. So, all the results we have achieved are acceptable.

REFERENCES

[1] Parasuraman, A., Zeithaml, V.A. and Berry, L.L., (1985). "A Conceptual Model of Service Quality and Its Implications for Future Research", Journal of Marketing, 49(4), 41-50.

[2] Soydal, İ., (2008). Web Bilgi Sistemlerinde Hizmet Kalitesi, Doktora Tezi, Hacettepe Üniversitesi Sosyal Bilimler Enstitüsü, Ankara.

[3] Eleren, A., Bektaş, Ç., and Görmüş, A. Ş., (2007). Hizmet Sektöründe Hizmet Kalitesinin SERVQUAL Yöntemi ile Ölçülmesi ve Hazır Yemek İşletmesinde Bir Uygulama, Finans Politik & Ekonomik Yorumlar, Cilt 44, Sayı 514.

[4] Armstrong, G. and Kotler, P., (2003). Marketing, International Edition, Prentice Hall.

[5] Anderson, C.R. and Zeithaml, C.P., (1984). Stage of Product Life Cycle, Business Strategy and business performance, Academy of Management Journal, 27, 5-24.

[6] Hoffman, K.D., and Bateson, J. E, (1997). Essential of Service Marketing, the Dryden Press, USA.

[7] Juran, J.M. and Gryna, F.M., (1998). Juran's Quality Control Handbook, McGraw Hill Co.,USA.

[8] Parasuraman, A, Zeithaml, V. and Berry, L., (1988). SERVQUAL: A Multiple-Item Scale for Measuring Consumer Perceptions of Service Quality, Journal of Retailing, 64, (Spring),12-40.

[9] Bulgan, U. ve Gürdal, G. (2005) "Hizmet Kalitesi Ölçülebilir mi? ÜNAK'05" Bilgi Hizmetlerinin Organizasyonu ve Pazarlanması, http://kaynak.unak.org.tr/bildiri/unak05/u05-22.pdf

[10] Chingang, N.D. and Berinyuy, L. P., (2010). Using the SERVQUAL Model to Assess Service Quality and Customer Satisfaction, Master Thesis.

[11] Hox, J.J. and Bechger, T.M., "An Introduction to Structural Equation Modeling, Family Science Review, 11, 354-373.

[12] Akgül, Y., (2010). Elektronik ticaret sitelerinde hizmet kalitesi ile müşteri bağlılığı arasındaki ilişkinin incelenmesi ve bir uygulama, İşletme Anabilim Dalı,

ICENS
INTERNATIONAL CONFERENCE ON ENGINEERING AND NATURAL SCIENCES
24-28 May 2016 /Sarajevo

Air Preheater Design And Optimization

Osman Ipek[1], Barıs Gurel[1], Mehmet Kan[1]

Abstract

The main heat recovering equipment air preheaters, one of the equipment of the boiler systems, are used in all boiler systems for pre heating combustion air. In tubular air pre heater, one of the different forms of the air pre heater systems, normally, flue gas (FG) flows inside the tubes while air flows across outside the tubes in cross flow form and carbon steel tubes are generally used in the system. In air pre heaters, air is pre heated by using hot flue gases from the boiler or heater. The energy from the hot flue gases is transferred to flowing cold air. Air pre heaters make a considerable contribution to the increasing efficiency of power plants fuelled with fossil fuel.

In the present study, tubular air pre heater has been investigated with analytical method using EES software with theoretical value. And then, theoretical design of air pre heater has been analyzed depending on analytical results. CFD analysis of the tubular air preheater is carried out using Ansys - Fluent 16.2 commercial software. The analyses of flue gas flow and air flow have been performed using Turbulence model and k-ε model. The parameters like temperature distribution, pressure drop, velocity, are also discussed. It has been planned to be used the designed air pre heater for industrial boiler application with 5 MW_{th} power. The first stage of the air pre heater with 5 stage has been analyzed in this study. Mass flow of flue gas is 2.52 kg/s and inlet temperature of flue gas is 190 ^{o} C while mass flow of air is 2.26 kg/s and inlet temperature of air is 27.36 ^{o} C in analyzed tubular air pre heater. In the study results have been shown outlet temperature of flue gas is 156.98 ^{o} C and outlet temperature of air is 78.09 ^{o} C in analyzed tubular air pre heater

Keywords: *Tubular air pre heater, Turbulence method, k-ε model, EES software, Numerical analysis*

NOMENCLATURE

$\dot{m_{air}}$	*Air Mass Flow*
$\dot{m_{FG}}$	*Flue Gas Mass Flow*
$T_{air\ i}$	*Air Inlet Temperature*
$T_{air\ o}$	*Air Outlet Temperature*
$T_{FG\ i}$	*Flue Gas Inlet Temperature*
$T_{FG\ o}$	*Flue Gas Outlet Temperature*
C_{pair}	*Specific Heat Of Air*
C_{pFG}	*Specific heat of Flue Gas*
S_T	*Transverse Pitch*
S_L	*Longitudinal Pitch*
d_o	*Outer Diameter Of The Tube*
d_i	*Tube Inner Diameter*
v_{FG}	*Velocity Of Flue Gas*
v_{air}	*Velocity Of Air*
U	*Overall Heat Transfer Coefficient*
h_i	*Heat Transfer Coefficient Of Flue Gas-Side*
h_o	*Heat Transfer Coefficient Of Flue Gas-Side*
ρ_{FG}	*Density Of Flue Gas*
N_w	*Number Of Tubes In Depth Of The Air Preheater*
N_H	*Number Of Tubes In Depth Of The Air Preheater*

1.INTRODUCTION

Air-pre heater is an important equipment which provides preheating of primary and secondary combustion air in the power plants fueled with fossil fuel. In this study, authors have investigated temperature and pressure and velocity distributions in the first stage of the air pre heater in the Circulating Fluidized - Bed Boiler (CFB) having 5 MW_{th} power. This study includes analytic and numerical solutions of the air pre heater and their results. Literature studies with article subject have been shown at the below. Heat transfer and pressure drop characteristics of the tube-side of a shell-and-tube heat exchanger fitted with full-length twisted tape inserts have been numerically investigated by Dumitru and Viorica [1]. Authors analyzed four different twist ratios of twisted tape. In their study results, it was found that the average heat transfer coefficient and pressure drop, respectively, for tubes with twisted tape inserts is 2.1 and 2.6 and 4.1-5.6 times higher than that of the plain tube. Gulberg, in

[1] *Suleyman Demirel University, Engineering Faculty , Mechanical Engineering Department, 32260 Isparta - Turkey*

the master thesis[2], have made measurements of the vibration and calculated some of the natural frequencies of the structure. In the results obtained in this thesis agree with the flow phenomenon described for off-resonant tube bundle flows in the literature. The rows in the pre-heater with a large space in the flow direction allow for vortex shedding as a flow mechanism. H. Vishwanath, G., Thammaiah at all, in their study [3, a theoretical design of Recuperative Primary Air preheater with In-line tube arrangement and a combination of fluid dynamics analysis with theoretical value. The model enables heat transfer of the flue-gas flow through the air preheater as well as the tubular heat transfer and the resulting temperature distribution in the matrix of the preheater. Sivakumar et.all., in their study[4], have analyzed air preheater with using computational fluid dynamics. In their study results, authors have shown air duct modification of inclined position gives the more performance than the straight bend air duct. Steam pre-heater increase the temperature from 40˚C to 68˚C and supply air temperature is increased by 20˚C at the same time combustion temperature is increased by 1 % and efficiency also increased by 3 %. Patil et.all., in their study[5], summaries a wide range of ongoing applications of CFD in the sugar industry. Their study demonstrated that the full benefits of CFD in the delivery of commercial between code development and validation via full-scale plant simulation. This two-way interaction enhances the code fundamentals by focusing on practical issues and increases the confidence of end-users in the capabilities and accuracy of the CFD predictions, to an extent that justifies firm engineering decisions on commercial plant based solely on the characteristics predicted by the code. Suresh et. all., In their study[6], have been evaluated the performance of primary and secondary air preheaters. In their study results, they have shown condition of the air heater seals indicated the air heater leakage. Rao, in his study[7], has studied on modeling of fabrication and CFD analysis of shell and tubular air preheater. The aim of this study is numerically and analytically to determine thermal and dynamic parameters of first stage of the air-preheater with five stage and compared with results.

2. MATERIALS AND METHODS

2.1. Boundary Conditions

Air pre heater with five stages and its details are shown in Figure 1. In our investigation, the first stage of the air pre heater with 5 stage has been analyzed. For boundary conditions parameters used in first stage of tubular air pre heater, flue gas mass flow and flue gas inlet temperature have been taken as 2.52 kg/s and 190 ^{o} C respectively. The same way, air mass flow and air inlet temperature have taken as 2.26 kg/s and 27.56 ^{o} C respectively.

2.2. Numerical Analysis

In this study, it has been used finite volume method in numerical analysis using ANSYS Fluent 16.2. As seen equation 1 and equation 2, standart k-e turbulence method has been used in the numerical analysis.

$$\frac{\partial}{\partial t}(\rho k) + \frac{\partial}{\partial x_i}(\rho k u_i) = \frac{\partial}{\partial x_j}\left[\left(\mu + \frac{\mu_t}{\sigma_k}\right)\frac{\partial_k}{\partial x_j}\right] + G_k + G_b - \rho\varepsilon - Y_M + S_k \quad (1)$$

$$\frac{\partial}{\partial t}(\rho \varepsilon) + \frac{\partial}{\partial x_i}(\rho \varepsilon u_i) = \frac{\partial}{\partial x_j}\left[\left(\mu + \frac{\mu_t}{\sigma_\varepsilon}\right)\frac{\partial_\varepsilon}{\partial x_j}\right] + C_{1\varepsilon}\frac{\varepsilon}{k}(G_k + C_{3\varepsilon}G_b) - C_{2\varepsilon}\rho\frac{\varepsilon^2}{k} + S_\varepsilon \quad (2)$$

In these equations, G_k represents the generation of turbulence kinetic energy due to the mean velocity gradients, G_b is the generation of turbulence kinetic energy due to buoyancy. Y_M represents the contribution of the fluctuating dilatation in compressible turbulence to the overall dissipation rate, $C_{1\varepsilon}$, $C_{2\varepsilon}$, and $C_{3\varepsilon}$ are constants. σ_K and σ_ε are the turbulent Prandtl numbers for k and Ɛ, respectively. S_k and S_ε are user-defined source terms.

2.3. Analytical Solution

In this study, flue gas flows outside the tubes, flue gas heat transfers to the inside tubes. Parameters are evaluated in SI units. The heat transfer rate can be calculated from equation 3 as

$$\dot{Q} = \dot{m_{FG}}\, C_{pFG}(T_{FG\,i} - T_{FG\,o}) = \dot{m_{FG}}\, C_{pair}(T_{air\,o} - T_{air\,i}) \quad (3)$$

Using density, velocity of flue gas and tube inner diameter, number of tubes can be calculated from equation 4[3] as

$$N_t = 1.25\left[\frac{\dot{m_{FG}}}{d_i^2\ x\ \rho_{FG}\ x\ v_{FG}}\right] \quad (4)$$

Flue gas velocity is in the range of 12.19 – 21.24 (m/s). According to the space requirement the width and depth of the air preheater can be calculated from equations 5 and 6 as

$$W = N_w\ x\ S_T \quad (5)$$

$$H = N_h\ x\ S_L \quad (6)$$

Heat transfer coefficient of both flue gas side and air side has been calculated using equations 7 and 8 respectively.

$$h_i = f_{hi}\left[\frac{\dot{m_{FG}}}{N_t}\right]^{n_i}\left[\frac{C}{d_i^{1.8}}\right] \quad (7)$$

$$h_o = f_{ho}\ G_{air}^{n_o} \quad (8)$$

Where, C and F are temperature factors evaluated at average flue gas temperature and film temperature respectively obtained from equations 9 and 10 as

$$G_{air} = \left[\frac{\dot{m}_{air}}{FGA}\right] \quad (9)$$

$$FGA = (S_T - d_o)N_w L \quad (10)$$

The overall heat transfer coefficient U is calculated by using flue gas side and air - side heat transfer coefficient from equation 11.

$$\frac{1}{U} = \left[\frac{d_o}{h_i\, d_i} + \frac{1}{h_o}\right] \quad (11)$$

Total heat transfer is also given by from equation 12.

$$Q = U\ x\ A\ x\ \Delta T \quad (12)$$

The area of heat transfer can be calculated from equation 13 using the actual length of the tube and numbers of the tubes and outer diameter of the tubes as

$$A = \pi\ x\ d_o\ x\ N_t\ x\ L \quad (13)$$

The flue gas - side and air - side pressure drops are given by following equation 14 and 15 respectively.

$$\Delta P_{FG} = f_{PFG}\ \left[\frac{\dot{m}_{FG}}{N_t}\right]^2 \left[\frac{L + 5d_i}{\rho_{FG}\ x\ d_i^5}\right] \quad (14)$$

$$\Delta P_{air} = f_{Pair}\ N_h \quad (15)$$

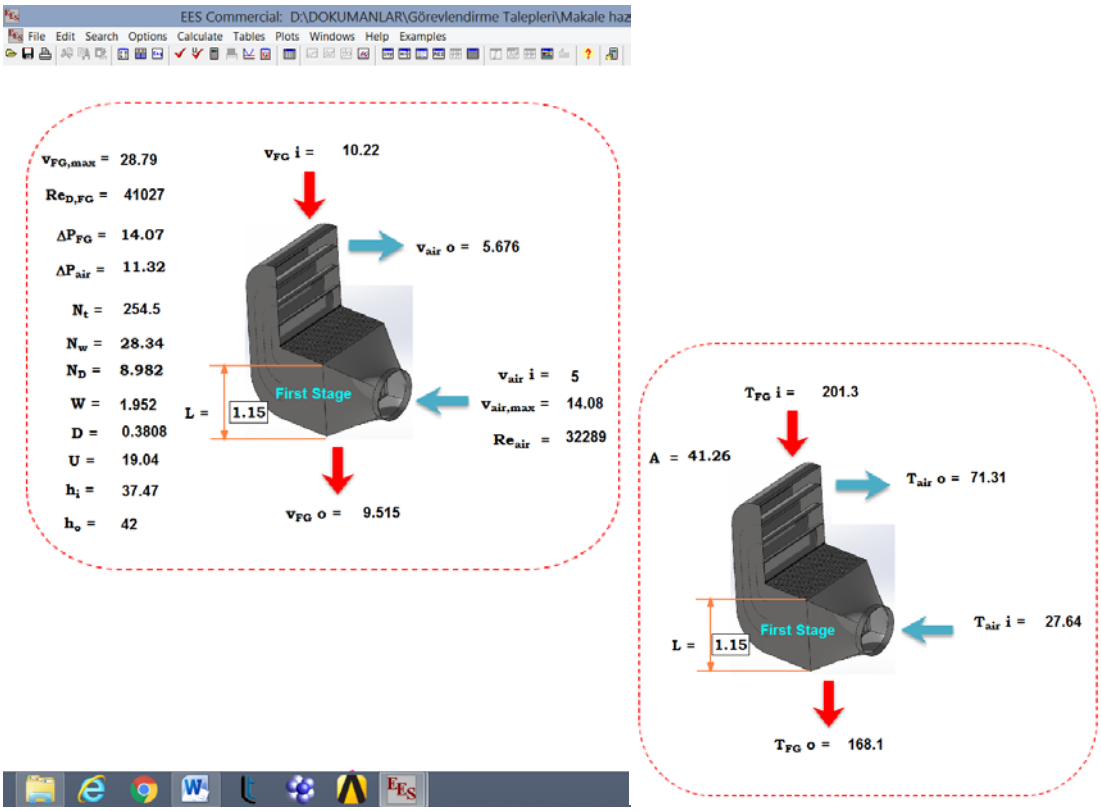

Figure 2: Analytical Model Description And *Results From Analytical Solutions By Using Engineering Equations Solver (EES)*

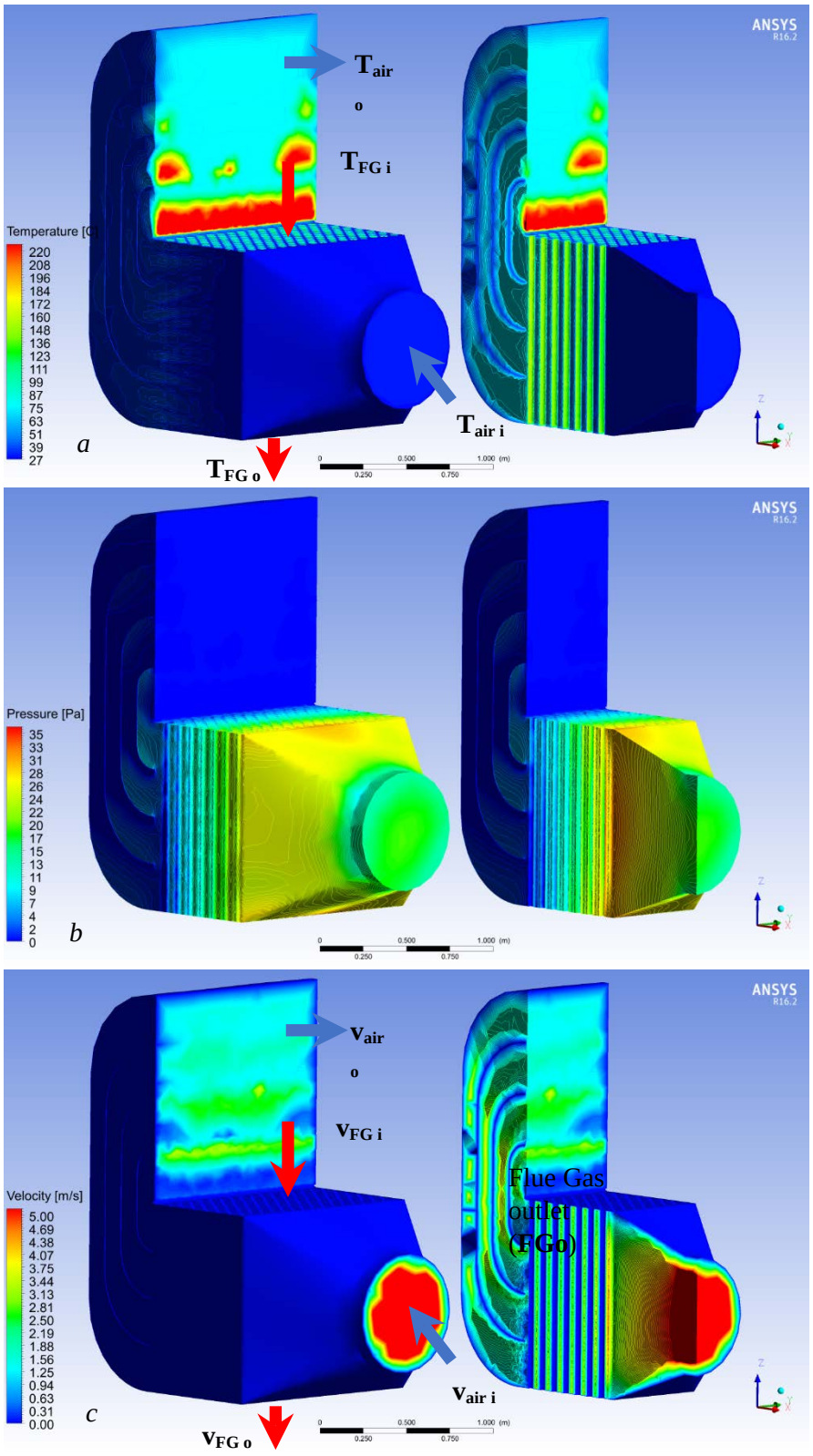

Figure 3: Air Flow Phenomenon *(a)* Temperature Contours Plot , *(b) Pressure Drop* Contours Plot *And (c) Velocity* Contours Plot *In Air- Side Of The Air Pre Heater*

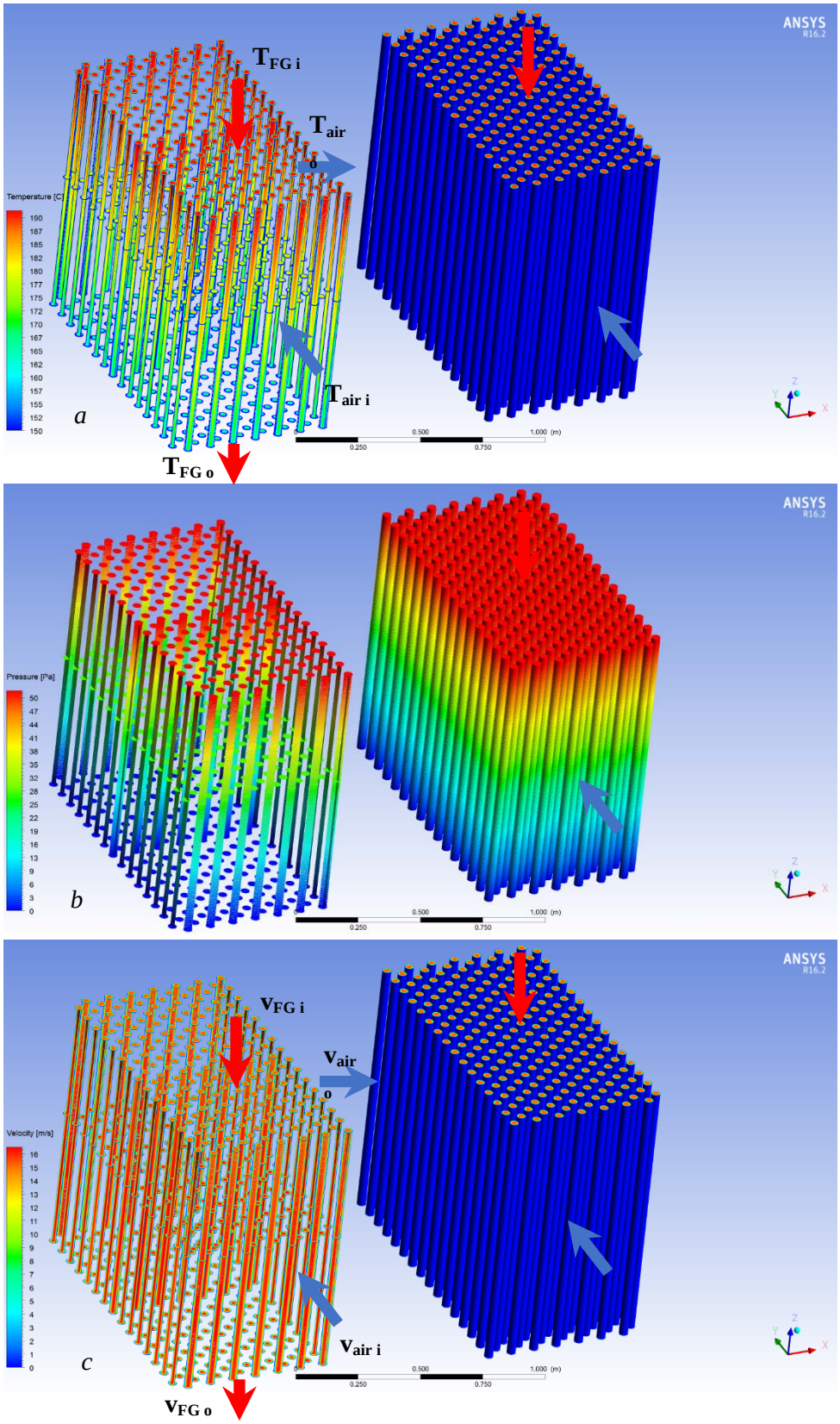

Figure 4: Flue Gas Flow Phenomenon *(a) Temperature Contours Plot (b) Pressure Drop Contours Plot And (c) Velocity Contours Plot In Flue Gas- Side Of The Air Pre Heater*

3. RESULTS AND DISCUSSION

In this study, authors have investigated on first stage of the air-pre heater thermal and dynamic parameters using analytical and numerical solution. Analytical model description and results are given in Figure 2. As seen Figure 2, air - side Reynolds number is 32289 and flue gas side Reynolds number is 41027. As shown in Figure 2, flue gas inlet temperature is 201.3 ˚C and flue gas outlet temperature is 168.1 ˚C. Air- side inlet temperature is 27.64 ˚C and air - side outlet temperature is 71.31 ˚C. Air- side pressure drop is 11.32 Pa and flue gas - side pressure reduce is 14.07 Pa, additional, air side inlet velocity 5 m/s and air side outlet velocity is 5.72 m/s, in addition to, flue gas side inlet velocity is 10.22 m/s, flue gas side outlet velocity is 9.515 m/s. Air - side temperature, pressure and velocity contour plots obtained from numerical calculations in the first stage of air-pre heater are given in Figure 3. At the same way, Flue gas- side temperature, pressure and velocity contour plots obtained from numerical calculations are given in Figure 4. Also, numerical analysis flue gas - side and air - side inlet and outlet temperature, pressure and velocity results values are given in Table 1. In the study results have been shown outlet temperature of flue gas is 168.1 ^{o} C and outlet temperature of air is 71.31 ^{o} C in analyzed tubular air pre heater.

Table 1. Temperature, Pressure And Velocity Inlet And Outlet Results Of Air-Preheater First Stage

Inlet And Outlet Parameter	*Results from Analytical Solutions*		*Results from Numerical Solutions*	
	Air - Side	*Flue Gas - Side*	*Air - Side*	*Flue Gas - Side*
Mass Flow (kg/s)	*2.36*	*2.52*	*2.36*	*2.52*
Density (kg/m3)	*1.174*	*0.7791*	*1.174*	*0.7791*
Inlet Temperature	*27.64*	*201.3*	*27.36*	*190*
Outlet Temperature (˚C)	*71.31*	*168.1*	*78.09*	*156.98*
Pressure Drop (Pa)	*11.32*	*14.07*	*17.11*	*50.61*
Inlet Velocity (m/s)	*5*	*10.22*	*5.61*	*14.71*
Outlet Velocity (m/s)	*5.27*	*9.515*	*2.02*	*13.63*
Reynolds Number	*32289*	*41027*	*17999*	*53642*
Heat Transfer Coefficient Of Flue Gas-Side(W/m^2 K)	*37.47*			
Heat Transfer Coefficient Of Air-Side(W/m^2 K)	*42*			
Overall Heat Transfer Coefficient(W/m^2 K)	*19.04*			
Depth of The Pre Air Heater (m)	*0.505*		*0.505*	
Width of The Pre Air Heater (m)	*1.625*		*1.625*	
Length Of Pre Air Heater (m)	*1.15*		*1.15*	
Number of Tubes	*255*		*250*	
Heat Transfer Area Of First Stage Air Pre Heater (m^2)	*41.26*			

As given in Table 1, air - side Reynolds number is 17999 while flue gas - side Reynolds number is 53642. Air -side inlet temperature is 27.36 ˚C and air - side outlet temperature is 78.09 ˚C. Flue gas –side inlet temperature is 190 ˚C and flue gas –side outlet temperature is 156.98 ˚C. Furthermore, air- side pressure drop is 17.11 Pa an flue gas - side pressure drop is 50.61 Pa. Air - side inlet velocity is 5.61 m/s and air - side outlet velocity is 2.02 m/s, flue gas - side inlet velocity is 14.72 m/s and flue gas - side outlet velocity is 13.79 m/s.

4. CONCLUSIONS

The objective of this work is to investigate the behavior of thermal and dynamic parameters of the tubular air-pre heater by using analytical and numerical approaches and compare with their results. Analytical solutions have been performed by energy equation solver (EES) software while numerical solutions have been carried out using Ansys-Fluent R16.2. The temperature distribution , pressure drops and velocity of both flue gas –side and air –side and are reported in this study. As seen in Table 1, results are compatible exclude of partial differences. Analytical and numerical results are given together in Table 1. Because of compatible this results, air-pre heater design will manufacturing and will use in the Circulating Fluidized Bed Boiler (CFB). From Figure 3(a, b, c), air pre heater is providing the decrease of the temperature to the flow path of flue gas.

REFERENCES

[1].C.Dumitru and C. Viorica, *Numerıcal Study Of A Shell-And-Tube Heat Exchanger For Heatıng Rıch Monoethanolamıne Usıng Hot Flue Gases. Part Iı: Tube-Sıde Heat Transfer Enhancement,* Proceeding of the 3rd International Conference on Thermal Engines and Environmental Engineering, 143-147, 2009.

[2]. M.Gulberg, *Unsteady Simulation Of Air Pre-heater*, Master Thesis of Lulea University Of Technology, Sweden, 2010.

[3]. H. Vishwanath, G., Thammaiah at all, Heat Transfer Analysıs Of Recuperatıve Aır Preheater International Journal Of Innovative Research in Science, Engineering and Technology, Vol. 2, Issue 7, July 2013

[4]. K.Sivakumar, J. Boopathy, F. Sudeep, K. Arun, Computational Fluid Dynamics Analysis of Airpreheater Cold End, IOSR Journal of Mechanical and Civil Engineering (IOSR-JMCE), Volume 11, Issue 3 Ver. II (May- Jun. 2014), PP 88-94, 2014.

[5]. B.M. Patil, B. Vijaykumar and B. Chanashetty, *Applıcatıon Of Cfd Analysıs In Sugar Industrıes,* Proceeding of NCRIET-2015 & Indian J.Sci.Res. 12(1):312-323, 2015.

[6]. B.V.Suresh, Y. Shireesha and Dr.B. Sateesh, *Evolution Of Performance Of Primary And SecondaryAir Preheaters*, International Journal of Engineering Trends and Technology (IJETT) – Volume22 Number 7- April 2015.

[7]. M.N.Rao, *Improving the Overall heat transfer coefficient of an Air Preheater by Design, Fabrication and CFD Analysis,* NATIONAL CONFERENCE on Developments, Advances & Trends in Engineering Sciences (NCDATES- 09th & 10th January, 2015.

Investigation of Heat Transfer Performance for Different Mass Flow Rate in Compact Plate Heat Exchanger

Osman Ipek[1], Mehmet Kan[1], Barıs Gurel[1]

Abstract

In this study, thermal treatment in different well angles and flow rates of a compact heat exchanger by Direct Metal Laser Sintering technique instead of a sealed and soldered one used in many areas has been investigated. Channel angles have been examined according to a sealed plate heat exchanger experimental set available in the laboratory. 3D designs of the compact heat exchanger in 60°,channel angle have been made. By using ANSYS-FLUENT software, inflow, outflow and thermal treatment of liquids circulating in the system have been analyzed according to boundary conditions in three different flow rates relatively 0,2 kg/s, 0,3 kg/s and 0,43 kg/s . Heat transfers occurring between heat channels and walls of heat exchangers in different flow rates of heat exchangers have been calculated. In this analysis, hot fluid inlet temperature is 60 °C and cold fluid inlet temparature is 15 °C. As a result of the analysis, 0,43 kg/s mass flow rate conditions is shown maximum performance for heat transfer rate.

***Keywords**: Compact Heat Exchangers, Micro Channel Heat Exchanger, Compact Design*

1.INTRODUCTION

The devices which are referred to as heat exchanger providing heat exchange between two or more fluids at different temperatures. Heating, cooling and ventilation applications, the required high productivity and economic efficiency, compact design in different geometries can be accessed through the heat exchanger. Replace pipe type heat exchanger and the speed with higher heat transfer coefficient of plate heat exchanger plate heat exchanger with getting the heat exchanger industry has had a larger market share. In various sizes and materials are manufactured, wide selection range of the plate, the plate material is the wide range of choice and to have the desired plate sizes and plate heat exchanger in terms of usage and flexibility are superior to. Plate heat exchangers, thermal power plants, chemical industry, heating, air conditioning, refrigeration installations, vehicles, electronic devices, alternative energy sources, the cryogenic applications, satellites (high performance working in the heat-generating private satellite electronic circuit to cool), special-purpose small electronic circuits, heat storage, electronics, avionics, metrology, robotics, medical, industrial processes (pasteurization, desalination, cryogen), telecommunications, automotive, aerospace, aviation (liquid-cooled electronic equipment, unmanned aerial vehicles thermal cameras cooling applications), defense industry, the energy sector (gas and steam turbine) and overall thermal management has a wide field of applications [1]. The amount of heat transfer in heat exchangers fall leads to poor performance of the heat exchanger. In this case, the system that uses the heat exchanger more fluids flow, pump flow and greater thermal energy use because it requires higher temperatures increase cost. Due to this reason, sometimes it is necessary to increase the capacity of the heat exchanger but the size of the amplification is not possible in some applications. Therefore improving heat transfer size of the system to be kept in appropriate sizes and with it the cost of the system and enables the reduction of operating costs [2]. Skilled cooling can be made, micro-scale, multi-purpose indoor heat exchanger and the flow channel geometry to obtain the same surface by forming more micro scale flow channels will be possible [3].For improving heat transfer in the flow channel, the numerical and experimental studies are found in the literature. Hopkinson et al., studied by the method of Direct Laser Metal Melting System different geometries made of bronze heat transfer on the cooling and heating channels experimentally. Heat transfer and temperature distribution in the channels belonging to the correlations were derived [4]. Gut et al., were determined the flow of heat transfer in the plate heat exchanger is related to the distribution experimentally. The flow of heat transfer in the plate heat exchanger distribution correlations were derived [5]. Franco et al., were made plate-fin heat exchangers, counter-flow heat exchanger and analyzed using compact heat exchangers [6]. Kargıcı et al., worked on the optimum design of heat exchangers. Optimum design methods have used excessive descent method. For the optimal solution, the heat transfer coefficient inside of the tube, the heat transfer coefficient outside the tube, outside the heat transfer area of the temperature difference and have been

[1] *Suleyman Demirel University, Engineering Faculty , Mechanical Engineering Department, 32260 Isparta - Turkey*

determined the importance of the tube are [7]. Erek et al., were examined numerically change in plate finned tube heat exchanger of the blade geometry of its effect on heat transfer and pressure drop [8]. Riverol et al., worked plate heat exchangers using artificial neural networks in the critical time, the average heat transfer coefficient and has tried to estimate the layer thickness [9]. Kim et al., have worked the data obtained from experimental data with the optimum design of flat plate finned tube heat exchangers on the wing tilt [10]. Atmaca et al., concentrically nested hot fluid and cold fluid in tube heat exchanger heat transfer coefficient and overall heat transfer coefficient. They found experimentally, parallel flow in opposite directions in the same direction and parallel-flow heat exchanger types were compared with each other [11]. Wen et al., worked about CFD modeling and measurement of flow velocity (PIV) experimental data for the same conditions using the plate-fin heat exchangers have characterized the turbulent flow at the inlet [12]. Durmuş et al., experimentally studied for three different plate heat transfer surface geometry, friction factor and exergy loss [13]. Dovic et al., investigated the plate surface angle β = 28 ° and β = 61 ° chevron type plate heat exchanger, which flow properties. Working within the flow channels in the plate Fanning friction factor and Nusselt number for use in estimating the correlations were derived [14]. Yildirim et al., have examined. in the micro-channel heat exchanger thermal performance of the structure and fluid analyzes Temperature distribution and the efficiency of the heat exchanger have derived correlations [15]. Gherasim et al., were experimentally investigated laminar and turbulent flow conditions for the two-channel chevron type plate heat exchangers in the hydrodynamic and thermal fields [16]. Mancin et al., experimentally examined. different geometric feature and aspect ratio design for plate brazed plate exchanger prototypes R407C and R410A refrigerants in the extreme glow effects [17]. Faizal et al., used in applications where the temperature difference is small on the plate heat exchangers have made an experimental study [18]. Kılıç, has examined three different channel geometries (30 °, 45 ° and 60 ° angles channels) for the sealing plate heat exchanger in the thermal and dynamic parameters experimentally investigated and the different channel geometry, thermal and dynamic parameters of the effect. Channel observes that the increase in yield with increasing angle [3]. As seen above in the literature to improve the plate heat exchanger for heat transfer is done much. However, the heat exchanger is standard 192 mm in length, 74 mm in size heat exchanger for a heat exchanger for different blade angles to a numerical modeling and optimization studies were encountered in the literature. In this study, 30 °, 45 ° and 60 ° in terms of channels in the standard size of a compact heat exchanger is made of 3D design. This design in three different flow boundary conditions in the system according to the circulating fluid using ANSYS-FLUENT software, input, output and canal flow and thermal behavior were investigated. Angle channels of the different channels of heat exchangers and heat the heat transfer occurring between the channel walls and the efficiency of the heat exchanger is calculated.

4.2. Nomenclature and Units

C_{ph} Hot fluid specific heat, [kJ/kg°C]
C_{pc} Cold fluid specific heat, [kJ/kg°C]
D_h Hydraulic diameter, [m]
h Heat transfer coefficient, [W/ m^2°C]
k Thermal conductivity, [W/m°C]
Nu Nusselt number
Pr Prandtl number
T_{hi} Inlet temperature of hot fluid, [°C]
T_{ci} Inlet temperature of cold fluid, [°C]
$T_{hç}$ Outlet temperature of hot fluid, [°C]
$T_{cç}$ Outlet temperature of cold fluid, [°C]
ΔT_m Average logarithmic mean temperature difference, [°C]
$\dot{m}_h$ Mass flow rate of the hot fluid, [kg/s]
$\dot{m}_c$ Mass flow rate of the cold fluid, [kg/s]
β Angle of channel, [°]
ε Effectiveness

2.MATERIALS AND METHODS

Numerical modeling of this study will be the geometric characteristics of the heat exchanger and process parameters are given in Table 1. 3-D CAD program specified geometric features with design of the heat exchanger shown in Figure 1 is the solid model.

Table 1. The geometric properties of the heat exchanger and process parameters

The length of the compact heat exchanger	192 (mm)
The width of the compact heat exchanger	74 (mm)
Number of plates	10
Hot water inlet temperature	60 (°C)
Cold water inlet temperature	15 (°C)
Environment temperature	27(°C)
Channel angles	60°

Hot water and cold water flow rates	0,2, 0,3, 0,43 (kg/s)

3D-CAD program specified geometric features with design of the heat exchanger shown in Figure 1 is the solid model.

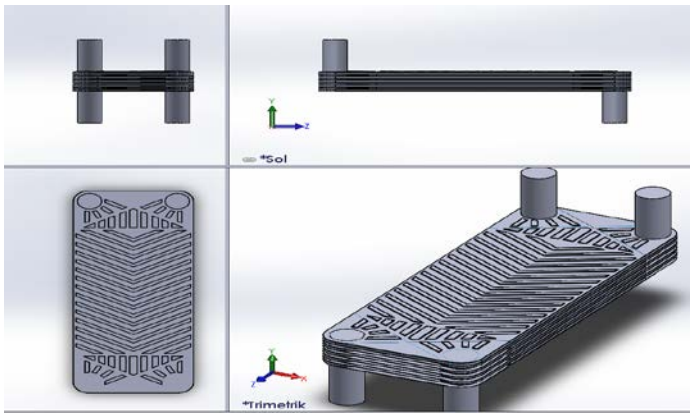

Figure 1. Solid model of the heat exchanger

3-D CAD solid model design made with the program tetrahedral mesh of the heat exchanger geometry software mesh structure was formed with the finite volume. This mesh structure is formed 10000000 tetrahedral mesh. In Figure 2 the plate 30 ^{0}, 45 ^{0}, 60 ^{0} angles plate channel mesh structures are observed in the finite volume.

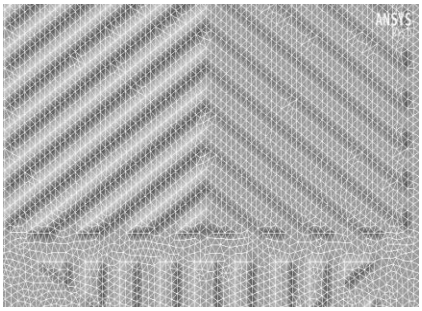

Figure 2. In a heat exchanger to 30 ° channel angles mesh structure

2.1.Boundary Conditions

Under the work done with three different channel angles metal powder DMLS (Direct Metal Laser Sintering) can be produced by the method is designed for compact heat exchangers. DMLS method when making design suitable for production of brazed plate heat exchangers are based on dimensions. Brazed plate heat exchanger technical specifications are shown in Table 1. 60 ° angle, three different channels of the compact heat exchanger 0.2 kg / s, 0.3 kg / s, 0.43 kg / s, hot water inlet temperature of 60 ° C and the cold water inlet temperature analyzes were carried out for 15 ° C (Figure 3). Environment temperature 27 ° C has been considered.

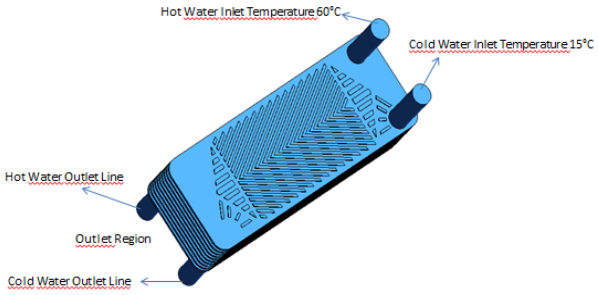

Figure *3. Compact Heat Exchanger Design*

2.2.Numerical Modeling

In this study based on the finite volume method is used ANSYS-FLUENT software. Software from ANSYS-meshing mesh files by applying boundary conditions and parameters of the system solution is made. ANSYS-FLUENT software, the system delivers the solution is to use the following equation in the background.

Continuity Equation;

$$\frac{\partial u}{\partial x}+\frac{\partial v}{\partial y}+\frac{\partial w}{\partial z}=0 \quad (1)$$

Conservation of momentum equation;

$$\frac{\partial}{\partial t}\left(\rho\vec{V}\right)+\nabla.\left((\rho\vec{V})\vec{V}\right)=-\nabla p+\nabla.\left(\bar{\bar{T}}\right)+\rho\vec{g}+\vec{F} \quad (2)$$

shaped.

Where P is the static pressure, stress tensor T, g is the gravitational acceleration; F can be given by the user the term refers to other sources.

Energy equation;

$$\frac{\partial(\rho E)}{\partial t}+\nabla.\left(\vec{V}\left(\rho E+p\right)\right)=\nabla\left[k_{eff}\,\nabla T-\sum_j h_i\,J_i+\left(\bar{\bar{T}}_{eff}.\vec{V}\right)\right]+S_h \quad (3)$$

is shown in.

In this equation E unit of energy, $k_{eff}\ \nabla T$ transmission, $\sum_j h_i\ J_i$ diffusion and $(\bar{\bar{T}}_{eff}.\vec{V})$ viscous energy loss (disposition) is represents [19]. Numerical solutions of equations modeling parameters are given in Table 2.

Table 2. Numerical modeling parameters used solution

Simulation Condition	Steady-state
Solver Type	Pressure Based
Mesh Structure / Mesh Number	Tetrahedral/ 10 Million
Turbulence Model	Standard k-ε Turbulence Model
Wall-Turbulence Interaction	Standard Wall-function
Speed - Pressure Interaction	SIMPLE algorithm
Decomposition Method	Second Order Upwind

3.RESULTS AND DISCUSSIONS

In Figure 4, the temperature in the heat exchanger compact vector is shown.

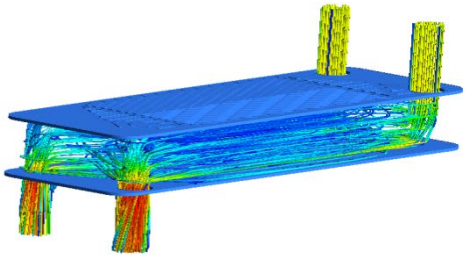

Figure 4. The Temperature Vectors Compact Heat Exchangers

Table 3 at 60 ^{0} plate channel angle, 0.2,0.3 and 0.43 kg / s liquid flow also work done during the 3 for analysis, the hot water outlet temperature, cold water outlet temperature, heat transfer amount value and effectiveness of the results are tabulated. As shown in Table 3 0.2 kg / s and 0.3 kg / s at 60 ^{0} on fluid flow channel angle is increased amount of heat transfer increases. 0,43 kg / s channels from the 60 ^{0} angle increases the amount of heat transfer is reduced and a maximum heat transfer 0,43 kg / s in fluid flow.

Table 3. Wing Angle and Different in Different Flow in Plate Heat Exchanger Temperature Chang

Analysis No	Channel Angle	Fluid Flow (kg/s)	Hot Water Inlet Temperature (°C)	Cold Water Inlet Temperature (°C)	Hot Water Outlet Temperature (°C)	Cold Water Outlet Temperature (°C)	Amount of Heat Transfer (W)	Effectiveness (Ɛ)
1	60	0,2	60	15	51,59	23,51	7031	0,187
2	60	0,3	60	15	53,63	21,75	7988	0,141
3	60	0,43	60	15	54,82	18,66	9310	0,115

Comparison of heat exchangers with each other and which is most suitable for the heat exchanger in the heat exchanger effectiveness of the selected parameter is utilized.[13] Heat effectiveness can be written as follows;

$$\varepsilon = \frac{t_{hg} - t_{hç}}{t_{hg} - t_{cç}} = \frac{C_c(t_{cç} - t_{cg})}{C_h(t_{hg} - t_{cç})} \qquad (4)$$

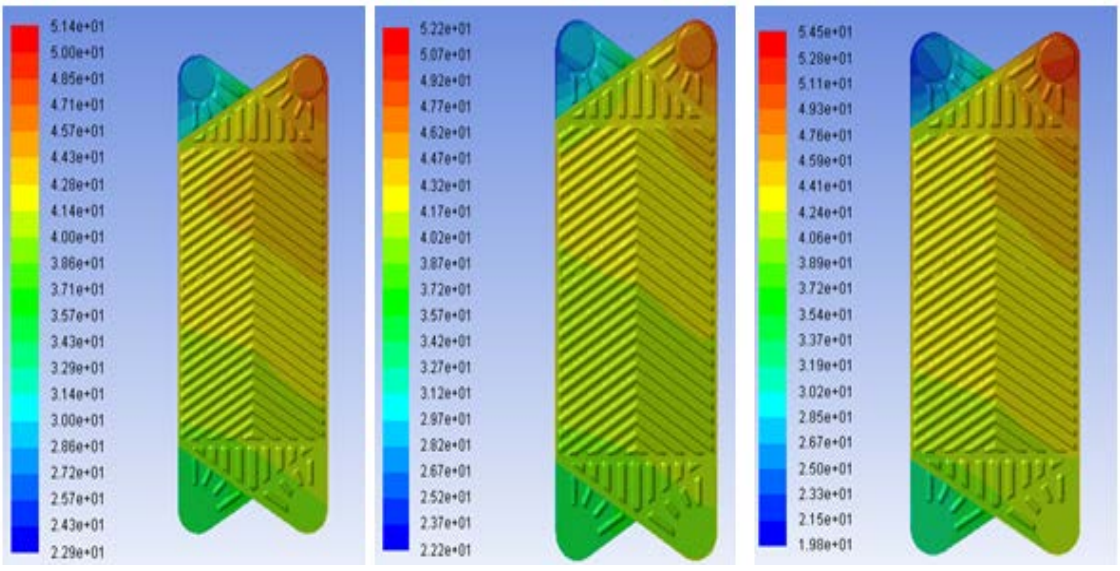

Figure 5. 60 ° angle for the different mass flow rate in the heat exchanger temperature changes

As shown in Figure 5, respectively 60° angle for the 0.2 kg/s, 0.3 kg/s and 0.43 kg/s mass flow rate in the heat exchanger temperature changes. As could be seen Figure 5, 0.43 kg/s is the best effectiveness in terms of process parameters and channel angle.

4.CONCLUSIONS

According to the study results obtained with the increase in mass flow increases the heat transfer rate. However, the mass flow rate is low and cold water outlet temperature of the hot water outlet temperature values showed no further change. In future studies, the results of the study, taking into consideration the specific application used in micro-scale heat exchanger design can be made. Micro-sized heat exchangers designed with a new manufacturing method DMLS (Direct Metal Laser Sintering) can be manufactured in one piece using the apparatus. DMLS heat exchanger to be manufactured by the method again, and the information obtained in the study of literature that is determined considering the flow of the heat exchanger can be made with the sets of experimental analysis.As a result, the numerical analysis of the compact plate heat exchanger in the manufacture, design and optimization stage has emerged in the matter.

REFERENCES

[1]. Shah R. K., 1983,Heat Exchanger Basic Design Methods, in Low Reynolds Number Flow Heat Exchangers, S. Kakac, R.K. Shah, and A. E. Bergles, eds., Hemisphere Publishing, Washington, DC, pp. 21-72.
[2]. Kays W. M., London, A. L., 1998,Compact Heat Exchangers, Krieger Publishing Company.Malabar, Florida, USA.
[3]. Kılıç, B., 2013, "Plakalı Isı Eşanjörlerinde Plaka Geometrisi İle Dinamik ve Termal Paramerelerin Isı Transferine Etkilerinin Deneysel Olarak Araştırılması", Doktora Tezi, 50-52.
[4]. Hopkinson, N., Dickens, P., 2000, Conformal Cooling and Heating Channels Using Laser Sintered Tools. Utwired.
[5]. Gut, J.A.W., Pinto, J.M., 2004, Optimal Configuration Desing for Plate Heat Exchangers. International Journal of Heat and Mass Transfer, 47, 4833-4848.
[6]. Franco, A., Giannini, N., 2004, Optimum Thermal Desing of Modular Compact Heat Exchangers Structure for Heat Recovery Steam Generators. Applied Thermal Engineering, 25, 1293-1313.
[7]. Kargıcı, S., Unuvar, A., 2004, An Approach for the Optimum Desing of Heat Exchangers. International Journal of Energy Research,28, 1379-1392.
[8]. Erek, A., Özerdem, B., Bilir, L., İlken, Z., 2005, Effect of Geometrical Parameters on Heat Transfer and Pressure Drop Characteristics of Plate Fin and Tube Heat Exchangers. Applied Thermal Engineering, 25, 2421-2431.
[9]. Riverol, C., Napolitano, V., Estimation of Fouling in a Plate Heat Exchangers Through the Application of Neural Networks. Journal of Chemical Technology and Biotechnology, (2005). 80, 594-600.
[10]. Kim, Y., Kim, Y., 2005, Heat Transfer Characteristics of Flat Plate Finned-Tube Heat Exchangers with Large Fin Pitch. International Journal of Refrigeration, 28, 851-858.
[11]. Atmaca, M., 2006, Klasik Tip Eş Eksenli (merkezli) İç İçe Borulu Isı Değiştiricisinde Isı Transferi ve Basınç Kaybının Deneysel Olarak İncelenmesi. Makine Teknolojileri Elektronik Dergisi, 4, 1-14.
[12]. Wen, J., Li, Y., Zhou, A., Zhang, K., 2006, An Experimental and Numerical Investigation of Flow Patterns in the Entrance of Plate-Fin Heat Exchanger. International Journal of Heat and Mass Transfer, 49, 1667-1678.
[13]. Durmus, A. Benli, H., Kurtbas, I., Gul, H., 2009, Investigation of Heat Transfer and Pressure Drop in Plate Heat Exchangers Having Different Surface Profiles. International Journal of Heat and Mass Transfer, 52, 1451-1457.
[14]. Dovic, D., Palm, B., Svaic, S., 2009, Generalized Correlations for Predicting Heat Transfer and Pressure Drop in Plate Heat Exchanger Channels of Arbitrary Geometry. International Journal of Heat and Mass Transfer, 52, 4553-4563.
[15]. Yildirim, O., Guo, Z., 2011, A High-efficiency Micro Channel Regeneretive Heat Exchanger for Fluid Processing. Comsol User Conference.
[16]. Gherasim, I., Taws, M., Galanis, N., Nguyen, 2011, Heat Transfer and Fluid Flow in a Plate Heat Exchanger part I. Experimental Investigation. International Journal of Thermal Sciences, 50,1492-1498
[17]. Mancin, S., Col, D.D., Rossetto, L., 2012, Partial Condensation of R407C and R410A Refrigerants inside a Plate Heat Exchanger. Experimental Thermal and Fluid Science, 36,149-157.
[18]. Faizal, M., Ahmed, M.R., 2012, Experimental Studies on a Plate Heat Exchanger for Small Temperature Different Applications. Experimental Thermal and Fluid Science, 36, 242-248.
[19]. Fluent, 2013, Version 14.0 User's Guide, Fluent Inc., Lebanon, NH, USA.

ICENS
INTERNATIONAL CONFERENCE ON ENGINEERING AND NATURAL SCIENCES
24-28 May 2016 /Sarajevo

Numerical Investigation on Hydrodynamic Behaviour in 8 MW_{th} Circulating Fluidized Bed

Osman Ipek[1], Barıs Gurel[2], Mehmet Kan[3]

Abstract

Multi-Phase flows is one of the types of flow which is frequently observed in natural phenomena and engineering applications. Circulating Fluidized Beds(CFB) constitute an important application of multi-phase flow. The combustion and emission behaviours in CFB's are determined by hydrodynamic of bearing. The most appropriate combustion can be provided with the hydrodynamic structure of bearing; taking into account fuel and operating parameters. Therefore, the hydrodynamic structure of CFB should be displayed with mathematical/physical modelling and simulation approach for its analysis and synthesis. Mathematical analysis in today's conditions is very difficult or impossible because of excessive turbulence, unstable and two-phase flow characteristics of the bed. Therefore, the most effective way to do this is the use the physical modelling and simulation approach. In this study, 8 MW_{th} CFB hydrodynamic analysis are made by ANSYS-FLUENT R14 commercial CFD code. This analysis results show CFD analysis compatible with literature experimental studies. 6 m/s superficial velocity is enough fluidization in CFB.

Keywords - *Circulating fluidized bed, Hydrodynamic analysis, Multi-phase flow, Clean Coal Technology.*

1. INTRODUCTION

Turkish %88 lignite which is named low quality lignite that is lower than 8000 kJ/kg calorific value. CFBB(Circulating Fluidized Bed Boiler)system is most convenient and newest clean coal technology for combustion to low calorific value coals that include high moisture and high ash. Coal, bed material, sulphur and air mixers in combustion chamber for CFBB system. Also, NO_x emissions value is low because this value maintained under lower than 1200 K. In addition, high combustion efficiency and fuel flexibity are being provided because low-quality lignite combustion process occurs below the fuel ash melting temperature. CFBB is obtained 4.5 MW/m^2 thermal power, While bubling fluidized bed is obtained 1.3 MW/m^2. Additionally particles are separated from the flue gas in the cyclone, and are returned in the boiler. As a result decreases the proportion of unburned carbon particles.

Some studies in the literature about CFBB combustion system are indicated as follows.

Gungor ve Eskin have been developed two dimensional hydrodynamic model for CFBB. They calculated axial and radial voidage distribution, gas and solid phase pressure drop, solid volume fraction in solid phase and particle dimension distribution with simulation. They compared and validated model results and experimental results on cold flow CFBB system in literature[1].

Dülger intended to provide an efficient and low emissions combustion in circulating fluidized bed with using specified algorithm in his Ph.D. They generated a feedback signal that obtained disposed sensors by collecting necessary data from the reactor and the flue gas according to the predetermined algorithm and thus have checked the coal supply motor and air flow fan. He reported CFBB combustion system don't need additional filter system to keep the specified limit emissions and consequently, they reported this advantage of in therms of installation cost, that one of the major factors to the fore other compared combustion systems [2].

Mirek et all., investigated as numerical and experimental that under similar operating conditions air nozzles effect on temperature and NO_x emissions in a large scale fluidized bed boiler. They showed change of the primary air distribution in the lower part of the combustion chamber effect on combustion process strength and temperature distribution along the boiler height [3].

Erbaş et all., in their works has been experimental studied that effect of heat transfer within the bed from the wall heating surface. Their study results are stated higher than heat transfer coefficient was obtained when the particle diameter decreased and gas velocity increased [4].

Weng and Plackmeyer, in their works, they compared experimental results and 3-D numerical analysis results by Barracuda CPFD software for Duisburg Circulating Fluidized Bed Boiler. They stated that this study results were very convenient and Barracuda CPFD program will very important tool detecting hydrodynamic, temperature and emissions in fluidized bed in the future optimization studies [5].

Kumar and Pandey , in their works, They made two three dimensional analysis of burning in CFB boiler. They have reached temperature, velocity, pressure and, turbulence kinetic energy contours in the boiler for different fluidization velocity. As a result of the studies, they stated that 6 m/s fluidization velocity more appropriate than 4 m/s and 5 m/s fluidization velocity for fluidized bed combustion [6].

Simanjuntak, vd., in their works, they made numerical and experimental studies for hydrodynamic in circulating bubbling fluidized bed that was generated internally cylinder. They have used the FLUENT 6.3 software for CFD simulations in the

study that was used Eulerian-Eulerian model for solid particle flow. The study noted that in compliance with the experimental results and simulation results and it was stated that the fluidization in the simulation were affected by flow rate in the flow pipe, air flow rate, initial bed static height and the orifice diameter [7].
Hydrodynamic,Analysis of A CFBB System have been maken for 8 MW_{th} .

2. NUMERICAL MODELLING

In this study, combustion and emission features have been investigated in CFBB. In this spirit, before CFBB that shown in Figure 1 have been designed with 3-D CAD programme then, boundary conditions that shown in Ansys Design Modeler have been created and mesh structure that include 2.000.000 polygonal mesh element have been created as shown in Figure 2. etc.

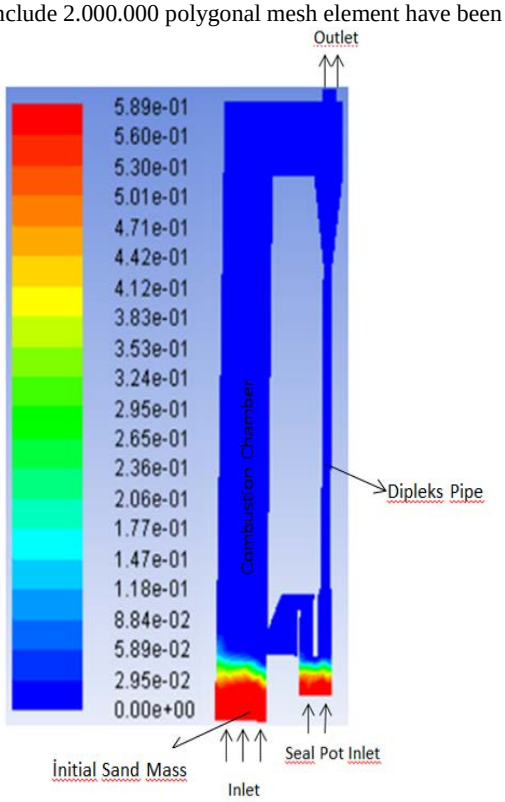

Figure 1. Boundary Conditions of CFB

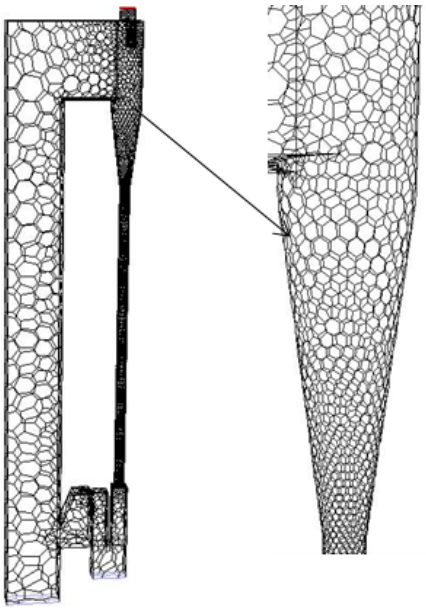

Figure 2. Mesh of CFB Geometry

Hydrodynamic analysis of CFBB system have been made for 2.1 kg/s primary air flow rate, 1.5 m bed material initial bed height, 0.5 kg/s seal pot air flow rate and 0,2 m bed material initial bed height. Realizable k-e turbulence method [8,9,14], Eulerian-Eulerian multiphase method [10,11] have been made in the numerical analysis. Bed material diameter that was made in the analysis is 300 μm. Primary air and seal pot air temperature, viscosity and density has been used respectively 500 K, 2.1e-5 kg/m-s and 0.6964 kg/m^3 in the hydrodynamic analysis. Initial bed material volume fraction and viscosity has been used respectively 0,589 [2],0.001003[12,13].

Table 1. Equations That Was Used Multiphase Flow Hydrodynamic Analysis[14]

Conservation Equations

Continuity

$$\frac{\partial}{\partial t}(\alpha_q \rho_q) + \nabla.(\alpha_q \rho_q \underline{v}_q) = 0 \quad (1)$$

$$\alpha_q + \alpha_s = 1 \quad (2)$$

Feature Equations

$$\frac{\partial}{\partial t}(\alpha_q \rho_q X_q^t) + \nabla.(\alpha_q \rho_q X_q^t) = \nabla.(\alpha_q \rho_q D_k^t \nabla X_q^t) + S_q$$

Momentum

$$\frac{\partial}{\partial_t}(\alpha_q \rho_g \underline{v}_q) + \nabla.(\alpha_q \rho_q v \underline{v}_q) = \nabla.\bar{\bar{\tau}}_q - \alpha_q \nabla_p + \alpha_q \rho_g \underline{g} + F_q \quad (4)$$

For Gas Phase

$$F_q = K_{qs}(\underline{v}_s - \underline{v}_q) \quad (5)$$

$$\bar{\bar{\tau}}_q = \alpha_g \mu_{g,eff}\left(\nabla \underline{v}_g + \nabla_{\underline{v}_g}{}^T\right) + \alpha_g\left(\lambda_g - \frac{2}{3}\mu_g\right)\nabla.\underline{v}_q \bar{\bar{I}} \quad (6)$$

$$\mu_{g,eff} = \mu_g + \mu_{g,t} \quad (7)$$

For Solid Phase

$$F_q = K_{sq}(\underline{v}_q - \underline{v}_s) \quad (8)$$

$$\bar{\bar{\tau}}_s = -P_s \bar{I} + \alpha_s \mu_s(\nabla \underline{v}_s + \nabla \underline{v}_s{}^T) + \alpha_s\left(\lambda_s - \frac{2}{3}\mu_s\right)\nabla.\underline{v}_s \bar{\bar{I}} \quad (9)$$

$$\lambda_s = \frac{4}{3}\alpha_s \rho_s d_s g_{0,ss}(1 + e_{ss})\left(\frac{\Theta_s}{\pi}\right)^{1/2} \quad (10)$$

Table 2. GLİ-Tunçbilek Coals That was used in analysis Elementel And Proximate Analysis(%)

Coal elementel(ultimate) analysis	C	72,9
	H	5
	O	14,7
	N	2,5
	S	4,9
Proximate aanalysis	Ash	32,6
	Moisture	13
	Volatile Material	14,8
	Fixed Carbon	39,53

3. RESULTS ANS DISCUSSIONS

Hydrodynamic Anaysis Results:

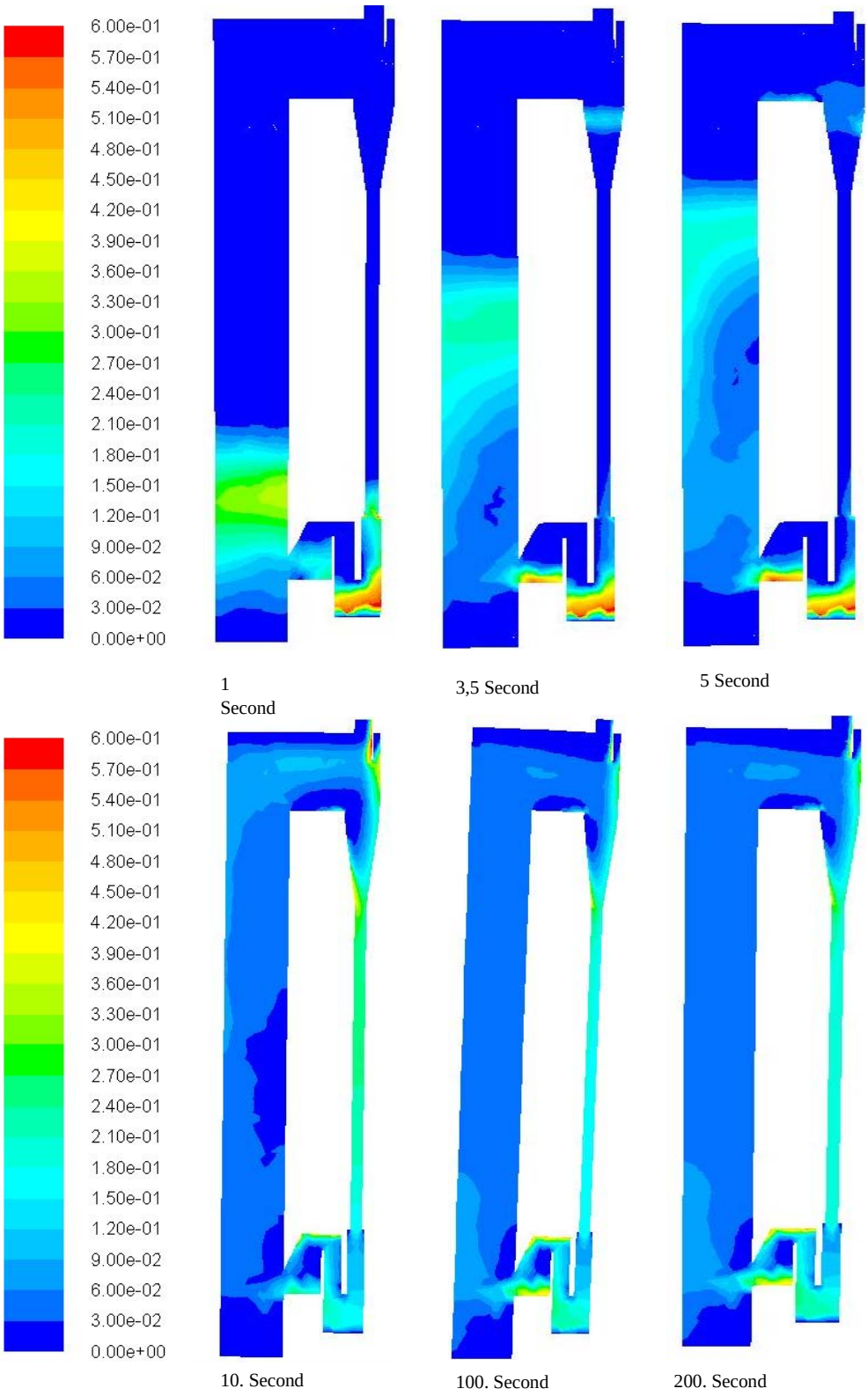

Figure 3. Changing Of Temporal Sand Volume Fraction In Solid Circulating System

As could be seen Figure 3, Sand volume fraction in CFB furnace that didn't change after 200 second from started up conditions. In this analysis results, sand volume fraction was respectively, %5-8 in combustion chamber, %6-9 in dip-leg pipe and %15-18 in loop-seal.

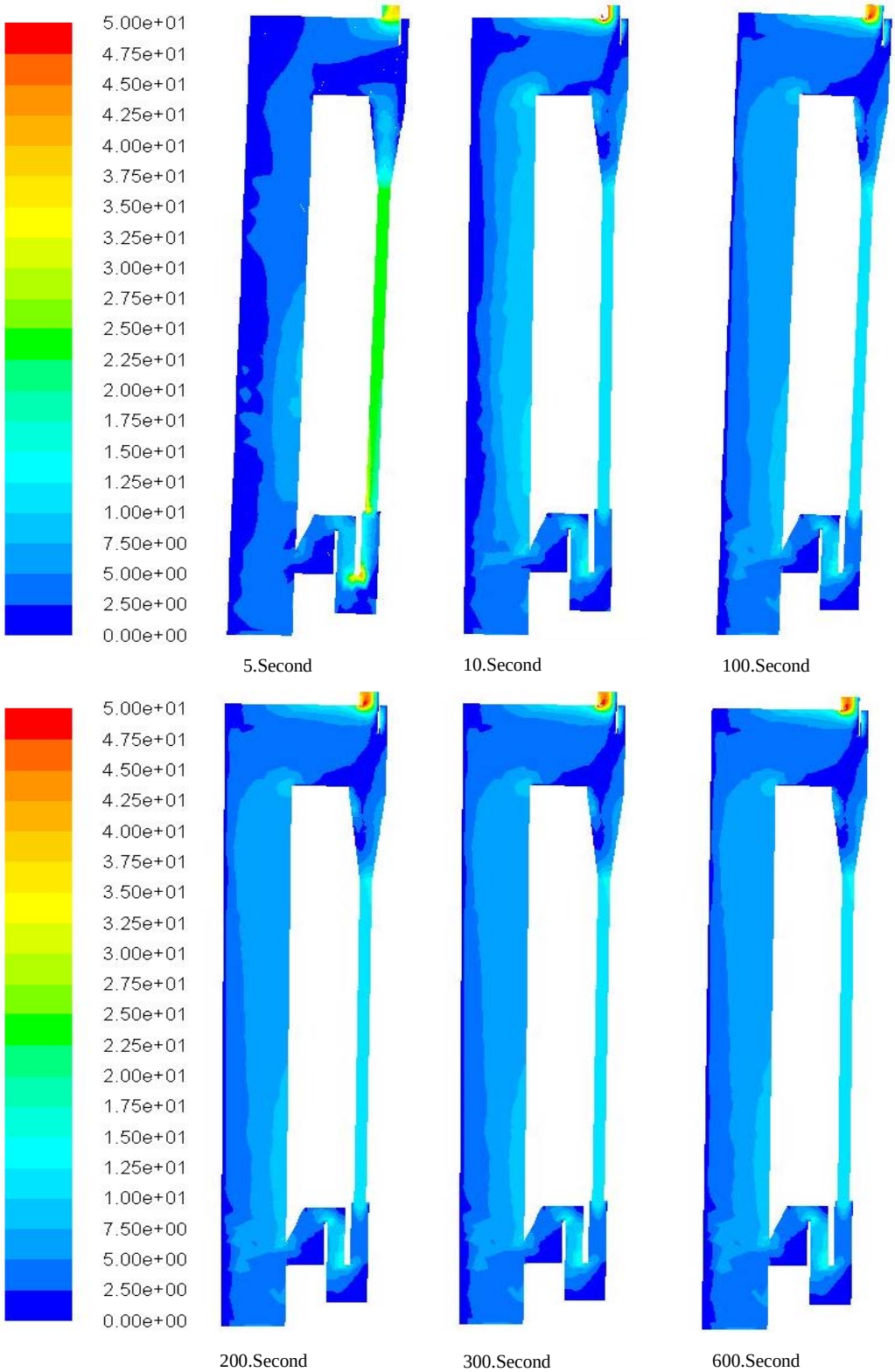

Figure 4. Changing of Temporal Air Velocity In Solid Circulating System

As could be seen Figure 4, Air velocity in CFB furnace that didn't change after 200 second from started up conditions. In this analysis results, air velocity was respectively 5-7,5 m/s in combustion chamber and cyclone, 15-17,5 m/s in dip-leg pipe and 0,2-5 m/s in loop-seal.

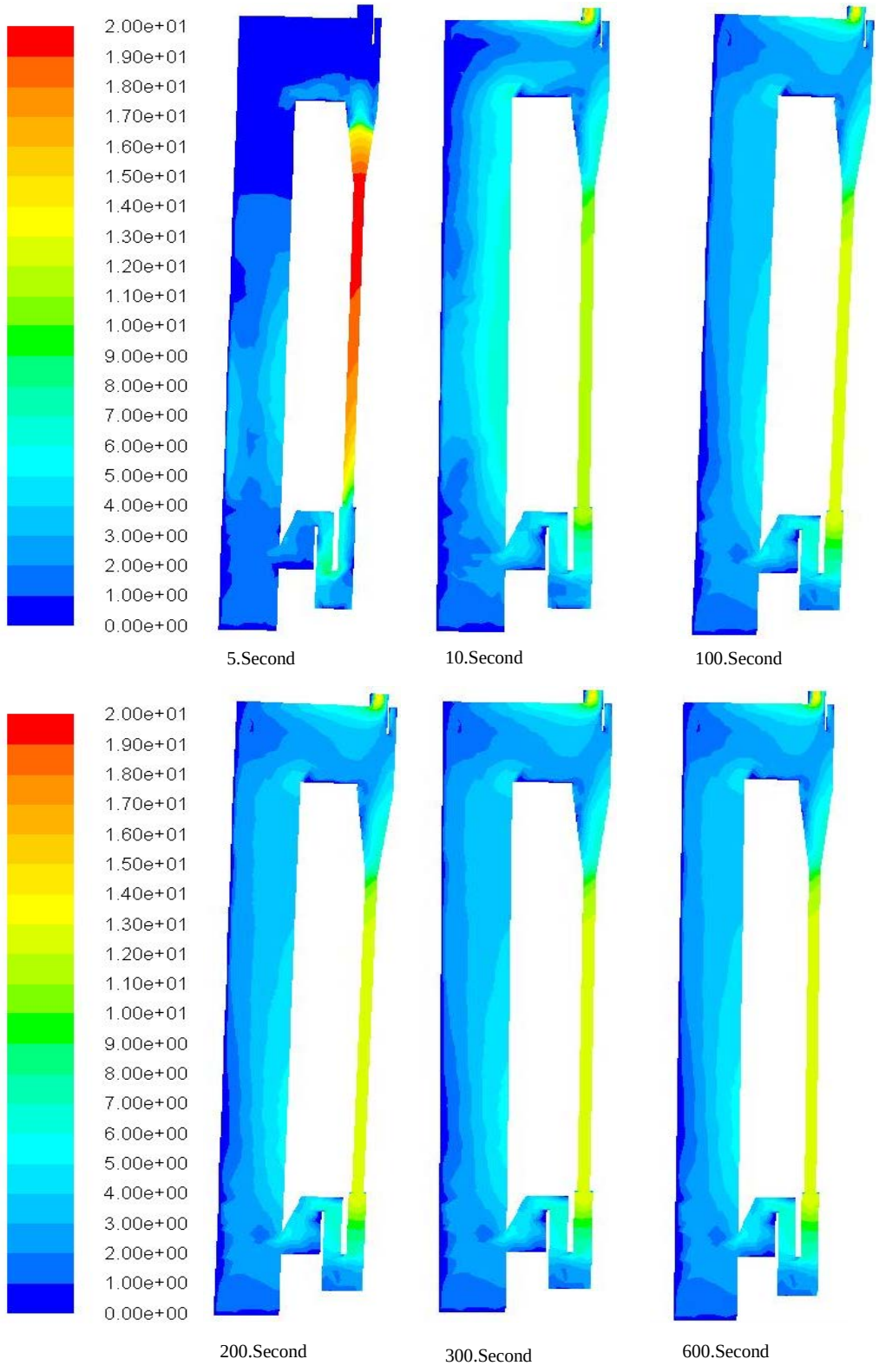

Figure 5. Changing of Temporal Air Velocity In Solid Circulating System

As could be seen Figure 5, Sand velocity in CFB furnace that didn't after 200 second from started up conditions. In this analysis results sand velocity was respectively 3-5 m/s in combustion chamber, 5-6 m/s in cyclone, 12-15 m/s in dip-leg pipe and 0-3 m/s in loop seal.

As could be seen Figure 4, air velocity in combustion chamber is 6 m/s for steady-state conditions. Also, sand velocity in combustion chamber is 4 m/s. 2,8 kg/s air is used for combustion of 0,36 kg/s Tunçbilek lignite at 1,2 stoichiometric rate.

4. RESULTS

Circulating Fluidized Bed processing is known as most clean and efficiency coal combustion technologies. In this study, GLİ-Tunçbilek coal which contains high moisture and ash, combustion and hydrodynamic characteristic was investigated in 8 MW_{th} circulating fluidized bed combustor. Air combustion chamber inlet and combustion chamber mean velocity was observed 6 m/s. This analysis results revealed that Circulating Fluidized Bed Combustors are most convenient combustor for low quality (8000 kJ/kg) Turkish lignites. Next studies, oxy-fuel combustion, staged secondary air and solar energy assisted innovations will include in CFBC combustion process and will investigate temperature and NO_x, SO_x emissions results in developed process.

REFERENCES

[1] A. Güngör and N. Eskin, "Dolaşımlı Akışkan Yataklı Yakıcıların Farklı İşletme Şartlarında İncelenmesi " , 84: 7, 2004.
[2] S. Dülger,'' Akışkan Yataklı Kömür Yakma Sistemlerinde Otomatik Kontrol Tasarım Ve Uygulaması, Gazi Üniversitesi Fen Bilimleri Enstitüsü, 172 s., Ankara, 2008.
[3] P. Mirek, R. Sekret and W. Nowak, "The influence of Air Nozzles'Shape on the NOx Emission in the Large Scale 670 MWT CFB Boiler": 8, 2007.
[4] O. Erbaş, H. Topal and A. Durmaz, "Effects of the Sıze Distribution of fuel particulate on the heat gate in the inner surface of fluidized bed ", Dumlupınar Üniversitesi Fen Bilimleri Enstitüsü Dergisi 16: 91-96, 2008.
[5] M. Weng and J. Plackmeyer, "Comparison Between Measurements and Numerical Simulation of Particle Flow and Combustion a the CFBC Plant." 8, 2011.
[6] K.M. Pandey and R. Kumar, "Numerical Analysis of Coal Combustion in Circulating Fluidized Bed." International Journal of Chemical Engineering and Applications **2**: 5. DOI: 10.7763/IJCEA.2011.V2.140, 2011.
[7] J.P.Simanjuntak, Z.A. Zainal and M. Z. Abdullah, "Hydrodynamic simulation and experimental studies of an internally circulating bubbling fluidized bed with concentric cylinders." 18, 2014.
[8] P. Stopford, "Recent applications of CFD modelling in the power generation and combustion industries", Applied Mathematical Modelling, 26, 351–374. DOI:10.1016/S0307-904X(01)00066-X, 2002.
[9]M. Gharebaghi., R.M.A. Irons, L. Ma, M. Pourkashanian, A. Pranzitelli., "Large eddy simulation of oxy-coal combustion in an industrial combustion test facility", International Journal of Greenhouse Gas Control, 5S, S100-S110. DOI:10.1016/j.ijggc.2011.05.030, 2011.
[10] H. Liu, A. Elkamel, A. Lohi, M. Biglari, " Computational Fluid Dynamics Modeling of Biomass Gasification in Circulating Fluidized-Bed Reactor Using the Eulerian–Eulerian Approach", Ind. Eng. Chem. Res.,, 52 (51), pp 18162–18174, 2013.
[11] L. G. Gibilaro, R. Di Felice and S. P. Waldram. "Generalized Friction Factor and Drag Coefficient Correlations for Fluid-particle Interactions". Chem. Eng. Sci.. 40(10). 1817-1823. 1985. DOI:10.1016/0009-2509(85)80116-0
[12] ANSYS FLUENT 14 User's Guide, Fluent Inc.,2013, USA.
[13] F. Kumaş, "Akışkan yatakta hidrodinamik yapının sistem davranışına etkisi", Dumlupınar Üniversitesi Fen Bilimleri Enstitüsü Yüksek Lisans Tezi, Kütahya, 2009.
[14] B. Gurel, O. İpek, M. Kan, "Numerıcal Analysis In Pulverised Coal Fired Furnace For Different Burner Geometries", International Conference On Computatıonal And Experimental Science And Engineering, Antalya, Turkey, 2014.

ICENS
INTERNATIONAL CONFERENCE ON ENGINEERING AND NATURAL SCIENCES
24-28 May 2016 /Sarajevo

Offshore Wind Farm Layout Optimization Using Mathematical Modeling

Ilayda Ulku[1], Cigdem Alabas Uslu[2]

Abstract

Wind energy is a main renewable energy source comparing with the other renewable energy resources such as geothermal energy, solar energy, bio energy, and heat pump. Wind turbines extract kinetic energy from wind and convert it into electricity. A group of turbines is called wind farm which can be located in land or in bodies of water. The latter is named offshore wind farm while the first is onshore. Offshore wind power is a charming alternative to generate energy in the future since it has better wind regime than that of onshore. Therefore, this study focuses on layout of offshore wind farms to decide the locations of the turbines relative to each other and electrical cable connections between each pair of turbines installed. Objectives of this layout design problem is to both maximize total power generated via the installed turbines and minimize total cost of the cables between these turbines. With this study, a mixed integer non-linear mathematical model is proposed for layout of small sized offshore wind farms. Since the total installation cost of offshore wind farms is quite expensive, small sized farms are generally preferred in the real case applications. An optimum layout design would provide a considerable saving in the cost besides providing increment in the total energy generated. An experimental study has been carried out to show the usability of the proposed mathematical model on different test problems.

Keywords: *Layout design, mixed integer non-linear model, wind farm.*

1. INTRODUCTION

With the rapid increase in energy demand, existing energy resources will be exhausted in the future. Thus, the use of renewable energy sources around the world has become obligate. Because of the continuity and sustainability opportunities of renewable energy, it has been considered as an alternative energy resource in the developed countries. Also, greenhouse gas emissions is one of the main global warming effects that must be solved around the world [1]. Therefore, the use of renewable energy sources has become inevitable around the world. Renewable energy is one of the major energy resource for the countries in terms of continuity and sustainability for the energy production.

Instead of importing energy at high cost, investment cost of renewable energy which consists of research and development, plant installation, technology, materials and manpower can be afforded. Investment in renewable energy is permanent for the country where it is installed and becomes a source for the local economy. Wind energy, solar energy, geothermal energy, bio energy, heat pump, and grid energy storage are alternative renewable energy sources. Among these alternatives wind energy becomes a key source of renewable energy because of its high potential to provide the required energy capacity [2]. Wind power extracts the kinetic energy from the wind and converts it into electricity with the help of turbines [3]. If a group of turbines is located in-land it is called onshore wind farm and if a group of turbines is located in bodies of water, then it is called offshore wind farm. Offshore wind power has better wind regime than onshore which makes it a charming alternative to generate energy in the future ([4], [5]). Therefore, this study focuses on offshore wind farms which has the highest potential to become energy resource for the developed countries. Determination of turbine locations in an offshore farm and cable connections between the located turbines and transmitter are the parts of offshore wind farm layout problem. With this study, we propose a non-linear mixed integer programming model in which these parts of the problem are included.

In the next section, there is a brief survey of the literature. In section 3, offshore wind farm layout problem is explained in detail considering the related aspects of the problem which effect the proposed model in this study. Proposed mathematical model is given in section 4 and the results obtained from the model on several test problems are reported in section 5. Finally, conclusions are given in the last section.

2. LITERATURE SURVEY

As electricity demand is increasing worldwide, wind power is expected as a major player in the future electricity production. However, there are significant obstacles to withstand the widespread deployment such as turbine development, electric grid

[1]*Corresponding author: Istanbul Kültür University, Faculty of Engineering, Industrial Engineering Department, 34191, Bakırköy/İstanbul, Turkey. i.karabulut@iku.edu.tr*

[2]*Marmara University, Faculty of Engineering, Industrial Engineering Department, 34722, Kadıköy/İstanbul, Turkey. cigdem.uslu@marmara.edu.tr*

design and integration, capacity factors, operation and maintenance costs, sustainable performance in a long run. In this section, studies in the literature which focus on the placement of turbines, cable layout (connection of turbines and transmitter) or power generation are given.

Placement of turbines is considered to decide optimal location of the turbines where maximum power is obtained. Energy loss and cost models are represented to find the placement of turbines to design the wind farm [21]. First model based on genetic algorithm is introduced in 1994 by Mosetti et al. [22] to find optimal placement of the wind turbines. A test case is generated by dividing a square into 100 square cells where possible turbine locations can be arranged. This type of the placement design is called grid design in the literature. Constant wind speed with variable direction, single direction, and variable wind speed with variable direction are considered for the given test case. After Mosetti et al. [22] introduced their study, some comparative studies which use the test case of [22] have been presented to the literature. Ozturk and Norman [23] propose a greedy improvement heuristic methodology to increase the efficiency of a wind farm [23]. They have tested the methodology on the test case of [22] and on additional test instances generated. A genetic algorithm is developed by Grady et al. [24] to find optimal placement of turbines, where the number of installed turbines are limited, to obtain maximum capacity under three considerations: non-uniform wind with several directions, single direction uniform wind, and uniform wind with several directions. A Monte Carlo simulation method determines optimal turbine placement in the study of Marmidis et al [25]. Also in this research, grid design of the wind farm is assumed and the researchers give a comparative study with their results and the results of Mosetti et al. [22] and Grady et al. [24]. Sood et al. [26] also develop a Monte Carlo based algorithm which gives various different turbine placement with the proposed mathematical method and determines the best turbine placement related with their objective. They apply their methodology to various scenarios related with multiple wake effects with four wind turbines. Pérez et al. [32] suggest a problem specific heuristic method to find initial layout configuration and then a nonlinear mathematical programming technique is proposed to optimize starting from the initial layout. The proposed model is tested by using real data with the increasing number of turbines up to 22 turbines. Gao et al. [27] propose a multi-population genetic algorithm to find the placement of turbines where constant wind speed with single wind direction, variable wind speed with variable wind directions, and constant wind speed with variable wind direction are used to generate test scenarios with different turbine sizes up to 46 turbines.

As the distances between tribunes are decreases, cable cost also decreases; however the closeness of the turbines results in wake effect which causes loss in the generated power. Therefore, cable layout has a significant effect on the wind farm design. Various studies focus on the cable layout problem. Lundberg [21] investigates the effects of different electrical cable types on the investment cost and power generated. Bauer et al. [28] focus on effects of system efficiency on electrical cable layout cost. Zhao et al. [29] optimize cable layout aiming both production cost and system reliability where the production cost includes investment and maintenance costs, cost of wind power production under wake effect and the system reliability is related with the failures of components. Another study by Zhao et al. [30] is an application of several genetic algorithms to find good solutions to the electrical cable layout for a real offshore wind farm. Lumbreras and Ramos [31] propose a Benders' decomposition method to optimize electrical cable layout taking into account stochasticity in wind scenarios and component failures. They solve a real case problem with 30 turbines and given locations. Hou et al. [33] model the cable layout problem as a minimum spanning tree and use the Prim's algorithm to decrease the cable cost. For the cable layout problem, Dahmani et al. [34] propose a genetic algorithm in which population of the network configurations is locally optimized by the Prim's algorithm.

Offshore wind farms are quite expensive investments. Therefore any improvement in the investment cost will be quite valuable. With this research, placement of the tribunes and cable layout between these turbines are addressed by proposing a non-linear mixed integer programming model. Objective of the proposed model is to optimize the tradeoff between power generation and cable cost in an offshore wind farm. Different scenarios are generated to see the effectiveness and efficiency of the proposed model.

The paper continues with the problem definition in section 3 and the introduced methodology is explained in section 4 in detail. In section 5, experimental study conducted is presented and finally conclusions and future remarks are given in the last section.

3. LAYOUT OF OFFSHORE WIND FARMS

There are several problems to be solved before generating the power using an offshore wind farm. First of all, selection and determination of the wind farm location, electrical infrastructure and cable layout, wake losses, operations, and also maintenance issues are significant problems that must be considered in the layout of an offshore wind farm. Since, total installation cost of an offshore wind farms is quite expensive, an optimum layout design would provide a considerable saving in the cost besides providing increment in the total energy generated. Table 1 represents the cost distribution of an offshore wind turbine installation. Cable installation cost even takes only 7% of the total, any improvement in the cable layout will be valuable because of the high total cost.

Table 6. Offshore wind turbine installation costs [20]

Turbines and its components	73%
Cable	10%
Grid Connection	10%
Cable Installation	7%

In this study, turbine/transmitter location problem under the wake effect and also cable layout problem are considered concurrently to minimize total installation costs given in Table 1. In the next two sections, turbine/transmitter location and wake effect, cable layout are described, respectively. Prediction of the power output which is necessary in the explanation of the proposed model is also given subsection 3.3.

3.1. Turbine/Transmitter Location Problem and Wake Effect

A wind turbine converts the wind power into electricity. Wind turbines are consisted of some electrical network such as battery charging circuits, grids, power systems, etc. to generate electricity. After the selection of wind farm location, position of each turbine and one or more transmitters relative to each other turbine/transmitter must be determined. This problem is called turbine/transmitter location problem. Besides the technical requirements which effect the distances between turbines depending on the type of the turbine there occurs an additional layout problem called wake effect. Positioning of the turbines relative to each other effects the direction and also velocity of the wind which the turbines can benefit. This is known as wake effect and results in decrease in the power generated by turbines effected by wake.

Jensen [19] has been published a wake model where the wake is expanding linearly with a velocity deficit and it is depended to the distance behind the rotor. An illustration of Jensen model is explained in Figure 1 where the wake effect between turbines with a distance x is represented [22]. The wind blows with a wind speed u_0 from the left and passes through the wind turbine with the rotor radius r_r . After the wind hits the wind turbine, the wake radius becomes $r_1 = \alpha x + r_r$. The α value in the equation (1) represents the enlargement of the wake with the given distance between the turbines. Hub height where the wake begins is defined as z and surface roughness is presented as a constant value z_0.

$$\alpha = \frac{0.5}{ln\frac{z}{z_0}} \tag{1}$$

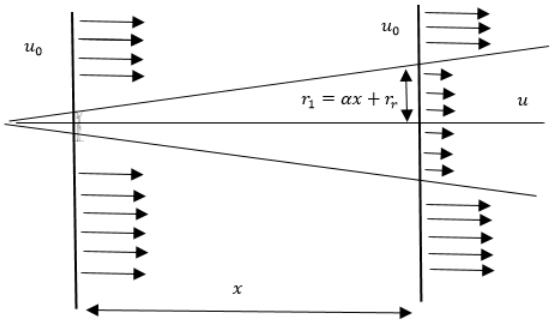

Figure 9. Wake effect representation [22]

Let i to be a turbine position where wake is beginning, j is the turbine which is effected by this wake. Also, u_0 is the wind speed of surrounding and u_j is at position j. Equation (2) gives the balance of the wind speed at position j by induced Vd_{ij} which is the velocity deficit on position j by wake generated on position i. Velocity deficit, Vd_{ij} is given in equation (3) where a is the axial induction factor, the distance from position i to j is x_{ij}, and downstream rotor radius is r_d which is also calculated in equation (5).

$$u_j = u_0(1 - Vd_{ij}) \tag{2}$$

$$Vd_{ij} = \frac{2a}{1 + \alpha\left(\frac{x_{ij}}{r_d}\right)^2} \tag{3}$$

In equation (4), calculation of the axial induction factor a is depend on thrust coefficient, C_T, of the turbine. It measures the wind speed losses due to wake effects.

$$a = 0.5\left(1 - \sqrt{1 - C_T}\right) \tag{4}$$

$$r_d = r_r\sqrt{\frac{1-a}{1-2a}} \tag{5}$$

As Vd_{ij} represents the velocity deficit for one turbine, the total velocity deficit, $V_{def}(j)$ is defined in equation (6) that $w(j)$ represents the turbines' set which generate wake and effect the position j.

$$V_{def}(j) = \sqrt{\sum_{i \in w(j)} V d_{ij}^{\,2}} \quad (6)$$

3.2. Cable Layout Problem

Cable connection which links wind turbines with electrical cables is a major problem called cable layout. There are medium voltage and high voltage cables in the system. Medium voltage cables, in general, are used to connect the turbines to each other while high voltage cables are used to connect transmitter with one or more turbines. Generated power at each turbine is transmitted via the cable layout to the transmitter. Thus, the cable layout takes a critical place not only for turbines but also for transmitter to transfer the power. As the cables are installed under the water once it will stay for a lifetime. As cable layout has a fundamental effect both for layout cost and reliability of the power generation, it takes an important place to be optimized.

3.3. Power Output Prediction

Related with the turbine type and wind speed the output of power differs and there exist a characteristic power performance curve as shown in Figure 2. With various turbine height and wind speed, there can occur different electrical power output values.

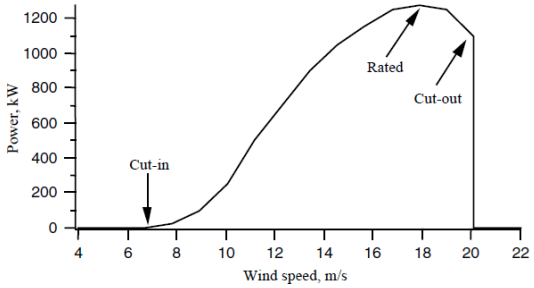

Figure 10. Power Generation of a wind turbine [2]

Performance of a wind turbine generator depends on three key points on the velocity scale which are cut-in speed, rated speed, and cut-out speed. The minimum wind speed where the blades of turbine begin to rotate and the generator executes the power is represented as cut-in speed. The electrical output power increases as the wind speed rises above the cut-in speed. Related with the capacity of the electrical generator, there is a limit called the rated wind speed. Although wind speed is increased, the design of the turbine stabilize the power to this limit which is the maximum level of the power output. This is done with the blade angles which are adjusted to stabilize the power at the constant level [13]. As the rated wind speed is raised, the forces on the turbine is increased which can occur a damage to the rotor. Thus, cut-out speed is related with the maximum wind speed. Due to safety considerations and also restricted engineering design of the turbine the generated power is, therefore, limited.

Equation (7) represents the generated power. The available power is proportional to the cube of the wind speed where mass flow rate of wind is a function of air density. In the literature, the wind power per unit area or the wind power density is calculated as given in equation (7) where ρ is the air density and and U is the air velocity (assumed uniform) [17].

$$\frac{P}{A} = \frac{1}{2}\rho U^3 \quad (7)$$

The wind power density is proportional to the cube of the wind velocity U^3, and the wind power is proportional to the area swept by the rotor diameter [2]. Therefore, any rise in wind speed would result in an increase in generated power.

4. METHODOLOGY

To model turbine location and cable connection problem under the grid-layout assumption, a mixed-integer non-linear programming formulation is suggested in this study. The parameters in the model are given as follows:

TotalNumberOfTurbines is used to limit turbine placement for each grid scenario. Cable cost between turbines (EUR per m) is used as *cost*, and cable cost between turbines and the transmitter (EUR per m) is used as *costT*. The distances between turbine i and j (m) is d_{ij}.

Decision variables of the problem are described as:

$$x_i = \begin{cases} 1, & if\ there\ is\ a\ turbine\ at\ position\ i; \\ 0, & otherwise \end{cases}$$

$$y_{ij} = \begin{cases} 1, & if\ there\ is\ a\ cable\ connection\ between\ turbine\ i\ turbine\ j\ ; \\ 0, & otherwise \end{cases}$$

$$yy_{i,T} = \begin{cases} 1, \ if\ there\ is\ a\ cable\ connection\ from\ turbine\ i\ to\ transmitter, T \\ 0, otherwise \end{cases};$$

Total power generated through the wind farm is *TotalPOWER*, and total cost for the cable layout is *Total* Cost. Objective function is defined as *z*.

The proposed mixed-integer non-linear programming model aims to find an efficient solution of turbine placement and connections between the turbines. Therefore, the objective is a bundle function that balances the generated total power and the cable cost used to connect the turbines and the transmitter taking into account coefficients α_1 and α_2.

$$\max z = \alpha_1 TotalPower - \alpha_2 \left[\left(\sum_{ij} y_{ij}\, d_{ij} \right) cost + \left(\sum_{i} yy_{i,T} d_{i,T} \right) costT \right] \quad (10)$$

$$min\{d_{ij}\} x_i = we_i \qquad \forall_i \quad (11)$$

$$Vd_{ij} = \frac{2a}{1 + \alpha \left(\frac{we_i}{r_d} \right)^2} \qquad \forall_i \quad (12)$$

$$P_i = \frac{1}{2} \rho \pi (r^r)^2 (u_0)(1 - Vd_i) x_i \qquad \forall_i \quad (13)$$

$$TotalPower = \sum_i P_i \quad (14)$$

$$TotalNumberOfTurbines = \sum_i x_i \quad (15)$$

$$y_{ij} + y_{ji} \leq x_i \qquad \forall_{ij} \quad (16)$$

$$\sum_{ij} y_{ij} \leq (TotalNumberOfTurbines - 1) \quad (17)$$

$$yy_{i,T} \leq x_i \qquad \forall_i \quad (18)$$

$$\sum_i yy_{i,T} \geq x_T \quad (19)$$

$$y_{ii} = 0 \qquad \forall_i \quad (20)$$

$$x_T = 1 \quad (21)$$

The wake effect is calculated with the equation (11) and (12). Positioned turbine effects the other turbines around itself. Therefore, minimum distance in the grid is considered to determine related wake effect for each turbine [23]. Power of one wind turbine is calculated with equation (13) where ρ is the air density (kg/m^3), $\pi(r^r)^2$ is the swept area (m^2) of wind turbine with radius r^r. Total power output of the set of turbines in a wind farm is calculated with equation (14) where the sum of all turbines' generated power in the wind farm is calculated. Maximum number of turbines are given with equation (15). Connectivity between turbines is represented in equation (16) - (19). If there is a turbine, there is a cable connection either to another turbine or to the transmitter. Total number of connections is less than total number of placed turbines in order to prevent the cycling which is shown in equation (17). With equation (17) the requirement for the minimum spanning tree is satisfied to prevent the loop between the connected turbines. Also, with equation (18) the connections thought the grid is strengthened. Generated power must be transformed through the cables to the transmitter. Thus, at least one turbine can be connected to the transmitter. This situation is represented by equation (19). Moreover, to avoid the redundant cable connections from one turbine to the same turbine equation (20) is used. The location of transmitter is given with equation (21).

5. EXPERIMENTAL STUDY

To test the proposed model, three different scenarios assuming the grid layout are considered. Each scenario consists of the changes in the grid size and total number of turbines. Changes in α_1 and α_2 are also evaluated for each scenario where α_1 is a coefficient for the total generated power from the wind farm and α_2 is that of the cable cost used in the layout. Proposed model is formulated in GAMS 23.1.2 and solved by using BONMIN solver in order to obtain the optimal results. The runs were executed on a 1.70 GHz Intel Core i5 notebook with 6 GB of RAM.

3x3 grid size is used to place 3 turbines and to find the connections between turbines and transmitter. When total power is compared with total cost for 3x3 grid size for different α_1 and α_2 values, best solution is found when α_1 is 0.4 and α_2 is 0.6. Total generated power in 3x3 grid size is 27691.09 kW with 9660 dollars total cable layout cost.

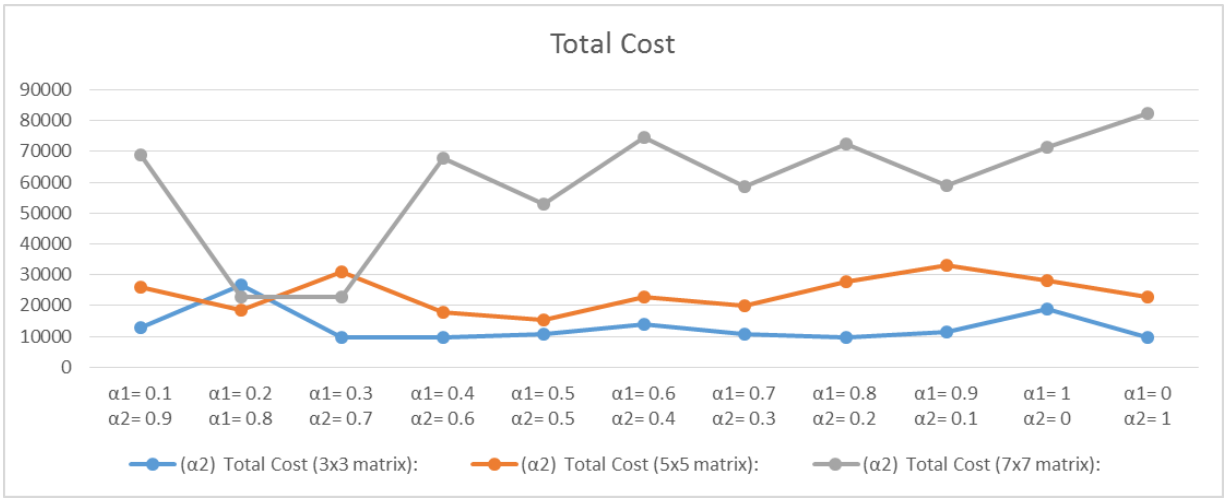

Figure 11. Total cost comparison of 3x3, 5x5, and 7x7 grid size for alpha values

Also, 5x5 grid size is used to place 4 turbines and to find the connections between turbines and transmitter. Best solution is when α_1 is 0.4 and α_2 is 0.6 with total generated power 27691.09 kW and total cable layout cost 17818.734 dollars.

As last generated scenario, 7x7 grid size is used to place 5 turbines and to find the connections between turbines and transmitter. When total power and total cost is compared for 7x7 grid size, total generated power is found as 55382.18 kW and total cable layout cost is concluded as 22962.45 dollars. However, best α_1 is 0.3 and α_2 is 0.7 which are different from the results obtained in the previous scenarios. All scenarios for possible alpha values are represented in figure 3 for the turbine placements in 3x3, 5x5, and 7x7 grid size.

In figure 4, grid layouts of the optimal solutions is given for each scenario. Execution times are 0.016 seconds, 0.094 seconds, and 0.078 seconds for 3x3, 5x5, and 7x7 grid sizes respectively.

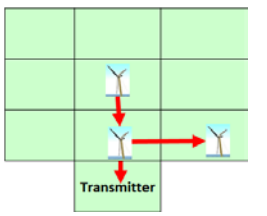

(a) Layout of 3x3 grid size

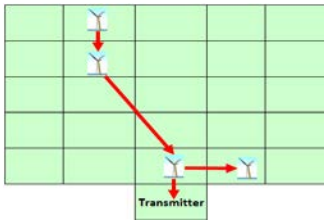

(b) Layout of 5x5 grid size

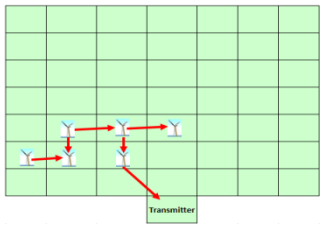

(c) Layout of 7x7 grid size

Figure 12. Grid Layouts of the optimal solutions

6. CONCLUSION

In this research, location of the turbines and the connection of the located turbines and a transformer are addressed. The structure of the complete problem is non-linear thus, a non-linear programming model is proposed to optimize the problem. There are two conflicting decisions in the problem which are related with power generation and cable cost through the layout. As the turbines are located close to each other generated power decreases because of the wake effect, on the other hand the cable cost decreases. Therefore, we generate different scenarios to analyze these conflicting decisions. Cable cost and power generated are weighted in the same objective function resulting in a composite function. Therefore, we aim to decrease the investment cost while increasing the generated power simultaneously. Offshore wind farms are rather expensive to invest and any improvement in the investment cost will be quite valuable. Since this study aims to develop an optimization based solution approach, it is certain to get cost savings for a planned wind farm.

REFERENCES

[1]. RWE Group, Environmental Statement – Non Technical Summary, Npower Renewables, 2005.
[2]. J. F. Manwell, J. G. McGowan, A. L. Rogers, *Wind Energy Explained Theory, Design, and Application*, West Sussex: John Wiley and Sons, Ltd., 2008.
[3]. *Onshore and Offshore Wind Energy Generation Technologies*, http://www.gridtech.eu/project-scope/technologies/12-technologies/13-onshore-and-offshore-wind-energy-generation-technologies (Accessed: 20.12.2015).
[4]. S. Lumbreras, and A. Ramos, *Offshore wind farm electrical design: a review*. Wind Energy, 2013. 16(3): p. 459-473.
[5]. S. Relevan, Offshore and Onshore: The Debate in Wind Energy, http://relevansi.com/blog/offshore-onshore-debate-wind-energy/, 2011 (Accessed: 20.12.2015).
[6]. A. Readyhough, *Lessons Learned: Offshore Cable Installation*, Global Marine Energy, 2010.

[7]. A. Arapogianni, J. Moccia, D. Williams, J. Phillips, *Wind in our Sails*. Technical Report. European Wind Energy Association, 2011.
[8]. (2016) *RES Power for Good*. [Online]. Available: http://www.res-anatolia.com/what-we-do/wind-energy/project-development?lang=Tks
[9]. J. W. Cleijne. *Results of Sexbierum wind farm; single wake measurements*. Technical Report TNO-Report 93-082, TNO Institute of Environmental and Energy Technology, 1993.
[10]. S. Lumbreras and A. Ramos, *Optimal Design of the Electrical Layout of an Offshore Wind Farm Applying Decomposition Strategies*, IEEE Transactions on Power Systems, 2013, 28(2): p. 1434-1441.
[11]. S. Lumbreras, A. Ramos, P. Sánchez, *Offshore wind farm electrical design using a hybrid of ordinal optimization and mixed-integer programming*, Wind Energy, 2015, 18(12): pp. 2241-2258.
[12]. (2013) AWEA, *Anatomy of a Wind Turbine*, American Wind Energy Association. [Online]. Available: http://www.awea.org/Resources/Content.aspx?ItemNumber=5083
[13]. (2016) *Wind turbine power ouput variation with steady wind speed*. [Online]. Available: http://www.wind-power-program.com/turbine_characteristics.htm
[14]. (2016) EWEA, *Wind in Power 2015 European Statistics*,. [Online]. Available: http://www.ewea.org/fileadmin/files/library/publications/statistics/EWEA-Annual-Statistics-2015.pdf,
[15]. B. Sanderse, *Aerodynamics of wind turbine wakes: literature review*. Energy Research Centre of the Netherlands (ECN); 2009. Report ECN-E-09-016.
[16]. K. E. Diamond, E. J. Crivella, *Wind Turbine Wakes, Wake Effect Impacts, and Wind Leases: Using Solar Access Laws As The Model For Capitalizing On Wind Rights During The Evolution Of Wind Policy Standards*, 2011, Duke Environmental Law and Policy Forum Wind Rights and Solar Access Laws, 22: p. 195-244.
[17]. M. Samorani, *The Wind Farm Layout Optimization Problem*, Handbook of Wind Power Systems, Energy Systems, DOI: 10.1007/978-3-642-41080-2_2, Springer-Verlag Berlin Heidelberg 2013.
[18]. G. Mosetti, C. Poloni, D. Diviacco, *Optimization of wind turbine positioning in large wind farms by means of a Genetic algorithm*, J Wind Eng Ind Aerody, 1994, 51: pp.105–116.
[19]. N. O., Jensen. *A note on wind generator interaction*. Risø-M-2411, Risø National Laboratory, 1983.
[20]. A. Readyhough, *Lessons Learned: Offshore Cable Installation*, Global Marine Energy, 2010.
[21]. S. Lundberg, *Evaluation of wind farm layouts*, EPE Journal 2006; 16: 14.
[22]. G. Mosetti, C. Poloni, B. Diviacco, *Optimization of wind turbine positioning in large wind farms by means of a genetic algorithm*, J Wind Eng Ind Aerodyn, 1994, 51(1): pp. 105–116.
[23]. U. A., Ozturk, B. A. Norman, *Heuristic methods for wind energy conversion system positioning*, Electric Power Systems Research 70, 2004: pp. 179–185
[24]. S. A. Grady, M. Y. Hussaini, M. M. Abdullah, *Placement of wind turbines using genetic algorithms*, Renew Energy, Elsevier, 2005, 30: pp. 259–70.
[25]. G. Marmidis, S. Lazarou, E. Pyrgioti, *Optimal placement of wind turbines in a wind park using Monte Carlo simulation*, Renewable Energy, 2008, 33: pp. 1455-1460.
[26]. P. Sood, V. Winstead, P. Steevens, *Optimal placement of wind turbines: a Monte Carlo approach with large historical data set*, 2010 IEEE International Conference on Electro/Information Technology (EIT), United States of America, 2010: pp. 1–5.
[27]. X. Gao, H. Yang, L. Lua , P. Koo, Wind turbine layout optimization using multi-population genetic algorithm and a case study in Hong Kong offshore, J. Wind Eng. Ind. Aerodyn, 2015, 139: pp. 89–99.
[28]. P. Bauer, S. W. H. De Haan, C. R. Meyl, J. T. G. Pierik, *Evaluation of electrical system for offshore wind farms*, Proc. IAS'00, 2000, 3: pp. 1416– 1423.
[29]. M. Zhao, Z. Chen, F. Blaabjerg, *Optimisation of electrical system for offshore wind farms via genetic algorithm. IET* Renewable Power Generation, 2009; 3: pp. 205–216.
[30]. M. Zhao, Z. Chen, J. Hjerrild, *Analysis of the behaviour of genetic algorithm applied in optimization of electrical system design for offshore wind farms*, IECON 2006, 32nd Annual Conference on IEEE Industrial Electronics (IEEE Cat. no. 06CH37763), Paris, France, 2006.
[31]. S. Lumbreras, A. Ramos, *A benders' decomposition approach for optimizing the electrical system of offshore wind farms*, IEEE TRANSACTIONS ON POWER SYSTEMS, 2013, 28, 2: pp. 1434-1441.
[32]. B. Pérez, R. Mínguez, R. Guanche, *Offshore wind farm layout optimization using mathematical programming techniques*, Renewable Energy, 2013, 53: 389-399.
[33]. P. Hou, W. Hu, Z. Chen, *Offshore Substation Locating in Wind Farms Based on Prim Algorithm*, 2015 IEEE Power & Energy Society General Meeting, 2015, pp.1-5.
[34]. O. Dahmani, S. Bourguet, M. Machmoum, P. Guérin, P. Rhein, L. Jossé, *Optimization of the Connection Topology of an Offshore Wind Farm Network*, IEEE SYSTEMS JOURNAL, 2015, 9, 4: pp. 1519-1528.

Hydrogeochemical and Isotopic Investigation of the Seydişehir-Ilıca Thermal Spring, Turkey

Ayla Bozdag[1]

Abstract

Ilıca thermal spring (ITS) is located in Seydişehir town, about 90 km southwest of Konya Province in the Central Anatolia, Turkey. The geothermal spring has a temperature of 31.3 °C, with total dissolved solids (TDS) ranging from 741 to 786 mg/l. The Ilıca thermal spring has low Na and K contents but high Ca and HCO_3 concentrations and ionic abundances are Ca> Mg > (Na + K) and HCO_3 > Cl > SO4. According to IAH classification, the Ilıca thermal spring is Ca-Mg-HCO_3 water type. Cold ground waters are mainly of Ca-HCO_3 and Ca-Mg-HCO_3 types, with TDS ranging from 282 to 702.5 mg/l. The chemical geothermometers applied in the Ilica thermal spring yielded ranging from 52 to 59 °C according to the silica geothermometers. The Ilıca thermal spring are undersaturated with respect to gypsum and anhydrite minerals, and oversaturated with respect to calcite, dolomite and aragonite at discharge temperatures corresponding to travertine precipitation in the discharge area. The calcite, dolomite and aragonite minerals possibly caused scaling when obtaining the thermal waters in the Ilıca thermal area. Based on the results of $\delta^{18}O$, $\delta^{2}H$ and ^{3}H isotope analyses, the Ilıca thermal spring and cold groundwaters have a meteoric origin. The meteoric waters infiltrate along fractures and faults, get heated at depth with the high geothermic gradient and then returns to surface through hydrothermal conduits. The $\delta^{13}C$ ratio for dissolved inorganic carbonate in the spring is between 0.76 and 1.33 ‰, indicating that it originates from the dissolution of marine carbonates.

Keywords: *Geothermometry, Hydrogeochemistry, Ilıca thermal spring, Isotope, Seydişehir*

1.INTRODUCTION

Geothermal exploration in Turkey started in the early 1960s yet Turkey's low and medium temperature resources have not completely explored and/or evaluated. The Ilıca thermal spring, a low temperature resource, is located in Seydişehir town, about 90 km southwest of Konya Province in the Central Anatolia, Turkey (Figure 1). The Ilıca thermal spring region and its vicinity were studied for different aspects ([1] - [5]).

The climate of the region is characterized by hot and dry summers, and cold and wet winters. The total annual precipitation in the region is about 679 mm. The Ilıca thermal spring has discharge rate of 1.36 l/s and its temperature is 31.3 °C. Unfortunately, this thermal spring is not presently used for any purposes. The aim of this study is to determine chemical characteristics, the origin and isotopic composition of Ilıca thermal waters and to make suggestions for their utilization.

Geologic and hydrogeologic settings

The Lower-Middle Cambrian aged Çaltepe formation form the basement rocks in the study area and consist of crystallized limestone, dolomite, dolomitic limestone [1]. The basement unit is conformably overlain by the Upper Cambrian-Lower Ordovician aged Seydişehir formation which are composed of greenish gray, green and brown in color metasandstone, metasiltstone, schist, phyllite, quartzite. The Middle-Upper Triassic aged Tarasçı formation which is represented by limestones including fossiliferous and bituminous levels overlies the Seydişehir formation with an angular unconformity. The Tarasçı formation is conformably overlain by the Upper Triassic-Lower Jurassic aged Sarpyardere formation which is composed of sandstone, claystone, siltstone, marl and limestone [6]. These formations outcrop in the south-southwest of the region and do not have wide distribution. All these units have been overlain unconformably by the Upper Miocene-Pliocene aged İnsuyu formation and Erenlerdağ volcanics. İnsuyu formation is made up of limestones, marl, conglomerates, sandstones, tuff, claystone and siltstone [7]. Erenlerdağ volcanics outcropping at the east of the region are composed of dacite, andesite and basalt with columnar jointing, the agglomerate, loosely-cemented conglomerate and the tuff [8]. All these units are covered unconformably by alluvial deposits, and travertine occurrences around the thermal spring (Figure 1).

[1] *Corresponding author: Selcuk University, Department of Geological Engineering, 42079, Konya, Turkey.* aayaz@selcuk.edu.tr

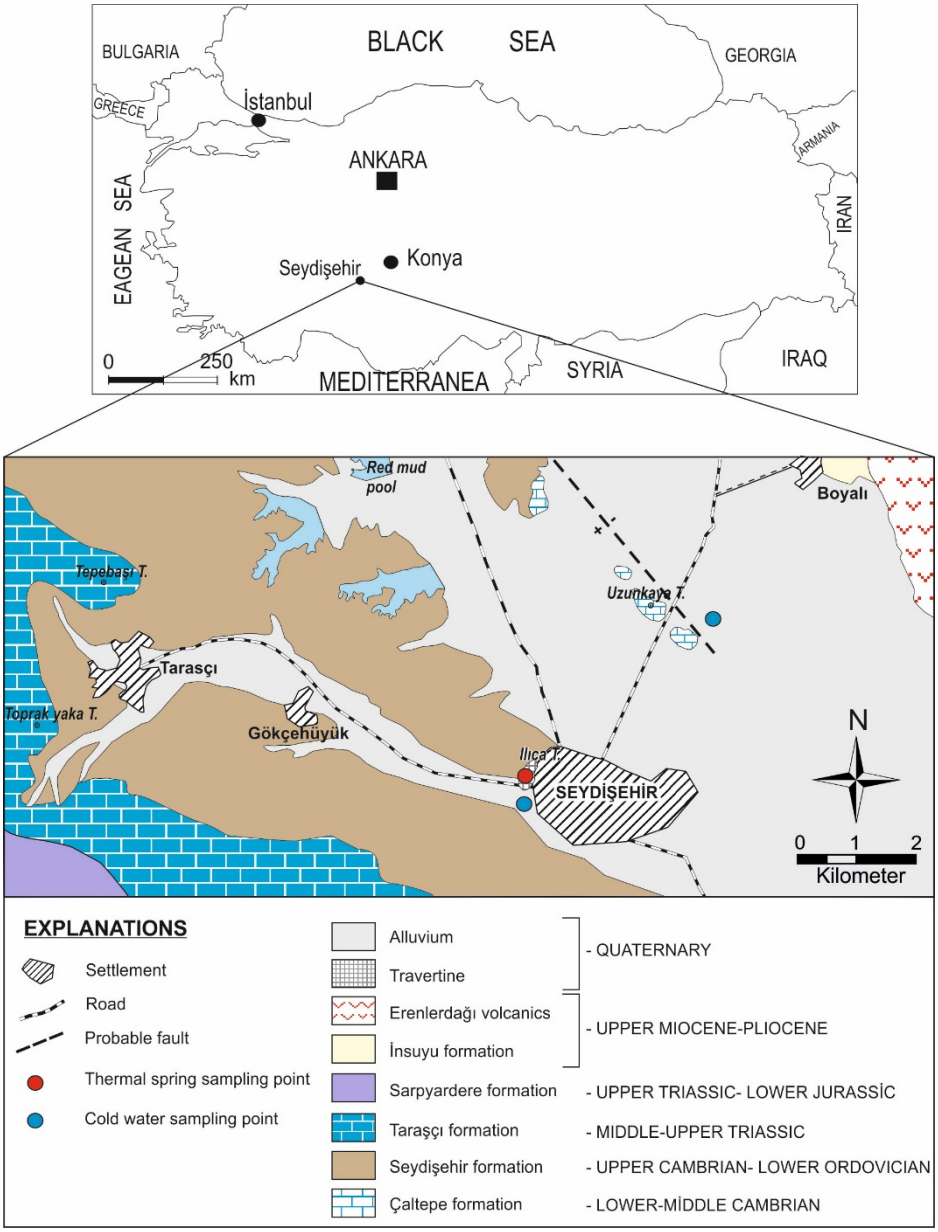

Figure 1. Location and geology maps, sampling location in the study area

The Lower-Middle Cambrian aged Çaltepe formation are highly fractured and karstified and form aquifer for thermal waters. Fine grained metasandstone, metasiltstone and phyllite within the Upper Cambrian-Lower Ordovician aged Seydişehir formation have relatively low permeability and therefore act as the cap rock for the thermal system. Fractured parts of quartzite and marble units within the Seydişehir formation also act as aquifers for thermal and cold groundwaters. The Middle-Upper Triassic aged Tarasçı limestones are permeable; whereas the bituminous levels negatively affect permeability. Claystones and siltstone of the the Upper Triassic -Lower Jurassic aged Sarpyardere formation are impervious. The tuffs belonging to the Upper Miocene-Pliocene Erenlerdağ volcanics are impervious, but dacites, andesites and basalts are permeable. The Upper Miocene-Pliocene aged İnsuyu formation and alluvium form aquifers for most of cold groundwaters.

The NW-SE trending Beysehir-Seydişehir Fault Zone [4] is the most important tectonic structure in the region. Although fault cannot be traced around the Ilıca thermal spring, the presence of thermal spring and changes in topography can be the indicators of possible faulting. The thermal spring has total discharge rate of 1.36 l/s and its temperatures is average 31 ^{o}C.

2.RESULT AND DISCUSSIONS

2.1.Water chemistry

The results of chemical analysis of Ilıca thermal spring and cold ground waters from study area are given in Table 1. Temperature of the ITS is average 31 ^{o}C and those of ICW and UCW is between 12.7 and 15.2 ^{o}C. The pH values are between

6.8 and 6.9 for thermal spring, 7.2 and 7.8 for cold groundwaters. Electrical conductivity (EC) values are in the range 828-874 µS/cm in ITS, 301-320 µS/cm in ICW and 840-850 µS/cm in UCW. TDS values range from 741 and 786 mg/l in ITS, 267 to 282 mg/l in ICW, and 680 to 703 mg/l in UCW. According to the International Association of Hydrogeologists [9], the studied thermal water is classified as Ca-Mg-HCO_3 type.

The distribution of ions in the Ilıca thermal spring and cold groundwaters is plotted on the Piper diagram [10] (Figure 2a). The ITS is of Ca-Mg-HCO_3 water type; ICW is of Ca-HCO_3 water type and UCW is of Ca-Mg-HCO_3 water type. Furthermore, all thermal and cold waters can be classified with carbonate hardness of more than 50%. Compositions of thermal and cold waters were compared in a Schoeller diagram (Figure 2b). In semi-logarithmic Schoeller diagram of thermal and mineral waters, the lines connecting the milli-equivalent values of ions are almost parallel indicating that waters are of similar origin.

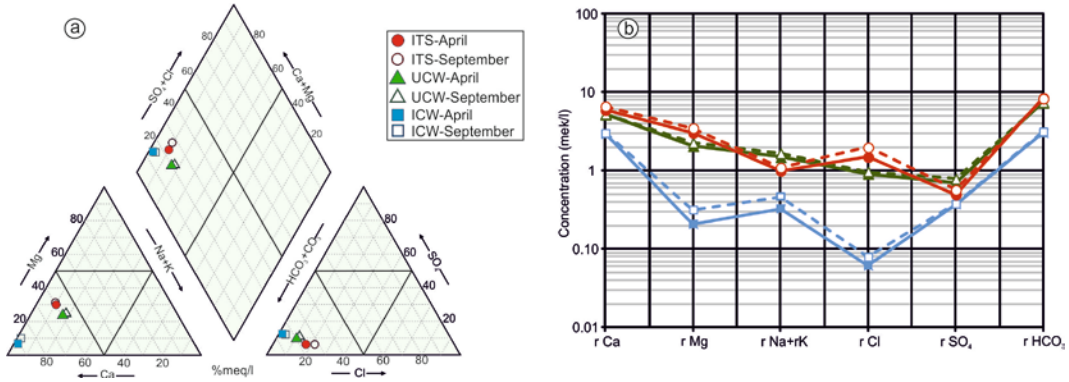

Figure 2. (a) Piper diagrame of water samples *(b) Schoeller diagrame of the water samples*

Calcium (119 and 133 mg/l) is the dominant cation and HCO_3 (518 and 543 mg/l) is dominant anion in the thermal water. Magnesium (37 and 42 mg/l) is the second most common ion in ITS (Table 1). Calcium in cold ground waters is still the dominant cation but its concentration is lower than that of the thermal water, and cold waters have relatively lower values of dissolved solids. TDS values of the thermal water are much higher than those of the cold waters and higher TDS values in the thermal water probably reflect longer circulation and residence times. Calcium is the dominant cation in thermal and cold ground waters indicating that carbonate rocks are the main reservoir rocks for these waters. The main process that controls the chemical properties of water is the dissolution of limestone and dolomite. Relatively high strontium content of thermal water probably reflects interaction between the thermal waters and carbonate rocks [11]. Fe and Al concentrations in the thermal water are lower than those of the cold waters suggesting that they have been removed from solution by secondary hydrothermal mineral formation.

2.2.Evaluation of isotope data

$\delta^{18}O$, $\delta^{2}H$ and ^{3}H and $\delta^{13}C$ isotopes were analyzed to determine the origin of thermal and cold waters, recharge altitude, and groundwater circulation (Table 1). The stable isotope contents of thermal water range from -10.18 to -9.91 ‰ for $\delta^{18}O$ and from -64.7 to -62.8 ‰ for $\delta^{2}H$. The stable isotope contents of cold ground waters range from -9.15 to -8.12 ‰ for $\delta^{18}O$ and from -60.1 to -54.6 ‰ for $\delta^{2}H$. The relationship between the $\delta^{18}O$ and $\delta^{2}H$ values are plotted in Figure 3a, which also shows the Global Meteoric Water Line (GMWL; $\delta^{2}H = 8\delta^{18}O + 10$) of [12] and the Konya Meteoric Water Line (KMWL; $\delta^{2}H = 8\delta^{18}O + 16$) of [13]. The waters in the study area plot close to the GMWL suggesting that the origin of recharge is precipitation. However, thermal water has more negative $\delta^{18}O$ and $\delta^{2}H$ values than those of cold waters indicating that they were recharged by continental precipitation at higher altitudes.

Table 7. Results of chemical analyses and isotopic composition of the waters in the study area

		ITS	ITS	ICW	ICW	UCW	UCW
		Sampling Data					
	Concentrations	April	September	April	September	April	September
EC	EC okuma	828	874	301	320	840	850
TDS	mg/l	741	786	267	282	680	702.5
pH		6.8	6.9	7.6	7.8	7,2	7.3
T	°C	31.3	31	12,7	15,2	14	15

Ca	mg/l	119	133	56.8	61	104.3	106.4
Mg	mg/l	36.6	42	2.5	3,8	25.2	27.4
Na	mg/l	20.9	22.1	1.12	1.8	27.8	31.7
K	mg/l	4.2	3.4	0.3	0.4	11.2	11.2
HCO_3	mg/l	518.1	543.1	185.5	194	444.1	451.4
Cl	mg/l	53.3	70.7	2.2	2.8	32.2	34.8
SO_4	mg/l	24.7	27.4	18	18.2	33.9	37.9
SiO_2	mg/l	14.6	n.d.	6.67	n.d.	5.8	n.d.
Al	ppb	7	n.d.	19.8	n.d.	50	n.d.
As	ppb	94.6	n.d.	16.6	n.d.	161.4	n.d.
B	ppb	229	n.d.	25	n.d.	364	n.d.
Ba	ppb	443.9	n.d.	170.4	n.d.	132.6	n.d.
Br	ppb	62	n.d.	27	n.d.	98	n.d.
Cu	ppb	0,7	n.d.	1.1	n.d.	2,9	n.d.
Fe	ppb	130	n.d.	217	n.d.	920	n.d.
Li	ppb	39.2	n.d.	2.5	n.d.	21.7	n.d.
Mn	ppb	14.7	n.d.	29.5	n.d.	76.19	n.d.
Rb	ppb	20.4	n.d.	2.6	n.d.	19.7	n.d.
Sr	ppb	956.6	n.d.	377.3	n.d.	406.4	n.d.
$\delta^{18}O$	(‰)SMOW	-9.91	-10.18	-8.12	-8.56	-8.96	-9.15
$\delta^{2}H$	(‰)SMOW	-62.8	-64.7	-54.6	-55.2	-57.8	-60.1
^{3}H	TU	0.96	1.78	6.28	n.d.	5.23	4.67
$\delta^{13}C$	(‰)VPDB	0.76	1.33	n.d.	n.d.	-10.94	-11.47

n.d.: not detected, TDS: total dissolved solids, EC: electric conductivity

Tritium value of the Ilıca thermal water range from 0.96 to 1.78 TU and those of cold waters vary between 4.67 and 6.28 TU. The tritium values are depleted due to the radioactive decay of tritium isotope representing the increases of the residence time of meteoric originated waters [14]. Tritium-chloride relationship is a method to separate shallowly and deeply circulating waters [15]. Tritium-chloride graph shows that deeply circulated thermal water has long residence time within the aquifer but shallowly circulated cold waters have short residence time within the aquifer.

$\delta^{13}C$ contents of thermal and cold waters in the study area range from 0.76 to 1.33 ‰ and from -11.47 to -10.94 ‰, respectively (Table 1). Carbon in the thermal water originates from the dissolution of marine carbonates. The carbon in cold waters is controlled by CO_2 that is accumulated in pores of soil or rocks [16].

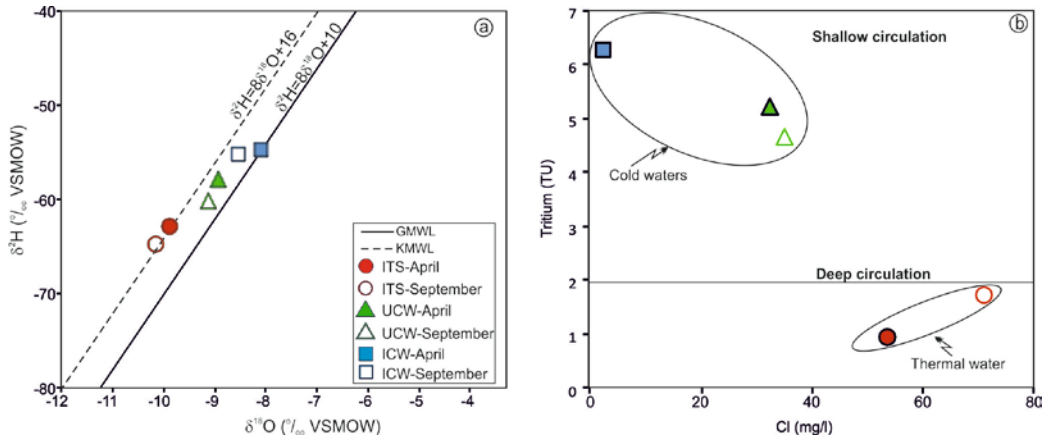

Figure 3. (a) $\delta^{18}O$ and $\delta^{2}H$ relation for thermal and cold waters (b) Tritium-Cl relation for thermal and cold waters

2.3.Geothermometry applications

To determine reservoir temperatures of the Ilıca thermal water, various silica and cation geothermometers were used (Table 2). The silica geothermometer is based on an absolute concentration, not concentration ratios, and is therefore affected by boiling and dilution more than the cation geothermometers [17]. The calculated temperatures using chalcedony geothermometers varied from about 20 to 28 ^{o}C. Results of calcedony geothermometers are not realistic since they are lower than the measured surface temperatures. The calculated temperatures using quartz geothermometers varied in the range of about 52-59 ^{o}C (Table 2). In the Giggenbach diagrame [18], the thermal spring water move away from the equilibrium/partial equilibrium field and plot near the Mg corner, reflecting conductive cooling or mixing with colder meteoric waters during the rise towards the spring (Figure 4). The non-equilibrium conditions suggest that quartz geothermometers provide more reliable results than cation geothermometers.

Table 2. Geothermometer results (^{o}C) of Ilıca thermal water

Geothermometer (^{o}C)	TS1	Geothermometer (^{o}C)	TS1
T ^{o}C measured	30.3	T ^{o}C measured	30.3
Quartz[a] no steam loss	52.1	N-K[d]	1284
Quartz[a] max steam loss	58.8	N-K[e]	1248
Chalcedony[b] no steam loss	19.6	Na-K-Ca[f]	23.2
Chalcedony[c] no steam loss	27.9	K-Mg[e]	35.8
Chalcedony[b] max steam loss	19.5	Li-Mg[g]	1067

Sample numbers and names as in Table 1. a: [19], b: [20], c: [21], d: [22], e: [18], f: [23], g: [24]

2.4.Mineral equilibration

Mineral saturation indices (SI) of the thermal spring were calculated by the PHREEQC Interactive 2.8 computer code [25] on the basis of outlet temperature and pH, and given in Table 3. It is important to know SI for some minerals to predict which minerals may precipitate during extraction and use of thermal waters.

A saturation indices of zero indicates that ion activity product and the solubility product are equal, and that thermodynamic equilibrium exists with the solid phase. A positive or negative indices show oversaturation or undersaturation conditions, respectively [26]. The results show that Ilıca thermal water is undersaturated with respect to gypsum, anhydrite and halite minerals. Calcite, dolomite, aragonite, quartz and chalcedony minerals are supersaturated at outlet temperature and pH values. Scaling of the carbonate minerals like calcite, dolomite and aragonite is expected for the Ilıca thermal spring.

Table 3. Saturation indices (SI) for Ilıca thermal water

	Calcite	Aragonite	Dolomite	Gypsum	Anhydrite	Halite	Quartz	Chalcedony
ITS	0.21	0.07	0.33	-2.12	-2.35	-7.54	3.04	2.58

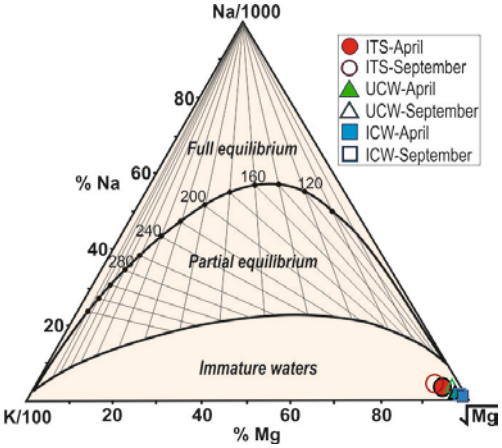

Figure 4. Plot of Na-K-Mg equilibrium diagram for waters in the study area.

3.CONCLUSION

The Ilıca thermal water has a low temperature (about 31 ^{o}C) and is classified as Ca-Mg-HCO_3 type. pH value of the ITS ranges from 6.8 to 6.9, and EC value varies between 828 and 874 µS/cm. Calcium (119 and 133 mg/l) is the dominant cation and HCO_3 (518 and 543 mg/l) is dominant anion in the thermal water. Magnesium (37 and 42 mg/l) is the second most common ion.

The Lower-Middle Cambrian aged Çaltepe formation are highly fractured and karstified and form aquifer for thermal waters. Fine grained metasandstone, metasiltstone and phyllite within the Upper Cambrian-Lower Ordovician aged Seydişehir formation have relatively low permeability and therefore act as the cap rock for the thermal water.

The thermal water falls into the field of immature waters in the Giggenbach diagram. Therefore, the silica geothermometers are more appropriate than cation geothermometers for the estimation of reservoir temperature. According to the quartz geothermometers, the temperature of the reservoir ranges between about 52 and 59 ^{o}C.

The isotopic data show that the thermal and cold ground waters have a meteoric origin. However, thermal water has more negative $\delta^{18}O$ and $\delta^{2}H$ values than those of cold waters indicating that they were recharged by continental precipitation at higher altitudes. Tritium value of the Ilıca thermal water range from 0.96 to 1.78 TU and those of cold waters vary between 4.67 and 6.28 TU. According to the tritium-chloride relationship, deeply circulated thermal water has long residence time within the aquifer but shallowly circulated cold waters have short residence time within the aquifer. Carbon in the thermal water originates from the dissolution of marine carbonates.

The discharge rate of the Ilıca thermal spring is 1.36 l/s. However, the discharge rate can be increased by drilling of deep wells. Therefore, the Ilıca thermal water can be used in different sectors such as spas, fishing and swimming pools, tourism and greenhouses.

ACKNOWLEDGMENT

This study was financially supported by Selcuk University Scientific Research Projects (BAP) (Project no. 15401019) (Konya, Turkey)

REFERENCES

[1]. W.T. Dean, and O. Monod, “The Lower Paleozoic stratigrahy and faunas of the Taurus Mountains near Beyşehir, Turkey,” *1 Stratigraphy: Bull. Brit. Mus. (Nat. Hist), Geol.*, vol., 19, issue 8, pp 411-426, 1970.
[2]. A.F. Bayram, “Seydişehir ve Kaşaklı Sıcaksu Kaynaklarının hidrojeoloji İncelemesi” Master's thesis. Institute of Science, Selcuk University, Konya, Turkey, Aug., 1992.
[3]. İ. Kara, and M. Durdu, “Konya-Ereğli-Karapınar-Seydişehir-Beyşehir çevresinin enerji olanakları,” MTA Tech. Rep. (unpublished), Ankara, 1999.
[4]. N. Özgül, “Bozkır-Hadim-Taşkent (Orta Toroslar’ın batı kesimi) dolayında yer alan tektono-stratigrafik birliklerin stratigrafisi,” MTA Tech. Rep. 119, pp 113-174, 1997.
[5]. W.T. Dean, “Trilobites from the Çal Tepe Formation (Combrian), Near Seydişehir, Central Taurides, Southwestern Turkey,” *Turkish J. Earth Sci.* vol. 14, pp 1-71, 2005.
[6]. O. Monod, “Resherches geologiques dansle Taurus occidental du sud de Beyşehir (Turquie),” These, I’ Univercity de Paris Sud Centre d’Orsay Docteur es Csinces, Orsay, 442 p. 1977.
[7]. Ü. Ulu, A.K. Bulduk, E. Ekmekçi, M. Karakaş, H. Öcal, A. Abbas, L. Saçlı, M.A. Taşkıran, M. Adır, S. Sözeri, M. Karabıyıkoğlu, “Geology of İnlice-Akkise and Cihanbeyli-Karapinar Area,” MTA Tech. Rep., 9720, Ankara (in Turkish), 1994.
[8]. M., Görmüş, “Kızılören (Konya) dolayının jeoloji incelemesi,” Master's thesis. Institute of Science, Selcuk University, Konya, Turkey, 1984.
[9]. IAH (International Association of Hydrogeologist), “Map of mineral and thermal water of Europe. Scale 1:500,000,” International Association of Hydrogeologist, 1979.

[10]. A.M. Piper, "A graphic procedure in the geochemical interpretation of water analyses,". *Am Geophys Union Trans.*, vol., 25, pp 914-923, 1944.
[11]. D.N. Han, X. Liang, M.G. Jin, M.J. Currell, X.F. Song, C.M. Liu, "Evolution of groundwater hydrochemical characteristic and mixing behavior in the Daying and Qicun geothermal systems. Xinzhou Basin," *J. Volcanol. Geotherm. Res.*, vol. 189, pp 92-104, 2010.
[12]. H. Craig, "Isotopic variations in meteoric waters," *Science*, 133, pp 1702-1703, 1961.
[13]. F. Şentürk, S. Bursali, Y. Omay, I. Eran, S. Güler, H. Yalçın, E. Önhon, "Isotope techniques applied to groundwater movement in the Konya plain," *Isotope Hydrology. Proc. Symp. Vienna, IAEA*, p. 153, 1970.
[14]. M. Afşin, İ. Kuşcu, H. Elhatip, K. Dirik, "Hydrogeochemical properties of CO_2-rich thermal-mineral waters in Kayseri (Central Anatolia), Turkey," *Environ Geol.*, vol. 50, pp. 24-36, 2006.
[15]. O. Çelmen, M. Çelik, "Hydrochemistry and environmental isotope study of the geothermal water around Beypazarı granitoids, Ankara, Turkey," *Environ. Geol.*, vol.,58, pp 1689-1701, 2009.
[16]. I. Clark, P. Fritz, "*Environmental isotopes in hydrogeology*," Lewis Publishers, New York, 1997.
[17]. A. Davraz, "Hydrogeochemical and hydrogeological investigations of thermal waters in the Usak Area (Turkey)," *Environ Geol.*, vol. 54, pp 615-628, 2008.
[18]. W.F. Giggenbach, "Geothermal solute equilibria. Derivation of Na-K-Mg-Ca geoindicators," *Geochimica et Cosmochimica Acta*, vol., 52, pp. 2749-2765, 1988.
[19]. R.O. Fournier, "Silica in thermal waters: laboratory and field investigations," *In: Proceedings of international symposium on hydrogeochemistry and biogeochemistry*, 1973, Tokyo, pp 132-139.
[20]. R.O. Fournier, "Chemical geothermometers and mixing models for geothermal systems," *Geothermics*, issue 5, pp 41-50, 1977.
[21]. S. Arnorsson, E. Gunnlaugsson, H. Svavarsson, "The chemistry of geothermal waters In Iceland. III. Chemical geothermometry investigations," *Geochim Cosmochim Acta*, vol., 47, pp 567-577, 1983
[22]. R.O. Fournier, "Geochemical and hydrological considerations and the use of enthalpy-chloride diagrams in the prediction of underground conditions in hot-spring systems," *J. Volcanol. Geotherm. Res.*, vol., 5, pp 1-16. 1979.
[23]. R.O. Fournier, A.H. Truesdell, "An Empirical Na-K-Ca Geothermometer for Natural Waters," *Geochimica et Cosmochimica Acta*, vol., 37, pp 1255-1275,1973.
[24]. Y.K. Kharaka, R.H. Mariner, "*Chemical geothermometers and their application to formation waters from sedimentary basins*," In: Naeser, N.D., McCulloh, T.H. (Eds.), Thermal History of Sedimentary Basins, Methods and Case Histories. Springer-Verlag, 1988.
[25]. D.L. Parkhurst, C.A.J. Appelo, "User's guide to PHREEQC (version 2) - a computer program for speciation, batch-reaction, one-dimensional transport, and inverse geochemical calculations:" U. S. Geol. Surv. Water-Resour. Invest. Rep. 99-4259, 312 p., 1999.
[26]. A. Gokgoz, G. Tarcan, "Mineral equilibria and geothermometry of the Dalaman-Kooycegiz thermal springs, southern Turkey," *Applied Geochemistry*, vol., 21, pp 253-268, 2006.

ICENS
INTERNATIONAL CONFERENCE ON ENGINEERING AND NATURAL SCIENCES
24-28 May 2016 /Sarajevo

New Generation Wireless Microcontroller Based Measurement System

Veysel Gokhan Bocekci [1], *Eyup Emre Ulku* [2]

Abstract

In this study, physical quantities such as humidity, temperature and pressure were measured by using new generation microcontroller systems. The measurement system is designed based on wireless communication protocol. Quantities that can be used in many applications such as humidity, temperature and pressure were measured by the sensors which are selected according to the application. Measurement values are transferred wirelessly to the receiver module. Thus, the display of these values is provided. The developed wireless measurement system has a low cost and compact design. The obtained results reveal that measurements can be performed with ± 2% margin of error.

Keywords: *Measurement, microcontroller based application, Wireless Sensor Network (WSN),*

1.INTRODUCTION

Wireless sensor networks (WSN) is used to collect information about various physical quantities needed. The purpose of gathering information is to provide the dissemination and visualization of information. Wireless sensors are devices which are powered by energy. These devices are used to detect physical quantities. In addition to this, wireless communications, data storage, signal processing and computing are other capabilities of wireless sensors [1].

WSN technology is one of the most significant technologies of the 21st century. One of the most important features of this technology is that it can be compatible with different network topologies and communication standards [2].

In radio frequency, WSN is defined as a system that includes transmitter, receiver, sensor, microcontroller and power supply [3].

Reducing cost, low power consumption, and multifunctional sensor nodes are the main concepts of the recent developments in the WSN technology [2].

Nowadays, WSN applications are trying to provide effective maximum area coverage with minimum collision. The main purpose of these studies is to increase benefits and reduce costs in WSN networks. These studies can be categorized into three groups. These three groups can be called as strength-based, grid based and computational geometry-based [4].

The WSN systems have a wide range of application areas. According to the projections WSN systems will become an important part of our lives in the coming years. Military, environmental, home and industrial applications are the major application areas of the WSN. [5].

Also, in the health sector there are important applications related with WSN technology. There are studies that aims to monitor and evaluate people's physical, physiological, psychological, behavioral, and cognitive features [6].

WSN technologies shows quite promising developments in monitoring and protection environment in recent years. One of the most sensitive studies on this subject is the development of real-time forest fire detection system using a wireless signal propagation characteristics [7].

For field biologists and ecologists, WSN technology provide quite great amenities in order to access and process the information. Important environmental data can be collected from some areas continuously with this technology such as; mountain peaks where transportation is difficult, lakes that are in high altitude etc. An application in this area is applied on Yang Lake where water temperature at different depths and oxygen levels are measured [8].

Besides, distorting effects such as fading in WSN networks is reduced in some studies where the aim is to recognize and interpret the channel statistics [9].

In our study, a measurement system is obtained where wireless communication protocol is supported by the various physical quantities. Developed system has a low cost and compact design. Today, wireless data collection and measurement system can be easily designed and performed with the selected system components. The measurement accuracy of the system is directly

[1] *Corresponding author: Marmara University, Faculty of Technology, Department of Electrical-Electronics Engineering, 34722, Göztepe/İstanbul, Turkey.* vgbocekci@marmara.edu.tr

[2] *Eyup Emre Ulku, Marmara University, Faculty of Technology, Department of Computer Engineering, 34722, Göztepe/İstanbul, Turkey.* emre.ulku@marmara.edu.tr

related with the characteristics of the sensors used in the system. Due to this situation, the measurement accuracy are susceptible to upgrading.

2.STUDY METHOD

In this study, the system that is conducted, measures the values of humidity, temperature and pressure. Communication and information transfer is obtained by RF transceiver module. The resulting measurement values are evaluated on the Arduino Uno platform that uses Atmel microcontrollers with relatively low cost and visualized on the LCD panel. All the components used in the system has a low power consumption feature. In the receiver and transmitter units, power consumption requirements is provided with a 9-volt batteries. Therefore, the system has been developed with a low cost and compact design.

2.1.Pressure sensor

In this study BMP180 pressure sensor is used which is designed to measure the height and pressure values. According to the manufacturer company, the sensor can measure pressure range from 300 hPA to 1100 hPA. When it is executed in low power consumption mode, data read range is 4.5 ms. On the other hand, when high resolution measurements is required, data read range is increased up to 25 ms. Figure 1 shows the connection between the sensor and Arduino microcontroller.

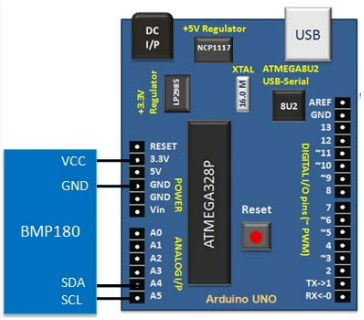

Figure 1. Connection of BMP 180 and Arduino Uno

2.2.Temperature and Humidity Sensor

DHT 11 sensor is used to measure temperature and humidity. With this sensor and negative temperature coefficient (NTC) sensor, resistance-based humidity measurement is performed. The temperature measurement range is given as 0-50^{o} and the humidity measurement range is given between 20% and 90% by the manufacturer company. The connection of the sensor to the Arduino microcontroller is given in figure 2.

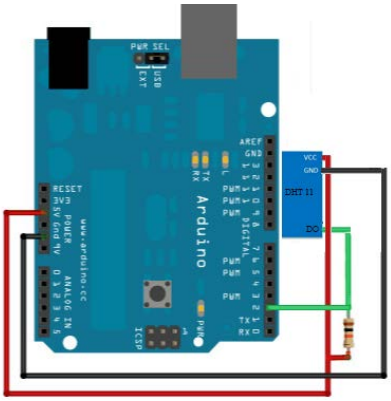

Figure 2. Connection of DHT 11 and Arduino Uno

2.3.RF 433 MHz Transmitter Receiver Units

The connection between the sensors and the main terminal unit is performed with the 433 MHz frequency transmitter receiver module. ASK modulation is used in the module. In figure 3, (a) represents the RF transmitter module and (b) shows the RF receiver module.

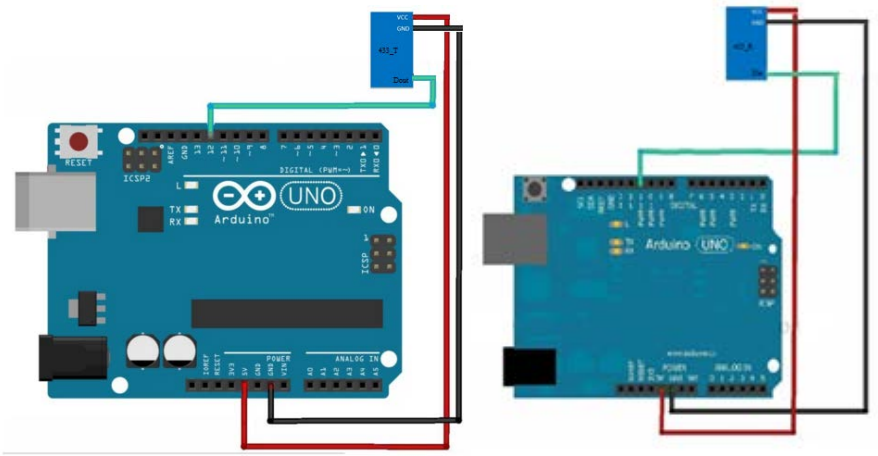

Figure 3. (a) 433 MHz transmitter module (b) receiver module

2.4.Performed WSN System

Figure 4 represents the WSN system block diagram that we obtain in a compact design and low cost. WSN system contains the sensors in the transmitter side and after the collected data is compiled, it is transmitted to the receiver circuit. The measurement results are displayed on the LCD panel.

3.RESULTS

In the realized system temperature, humidity and pressure values are measured. The measurements and the experiments are conducted with distance on average of 30 meters between the transmitter and receiver terminals. As the temperature value, ambient temperature is considered primarily as 17.2 ° C. With the digital thermometer, the temperature is determined as 17.5 ° C for the same ambient. Also, similar results are obtained in the performed numerous measurements. The difference in the measurement results remain within the limits of the error margin of 2%. When ambient temperature is increased stepwise, the value of temperature and performed system is determined in a similar manner.

Humidity measurement is tested with the buried sensor in the ground. Humidity is determined as 42%. On the other hand, with the digital humidity meter, the humidity is identified as 40.5% for in the same ambient.

Atmospheric pressure value is measured as 1010 mbar with the pressure sensor. Besides, official data for the region is given as 1019.3 mbar for the relevant period.

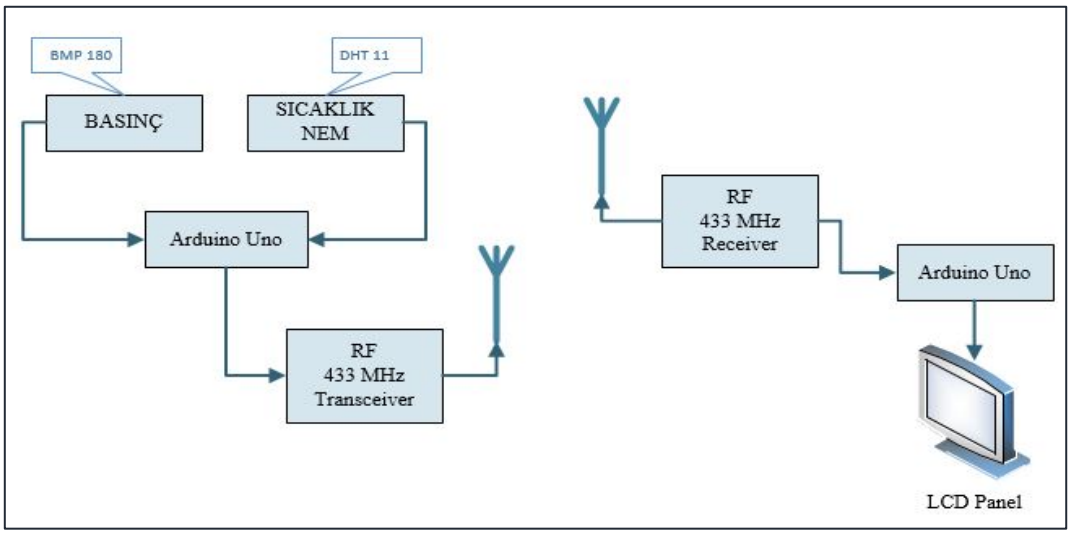

Figure 4. WSN system block diagram

4.CONCLUSIONS

In this study, low cost and a compact design of a WSN system is designed. In the realized system, sensor data is transferred on average of 30 meters to the receiver terminal. The measurement results are displayed on the LCD panel in a readable way. The

obtained results are within the error margin of 2%. To improve the obtained measurement results, the use of higher sensitivity sensor will be more appropriate. When cost rates and the simplicity of realization infrastructure are examined, WSN system applications will be increased in a diversification in the future.

REFERENCES

[1]. Li, Yingshu, and My T. Thai. *Wireless sensor networks and applications*. Springer Science & Business Media, 2008.
[2]. Ruiz-Garcia, Luis, et al. "A review of wireless sensor technologies and applications in agriculture and food industry: state of the art and current trends." *sensors* 9.6 (2009): 4728-4750.
[3]. Akyildiz, Ian F., et al. "Wireless sensor networks: a survey." *Computer networks* 38.4 (2002): 393-422.
[4]. Aziz, Nor Azlina Ab, Kamarulzaman Ab Aziz, and Wan Zakiah Wan Ismail. "Coverage strategies for wireless sensor networks." *World academy of science, Engineering and technology* 50 (2009): 145-150.
[5]. Akyildiz, Ian F., and Mehmet Can Vuran. *Wireless sensor networks*. Vol. 4. John Wiley & Sons, 2010.
[6]. Ko, JeongGil, et al. "Wireless sensor networks for healthcare." *Proceedings of the IEEE* 98.11 (2010): 1947-1960.
[7]. Zhang, Junguo, et al. "Forest fire detection system based on wireless sensor network." *Industrial Electronics and Applications, 2009. ICIEA 2009. 4th IEEE Conference on*. IEEE, 2009.
[8]. Porter, John, et al. "Wireless sensor networks for ecology." *BioScience* 55.7 (2005): 561-572.
[9]. Niu, Ruixin, Biao Chen, and Pramod K. Varshney. "Fusion of decisions transmitted over Rayleigh fading channels in wireless sensor networks." *Signal Processing, IEEE Transactions on* 54.3 (2006): 1018-1027.

Veysel Gokhan Bocekci was born in Istanbul, Turkey in 1980. He received his PhD and MSc degrees in Electronic and Computer Education (2011) and (2005) respectively in Marmara University. He received a B.Sc. degree in Electronics and Communication Engineering from Istanbul Technical University. He is an assistant professor in Department of Electrical and Electronics Engineering, Technology Faculty, Marmara University. He teaches photonics and communication technologies for undergraduate and graduate students. His research interests include optoelectronics, image processing and video processing applications.

Eyup Emre Ulku received a B.S. and M.Sc. degrees in Teacher Training in Computer and Control from Marmara University in 2009 and 2012, respectively. In 2009, he joined as a Research Assistant in Marmara University. He has begun his Ph.D. studies in Computer Engineering program at Turkish Air Force Academy, Istanbul, Turkey in 2012. He is currently a Research Assistant in Marmara University, Faculty of Technology, Computer Engineering Department. His current research interests are in wireless communications, ad hoc networks, and image processing.